THEORY AND APPLICATIONS OF APERIODIC (RANDOM) PHASED ARRAYS

A Dissertation

by

KRISTOPHER RYAN BUCHANAN

Submitted to the Office of Graduate and Professional Studies of
Texas A&M University
in partial fulfillment of the requirements for the degree of

DOCTOR OF PHILOSOPHY

Chair of Committee,	Gregory Huff
Committee Members,	Jean-Francois Chamberland-Tremblay
	Helen Reed
	Robert Nevels
Head of Department,	Chanan Singh

August 2014

Major Subject: Electrical Engineering

ABSTRACT

A need for network centric topologies using mobile wireless communications makes it important to investigate new distributed beamforming techniques. Platforms such as micro air vehicles (MAVs), unattended ground sensors (UGSs), and unpiloted aerial vehicles (UAVs) can all benefit from advances in this area utilizing advantages in stealth, enhanced survivability and maximum maneuverability. Moreover, in this dissertation, electromagnetic radiation is investigated such that the signal power of each element is coherently added in the far-field region of a specified target direction with net destructive interference occurring in all other regions to suppress sidelobe behavior. This provides superior range and resolution characteristics for a variety of applications including; early warning radar, ballistic missile defense and search and rescue efforts.

A wide variety of topologies can be used to confine geometrically these mobile random arrays for analysis. The distribution function for these topologies must be able to generalize the randomness within the geometry. By this means it is feasible to assume the random element distribution of a very large volumetric space will yield either a normal or Gaussian distribution. Therefore the underlying assumption stands that the statistically averaged beam pattern develops from an arrangement of uniformly or Gaussian distrusted elements; both confined to a variety of geometry of radius A and is further generalized using a simple theory based upon the Fourier Transform. Hence, this theory will be derived and serve as the foundation for advanced performance characteristics of these arrays such as its ability for sidelobe tapering, adaptive nulling and multi beam control. In addition it will be shown that for the most ideal of conditions a steerable beam pattern free of sidelobe behavior (better known as a Gaussian distribution) is quite possible. As well these random array structures will be shown to provide superior bandwidth capability over tradiational array structures since they are frequency independent. Last of all a summary of the random array analysis and its results concludes this dissertation.

ACKNOWLEDGEMENTS

NOMENCLATURE

Path length (Cartesian)	$Z_n \cos\psi_n = \vec{Z}_n \cdot \hat{a}_r = x_n \sin\theta\cos\phi + y_n \sin\theta\sin\phi + z_n \cos\theta$
Path length (cylindrical)	$Z_n \cos\psi_n = \vec{Z}_n \cdot \hat{a}_r = \rho_n \sin\theta\left(\cos(\phi - \phi_n)\right) + z_n \cos\theta$
Path Length (spherical)	$\vec{Z}_n \cdot \hat{a}_r = r_n \sin\theta_n \sin\theta\cos(\phi - \phi_n) + r_n \cos\theta_n \cos\theta$
Phase correction (Cartesian)	$Z_n \cos\psi_n - Z_n \cos\psi_{n0} = u_n \alpha(\theta,\phi) + v_n \beta(\theta,\phi) + \chi_n \xi(\theta)$
Phase correction (cylindrical)	$Z_n \cos\psi_n - r_n \cos\psi_{n0} = \upsilon^r_{n,x} \zeta^r_x(\theta,\phi) + \upsilon^r_{n,y} \zeta^r_y(\theta,\phi)$
Phase correction (spherical)	$Z_n \cos\psi_n - Z_n \cos\psi_{n0} = \Upsilon^r_{n,x} \zeta^r_x(\theta,\phi) + \Upsilon^r_{n,y} \zeta^r_y(\theta,\phi) + \Upsilon^r_{n,z} \zeta^r_z(\theta)$
Circular (x) random variable	$\upsilon^r_{n,x} \triangleq \tilde{\rho}_n \cos\phi_n$
Circular (y) random variable	$\upsilon^r_{n,y} \triangleq \tilde{\rho}_n \sin\phi_n$
Spherical (x) random variable	$\Upsilon^r_{n,x} = \tilde{r}_n \sin\theta_n \cos\phi_n$
Spherical (y) random variable	$\Upsilon^r_{n,y} = \tilde{r}_n \sin\theta_n \sin\phi_n$
Spherical (z) random variable	$\Upsilon^r_{n,z} = \tilde{r}_n \cos\theta_n$
Cartesian (x) random variable	$u_n \triangleq \tilde{x}_n \triangleq \dfrac{x_n}{A}$
Cartesian (y) random variable	$v_n \triangleq \tilde{y}_n \triangleq \dfrac{y_n}{A}$
Cartesian (z) random variable	$\chi_n = \tilde{z}_n \triangleq \dfrac{z_n}{A}$
Beamsteering (x) Cartesian	$\alpha(\theta,\phi) \triangleq 2\pi\tilde{A}\left(\sin\theta\cos\phi - \sin\theta_o \cos\phi_o\right) = \hat{x}\cdot\left(\hat{r}(\theta,\phi) - \hat{r}_o(\theta_o,\phi_o)\right)$
Beamsteering (y) Cartesian	$\beta(\theta,\phi) \triangleq 2\pi\tilde{A}\left(\sin\theta\sin\phi - \sin\theta_o \sin\phi_o\right) = \hat{y}\cdot\left(\hat{r}(\theta,\phi) - \hat{r}_o(\theta_o,\phi_o)\right)$
Beamsteering (z) Cartesian	$\xi(\theta) \triangleq 2\pi\tilde{A}\left(\cos\theta - \cos\theta_o\right) = \hat{z}\cdot\left(\hat{r}(\theta,\phi) - \hat{r}_o(\theta_o,\phi_o)\right)$
Beamsteering (x) cylindrical and spherical	$\zeta^r_x(\theta,\phi) \triangleq 2\pi\tilde{A}\rho_o \cos\delta = \hat{x}\cdot\left(\hat{r}(\theta,\phi) - \hat{r}_o(\theta_o,\phi_o)\right)$
Beamsteering (y) cylindrical and spherical	$\zeta^r_y(\theta,\phi) \triangleq 2\pi\tilde{A}\rho_o \cos\delta = \hat{y}\cdot\left(\hat{r}(\theta,\phi) - \hat{r}_o(\theta_o,\phi_o)\right)$
Beamsteering (z) cylindrical and spherical	$\zeta^r_z(\theta,\phi) \triangleq 2\pi\tilde{A}\rho_o \cos\gamma = \hat{z}\cdot\left(\hat{r}(\theta,\phi) - \hat{r}_o(\theta_o,\phi_o)\right)$
Beamsteering directional angle (z) spherical	$\gamma = \cos^{-1}\left(\rho_0^{-1}\left(\cos\theta - \cos\theta_0\right)\right)$

Beamsteering directional angle (x, y) cylindrical and spherical $\delta = \tan^{-1}\left[\dfrac{\sin\theta\sin\phi - \sin\theta_o \sin\phi_o}{\sin\theta\cos\phi - \sin\theta_o \cos\phi_o}\right]$

Steering magnitude cylindrical and spherical	..
Azimuthal random variable	$\tilde{\phi}_n \triangleq \phi_n - \delta$
Elevation random variable	$\tilde{\theta}_n \triangleq \theta_n$
Radial random variable (cylindrical)	$\tilde{\rho}_n \triangleq \dfrac{\rho_n}{A}$, $\rho_n = \sqrt{x_n^2 + y_n^2}$
Radial random variable (spherical)	$\tilde{r}_n \triangleq \dfrac{r_n}{A}$, $r_n = \sqrt{x_n^2 + y_n^2 + z_n^2}$
Largest diameter of array	D
Effective aperture size	$A = D/2$
Normalized aperture size	$\tilde{A} = A/\lambda$
Beamsteering coefficients	$\mathrm{X} = \left(\Psi_x + \Psi_y + \Psi_z\right) = \left(\hat{x} + \hat{y} + \hat{z}\right) \cdot \left(\hat{r}(\theta,\phi) - \hat{r}_o(\theta_o,\phi_o)\right)$
Gaussian beamsteering coefficients (x)	$\vec{Z}_n \cdot \hat{x} = U$
Gaussian beamsteering coefficients (y)	$\vec{Z}_n \cdot \hat{y} = V$
Gaussian beamsteering coefficients (z)	$\vec{Z}_n \cdot \hat{z} = W$

TABLE OF CONTENTS

LIST OF FIGURES

xv

LIST OF TABLES

CHAPTER I

INTRODUCTION

1.1 Background

Applications today require radiation characteristics with high values of directivity and bandwidth, which are not often achievable by a single antenna operating on its own behalf. Ultra wide band (UWB) antennas persist to mitigate some of the bandwidth limitations and accommodate high-resolution scanning capabilities [1]-[18] with low probability intercept (LPI) and ELINT hardening. A single one of these broadband antennas operating on its own behalf will routinely not provide the sufficient amount of both bandwidth [19]-[22] and directivity. Therefore "to design antennas with very large directivities, it is usually necessary to increase the electrical size of the antenna. This can be accomplished by enlarging the electrical dimensions of the chosen single element. However, mechanical problems are frequently associated with very large elements [23]. For example, a parabolic dish is an excellent choice as a single element, but its size is limited by gravitational and thermal stresses to a few hundred feet. In addition, its silhouette is often unacceptable and aerodynamic drag precludes its use on an aircraft. Last of all, its very attractiveness with respect to its ease of scan, limits the microwave dish to a sequential scan only; for random access a phased array is required.

"An alternative way to achieve large directivities, without increasing the size of the individual elements, is to use multiple single elements to form an array. An array is a sampled version of a very large single element. In an array, the mechanical problems of large single elements are traded for the electrical problems associated with the feed networks of arrays [23]." Further this collection or distribution of radiating elements form an aggregate geometrical arrangement (called an array), capable of providing adequate radiation characteristics of large values of directivity and bandwidth [24]-[27]. Plus today's solid-state technology, very efficient (reduced equipment size and power consumption) and low-cost feed networks can be designed and integrated into these arrays offering some of the most versatile of antenna systems. However, just as size has a natural limit for the parabolic dish, so too do cost and certain physical and electrical phenomena limit the natural size of the phased array. Techniques for extending the size of phased arrays are investigated by the use of random arrays. These random and sparse distributions of radiating elements (called an aperiodic array) can be utilized to achieve more illustrious behavior when compared to the well-populated periodic distribution [28]-[37]. Random arrays even mitigate array spacing and spatial constraints provided, which allows for considerably superior broadband behavior. An illustration of a large parabolic dish, periodic phased array and random array is shown in Figure 1. Other insightful studies for random arrays are provided by the works [38]-[101].
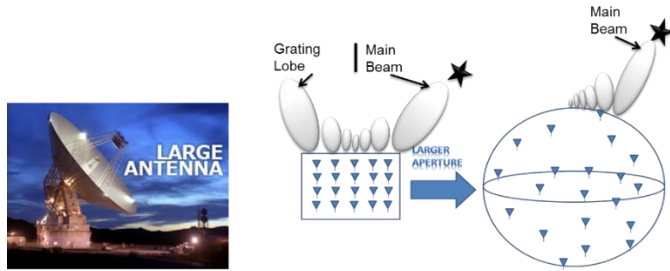
Figure 1. Illustration of a large single element (left), periodic phased array (middle) and random array (right).

(a) Directivity and beam resolution

In the periodic array half-wavelength spacing is common especially when the elements have a narrow bandwidth. This spatial guidance creates an acceptable beampattern, but for an array of electrically large antennas degradation due to mutual coupling prevails and prevents the full utilization of its instantaneous bandwidth [30], [36]-[39] (More specifically this can be analyzed and explained in a signal processing approach provided by Section 4.3). Further use of these electrically larger radiators are necessary for more broadband or wideband capabilities [40]-[44]. For example, sparsely populated and thinned arrays [45]-[48] are utilized to relax physical size restrictions on element dimensions and spacing, but should not to be confused with random array environments. In these situations elements are removed from the overall periodicity in formations, but overall periodicity is still maintained. The increased spacing significantly reduces the unintended effects of mutual coupling on scan impedance and is of course, very different from current sheet arrays (CSAs) and other densely populated or continuous [49]-[53] wideband array designs that exploit the inter-element interactions. The primary difference between beamforming techniques using random arrays and CSAs or other more widely recognized arrangements (planar and volumetric) is the absence of periodicity. Hence the overall solution to sparse, thinned and periodic array problems is to just remove the periodicity and space the *N* elements aperiodically into a larger aperture. This allows for greater bandwidth in beamforming across larger distances [26], [27], [32] and [35]. More so it reduces the need to have elements spaced close to each other inducing mutual coupling issues. For instance, experimentally limited studies have been performed to verify whether mutual coupling (occurring by radiation, from paths within the feed structure, surface paths, or reflections at the antenna terminal due to impedance mismatches illustrated in Figure 2) issues are minimal or not for these random arrays. But, insightful studies were performed in [32] and [37], and assessed therein demonstrating two petty outcomes. First minor increases in sidelobe level may result from small average spacing of less than two and a half wavelengths. This is also shown by the coupling magnitude of the coupling coefficients calculated in (1) for isotropic elements [102] and illustrated in Figure 3 relating the current flowing into

the nth element due to the current from the mth element. Second coupling may produce small fluctuations of main-beam amplitude as a function of the scan angle. Henceforward, this dissertation ignores the effects of mutual coupling, which were shown to be minimal anyway [32]. In addition, Chapter XIII derives an informal proof toward displaying, frequency independence characteristics of these random arrays for the first time in their history.

$$c_{mn} = \frac{\sin(kd_{mn})}{(kd_{mn})} \quad (\text{isotropic elements}) \tag{1}$$
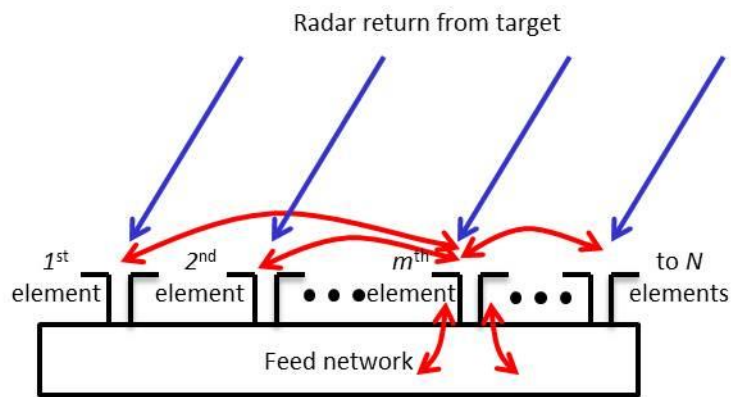
Figure 2. Mutual coupling between elements of an antenna array. [103]
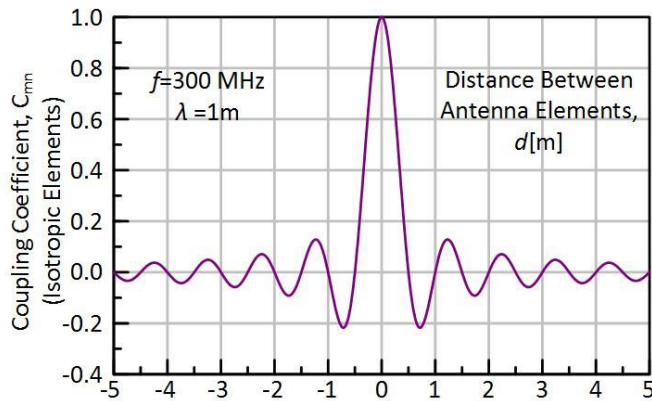
Figure 3. Mutual coupling coefficient (isotropic elements) vs. separation distance (*d*).

Nevertheless, it should be noted that it is theoretically possible to calculate the effects of mutual coupling, but in reality this is not easily measured and is generally unstable with scan angle. Thus, to

reduce these effects it is seen from the envelope of Figure 3 that increasing the element spacing greater than $\lambda/2$ is the best course of action for neglible mutual coupling. However, for periodic spacing thinning must be utilized, which again typically induces higher sidelobes and at times does not totally eliminate the grating lobes. On the other hand increasing the element spacing or aperture size too large for a random array induces unrealistic requirements on the phase shifter accuracy, which will also be demonstrated in this dissertation (Appendix I). Thus, a set of design guidelines are presented in regard to this accuracy for the first time.

Radiation characteristics and beamsteering of these random arrays can be controlled via adequate phase control and synchronization such that a coherence of signals superimpose upon one another in the desired target direction. The added benefit is the arrays randomized phase information causes a net destructive interference to occur outside this region, and for a large number of elements predictable sidelobes are formed adjacent to the mainlobe region based upon the Fourier transform illustrated by the vector diagrams of Figure 4. The most notable results from this randomization include a reduction in side-lobe levels without amplitude tapering and the mitigation of grating lobes over wide bandwidths [27]-[33]. A narrower beam is typically achieved in these arrays and the directive gain reaches a fundamental limit of order N when the element distribution is sparse. The resolution of this beam depends mainly upon the effective aperture dimension in wavelengths and N, but also on the probability density function to which the elements are placed. Accordingly, the resolution of the aperture can be improved for a fixed number of elements by spreading them over a larger aperture. This can also be used to eliminate high peaking sidelobes [31] that are undesirable.
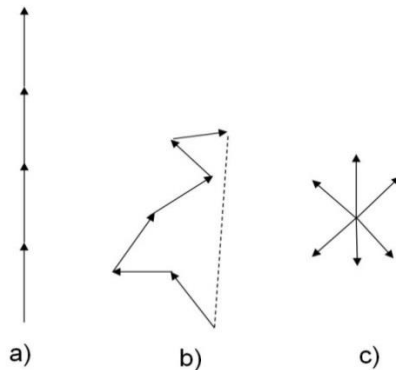
Figure 4. Phasor diagram representation of N randomly spaced elements forming (a) mainbeam (b) sidelobe (c) null, but mean power grows as N). [102]

(b) Bandwidth and applications

Frequency independence attributes are critical in current applications since bandwidth is a major design challenge in current electronic support equipment, typically operating in the range of 2 GHz to 20 GHz. [104] For the multifunctional needs of any architecture, it is a typical fact that different functions need different bands for applications in surveillance, tracking, communications, direction finding and weapons guidance purposes. Even more though frequencies below 2 GHz are still of importance as electronic warfare operators typically have trouble detecting radars operating in the UHF band, due to the dense electronic environment. Lower HF, VHF and UHF bands can be especially effective in random array applications exploiting the advantage of their widespread use in long distance communications Table 1. This can even be extended in many applications such as: man portable networks, UAV swarms or even wirelessly networked digital array radars. [102]-[125]

Table 1. Radar Bands and Usage.

Band Designation	Frequency Range	Usage
HF	3-30 MHz	OTH Surveillance
VHF	30-300 MHz	Very-long-range surveillance
UHF	300-3,000 MHz	Very-long-range surveillance
L	1-2 GHz	Long-range surveillance
S	2-4 GHz	En route traffic control
C	4-8 GHz	Moderate-range surveillance Terminal traffic control
X	8-12 GHz	Short-range tracking Missile guidance Mapping marine radar Airborne intercept
K_u	12-18 GHz	High-resolution mapping Satellite altimetry
K	18-27 GHz	Little use (water vapor)
K_a	27-40 GHz	Very-high-resolution mapping Airport surveillance
Millimeter	40-100+ GHz	Experimental

The incorporation of beamforming in the HF range will have significant impacts in SIGINT since the sky wave may be utilized illustrated in Figure 5-Figure 7. These characteristics provide extremely long range and high power jamming capabilities down to frequencies as low as 3 MHz. Also employing more elements at this band allows for greater power constraints and again provides significant advantages in distance. Moreover, the improvements for these lower frequencies bands will play a vital role in future applications that overcome difficulties of current phased array architectures and large antenna sizes at these low frequency ranges. [105]

HF Coastal Radar (CODAR)

Characteristic	Value
Operating frequency	27.65 MHz
Transmitted power	30 W
Working range (35 PSU salinity)	up to 50 km
Length of sea surface wave (Bragg)	5.42 m
Depth over which current is averaged	~0.5 m
Range resolution	0.3 km, 0.6 km, 1.2 km
Azimuthal resolution (Direction Finding)	1 degree
Azimuthal resolution (Beam Forming)	+/-3 degrees
Integration time	9 minutes, 18 minutes
Accuracy of radial component	1...2~cm/s
Accuracy of current field	1...5~cm/s

Surface current map
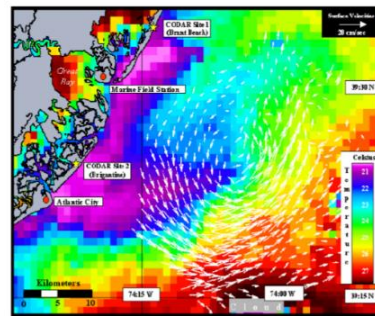
University of Hamburg WERA HF radar

Figure 5. High frequency (HF) codar random array application. [106]
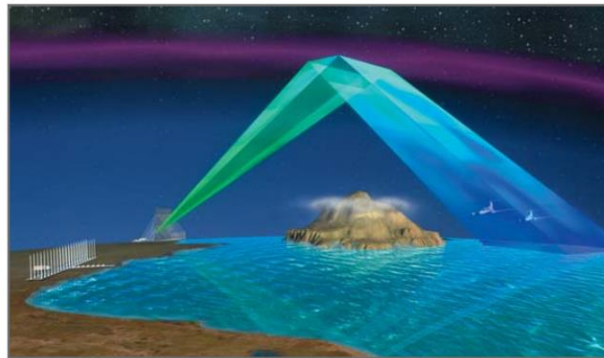
Figure 6. Illustration of the sky wave for over the horizon (OTH) capability. [107]

Figure 7. Relocatable over the horizon (ROTHR) random array application. [107]

Bandwidth increases will also lead to more troubling architectures. Hence, it will be more important than ever to have the necessary technological advancements ready for these mobile random array environments. Receiver and transmitter type architectures are the most critical of such needs and will need to handle these large bandwidths for data processing. Digital signal processing techniques will be needed and serve as the backbone for down conversion over increasingly wide frequency bandwidths and use in the recovery of transmitted signals. Additional incorporation of independent receivers in these architectures will reduce, if not eliminate performance inhibitors of the homodyne or direct conversion architecture. Hence, once these advancement are established incorporation of these technologies may be implemented into UAVs so that they can be launched in order to obtain video imagery containing real time video signals and time sensitive *ISR* (Information Surveillance and Reconnaissance) information. Tracking and delivering of this information will be vital as it alleviates the necessity of sending out reconnaissance parties for intelligence gathering purposes. Even more the incorporation of additional bandwidth will allow for these video images to be broadcast to other units in the nearby vicinity or even back to rear HQs for dissemination. [105]

(c) LPI integration

In today's operational environment radars have to contend with very capable and advanced threats ranging "from antiradiation missiles (ARMs), radar warning receivers (RWRs), electronic warfare support (ES) interception capabilities, and electronic attack (EA) systems. All of these are designed to contribute to the degradation of radar performance by jamming, evasion, or destruction." [108] To counteract these threats and survive it is critical for these radars to mask their presence and hide their emissions from hostile receivers. For this purpose, radars composed of random arrays will be essential for masking their presence; benefits of utilizing a wider operational bandwidth for high duty cycle/wide band transmission containing enough frequency agility will be vital to not be seen. Also employing irregular and advanced scan patterns (modulations), power management control, and ultra-low side lobe levels (-45 dB and below for LPI radar) will further benefit. Accordingly, these architectures provide what is "called

Low Probability of Intercept (LPI) radars and they use techniques *to see and not to be seen* by modern and capable intercept receivers. In fact, so called LPI performance is a probability event" [108]. Last of all, the overall incorporation of LPI capability integrated into random arrays offers momentous advancements in *monostatic/bistatic* and *multistatic* configurations, coherent detection and high processing gains illustrated in Figure 8.
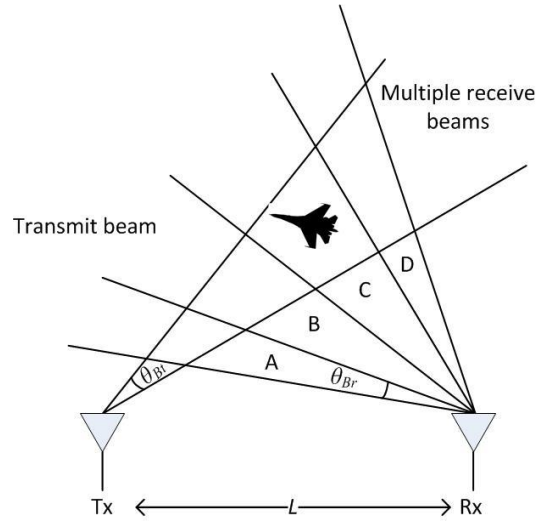
Figure 8. Notional example of bistatic radar from the notes of [109].

Another advantage of wide-bandwidth characteristics of these random arrays will help LPI radars in effort toward spreading their radiated energy over a wider spectrum of frequencies. This allows the LPI radar the ability exploit the time bandwidth product and reduce its peak transmitted power so low such that it is buried within the environmental noise floor. As a consequence it becomes exceptionally difficult for an ES receiver to detect the LPI radar since it must search these tremendously large bandwidths to find the transmitting LPI radar. In addition, "due to the mismatch in waveforms for which the ES receiver is tuned, the LPI radar is effectively invisible to the ES receiver, since the high peak power transmitted by the pulsed radar can easily be detected by ES receivers." [108] Therefore continuous wave (CW) radars are a very popular choice, because they have the ability to send very low power while still maintaining the required energy profile by taking advantage of energy superposition across these large bandwidths. An illustration of other available waveforms are presented in Figure 9 as alternatives. However though, it should be noted that the increased bandwidth and incorporation of FMCW will also alleviate issues of range gating once again making it a better choice.
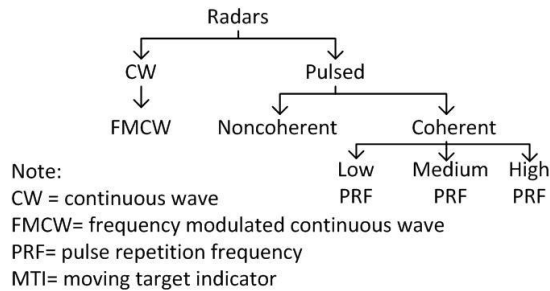
Figure 9. Examples of common waveforms. [109]

Another perpetual benefit of very large bandwidths permit the utilization of the uncommon frequencies used as the carrier frequencies. "An LPI radar can use frequencies of 22, 60, 118, 183, and 320 GHz at which peak absorption occurs. This will serve to maximize attenuation in order to mask the transmit signal and limit reception by hostile receivers (atmospheric attenuation shielding). Because of the high absorption of the emitter's energy, this technique is always limited to short range systems." [108] However, when incorporated into random arrays and collaborative coherent beamforming type situations, limitations in range can be assuredly overcome, but at a burdensome expense of wasted power. Hence, this is not one of the more green (energy efficient) of choices, but provides as an example. An illustration of these troublesome frequencies is provided below in Figure 10.
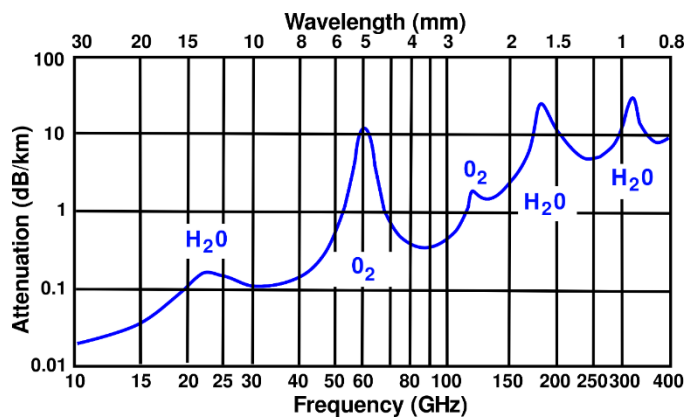
Figure 10. Attenuation of radio waves vs. frequency. [110]

The only misfortune of incorporating LPI capability into random array radar is the ability to also counter it using another random array. For instance an ES receiver composed of a random array may be

designed to contain the same sensitivity of the CW signal using conventional pulse signals. The process does this by employing a technique known as dereamping. This process "forms an adaptive matched filter to the linear FMCW LPI radar signal in order to achieve the processing gain that is equal to the received signal's time-bandwidth product." [111] Hence, the overall processing gain may end up being countered, however the likelihood of this must be further investigated first.

(d) Spatial division multiple access (SDMA)

Another advantage of collaborative beamforming whether it applies classically or distributedly is the ability to take advantage of modern Space-Division Multiplex Access (SDMA) technology. This architecture enables channeling of radio signals based upon a mobile devices location and is a MIMO (Multiple-Input-Multiple-Output) architecture. This is primarily suitable for mobile ad-hoc networks, because it sets up a one-to-one type mapping between a networks bandwidth division and identified spatial division. A more in depth analysis of this procedure will be covered in Appendix I Chapter XXI of this dissertation.

1.2 Previous Work (Non-Theoretical Historical Advancement)

The analysis of random arrays was considered initially by numerous researchers from [26], and [34]-[36]. The more widely recognized probabilistic approach for analysis of random arrays in linear and planar topologies contexts was examined in rigor by Lo *et al.* in [28]-[31] and benchmarked experimentally in [37] for planar topology. These works provided a foundation for further studies (e.g., [6]-[14]), which extended the theory into the treatment of other canonical geometries. For example, periodically spaced phased arrays have been known for decades, and the most popular types are planar. For these arrays, it is known the main beam tends to deteriorate rapidly as it's scanned towards the plane of the array [58]-[62]. This demise makes geometries like circular and spherical topology of greater interest. However, difficulty arises since these arrays are not expressed in terms of simple polynomials and when the array is random; these types of arrays have a tendency to become very complex.

The investigation of randomly spaced circular and spherical arrays was first done by [58] in the late 60's and later in the late 70's [59]-[61]. For the time being it was believed, "no particular element arrangement on the circle or sphere of a random array could result in mathematical simplicity, thereby leading to a closed form solution except for the special case of very small element spacing's where some approximate solution could be found [58]. Conversely, it is shown in this dissertation that a structure of mathematical simplicity does exist and is used to formulate simple closed form solutions for any simple Euclidean topology. In addition, Panicali and Lo simulated experiments using the Monte Carlo method to test the validity of their theory. Instead, this dissertation will not use the Monte Carlo method since simple closed form solutions are now known to exist.

Synthesis of random arrays remains an open problem today since optimizations techniques present non-unique solutions; such that an infinite number of variations of the solution exist. Yet, a

number of attempts have been made to optimize these topologies. For example, an examination from [55] has determined null locations may be prescribed to a pattern when elements are known with a tolerance of approximately one wavelength or better. Alternative synthesis approaches have been investigated from [56] to optimize the aperture with a fixed set of elements to provide better performance characteristics. Overall, the optimization or synthesis of random arrays will not be covered in this dissertation, but its implications may serve to be of vital importance in future applications (especially allocated to mobile distributions).

Other studies have determined a random array typically loses effectiveness in scanning the main beam when the total number of elements is too low. In so doing this produces higher sidelobes in the pattern and predictability in the pattern is lost; past the third null of the main beam [57]. For this reason, low resolution will induce a large collection of artifacts to be collected during conventional radar scans. Last of all fewer elements reduces gain such that the periodic structure of the same aperture size, element type and feed structure becomes superior [57].

Finally it is important to note that other interesting work for random arrays has been ongoing for over a decade at the Naval Post Graduate School under the mentorship of Dr. David C. Jenn. This research is explicitly related to radar applications based on opportunistic arrays and includes a number of master thesis's [112]-[125].

1.3 Scope of Research or Dissertation Objective

In the past random arrays have suffered from limited knowledge of radiative properties. In addition, complexity of analysis, synthesis, and cost to test made them disadvantageous to implement in real time. However, over the past few decades further contributions have been added to the literature of random arrays. In part this is due, because of an increasing interest in ultra-wide band antennas structures, networks on the move and increased technology developments. Hence, these radiative properties will be fully defined in this dissertation.

The goal of this work is to provide a summary of an alternate and potentially more tractable formulation for the previously mentioned works on random array studies provided in [9]-[12]. By the same token, this dissertation along with other recent papers [6]-[14] is designed to provide better insight into the characteristics of random arrays. Care has been taken in the derivations such that the topic is traced easily to its origins from [26], [31], and [34]-[36]. In addition, the understanding framework of the theory makes more advanced concepts easier to grasp. Even more the fundamental theory is the foundation of ongoing systems and it's important to understand since the future main objective is to incorporate such theory into applications such as Wirelessly Networked Distributed Digital Random Array Radar (WNDDRAR) shown in Figure 11 (also called an opportunistic array) [103] or other natural beamforming scenarios of: swarming, flocking, herding or shoaling. Also of interest will be the incorporation of WNDDRAR's and random array distributions into Wide Sensor Networks (WSN) shown in Figure 12. Moreover, the current

state of this research is a mixture of the digital beamformer and the analog beamformer shown in Figure 11.
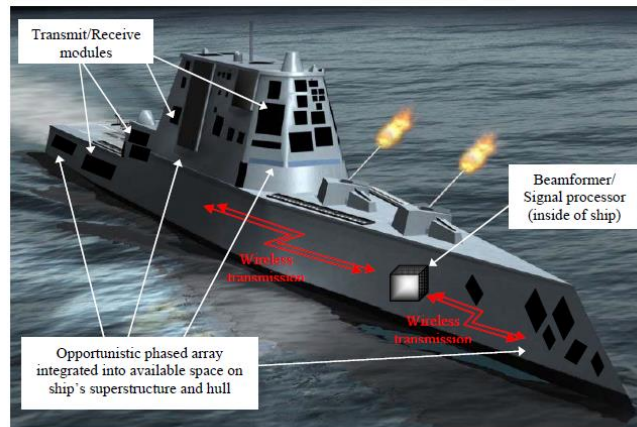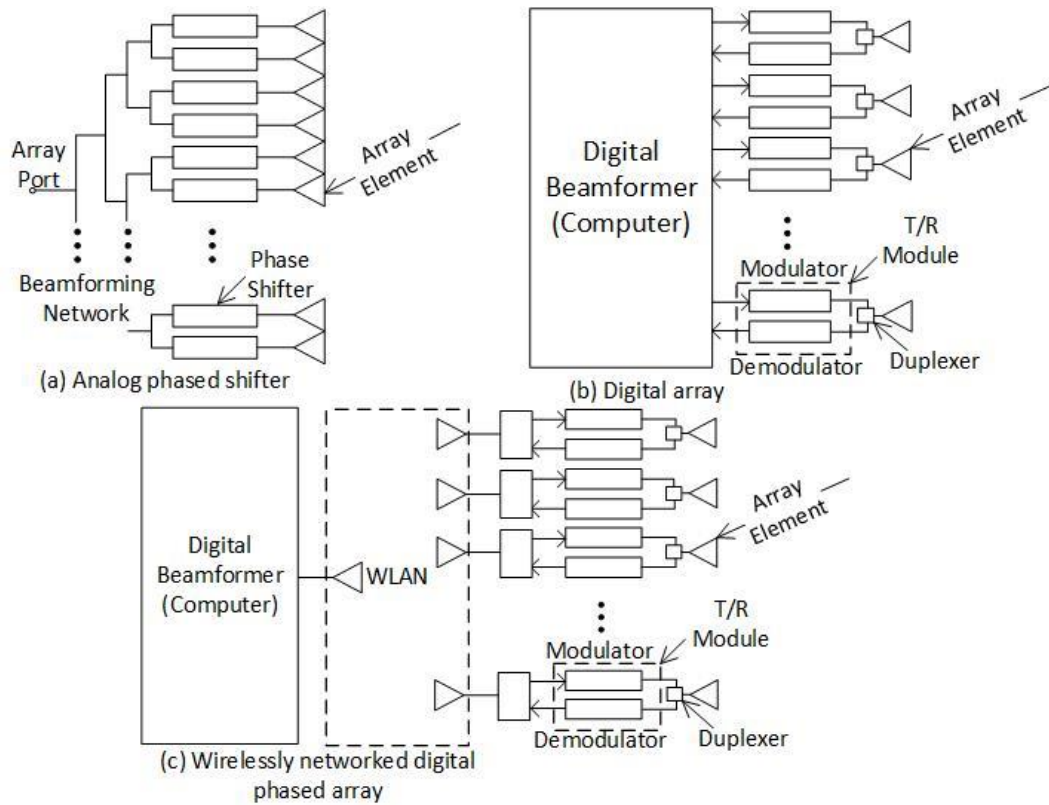
Figure 1.   Major systems onboard the DDX (After [1]).

Figure 11. Example of a WNDDRAR (top) and opportunistic array (bottom). [124]
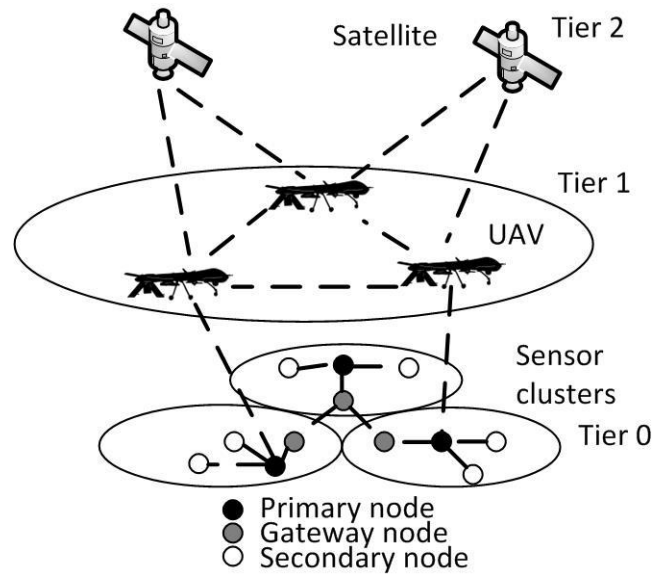
Figure 12. Example of a three tier wireless sensor network. [57]

This architecture employs a digital beamformer (computer processor) and controller to compute beam control data (phase and amplitude weights) for each element differently from the conventional microwave beamforming network. These latter systems are bulky and contain complicated mechanical gimbal systems, servos and rotary joints to steer the beam of the antenna and are thereby eliminated; making digital phase shifting a premier advantage. Even more no mechanical wear and tear is tied to these systems, hence eliminating preventative maintenance and additional power requirements for control of these devices. Hence, a multitude of applications benefit: multiple simultaneous beams can be achieved by the means of *digital-beam-forming* (DBF) (multiple tracking); ultra-low sidelobes (-45 dB), narrow beams for low probability intercept (LPI) capability (with minimum mutual interference effects), pattern control and null positioning in the direction of noise jammers, adaptive beamwidth, data rate reconfiguration for tracking purposes and last of all clutter suppression (range degradation). Perhaps providing the arrays most central advantage, multi-functionality, and integrated value into many applications such as communications, data-links, radar (search and track), and electronic warfare (EW).

Lastly, a Wirelessly Networked Distributed Digital Random Array Radar (WNDDRAR) offers the opportunity to compensate for the failure of hundreds to thousands of elements in the design. Damage, destruction or defects from several elements will not shut down the entire system down, but instead, provide graceful degradation. Even a single source of error can be found and associated to a single damaged element. With this knowledge a hot swap of the damaged element can be made improving the systems mean-time between failures and repair time contrasted to conventional techniques. More

13

advanced predictors of the peaking sidelobe versus number of elements will be provided in Chapter 14 to serve as a guide for the required number of elements.

Henceforth, as previously stated the overall main objective of this dissertation is to completely and fully understand the internal workings of random arrays. Next is to merge the theoretical concepts of random arrays into practical applications to include:

- 1. Wirelessly Networked Distributed Digital Random Array Radar (WNDDRAR) for long range radar capability
- 2. Man Portable Network (MPN) with improved range and network capability
- 3. Unpiloted Aerial Vehicle (UAV) swarm for enhanced Information, Surveillance, and Reconnaissance (ISR) applications.

Hardware for the proposed applications can be found in the sources of [1], [5], [102]-[125]. These applications will be seen to benefit from ad hoc configurations relating to the vigorously derived closed form pattern solutions of this dissertation. Noting that certain outstanding difficulties still exist, the overall conclusion is that merging the theoretical and design concepts of distributed beamforming is viable and yields operational advantages in terms of both military and civilian applications.

1.4 Organization of Dissertation

This dissertation comprises a variety of aperiodic arrays structures and a more thorough examination and emphasis is placed into determining characteristics for circular and spherical topology. Chapter II begins with simple electromagnetic theory of which the goal is to derive the free space Greens functions. Chapter III presents simple array theory and derives the array factor and radiation pattern given a set of assumptions that are used in throughout this dissertation. Chapter IV applies statistics to the radiation pattern and results with the mean valued radiation pattern. Chapter V relates the derived volumetric radiation pattern to previous works. Chapter VI-Chapter X derive pattern statistics of the main beam such that: Chapter VI presents a method for creating nulls in the pattern, Chapter VII shows the characteristic modes of circular and spherical random array, Chapters VIII and X derive the taper functions for the main beam and Chapter IX derives the procedures for creating multiple beams. Moreover, the reason why Chapter X follows Chapter IX is because it will be shown that a Gaussian is nothing more than the self-convolution of a distribution over and over again (or multiplication of itself over and over again in the Fourier domain), which makes Chapter IX a predecessor of Chapter X. An experimental campaign of these results is verified in Chapter XI. The next part of this dissertation derives the element correction procedures for tilted elements in Chapter XII and frequency independence of a random array in Chapter XIII. A more statistical formulation is derived in Chapter XIV in order to derive the maximum peaking sidelobe in the beampattern of a random array, which is a critical design feature for array designers. Chapter XV continues with this statistical analysis by deriving the maximum phase shifter and range error allowed for the random array. After this a near field analysis is derived for deriving the

radiation pattern anywhere and everywhere, which is not exclusive to the Fraunhofer region! Chapter XVII ends with a conclusion of random arrays. Also for more in depth analysis and application extension of applicable use an appendix is provided in Appendix I. Appendix II-XV are provided as additional extended explanations and derivations of these random arrays.

CHAPTER II

A REVIEW OF MAXWELL'S EQUATIONS, VECTORS AND SCALAR

POTENTIALS

Mathematical notation and foundations will follow throughout this dissertation and clarity of these foundations is the goal. This chapter is closely followed from the notes found online by [67]. The goal of this chapter is to set up the notation and foundation of which will be used for establishing standard notation with deeper understanding of the physical process and behavior of random antenna arrays. First Maxwell's equations are established in (2)-(8).

2.1 Maxwell's Equations

(a) The law of induction (Faraday's law)

$$-\vec{\nabla} \times \vec{E} = \frac{\partial \vec{B}}{\partial t} + \vec{M} \tag{2}$$

$$e = \oint_c \vec{E} \cdot d\vec{c} = -\frac{\partial}{\partial t} \iint_{S_{[c]}} \vec{B} \cdot d\vec{s} = -\frac{\partial \Psi}{\partial t} \tag{3}$$

Where $\vec{E}(V/m)$ is the electric field intensity, $\vec{B}(T = Wb/m^2)$ is the magnetic field density, $\vec{M}(V/m^2)$ is the magnetic currenty density, $\Psi(Wb = V \cdot s)$ is the magnetic flux and $e(V)$ is the electromotive force.

(b) Ampere's law, generalized by Maxwell to include the displacement current $\partial \vec{D}/\partial t$

$$\vec{\nabla} \times \vec{H} = \frac{\partial \vec{D}}{\partial t} + \vec{J} \tag{4}$$

$$I = \oint_c \vec{H} \cdot d\vec{c} = \iint_{S_{[c]}} \left(\frac{\partial \vec{D}}{\partial t} + \vec{J} \right) \cdot d\vec{s} \tag{5}$$

Where $\vec{H}(A/m)$ is the magnetic field intensity, $\vec{D}(C/m^2)$ is the magnetic field density, $\vec{J}(A/m^2)$ is the electric current density and $I(A)$ is the electric current.

(c) Gauss' electric law

$$Q = \oiint_S \vec{D} \cdot d\vec{s} = \iiint_{V_{[s]}} (\vec{\nabla} \cdot \vec{D}) dv = \iiint_{V_{[s]}} \rho dv \tag{6}$$

Where $\rho\left(C/m^3\right)$ is the electric charge density and $Q(C)$ is the electric charge. This also includes the continuity relation (7); due to taking the divergence of both sides of (4):

$$\vec{\nabla}\cdot\vec{J}=-\frac{\partial\rho}{\partial t} \tag{7}$$

(d) Gauss' magnetic law

$$Q_m=\oiint_{S}\vec{B}\cdot d\vec{s}=\iiint_{V_{[s]}}\left(\vec{\nabla}\cdot\vec{B}\right)dv=\iiint_{V_{[s]}}\rho_m dv \tag{8}$$

Provided that $\vec{M}=0$, contributes $\vec{\nabla}\cdot\vec{B}=0$ from(2).

Maxwell's equations (a-d) are insufficient to solve for the four vector quantities: $\vec{E},\vec{D},\vec{H}$ and $\vec{B}$ (twelve scalar quantities) and in consequence two additional vector equations are needed.

(e) Constitutive relationships

The constitutive relationships in (9) and (10) describe the properties of matter with respect to electric and magnetic forces. In an anisotropic medium, the dielectric permittivity and magnetic permeability are tensor quantities whereas in an isotropic or vacuum, they are constants (or tensors whose diagonal elements only are nonzero and are the same): $\varepsilon_0 8.854187817\times10^{-12}\,F/m$, $\mu_0=4\pi\times10^{-7}\,H/m$. This dissertations interest will focus upon an isotropic medium, such that the vectors $\vec{D}$ and $\vec{E}$ are collinear. Hence, the vectors $\vec{B}$ and $\vec{H}$ take the simple form $\vec{B}=\mu_0\mu_r\vec{H}$ and $\vec{D}=\varepsilon_0\varepsilon_r\vec{E}$ such that ε_r is the relative permittivity and μ_r is the relative permeability.

$$\vec{D}=\|\varepsilon\|\cdot\vec{E} \tag{9}$$

$$\vec{B}=\|\mu\|\cdot\vec{H} \tag{10}$$

In a lossy medium (non-vacuum) the dielectric properties of both permittivity and permeability loss are represented respectively by the loss angles δ_d (11) and δ_m (12).

$$\bar{\varepsilon}=\varepsilon'\left[1-j\left(\frac{\varepsilon''}{\varepsilon'}+\frac{\sigma}{\omega\varepsilon'}\right)\right]=\varepsilon'\left[1-j\left(\tan\delta_d+\frac{\sigma}{\omega\varepsilon'}\right)\right] \tag{11}$$

$$\bar{\mu}=\mu'-j\mu''=\mu'\left[1-j\left(\frac{\mu''}{\mu'}\right)\right]=\mu'\left[1-j\left(\tan\delta_m\right)\right] \tag{12}$$

(f) Time-harmonic field analysis

Field phasors relationships (13) and (14) are introduced in the analysis of time harmonic electromagnetic fields where the notation of time-dependent field vectors are represented by the lower-case letters, while their phasor relationship is denoted with upper-case letters.

$$\vec{e}(x,y,z,t) = \text{Re}\left\{\vec{E}(x,y,z)e^{j\omega t}\right\} \tag{13}$$

$$\vec{h}(x,y,z,t) = \text{Re}\left\{\vec{H}(x,y,z)e^{j\omega t}\right\} \tag{14}$$

2.2 Vector and Scalar Potentials

In a linear medium, a field can be found by superimposing the partial field due to the electric sources $\left(\vec{F}\right)$ only and the one due to the magnetic sources $\left(\vec{A}\right)$ only. A collection of these results are shown in Table 2.

Table 2 Field Vectors in Terms of Vector Potentials

Magnetic vector-potential $\vec{A}$ (electric sources only)	Electric vector-potential $\vec{F}$ (magnetic sources only)
$\vec{B} = \vec{\nabla} \times \vec{A}, \ \vec{H} = \dfrac{1}{\mu}\vec{\nabla} \times \vec{A}$	$\vec{D} = -\vec{\nabla} \times \vec{F}, \ \vec{E} = -\dfrac{1}{\varepsilon}\vec{\nabla} \times \vec{F}$
$\vec{E} = -j\omega\vec{A} - \dfrac{j}{\omega\mu\varepsilon}\vec{\nabla}\vec{\nabla}\cdot\vec{A} \ \ or$	$\vec{H} = -j\omega\vec{F} - \dfrac{j}{\omega\mu\varepsilon}\vec{\nabla}\vec{\nabla}\cdot\vec{F} \ \ or$
$\vec{E} = \dfrac{1}{j\omega\mu\varepsilon}\vec{\nabla}\times\vec{\nabla}\times\vec{A} - \dfrac{\vec{J}}{j\omega\varepsilon}$	$\vec{H} = \dfrac{j}{\omega\mu\varepsilon}\vec{\nabla}\times\vec{\nabla}\times\vec{F} - \dfrac{\vec{M}}{j\omega\mu}$
$\nabla^2\vec{A} - \gamma^2\vec{A} = -\mu\vec{J}$ $\gamma = \alpha + j\beta$	$\nabla^2\vec{F} - \gamma^2\vec{F} = -\varepsilon\vec{M}$

2.3 Retarded Potentials

"*Retarded potential* is a term usually used to denote the solution of the inhomogeneous Helmholtz' equation (in the frequency domain) or that of the inhomogeneous wave equation (in the time domain) in an unbounded region." [67] For example, consider the *z-directed* electric current density $\vec{J} = \hat{z}J_z$. Then, according to Table 2, the magnetic vector potential $\vec{A}$ also has only a *z-component* governed by the following equation in a lossless medium:

$$\nabla^2 A_z + \beta^2 A_z = -\mu J_z \tag{15}$$

Eq. (15) is a Helmholtz equation and its solution (16) in open space is determined by the integral where $G(P,Q)$ is the open source Green's function of the Helmholtz equation, P is the observation point and Q is the source point.

$$A_z(P) = \iiint_{V_Q} G(P,Q) \cdot \left[-\mu J_z(Q)\right] dv_Q \tag{16}$$

Substituting the free space Green's function [65] provides

$$A_z(P) = \iiint_{V_Q} \frac{e^{-j\beta R_{PQ}}}{4\pi R_{PQ}} \mu J_z(Q) dv_Q \tag{17}$$

To further generalize the above formula, one assumes the existence of source currents of arbitrary directions, which would produce partial magnetic vector potentials in any direction. Note that a current element in the $\hat{\psi}$ direction results in a vector potential $\vec{A} = A_\psi \hat{\psi}$ in the same direction (unless the medium is inhomogeneous and/or anisotropic). Thus,

$$\vec{A}(P) = \iiint_{v_Q} \mu \vec{J}(Q) \frac{e^{-j\beta R_{PQ}}}{4\pi R_{PQ}} dv_Q \tag{18}$$

The solution for the electric vector potential due to magnetic current sources $\vec{M}(Q)$ is analogous: (and will not be used in this dissertation)

$$\vec{F}(P) = \iiint_{v_Q} \varepsilon \vec{M}(Q) \frac{e^{-j\beta R_{PQ}}}{4\pi R_{PQ}} dv_Q \tag{19}$$

Finally, we recall that not only *volume* sources are used to model current distributions. A useful approximation, especially for currents on a conductor surface, is the surface current density (or simply surface current):

$$\vec{J}_s(x,y) = \lim_{\delta \to 0} \int_{-\delta/2}^{\delta/2} \vec{J}(x,y,z) dz, \; A/m \tag{20}$$

The magnetic vector potential $\vec{A}$ produced by distributed surface currents is then expressed as

$$\vec{A}(P) = \iint_s \mu \vec{J}_s(Q) \frac{e^{-j\beta R_{PQ}}}{4\pi R_{PQ}} ds_Q \tag{21}$$

Currents on a very thin wire are usually approximated by a linear source, which is the current, I flowing through the wire:

$$\vec{I}_z(z) = \lim_{\substack{\delta_x \to 0 \\ \delta_y \to 0}} \iint_{\delta_x \delta_y} \vec{J}(x,y,z) dxdy \tag{22}$$

The potential of line current is given by (23). An example of a line and surface current is provided in Figure 13.

$$\vec{A}(P) = \int_L \mu I(Q) \frac{e^{-j\beta R_{PQ}}}{4\pi R_{PQ}} d\vec{l}_Q \tag{23}$$

(a) surface current on a sheet   (b) linear current on a thin wire
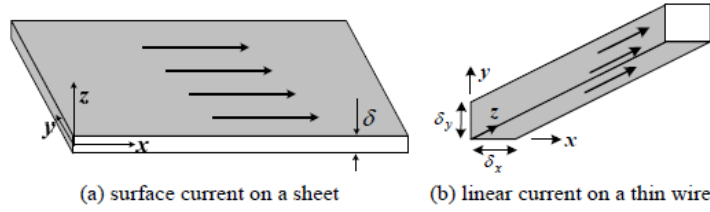
Figure 13. Examples of surface and line currents. [67]

The last of these cases would be a fictitious point source current. For this current the magnetic vector potential is just the multiplication of the greens function and exciting function shown normalized below. This is an invaluable result as a random array is assumed a superposition of point sources of this nature. More on this can be found throughout this dissertation in addition to Appendix II. Also this is similar to the method of moments except the current distribution is a sampled version of point sources. To relate back to the method of moments the trouble comes from having to know the element factor.

$$\vec{A} = \frac{\mu \vec{J}(r',\theta',\phi')}{4\pi} \frac{e^{-jk|r-r'|}}{|r-r'|} \quad \left(\begin{array}{l} \text{infinitesimal dipole located at the origin} \\ \text{no integration for a point source} \\ x' = y' = z' = 0 \end{array} \right)$$

$$\vec{A} = \frac{\mu I_0}{4\pi} \frac{e^{-jkr}}{r} \left(\hat{r} + \hat{\theta} + \hat{\phi} \right) \tag{24}$$

$$\vec{A} = \frac{e^{-jkr}}{4\pi r} \left(\hat{r} + \hat{\theta} + \hat{\phi} \right) \bigg|_{I_0 = \frac{1}{\mu}}$$

2.4 Far Fields and Vector Potentials

(a) Potentials

The further away from the antenna (observation point), the more spherical like is the emanated wave causing the antenna to look like a point source regardless of physical shape. Hence, this region is known as the *far field* or *far zone*. These spherical like properties of the wave add similar to Huygens principal, but for now, are applied to the vector potential provided in (25) derived from the integral in (17).

$$\vec{A} = \left[\hat{r} \cdot A_r(\theta,\phi) + \hat{\theta} \cdot A_\theta(\theta,\phi) + \hat{\phi} \cdot A_\phi(\theta,\phi) \right] \frac{e^{-jkr}}{r}, \quad r \to \infty \tag{25}$$

Another way of describing the free space Green's function is "it demonstrates spherical like properties of the wave as the term e^{-jkr} shows propagation along $\hat{r}$ away from the antenna at the speed of light. The term $1/r$ shows the spherical spread of the potential in space, which results in a decrease of its magnitude as the radius of the sphere increases. [67]" Most importantly it shows that the far-field potential

20

on the distance r is separable from the dependence on the observation angle (θ, ϕ), and it is the same for any antenna: e^{-jkr}/r regardless of the physical shape

To arrive at this expression we examine (17) in further detail such that when "the observation point P is very far from the source, the distance R_{PQ} between P and the integration points varies only slightly as Q sweeps the volume of the source. It is almost the same as the distance r from the origin to P since we usually position the origin of the coordinate system close to the source center [67]." Thus, it is the typical convention to use the following approximation (attributed to Kirchhoff) known as the *far-field approximation.*

$$\frac{e^{-jkR_{PQ}}}{R_{PQ}} \approx \frac{e^{-jk(r-\hat{r}\cdot\vec{r}')}}{r} \tag{26}$$

It is seen a first-order approximation is used for the amplitude, while a second order approximation is used for phase. This approximation is more critical for accuracy in the formulation and the approximation leads up to *22.5* degrees of inaccuracy as long as the three requirements are satisfied in the far field region.

Table 3. Near Field, Fresnel and Fraunhofer Regions.

Reactive near field	$0 \leq r \leq .62\sqrt{\dfrac{D^3}{\lambda}}$
Radiating near field (Fresnel Region)	$.62\sqrt{\dfrac{D^3}{\lambda}} \leq r \leq 2\dfrac{D^2}{\lambda}$
Far Field (Fraunhofer region)	1) $r \geq r_{ff} = \dfrac{2D^2}{\lambda}$ 2) $r \gg D$ 3) $r \gg \lambda$

A visual example of the phase approximation is illustrated in Figure 14 below.
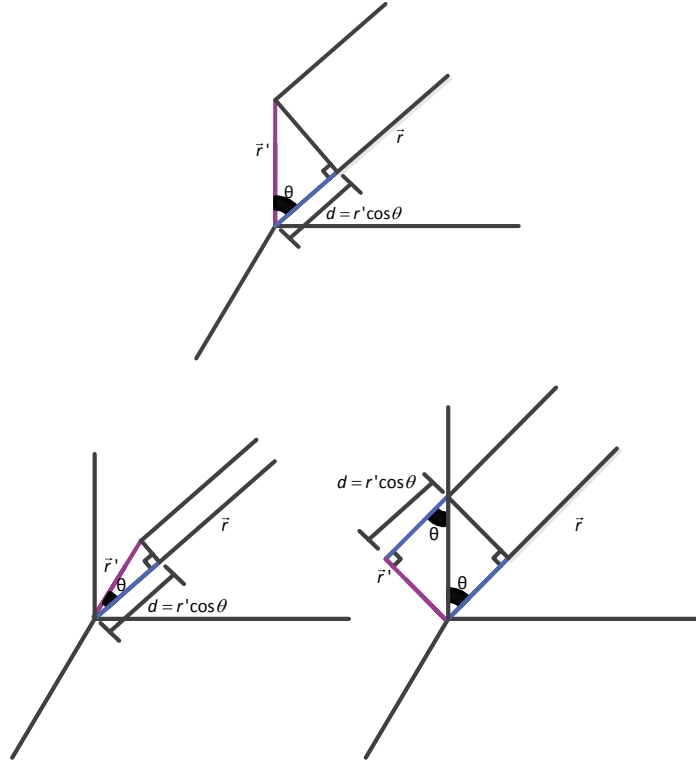
Figure 14. Path length approximations.

(b) Far-zone fields

Now applying the far-field approximation of the vector potential to the far-field vectors and assuming there are only electrical currents $\vec{F} = 0$. Then the EM fields are provided by those of (27)-(28).

$$\vec{E} = -j\omega\vec{A} - \frac{j}{\omega\mu\varepsilon}\vec{\nabla}\vec{\nabla}\cdot\vec{A} \qquad (27)$$

$$\vec{H} = \frac{1}{\mu}\vec{\nabla}\times\vec{A} \qquad (28)$$

The differential operators $\vec{\nabla}\times$ and $\vec{\nabla}\vec{\nabla}\cdot$ have to be expressed in spherical coordinates (29), which leads to the mathematical process of (30) and simplification (31).

$$-j\omega\begin{bmatrix}\hat{r}\cdot A_r(\theta,\phi)+ \\ \hat{\theta}\cdot A_\theta(\theta,\phi)+ \\ \hat{\phi}\cdot A_\phi(\theta,\phi)\end{bmatrix}\frac{e^{-jkr}}{r} - \frac{j}{\omega\mu\varepsilon}\vec{\nabla}\vec{\nabla}\cdot\left(\begin{bmatrix}\hat{r}\cdot A_r(\theta,\phi)+ \\ \hat{\theta}\cdot A_\theta(\theta,\phi)+ \\ \hat{\phi}\cdot A_\phi(\theta,\phi)\end{bmatrix}\frac{e^{-jkr}}{r}\right) \qquad (29)$$

22

$$
\begin{aligned}
=&-j\omega\begin{bmatrix}\hat{r}\cdot A_r(\theta,\phi)+\\ \hat{\theta}\cdot A_\theta(\theta,\phi)+\\ \hat{\phi}\cdot A_\phi(\theta,\phi)\end{bmatrix}\frac{e^{-jkr}}{r}-\frac{j}{\omega\mu\varepsilon}\vec{\nabla}\begin{bmatrix}\dfrac{1}{r^2}\dfrac{\partial}{\partial r}\left(\left[r^2 A_r(\theta,\phi)\right]\dfrac{e^{-jkr}}{r}\right)\hat{r}+\\[2mm] \dfrac{1}{r\sin\theta}\dfrac{\partial}{\partial\theta}\left(\begin{array}{l}\left[\sin\theta A_\theta(\theta,\phi)\dfrac{e^{-jkr}}{r}\right]+\\[2mm]\dfrac{\partial}{\partial\phi}\left[A_\phi(\theta,\phi)\right]\dfrac{e^{-jkr}}{r}\end{array}\right)\end{bmatrix}\\[4mm]
=&-j\omega\left[\hat{r}\cdot A_r(\theta,\phi)+\hat{\theta}\cdot A_\theta(\theta,\phi)+\hat{\phi}\cdot A_\phi(\theta,\phi)\right]\frac{e^{-jkr}}{r}-\\[2mm]
&\frac{j}{\omega\mu\varepsilon}\vec{\nabla}\begin{bmatrix}\dfrac{1}{r^2}e^{-jkr}\left[A_r(\theta,\phi)\right]-\dfrac{jk}{r}e^{-jkr}\left[A_r(\theta,\phi)\right]+\dfrac{e^{-jkr}}{r}\dfrac{\partial}{\partial r}\left[A_r(\theta,\phi)\right]\\[3mm]\dfrac{e^{-jkr}}{r}\dfrac{1}{r\sin\theta}\left(\begin{array}{l}\cos\theta\left[A_\theta(\theta,\phi)\right]+\\[1mm]\sin\theta\dfrac{\partial}{\partial\theta}\left[A_\theta(\theta,\phi)\right]+\\[1mm]\dfrac{\partial}{\partial\phi}\left[A_\phi(\theta,\phi)\right]\end{array}\right)\end{bmatrix}
\end{aligned}
\tag{30}
$$

$$
\begin{aligned}
=&-j\omega\left[\hat{r}\cdot A_r(\theta,\phi)+\hat{\theta}\cdot A_\theta(\theta,\phi)+\hat{\phi}\cdot A_\phi(\theta,\phi)\right]\frac{e^{-jkr}}{r}\\[2mm]
&-\frac{j}{\omega\mu\varepsilon}\left[\begin{array}{l}\left(\begin{array}{l}\dfrac{e^{-jkr}}{r}\left(\dfrac{\partial}{\partial r}\left[\begin{array}{l}\dfrac{1}{r}A_r(\theta,\phi)-jkA_r(\theta,\phi)+\dfrac{\partial}{\partial r}\left[A_r(\theta,\phi)\right]+\\[1mm]\dfrac{1}{r\sin\theta}\left(\cos\theta\left[A_\theta(\theta,\phi)\right]+\sin\theta\dfrac{\partial}{\partial\theta}\left[A_\theta(\theta,\phi)\right]+\dfrac{\partial}{\partial\phi}\left[A_\phi(\theta,\phi)\right]\right)\end{array}\right]\right)\\[5mm]+\dfrac{\partial}{\partial r}\left[\dfrac{e^{-jkr}}{r}\right]\left[\begin{array}{l}\dfrac{1}{r}A_r(\theta,\phi)-jkA_r(\theta,\phi)+\dfrac{\partial}{\partial r}\left[A_r(\theta,\phi)\right]+\\[1mm]\dfrac{1}{r\sin\theta}\left(\cos\theta\left[A_\theta(\theta,\phi)\right]+\sin\theta\dfrac{\partial}{\partial\theta}\left[A_\theta(\theta,\phi)\right]+\dfrac{\partial}{\partial\phi}\left[A_\phi(\theta,\phi)\right]\right)\end{array}\right]\end{array}\right)\hat{r}+\\[12mm]\dfrac{e^{-jkr}}{r^2}\left(\begin{array}{l}\dfrac{\partial}{\partial\theta}\left[\begin{array}{l}\dfrac{1}{r}A_r(\theta,\phi)-jkA_r(\theta,\phi)+\dfrac{\partial}{\partial r}\left[A_r(\theta,\phi)\right]+\\[1mm]\dfrac{1}{r\sin\theta}\left(\begin{array}{l}\cos\theta\left[A_\theta(\theta,\phi)\right]+\sin\theta\dfrac{\partial}{\partial\theta}\left[A_\theta(\theta,\phi)\right]\\[1mm]+\dfrac{\partial}{\partial\phi}\left[A_\phi(\theta,\phi)\right]\end{array}\right)\end{array}\right]\hat{\theta}+\\[10mm]\dfrac{1}{\sin\theta}\dfrac{\partial}{\partial\phi}\left[\begin{array}{l}\dfrac{1}{r}A_r(\theta,\phi)-jkA_r(\theta,\phi)+\dfrac{\partial}{\partial r}\left[A_r(\theta,\phi)\right]+\\[1mm]\dfrac{1}{r\sin\theta}\left(\begin{array}{l}\cos\theta\left[A_\theta(\theta,\phi)\right]+\sin\theta\dfrac{\partial}{\partial\theta}\left[A_\theta(\theta,\phi)\right]\\[1mm]+\dfrac{\partial}{\partial\phi}\left[A_\phi(\theta,\phi)\right]\end{array}\right)\end{array}\right]\hat{\phi}\end{array}\right)\end{array}\right]
\end{aligned}
\tag{31}
$$

All terms decrease as $1/r^2$ or faster are neglected for large r (32)-(33). In addition to the condition (34) hence the *EM* fields are simplified as (35)-(36) where, $\eta = \sqrt{\mu/\varepsilon}$ denotes the intrinsic impedance of the medium.

$$\vec{E} = \frac{1}{r}\left\{ -j\omega e^{-jkr}\left[\hat{\theta}A_\theta(\theta,\phi)+\hat{\phi}(\theta,\phi)\right]+\frac{1}{r^2}\{\ \}+\ldots,\ r\to\infty \right. \tag{32}$$

$$\vec{H} = \frac{1}{r}\left\{ j\frac{\omega}{\eta} e^{-jkr}\left[\hat{\theta}A_\theta(\theta,\phi)+\hat{\phi}(\theta,\phi)\right]+\frac{1}{r^2}\{\ \}+\ldots,\ r\to\infty \right. \tag{33}$$

$$\frac{e^{-jkr}}{r}\left[-2jk\frac{\partial}{\partial r}\left[A_r(\theta,\phi)\right]+\frac{\partial^2}{\partial r^2}\left[A_r(\theta,\phi)\right]\right]=0$$

where   (34)

$A_r(\theta,\phi)$ is not a function of r

$$\left.\begin{array}{l} E_r \simeq 0 \\ E_\theta \simeq -j\omega A_\theta \\ E_\phi \simeq -j\omega A_\phi \end{array}\right\} \vec{E}^A \simeq -j\omega\vec{A},\ \text{where } E_r^A \simeq 0 \tag{35}$$

$$\left.\begin{array}{l} H_r \simeq 0 \\ H_\theta \simeq +j\dfrac{\omega}{\eta}A_\phi = -\dfrac{E_\phi}{\eta} \\ H_\phi \simeq -j\dfrac{\omega}{\eta}A_\theta = +\dfrac{E_\theta}{\eta} \end{array}\right| \vec{H}^A \simeq -j\dfrac{\omega}{\eta}\hat{r}\times\vec{A} = \dfrac{1}{\eta}\hat{r}\times\vec{E}^A \tag{36}$$

In an analogous manner, if one assumes only magnetic sources are present the fields are:

$$\left.\begin{array}{l} H_r \simeq 0 \\ H_\theta \simeq -j\omega F_\theta \\ H_\phi \simeq -j\omega F_\phi \end{array}\right\} \vec{H}^F \simeq -j\omega\vec{F},\ \text{where } \mathrm{H}_r^F \simeq 0 \tag{37}$$

$$\left.\begin{array}{l} E_r \simeq 0 \\ E_\theta \simeq -j\omega\eta F_\phi = \eta H_\phi \\ H_\phi \simeq +j\omega\eta F_\theta = -\eta H_\theta \end{array}\right\} \vec{H}^A \simeq j\omega\eta\hat{r}\times\vec{F} = -\eta\hat{r}\times\vec{H}^F \tag{38}$$

"In summary, the far field of any antenna has the following important features which follow from equations (35) through (38) [67]." First there are no radial components of the fields $E_r = H_r = 0$ in the direction of propagation making it a TEM (Transverse Electro Magnetic Wave). Second the field vectors are mutually orthogonal to the direction of propagation. Third the magnitude(s) of the electric and magnetic field are related always as $|E| = \eta|H|$.

(c) Normalized (far) field electric field of a point source

The goal of this section is to define the electric field such that it matches to similar works in the field of random arrays by those of [6], [9], [10], [30], [58], [81] and [82]. Hence, the set up will describe the electric field composed from (24) and (35) as

$$\vec{E} \approx -j\omega\vec{A}_T = -j\omega\frac{e^{-jkr}}{4\pi r}\left(\hat{\theta}+\hat{\phi}\right) \tag{39}$$

With the following normalization,

$$\vec{E}_{Normalized} \approx \vec{A}_T = \frac{e^{-jkr}}{4\pi r}\left(\hat{\theta}+\hat{\phi}\right) \tag{40}$$

The result of (40) is used in Lo [58]. However, the theory expanded upon this result [9], [10], [81] and [82]. is much different than the more complex result of (40).

The works of [9], [10], [81] and [82] remove the $\hat{\phi}$ dependence due to assuming a symmetrically rotational pattern. This eases the mathematical analysis or otherwise the provided results in these works. Furthermore it is shown in [65] that the array factor and element factor are independent, such that pattern multiplication may be applied between the two. Hence, the works of [9], [10], [81] and [82] are correct in analysis in this sense. However, if one were to assume that that the magnitudes of the elements will differ such that the array factor and element factor are no longer independent. Then one could use the theory of [58].

CHAPTER III

SYSTEM MODEL AND SETUP OF THE RANDOM ARRAY

3.1 Initial Considerations

Use of the term *distributed* has two distinct meanings in the sense of distributed beamforming. The first meaning indicates that the antennas of the array themselves are distributed over the receiving [or transmitting] plane in some randomly structured fashion. This is a departure from traditional beamforming literature, which relies on a strict, uniform [or periodic] placement of the antenna elements to reduce the complexity of the analysis through the removal of dependence on the individual locations of nodes within the arrays. When the nodes are no longer structured so nicely, the location of each element must be considered on its own, rather than simply considering the location of the array as a whole. In this scenario, the elements are still controlled by some central source; hence the locations, phase offsets, and transmit capabilities of each node are known quantities to be taken advantage of during ideal weight calculations.

The second meaning builds on the first, implying that the elements are not only distributed in terms of location, but are also independent processing units, such as with a wireless sensor network in a field. This second scenario severely limits the quantity and quality of information available to a beamformer. In this case, methods for determining ideal complex weights must be distributed in the sense that they can be carried out by each node individually without sharing significant amounts of information. If the nodes were allowed to share the total amount of information about themselves, such as through some pre-communication phase, the second scenario would collapse into the first, where ideal weights could be calculated based on the global information and disseminated through the network by a single cluster head. Early work with systems where the global parameters. [126]

For an array of identical elements, there are five factors [102] that can be used to shape the overall radiation pattern. First is the geometrical configuration bounding the overall array. Second, the distribution of the elements bound to the overall array. Third the current excitation amplitudes of the elements used mainly for adaptive beamforming. Fourth the relative phase shift of the elements for beamsteering purposes. Last is the individual pattern of the elements.

For this study, a choice in topology to encompass a random cluster of radiating elements is the first step in random array analysis. Henceforth, a choice has been made to examine a volumetric spherically bound random array topology of *N* elements shown in Figure 15 [6], [81] and [82] with radiators in the array denoted $P_n(r_n, \theta_n, \phi_n)$ where $\theta \in [0, \pi]$, $\phi \in [0, 2\pi)$. The radius *A* of the encompassing topology is set by the outermost radiators (this ability for inclusiveness is a key feature of these types of arrays). Several assumptions are considered to enable the analysis of the array in Figure 15. These are:

- First: The location of each antenna is chosen randomly with uniform distribution inside a sphere of diameter A.
- Second: Each antenna is assumed to be an ideal isotropic radiator
- Third: All antenna elements transmit an equal amount of energy with equal path loss
- Fourth: No reflection or scattering of the signal exists (e.g., no multipath fading or shadowing)
- Fifth: Mutual coupling is mitigated under the assumption the antennas are separated sufficiently far away from one another
- Sixth: Adequate synchronization is available to ensure frequency offsets and phase jitter is not present
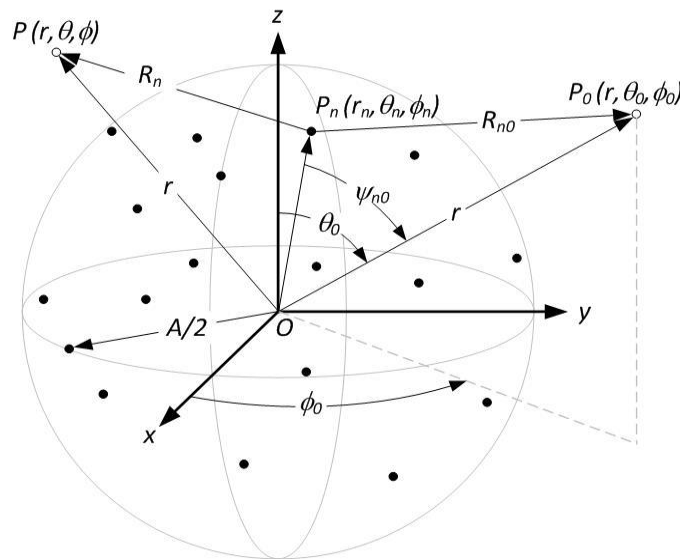
Figure 15. Random distribution of elements in a spherical volume.

3.2 Array Factor

The derivation of the array factor is demonstrated in this section for a uniformly distributed volumetric random array with perfect phase information bound to a Euclidean domain. It begins by examining the magnitude of the normalized electric field E in (41) of the array at an observation point $P(r,\theta,\phi)$ for randomly spaced elements at locations $P_n(r_n,\theta_n,\phi_n)$. This result is similar in respect to Huygens's principle which states that an excited surface $S(x,y,z)$ radiates as an independent source of strength $I(x,y,z)$ of which the field at any point external to the surface is the sum or superposition of the

27

radiations from all the elemental radiators given in (42). The element distance $R_n(\theta,\phi)$ in (43) provides the Euclidean distance between P_n and P. This distance is simplified by means of the binomial expansion given in (44) reducing (43) to (45).

$$E(R_n,\theta,\phi) = \frac{1}{N}\sum_{n=1}^{N} f_{no}(R_{no},\theta_{no},\phi_{no}) \frac{e^{-j\vec{k}\cdot\vec{R}_n(\theta,\phi|r_n,\theta_n,\phi_n)}}{R_n(\theta,\phi|r_n,\theta_n,\phi_n)}$$
$$\neg \vec{k} = k\hat{x} + k\hat{y} + k\hat{z}$$
$$\vec{R} = r\sin\theta\cos\phi\hat{x} + r\sin\theta\sin\phi\hat{y} + r\cos\theta\hat{z}$$
(41)

$$E(R_n,\theta,\phi) = K\oiiint I(x,y,z)\frac{e^{-jkR_n(\theta,\phi|r_n,\theta_n,\phi_n)}}{R_n(\theta,\phi|r_n,\theta_n,\phi_n)}$$
(42)

$$\neg K(\text{impedance of the medium})$$

$$R_n(\theta,\phi|r_n,\theta_n,\phi_n) = \left|\vec{R}_n(\theta,\phi|r_n,\theta_n,\phi_n)\right| = \left|\vec{r}-\vec{r}_n\right|$$

$$= \sqrt{(r\sin\theta\cos\phi - r_n\sin\theta_n\cos\phi_n)^2 + (r\sin\theta\sin\phi - r_n\sin\theta_n\sin\phi_n)^2 + (r\cos\theta - r_n\cos\theta_n)^2}$$

$$= \sqrt{r^2 + r_n^2 - 2rr_n\sin\theta\sin\theta_n(\cos\phi\cos\phi_n + \sin\phi\sin\phi_n + \cos\theta\cos\theta_n)}$$
(43)

$$= \sqrt{r^2 + r_k^2 - 2rr_n(\sin\theta\sin\theta_n\cos(\phi-\phi_n) + \cos\theta\cos\theta_n)}, \quad \begin{cases}\cos(\alpha-\beta) = \\ \cos\alpha\cos\beta - \sin\alpha\sin\beta\end{cases}$$

$$= r\sqrt{1 + \left(\frac{r_n}{r}\right)^2 - \frac{2r_n\cos\psi_n}{r}} \quad \{\cos\psi_n = \hat{r}_n\cdot\hat{r}\}$$

$$(1+x)^n = \binom{n}{0}x^0 + \binom{n}{1}x^1 + \binom{n}{2}x^2 + \ldots + \binom{n}{n-1}x^{n-1} + \binom{n}{n}x^n$$
(44)

$$\left|\vec{R}_n(\theta,\phi|r_n,\theta_n,\phi_n)\right| = |r-r_n|$$

$$\approx r + \frac{1}{2}r\left(-\frac{2\cos\psi_n r_n}{r} + \frac{r_n^2}{r^2}\right) - \frac{1}{8}r\left(-\frac{2\cos\psi_n r_n}{r} + \frac{r_n^2}{r^2}\right)^2 + \frac{1}{16}r\left(-\frac{2\cos\psi_n r_n}{r} + \frac{r_n^2}{r^2}\right)^3 + \ldots$$
(45)

$$= r - r_n\cos\psi_n + \frac{1}{r}\left(\frac{r_n^2}{2}\sin^2\psi_n\right) + \frac{1}{r^2}\left(\frac{r_n^3}{2}\cos\psi_n\sin^2\psi_n\right) + \ldots$$

If P is assumed to reside in the far field of the array, the common approximations are a first order approximation for the magnitude $R_n \approx r$ and second order approximation for phase $R_n \approx r - r_n\cos\psi_n$ [65]. This is a consequence of the denominator $\left(R_n(\theta,\phi|r_n,\theta_n,\phi_n)\right)$ since it varies slightly over either integral or summation of (41)-(42), but the variation of $\left(R_n(\theta,\phi|r_n,\theta_n,\phi_n)\right)$ in the exponent is much more significant, since $\exp\left(-j\vec{k}\cdot\vec{R}_n(\theta,\phi|r_n,\theta_n,\phi_n)\right)$ rotates 360° as the wave travels a distance over one wavelength. Last of all this additional path length contribution can be calculated with ease by linking the

direction vectors $\hat{r}$ from the origin (46) and $\hat{r}_n$ from P_n (47) to P through the direction cosine in (48). This process results through the spherical addition theorem (first order), and includes the angular phasing information of each source required toward steering the main beam (e.g., the direction of constructive superposition) in the desired direction of P_0. Furthermore it is assumed that the dot product $\vec{k} \cdot \vec{R}_n \left(\theta, \phi | r_n, \theta_n, \phi_n \right)$ approximates as $k\hat{r} \cdot \left(r - r_n \cos \psi_n \right) \hat{r} = k \left(r - r_n \cos \psi_n \right)$ simplifying the waves direction of travel.

$$\hat{r} = \hat{x} \sin \theta \cos \phi + \hat{y} \sin \theta \sin \phi + \hat{z} \cos \theta \tag{46}$$

$$\hat{r}_n = \hat{x} \sin \theta_n \cos \phi_n + \hat{y} \sin \theta_n \sin \phi_n + \hat{z} \cos \theta_n \tag{47}$$

$$\cos \psi_n = \hat{r}_n \cdot \hat{r} = \sin \theta_n \sin \theta \cos \left(\phi - \phi_n \right) + \cos \theta_n \cos \theta \tag{48}$$

It should be further noted that neglecting a third order approximation with antennas greater than $\left(A > \lambda \right)$ produces a maximum phase error of $\left(22.5° \right)$ [65]. Hence, this neglection can be critical and unfavorable in certain applications. The exception is that such an approximation considerably simplifies the results leading to mathematical insight on the behavior of these random array structures.

Inserting an excitation coefficient $f_{no} \left(r_n, \theta_{no}, \phi_{no} \right) = I_n e^{jkr_n \cos \psi_{no}}$ into (48) where I_n is the amplitude and $\cos \psi_{no}$ is the phase information for the nth element (49). Using the definition of the array factor $F \left(\theta, \phi | r_n, \theta_n, \phi_n \right)$ the electric field distribution simplifies to (50) and to (51) for a uniform amplitude distribution $I_n = I_o = 1$ (isotropic source). The approximation symbol has been included to show a far field approximation has been made; the exact expression is calculated using (41).

$$E \left(r, \theta, \phi | \vec{r}_n, \vec{\theta}_n, \vec{\phi}_n \right) = \frac{1}{N} \frac{e^{-jkr}}{r} \sum_{n=1}^{N} I_n e^{jkr_n \left(\cos \psi_n - \cos \psi_{no} \right)} \tag{49}$$

$$E \left(r, \theta, \phi | r_n, \theta_{no}, \phi_{no} \right) = F \left(\theta, \phi | r_n, \theta_{no}, \phi_{no} \right) \frac{e^{-jkr}}{r} \tag{50}$$

$$F \left(\theta, \phi | r_n, \theta_{no}, \phi_{no} \right) = \frac{1}{N} \sum_{n=1}^{N} e^{j\vec{k} \cdot \left(\vec{R}_n (\theta, \phi) - \vec{R}_{no} (\theta_o, \phi_o) \right)} \approx \frac{1}{N} \sum_{n=1}^{N} e^{jkr_n \left(\cos \psi_n - \cos \psi_{no} \right)} \tag{51}$$

Last of all for completeness of this topic it should be noted that if beamforming is expected to take place in the near field or Fresnel region of the array then a total array factor of (52) should be utilized. The first exponential of the summation is the Fourier kernel whereas the second exponential is the Fresnel kernel. Moreover, when the current excitation is such that $\left(\cos \psi_n - \cos \psi_{n0} \right) = 0 \rightarrow \left(\sin \psi_n - \sin \psi_{n0} \right) = 1$ the beampattern is considered to lie at the target location, such that the summation of (52) reduces to the Cornu spiral summation relation given by (53). It is determined that a change of variables of (54), and normalization by that of (55) provides the essential tools necessary of defining an acceptable tolerance level of field loss at these target locations. For instance, a typical tolerance value of the field strength at the

target location is .9, which represents a 1dB total loss. Hence, from Figure 16 a value of $v=1$ is found to satisfy this tolerance threshold as given in (56). This relation is also known as the far-field condition and is known as the closest distance at which phase-front curvature may be ignored. In the work of [65] this distance is given as $2(2\tilde{A}^2)/\lambda$ and in [101] the mean between these two distances being $(2\tilde{A}^2)/\lambda$. For this work the far field is considered to be the typical $2(2\tilde{A}^2)/\lambda$ distance used in most of the literature.

$$F\left(\theta,\phi \big| r_n,\theta_{no},\phi_{no}\right)=\frac{1}{N}\sum_{n=1}^{N}e^{j\vec{k}\cdot\left(\vec{R}_n(\theta,\phi)-\vec{R}_{no}(\theta_o,\phi_o)\right)}\approx\frac{1}{N}\sum_{n=1}^{N}e^{jk\left(r_n\cos\psi_n-r_n\cos\psi_{no}\right)}e^{jk\left(-\frac{r_n^2\sin^2\psi_n}{2r}+-\frac{r_n^2\sin^2\psi_{n0}}{2r}\right)} \tag{52}$$

$$F\left(\theta_0,\phi_0 \big| r_n,\theta_{no},\phi_{no}\right)=\frac{1}{N}\sum_{n=1}^{N}e^{j\vec{k}\cdot\left(\vec{R}_n(\theta,\phi)-\vec{R}_{no}(\theta_o,\phi_o)\right)}\approx\frac{1}{N}\sum_{n=1}^{N}e^{jk\left(-\frac{r_n^2}{2r}\right)} \tag{53}$$

$$\frac{\pi T^2}{2}=k\frac{r_n^2}{2r} \quad\Rightarrow T=r_n\sqrt{\frac{2}{\lambda r}} \tag{54}$$

$$\frac{F\left(\theta_0,\phi_0 \big| r_n,\theta_{no},\phi_{no}\right)}{F_{\max}\left(\theta_0,\phi_0 \big| r_n,\theta_{no},\phi_{no}\right)}=\frac{\int_0^v e^{\left(-\frac{j\pi T^2}{2}\right)}dT}{\int_0^v dT}=\frac{1}{v}\left|\int_0^v e^{\left(-\frac{j\pi T^2}{2}\right)}dT\right| \tag{55}$$
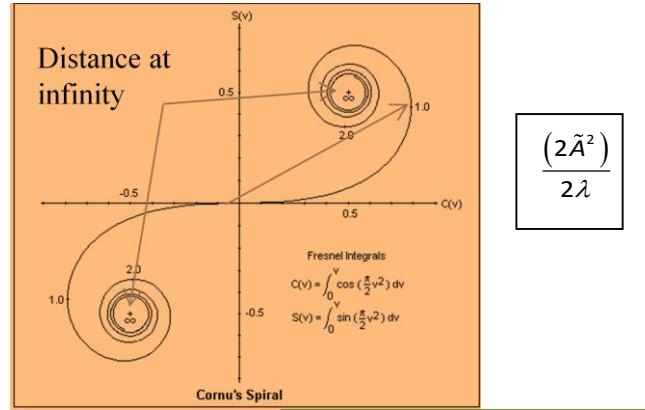
$$v=\frac{\tilde{A}}{\sqrt{2\pi r}}$$

$$\frac{\tilde{A}}{\sqrt{2\pi r}}=1 \quad or \quad r=\frac{\tilde{A}^2}{2\lambda} \tag{56}$$
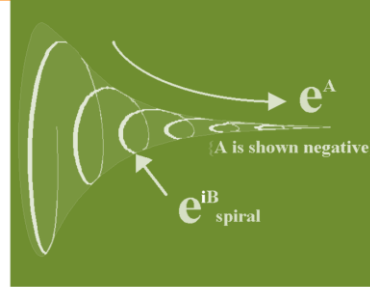
Figure 16. Cornu spiral. [127]

3.3 Radiation Intensity and Beamforming

Precise phase information is assumed herein to examine beamsteering in a direction of $P_o(r, \theta_o, \phi_o)$; accurate position and/or location of the nth element is also assumed known with respect to the direction vector $\hat{r}(\theta_o, \phi_o)$ pointing from the origin to P_o. Thereof calculation of the phase factor in (57) leads to (58). Other methods for obtaining phase information include the use of known reference positions. In either case the proliferation of Global Positioning Systems (GPS) and other technologies have and will continue to improve the ability to accurately calculate these distances. With this in mind, it is clear that ad hoc random arrays are developing into an exciting motivation and a reason to as to why the theory should be built up from the probabilistic sense.

$$\vec{k} \cdot \vec{r}_{no} = kr_n \cos\psi_{no} = kr_n \left(\hat{r}(\theta_o, \phi_o) \bullet \hat{r}_n \right) = kr_n \left(\sin\theta_n \sin\theta_0 \cos(\phi_0 - \phi_n) + \cos\theta_n \cos\theta_0 \right) \qquad (57)$$

$$F(\theta, \phi | r_n, \theta_n, \phi_n) = \frac{1}{N}\sum_{n=1}^{N} e^{jk(R_n(\theta,\phi) - R_{no}(\theta_o,\phi_o))} \approx \frac{1}{N}\sum_{n=1}^{N} e^{jkr_n(\cos\psi_n - \cos\psi_{no})} \qquad (58)$$

The array factor in (58) will be analyzed throughout the rest of this paper. It can be rewritten by expanding the angular information (48) in the exponential term of (51) according to (59) using (60)-(64) to

give (65). It is important to note that (59) provides a compact expression for the azimuthal and elevation information while maintaining the integrity of each random variable $\{r_n, \theta_n, \phi_n\}$.

$$kr_n\left(\cos\psi_n - \cos\psi_{no}\right) = kr_n\rho_o\left(\cos\left(\phi_n - \delta\right) + \cos\theta_n\cos\gamma\right) = \\ \rho_o\left(\cos\phi_n\cos\delta + \sin\phi_n\sin\delta + \cos\theta_n\cos\gamma\right) \tag{59}$$

$$\rho_o = \left[\left(\sin\theta_o\cos\phi_o - \sin\theta\cos\phi\right)^2 + \left(\sin\theta_o\sin\phi_o - \sin\theta\sin\phi\right)^2\right]^{\frac{1}{2}} \tag{60}$$

$$\cos\delta = \rho_0^{-1}\left(\sin\theta_o\cos\phi_o - \sin\theta\cos\phi\right) \tag{61}$$

$$\sin\delta = \rho_0^{-1}\left(\sin\theta_o\sin\phi_o - \sin\theta\sin\phi\right) \tag{62}$$

$$\delta = \tan^{-1}\left[\frac{\sin\theta\sin\phi - \sin\theta_o\sin\phi_o}{\sin\theta\cos\phi - \sin\theta_o\cos\phi_o}\right] \tag{63}$$

$$\cos\gamma = \rho_0^{-1}\left(\cos\theta_o - \cos\theta\right) \tag{64}$$

$$F\left(\theta,\phi|r_n,\phi_n,\theta_n\right) = \frac{1}{N}\sum_{n=1}^{N}e^{jkr_n\rho_o\left(\sin\theta_n\left(\cos\phi_n\cos\delta + \sin\phi_n\sin\delta\right) + \cos\theta_n\cos\gamma\right)} \tag{65}$$

The radiation intensity in a given direction (67) is defined as the power radiated from the antenna per unit solid angle. This is obtained by multiplying the radiation density (66) by the square of the distance (67). Normalized radiation intensity is given by (68) and will also be used throughout this paper where the parameter Z holds as a placeholder for an appropriate set of random variables dependent upon the coordinate system i.e. (spherical, Cartesian, or polar).

$$W_{rad}\left(\theta,\phi|\vec{r}_n,\vec{\theta}_n,\vec{\phi}_n\right) = \frac{1}{2\eta}\left|\vec{E}\left(r,\theta,\phi|\vec{r}_n,\vec{\theta}_n,\vec{\phi}_n\right)\right|^2 \simeq \frac{1}{2\eta}\left[\left|E_\theta\left(r,\theta,\phi|\vec{r}_n,\vec{\theta}_n,\vec{\phi}_n\right)\right|^2 + \left|E_\phi\left(r,\theta,\phi|\vec{r}_n,\vec{\theta}_n,\vec{\phi}_n\right)\right|^2\right]$$

$$= \frac{1}{\eta}\left[\left|\frac{F\left(\theta,\phi|\vec{r}_n,\vec{\theta}_n,\vec{\phi}_n\right)}{r}\right|^2\right]\left(\text{For an isotropic radiator}\right) \tag{66}$$

$E_\theta, E_\phi =$ Far-zone electric field of the antenna $\left(\textit{Element Factor}\right) = \left(1 \text{ for an isotropic radiator}\right)$

$$U\left(\theta,\phi|\vec{Z}\right) = r^2 W_{rad}\left(\theta,\phi|\vec{Z}\right) = \frac{\left|F\left(\theta,\phi|\vec{Z}\right)\right|^2}{\eta} \tag{67}$$

$$U\left(\theta,\phi|\vec{Z}\right) \overset{Normalized}{=} \left|F\left(\theta,\phi|\vec{Z}\right)\right|^2 \tag{68}$$

An example of this process is provided for the spherical random array. I.e., let the array factor for an independent and identically distributed (i.i.d.) distribution of isotropic elements be provided as (69) or by using the complex superposition (Euler's identity) with spherical random variables (70) and steering functions (71). These connotations are utilized to provide the outmost compactness and ease in the general process from the array factor provided in (65). Similarly the array factor for a circular random array is

provided by (72) with circular random variables (73). Last of all, an orthonormal steering vector will be defined as $\zeta^{\vec{r}}(\theta,\phi) \triangleq \left(\zeta_x^r(\theta,\phi), \zeta_y^r(\theta,\phi), \zeta_z^r(\theta)\right)$ for simplicity in analysis when referring to the beamsteering functions.

$$F\left(\theta,\phi\middle|x_n,y_n,z_n\right) = \frac{1}{N}\sum_{n=1}^{N} e^{jkr_n\rho_0\left(\sin\theta_n\cos(\phi_n-\xi)+\cos\theta_n\cos\gamma\right)} =$$

$$F\left(\theta,\phi\middle|\Upsilon_n^x,\Upsilon_n^y,\Upsilon_n^z\right) = \frac{1}{N}\sum_{n=1}^{N} e^{j\left(\zeta_x^r(\theta,\phi)\Upsilon_n^x+\zeta_y^r(\theta,\phi)\Upsilon_n^y+\zeta_z^r(\theta)\Upsilon_n^z\right)} = \quad (69)$$

$$\frac{1}{N}\sum_{n=1}^{N}\left(u_n+jv_n\right) = \frac{1}{N}\left(U+jV\right)$$

$$\begin{aligned}
\Upsilon_n^x &= \tilde{r}_n\sin\theta_n\cos\phi_n, \quad -1\le\Upsilon_n^x\le 1\\
\Upsilon_n^y &= \tilde{r}_n\sin\theta_n\sin\phi_n, \quad -1\le\Upsilon_n^y\le 1\\
\Upsilon_n^z &= \tilde{r}_n\cos\theta_n, \quad\quad\quad -1\le\Upsilon_n^z\le 1\\
\tilde{r}_n &= r_n/A, r_n = \sqrt{x_n^2+y_n^2+z_n^2}
\end{aligned} \quad (70)$$

$$\zeta_x^r(\theta,\phi) = \cos(\delta)\zeta(\theta,\phi), \zeta_y^r(\theta,\phi) = \sin(\delta)\zeta(\theta,\phi)$$

$$\zeta_z^r(\theta) = \cos(\gamma)\zeta(\theta,\phi), \zeta(\theta,\phi) \triangleq 2\pi\tilde{A}\rho_o, \tilde{A} = A/\lambda$$

$$\rho_o = \sqrt{\left(\frac{\sin\theta\cos\phi-}{\sin\theta_o\cos\phi_o}\right)^2 + \left(\frac{\sin\theta\sin\phi-}{\sin\theta_o\sin\phi_o}\right)^2} \quad (71)$$

$$\delta = \tan^{-1}\left[\frac{\sin\theta\sin\phi-\sin\theta_0\sin\phi_0}{\sin\theta\cos\phi-\sin\theta_0\cos\phi_0}\right]$$

$$\gamma = \cos^{-1}\left(\rho_0^{-1}\left(\cos\theta-\cos\theta_0\right)\right)$$

$$F\left(\theta,\phi\middle|\upsilon_n^x,\upsilon_n^y\right) = \frac{1}{N}\sum_{n=1}^{N} e^{j\left(\zeta_x^r(\theta,\phi)\upsilon_n^x+\zeta_y^r(\theta,\phi)\upsilon_n^y\right)} =$$

$$\frac{1}{N}\sum_{n=1}^{N}\left(u_n+jv_n\right) = \frac{1}{N}\left(U+jV\right) \quad (72)$$

$$\begin{aligned}
\upsilon_n^x &= \tilde{\rho}_n\cos\phi_n,\\
\upsilon_n^y &= \tilde{\rho}_n\sin\phi_n,\\
\tilde{\rho}_n &= \rho_n/A, \rho_n = \sqrt{x_n^2+y_n^2}
\end{aligned} \quad (73)$$

These constitutive parameters provide enough information to give the normalized mean power pattern

$$U\left(\theta,\phi\middle|\vec{\Upsilon}^{\vec{r}}\right) = \frac{\left|F\left(\theta,\phi\middle|\vec{\Upsilon}^{\vec{r}}\right)F^*\left(\theta,\phi\middle|\vec{\Upsilon}^{\vec{r}}\right)\right|_{Normalized}}{\eta} =$$

$$\frac{1}{N}+\frac{1}{N^2}\sum_{n=1}^{N}\sum_{\substack{m=1\\m\ne n}}^{N} e^{j\zeta_x^r(\theta,\phi)\left(\Upsilon_{x,n}^r-\Upsilon_{x,m}^r\right)} e^{j\zeta_x^r(\theta,\phi)\left(\Upsilon_{y,n}^r-\Upsilon_{y,m}^r\right)} e^{j\zeta_x^r(\theta)\left(\Upsilon_{z,n}^r-\Upsilon_{z,m}^r\right)} = \quad (74)$$

$$\frac{1}{N}+\frac{1}{N^2}\sum_{n=1}^{N}\sum_{\substack{m=1\\m\ne n}}^{N} e^{j\zeta^{\vec{r}}(\theta,\phi)\left(\Upsilon_n^{\vec{r}}-\Upsilon_m^{\vec{r}}\right)}$$

33

The form of (74) may present itself in the form of a spherical solution, however it is also serves as the radiation intensity of a linear, planar, circular, cylindrical, and cubical random array in disguise. For instance, for the circular random array $\theta_n = 90°$ giving (75) and in order to convert (75) to a planar type the trigonometric identity of (76) is used to achieve (77)-(79).

$$U\left(\theta,\phi\big|\vec{\Upsilon}\right) = \frac{1}{N} + \frac{1}{N^2}\sum_{n=1}^{N}\sum_{\substack{m=1\\m\neq n}}^{N} e^{j\zeta(\theta,\phi)\left(\Upsilon_{x,y,n}^{r} - \Upsilon_{x,y,m}^{r}\right)} e^{j\zeta_z^{r}(\theta,\phi)\left(\Upsilon_{z,n}^{r} - \Upsilon_{z,m}^{r}\right)}$$

(75)

$$\vec{\Upsilon}_{x,y}^{r} = \tilde{r}_n \cos\left(\phi_n - \delta\right) \text{ with } -1 \le \vec{\Upsilon}_{x,y}^{r} \le 1$$

$$\cos\left(\alpha - \beta\right) = \cos\alpha\cos\beta - \sin\alpha\sin\beta$$

(76)

$$\vec{\Upsilon}_{x,y}^{r} = \tilde{r}_n\left(\cos\phi_n\cos\delta - \sin\phi_n\sin\delta\right) \text{ with } -1 \le \vec{\Upsilon}_{x,y}^{r} \le 1$$

(77)

$$\vec{\Upsilon}_{x,y}^{r} = \tilde{x}_n\cos\delta - \tilde{y}_n\sin\delta \text{ with } -1 \le \vec{\Upsilon}_{x,y}^{r} \le 1$$

(78)

$$U\left(\theta,\phi\big|\vec{x},\vec{y}\right) = \frac{1}{N} + \frac{1}{N^2}\sum_{n=1}^{N}\sum_{\substack{m=1\\m\neq n}}^{N} e^{j2\pi\tilde{A}\rho_o\left(\tilde{x}_n\cos\delta - \tilde{y}_n\sin\delta - \tilde{x}_m\cos\delta - \tilde{y}_m\sin\delta\right)}$$

$$= \frac{1}{N} + \frac{1}{N^2}\sum_{n=1}^{N}\sum_{\substack{m=1\\m\neq n}}^{N} e^{j2\pi\tilde{A}\left(\left(\tilde{x}_n - \tilde{x}_m\right)\left(\sin\theta\cos\phi - \sin\theta_o\cos\phi_o\right) + \left(\tilde{y}_n - \tilde{y}_m\right)\left(\sin\theta\sin\phi - \sin\theta_o\sin\phi_o\right)\right)}$$

(79)

In fact, one should be aware that the orthonormal steering vector simplifies as

$$\begin{aligned}
\zeta_x^{r}\left(\theta,\phi\right) &= \cos\left(\delta\right)\zeta\left(\theta,\phi\right) = \hat{x}\cdot\left(\hat{r}\left(\theta,\phi\right) - \hat{r}\left(\theta_0,\phi_0\right)\right), \\
\zeta_y^{r}\left(\theta,\phi\right) &= \sin\left(\delta\right)\zeta\left(\theta,\phi\right) = \hat{y}\cdot\left(\hat{r}\left(\theta,\phi\right) - \hat{r}\left(\theta_0,\phi_0\right)\right), \\
\zeta_z^{r}\left(\theta\right) &= \cos\left(\gamma\right)\zeta\left(\theta,\phi\right) = \hat{z}\cdot\left(\hat{r}\left(\theta,\phi\right) - \hat{r}\left(\theta_0,\phi_0\right)\right), \\
\zeta^{\vec{r}}\left(\theta,\phi\right) &= \left\langle \hat{x}\cdot\left(\hat{r}\left(\theta,\phi\right) - \hat{r}\left(\theta_0,\phi_0\right)\right), \hat{y}\cdot\left(\hat{r}\left(\theta,\phi\right) - \hat{r}\left(\theta_0,\phi_0\right)\right), \hat{z}\cdot\left(\hat{r}\left(\theta,\phi\right) - \hat{r}\left(\theta_0,\phi_0\right)\right) \right\rangle
\end{aligned}$$

(80)

3.4 Ground Plane Factor

For some applications the random array may be place above a ground plane. In these situation the ground plane factor (*GF*) is calculated for a two-element linear array along the *z-axis*, with vertically polarized elements (in phase image) where the parameter *h* is the height above the ground plane.

$$GF = e^{jkh\cos\theta} + e^{-jkh\cos\theta} = 2\cos\left(kh\cos\theta\right)$$

(81)

Thus the total array factor is rewritten as a pattern multiplication of the array factor, ground plane factor and element factor.

$$\begin{aligned}
\vec{AF}\left(\theta,\phi\right) &= F\left(\theta,\phi\right)_{norm} GF_{norm} \vec{EF}_{norm} \\
&= \left(F\left(\theta,\phi\right)\cdot GF\cdot\vec{EF}\right)_{norm} \\
&= F\left(\theta,\phi\right)_{norm}\cos\left(kh\cos\theta\right)\vec{EF}_{norm}
\end{aligned}$$

(82)

In general, the element factor will have both Θ and ϕ components as shown in (86) (dipole). Hence, the array factor can be analyzed similar to [58]. This causes the total *AF* to have both azimuthal and elevation components as well. For example, if two half wave dipoles are aligned with the x axis ($\hat{I} = \hat{x}$, horizontal polarization) the element factor can be found from (83) [105] giving (84)-(86).

$$\vec{E}(\theta,\phi) = -\frac{j\eta_0 I_m e^{-jkr}}{2\pi r}\left[\frac{\cos\left(\frac{\pi}{2}\hat{r}\cdot\hat{I}\right)}{1-\left(\hat{r}\cdot\hat{I}\right)^2}\right]\cos\theta\cos\phi \tag{83}$$

$$EF_\theta = -\frac{j\eta_0 I_m e^{-jkr}}{2\pi r}\left[\frac{\cos\left(\frac{\pi}{2}\sin\theta\cos\phi\right)}{1-\sin^2\theta\cos^2\phi}\right]\cos\theta\cos\phi \tag{84}$$

$$\hat{\theta}\cdot\hat{I} = \cos\theta\cos\phi$$

$$EF_\phi = \frac{j\eta_0 I_m e^{-jkr}}{2\pi r}\left[\frac{\cos\left(\frac{\pi}{2}\sin\theta\cos\phi\right)}{1-\sin^2\theta\cos^2\phi}\right]\sin\phi \tag{85}$$

$$\hat{\phi}\cdot\hat{I} = -\sin\phi$$

$$\vec{EF}_{norm} = \vec{E}_{Normalized} \approx \vec{A}_T = \frac{e^{-jkr}}{4\pi r}\left(\hat{\theta}+\hat{\phi}\right) \tag{86}$$

To normalize these equations the leading factor $j\eta_0 I_m e^{-jkr}/2\pi r$ is simply removed and then the array factor would have two components associated with it like that of [58] provided in (82). Otherwise one could obtain the array factor independently of the element factor, which is done in this dissertation. Also no loss of generality occurs due to the independency of pattern multiplication. Lastly, the ground plane factor will be ignored in this dissertation, but was shown for completeness of array theory.

3.5 Mean Valued Radiation Intensity

Collaborative beamforming is perhaps one of the most popular and one of the newest techniques in the application of wireless communications and array theory. The technique is responsible for the generation of a beampattern using a randomly distributed antenna array with fitting phase coefficient for the elements. However, the mechanisms of the process are so complicated that a complete description of the pattern is impractical. Hence, insofar as system analysis is concerned, an average characterization of the beampattern phenomenon is adequate for the problem at hand. This type of solution gives more insight of the beampattern by giving a mathematical description; whereas previous analysis describes these type of phenomenal formulates by means of diffraction patterns. Such studies of randomly located dots in a

Bravais lattice [74]-[75] uses the fast Fourier transform (FFT) to explain the structure of crystals. The FFT thereby gives one the desired and necessary diffraction pattern of the phenomena, but the method loses mathematical foundation and description of the generated pattern. Additional analysis of diffraction patterns is found for circular and rectangular apertures in [76] using the Fourier Bessel transform. This type of solution helps provide one with mathematical clarity of the generated diffraction patterns. Now a newly developed theory has been observed and will be shown in this paper for transforming between the Bessel Fourier transform and Fourier transform. This method aids in the calculation of these radiation characteristics or so-called diffraction patterns and will be shown in application to those of random array environments.

When discussing an aperiodic (random) array it interesting to find the mean or expected value of the beampattern in order to obtain clearer understanding of its radiative characteristics. This average radiation intensity can be calculated by taking the expectation of the beampattern (87). Therefore, when (87) is applied to (68) one will have the appropriate recipe of calculating an average radiation intensity given in (88).

$$E_Z\left|U\left(\theta,\phi\middle|\vec{Z}\right)\right| = \sum_{m=1}^{N}\sum_{n=1}^{N}\int_{-\infty}^{\infty}\int_{-\infty}^{\infty}U\left(\theta,\phi\middle|\vec{Z}\right)f\left(Z_n\right)f\left(Z_m\right)dZ_n dZ_m \tag{87}$$

$$E_Z\left|U\left(\theta,\phi\middle|\vec{Z}\right)\right| = \int_{-\infty}^{\infty}\int_{-\infty}^{\infty}\left(\frac{1}{N} + \frac{1}{N^2}\sum_{m=1}^{N}\sum_{\substack{n=1\\n\neq m}}^{N}e^{j(Z_n(\theta,\phi)-Z_m(\theta,\phi))}\right)f\left(Z_n\right)f\left(Z_m\right)dZ_n dZ_m \tag{88}$$

For the spherical coordinate system (88) takes the form of (89).

$$E_{\Upsilon^{\vec{r}}}\left|U\left(\theta,\phi\middle|\vec{\Upsilon}^{\vec{r}}\right)\right| = \int_{-\infty}^{\infty}\int_{-\infty}^{\infty}\left(\frac{1}{N} + \frac{1}{N^2}\sum_{m=1}^{N}\sum_{\substack{n=1\\n\neq m}}^{N}e^{j\zeta^{\vec{r}}(\theta,\phi)\left(\Upsilon_n^{\vec{r}}-\Upsilon_m^{\vec{r}}\right)}\right)f\left(\Upsilon_n^{\vec{r}}\right)f\left(\Upsilon_m^{\vec{r}}\right)d\Upsilon_n^{\vec{r}}d\Upsilon_m^{\vec{r}} =$$

$$E_{\Upsilon_x^r,\Upsilon_x^r,\Upsilon_z^r}\left|U\left(\theta,\phi\middle|\vec{\Upsilon}_x^r,\vec{\Upsilon}_y^r,\vec{\Upsilon}_z^r\right)\right| = \int_{-\infty}^{\infty}\int_{-\infty}^{\infty}\int_{-\infty}^{\infty}\int_{-\infty}^{\infty}\int_{-\infty}^{\infty}\int_{-\infty}^{\infty}\left(\frac{1}{N} + \frac{1}{N^2}\sum_{m=1}^{N}\sum_{\substack{n=1\\n\neq m}}^{N}\left[\begin{array}{c}e^{j\zeta_x^r(\theta,\phi)\left(\Upsilon_{x,n}^r-\Upsilon_{x,m}^r\right)}\\e^{j\zeta_y^r(\theta,\phi)\left(\Upsilon_{y,n}^r-\Upsilon_{y,m}^r\right)}\\e^{j\zeta_z^r(\theta,\phi)\left(\Upsilon_{z,n}^r-\Upsilon_{z,m}^r\right)}\end{array}\right]\right)$$
$$f\left(\Upsilon_{x,n}^r\right)f\left(\Upsilon_{x,m}^r\right)d\Upsilon_{x,n}^r d\Upsilon_{x,m}^r$$
$$f\left(\Upsilon_{y,n}^r\right)f\left(\Upsilon_{y,m}^r\right)d\Upsilon_{y,n}^r d\Upsilon_{y,m}^r$$
$$f\left(\Upsilon_{z,n}^r\right)f\left(\Upsilon_{z,m}^r\right)d\Upsilon_{z,n}^r d\Upsilon_{z,m}^r \tag{89}$$

Interchanging integration with summation leads to (90) and it is observed that the term *1/N* separates from the expression since the integration is done over the entire distribution space; or in other words the cumulative distribution over the entire space is equal to one. Now applying a summation identity [81] of (91) in succession provides (92). Also since the orthonormal beamsteering coefficient and orthonormal

compound random array are independent as illustrated in (89) the mean valued array factor of (93) can also be rewritten as that of (94), which will be used throughout this dissertation.

$$E_{\vec{\Upsilon}^{\vec{r}}}\left|U\left(\theta,\phi\middle|\vec{\Upsilon}^{\vec{r}}\right)\right| = \frac{1}{N} + \frac{1}{N^2}\sum_{m=1}^{N}\sum_{\substack{n=1\\n\neq m}}^{N}\int_{-\infty}^{\infty}\int_{-\infty}^{\infty}e^{j\zeta^{\vec{r}}(\theta,\phi)\left(\Upsilon_n^{\vec{r}}-\Upsilon_m^{\vec{r}}\right)}f\left(\Upsilon_n^{\vec{r}}\right)f\left(\Upsilon_m^{\vec{r}}\right)d\Upsilon_n^{\vec{r}}d\Upsilon_m^{\vec{r}} \qquad (90)$$

$$\sum_{m=1}^{N}\sum_{\substack{n=1\\n\neq m}}^{N}e^{j\alpha(x_n-x_m)}e^{j\beta(y_n-y_m)}e^{j\chi(z_n-z_m)} =$$

$$N(N-1)\begin{bmatrix}\cos\left(\alpha(x_n-x_m)+\beta(y_n-y_m)+\chi(z_n-z_m)\right)+\\ j\sin\left(\alpha(x_n-x_m)+\beta(y_n-y_m)+\chi(z_n-z_m)\right)\end{bmatrix} \qquad (91)$$

$$E_{\Upsilon^{\vec{r}}}\left|U\left(\theta,\phi\middle|\vec{\Upsilon}^{\vec{r}}\right)\right| =$$

$$\frac{1}{N}+\left(1-\frac{1}{N}\right)\int_{-\infty}^{\infty}\int_{-\infty}^{\infty}\begin{pmatrix}\cos\left(\zeta^{\vec{r}}(\theta,\phi)\left(\Upsilon_n^{\vec{r}}-\Upsilon_m^{\vec{r}}\right)\right)+\\ j\sin\left(\zeta^{\vec{r}}(\theta,\phi)\left(\Upsilon_n^{\vec{r}}-\Upsilon_m^{\vec{r}}\right)\right)\end{pmatrix}f\left(\Upsilon_n^{\vec{r}}\right)f\left(\Upsilon_m^{\vec{r}}\right)d\Upsilon_n^{\vec{r}}d\Upsilon_m^{\vec{r}} \qquad (92)$$

$$\bar{U}(\theta,\phi) = E_{\Upsilon^{\vec{r}}}\left|U\left(\theta,\phi\middle|\vec{\Upsilon}^{\vec{r}}\right)\right| = \frac{1}{N}+\left(1-\frac{1}{N}\right)|\Lambda|^2$$

$$= \left|\Lambda\left(\zeta_x^r(\theta,\phi)\right)\Lambda\left(\zeta_y^r(\theta,\phi)\right)\Lambda\left(\zeta_z^r(\theta)\right)\right|^2, \qquad (93)$$

$$\Lambda = \left[\text{Main Lobe Factor}\right] = \left|\text{Characteristic Function}\right|^2$$

$$\bar{U}(\theta,\phi) = E_{\Upsilon^{\vec{r}}}\left|U\left(\theta,\phi\middle|\vec{\Upsilon}^{\vec{r}}\right)\right| = \frac{1}{N}+\left(1-\frac{1}{N}\right)\left|\Lambda\left(\zeta_x^r(\theta,\phi)\right)\right|^2\left|\Lambda\left(\zeta_y^r(\theta,\phi)\right)\right|^2\left|\Lambda\left(\zeta_z^r(\theta)\right)\right|^2, \qquad (94)$$

The resultant radiation pattern exhibits a convenient addition of two distinct terms. The first parameter represents the average power level of the side lobes; it is interesting to note this term is independent of location. The second term represents the main beam and one sees that this is represented by taking the Fourier transform of the probability density function. Or in probability theory this type of equation is commonly known as the characteristic function and completely describes the main beam of the array. These characteristic functions [31], [77]-[79] provide a useful method for analyzing probability distributions. For this dissertation and in most instances, the domain is taken to be Euclidean space and although the integral transforms may not have a simple expression, some qualitative features about the radiation characteristics of the underlying probability distribution can often be extracted. Research efforts in spaces more complicated than the Euclidean case, offer very little on characteristic functions and limited availability on probability distributions of these general domains [80]. Therefore, characteristic functions for a uniform and Gaussian distribution are explored on a general Euclidean domain since these distributions are highly likely in practice once the number of elements is large enough. In summary it has been found that for the random array problem Fourier transforms are taken with respect to the irreducible representations thereby producing a concrete expression of which the characteristic function is obtained in its complete solution.

Next one must consider that a spherical random array of isotropic radiators will present unique features of its overall mean valued radiation pattern. For example, there should be no fundamental difference as to whether the beam is scanned at broadside or endfire. Hence, these typical notations should essentially lose their physical meaning for a spherical random array, except when applied mathematically to the steering vector in (71). By this deduction it is seen that Figure 17 behaves correctly while Figure 18 does not. Second the random variables Υ_n and T_n utilized in [6], [81]-[82] have been replaced by the correctly defined orthonormal random variable $\Upsilon_n^{\vec{r}} \triangleq \{ \quad \Upsilon_n^x = \tilde{r}_n \sin\theta_n \cos\phi_n, \Upsilon_n^y = \tilde{r}_n \sin\theta_n \sin\phi_n \quad$ and $\Upsilon_n^z = \tilde{r}_n \cos\theta_n \}$. Furthermore, the compound random variable T_n was thought to be constructed as a double sided Wigner semi-circle distribution as it appeared from the work in [82], which has appeared to be incorrect by the results of Figure 18 and (95). The fundamental error with this is that the random variable $\tilde{r}_n$ is spherically defined rather than cylindrically $\tilde{\rho}_n$. As a consequence, $\Upsilon_n^z = \tilde{r}_n \cos\theta_n$ is considered to rather be a parabolic (or spherical) distribution. Hence, the orthonormal random variable is distributed the same along all three coordinates with corrected mean radiation intensity of a spherical $\tilde{A} = 2.77$ and circular random array $\tilde{A} = 2$ specified in (96)-(97) illustrated in Figure 17-Figure 25.
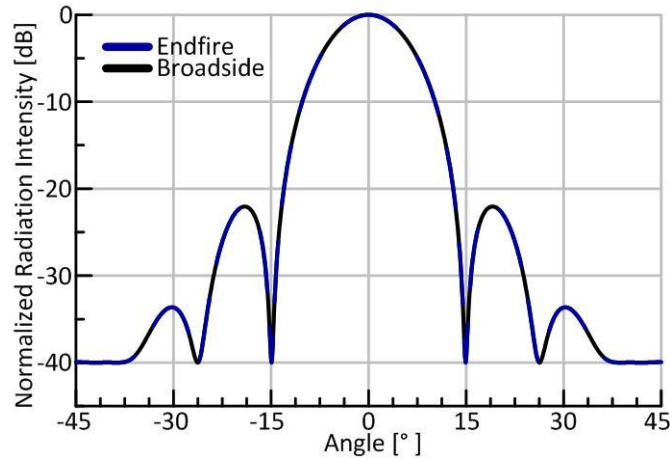
Figure 17. SRA pattern with corrected analysis (96) from [6]-[14] and [81]-[82].
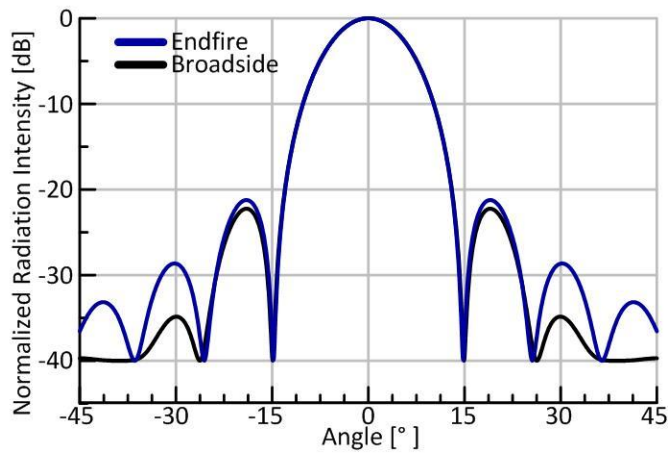
Figure 18. SRA pattern with incorrect analysis (95) from [6]-[14] and [81]-[82].
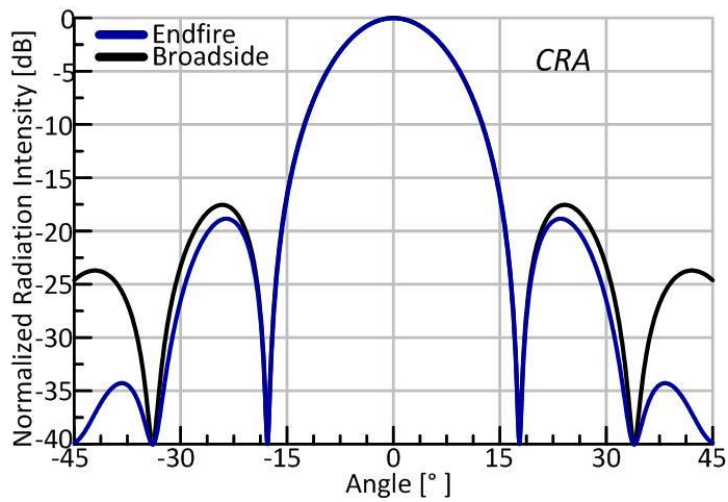
Figure 19. CRA pattern with corrected analysis (97) from [6]-[14] and [81]-[82].
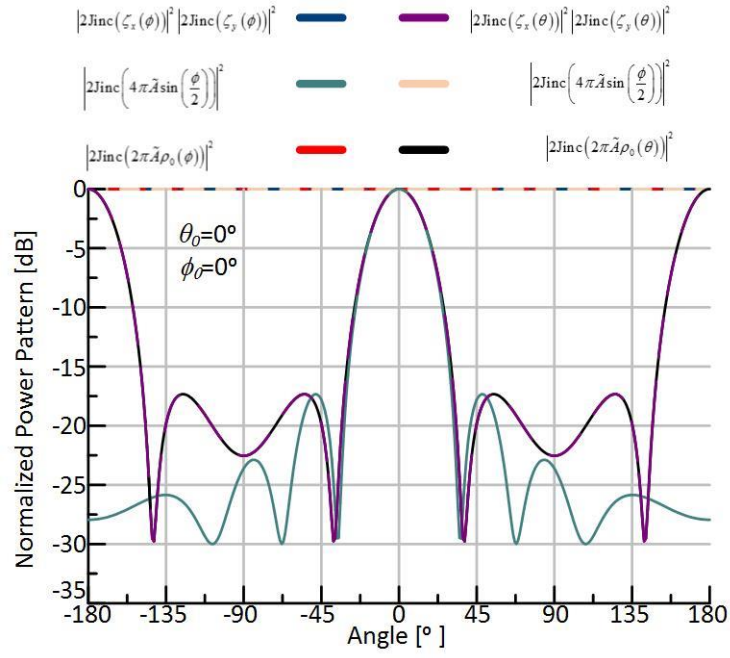
Figure 20. Comparison of the CRA solutions at broadside $\tilde{A} = 1$.
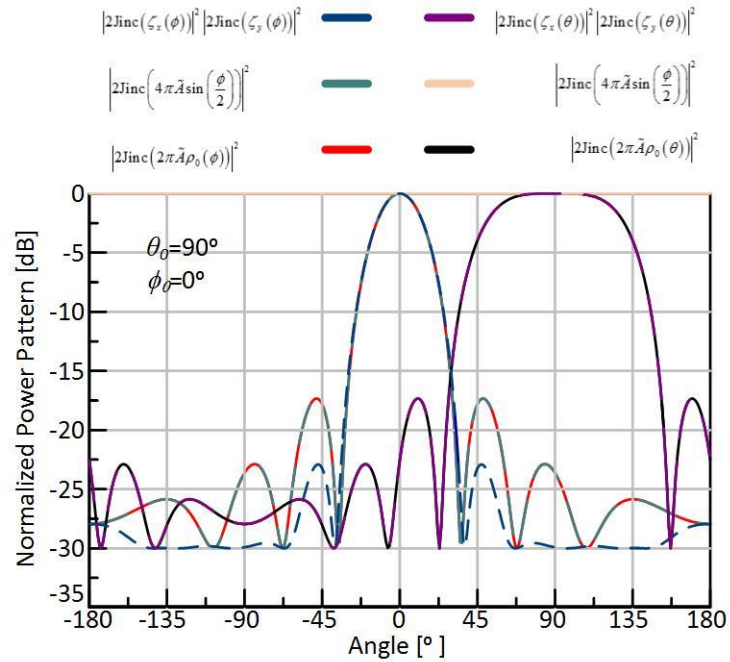
Figure 21. Comparison of the CRA solutions at endfire $\tilde{A} = 1$.

40
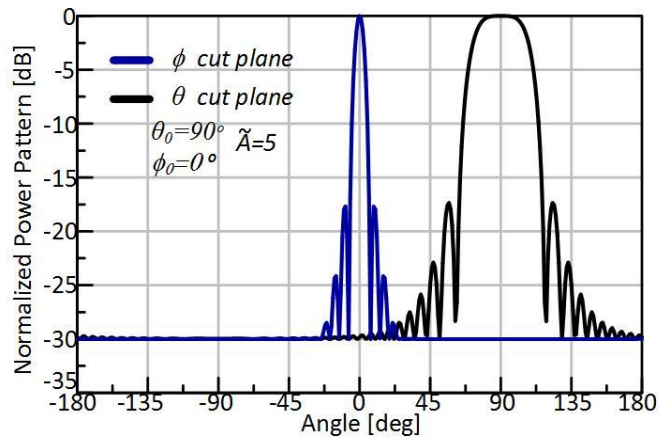
Figure 22. CRA pattern with corrected analysis (97) in both cut planes.
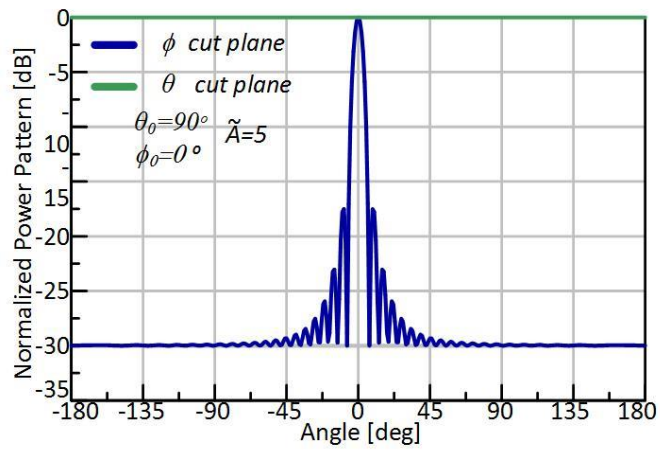
Figure 23. CRA pattern with incorrect analysis in both cut planes.
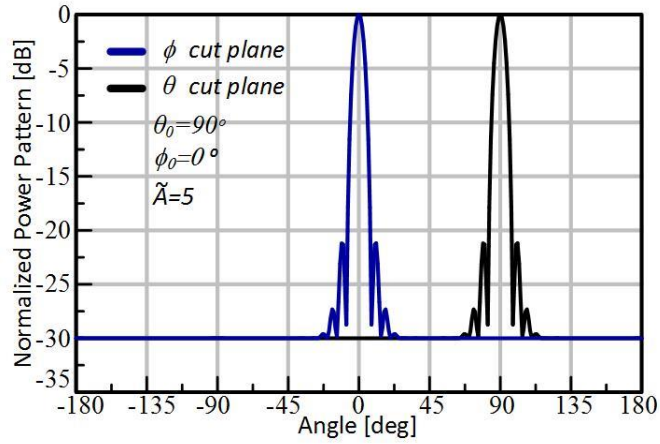
Figure 24. SRA pattern with corrected analysis (96) in both cut planes.
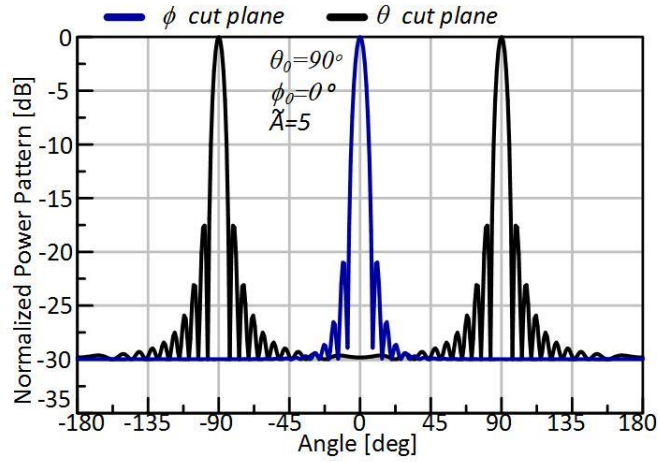
Figure 25. SRA pattern with incorrect analysis in both cut planes.

$$F\left(\theta,\phi\,|\,\Upsilon_n,\mathrm{T}_n\right) = \frac{1}{N}\sum_{n=1}^{N} e^{j\zeta(\theta,\phi)\Upsilon_n + \xi(\theta)\mathrm{T}_n}$$

$$\Upsilon_n = \tilde{r}_n \sin\theta_n \cos\tilde{\phi}_n, \quad -1 \le \Upsilon \le 1 \tag{95}$$

$$\mathrm{T} = \tilde{r}_n \cos\theta_n, \qquad -1 \le \mathrm{T} \le 1$$

$$\tilde{\phi}_n = \phi_n - \delta$$

$$\bar{U}\left(\theta,\phi\right) \overset{Sph}{=} \frac{1}{N} + \left(1 - \frac{1}{N}\right)\begin{bmatrix} 3\mathrm{tinc}\left|\zeta_x^r\left(\theta,\phi\right)\right|^2 \\ 3\mathrm{tinc}\left|\zeta_y^r\left(\theta,\phi\right)\right|^2 \\ 3\mathrm{tinc}\left|\zeta_z^r\left(\theta\right)\right|^2 \end{bmatrix}, \mathrm{tinc}\left(x\right) = \frac{j_1\left(x\right)}{x} \tag{96}$$

42

$$\bar{U}(\theta,\phi) \overset{Cir}{=} \frac{1}{N} + \left(1 - \frac{1}{N}\right)\left[\begin{array}{c} 2\mathrm{jinc}\left|\zeta_x^r(\theta,\phi)\right|^2 \\ 2\mathrm{jinc}\left|\zeta_y^r(\theta,\phi)\right|^2 \end{array}\right], \mathrm{jinc}(x) = \frac{J_1(x)}{x} \tag{97}$$

3.6 Focal Distance

The distance between the nth element and the origin can be calculated in multiple fashions. I.e. one may truncate the binomial expansion of the length by any one of the following series below where the array is assumed phase at the point of interest $\psi = 0$. For instance, the solution of (98) is due when the pattern is taken in the near field or Fresnel zone. The transform contains the quadratic term and introduces a phase shift of $-(1/2r)$ and has the possibility of canceling the quadratic term since $r_n^2\left(\frac{1}{2r} - \frac{1}{2r}\right) = 0$. More so at this range the beam pattern is equivalent to the beam pattern at infinity. Or mathematically the mean valued radiation intensity is reduced to that of (99).

$$\left|\vec{R}_n\left(\theta,\phi\middle|r_n,\theta_n,\phi_n\right)\right| = \left|r - r_n\right| \approx r + \frac{1}{2}r\left(-\frac{2\cos\psi_n r_n}{r} + \frac{r_n^2}{r^2}\right) = r - r_n + \left.\frac{r_n^2}{2r}\right|_{\psi=0} \tag{98}$$

$$\bar{U}(r,\theta,\phi) = \bar{U}(\theta,\phi) \tag{99}$$

Alternatively the mean valued array factor can be written as (100) where r_0 is the focal distance and the term $r_n^2/2r$ is the correction factor in the near field.

$$\bar{F}\left(r,\theta,\phi\middle|r_n,\theta_n,\phi_n\right) = \bar{F}\left(r,\theta,\phi\middle|r_n,\cos\psi_n\right) =$$
$$\int pdf\left(r_n,\psi_n\right)\exp\left[jk\left(r_n\cos\psi_n + \frac{r_n^2}{2r_0} - \frac{r_n^2}{2r}\right)\right]r_n^2\sin\theta_n dr_n d\theta_n d\phi_n \tag{100}$$

For simplicity a linear random array is assumed along the x axis reducing (100) on axis (beamsteered to $-r_n\cos\psi_{n0}$) to

$$\bar{F}(r,\theta,\phi|x_n,0) = \int pdf\left(x_n\right)\exp\left[jkx_n^2\left(\frac{1}{2\Delta r}\right)\right]dx_n \tag{101}$$

A notional example of the depth of the field Δr is shown in Figure 26 and is the factor of interest now of which it will be determined within what range the pattern can be taken such that it is within 3dB of its peak value. This is also referred to as the half-power beamwidth in range. "This expression for the depth of field is appropriate only when it is small compared to the focal distance. When the focal point approaches the near-field-far-field transition, the depth of field approaches the focal distance." [101] By this means the hyperfocal distance is to be defined as the given focal distance of which is in focus out to infinity and on axis i.e. $(\cos\psi - \cos\psi_0) = 0$. Furthermore the hyperfocal distance is 3dB above the field

strength at infinity (ignoring geometrical spreading i.e. path loss). For simplicity again assume a linear random array oriented along the *x-axis* and let $r_0 = r_h$ with array factor

$$F\left(r_h | x_n\right) = \frac{1}{2A} \int_{-A/2}^{A/2} 1\, dx = 1 \tag{102}$$
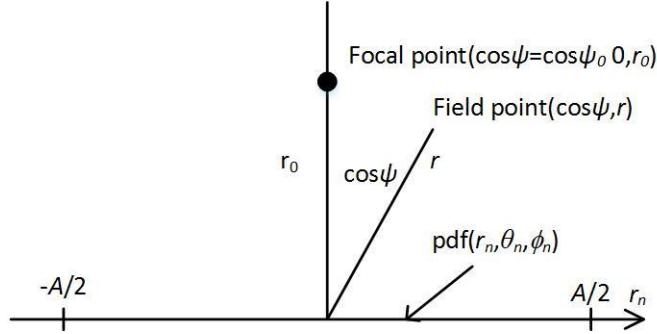
Figure 26. Focused aperture and field point.

The corresponding value at infinity is provided as

$$F\left(r_h = \infty | x_n\right) = \frac{1}{2A} \int_{-A/2}^{A/2} \exp\left(j\frac{kx_n^2}{2r_h}\right) dx = \frac{2}{2A} \int_{0}^{A/2} \exp\left(j\frac{kx_n^2}{2r_h}\right) dx \tag{103}$$

Now since the power is 3dB greater at the hyperfocal distance

$$F\left(r_h = \infty | x_n\right) = \frac{1}{\sqrt{2}} F\left(r_h | x_n\right) = \frac{1}{\sqrt{2}} \tag{104}$$

Next combining (103) and (105) yields

$$\int_{0}^{A/2} \exp\left(j\frac{kx_n^2}{2r_h}\right) dx = \frac{2A}{2\sqrt{2}} \tag{106}$$

Now rewriting this in the form

$$\int_{0}^{A/2} \exp\left(j\frac{\pi t^2}{2r_h}\right) dt = \frac{X}{\sqrt{2}}$$

$$t = x\sqrt{2/\lambda r_h}, \ X = \frac{2A}{\sqrt{2\lambda r_h}} \tag{107}$$

Which is easily evaluated using the Cornu spiral one finds $X = .94\sqrt{2}$. Hence, the hyperfocal distance becomes

$$r_h = \frac{(2A)^2}{3.5\lambda} \tag{108}$$

Which is approximately 1/3 the distance of the far field condition $2(2A)^2/3.5\lambda$. Differently the 3dB near-focal distance r_1 is the distance on the near side of the hyperfocal distance again on axis and can be calculated as

$$F(r_1|x_n) = \frac{1}{2A} \int_{-A/2}^{A/2} \exp\left(j\frac{kx_n^2}{2}\left(\frac{1}{r_h} - \frac{1}{r_1} \right) \right) dx = \frac{1}{\sqrt{2}} \tag{109}$$

In order to calculate r_1 we first observe that (110) contains two solutions by being quadratic. One solution is out at infinity by definition. Hence this reduces as

$$F(r_1 = \infty | x_n) = \frac{1}{2A} \int_{-A/2}^{A/2} \exp\left(j\frac{kx_n^2}{2}\left(\frac{1}{r_h} \right) \right) dx = \frac{1}{\sqrt{2}} \tag{111}$$

Thus, the term $kx_n^2/2r_h$ is one of the solutions. Also since this is a quadratic equation $-kx_n^2/2r_h$ is also a solution such that

$$j\frac{kx_n^2}{2}\left(\frac{1}{r_h} - \frac{1}{r_1} \right) = -j\frac{kx_n^2}{2}\left(\frac{1}{r_h} \right) \tag{112}$$

$$\left(\frac{1}{r_h} - \frac{1}{r_1} \right) = -\left(\frac{1}{r_h} \right) \tag{113}$$

$$r_1 = \frac{r_h}{2} \tag{114}$$

Now upon substitution of the hyperfocal distance of (115) the near field hyperfocal range is

$$r_1 = \frac{(2A)^2}{7\lambda} \tag{116}$$

The results of these expressions are shown such that the array is focused at infinity in Figure 27. Here it is seen that rays propagate as linear lines out to infinity after leaving the length of the aperture (2A). Alternatively if one is to measure at the hyperfocal distance the rays are uniformly excited upon the hyperfocal distance as shown in Figure 28. Hence, the hyperfocal distance, near-field-far-field transition range, the hyperfocal distance and the near-focal distance are all readily visualized.
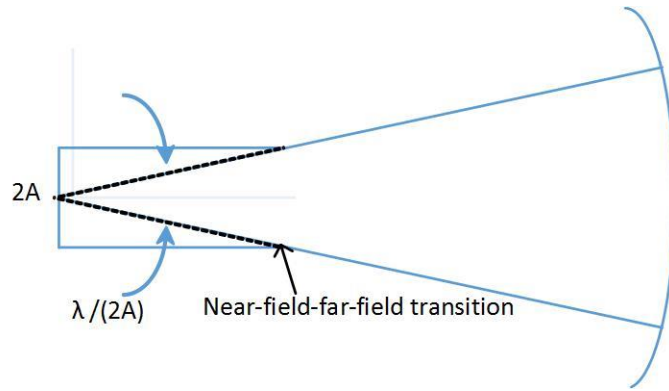
Figure 27. Focused at infinity.
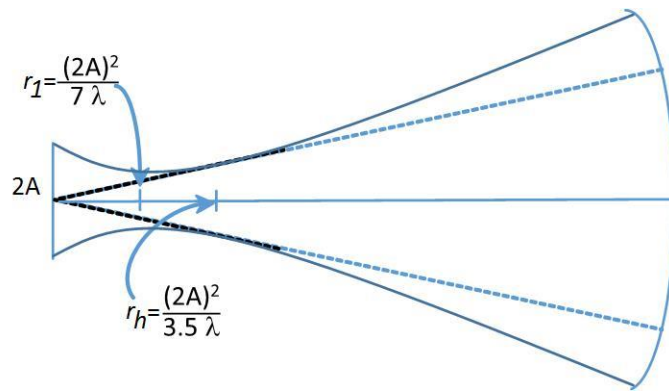
Figure 28. Focused at the hyperfocal distance (near focal range also shown).

Last of all this section followed in analysis similar to [101], which found the hyperfocal distance and near focal range of a linear random array. Instead to find these parameters for other types of distributions namely circular and spherical, which have been the main interest presented in this work. One should change the distribution of (102) with the appropriate distribution function. From there the mechanics are the same and it is assumed that the solutions will vary slightly from the solutions derived in this section. Also the same type of analysis can be repeated for hyperfocal distances of higher order by solving the solutions of (117) and (118). These will likely have three solutions for (117) and four solutions for (118). They will be much more difficult to solve and at the present their total value worth in doing so is unknown.

$$\left| \vec{R}_n \left(\theta, \phi \middle| r_n, \theta_n, \phi_n \right) \right| = \left| r - r_n \right|$$

$$\approx r + \frac{1}{2} r \left(-\frac{2\cos\psi_n r_n}{r} + \frac{r_n^2}{r^2} \right) - \frac{1}{8} r \left(-\frac{2\cos\psi_n r_n}{r} + \frac{r_n^2}{r^2} \right)^2 \tag{117}$$

$$= r - r_n + \frac{r_n^3}{2r^2} - \frac{r_n^4}{8r^3} \Bigg|_{\psi=0}$$

$$\left| \vec{R}_n \left(\theta, \phi \middle| r_n, \theta_n, \phi_n \right) \right| = \left| r - r_n \right|$$

$$\approx r + \frac{1}{2} r \left(-\frac{2\cos\psi_n r_n}{r} + \frac{r_n^2}{r^2} \right) - \frac{1}{8} r \left(-\frac{2\cos\psi_n r_n}{r} + \frac{r_n^2}{r^2} \right)^2 + \frac{1}{16} r \left(-\frac{2\cos\psi_n r_n}{r} + \frac{r_n^2}{r^2} \right)^3 + \ldots \tag{118}$$

$$= r - r_n + \frac{5r_n^4}{8r^3} - \frac{3r_n^5}{8r^4} + \frac{r_n^6}{16r^5} \Bigg|_{\psi=0}$$

CHAPTER IV

THE MEAN VALUED RADIATION PATTERN OF PLANAR, CYLINDRICAL AND

SPHERICAL RANDOM ARRAYS

A complete unified theory of the deterministic aperiodic array ceases to exist, but curiously enough such a theory for the random array has been developed even though many of the properties are considered peculiar and unexpected. This theory exists because the mathematics of random processes, that is, statistics, can be applied. [59]

4.1 Mean Valued Radiation Intensity of a Circular Random Array without Using Compound Random Variables

To simplify the analysis and illustration of the process this section focuses upon a circular random array's beampattern (119).

$$U_{av}(\theta,\phi) = E_{\rho,\phi}\left|U\left(\theta,\phi\middle|\tilde{\rho}_n,\tilde{\phi}_n\right)\right| = \frac{1}{N} + \left(1-\frac{1}{N}\right)\left|\int_0^1\int_0^{2\pi} e^{j\tilde{\rho}_n\cos\tilde{\phi}_n\left(\zeta_x^r(\theta,\phi)+\zeta_y^r(\theta,\phi)\right)}\frac{1}{2\pi}d\tilde{\phi}_n 2\tilde{\rho}_n d\tilde{\rho}_n\right|^2 \quad (119)$$

The main lobe factor of (119) is found by means of taking the Fourier Bessel transform. In order to solve this one uses a Bessel identity (120) to obtain (121). Identity (122) solves the successive integral relation providing (123) in final form.

$$J_0(x) = \frac{1}{2\pi}\int_0^{2\pi} e^{jx\cos\phi}d\phi \quad (120)$$

$$= \frac{1}{N} + \left(1-\frac{1}{N}\right)\int_0^1\int_0^1 J_0\left(\zeta(\theta,\phi)\tilde{\rho}_n\right)J_0\left(\zeta(\theta,\phi)\tilde{\rho}_m\right)2\tilde{\rho}_n 2\tilde{\rho}_m d\tilde{\rho}_m d\tilde{\rho}_n \quad (121)$$

$$\int_0^z xJ_o(x)dx = zJ_1(z) \quad (122)$$

$$\bar{U}(\theta,\phi) = \frac{1}{N} + \left(1-\frac{1}{N}\right)\left|2\frac{J_1\zeta_x^r(\theta,\phi)}{\zeta_x^r(\theta,\phi)}2\frac{J_1\zeta_y^r(\theta,\phi)}{\zeta_y^r(\theta,\phi)}\right|^2 =$$
$$\frac{1}{N} + \left(1-\frac{1}{N}\right)\left|2\,\mathrm{jinc}\left(\zeta_x^r(\theta,\phi)\right)\right|^2\left|2\,\mathrm{jinc}\left(\zeta_y^r(\theta,\phi)\right)\right|^2 \quad (123)$$

A spatially damped oscillatory sinusoid known as the jinc function [84] characterizes the beampattern. More comprehensive analyses of the jinc function may be found in [73].

The same approach used to obtain (123) can similarly be used to obtain the average radiation intensity of a spherical random array given in (124). Although this process involves taking both spherical and Bessel Fourier transform (124). As a consequence, pattern multiplication consists this time around in

the main described by spatially damped oscillatory sinusoids (better known as the jinc function and tinc functions) [68] and [73].

$$U_{av}(\theta,\phi) = E_{\rho,\phi}\left|U\left(\theta,\phi\middle|\tilde{r}_n,\tilde{\theta}_n,\tilde{\phi}_n\right)\right|$$

$$= \frac{1}{N} + \left(1 - \frac{1}{N}\right)\left|\int_0^1\int_0^\pi\int_0^{2\pi}\Re e\left[e^{j\zeta_x^r(\theta,\phi)\left(\tilde{r}_n\sin\tilde{\theta}_n\cos\tilde{\phi}_n\right)}e^{j\zeta_y^r(\theta,\phi)\left(\tilde{r}_n\sin\tilde{\theta}_n\sin\tilde{\phi}_n\right)}e^{j\zeta_z^r(\theta)\left(\tilde{r}_n\cos\tilde{\theta}_m\right)}\right]\frac{3}{4\pi}\tilde{r}_n^2\sin\tilde{\theta}_n\,d\tilde{\phi}_n\,d\tilde{\theta}_n\,d\tilde{r}_n\right|^2 \quad (124)$$

$$= \frac{1}{N} + \left(1 - \frac{1}{N}\right)\left|3\mathrm{tinc}\left(\zeta_x^r(\theta,\phi)\right)\right|^2\left|3\mathrm{tinc}\left(\zeta_y^r(\theta,\phi)\right)\right|^2\left|3\mathrm{tinc}\left(\zeta_z^r(\theta)\right)\right|^2$$

4.2 Mean Valued Radiation Intensity of a Circular Random Array Using Compound Random

Variables

The radiation intensity of a circular random array rewritten in terms of compound random variables (75) defines a mainlobe factor in terms of the Fourier transform. This appears as an alternative to the Bessel Fourier transform (119) and the corresponding integral relation is shown in (125) giving (126).

$$U_{av}(\theta,\phi) = \frac{1}{N} + \left(1 - \frac{1}{N}\right)\left|\int_{-1}^1\cos\left(\left(\zeta_x^r(\theta,\phi) + \zeta_y^r(\theta,\phi)\right)\upsilon_n\right)\frac{2}{\pi}\sqrt{1-\upsilon_n^2}\,d\upsilon_n\right|^2 \tag{125}$$

$$U_{av}(\theta,\phi) = \frac{1}{N} + \left(1 - \frac{1}{N}\right)\left|2\frac{J_1\zeta_x^r(\theta,\phi)}{\zeta_x^r(\theta,\phi)}2\frac{J_1\zeta_y^r(\theta,\phi)}{\zeta_y^r(\theta,\phi)}\right|^2 =$$

$$\frac{1}{N} + \left(1 - \frac{1}{N}\right)\left|2\mathrm{jinc}\left(\zeta_x^r(\theta,\phi)\right)\right|^2\left|2\mathrm{jinc}\left(\zeta_y^r(\theta,\phi)\right)\right|^2 \tag{126}$$

The final form of (123) and (126) are shown to be equal; but derived in two different fashions. One method derives the relation by means of the Fourier Bessel transform whereas the second method used the Fourier transform. The benefit of introducing compound random variables is seen to reduce the number of integrals required to solve the problem at hand. In addition it relates the main beam to a more well-known and understood Fourier transform relation. Further examples and demonstrations of this process can be found in [6] and [82].

4.3 Discrete Fourier Transform Radiation Intensity

For a discrete uniform Distribution the probability mass function is given as (127). Like in previous examples the expected beampattern is solved by simply looking at the characteristic function of the distribution. I.e. for the case of a uniform linear distribution one finds a radiation intensity given by the process in (128)-(130) and for one centered at the origin (131) [128].

$$f(x) = \frac{1}{n} \quad a \le x \le b$$

$$n = b - a + 1 \tag{127}$$

$$E_x\left|U\left(\theta,\phi\middle|\vec{x}\right)\right| = \frac{1}{N} + \left(1 - \frac{1}{N}\right)\sum_{n=-a}^b\sum_{m=-a}^b e^{j\alpha(\theta,\phi)(x_n-x_m)}f(x_n)f(x_m)\,dx_n\,dx_m \tag{128}$$

49

$$E_x\left|U\left(\theta,\phi|\vec{x}\right)\right| = \frac{1}{N} + \left(1 - \frac{1}{N}\right)|\Lambda|^2 \tag{129}$$

$$E_x\left|U\left(\theta,\phi|\vec{x}\right)\right| = \frac{1}{N} + \left(1 - \frac{1}{N}\right)\left|\frac{e^{ja\alpha(\theta,\phi)} - e^{j(b+1)\alpha(\theta,\phi)}}{n\left(1 - e^{j\alpha(\theta,\phi)}\right)}\right|^2 \tag{130}$$

$$E_x\left|U\left(\theta,\phi|\vec{x}\right)\right| = \frac{1}{N} + \left(1 - \frac{1}{N}\right)\left|\frac{1}{\left(2\tilde{A}+1\right)}\frac{\sin\left(\frac{\left(2\tilde{A}+1\right)}{2}\alpha(\theta,\phi)\right)}{\sin\left(\frac{\alpha(\theta,\phi)}{2}\right)}\right|^2 \tag{131}$$

Equation (131) is equivalent to the solution of a uniformly distributed periodic linear array. The result samples all possible realizations of the random variable x_n such that it is done periodically. The number of samples n in (128) is dependent upon the effective aperture size. For instance when the aperture size $\tilde{A} = 1$ one results in sampling the distribution three times ($n=3$); when $\tilde{A} = 2$ the sample size is ($n=5$). Thus, for the case $\tilde{A} = 1$ the aperture is essentially sampled at one wavelength spacing and for $\tilde{A} = 2$ two wavelength spacing, Hence, the number of mainbeams is expressed such that $2\tilde{A}+1 = N$ mainbeams and an example is shown in Figure 29 with added comparison to a periodic linear array in Figure 30.
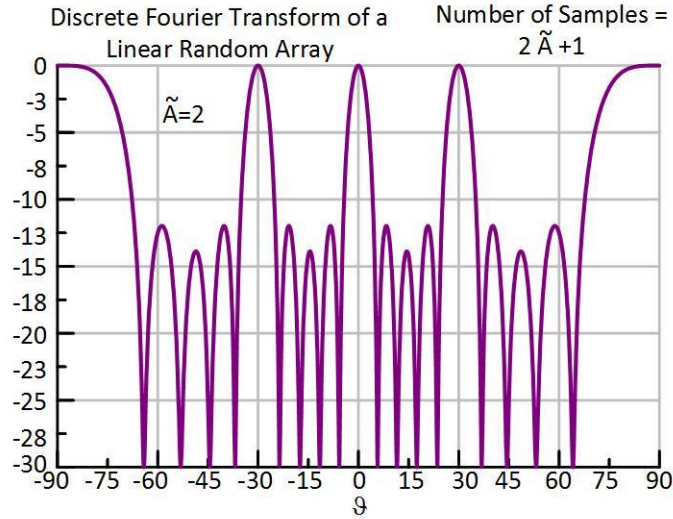
Figure 29. Example of the discrete Fourier transform of a random array.
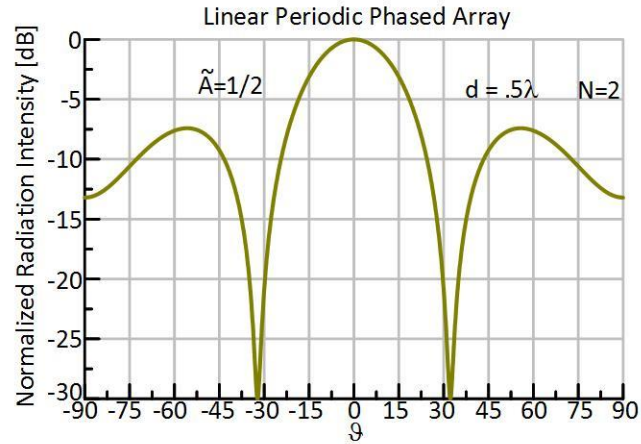
Figure 30. DFT of a linear random array is the same as a periodic linear array for spacing less than half a wavelength.

On a final note the discrete Fourier transforms relation to a periodic array is shown in Figure 31-Figure 33 for a periodic array with one wavelength spacing. In this window it is seen that the periodic array characteristic function (132) suffers from aliasing, i.e. since the pulse train appears in the operating regime ($u = \sin\theta\cos\phi|_{\phi=0°} = \sin\theta,\ |u| \leq 1$) of the characteristic function. Differently Figure 34-Figure 36 demonstrate how the periodic linear array with half wavelength spacing does not suffer from grating lobes since the pulse train is not in the operating regime of the characteristic function of a linear random array. Finally it is important to note that the 3dB beamwidth has been approximated to $\lambda/2(2A) = \lambda/2D$ where it is actually $.88x\lambda/2D$ [101]. Also the u space has been utilized for convenience, however this spaces results with loss of the actual pattern, which is shown in Chapter 11 section 8 and Chapter 14 section 6 (pattern shape is invariant to scan angle). Therefore the u, v, and w should not be utilized expect for circumstances such as these.

$$i(x) = \text{rect}(A) \cdot \sum_{n=-\infty}^{\infty} \delta(x - nd)$$

$$U = \Im\{\text{rect}(A)\} * \Im\left\{\sum_{n=-\infty}^{\infty} \delta(x - nd)\right\} \tag{132}$$

$$= \frac{\sin\left(\frac{2\pi Au}{\lambda}\right)}{\frac{2\pi Au}{\lambda}} * \sum_{m=-\infty}^{\infty} \delta\left(u - \frac{m\lambda}{d}\right) = \sum_{m=-\infty}^{\infty} \frac{\left[\sin\left(\frac{2\pi Au}{\lambda}\right)\right]\left(u - \frac{m\lambda}{d}\right)}{\frac{2\pi A}{\lambda}\left(u - \frac{m\lambda}{d}\right)}$$

51

$d=\lambda$ $N=10$
$A=d \times N=10\lambda$
$D=2A=20\lambda$

1.0

0.5 $\lambda/(2D)$

- 0.02   - 0.01   0.01   0.02

$\lambda/(D)=.05$

-0.5

-1.0
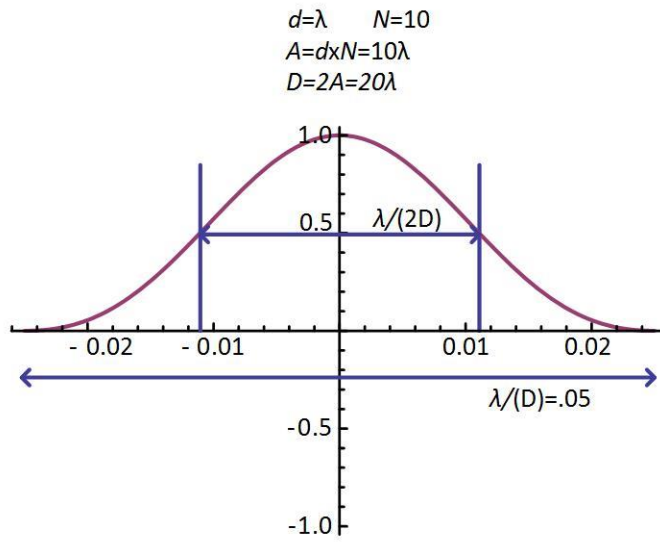
Figure 31. Linear random array pattern beamwidth only (lambda equivalent periodic array spacing).

$\lambda/(d)=1$ $\times$ $\lambda/(d)=1$

1.0

0.8

0.6

0.4

0.2

-1.0   -0.5   0.0   0.5   1.0
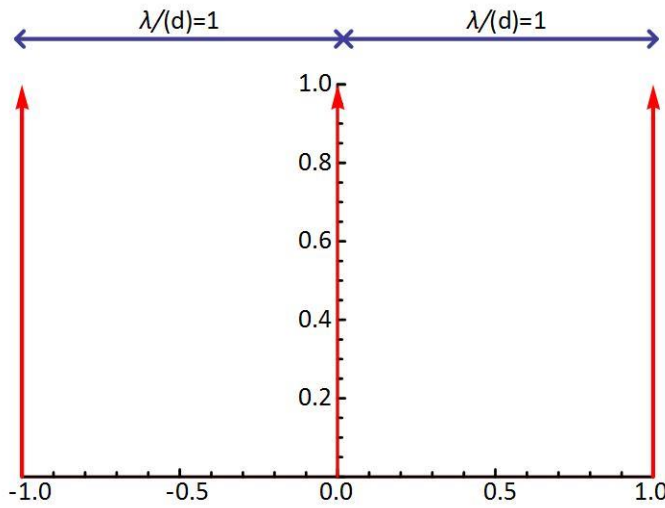
Figure 32. Pulse train sampling of a lambda equivalent periodic spacing array with $N=10$.

52
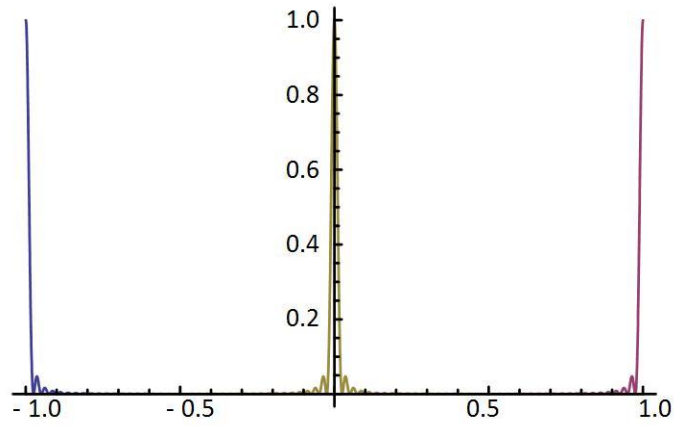
Figure 33. The pattern of a linear periodic array is nothing more than the convolution of Figure 31 and Figure 32. Grating lobes are produced for lambda spacing.
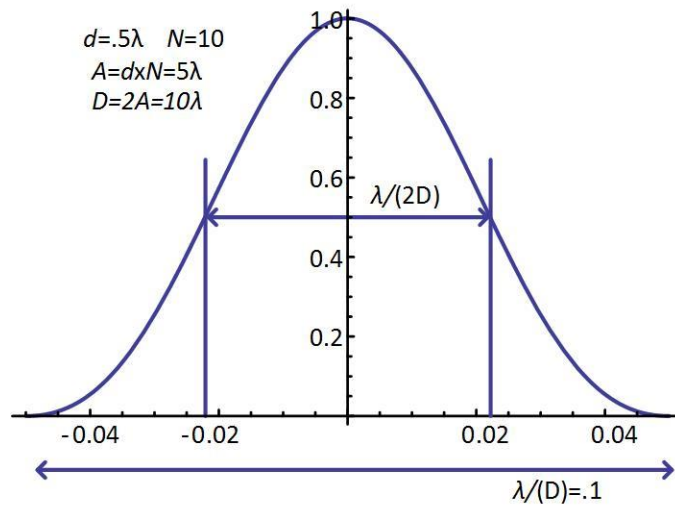
Figure 34. Linear random array pattern beamwidth only (.5 lambda equivalent periodic array spacing).
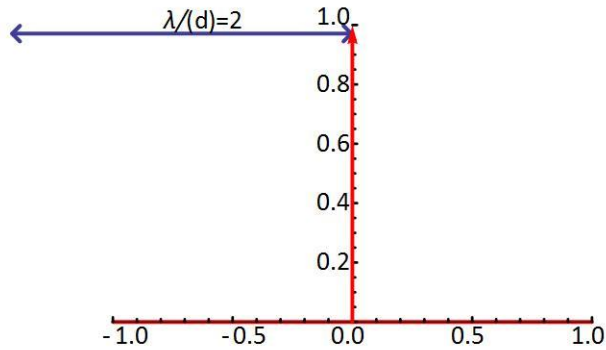
Figure 35. Pulse train sampling of a .5 lambda equivalent periodic spacing array with *N*=10.
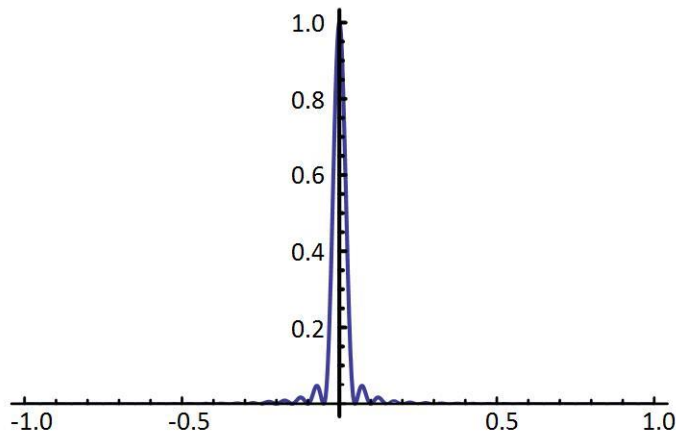
Figure 36. The pattern of a linear periodic array is nothing more than the convolution of Figure 34 and Figure 35. Grating lobes are not produced for .5 lambda spacing as the pulse train is not in the window of the characteristic functions operating regime.

In conclusion, grating lobes do not occur in a uniform periodic phased array for spacing $d \leq \lambda/2$. This closely relates to the Nyquist Sampling Theorem. The number of independent samples required to measure a waveform bandlimited to W during duration T is $2TW$. The average sampling interval required to measure the waveform with neither ambiguity nor loss of accuracy is $\tau \leq 1/2W$. For an array we rewrite $d \leq \lambda/2 = c/2f \Rightarrow d/c \leq 1/2f$. This gives the spatial sampling equivalent interval of a radiation field of the Nyquist condition $\tau \leq 1/2f$.

4.4 Fourier Series Radiation Intensity

The expected beampattern for both helical [68] (133) and spiral [129] (134) random array exhibits rotational symmetry; the helix is periodic in the *z-axis*, and the spiral is periodic in the *xy-plane*. Thus, it is expected that the Fourier transform be discrete – that is, a Fourier series – in the f_z variable for

the helix and f_x and f_y variable for the spiral. More information on the transform of a helix can be found by classic papers [130]-[135]. The analytical solution of a spiral and helical random array is shown in Figure 37 for N=100.

$$\Lambda = \left(\sum_{n=-\infty}^{\infty} J_n\left(2\pi\sqrt{f_x^2 + f_y^2}\right) e^{jn\tan^{-1}\left(\frac{f_x}{f_y}\right)} \delta\left(f_z - \frac{n}{2\pi}\right) \right) \tag{133}$$

$$\Lambda = \frac{2\lambda}{P} \left(\begin{array}{l} \left(\frac{D^2}{\lambda^2}\right)\mathrm{jinc}\left(\frac{Dq}{\lambda}\right) + \\ \left(\frac{D}{\lambda}\right)^{3/2} \sum_{n=1}^{\infty} \frac{1}{\left(\frac{4\pi n\lambda}{P}\right)^{1/2}} \left\{ \mathrm{sinc}^{1/2}\left[\frac{D}{\lambda}\left(q - \frac{2n\lambda}{P}\right)\right] \sin\left(2n\phi\right) \right\} \end{array} \right)$$

P: Pitch-radial distance an arm moves outward over one turn

N: Number of turns   (134)

D: Total diameter = 2NP

q: Radial coordinate in the transform plane
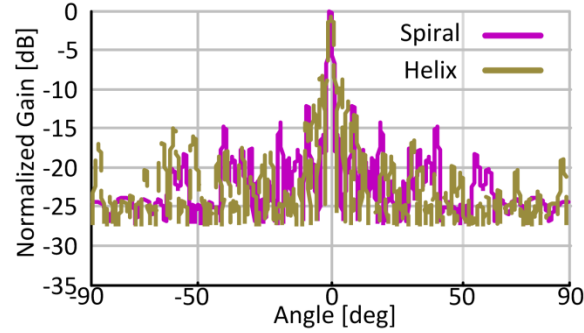
Figure 37. Analytical solution of a spiral and helical random array with N=512.

4.5 Mean Valued Radiation Intensity Amplitude Distribution

The power pattern of a random array with a uniform amplitude distribution going from 0 to 1 is

$$\frac{\overline{a^2}}{N} + \left(1 - \frac{1}{N}\right)\overline{a}^2 |\Lambda|^2 \tag{135}$$

Where

$$\bar{a} = \int_0^1 a\, w(a)\, da$$

$$\overline{a^2} = \int_0^1 a^2\, w(a)\, da$$

For a uniform distribution in Cartesian coordinates $w(a)=1$ and

$$\bar{a} = \int_0^1 a\, da = \frac{1}{2} \quad (\textit{first moment mean})$$

$$\overline{a^2} = \int_0^1 a^2\, da = \frac{1}{3}$$

$$\sigma_a^2 = \overline{a^2} - \left(\bar{a}\right)^2 \quad (\sec ond\ moment\ \text{var} iance)$$

Now for a linear random array with beamsteering coefficient X the mean valued radiation pattern is

$$\bar{U}(\theta,\phi) = \frac{\left(\dfrac{1}{3}\right)}{N} + \left(1-\frac{1}{N}\right)\left(\frac{1}{2}\right)^2\left|\frac{\sin X}{X}\right|^2 = \frac{1}{3N} + \left(1-\frac{1}{N}\right)\left|\frac{1}{2}\frac{\sin X}{X}\right|^2 \tag{136}$$

An illustration of this for both a linear random array and spherical random array is provided below in illustrations Figure 38 and Figure 39 respectively. More importantly these types of distributions will be of vital importance to random arrays if the amplitude distribution is not accounted for. Or if the path loss incurred at the transceiver is not corrected appropriately.
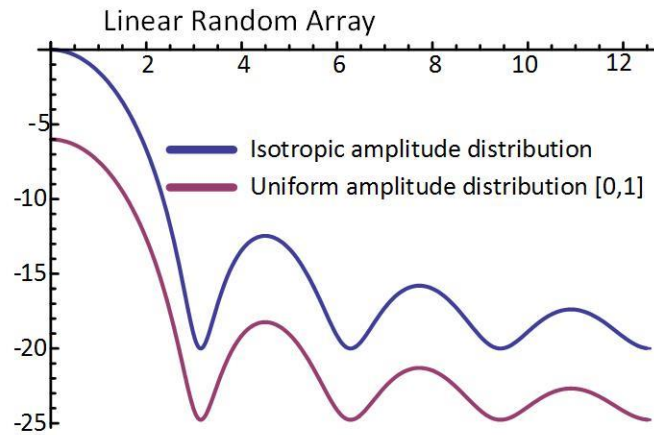
Figure 38. Uniformly distributed linear random array with uniform amplitude distribution.
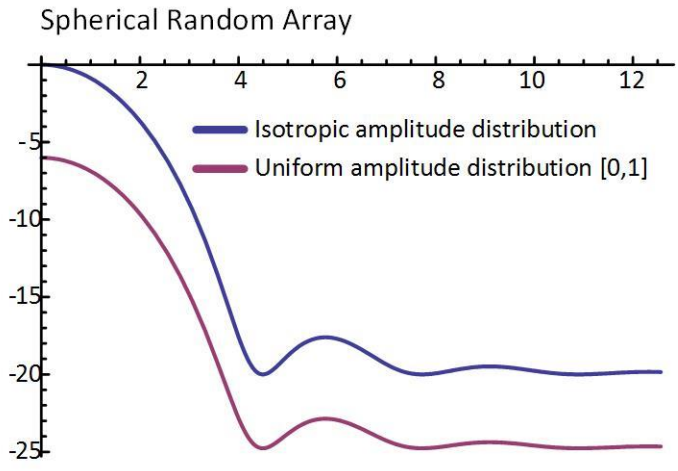
Figure 39. Uniformly distributed spherical random array with uniform amplitude distribution.

CHAPTER V

ANALYTICAL RELATION TO PREVIOUS WORK

The earliest work pertinent to the random array was investigated in 1952 by John Ruze [136]. The work did not exclusively focus upon the random array, but instead the mathematics therein was applicable; effects of random amplitude and phase errors were investigated and degenerate effects of these results showed how the radiation pattern of an aperture is modified from its ideal state. Additional work on this subject was provided by Gilbert and Morgan in 1955 [137] with an exhaustive report done by John Allen in 1961. The most significant work on random arrays is found in [9]-[14], and [35]-[61] with earlier work done by Y. T. Lo and his associates (S.W. Lee, R.J. Simcoe, A. R. Panicali and V.D. Agrawal) in [28]-[33], [58] and [37]. For these earlier works a detailed rigorous solution of the peak sidelobe of a random array was missing, but this statistic, also derived in a statistical sense was provided in later works by [101]-[186]. In [85] it was found that the peak sidelobe is relatively insensitive to array size, beam-steering angle or taper where approximations are utilized to obtain this fact. Differently [9] and [10] derive statistics using no approximations for uniform circular and Gaussian distributed random arrays. Furthermore this dissertation also extends the results to both spherical uniform and Gaussian random arrays and has verified the assumptions from [85].

In general one of the most profound papers for random arrays was given by [31] wherein this paper a mean valued array factor is found in the following fashion.

$$F_{av}\left(\theta,\phi\right) = E_Z\left|F\left(\theta,\phi\middle|\vec{Z}\right)\right| = N\int_{-\infty}^{\infty}\left(\frac{1}{N}\sum_{n=1}^{N}e^{j(Z_n(\theta,\phi)-Z_m(\theta,\phi))}\right)f\left(Z_n\right)dZ_n \tag{137}$$
$$= Mean\,Valued\,Array\,Factor$$

This formulation laid the ground work for random arrays. The relation states that squaring the mean valued array factor results a main lobe factor for the random array based upon a well-known Fourier transform pair of the probability density function $f\left(Z\right)$. The result essentially determined that the mainbeam pattern of a random array is deterministic and dependent upon the spatial distribution of the elements. This was also verified from the variance relations of the beampattern of Y.T. Lo's work provided in (138)-(139). For example, the spatial function $Z\left(\theta_0,\phi_0\right)=1$ at the target location and hence, the variance relations of (138)-(139) reduce to zero $\left\{\sigma_x^2\left(\theta_0,\phi_0\right)=\frac{1}{2N}\left[1+1\right]-\frac{1}{N}=0, \ \ \sigma_y^2\left(\theta_0,\phi_0\right)=\frac{1}{2N}\left[1-1\right]=0\right\}$; which means the mainbeam is deterministic at the target location.

$$\sigma_x^2 = \frac{1}{2N}\Big[1 + \Lambda\big(2Z(\theta,\phi)\big)\Big] - \frac{1}{N}\Lambda\big(Z(\theta,\phi)\big)^2 \tag{138}$$

$$\sigma_y^2 = \frac{1}{2N}\Big[1 - \Lambda\big(2Z(\theta,\phi)\big)\Big] \tag{139}$$

A different type of formulation for the mean valued radiation intensity was observed in (126) and was derived using compound random variables in [9] for use in wireless sensor networks (WSN) (approximately 40 years later). However, [101] was the first paper to derive this result back in the 1970's without the use of compound random variables, and its derivation is shown differently below.

$$
\begin{aligned}
U_{av}\left(\phi\right) &= U_{av}\left(\theta=\frac{\pi}{2},\phi\right) = \bar{U}\left(\theta=\frac{\pi}{2},\phi\right) = \left|F\left(\phi|\vec{x}\right)\right|^2 = F\left(\phi|\vec{x}\right)F\left(\phi|\vec{x}\right)^* \\
&= \frac{1}{N^2}\sum_n^N\sum_m^N \overline{e^{\left(jk(x_n-x_m)\alpha(\phi)\right)}} \\
&= \frac{1}{N^2}\left[N + \overline{e^{\left(jkx\alpha(\phi)\right)}}\,\overline{e^{\left(-jkx\alpha(\phi)\right)}}\left(N^2-N\right)\right] \\
&= \frac{1}{N^2}\left[N + \Lambda\big(\alpha(\phi)\big)\Lambda\big(\alpha(\phi)\big)^*\left(N^2-N\right)\right] \\
&= \frac{1}{N} + \left(1-\frac{1}{N}\right)\left|\Lambda\big(\alpha(\phi)\big)\right|^2
\end{aligned}
\tag{140}
$$

Extension of this new analysis brought into play novelty, providing new fundamental parameters in regard to random array analysis. The extension of an analytic simplification of the double summation term in (91) led to a clearer understanding of the random array theory. The lack of neglecting the summation identity (91) left Y.T. Lo's theory on random arrays incomplete. Even more the main difference in the derivations of [9] and [101] is that the derivation is done for a linear random array and usefulness of using compound random variables for derivations for volumetric random arrays [82] was not shown.

As mentioned previously the first parameter being $(1/N)$ of (93) represents the average sidelobe level or the average side lobe floor. The second term is driven by multiplication of a linearly decreasing coefficient $(1-1/N)$ again found due to the summation identity. Moreover, this term multiplies with the main beam factor (137) and provides complete description of the mean valued beam pattern in (93). The complete expression of (93) shows additional interesting features; as the number of element go to infinity one obtains a mean valued radiation intensity given by simply squaring (137). Or in other words the mean valued radiation intensity approaches that of a continuous aperture distribution in the $\lim_{N\to\infty}$.

Also differently from [9], [31], and [101] is that prior work for one and two-dimensional results did not identify pattern multiplication in the main beam region like those volumetric types of arrays (124). These works only come across as using either one random variable [101] or using one compound random

variable [9] (when avoiding error analysis [9]). For example, a one dimensional structure does not contain the pattern multiplication seen in planar and volumetric arrays. Moreover, this lack of description was missing for that of a circular random array in [9]-[14].

Now expanding previous theory in [9]-[14] one is to rewrite the results of a circular random array by that of (126) to a more general method shown in (141). Thus, for the three generic coordinate systems (141) is written as (142) for Cartesian, (143) for spherical, and (144) for polar coordinates. Now one can observe that a main lobe factor will be given by an n dimensional Fourier transform relation for Cartesian coordinates (142) and an n dimensional Bessel Fourier transform in polar (119) and spherical coordinates (124). However, due to symmetry in most uniform distributions derived thus far in addition to the coupling of coordinates in spherical and polar topology one is able to re-derive (119) and (124) using compound random variables. This reduces the previous methods such that the spherical and polar Bessel Fourier transform convert to an n dimensional Fourier transform relation (143), and (144). A complete list of all parameters is given by (145) for reference. It should be noted that the beamsteering functions $\zeta_x^r(\theta,\phi)$, $\zeta_y^r(\theta,\phi)$ and $\zeta_z^r(\theta)$ were previously derived in [81] since we were trying to simplify the true pattern multiplication of the solution. In other words we assumed that δ was a constant offset angle, which caused $\zeta_x^r(\theta,\phi)$ and $\zeta_y^r(\theta,\phi)$ to simplify to just $\zeta(\theta,\phi)$. Hence, the solution only was composed of pattern multiplication of two symmetries the volume and surface area. This solution though is incorrect and more so $\zeta_x^r(\theta,\phi)$, $\zeta_y^r(\theta,\phi)$ and $\zeta_z^r(\theta,\phi)$ are preferred since $\alpha(\theta,\phi)$, $\beta(\theta,\phi)$ and $\chi(\theta)$ are already overloaded with meaning. Typically α serves as attenuation and β is sometimes referred as the wave number (k in this dissertation).

$$E_Z\left|U\left(\theta,\phi\middle|\vec{Z}\right)\right| = \frac{1}{N} + \left(1 - \frac{1}{N}\right)\left|\prod_{p=1}^{\#Dim}\int_{-\infty}^{\infty}e^{j(Z_n(\cos\psi_n - \cos\psi_{n0}))}\left(f\left(Z_n\right)dZ_n\right)_p\right|^2 =$$

$$E_Z\left|U\left(\theta,\phi\middle|\vec{Z}\right)\right| = \frac{1}{N} + \left(1 - \frac{1}{N}\right)\left|\prod_{p=1}^{\#Dim}\int_{-\infty}^{\infty}e^{j(Z_n(X))}\left(f\left(Z_n\right)dZ_n\right)_p\right|^2$$

(141)

$$U_{av}\left(\theta,\phi\right) = \frac{1}{N} + \left(1 - \frac{1}{N}\right)\left|\int_{-1}^{1}e^{j\xi(\theta)(\chi_n - \chi_m)}\frac{1}{2}d\chi_n\int_{-1}^{1}e^{j\beta(\theta,\phi)(v_n - v_m)}\frac{1}{2}dv_n\int_{-1}^{1}e^{j\alpha(\theta,\phi)(u_n - u_m)}\frac{1}{2}du_n\right|^2$$ (142)

$$\bar{U}(\theta,\phi) = \frac{1}{N} + \left(1 - \frac{1}{N}\right) \left| \begin{array}{c} \int\limits_{-1}^{1} e^{j\zeta_x^r(\theta,\phi)\left(\Upsilon_{x_n}^r\right)} \frac{3}{4}\left(1 - \left(\Upsilon_{x_n}^r\right)^2\right) d\Upsilon_{x_n}^r \\ \int\limits_{-1}^{1} e^{j\zeta_y^r(\theta,\phi)\left(\Upsilon_{y_n}^r\right)} \frac{3}{4}\left(1 - \left(\Upsilon_{y_n}^r\right)^2\right) d\Upsilon_{y_n}^r \\ \int\limits_{-1}^{1} e^{j\zeta_z^r(\theta)\left(\Upsilon_{z_n}^r\right)} \frac{3}{4}\left(1 - \left(\Upsilon_{z_n}^r\right)^2\right) d\Upsilon_{z_n}^r \end{array} \right|^2 =$$

$$\frac{1}{N} + \left(1 - \frac{1}{N}\right) \left[\begin{array}{c} \left| \int\limits_{-1}^{1} e^{j\zeta_x^r(\theta,\phi)\left(\Upsilon_{x_n}^r\right)} \frac{3}{4}\left(1 - \left(\Upsilon_{x_n}^r\right)^2\right) d\Upsilon_{x_n}^r \right|^2 \\ \left| \int\limits_{-1}^{1} e^{j\zeta_y^r(\theta,\phi)\left(\Upsilon_{y_n}^r\right)} \frac{3}{4}\left(1 - \left(\Upsilon_{y_n}^r\right)^2\right) d\Upsilon_{y_n}^r \right|^2 \\ \left| \int\limits_{-1}^{1} e^{j\zeta_z^r(\theta)\left(\Upsilon_{z_n}^r\right)} \frac{3}{4}\left(1 - \left(\Upsilon_{z_n}^r\right)^2\right) d\Upsilon_{z_n}^r \right|^2 \end{array} \right] \tag{143}$$

$$U_{av}(\theta,\phi) = \frac{1}{N} + \left(1 - \frac{1}{N}\right) \left| \begin{array}{c} \int_{-1}^{1} e^{j\left(\upsilon_{x_n}^r \zeta_{x_n}^r(\theta,\phi)\right)} \frac{2}{\pi} \sqrt{1 - \left(\upsilon_{x_n}^r\right)^2} \, d\upsilon_{x_n}^r \\ \int_{-1}^{1} e^{j\left(\upsilon_{y_n}^r \zeta_{y_n}^r(\theta,\phi)\right)} \frac{2}{\pi} \sqrt{1 - \left(\upsilon_{y_n}^r\right)^2} \, d\upsilon_{y_n}^r \\ \int_{-1}^{1} e^{j\left((\chi_n)\zeta_z^r(\theta)\right)} \frac{1}{2} \, d\chi_n \end{array} \right|^2$$

$$= \frac{1}{N} + \left(1 - \frac{1}{N}\right) \left[\begin{array}{c} \left| \int_{-1}^{1} e^{j\left(\upsilon_{x_n}^r \zeta_{x_n}^r(\theta,\phi)\right)} \frac{2}{\pi} \sqrt{1 - \left(\upsilon_{x_n}^r\right)^2} \, d\upsilon_{x_n}^r \right|^2 \\ \left| \int_{-1}^{1} e^{j\left(\upsilon_{y_n}^r \zeta_{y_n}^r(\theta,\phi)\right)} \frac{2}{\pi} \sqrt{1 - \left(\upsilon_{y_n}^r\right)^2} \, d\upsilon_{y_n}^r \right|^2 \\ \left| \int_{-1}^{1} e^{j\left((\chi_n)\zeta_z^r(\theta)\right)} \frac{1}{2} \, d\chi_n \right|^2 \end{array} \right] \tag{144}$$

Path Length (Cartesian, Cylindrical, Spherical)

$$Z_n \cos \psi_n = \vec{Z}_n \cdot \hat{a}_r = x_n \sin\theta\cos\phi + y_n \sin\theta\sin\phi + z_n \cos\theta$$

$$Z_n \cos \psi_n = \vec{Z}_n \cdot \hat{a}_r = \rho_n \sin\theta \left(\cos(\phi - \phi_n) \right) + z_n \cos\theta$$

$$Z_n \cos \psi_n = \vec{Z}_n \cdot \hat{a}_r = r_n \sin\theta_n \sin\theta \cos(\phi - \phi_n) + r_n \cos\theta_n \cos\theta$$

Phase Correction (Cartesian, Cylindrical, Spherical)

$$Z_n \cos\psi_n - Z_n \cos\psi_{n0} = u_n \alpha(\theta,\phi) + v_n \beta(\theta,\phi) + \chi_n \xi(\theta)$$

$$Z_n \cos\psi_n - r_n \cos\psi_{n0} = \upsilon_{n,x}^r \zeta_x^r(\theta,\phi) + \upsilon_{n,y}^r \zeta_y^r(\theta,\phi)$$

$$Z_n \cos\psi_n - Z_n \cos\psi_{n0} = \Upsilon_{n,x}^r \zeta_x^r(\theta,\phi) + \Upsilon_{n,y}^r \zeta_y^r(\theta,\phi) + \Upsilon_{n,z}^r \zeta_z^r(\theta)$$

$$\upsilon_{n,x}^r \triangleq \tilde{\rho}_n \cos\phi_n, \quad \upsilon_{n,y}^r \triangleq \tilde{\rho}_n \sin\phi_n, \quad \Upsilon_{n,x}^r = \tilde{r}_n \sin\theta_n \cos\phi_n, \Upsilon_{n,y}^r = \tilde{r}_n \sin\theta_n \sin\phi_n, \Upsilon_{n,z}^r = \tilde{r}_n \cos\theta_n,$$

$$u_n \triangleq \tilde{x}_n \triangleq \frac{x_n}{A}, \ v_n \triangleq \tilde{y}_n \triangleq \frac{y_n}{A}, \quad \chi_n = \tilde{z}_n \triangleq \frac{z_n}{A} \exists \left(|\Upsilon_n| \le 1, |\upsilon_n| \le 1, |T_n| \le 1, |u_n| \le 1, |v_n| \le 1, |\chi_n| \le 1 \right)$$

$$\alpha(\theta,\phi) \triangleq 2\pi \tilde{A} (\sin\theta\cos\phi - \sin\theta_o \cos\phi_o) = \hat{x} \cdot (\hat{r}(\theta,\phi) - \hat{r}_o(\theta_o,\phi_o)),$$

$$\beta(\theta,\phi) \triangleq 2\pi \tilde{A} (\sin\theta\sin\phi - \sin\theta_o \sin\phi_o) = \hat{y} \cdot (\hat{r}(\theta,\phi) - \hat{r}_o(\theta_o,\phi_o)),$$

$$\xi(\theta) \triangleq 2\pi \tilde{A} (\cos\theta - \cos\theta_o) = \hat{z} \cdot (\hat{r}(\theta,\phi) - \hat{r}_o(\theta_o,\phi_o)),$$

$$\zeta_x^r(\theta,\phi) \triangleq 2\pi \tilde{A} \rho_o \cos\delta = \hat{x} \cdot (\hat{r}(\theta,\phi) - \hat{r}_o(\theta_o,\phi_o)),$$

$$\zeta_y^r(\theta,\phi) \triangleq 2\pi \tilde{A} \rho_o \cos\delta = \hat{y} \cdot (\hat{r}(\theta,\phi) - \hat{r}_o(\theta_o,\phi_o)),$$

$$\zeta_z^r(\theta,\phi) \triangleq 2\pi \tilde{A} \rho_o \cos\gamma = \hat{z} \cdot (\hat{r}(\theta,\phi) - \hat{r}_o(\theta_o,\phi_o)),$$

$$\cos\gamma = \rho_0^{-1} (\cos\theta - \cos\theta_0), \widetilde{\phi_n} \triangleq \phi_n - \delta, \ \tilde{\theta}_n \triangleq \theta_n, \ \tilde{\rho}_n \triangleq \frac{\rho_n}{A}, \ \tilde{r}_n \triangleq \frac{r_n}{A}, \tag{145}$$

$$\rho_o = \sqrt{(\sin\theta\cos\phi - \sin\theta_o \cos\phi_o)^2 + (\sin\theta\sin\phi - \sin\theta_o \sin\phi_o)^2}, \delta = \tan^{-1} \left[\frac{\sin\theta\sin\phi - \sin\theta_o \sin\phi_o}{\sin\theta\cos\phi - \sin\theta_o \cos\phi_o} \right]$$

The result of taking an n-dimensional Fourier Transform in Cartesian Coordinates or an n dimensional Fourier Transform in polar and spherical coordinates leads to a main lobe factor comprised of pattern multiplication based upon the number of Fourier transforms taken.

A three dimensional Cartesian coordinate system is comprised of three uncoupled coordinates and consequently gives up to three unique solutions due to orthogonality; One solution for a linear array, two for a planar array and three for a volumetric array. However, differently in the work of [6]-[14] and [81]-[82] it was studied that a three dimensional spherical and polar coordinate system contained coupled coordinates and because of this pattern multiplication only consisted of up to two solutions, which is incorrect. For example, previously it was thought that the two solution answer was unique in the sense that it described symmetry in the topology. For example, the solution of a spherical random array in the work of [6]-[14] and [81]-[82] describes the volumetric symmetry of the sphere by the $\mathrm{tinc}(\Psi_\upsilon)$ function and circular symmetry found in the surface area by the $\mathrm{jinc}(\Psi_\mathrm{T})$ function. Then the cylindrical random array characteristic function describes volumetric circular symmetry by the $\mathrm{jinc}(\Psi_\upsilon)$ function and linear

surface area symmetry in terms of elevation given by the $\text{sinc}(x)$ function. However, by once again comparing the results of Figure 17-Figure 19 it is seen that this assumption is incorrect as the pattern of a sphere is composed of three tinc functions (namely defining volumetric symmetry).

Last of all, until recently results of pattern multiplication were thought to have been a new addition to the previous theory, but it has been found that the main beam factor of a cylindrical random array is provided in [187] showing the pattern multiplication as defined above. The difference, however is this earlier paper derives the results based upon an acoustic array of buoys distributed in a cylindrical body in the ocean, but does not show the derivation of the result. In addition, it is unclear as to whether a Fourier Bessel transform or Fourier transform pair is utilized to derive the mean valued beampattern. Also this paper does not mention or generalize that the volumetric array pattern is composed according to the symmetry it contains: volumetric, circular or linear with an induced pattern multiplication. Hence, this in depth explanation is somewhat new and is not expressed in the literature at the least for spherical random arrays (from the author's familiarity and ongoing research thus far).

CHAPTER VI

ANNULAR CIRCULAR AND SPHERICAL RANDOM ARRAY

6.1 Initial Consideration and Problem Setup

A new approach in the field of adaptive beamforming is presented by means of circular and spherical ring random arrays. This process follows a different approach from more traditional approaches in the art of adaptive and nulling techniques found in traditional phased array and aperiodic array literature. This process avoids expansions of large polynomial equations and matrices aiding the designer in the overall process providing its most beneficial advantage yet; ease in this general process.

In general adaptive beamforming is a popular technique applied in "modern wireless communication systems to combat interference and multi-path fading and thereby increase system capacity." [188] This process determines a set of complex weights to be applied to the elements such that suppression of the radiation pattern is achieved in directions of unwanted interferes. By doing so, the signal to interference ratio can be maximized in target direction while minimized at nearby interferes. This technique is suitable for stationary systems or traditional periodically spaced phased arrays since simple polynomial equations may be derived. The simplicity in these architectures arises from using a polynomial root finding algorithm in order to find these complex weights. However, for the random or aperiodic array the processes this process is much more difficult. In these scenarios, a proposed technique is to truncate the element spacing to an acceptable level such that the *Z transform* may be used to approximate a polynomial equation and find the complex roots. [189]

Another approach for adaptive beamforming in the random array environment is to solve a general linear system of equations. However, the solution of these general linear systems provides an infinite number of solutions. I.e., studies performed by [190] demonstrate that an optimization of these solutions can be done from a minimum variance standpoint. The approach is acceptable; however it becomes exceedingly computationally demanding for planar and volumetric topologies.

A new method proposed in the art of array nulling is found in [158]. Different from traditional adaptive beamforming techniques [188] and computationally demanding matrix solutions [189]. It utilizes circular ring random arrays in order to place nulls in those direction of interferes. This topology also provides advantages and reductions in network energy waste and disconnectivity issues. This work extends the results in [158] from the given planar environment into a more robust three dimensional space. This work has identified that the same analysis can be applied to spherical rings providing results similar to those of [158].

Yet, the only discrepancy is that the work of [9] proposed a discrepancy in the calculation of the compound random variables utilized therein of which induced errors in the mean valued radiation pattern.

This error continued into the analysis of soon after [12] then [158] and even carried on into the works [6], [81]-[82] before it was corrected in the work of [191]. Hence, this work begins with the amended work, but diverges such that necessary approximations are applied causing the overall process to become similar in fashion to [158]. Hence, even though the work of [158] utilized the incorrect expression for the mean valued radiation pattern it induces no loss in generality when inducing nulls in the neighborhood of the main beam.

A review of the process found in [190] will be presented first with the intent of creating a greater ease in understanding from the work in [190]. Next the new approach is presented such that the average beampattern expression is derived for the case that all the elements are uniformly distributed about a spherical random ring. For completeness the statistical results of the spherical ring patterns are compared against those of the circular ring patterns given in [158].

6.2 Relation to Previous Work

Up to this point it has been assumed that we feed the elements with a uniform amplitude distribution $I_n = I_o = 1$. When this is not the case it is possible to force null positions in the beam pattern by the following method similar to [190].

The array factor is rewritten as (146) and its corresponding beam pattern in (147) for a non-uniform amplitude distribution.

$$F\left(\theta,\phi|\vec{Z}\right) = \sum_{n=0}^{N-1} I_n e^{j\alpha(\theta,\phi)x_n} \tag{146}$$

$$U\left(\theta,\phi|\vec{Z}\right) = \frac{1}{N}\frac{1}{M}\sum_{m=0}^{N-1}\sum_{n=0}^{M-1} I_n I_m^* e^{j\alpha(\theta,\phi)(x_n-x_m)} \tag{147}$$

Now upon taking the expected value we remodel (147) as (148) in matrix form. Equation (149) is used to state that we will force null positions at those points equated to zero in (149), but with the tradeoff that the respective gain will be attenuated by the coefficient α.

$$
\begin{aligned}
U_{av}\left(\theta,\phi\right) &= E\left[U\left(\theta,\phi|\vec{x}\right)\right] \\
&= \begin{bmatrix}
1 & E\left[e^{j\alpha(\theta,\phi)(x_1-x_2)}\right] & \cdots & E\left[e^{j\alpha(\theta,\phi)(x_1-x_N)}\right] \\
E\left[e^{j\alpha(\theta,\phi)(x_2-x_1)}\right] & 1 & \cdots & \vdots \\
\vdots & \vdots & \cdots & E\left[e^{j\alpha(\theta,\phi)(x_{N-1}-x_N)}\right] \\
E\left[e^{j\alpha(\theta,\phi)(x_N-x_1)}\right] & E\left[e^{j\alpha(\theta,\phi)(x_N-x_2)}\right] & \cdots & 1
\end{bmatrix} = c
\end{aligned} \tag{148}
$$

$$c = \begin{vmatrix} \begin{matrix} \alpha \\ \begin{Bmatrix} 0 \\ \vdots \\ 0 \end{Bmatrix} M \end{matrix} \end{vmatrix} \tag{149}$$

$$M \triangleq \text{degrees of freedom for nulling}$$

The exponential of (148) is rewritten as (150) in the fashion that a substitution of variables is made for the corresponding probability distribution letting the nominal position of the ith element be a_i. This substitution of variables leads to the form of (151). The parameter $\eta(\alpha(\theta,\phi))$ is observed to be the inverse Fourier transform of the pdf $p(y_i)$ and a function of the spatial function $\alpha(\theta,\phi)$.

$$E\left[e^{j\alpha(\theta,\phi)(x_i)} \right] = \int_{-\infty}^{\infty} p(x_i - a_i) e^{j\alpha(\theta,\phi)(x_i)} dx_i$$
$$y_i = x_i - a_i \tag{150}$$

$$E\left[e^{j\alpha(\theta,\phi)(x_i)} \right] = \int_{-\infty}^{\infty} p(y_i) e^{j\alpha(\theta,\phi)(y_i)} e^{-j\alpha(\theta,\phi)(a_i)} dy_i \tag{151}$$

$$E\left[e^{j\alpha(\theta,\phi)(x_i)} \right] = e^{-j\alpha(\theta,\phi)(a_i)} \eta(\alpha(\theta,\phi))$$
$$\eta(\alpha(\theta,\phi)) = \int_{-\infty}^{\infty} p(y_i) e^{j\alpha(\theta,\phi)(y_i)} \tag{152}$$

Now when multiplying the result of (152) by non-uniform amplitude distribution $A_{i,s}$ and setting this equal to the constraint vector c one obtains (153).

$$U_{av}(\theta,\phi) = I_n I_m^* E\left[U(\theta,\phi|\vec{x}) \right] = c$$
$$= \frac{I_n I_m^*}{N} + \frac{1}{N^2} I_n I_m^* \eta^2 (\alpha(\theta,\phi)) \sum_{\substack{m=1 \\ m \neq n}}^{N} \sum_{n=1}^{N} e^{j(a_m - a_n)\alpha(\theta,\phi)} \tag{153}$$

$$U_{av}(\theta,\phi) = |I|^2 \left(\frac{1}{N} + \frac{1}{N^2} \eta^2 (\alpha(\theta,\phi)) \sum_{\substack{m=1 \\ m \neq n}}^{N} \sum_{n=1}^{N} e^{j(a_m - a_n)\alpha(\theta,\phi)} \right) = c \tag{154}$$

$$|I|^2 = \left(R^{-1} \right)^* c$$
where $\tag{155}$
$$R = \left(\frac{1}{N} + \frac{1}{N^2} \eta^2 (u) \sum_{\substack{m=1 \\ m \neq n}}^{N} \sum_{n=1}^{N} e^{j(a_m - a_n)\alpha(\theta,\phi)} \right)$$

Similar to [55] we find the variance of the array factor as given by the procedure in (156)-(158). Once the variance (158) of the array factor is found we use (147) to minimize this result. The result that minimizes the variance is given by [55] in (159). Where in (159) $\alpha(\theta_0,\phi_0)$ is given to be the mainbeam location which equals one for a normalized beam pattern giving (160) . With this the degradation factor

becomes (161) [55]. Lastly, for then non-constrained case it is seen that when M=0 that I=N and gives (162) of which is equivalent (163) for completeness.

$$\sigma^2 = E\left[F(u)^2\right] - E\left[F(u)F(u)^*\right] = E\left[F(u)^2\right] - E\left[F(u)\right]E\left[F(u)^*\right]$$
$$= \frac{I_n I_m^*}{N} + \frac{1}{N^2}\eta^2(u)\sum_{\substack{m=1 \\ m\neq n}}^{N}\sum_{n=1}^{N} I_n I_m^* e^{j(a_m-a_n)\alpha(\theta,\phi)} - I_n I_m^*\eta(u)^2 \tag{156}$$

$$\sigma^2 = \frac{|I|^2}{\alpha N} + \frac{|I|^2}{(\alpha N)^2}\eta^2(u)\sum_{\substack{m=1 \\ m\neq n}}^{N}\sum_{n=1}^{N} e^{j(a_m-a_n)\alpha(\theta,\phi)} - \eta(u)^2 \tag{157}$$

$$\sigma^2 = |I|^2\left(\frac{1}{\alpha N} + \eta^2(u)\left(\frac{1}{(\alpha N)^2}\sum_{\substack{m=1 \\ m\neq n}}^{N}\sum_{n=1}^{N} e^{j(a_m-a_n)\alpha(\theta,\phi)} - 1\right)\right) \tag{158}$$

$$|I|^2 = \frac{\alpha^2 N^2}{\eta(\alpha(\theta_0,\phi_0))(N-M)} \tag{159}$$

$$|I|^2 = \frac{\alpha^2 N^2}{(N-M)} \tag{160}$$

$$\alpha^2 = \frac{\eta(\alpha(\theta_0,\phi_0))(N-M)}{N}$$
$$\alpha^2 \overset{Normalized\ Beampattern}{=} \frac{(N-M)}{N} \tag{161}$$

$$U_{av}(\theta,\phi) = \left(N + \eta^2(\alpha(\theta,\phi))\sum_{\substack{m=1 \\ m\neq n}}^{N}\sum_{n=1}^{N} e^{j(a_m-a_n)\alpha(\theta,\phi)}\right) = c = \begin{bmatrix} 1 \\ \vdots \\ 1 \end{bmatrix}$$

$$U_{av}(\theta,\phi) \equiv N + (N^2 - N)\eta^2(\alpha(\theta,\phi)) \tag{162}$$

$$U_{av}(\theta,\phi) \overset{Normalized}{=} \frac{1}{N} + \left(1 - \frac{1}{N}\right)\eta^2(\alpha(\theta,\phi))$$

$$E_{\Upsilon^{\vec{r}}}\left|U\left(\theta,\phi\big|\vec{\Upsilon}^{\vec{r}}\right)\right| = \frac{1}{N} + \left(1 - \frac{1}{N}\right)|\Lambda|^2$$

$$\Rightarrow \eta^2(\alpha(\theta,\phi)) \equiv |\Lambda|^2 \tag{163}$$

The problem with (163) is that it is computationally demanding. Hence, the next section displays an alternative to this process by using randomly distributed circular and spherical rings.

6.3 Annular Circular and Spherical Random Arrays

(a) Initial consideration and problem setup

Consider a spherically bound random array whose elements are uniformly distributed on $S_{sph}\left(0,\tilde{A}_{\max}\right)$, the sphere centered at O with normalized radius $\tilde{A}_{\max} = A_{\max}/\lambda$. Like in [158] let $S_{sph}\left(0,\tilde{A}_{i,s},\tilde{A}_{0,s}\right)$ denote the spherical ring centered at O with the inner radius $\tilde{A}_{i,s} \geq 0$ and the outer radius $\tilde{A}_{o,s} \leq \tilde{A}_{\max}$. It is assumed that $\tilde{A}_{i,s}$ and $\tilde{A}_{o,s}$ are selected such that $S_{sph}\left(0,\tilde{A}_{i,s},\tilde{A}_{0,s}\right)$ has an area (164) large enough to include at least N (L in the inner sphere and K in the annular region) nodes with a high probability as shown in Figure 40. The area of the circular disk random array $S_{disk}\left(0,\tilde{A}_{\min},\tilde{A}_{\max}\right)$ is given by that of (165) for completeness.
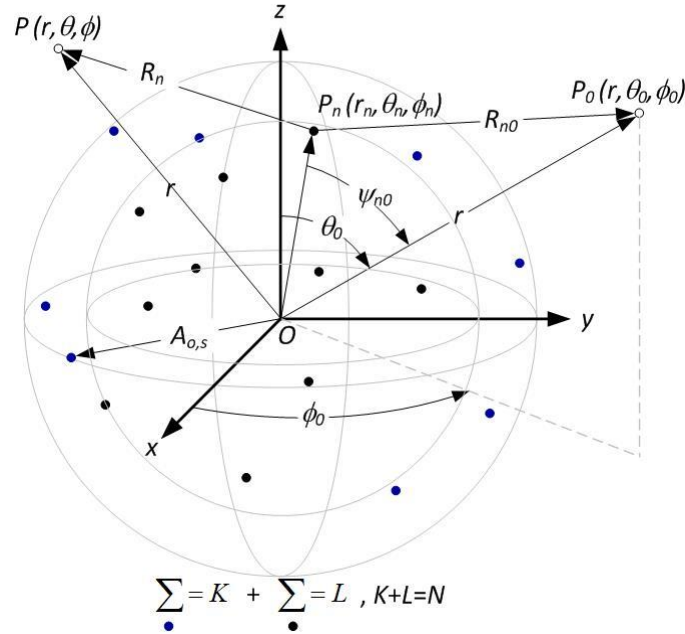
Figure 40. Random distribution of elements in a spherical volumetric shell.

$$V_{sph} = \frac{4}{3}\pi\left(\tilde{A}_{o,s}^{3} - \tilde{A}_{i,s}^{3}\right)$$

$$\Rightarrow A_{sph} = \frac{d\left(V_{sph}\right)}{d\tilde{A}} = 4\pi\left(\tilde{A}_{o,s}^{2} - \tilde{A}_{i,s}^{2}\right) \tag{164}$$

68

$$A_{disk} = \pi \left(\tilde{A}_{o,s}^2 - \tilde{A}_{i,s}^2 \right) \tag{165}$$

The nodes are assumed uniformly distributed on a large volume, and they are points of a homogenous three-dimensional Poisson process [170], [172]. Therefore, having at least N nodes on $S_{sph}\left(0, \tilde{A}_{i,s}, \tilde{A}_{0,s}\right)$ with a probability not less than ι is given by (166) where ρ is the node density and $\Gamma(.,.)$ is the incomplete Gamma function.

$$\sum_{n=0}^{N-1} e^{-\rho A_{sph}} \frac{\left(\rho A_{sph}\right)^n}{n!} = \frac{\Gamma\left(N, \rho A_{sph}\right)}{(N-1)!} \leq 1 - \iota \tag{166}$$

This result is useful since given ι, N, and ρ, the minimum feasible A_{sph} can be obtained from (166). Selecting a ι close to one will ensure the presence of at least N nodes on the sphere $S_{sph}\left(0, \tilde{A}_{i,s}, \tilde{A}_{0,s}\right)$ with a high probability.

Once the total numbers of nodes are selected from the ring the total in the spherical distribution will be decreased such that $K \leq N$ nodes participate in beamforming. Hence, a decrease in the number of nodes will typically occur. This will have impacts on the maximum gain achievable going from N to K, however it will be seen that a number of advantages can occur to include: beampattern nulling, and thinning the mainbeam.

(b) Circular and spherical array factor

The array factor for an independent and identically distributed (i.i.d.) distribution of isotropic elements is provided as (167) with spherical random variables (168) and steering functions (169). Similarly the array factor for a circular random array is provided by (170) with circular random variables (171).

$$F\left(\theta, \phi \big| x_n, y_n, z_n\right) = \frac{1}{N} \sum_{n=1}^{N} e^{jkr_n\rho_0\left(\sin\theta_n \cos(\phi_n-\xi)+\cos\theta_n \cos\gamma\right)} =$$

$$F\left(\theta, \phi \big| \Upsilon_n^x, \Upsilon_n^y, \Upsilon_n^z\right) = \frac{1}{N} \sum_{n=1}^{N} e^{j\left(\zeta_x^r(\theta,\phi)\Upsilon_n^x + \zeta_y^r(\theta,\phi)\Upsilon_n^y + \zeta_z^r(\theta)\Upsilon_n^z\right)} \tag{167}$$

$$
\begin{aligned}
\Upsilon_n^x &= \tilde{r}_n \sin\theta_n \cos\phi_n, \quad -1 \leq \Upsilon_n^x \leq 1 \\
\Upsilon_n^y &= \tilde{r}_n \sin\theta_n \sin\phi_n, \quad -1 \leq \Upsilon_n^y \leq 1 \\
\Upsilon_n^z &= \tilde{r}_n \cos\theta_n, \qquad\quad -1 \leq \Upsilon_n^z \leq 1 \\
\Upsilon_n^{\tilde{r}} &\triangleq \left\langle \Upsilon_n^x, \Upsilon_n^y, \Upsilon_n^z \right\rangle \\
\tilde{r}_n &= r_n / A, r_n = \sqrt{x_n^2 + y_n^2 + z_n^2}
\end{aligned}
\tag{168}
$$

$$\zeta_x^r(\theta,\phi) = \cos(\delta)\zeta(\theta,\phi), \zeta_y^r(\theta,\phi) = \sin(\delta)\zeta(\theta,\phi)$$

$$\zeta_z^r(\theta) = \cos(\gamma)\zeta(\theta,\phi), \zeta(\theta,\phi) \triangleq 2\pi\tilde{A}\rho_o$$

$$\rho_o = \sqrt{\left(\frac{\sin\theta\cos\phi -}{\sin\theta_o\cos\phi_o}\right)^2 + \left(\frac{\sin\theta\sin\phi -}{\sin\theta_o\sin\phi_o}\right)^2} \tag{169}$$

$$\delta = \tan^{-1}\left[\frac{\sin\theta\sin\phi - \sin\theta_0\sin\phi_0}{\sin\theta\cos\phi - \sin\theta_0\cos\phi_0}\right]$$

$$\gamma = \cos^{-1}\left(\rho_0^{-1}\left(\cos\theta - \cos\theta_0\right)\right)$$

$$F\left(\theta,\phi\big|\upsilon_n^x,\upsilon_n^y\right) = \frac{1}{N}\sum_{n=1}^{N} e^{j\left(\zeta_x^r(\theta,\phi)\upsilon_n^x + \zeta_y^r(\theta,\phi)\upsilon_n^y\right)} =$$

$$\frac{1}{N}\sum_{n=1}^{N}\left(u_n + jv_n\right) = \frac{1}{N}\left(U + jV\right) \tag{170}$$

$$\upsilon_n^x = \tilde{\rho}_n\cos\phi_n,$$

$$\upsilon_n^y = \tilde{\rho}_n\sin\phi_n, \tag{171}$$

$$\tilde{\rho}_n = \rho_n \big/ A, \ \rho_n = \sqrt{x_n^2 + y_n^2}$$

The spatial beamsteering function will be defined as $\zeta^{\vec{r}}(\theta,\phi) \triangleq \left(\zeta_x^r(\theta,\phi), \zeta_y^r(\theta,\phi), \zeta_z^r(\theta)\right)$ and will be referred as an orthonormal steering vector for simplicity in analysis when referring to the beamsteering functions. At the meridian elevation angle $\left(\theta = \theta_0 = \pi/2, \phi_0 = 0, \phi\right)$ this function reduces to $\zeta_{endfire}^{\vec{r}}(\phi) = 2\pi\tilde{A}\langle\cos\phi - 1, \sin\phi, 0\rangle$ for either spherical or circular random array (since no z-component exists for the CRA). At the meridian angle the spatial function $\zeta_{endfire}^{\vec{r}}(\phi)$ is defined in [82] as (9), but will be redefined as (10).

$$\zeta_{endfire}^{\vec{r}}(\phi) = 2\pi\tilde{A}\langle\cos\phi - 1, \sin\phi, 0\rangle \tag{172}$$

$$\zeta_{endfire}^{\vec{r}}(\phi) = 2\pi\langle\cos\phi - 1, \sin\phi, 0\rangle \tag{173}$$

This makes it easier to view the solutions to characteristic functions with annular regions or multiple radii and additionally keeps $\zeta_{endfire}^{\vec{r}}(\phi)$ independent of radius, which maintains its consistency with [158]. Differently the orthonormal steering vector is not consistent at broadside for spherical and circular random array. Instead, at the zenith elevation angle $\left(\phi = \theta_0 = \phi_0 = 0, \theta\right)$ this function reduces to $\zeta_{broadside}^{\vec{r}}(\theta) = 2\pi\tilde{A}\langle\sin\theta, 0, \cos\theta - 1\rangle$ for the SRA and $\zeta_{broadside}^{\vec{r}}(\theta) = 2\pi\tilde{A}\langle\sin\theta, 0\rangle$ for the CRA.

(c) Expected power patterns of the circular and spherical random array

The mean valued radiation patterns of the array factor of either spherical and circular random array is given respectively by (174) and (175).

$$\bar{U}(\theta,\phi) \overset{Sph}{=} \frac{1}{N} + \left(1 - \frac{1}{N}\right)\left[\left|3\text{tinc}\left(\zeta^{\vec{r}}(\theta,\phi)\right)\right|^2\right]$$

$$3\text{tinc}\left|\zeta^{\vec{r}}(\theta,\phi)\right|^2 = \begin{bmatrix} \left|3\text{tinc}\left(\zeta_x^r(\theta,\phi)\right)\right|^2 \\ \left|3\text{tinc}\left(\zeta_y^r(\theta,\phi)\right)\right|^2 \\ \left|3\text{tinc}\left(\zeta_z^r(\theta,\phi)\right)\right|^2 \end{bmatrix} = \begin{bmatrix} \left|3\text{tinc}\zeta_x^r(\theta,\phi)\right|^2 \\ \left|3\text{tinc}\zeta_y^r(\theta,\phi)\right|^2 \\ \left|3\text{tinc}\zeta_z^r(\theta)\right|^2 \end{bmatrix}, \text{tinc}(x) = \frac{j_1(x)}{x} \tag{174}$$

$$\bar{U}(\theta,\phi) \overset{Cir}{=} \frac{1}{N} + \left(1 - \frac{1}{N}\right)\left[\left|2\text{jinc}\left(\zeta^{\vec{r}}(\theta,\phi)\right)\right|^2\right]$$

$$2\text{jinc}\left|\zeta^{\vec{r}}(\theta,\phi)\right|^2 = \begin{bmatrix} \left|2\text{jinc}\left(\zeta_x^r(\theta,\phi)\right)\right|^2 \\ \left|2\text{jinc}\left(\zeta_y^r(\theta,\phi)\right)\right|^2 \end{bmatrix} = \begin{bmatrix} \left|2\text{jinc}\left(\zeta_x^r(\theta,\phi)\right)\right|^2 \\ \left|2\text{jinc}\left(\zeta_y^r(\theta,\phi)\right)\right|^2 \end{bmatrix}, \text{jinc}(x) = \frac{J_1(x)}{x} \tag{175}$$

However, this type of solution leads to multiple orthogonal solutions composed of the independent coordinates of the orthonormal steering vector set. As a consequence the mean valued beampattern of a circular random array (CRA) and spherical random array (SRA) proceeds upon non-linear solution sets. This causes overwhelming difficulty in the process when solving for mean peak and null locations such that an alternate approach is desirable. Hence, an alternative approach will be followed similar to the works of [6]-[14], [81]-[82] and [158] of which unknowingly simplified the patterns of (174)-(175) to (176)-(177). For instance, this approximation assumes that the angle δ is nothing more than a constant offset angle of which in not entirely accurate; although this simplification causes no major loss in generality when trying to find the mean peak and null locations (in the neighborhood of the mainbeam region). This is due since the mean null and peak locations closely approximate to the true pattern of a CRA or SRA as shown in Figure 41 and Figure 42. This induces the simplified pattern in the form of a monotonically decaying transcendental solution of which determining the peaks and nulls of the characteristic function is trivial; Though in this analysis a determination of the mean peaks and nulls will be approximated using the correct mean valued radiation pattern. This type of approach will follow suit to popular methods of determining the peaks and null locations of the beampattern in periodic lattice array architectures.

$$\bar{U}(\theta,\phi) \overset{Sph}{\approx} \frac{1}{N} + \left(1 - \frac{1}{N}\right)\left[3\text{tinc}\left|\zeta(\theta,\phi)\right|^2\right] \tag{176}$$

$$\bar{U}(\theta,\phi) \overset{Cir}{=} \frac{1}{N} + \left(1 - \frac{1}{N}\right)\left[2\text{jinc}\left|\zeta(\theta,\phi)\right|^2\right] \tag{177}$$
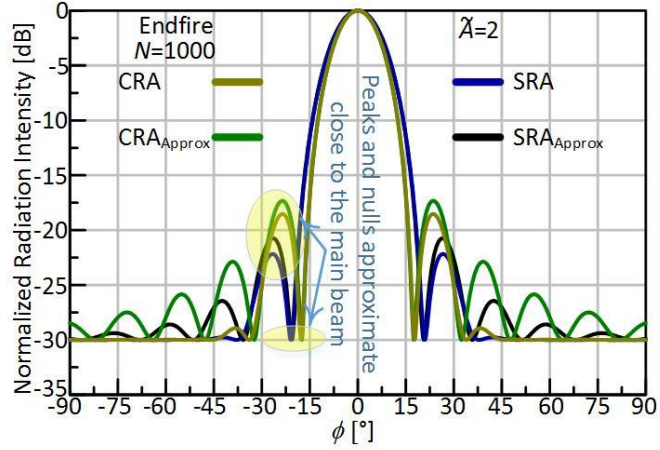
Figure 41. Analytical comparison of (96)-(97) and (176)-(177) at the meridian elevation angle.
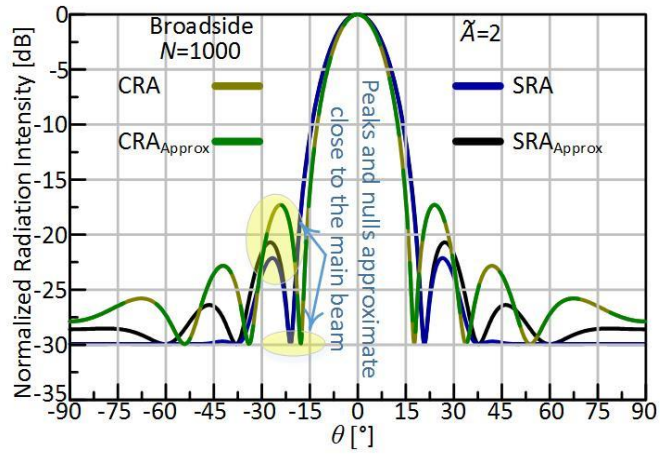
Figure 42. Analytical comparison of (96)-(97) and (176)-(177) at the zenith elevation angle.

(d) *Annular circular and spherical ring random array*

The joint distribution of a semicircular distribution is given in (178). The marginal distribution is given by both (179) and (180) and differs from (Equation 9, [158]), however this mistake in [158] did not lead to any loss in generality as [158] still obtains the correct expected value of the radiation pattern as given by (181).

$$
\int_0^{2\pi} \int_{A_{i,s}}^{A_{0,s}} f(u,\upsilon) u \, du \, d\upsilon
$$
$$
f_{u_n,\upsilon_n}(u,\upsilon) = \frac{1}{\pi\left(\tilde{A}_{0,s}^2 - \tilde{A}_{i,s}^2\right)}
$$

(178)

$$f_{v_n}(v) = \int_{-\sqrt{A_{i,s}^2 - v^2}}^{\sqrt{A_{i,s}^2 - v^2}} f_{u_n,v_n}(u,v)\,du = \frac{2}{\pi\left(A_0^2 - A_{i,s}^2\right)}\sqrt{A_{i,s}^2 - v^2}$$

$$0 \le |v| \le A_{i,s}$$

(179)

$$f_{v_n}(v) = \int_{-\sqrt{\tilde{A}_{o,s}^2 - v^2}}^{\sqrt{\tilde{A}_{o,s}^2 - v^2}} f_{u_n,v_n}(u,v)\,du - \int_{-\sqrt{\tilde{A}_{i,s}^2 - v^2}}^{\sqrt{\tilde{A}_{i,s}^2 - v^2}} f_{u_n,v_n}(u,v)\,du$$

$$= \frac{2}{\pi\left(\tilde{A}_0^2 - \tilde{A}_{i,s}^2\right)}\left(\sqrt{\tilde{A}_{o,s}^2 - v^2} - \sqrt{\tilde{A}_{i,s}^2 - v^2}\right) \quad \tilde{A}_{i,s} \le |v| \le \tilde{A}_{o,s}$$

(180)

$$U_{av}(\phi) = \frac{1}{K} + \left(1 - \frac{1}{K}\right)|\Lambda|^2$$

$$\Lambda = \frac{2}{\tilde{A}_{o,s}^2 - \tilde{A}_{i,s}^2}\frac{\tilde{A}_{o,s}J_1\left(\tilde{A}_{o,s}\zeta^{\bar{r}}(\phi)\right) - \tilde{A}_{i,s}J_1\left(\tilde{A}_{i,s}\zeta^{\bar{r}}(\phi)\right)}{\zeta(\phi)}$$

(181)

Following the same technique it can be shown that for a random variable distributed according to (182), one obtains a similar result as that of (181) given by (183). It is noteworthy to observe that when $\tilde{A}_{i,s} = 0$ that is the spherical ring $S_{sph}\left(0,\tilde{A}_{i,s},\tilde{A}_{0,s}\right)$ transforms to a spherical uniform distribution $S_{sph}\left(0,\tilde{A}_{0,s}\right)$ being a sphere centered at the origin O with radius $\tilde{A}_{o,s}$, and (183) simplifies to (184).

$$f_{v_n}(v) = \frac{3}{4\pi\left(\tilde{A}_0^2 - \tilde{A}_{i,s}^2\right)}\sqrt{\tilde{A}_{i,s}^2 - v^2} \qquad 0 \le |v| \le \tilde{A}_{i,s}$$

$$= \frac{3}{4\pi\left(\tilde{A}_0^2 - \tilde{A}_{i,s}^2\right)}\left(\sqrt{\tilde{A}_{o,s}^2 - v^2} - \sqrt{\tilde{A}_{i,s}^2 - v^2}\right)\tilde{A}_{i,s} \le |v| \le \tilde{A}_{o,s}$$

(182)

$$U_{av}(\phi) = \frac{1}{K} + \left(1 - \frac{1}{K}\right)|\Lambda|^2$$

$$\Lambda = \frac{3}{\tilde{A}_{o,s}^2 - \tilde{A}_{i,s}^2}\frac{\tilde{A}_{o,s}j_1\left(\tilde{A}_{o,s}\zeta^{\bar{r}}(\phi)\right) - \tilde{A}_{i,s}j_1\left(\tilde{A}_{i,s}\zeta^{\bar{r}}(\phi)\right)}{\zeta^{\bar{r}}(\phi)}$$

(183)

$$U_{av}(\phi) = \frac{1}{K} + \left(1 - \frac{1}{K}\right)|\Lambda|^2$$

$$\Lambda = \frac{3}{\tilde{A}_{o,s}}\left\{\frac{j_1\left(\tilde{A}_{o,s}\zeta(\phi)\right)}{\zeta(\phi)}\right\} = 3\text{tinc}\left(\zeta^{\bar{r}}(\phi)\right)\Big|_{\tilde{A}_{o,s}=1}$$

(184)

Equation (184) has been obtained in [6], [81] and [82], but it will be seen that there are advantages towards choosing $\tilde{A}_{i,s} \ne 0$ similar to [158].

73

(e) Mainlobe of the average beampattern for circular and spherical apertures

For enhanced stealth and point to point architectures it is critical to have a very narrow beam. This reduces the probability of interception to unintended receivers. In addition, if multiple target receivers are in close proximity to other clusters of receivers, a narrow mainbeam will be critical for reducing unintended interference. In what follows, we analyze the mainbeam to be narrow enough such we rewrite the beampatterns first null $\phi_{(n),1}$ as a function of $\alpha \triangleq \tilde{A}_{i,s} / \tilde{A}_{0,s}$ for the spherical ring random array given in (185) and also for the circular ring random array given in (186) [158].

$$f(x,\alpha) = \frac{3}{(1-\alpha^2)} \left\{ \frac{j_1(x)}{x} - \frac{\alpha}{x} j_1(\alpha x) \right\} \tag{185}$$

$$f(x,\alpha) = \frac{2}{\tilde{A}_{o,s}^2 \left(1 - \frac{\tilde{A}_{i,s}^2}{\tilde{A}_{o,s}^2}\right)} \left\{ \frac{A_{o,s} J_1\left(\tilde{A}_{o,s} \zeta^{\bar{r}}(\phi)\right) - \tilde{A}_{i,s} J_1\left(\tilde{A}_{i,s} \zeta^{\bar{r}}(\phi)\right)}{\zeta^{\bar{r}}(\phi)} \right\}$$

$$= \frac{2 \left\{ \frac{J_1\left(\tilde{A}_{o,s} \zeta^{\bar{r}}(\phi)\right)}{\tilde{A}_{o,s} \zeta^{\bar{r}}(\phi)} - \frac{\tilde{A}_{i,s}}{\tilde{A}_{o,s}^2 \zeta^{\bar{r}}(\phi)} J_1\left(\frac{\tilde{A}_{i,s} \tilde{A}_{o,s} \zeta^{\bar{r}}(\phi)}{\tilde{A}_{o,s}}\right) \right\}}{\left(1 - \frac{\tilde{A}_{i,s}^2}{\tilde{A}_{o,s}^2}\right)} \tag{186}$$

$$= \frac{2}{(1-\alpha^2)} \left\{ \frac{J_1(x)}{x} - \frac{\alpha}{x} J_1(\alpha x) \right\}$$

To determine the mean valued peak and null locations of the beampattern of a CRA one must first identify which, of the orthogonal pattern multiplier decays faster or in essence dominates the shape of the patter. For instance, plotting $\left| 2\mathrm{jinc}\zeta_x^r(\theta,\phi) \right|^2$ comparative to $\left| 2\mathrm{jinc}\zeta_y^r(\theta,\phi) \right|^2$ will allow one to identify that the $\zeta_y^r(\theta,\phi)$ orthonormal steering vectors dominates the pattern. Hence, the first null of the circular random array can be found by that of (187). In addition, by [158] is can be shown that there is some $x^*(\alpha)$ such that $f(x^*(\alpha),\alpha) = 0$ and for any given $\tilde{A}_{o,s}, \phi_{(n),1}$ (186) is a decreasing function of some $\tilde{A}_{i,s}$. Otherwise if $\tilde{A}_{i,s} = 0$, or, equivalently, $\alpha = 0$, one obtains (187). Meanwhile, increasing $\tilde{A}_{i,s}$ results in increasing α, which, according to (188), decreases $\phi_{(n),1}$. The steady decrease in $\phi_{(n),1}$ continues until $\tilde{A}_{i,s}$ approaches $\tilde{A}_{o,s,}$, or, in other words, $\alpha \approx 1$. In such a case, the first null of the ring is given by (189) where $v_1 \approx 3.8317$ and $v_0 \approx 2.4048$ are the first positive roots of $J_1(x)$ and $J_0(x)$, respectively for any $\alpha \in (0,1)$.

$$\phi_{(n),1} = \arcsin\left(\frac{\nu_1}{2\pi \tilde{A}_{o,s}}\right), \quad \alpha = 0 \tag{187}$$

$$\frac{dx^*(\alpha)}{d\alpha} < 0 \tag{188}$$

$$\phi_{(n),1} = \arcsin\left(\frac{\nu_0}{2\pi \tilde{A}_{o,s}}\right), \quad \alpha \approx 1 \tag{189}$$

Similarly for the spherical aperture it can be shown that if $\tilde{A}_{i,s} = 0$, or, equivalently, $\alpha = 0$, one obtains the first null of the spherical random array as (190) and for $\alpha \approx 1$ given by that of (191)

$$\phi_{(n),1} = \arcsin\left(\frac{\nu_1}{2\pi \tilde{A}_{o,s}}\right), \quad \alpha = 0 \tag{190}$$

$$\phi_{(n),1} = \arcsin\left(\frac{\nu_0}{2\pi \tilde{A}_{o,s}}\right), \quad \alpha \approx 1 \tag{191}$$

where $\nu_1 \approx 4.49$ and $\nu_0 \approx \pi$ are the first positive roots of $j_1(x)$ and $J_{1/2}(x)$ or $j_0(x)$, respectively. For any $\alpha \in (0,1)$

Note from (189) and (191) that, a narrow mainlobe, or, equivalently, a small $\phi_{(n),1}$, requires having a large $\tilde{A}_{o,s}$. This implies that $\tilde{A}_{i,s}$ may be very close to $\tilde{A}_{o,s}$ in practice without making A_{sph} so small that the number of nodes on $S_{sph}\left(0, \tilde{A}_{i,s}, \tilde{A}_{0,s}\right)$ drops below N. In other words, $S\left(0, \tilde{A}_{i,s}, \tilde{A}_{0,s}\right)$ and $S_{sph}\left(0, \tilde{A}_{i,s}, \tilde{A}_{0,s}\right)$ can be a narrow ring or narrow spherical ring but can still be large enough to include at least K nodes.

It follows from (187)-(189) and (190)-(191) that, when $\tilde{A}_{o,s}$ is large $\phi_{(n),1} \approx \nu_1/2\pi \tilde{A}_{o,s}$, for $\tilde{A}_{i,s} = 0$ while $\phi_{(n),1} \approx \nu_0/2\pi \tilde{A}_{o,s}$ for $\tilde{A}_{i,s} \approx \tilde{A}_{o,s}$. The following results are directly obtained from the above observation.

- For the spherical annular random array the first null can be reduced by up to 30% whereas for the circular annular array up to 37% [158] when increasing $\tilde{A}_{i,s}$ from zero to a close proximity of $\tilde{A}_{o,s}$. Interestingly, this means it is possible to considerably shrink the mainlobe of $U_{av}(\phi)$ simply by selecting a cluster of active nodes from within some close vicinity of the perimeter of $\left\{D\left(0, \tilde{A}_{0,s}\right), D_{sph}\left(0, \tilde{A}_{0,s}\right)\right\}$ while leaving all other nodes in the sleeping mode to preserve energy.

- Without having any effect on the target $\phi_{(n),1}$, the outer radius of $\{S_{disk}, S_{sph}\}$ can be reduced

from $\tilde{A}_{o,s} \approx \left(\dfrac{\lambda v_1}{2\pi\phi_{(n),1}} \right)$ to $\tilde{A}_{o,s} \approx \left(\dfrac{\lambda v_0}{2\pi\phi_{(n),1}} \right)$ by increasing the inner radius $\tilde{A}_{i,s}$ from zero to

$\tilde{A}_{i,s} \approx \tilde{A}_{o,s} \approx \left(\dfrac{\lambda v_0}{2\pi\phi_{(n),1}} \right)$. This property can be real useful when $\tilde{A}_{max}$ is smaller than $\left(\dfrac{\lambda v_1}{2\pi\phi_{(n),1}} \right)$.

(f) Approximate peak and null locations of the sidelobes

As discussed previously the practical interest in forming a narrow mainlobe necessitates $\phi_{(n),1}$ to

be small. According to the developments in the same subsection $\phi_{(n),1}$, is inversely proportional to $\tilde{A}_{o,s}$.

Therefore, a narrow mainlobe can be in fact associated with a large $\tilde{A}_{o,s}$. Hence, a large network may

benefit energy preservation and network connectivity by choosing A_{sph} and A_{disk} just large enough to

ensure $S\left(0, \tilde{A}_{i,s}, \tilde{A}_{0,s}\right)$ and $S_{sph}\left(0, \tilde{A}_{i,s}, \tilde{A}_{0,s}\right)$ includes K nodes [158]. It is direct to show that increasing

$\tilde{A}_{o,s}$ while keeping A_s fixed results in an $\tilde{A}_{i,s}$ that is close to $\tilde{A}_{o,s}$, or, equivalently, a large narrow ring

$S\left(0, \tilde{A}_{i,s}, \tilde{A}_{0,s}\right)$ or narrow spherical ring $S_{sph}\left(0, \tilde{A}_{i,s}, \tilde{A}_{0,s}\right)$. For such a scenario, $U_{av}(\phi)$ in (181) and (183)

can be approximated as shown by (192) and (193).

$$U_{av}(\phi) \approx \lim_{A_{i,s} \to A_{o,s}} \left(\frac{1}{K} + \left(1 - \frac{1}{K}\right) \left\| \frac{2}{\tilde{A}_{o,s}^2 - \tilde{A}_{i,s}^2} \left(\frac{\tilde{A}_{o,s}}{\zeta^{\tilde{r}}(\phi)} J_1\left(\tilde{A}_{o,s}\zeta^{\tilde{r}}(\phi)\right) - \frac{\tilde{A}_{i,s}}{\zeta^{\tilde{r}}(\phi)} J_1\left(\tilde{A}_{i,s}\zeta^{\tilde{r}}(\phi)\right) \right) \right\|^2 \right) =$$

$$\lim_{A_{i,s} \to A_{o,s}} \left(\frac{1}{K} + \left(1 - \frac{1}{K}\right) \left\| \frac{2\zeta^{\tilde{r}}(\phi)}{\left(\tilde{A}_{o,s} - \tilde{A}_{i,s}\right)\left(\tilde{A}_{o,s} + \tilde{A}_{i,s}\right)\zeta^{\tilde{r}}(\phi)} \left(\frac{\frac{\tilde{A}_{o,s}}{\zeta^{\tilde{r}}(\phi)} J_1\left(\tilde{A}_{o,s}\zeta^{\tilde{r}}(\phi)\right) -}{\frac{\tilde{A}_{i,s}}{\zeta^{\tilde{r}}(\phi)} J_1\left(\tilde{A}_{o,s}\zeta^{\tilde{r}}(\phi)\right)} \right) \right\|^2 \right) =$$

$$\frac{1}{K} + \left(1 - \frac{1}{K}\right) \left\| \frac{2}{2\tilde{A}_{o,s}\zeta^{\tilde{r}}(\phi)} \lim_{\tilde{A}_{i,s} \to \tilde{A}_{o,s}} \frac{\tilde{A}_{o,s}\zeta^{\tilde{r}}(\phi) J_1\left(\tilde{A}_{o,s}\zeta^{\tilde{r}}(\phi)\right) - \tilde{A}_{i,s}\zeta^{\tilde{r}}(\phi) J_1\left(\tilde{A}_{o,s}\zeta^{\tilde{r}}(\phi)\right)}{\tilde{A}_{o,s}\zeta^{\tilde{r}}(\phi) - \tilde{A}_{i,s}\zeta^{\tilde{r}}(\phi)} \right\|^2 = \tag{192}$$

$$\frac{1}{K} + \left(1 - \frac{1}{K}\right) \left\| \frac{1}{\tilde{A}_{o,s}\zeta^{\tilde{r}}(\phi)} \frac{\partial\left(\tilde{A}_{o,s}\zeta^{\tilde{r}}(\phi) J_1\left(\tilde{A}_{o,s}\zeta^{\tilde{r}}(\phi)\right)\right)}{\partial\left(\tilde{A}_{o,s}\zeta^{\tilde{r}}(\phi)\right)} \right\|^2$$

using the identity   thus

$$\frac{d}{dx}\left[x^m J_m(x)\right] = x^m J_{m-1}(x) \qquad = \frac{1}{K} + \left(1 - \frac{1}{K}\right) \left\| J_0\left(\tilde{A}_{o,s}\zeta^{\tilde{r}}(\phi)\right) \right\|^2$$

$$U_{av}(\phi) \approx \lim_{A_{i,s} \to A_{o,s}} \left(\frac{1}{K} + \left(1 - \frac{1}{K}\right) \left| \frac{3}{\tilde{A}_{o,s}^2 - \tilde{A}_{i,s}^2} \left(\frac{\tilde{A}_{o,s}}{\zeta^{\vec{r}}(\phi)} j_1\left(\tilde{A}_{o,s}\zeta^{\vec{r}}(\phi)\right) - \frac{\tilde{A}_{i,s}}{\zeta(\phi)} j_1\left(\tilde{A}_{i,s}\zeta^{\vec{r}}(\phi)\right) \right) \right|^2 \right) =$$

$$\lim_{A_{i,s} \to A_{o,s}} \left(\frac{1}{K} + \left(1 - \frac{1}{K}\right) \left| \frac{3\zeta^{\vec{r}}(\phi)}{\left(\tilde{A}_{o,s} - \tilde{A}_{i,s}\right)\left(\tilde{A}_{o,s} + \tilde{A}_{i,s}\right)\zeta^{\vec{r}}(\phi)} \left(\frac{\tilde{A}_{o,s}}{\zeta(\phi)} j_1\left(\tilde{A}_{o,s}\zeta^{\vec{r}}(\phi)\right) - \frac{\tilde{A}_{i,s}}{\zeta(\phi)} j_1\left(\tilde{A}_{i,s}\zeta^{\vec{r}}(\phi)\right) \right) \right|^2 \right)$$

$$= \frac{1}{K} + \left(1 - \frac{1}{K}\right) \left| \frac{3}{\left(2\tilde{A}_{o,s}\right)\zeta^{\vec{r}}(\phi)} \lim_{\tilde{A}_{i,s} \to \tilde{A}_{o,s}} \frac{\tilde{A}_{o,s}\zeta^{\vec{r}}(\phi) j_1\left(\tilde{A}_{o,s}\zeta^{\vec{r}}(\phi)\right) - \tilde{A}_{i,s}\zeta^{\vec{r}}(\phi) j_1\left(\tilde{A}_{i,s}\zeta^{\vec{r}}(\phi)\right)}{\tilde{A}_{o,s}\zeta^{\vec{r}}(\phi) - \tilde{A}_{i,s}\zeta^{\vec{r}}(\phi)} \right|^2 =$$

$$\frac{1}{K} + \left(1 - \frac{1}{K}\right) \left| \frac{3}{2\tilde{A}_{o,s}\zeta^{\vec{r}}(\phi)} \frac{\partial\left(\tilde{A}_{o,s}\zeta^{\vec{r}}(\phi) j_1\left(\tilde{A}_{o,s}\zeta^{\vec{r}}(\phi)\right)\right)}{\partial\left(\tilde{A}_{o,s}\zeta^{\vec{r}}(\phi)\right)} \right|^2$$

$$= \frac{1}{K} + \left(1 - \frac{1}{K}\right) \left| \frac{3}{2} \left(j_0\left(\tilde{A}_{o,s}\zeta^{\vec{r}}(\phi)\right) - \frac{j_1\left(\tilde{A}_{o,s}\zeta^{\vec{r}}(\phi)\right)}{\tilde{A}_{o,s}\zeta^{\vec{r}}(\phi)} \right) \right|^2 =$$

$$\frac{1}{K} + \left(1 - \frac{1}{K}\right) \left| \frac{3}{2} \left(\sqrt{\frac{\pi}{2\tilde{A}_{o,s}\zeta^{\vec{r}}(\phi)}} \left(J_{1/2}\left(\tilde{A}_{o,s}\zeta^{\vec{r}}(\phi)\right) - \frac{J_{3/2}\left(\tilde{A}_{o,s}\zeta^{\vec{r}}(\phi)\right)}{\tilde{A}_{o,s}\zeta^{\vec{r}}(\phi)} \right) \right) \right|^2$$

$$= \frac{1}{K} + \left(1 - \frac{1}{K}\right) \left| \frac{3}{2} \left(\operatorname{sinc}\left(\tilde{A}_{o,s}\zeta^{\vec{r}}(\phi)\right) - \operatorname{tinc}\left(\tilde{A}_{o,s}\zeta^{\vec{r}}(\phi)\right) \right) \right|^2 \tag{193}$$

Now using (194) $U_{av}(\phi)$ in (192) is further simplified to (195) for $\tilde{A}_{o,s}\zeta(\phi) \gg 1/4$ and (193) to (196) for $\tilde{A}_{o,s}\zeta(\phi) \gg 2$ since the orthonormal steering function $\zeta_y^r(\phi)$ dominates at endfire. This helps ease the process for finding the mean l^{th} null $\phi_{(n),l}$ and peak $\phi_{(p),l}$ positions of the average beampattern, where the zeroth order peak ($\phi_{(p),0} = \phi_0 = 0$) represents the mainlobe of the respective beampattern.

$$J_m(x) \approx \sqrt{\frac{2}{\pi x}} \cos\left(x - \frac{m\pi}{2} - \frac{\pi}{4}\right) \quad x \gg \left|m^2 - \frac{1}{4}\right|$$

$$\therefore$$

$$J_0(x) \approx \sqrt{\frac{2}{\pi x}} \cos\left(x - \frac{\pi}{4}\right) \quad x \gg \frac{1}{4} \tag{194}$$

$$J_{1/2}(x) \approx \sqrt{\frac{2}{\pi x}} \cos\left(x - \frac{\pi}{2} - \frac{\pi}{4}\right) = \sqrt{\frac{2}{\pi x}} \cos\left(x - \frac{3\pi}{4}\right) \quad x \gg 0$$

$$J_{3/2}(x) \approx \sqrt{\frac{2}{\pi x}} \cos\left(x - \frac{3\pi}{8} - \frac{\pi}{4}\right) = \sqrt{\frac{2}{\pi x}} \cos\left(x - \frac{5\pi}{8}\right) \quad x \gg 2$$

$$U_{av}(\phi) \approx \frac{1}{K} + \left(1 - \frac{1}{K}\right) \frac{2}{\pi \tilde{A}_{o,s}\zeta(\phi)} \cos^2\left(\tilde{A}_{o,s}\zeta(\phi) - \frac{\pi}{4}\right) \tag{195}$$

$$\left| \frac{3}{2}\left(\sqrt{\frac{\pi}{2\tilde{A}_{o,s}\varsigma(\phi)}}\left(\sqrt{\frac{2}{\pi\tilde{A}_{o,s}\varsigma(\phi)}}\cos\left(\tilde{A}_{o,s}\varsigma(\phi)-\frac{3\pi}{4}\right) - \frac{\sqrt{\frac{2}{\pi\tilde{A}_{o,s}\varsigma(\phi)}}\cos\left(\tilde{A}_{o,s}\varsigma(\phi)-\frac{5\pi}{8}\right)}{\tilde{A}_{o,s}\varsigma(\phi)}\right)\right)\right|^2$$

$$= \left| -\frac{3}{2\tilde{A}_{o,s}\varsigma(\phi)}\left(\cos\left(\tilde{A}_{o,s}\varsigma(\phi)-\frac{3\pi}{4}\right) - \frac{\cos\left(\tilde{A}_{o,s}\varsigma(\phi)-\frac{5\pi}{8}\right)}{\tilde{A}_{o,s}\varsigma(\phi)}\right)\right|^2$$

$$= \left| -\frac{3}{2}\left(\frac{\cos\left(\frac{\pi}{4}+\tilde{A}_{o,s}\varsigma(\phi)\right)}{\tilde{A}_{o,s}\varsigma(\phi)} - \frac{\sin\left(\frac{\pi}{8}-\tilde{A}_{o,s}\varsigma(\phi)\right)}{\left(\tilde{A}_{o,s}\varsigma(\phi)\right)^2}\right)\right|^2$$

$$= U_{av}(\phi) \approx \frac{1}{K}+\left(1-\frac{1}{K}\right)\left| -\frac{3}{2}\left(\frac{\cos\left(\frac{\pi}{4}+\tilde{A}_{o,s}\varsigma(\phi)\right)}{\tilde{A}_{o,s}\varsigma(\phi)} - \frac{\sin\left(\frac{\pi}{8}-\tilde{A}_{o,s}\varsigma(\phi)\right)}{\left(\tilde{A}_{o,s}\varsigma(\phi)\right)^2}\right)\right|^2$$

$$U_{av}(\phi) \overset{sph}{\approx} \frac{1}{K}+\left(1-\frac{1}{K}\right)\left| \frac{\cos\left(x-\frac{\pi}{2}\right)}{x}\right|^2, x=A_{o,s}\varsigma_y^r(\phi) \tag{196}$$

It follows from (195) that nulls (197) and peaks (198) are found for the circular ring array [158].[1] Similarly peaks (199) and (200) of (196) are also found in a similar manner where the zeroth peak and null location are offset by a factor of 1/8 due to the slightly less accurate approximation (196) for the spherical ring random array.

---

[1] The results of (197) and (198) were previously provided as $\phi_{(n),\ell}=2\sin^{-1}\left(\left(\ell-1/4\right)/4\tilde{A}_{0,s}\right)$ and $\phi_{(p),\ell}=2\sin^{-1}\left(\left(\ell+1/4\right)/4\tilde{A}_{0,s}\right)$ since a constant value of the orthonormal steering vector $\varsigma_{endfire}^{\vec{r}}(\phi)=4\pi\sin\left(\phi/2\right)$ was thought to of been correct. This value, however is in fact incorrect as $\varsigma_{endfire}^{\vec{r}}(\phi)$ is actually a vector due to the constant offset angle δ. Moreover, the magnitude of the orthonormal steering vector simplifies as $\varsigma_{endfire}^{\vec{r}}(\phi)=4\pi\sqrt{(1-\cos\phi)/2}$ whereas the factor $\sqrt{(1-\cos\phi)/2}$ cannot be reduced as $\sin\left(\phi/2\right)$ as it was previously expected. This is due, since the factor $(1-\cos\phi)/2=\sin^2\left(\phi/2\right)$ neglects the $\pm$ portion of the factor. However, all in all for small values of angle the factor $2\sin\left(\phi/2\right)$ approximated as ϕ causing no loss in generality in the works of [6]-[14], [81]-[82], but yet should be avoided in future use.

$$\cos^2\left(2\pi\tilde{A}_{0,s}\sin(\phi)-\frac{\pi}{4}\right)=0 \approx \text{produces a null}$$

$$2\pi\tilde{A}_{0,s}\sin(\phi)=\left(\ell\pm\frac{1}{2}\right)\pi+\frac{\pi}{4} \quad (\text{use minus}) \tag{197}$$

$$\phi_{(n),\ell}=\sin^{-1}\left(\frac{\ell-\frac{1}{4}}{2\tilde{A}_{0,s}}\right)$$

$$\cos^2\left(2\pi\tilde{A}_{0,s}\sin(\phi)\right)=1 \approx \text{produces a peak}$$

$$2\pi\tilde{A}_{0,s}\sin(\phi)=(\pm\ell\pi) \quad (\text{use plus because a peak follows a null}) \tag{198}$$

$$\phi_{(p),\ell}=\sin^{-1}\left(\frac{\ell+\frac{1}{4}}{2\tilde{A}_{0,s}}\right)$$

$$\phi_{(p),0}=\sin^{-1}\left(\frac{\ell+3/8}{2\tilde{A}_{o,s}}\right),\ell=0$$

$$\phi_{(p),\ell}=\sin^{-1}\left(\frac{\ell+1/2}{2\tilde{A}_{o,s}}\right),\ell=1,2,\ldots \tag{199}$$

$$\phi_{(n),0}=\sin^{-1}\left(\frac{\ell-1/8}{2\tilde{A}_{o,s}}\right),\ell=0$$

$$\phi_{(n),\ell}=\sin^{-1}\left(\frac{\ell}{2\tilde{A}_{o,s}}\right),\ell=1,2,\ldots \tag{200}$$

For $\ell=1,2,\ldots$ it is noteworthy that the approximate $\phi_{(n),\ell}$ obtained from (197) is in fact very close to the approximate derived in (191). Note also that, the approximations in (197)-(200) provide a simple technique to derive $\tilde{A}_{o,s}$ and $\tilde{A}_{i,s}$. Given a desired $\phi_{(n),\ell}$ or $\phi_{(p),\ell}$, one may determine the required $\tilde{A}_{o,s}$ from (199) and (200) and, then, use the preassigned A_{sph} to obtain $\tilde{A}_{i,s}$. We also obtain from (196) and (199)-(200) that the lth peak of the average sidelobe is approximately given by (201) [158]. For completeness in analysis the lth peak of the average sidelobe of the circular ring random array is also provided by that of (202) [158].

$$U_{av}\left(\phi_{(p),\ell}\right)\approx\frac{1}{K}+\left(1-\frac{1}{K}\right)\left(\frac{3}{2\left(\ell+\frac{1}{2}\right)\pi}\right)^2 \tag{201}$$

$$U_{av}\left(\phi_{(p),\ell}\right) \approx \frac{1}{K} + \left(1 - \frac{1}{K}\right)\frac{2}{2\pi\tilde{A}_{o,s}\sin\left(\arcsin\left(\frac{\left(\ell + \frac{1}{4}\right)}{2\tilde{A}_{o,s}}\right)\right)\pi}$$

$$= \frac{1}{K} + \left(1 - \frac{1}{K}\right)\frac{2}{\pi^2\left(\ell + \frac{1}{4}\right)}$$

(202)

(g) Average directivity

Average directivity is a parameter that measures the beamforming efficiency to concentrate the transmitted power towards the desired direction. Note that or in other words this is a damped sinusoidal. Therefore, as $\tilde{A}_{o,s}$ grows, the normalized average directivity converges to its maximum value of *N*. The average directivity of (192) is given by (203) whereas the average directivity of (193) is given by (204). These results are illustrated in Figure 43 and are useful since, as $\tilde{A}_{o,s}$ grows, the normalized average directivity converges to its maximum value of *K* (since the denominator is a dampened sinusoidal function).

$$D_{av} = \frac{K}{1 + (K-1)\,{}_2F_3\left[\frac{1}{2},\frac{1}{2};1,1,1;-\left(4\pi\tilde{A}_{o,s}\right)^2\right]}$$

(203)

$$\frac{K}{\left[1 + \frac{(K-1)\left(\left(\frac{8x - 4x^3 -}{6x^5}\right)J_0(2x) + \left(-8 + 8x^2 + 3x^4\right)J_1(2x)\right)}{10x^5} + \frac{(K-1)\pi\left(\frac{-5+}{6x^2}\right)\left(\begin{array}{c}-J_1(2x)H_0(2x)+\\J_0(2x)H_1(2x)\end{array}\right)}{20x^2}\right]}$$

(204)

$$x = 2\tilde{A}_{o,s}\pi$$
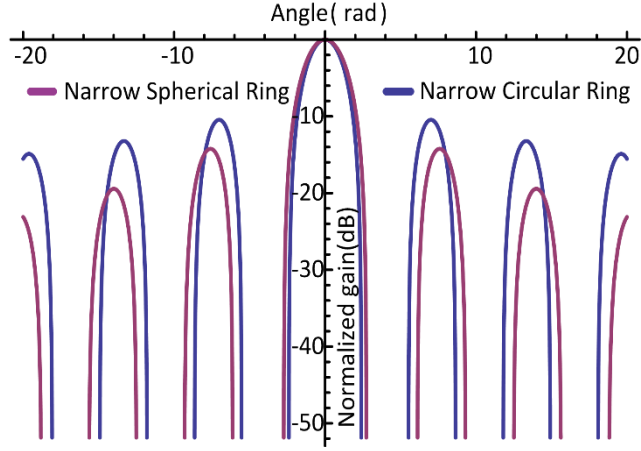
Figure 43. Comparison the characteristic functions (192) and (193).

(h) Extension to multiple concentric rings

As can be observed from (202), when $\tilde{A}_{i,s} \approx \tilde{A}_{o,s}$, the first and the largest sidelobe peak of the average beampattern is given by $U_{av}(\phi) \approx .16$ which is around 8 dB less than the mainlobe maximum value. For the spherical ring in (201) $\tilde{A}_{i,s} \approx \tilde{A}_{o,s}$, the first and the largest sidelobe peak of the average beampattern is given by $U_{av}(\phi) \approx .045$ which is around 13 dB less than the mainlobe maximum value. This reduction in sidelobe level will provide significant improvements for numerous applications. Elements may even be selected from multiple concentric rings of circles or spheres with a proper radii to reduce sidelobe peak value. With M concentric rings (circular or spherical) $S_{\{sph,disk\},m}\left(0,\tilde{A}_{i,s}^{m},\tilde{A}_{o,s}^{m}\right), m = 1,...,M$ where $\tilde{A}_{o,s}^{(m)} \leq \tilde{A}_{i,s}^{(m+1)}$ it can be shown from [158] that the characteristic function for circular concentric rings is given by (205) for that of concentric spherical rings (206).

$$U_{av}(\phi) = \frac{1}{K} + \left(1 - \frac{1}{K}\right)|\Lambda|^{2}$$

$$\Lambda = 2 \frac{\left\{ \sum_{m=1}^{M} \frac{\tilde{A}_{o,s}^{(m)} J_1\left(\tilde{A}_{o,s}^{(m)}\zeta^{\ddot{r}}(\phi)\right) - \tilde{A}_{i,s}^{(m)} J_1\left(\tilde{A}_{i,s}^{(m)}\zeta^{\ddot{r}}(\phi)\right)}{\zeta^{\ddot{r}}(\phi)} \right\}}{\sum_{m=1}^{M} \tilde{A}_{o,s}^{(m)2} - \tilde{A}_{i,s}^{(m)2}} \tag{205}$$

$$U_{av}(\phi) = \frac{1}{K} + \left(1 - \frac{1}{K}\right)|\Lambda|^2$$

$$\Lambda = 3 \frac{\left\{\sum_{m=1}^{M} \frac{\tilde{A}_{o,s}^{(m)} j_1\left(\tilde{A}_{o,s}^{(m)} \zeta^{\tilde{r}}(\phi)\right) - \tilde{A}_{i,s}^{(m)} j_1\left(\tilde{A}_{i,s}^{(m)} \zeta^{\tilde{r}}(\phi)\right)}{\zeta^{\tilde{r}}(\phi)}\right\}}{\sum_{m=1}^{M} \tilde{A}_{o,s}^{(m)2} - \tilde{A}_{i,s}^{(m)2}} \tag{206}$$

Now assume that $A_{disk_m} = \pi\tilde{A}_{o,s}^{(m)2} - \pi\tilde{A}_{i,s}^{(m)2} = \eta/M$ and $A_{sph_m} = 4\pi\tilde{A}_{o,s}^{(m)2} - 4\pi\tilde{A}_{i,s}^{(m)2} = \eta/M$ for $m = 1,\ldots,M$, that is, all rings have the same area while their total area is equal to η. As η is independent from $\tilde{A}_{o,s}^{(m)}$, if $\tilde{A}_{o,s}^{(m)}$ increases, $\tilde{A}_{i,s}^{(m)}$ grows as well such that η/M remains unchanged. Under this condition, $U_{av}(\phi)$ can be approximated for a large $\tilde{A}_{o,s}^{(1)}$ as shown in (207) similar to (45 in [158]) and (192). For a spherical ring the procedure is the same and the result is given in (208).

$$U_{av}(\phi) \approx \frac{1}{K} + \left(1 - \frac{1}{K}\right)\left|\frac{1}{M}\sum_{m=1}^{M} J_0\left(\tilde{A}_{o,s}^{(m)} \zeta(\phi)\right)\right|^2 \tag{207}$$

$$U_{av}(\phi) \approx \frac{1}{K} + \left(1 - \frac{1}{K}\right)\left|\frac{1}{M}\sum_{m=1}^{M} \frac{3}{2}\left(\text{sinc}\left(\tilde{A}_{o,s}^{(m)} \zeta(\phi)\right) - \text{tinc}\left(\tilde{A}_{o,s}^{(m)} \zeta(\phi)\right)\right)\right|^2 \tag{208}$$

Now using (195) in (207) and (196) in (208), simplifies the results of the concentric circular and spherical annular ring random array to that of (209) and (210). The result of these expressions indicates that the contributions of all rings (circular or spherical) apply independently to the average beampattern $U_{av}(\phi)$ through a simple summation. This fact facilitates a simple approach to determine $\tilde{A}_{o,s}^{(m)}, m = 1,\ldots,M$. I.e., assume that it is required to have a null positioned at ϕ^* then selecting $\tilde{A}_{o,s}^{(m)}$ in (211) for a circular rings or $\tilde{A}_{o,s}^{(m)}$ in (47) for spherical rings may be utilized for the design. This results in generating an average beampattern null at ϕ^* while substantially reducing the sidelobe peaks. As well all rings reinforce the null at ϕ^*, such that one may conjecture that the null width around ϕ^* increases as the number of rings grows. Numerical results are demonstrated in Figure 44-Figure 49 to verify this conjecture where $\phi^* = 1$. Furthermore, Figure 44-Figure 46 demonstrate the SARA ability to create a null at 1 degree using the nth null of the pattern in (212) given m =0 in Figure 44, m=1 in Figure 45, and m=2 in Figure 46. Furthermore these illustrations demonstrate that the pattern more directive and squeezed tighter in the corresponding viewing window as the nth null of the pattern is utilized. Also since the SRA contains a symmetric at broadside and endfire pattern as shown in Figure 41 and Figure 42 that these results will be the same at the SARA zenith elevation angle. However, differently the CRA is not

symmetric at the endfire and zenith locations. As a consequence, the pattern of the CARA is not the same at these angles and a comparison is made in Figure 47-Figure 49. From these results it is seen that the patterns are closely the same near the mainbeam, but diverge from each other far away such that the results of the CARA is likely to have higher values in sidelobe level.

$$U_{av}(\phi) \approx \frac{1}{K} + \left(1 - \frac{1}{K}\right) \left| \frac{\sqrt{2}}{M} \sum_{m=1}^{M} \frac{\cos\left(\tilde{A}_{o,s}^{(m)} \zeta^{\bar{r}}(\phi) - \frac{\pi}{4}\right)}{\sqrt{\pi \tilde{A}_{o,s}^{(m)} \zeta^{\bar{r}}(\phi)}} \right|^2 \tag{209}$$

$$U_{av}(\phi) \approx \frac{1}{K} + \left(1 - \frac{1}{K}\right) \left| \frac{1}{M} \sum_{m=1}^{M} \left(\frac{\cos\left(\tilde{A}_{o,s}^{(m)} \zeta^{\bar{r}}(\phi) - \frac{\pi}{2}\right)}{\tilde{A}_{o,s}^{(m)} \zeta^{\bar{r}}(\phi)} \right) \right|^2 \tag{210}$$

$$\tilde{A}_{o,s}^{(m)} = \frac{\lambda\left(m - \frac{1}{4}\right)}{4\sin\left(\frac{\phi^*}{2}\right)}, \quad m = 1, \ldots, M \tag{211}$$

$$\tilde{A}_{o,s}^{(m)} = \frac{\lambda(m - 1/8)}{2\sin(\phi^*)}, \quad m = 0$$

$$\tilde{A}_{o,s}^{(m)} = \frac{\lambda m}{2\sin(\phi^*)}, \quad m = 1, \ldots, M \tag{212}$$
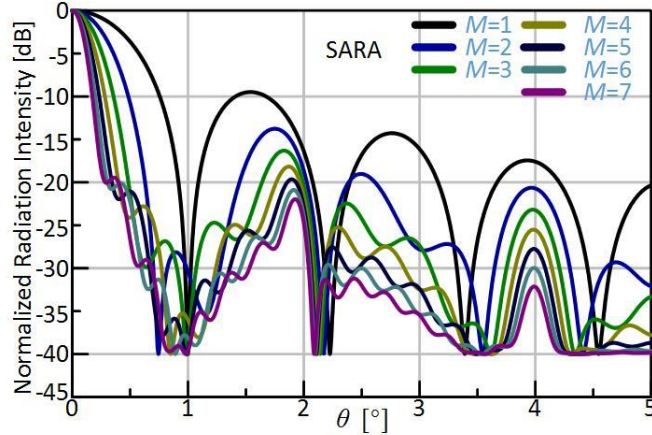
Figure 44. Spherical annular random array broadside (first null).
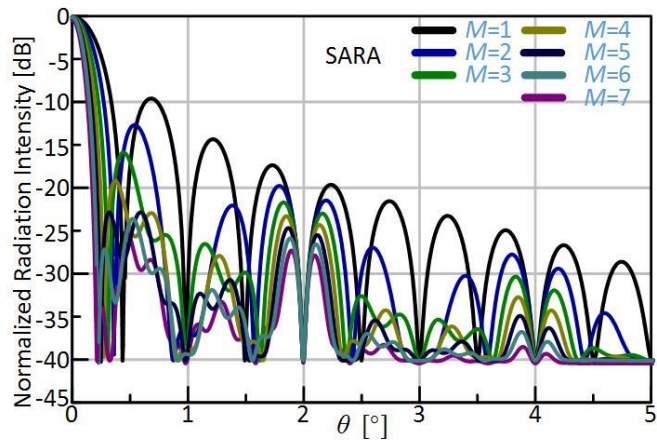
Figure 45. Spherical annular random array broadside (second null).
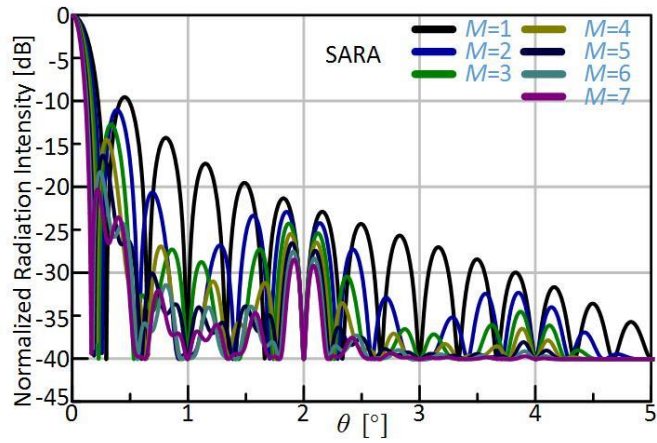
Figure 46. Spherical annular random array Sara broadside (third null).
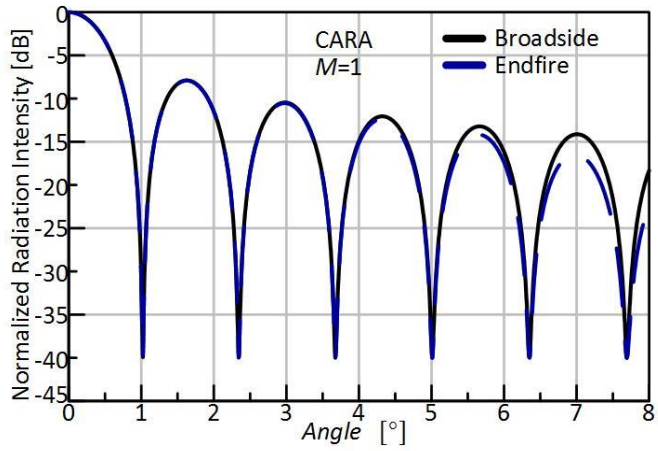
Figure 47. Circular annular random array broadside and endfire comparison (first null).
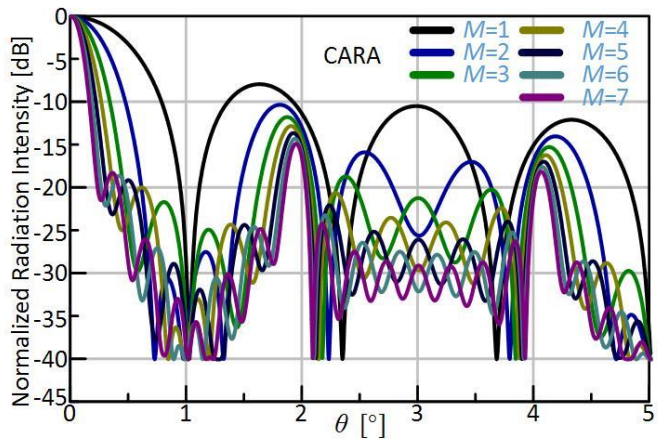
Figure 48. Circular annular random array broadside (first null).
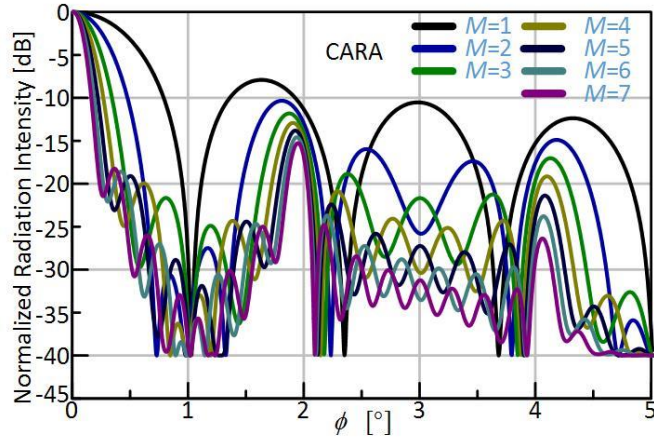
Figure 49. Circular annular random array endfire (first null).

It should be mentioned that, if multiple narrow rings are used, the inter-ring connectivity is maintained when $A_{o,s}^{(m+1)} - A_{o,s}^{(m)} < A_f$ for $m = 1, \ldots, M$. However, if the latter inequality does not hold for an m, some of the nodes located between the rings m and m+1 may be kept in the active mode and used to establish the connection between those rings. Alternative means to maintain the inter-cluster connectivity may be adopted for these means from to preserve these inter ring connections.

In conclusion this section has analyzed a new method in adaptive beamforming for aperiodic random arrays of which utilizes a shared aperture approach. A full rigorous derivation of this process was completed and it was seen that narrow circular or spherical rings may be utilized in terms of creating nulls at specified spatial locations. The approach mainly centered on the orthonormal meridian steering vector, but can be easily changed to the broadside steering vector. Furthermore results of both the meridian and zenith elevation steering vectors were illustrated in Figure 44-Figure 49. From these it was seen that the results of a spherical annular random array (SARA) is symmetric at all angles due to where the circular annular random array (CARA) is dependent upon scan angle. As a consequence, the CARA is likely to have greater sidelobe levels when scanned toward the zenith elevation angle as compared to when scanned at the plane of the array.

CHAPTER VII

CHARACTERISTIC MODES OF CIRCULAR AND SPHERICAL RANDOM ARRAYS (DIRECTIVE TAPERS)

7.1 Generalized Jinc Function Family for the Circular Random Array

A systematic treatment of the far-field diffraction patterns produced by circular sector apertures or annular versions has provided analytical solutions in terms of a series of Bessel functions known as the jinc family [73]. This family will be analyzed in this section in order to find the characteristic modes of circular random arrays.

It is well known that the diffraction pattern of a uniformly distributed circular aperture is given by $2\,\text{jinc}(x)$. This solution is similar to what one calls the dominant mode of a patch antenna and an integral form is written as (213): where $J_0(x)$ is the zero-order Bessel function of the first kind and v is the variable of integration. In fact the derivation of the Fraunhofer diffraction of circular apertures leads to a generalized Jinc family distribution (214). In fact the first several modes besides the dominant n=0 mode are given by (215)-(217) also similar to [73].

$$\text{Jinc}(x) = \frac{J_1(x)}{x} = \frac{1}{x^2}\int_0^x v J_0(v)\,dv \tag{213}$$

$$\text{Jinc}_n(x) = \frac{1}{x^{2n+2}}\int_0^x v^{2n+1} J_0(v)\,dv \quad n \geq 0 \tag{214}$$

$$\text{Jinc}_1(x) = \frac{J_1(x)}{x} - 2\frac{J_2(x)}{x^2} \tag{215}$$

$$\text{Jinc}_2(x) = \frac{J_1(x)}{x} - 4\frac{J_2(x)}{x^2} + 8\frac{J_3(x)}{x^3} \tag{216}$$

$$\text{Jinc}_3(x) = \frac{J_1(x)}{x} - 6\frac{J_2(x)}{x^2} + 24\frac{J_3(x)}{x^3} - 48\frac{J_4(x)}{x^4} \tag{217}$$

One can deduce that for large x all sub terms decrease much faster than the dominant mode and for large x the dominant mode approaches (218). In addition for the relation $J_0(v)=1 \cap \lim_{x\to 0}$ the integral of (214) reduces to that of (219) showing a convergence value of each maximum nth order Jinc mode. Also seen is each nth order mode decreases with increase of *n*.

$$\lim_{x\to\infty} \text{Jinc}_n(x) = \frac{J_1(x)}{x} \tag{218}$$

$$\text{Jinc}_n(0) = \frac{1}{2(n+1)} \tag{219}$$

This family of Jinc functions has similar curves gradually changing with a change in the order n. Also similar to [73] it can be shown from (214) as the $\lim_{n\to\infty}$, the normalized $\text{Jinc}_n(x)$ functions approach that of a zero order Bessel function $J_0(x)$ (220).

$$\lim_{n\to\infty} \text{Jinc}_n(x) = \frac{1}{2(n+1)} J_0(x) \tag{220}$$

7.2 Circular Random Array Modes

The second through fourth order modes of a circular random array will be shown in this section as an example for completeness and clarity. To find the second order mode it is necessary to find the probability density function leading itself toward the desired solution type. In order to find this distribution the integral relation in (214) is examined and it is seen that a ρ^2 type of distribution will lead itself to the second order mode solution. The joint distribution of the dominant mode of a circular path in (221) is modified to fit the second order mode given by (222). Next the marginal distribution function for each mode in terms of Cartesian coordinates is found respectively in (224) and (225). An illustration of the first four pdf modes are shown in Figure 50.

$$\int_0^1 \int_0^{2\pi} f_0(\rho,\phi)\rho \, d\rho \, d\phi = 1 \rightarrow f_0(\rho,\phi) = \frac{1}{\pi} \tag{221}$$

$$\int_0^1 \int_0^{2\pi} f_1(\rho,\phi)\rho^2 \, d\rho \, d\phi = 1 \rightarrow f_1(\rho,\phi) = \frac{2}{\pi} \tag{222}$$

$$\int_0^1 \int_0^{2\pi} f_2(\rho,\phi)\rho^4 \, d\rho \, d\phi = 1 \rightarrow f_2(\rho,\phi) = \frac{3}{\pi} \tag{223}$$

$$f_0(x) = \frac{1}{\pi} \int_{-\sqrt{1-x^2}}^{\sqrt{1-x^2}} 1 \, dy = \frac{2\sqrt{1-x^2}}{\pi} \tag{224}$$

$$f_1(x) = \frac{2}{\pi} \int_{-\sqrt{1-x^2}}^{\sqrt{1-x^2}} \left(x^2+y^2\right) dy = \frac{4\sqrt{1-x^2}}{3\pi}\left(1+2x^2\right) \tag{225}$$

$$f_2(x) = \frac{3}{\pi} \int_{-\sqrt{1-x^2}}^{\sqrt{1-x^2}} \left(x^2+y^2\right)^2 dy = \frac{2\sqrt{1-x^2}}{5\pi}\left(3+4x^2+8x^4\right) \tag{226}$$

$$f_3(x) = \frac{4}{\pi} \int_{-\sqrt{1-x^2}}^{\sqrt{1-x^2}} \left(x^2+y^2\right)^3 dy = \frac{8\sqrt{1-x^2}}{35\pi}\left(5+6x^2+8x^4+16x^6\right) \tag{227}$$
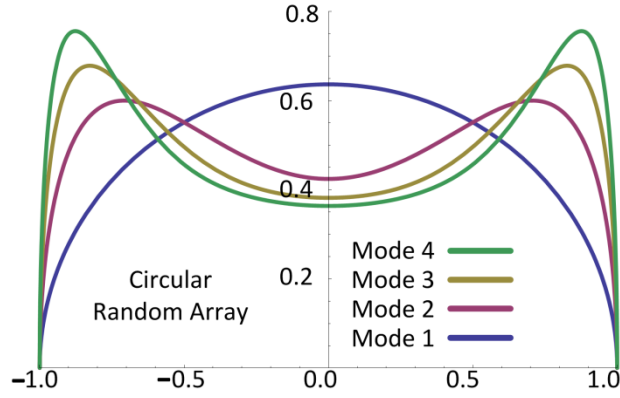
Figure 50. Pdfs of the first four modes of a circular random array.

This method in polar coordinates is shown in order to verify its representation to the jinc family integral representation in (214) given by the following formulation (228)-(230).

$$f(\rho) = \frac{2\rho^3}{\pi} \int_0^{2\pi} d\phi = 4\rho^3 \tag{228}$$

$$f(\phi) = \frac{2}{\pi} \int_0^1 \rho^3 d\rho = \frac{1}{2\pi} \tag{229}$$

$$F_{av}(\theta,\phi) = E_{\rho,\phi}\left|F\left(\theta,\phi\middle|\tilde{\rho}_n,\tilde{\phi}_n\right)\right| =$$

$$= \left(1-\frac{1}{N}\right)\left[\int_0^1\int_0^{2\pi} e^{j\zeta(\theta,\phi)\left(\tilde{\rho}_n\cos\tilde{\phi}_n\right)} \frac{1}{2\pi} d\tilde{\phi}_n 4\tilde{\rho}_n^3 d\tilde{\rho}_n\right]$$

$$= \left(1-\frac{1}{N}\right)\left[\int_0^1 4\tilde{\rho}_n^3 J_0\left(\zeta(\theta,\phi)\right) d\tilde{\rho}_n\right]$$

$$= \left(1-\frac{1}{N}\right)\frac{4}{\zeta(\theta,\phi)^4}\left[\int_0^{\zeta(\theta,\phi)} u_n^3 J_0(u) du_n\right]$$

$$= 4\left[\frac{J_1\left(\zeta(\theta,\phi)\right)}{\zeta(\theta,\phi)} - 2\frac{J_2\left(\zeta(\theta,\phi)\right)}{\zeta(\theta,\phi)^2}\right] \tag{230}$$

Taking the absolute value of (230) and squaring it gives the average array factor or mean valued radiation intensity of the second order mode (231). Again this solution was found using the Bessel Fourier transform, but could have been derived using a Fourier Transform and compound random variable representation (232). Again the first four characteristic functions are provided below in Figure 51.

$$U_{av}(\theta,\phi) = \left|4\left[\frac{J_1\left(\zeta(\theta,\phi)\right)}{\zeta(\theta,\phi)} - 2\frac{J_2\left(\zeta(\theta,\phi)\right)}{\zeta(\theta,\phi)^2}\right]\right|^2 \tag{231}$$

$$\Lambda = F_{av}(\theta,\phi) = \left(\int_0^1 e^{j\zeta(\theta,\phi)x} \frac{4\sqrt{1-x^2}}{3\pi} + \frac{8x^2\sqrt{1-x^2}}{3\pi} \right) dx = 4Jinc_1\left(\zeta(\theta,\phi)\right) \tag{232}$$
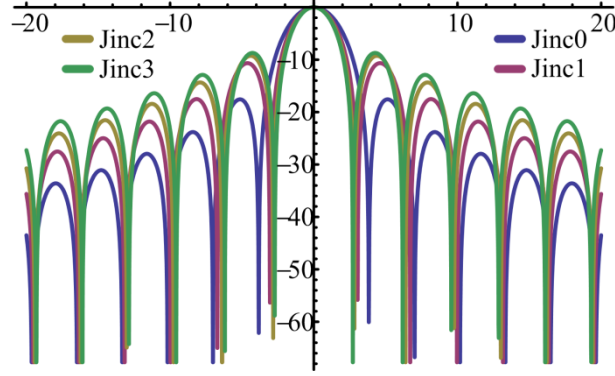
Figure 51. Comparison of the characteristic functions of the first four modes of a circular random array.

In Figure 51 it is seen that the ascending order modes are more directive then the dominant mode, but come at an expense of higher sidelobes. The loss of energy in the main beam is due to the conservation of energy meaning that the energy lost in the main lobe region is now displaced outside of the main lobe region or into the sidelobe region; also similar to the beams seen in tapered aperture distributions, which are shown in Chapters VIII – Chapter X.

7.3 Spherical Random Array Modes

The derivation of the Fraunhofer diffraction of spherical apertures at the meridian elevation angle $\theta = \theta_0 = \pi/2$ leads to a generalized Tinc family distribution, similar to (214) and given in (238). The difference in the abiding formulations are that Bessel functions of (214) are replaced by spherical Bessel functions. Several modes besides the dominant $n=0$ mode are given by (239)-(241) also similar to [73]. These pdfs are also illustrated in Figure 52. It should be noted that a meridian elevation angle is chosen not only to simplify the mathematics, but also to mimic the solution set of circular random array modes. The characteristic functions of these modes are also provided in Figure 53.

$$f_0(x) = \frac{3}{4\pi} \int_{-\sqrt{1-x^2-y^2}}^{\sqrt{1-x^2-y^2}} \int_{-\sqrt{1-x^2}}^{\sqrt{1-x^2}} 1 \, dz \, dy = \frac{3}{4}(1-x^2) \tag{233}$$

$$f_1(x) = \frac{5}{4\pi} \int_{-\sqrt{1-x^2-y^2}}^{\sqrt{1-x^2-y^2}} \int_{-\sqrt{1-x^2}}^{\sqrt{1-x^2}} (x^2+y^2+z^2) \, dz \, dy = \frac{5}{8}(1-x^4) \tag{234}$$

$$f_2(x) = \frac{7}{4\pi} \int_{-\sqrt{1-x^2-y^2}}^{\sqrt{1-x^2-y^2}} \int_{-\sqrt{1-x^2}}^{\sqrt{1-x^2}} \left(x^2 + y^2 + z^2\right)^2 dz dy = \frac{7}{12}\left(1 - x^6\right) \tag{235}$$

$$f_3(x) = \frac{7}{4\pi} \int_{-\sqrt{1-x^2-y^2}}^{\sqrt{1-x^2-y^2}} \int_{-\sqrt{1-x^2}}^{\sqrt{1-x^2}} \left(x^2 + y^2 + z^2\right)^3 dz dy = \frac{9}{16}\left(1 - x^8\right) \tag{236}$$

$$\text{Tinc}\left(\zeta(\theta,\phi)\right) = \int_0^1 v^2 j_0\left(\zeta(\theta,\phi)r\right) dr \quad n \geq 0 = \frac{1}{\zeta(\theta,\phi)^3} \int_0^{\zeta(\theta,\phi)} v^2 j_0(v) dv \quad n \geq 0$$

$$v = r\zeta(\theta,\phi) \quad , \quad v_1 = 0\zeta(\theta,\phi) = 0, \quad v_2 = 1\zeta(\theta,\phi) = \zeta(\theta,\phi) \tag{237}$$

$$dv = dr\zeta(\theta,\phi)$$

$$\text{Tinc}_n(x) = \frac{1}{x^{2n+3}} \int_0^x v^{2n+2} j_0(v) dv \quad n \geq 0 \tag{238}$$

$$\text{Tinc}_0(x) = \frac{j_1(x)}{x} \tag{239}$$

$$\text{Tinc}_1(x) = \frac{j_1(x)}{x} - 2\frac{j_2(x)}{x^2} \tag{240}$$

$$\text{Tinc}_2(x) = \frac{j_1(x)}{x} - 4\frac{j_2(x)}{x^2} + 8\frac{j_3(x)}{x^3} \tag{241}$$
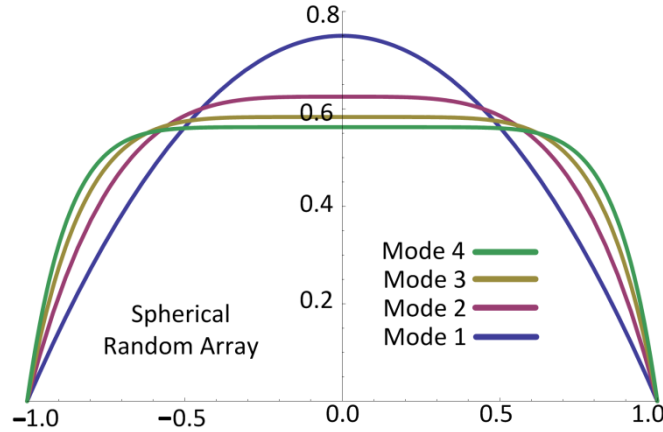
Figure 52. Pdfs of the first four modes of a spherical random array.
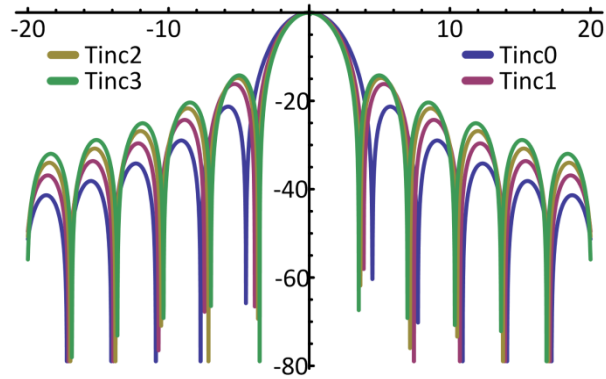
Figure 53. Comparison of the characteristic functions of the first four modes of a spherical random array.

In Figure 53., it is seen that the ascending order modes are more directive then the dominant mode, but come at an expense of higher sidelobes. The loss of energy in the main beam is due to the conservation of energy meaning that the energy lost in the main lobe region is now displaced outside of the main lobe region or into the sidelobe region; also similar to the beams seen in tapered aperture distributions, which are shown later in this dissertation. A comparison of the circular and spherical modes are shown in Figure 54.
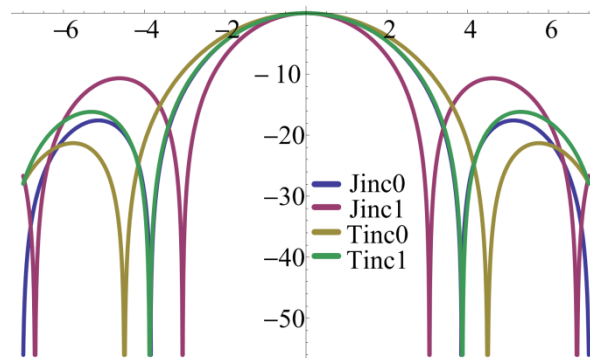
Figure 54. Comparison of the first two characteristic functions for the circular and spherical random array.

In Figure 54 it is seen that the main beam of the dominant mode for a circular random array is the same as that of the second mode of a spherical random array. However it is seen that the first sidelobe of the circular random array is smaller than that of the spherical random array.

Last of all it is likely that the jinc and tinc characteristic modes are in some way related to the spherical harmonics and multipoles illustrated in Figure 55-Figure 56. For example, integration of a plane

wave over a spherically symmetric volume can be expressed as an integration of the sum of spherical waves as

$$\frac{1}{V}\int_0^1\int_0^{2\pi}\int_0^{\pi} e^{j\vec{k}\cdot\vec{r}} = \frac{1}{V}\sum_{l=0}^{\infty}\int_0^1\int_0^{2\pi}\int_0^{\pi}(j)^l(2l+1)j_l(kr)P_l(\cos\psi)r^2\sin\theta d\theta d\phi \tag{242}$$

And since the spherical Hankel function of order zero h_0 represents the spherically symmetric wave field. Therefore upon integrating the zeroth order mode one obtains

$$3\mathrm{Tinc}(k) = \frac{3}{4\pi}\int_0^1\int_0^{2\pi}\int_0^{\pi} e^{j\vec{k}\cdot\vec{r}} = \frac{3}{4\pi}\int_0^1\int_0^{2\pi}\int_0^{\pi}(j)^0(2l+1)j_0(kr)P_0(\cos\psi)r^2\sin\theta d\theta d\phi \tag{243}$$

Or in other words since the Greens function of a finite spherical point source is calculated as

$$\frac{e^{-jk|\vec{r}-\vec{r}_n|}}{|\vec{r}-\vec{r}_n|} = jk\sum_{l=0}^{\infty}j_l(kr')h_l^{(1)}(kr)\sum_{m=-l}^{l}Y_l^m(\theta,\phi)Y_l^{m*}(\theta',\phi'),\ [r>r'] \tag{244}$$

For a theoretical point source we can calculate its far-field distribution by keeping the dominant term $n=0$

$$\frac{e^{-jk|\vec{r}-\vec{r}_n|}}{|\vec{r}-\vec{r}_n|} = jk\sum_{l=0}^{\infty}j_l(kr')h_l(kr)\sum_{m=-l}^{l}Y_{lm}(\theta,\phi)Y_{lm}^*(\theta',\phi')$$

$$\approx jkj_0(kr')h_0(kr)Y_{00}(\theta,\phi)Y_{00}^*(\theta',\phi') = \frac{jk}{4\pi}\left(\frac{\sin(kr')}{kr'} - j\frac{e^{jkr}}{kr}\right) \tag{245}$$

$$= \frac{e^{jkr}}{4\pi r}\bigg|_{r'=0}\ \{\text{point source}\}$$

And for multiple sources or sources offset from the origin we use a second order approximation for phase (43) and a first order approximation for path loss such that

$$\frac{e^{-jk|\vec{r}-\vec{r}_n|}}{|\vec{r}-\vec{r}_n|} \approx \frac{e^{-jkr}}{4\pi r}e^{jkr'\cos\psi} \tag{246}$$

This result is the mathematical description of a plane wave. It can be expanded by the Jacobi-Anger expansion which is useful in converting an expansion of plane waves into a series of cylindrical waves.

$$e^{jz\cos\psi} = \sum_{n=-\infty}^{\infty}J_n(z)e^{jn\psi} \tag{247}$$

And for integer n the expansion becomes

$$e^{jz\cos\psi} = J_0(z) + 2\sum_{n=1}^{\infty}j^n J_n(z)\cos(n\theta) \tag{248}$$

Therefore, we have seen that the monopole moment of a point source Greens function is given to be the familiar plane wave function of which can be transformed/expanded as a superposition of cylindrical waves. From this result we observe the far-field diffraction pattern composed of its cylindrical wave basis functions as:

$$\frac{e^{-jkr}}{4\pi r}\int_0^{2\pi}\int_0^1\left[J_0\left(kr'\right)+2\sum_{l=1}^{\infty}j^lJ_l\left(kr'\right)\cos\left(l\psi'\right)\right]r'dr'$$

$$=\frac{e^{-jkr}}{4\pi r}\int_0^{2\pi}\left(\frac{J_1\left(k\right)}{k}+\sum_{l=1}^{\infty}2^{-l}e^{jn\frac{\pi}{2}}k^l\cos\left(l\psi\right)\Gamma\left(1+\frac{l}{2}\right){}_1F_2\left[\left\{1+\frac{l}{2}\right\},\left\{2+\frac{l}{2},1+l\right\},-\frac{k^2}{4}\right]\right)d\psi'$$

$$=\frac{e^{-jkr}}{4\pi r}\left(\frac{J_1\left(k\right)}{k}2\pi+\sum_{l=1}^{\infty}2^{-l-1}e^{jn\frac{\pi}{2}}k^l\cos\left(l\psi\right)\Gamma\left(\frac{l}{2}\right){}_1F_2\left[\left\{1+\frac{l}{2}\right\},\left\{2+\frac{l}{2},1+l\right\},-\frac{k^2}{4}\right]\left(\sin2l\pi\right)\right)$$

$$=\frac{e^{-jkr}}{2r}\frac{J_1\left(k\right)}{k}\left\{\text{since } l\in\Im \rightarrow \sin2l\pi=0\right\}$$

(249)

Interestingly we see that diffraction pattern of the *n*=0 mode is equivalent to that diffraction pattern of a circular random array. This is also true since the term is angle independent. This consequently represents a uniform plane wave incident upon a circular aperture.

Alternatively, a plane wave can be expressed as a sum of spherical waves. This time (246) is expanded by the by converting an expansion of plane waves into a series of spherical waves.

$$e^{jkr'\cos\psi}=4\pi\sum_{l,m}\left(j\right)^lj_l\left(kr'\right)Y_{lm}\left(\theta,\phi\right)Y_{lm}^*\left(\theta',\phi'\right)$$

or for a axially symmetric term

(250)

$$e^{jkr'\cos\psi}=\sum_{l=0}^{\infty}\left(j\right)^l\left(2l+1\right)j_l\left(kr'\right)P_l\left(\cos\psi\right)$$

And for $l=0$ (250) reduces to

$$e^{jkr'\cos\psi}\underset{\substack{l=0\\ \text{monopole moment}}}{\doteq}j_0\left(kr'\right)$$

(251)

Now integrating the monopole moment over a spherical volume one obtains

$$\frac{e^{-jkr}}{4\pi r}\int_0^1\int_0^{2\pi}\int_{-\pi}^{\pi}j_0\left(kr'\right)r'^2\sin\theta'd\theta'd\phi'dr'=\frac{j_1\left(k\right)}{k}\frac{e^{-jkr}}{r}$$

(252)

Similarly, one can find by the same process that the dipole moment is (253) and the quadruple by that of (254). Or in essence the summation of all the these modes leads to a perfect plane wave as seen in

$$\frac{e^{jkr}}{r}\left(\frac{\left(krj-1\right)}{r}\frac{j_2\left(k\right)}{k}\cos^2\theta\right)$$

(253)

$$\frac{e^{jkr}}{r}\left(-\frac{jk}{r^2}\left(-3+3j\left(kr\right)+\left(kr\right)^2\right)\frac{\left(1+3\cos\left(2\theta\right)\right)^2}{192\pi}\frac{j_3\left(k\right)}{k}\right)$$

(254)
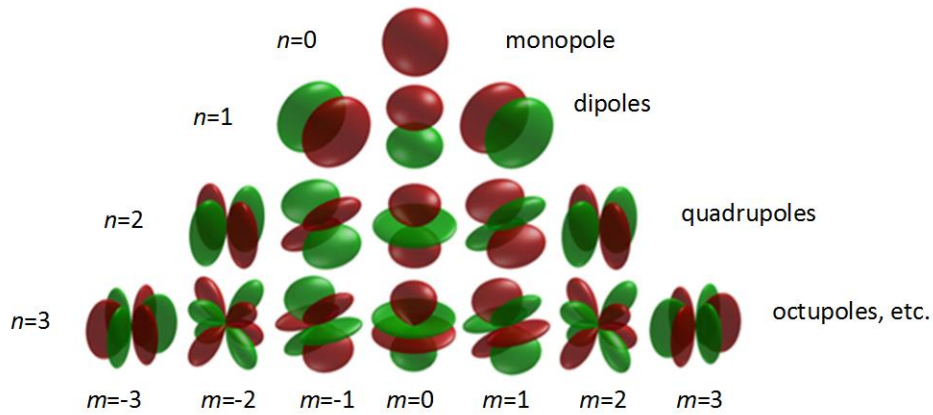
Figure 55. Spherical harmonics and multipoles.
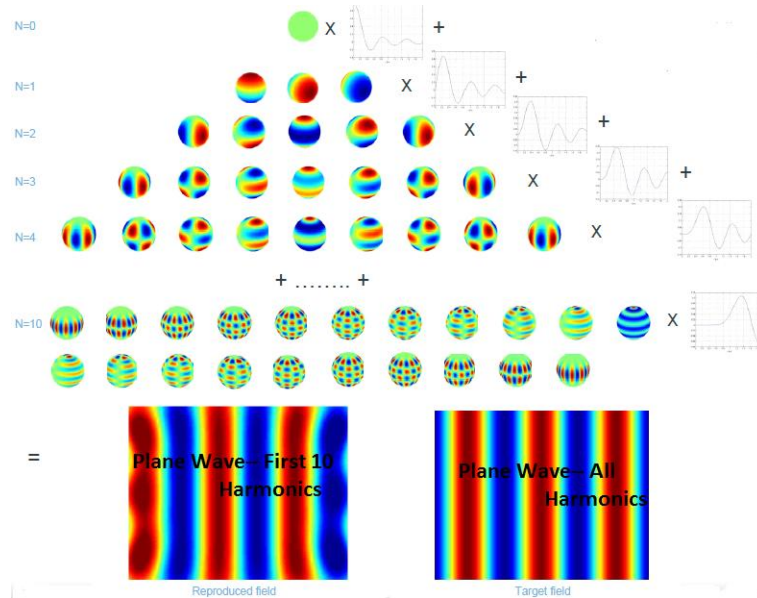
Fig. 1 Summation of Spherical Harmonics Leads to a Plane Wave in the Far Field.

Figure 56. Summation of the multiples in the plane wave solution. [143]

Also a more in detail explanation of the spherical random array moments is provided in the appendices. Moreover, it is found by summing the spherical random array modes independent of the spherical propagating Hankel function that the pattern is familiar to the common operating fields of the antenna as provided in Figure 57. Noted however, that all of the moments are normalized to $\exp[-jkr]/r$ or as (255). A more correct representation should decay as the ascending spherical Hankel function. Furthermore this solution is similar to those shown in [65].

$$\frac{e^{-jkr}}{r}\left[\frac{j_1(k)}{k}+\frac{j_2(k)}{k}+\frac{j_3(k)}{k}+\frac{j_4(k)}{k}\right] \tag{255}$$
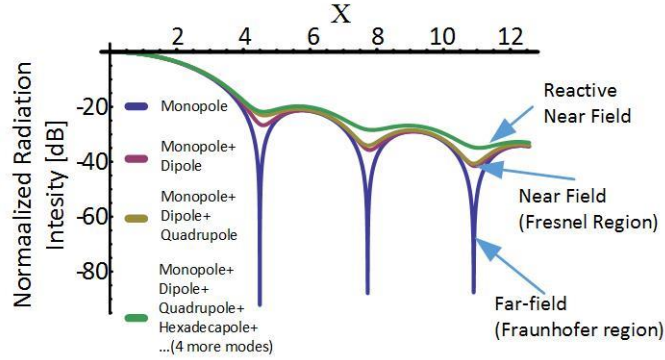
Figure 57. Addition of the spherical random array moments.

7.4 Sinc Family Characteristic Modes of Random Arrays

Similar to the previous section the characteristic modes of N-dimensional uniformly distributed spherical random arrays have many underlying connections to common topology. For instance, a generalized sinc family is given by the following equation (256). Applying the recurrence relation for the Bessel function similar to [143] and the lambda function in [146] derives the recurrence relation of (256) as (257).

$$\text{sinc}(n,x)=\Gamma\left(1+\frac{n}{2}\right)\frac{J_{n/2}(x)}{\left(\frac{x}{2}\right)^{n/2}} \tag{256}$$

$$\text{sinc}(n,x)=n\frac{(n+2)}{x^2}\left[\text{sinc}(n,x)-\text{sinc}(n-2,x)\right] \tag{257}$$

This recurrence relation splits the recursive progressions in terms of one odd and one even mode. The odd modes are expressed in terms of $\sin(x)$ and $\cos(x)$ while the even modes are expressed in terms of $J_0(x)$ and $J_1(x)$. Examples of these solutions are given below in (258)-(264).

$$\text{sinc}(-1,x)=\cos(x) \tag{258}$$

$$\text{sinc}(0,x)=J_0(x)\ [Ring\ 0-sphere] \tag{259}$$

96

$$\text{sinc}(1, x) = \frac{\sin(x)}{x} \quad [Line\ 1-ball] \tag{260}$$

$$\text{sinc}(2, x) = 2\frac{J_1(x)}{x} \quad [Circle\ 1-sphere] \tag{261}$$

$$\text{sinc}(3, x) = 3\frac{j_1(x)}{x} \quad [Sphere\ 2-sphere] \tag{262}$$

$$\text{sinc}(4, x) = 8\frac{J_2(x)}{x^2} \quad [Glome\ 3-sphere] \tag{263}$$

$$\text{sinc}(5, x) = 15\frac{j_2(x)}{x^2} \quad [4-sphere] \tag{264}$$

By observing these solutions it can be seen that $\text{sinc}(0, x)$ is the solution to a circular ring (Chapter VI), $\text{sinc}(1, x)$ is the solution to a linear random array, $\text{sinc}(2, x)$ is the solution to a circular random array and $\text{sinc}(3, x)$ is the solution to a spherical random array (ignoring pattern multiplication of the steering functions that is). Whereas for an N dimensional uniformly distributed random sphere the general solution takes on the form.

$$\text{sinc}(n, x), n \in Integers\ \&\ n > 1 \tag{265}$$

Also for more detail the zeroth order solution will be covered in more depth. The zeroth order solution is a unique solution of which appears to be the solution of a uniformly distributed point source or ring with singularity at the center. This solution is found in the following manner. A ring of thickness $\in$ and height $1/\in$, centered on a unit diameter and can be written as (266). Taking the Bessel Fourier transform the relation becomes (267) and in the $\lim_{\varepsilon \to 0}$ (268). A more complete derivation can be found in [146].

$$f(r) = \frac{1}{\varepsilon}\text{rect}\left(\frac{2r-1}{\in}\right) \tag{266}$$

$$F_{av} = 2\int_{\frac{1-\varepsilon}{2}}^{\frac{1+\varepsilon}{2}} r\frac{1}{\varepsilon}\text{rect}\left(\frac{2r-1}{\in}\right)J_0\left(2\zeta(\theta,\phi)r\right)dr \tag{267}$$

$$F_{av} = J_0\left(\zeta(\theta,\phi)\right) \tag{268}$$

Another probable solution comes from the pdf (269), which is similar to the inverse of the Wigner semicircle distribution (arcsine distribution). Thereof taking the Fourier transform of this distribution (270) leads to the $\text{sinc}(0, x) = J_0(x)$ solution (271). Also, for clarity a plot of this distribution (arcsine distribution) is shown in Figure 58. Moreover, this result matches the results of the ring random array presented in the Chapter VI.

$$p(x) = \frac{1}{\pi\sqrt{1-x^2}} \tag{269}$$

$$F_{av}(\theta,\phi) = \int_{-1}^{1} \frac{1}{\pi\sqrt{1-x^2}} e^{-j\zeta(\theta,\phi)} dx \tag{270}$$

$$= J_0\left(\zeta(\theta,\phi)\right) \tag{271}$$
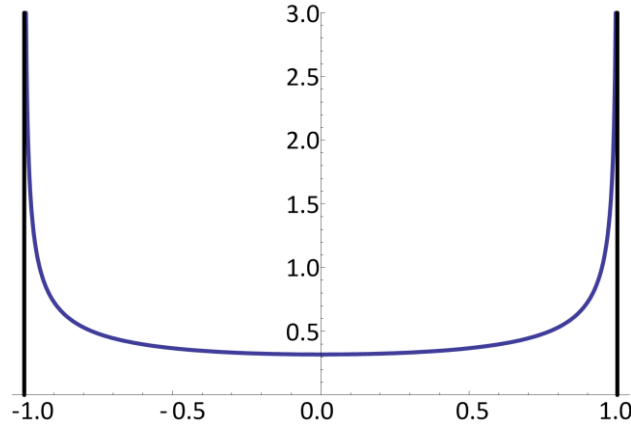
Figure 58. Probability distribution function of the inverse of the Wigner semicircle distribution or arcsine distribution, which is a special case of the beta distribution with $\alpha = \beta = 1/2$.

The recurrence relation in (257) can also be expressed for negative solutions. However, negative even solutions are undefined whereas odd solutions exhibit divergent oscillating functions rather than damped ones. Furthermore, a break-even point occurs for $n = -1$ as can be seen in (258), which neither is damped, nor diverges.

The $n = -1$ solution is like solving the integral shown in (272). It appears more than likely that this solution is related to a *0-sphere*. This type of sphere is described by a set of points $\{\pm R\}$. Thereby it is described by discrete topology for some R>0 and of which is also the only disconnected sphere. This is also like finding the array factor of an isotropic source placed above a ground plane.

Negative odd solutions of the generalized sinc family $n < -1$ are likely to represent leaky wave characteristic modes of a uniformly distributed random *n-sphere*. This is likely since a uniformly distributed circular random array for the case $n = -2$ would physically not make sense in the realm of leaky waves. The odd solutions would assume non-smooth surfaces and would therefore be prone to leaky waves. An example of the solution $n = -3$ is shown in (273). An example similar to the solution of a uniformly distributed spherical array, yet divergent instead of damped.

$$\int_{-\infty}^{\infty} w \sin(wt) = \int_{1}^{\pi/2} w \sin(wt) = \cos(w) \qquad (272)$$

$$\mathrm{sinc}(-3, x) = \cos(x) + x \sin(x) \qquad (273)$$

A secondary hypothesis is taken that these negative solutions are a consequence of the phenomena known as sphere eversion (turning a sphere inside-out allowing self-intersections without ripping it) [147]-[148].

7.5 Explanation of the Sinc Family Characteristic Modes

First one should wonder why the characteristic function of a shell provided in (193)? Hence, in order to explain this one needs to understand the illustration Figure 59 and the meaning of the N-sphere. Here it is seen that the zero sphere (i.e. periodic array) can be convolved into two ways without crossing. One way is to convolve the two into a line segment. The second of the two ways is to convolve the points into a ring. Furthermore these are the common solutions of any antenna problem. The 1-ball represents the TE modes of an electric dipole whereas the 1-sphere represents the TM-modes of a magnetic dipole. In addition, when comparing the characteristic functions of the ring, line, circle and sphere from the following Chapter VIII Figure 60 it is seen that the ring is a lower order mode (or taper) than the line. Again this is analogous to antenna theory and as to why the circular waveguides have lower order modes than those of planar waveguides. Moreoever, the original question is why the charactereistic function of a shell is a line minus a sphere and the way to understand this now is since the line fills the circle and then the sphere whereas the ring is the perimeter. Then the only way to delete the inside of the sphere by some form of convolution using a sphere, which contains both the line and the ring inside of it then it will need to delete the ring. Hence, it does this by some form of convolution, which essentially would be a 360 degree rotation in the elevation plane followed 360 times in the azimuth, which would delete the inside of the sphere. The next question of concern should be as to why these array form a taper family and furthermore why the negative solutions of the N-sphere are divergent. A quick explanation as to why this phenomena happens will be explained in Chapter X.

Inferometer
(0-sphere, bounded along a 1-
ball [line segment])
(0-ball, each individual point)

Convolves

Circular motion   Linear motion

Common TM modes   Common TE modes
(1-sphere)   (1-ball)

Convolve into a circle
(2-sphere)

Inside is filled by the
line outside is the ring

Convolves in a circular
motion (theta 0 to 360) to a
filled sphere (ring is still the
outside) line fills the inside

Moves in a plane radially in a
circular motion
(convolution) (glome)

Moves in a plane radially
about the elevation (theta 0
to 360) (convolution)
creating a 4-sphere

Figure 59. *N*-sphere convolution and representation diagram.

CHAPTER VIII

RANDOM ARRAY AMPLITUDE TAPER DISTRIBUTIONS IN CARTESIAN,

POLAR AND SPHERICAL COORDINATES (GAUSSIAN TAPERS)

As described in when the number of elements in a discrete element array approaches infinity one finds that the array factor summation reduces to an integral called the space factor. A space factor is given in (274) for a planar-source distribution. For completeness it should be noted that for an N dimensional orthogonal geometry (i.e. rectangular aperture) the aperture distribution is typically separable for current and phase distributions as shown in (275)-(276). To modify (274) for the case of a random array it is shown that one integrates relative to the distribution of the element population similar to (277). This type of integral relation will defined as the *RASF (Random Array Space Factor)* (278).

$$SF(\theta,\phi) = \int_{-l_x/2}^{l_x/2} \int_{-l_y/2}^{l_y/2} A_n(x',y') e^{j[kx'\sin\theta\cos\phi + ky'\sin\theta\sin\phi + \phi_n(x',y')]} dx'dy' \tag{274}$$

$$A_n(x',y') = I_x(x')I_y(y') \quad \text{current amplitude} \tag{275}$$

$$\phi_n(x',y') = \phi_x(x')\phi_y(y') \qquad \text{phase distriubtion along source} \tag{276}$$

$$E_{\Upsilon,T}\left|U(\theta,\phi|\vec{T},\vec{\Upsilon})\right| = \frac{1}{N} + \left(1 - \frac{1}{N}\right) \int_{-\infty}^{\infty}\int_{-\infty}^{\infty} \frac{\int_{-\infty}^{\infty}\int_{-\infty}^{\infty} \left(\cos\left(\begin{array}{c}\zeta(\theta,\phi)(\Upsilon_n - \Upsilon_m) \\ +\xi(\theta)(T_n - T_m)\end{array}\right)\right)}{f(\Upsilon_n)f(\Upsilon_m)f(T_n)f(T_m)} \\ d\Upsilon_n d\Upsilon_m dT_n dT_m \tag{277}$$

$$\Lambda = \text{RASF}(\theta,\phi)$$
$$= \int_{-\infty}^{\infty}\int_{-\infty}^{\infty} A_n(x)A_n(y)f(x)f(y) e^{j[k\tilde{x}_n\alpha(\theta,\phi) + k\tilde{y}_n\beta(\theta,\phi) + \phi_n(x',y')]} d\tilde{x}_n d\tilde{y}_n \tag{278}$$

Common line-source amplitude distributions are those of the triangular, cosine, cosine-squared, cosine on-a-pedestal, cosine squared on-pedestal, Gaussian, inverse taper, and edge [65]. The equivalence of these taper distributions for a random array in a two dimensional Cartesian coordinate system are shown in TABLE 5 in addition to other common distributions. This Table is also organized in terms of increasing beamwidths and decreasing sidelobe levels equivalent in concept to tapered aperture distributions [142]. It is also noted that "there is a trade-off between the beamwidth and the side lobe level based on the amplitude distribution." [65]

The random array space factor for a circular aperture(279) is similar to(278). For practical antennas such as a parabolic reflector, it is common to have distributions that taper toward the edges of the

apertures. These distributions are thus, approximated reasonably well by (280) and in terms of a random array, (280) takes the form given by (281).

The taper of a spherical aperture is similar to the taper of a circular aperture (280) and will not be explicitly shown for brevity, but to simplify the procedure for the spherical system the pattern is taken at the meridian elevation angle such that $\theta = \theta_0 = \pi/2$. This criteria is useful since pattern multiplication is avoided of which allows for ease in analysis.

$$\Lambda = \int_0^{2\pi} \int_0^1 f(\rho,\phi) A_n(\rho) e^{j\zeta(\theta,\phi)\tilde{\rho}_n \cos\phi_n} \tilde{\rho}_n d\tilde{\rho}_n d\phi_n$$
$$= 2\pi \int_0^1 f(\rho,\phi) A_n(\rho) J_0\left(\zeta(\theta,\phi)\tilde{\rho}_n\right) \tilde{\rho}_n d\tilde{\rho}_n \tag{279}$$

$$A_n(\rho') = \begin{cases} \left[\left[1-\left(\dfrac{\rho'}{a}\right)^2\right]\right]^n & 0 \le \rho' \le a \qquad n = 0,1,2,3 \\ 0 & elsewhere \end{cases} \tag{280}$$

$$\Lambda = 4\pi \int_0^1 f(r) f(\theta) f(\phi) A_n(r) \frac{\tilde{r}_n \sin\left(\tilde{r}_n \zeta(\theta,\phi)\right) d\tilde{r}_n}{\zeta(\theta,\phi)} \tag{281}$$

Comparison of the characteristic functions $|\Lambda|^2$ are provided in Table 4 and its taper functions (planar) are provided in TABLE 5. Furtheremore it is seen that these tapers provide a more directive main beam with larger side lobe levels compared to those tapers in Table 6 and Table 7. The spherical characteristic functions (Table 7) provide the broadest main beam with smallest sidelobe activity. Lastly, the solutions in Table 6 are shown to have a broader main beams region compared to those planar types, yet smaller than those spherical types. This also leads to sidelobe levels of which are in between the spherical and planar taper. A complete comparison of this description is shown in Figure 60. Last of all the odd tapers are provided in Table 8 and also include its tapers in increasing order, but for the most extreme tapers (Gaussian) Table 9 is provided for comparison.
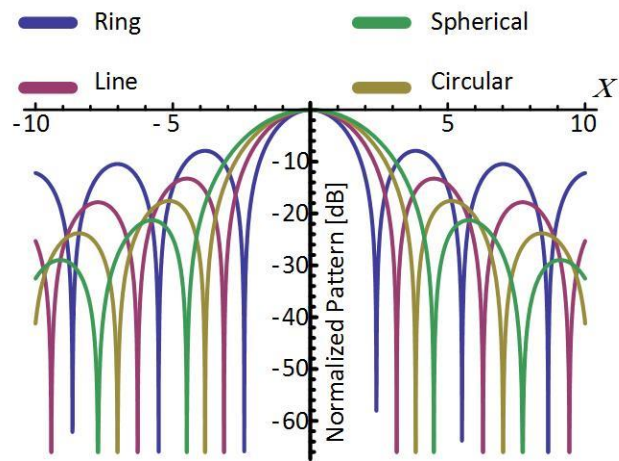
Figure 60. Comparison of the characteristic functions of planar, polar and spherical uniform distributions.

Table 4. Random Array Main Lobe Characteristic Functions (All Centered at the Origin) $\zeta_x^r(\theta,\phi), \Psi_y = \zeta_y^r(\theta,\phi)\ \Psi_z = \zeta_z^r(\theta)$

Linear

$$\Lambda = \mathrm{Sinc}\left(\left\{\Psi_x, \Psi_y, \Psi_z\right\}\right)^*$$

Semicircular

$$\Lambda = \mathrm{jinc}\left(\Psi_y\right)\mathrm{sinc}\left(\Psi_x\right)$$

Planar

$$\Lambda = \mathrm{Sinc}\left(\left\{\Psi_x, \Psi_y, \Psi_z\right\}_1\right)\mathrm{Sinc}\left(\left\{\Psi_x, \Psi_y, \Psi_z\right\}_2\right)^{**}$$

Triangle

$$\Lambda = -2\frac{(b-c)e^{ja\Psi_y} - (b-a)e^{jc\Psi_y} + (c-a)e^{jb\Psi_y}}{(b-a)(c-a)(b-c)\Psi_y^{\ 2}}\mathrm{Sinc}\left(\Psi_x\right)$$
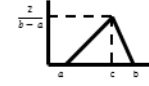
Cubic

$$\Lambda = \mathrm{Sinc}\left(\Psi_x\right)\mathrm{Sinc}\left(\Psi_y\right)\mathrm{Sinc}\left(\Psi_z\right)$$

Elliptical

$$\Lambda = \pi C a_1^2\left(\in_1 2\,\mathrm{jinc}\left(N_0\sqrt{X^2 + \in_1^4 Y^2}\right)\right)$$

Circular

$$\Lambda = \mathrm{Jinc}\left(\Psi_x\right)\mathrm{Jinc}\left(\Psi_y\right)$$

Annular Elliptical

$$\Lambda = \pi C a_1^2\left(\begin{array}{l}\in_1 2\,\mathrm{jinc}\left(N_0\sqrt{X^2 + \in_1^4 Y^2}\right) - \\ \in_2 \alpha^3\,\mathrm{jinc}\left(\alpha N_0\sqrt{X^2 + \in_1^2\in_2^2 Y^2}\right)\end{array}\right)$$

Cylindrical (Elevation z-plane, Circular xy-plane)

$$\Lambda = \mathrm{Jinc}\left(\Psi_x\right)\mathrm{Jinc}\left(\Psi_y\right)\mathrm{Sinc}\left(\Psi_z\right)$$

Diamond

$$\Lambda = \mathrm{Sinc}^2\left(\Psi_y\right)\mathrm{Sinc}^2\left(\Psi_x\right)$$

Spherical

$$\Lambda = \mathrm{Tinc}\left(\Psi_x\right)\mathrm{Tinc}\left(\Psi_y\right)\mathrm{Tinc}\left(\Psi_z\right)$$
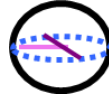
Ring

$$\Lambda = J_0\left(\zeta\left(\theta,\phi\right)\right)$$

Isosceles Right Triangle

$$\Lambda = \mathrm{Sinc}^2\left(\Psi_y\right)\mathrm{Sinc}\left(\Psi_x\right)$$

Inverted V

$$\Lambda = \mathrm{Sinc}^2\left(\Psi_y\right)$$

Circular Sectoral

$$\Lambda = \int_{-R\sin\left(\frac{\psi}{2}\right)}^{R\sin\left(\frac{\psi}{2}\right)}\int_{-1}^{1}\Re e\left[e^{j((\upsilon_n)\zeta(\theta,\phi))}\right]\left|\frac{2\left(\sqrt{1-\upsilon_n^2}\right) - |\upsilon_n|\cot\left(\frac{\psi}{2}\right)}{\psi}\right|$$

$$\upsilon_n d\upsilon_n d\psi$$
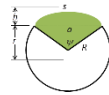
Circular Segment

$$\Lambda = \int_{-R\sin\left(\frac{\psi}{2}\right)}^{R\sin\left(\frac{\psi}{2}\right)}\int_{-1}^{1}\Re e\left[e^{j((\upsilon_n)\zeta(\theta,\phi))}\right]\left[\left(\frac{2\left(\sqrt{1-\upsilon_n^2}\right) - \cos\left(\frac{\psi}{2}\right)}{(\psi - \sin\psi)}\right)\upsilon_n\right.$$

$$\left. d\upsilon_n d\psi\right]$$
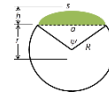
Table 5. Random Array Taper Distributions (Cartesian) $\zeta_x^r(\theta,\phi)$, $\Psi_y = \zeta_y^r(\theta,\phi)$ $\Psi_z = \zeta_z^r(\theta)$
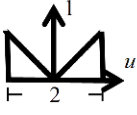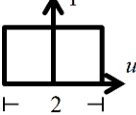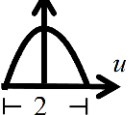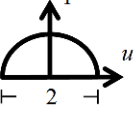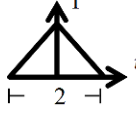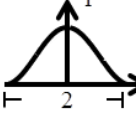
DISTRIBUTION	V	UNIFORM	PARABOLIC	COSINE	TRIANGULAR	COSINE-SQUARED
Element Distribution $\|u\| \le 1$ $u = Z_n / A$						
Distribution (Taper)	$\|u\|$	1	$(1-u^2)$	$\cos\left(\dfrac{\pi}{2}u\right)$	$(1-\|u\|)$	$\cos\left(\dfrac{\pi}{2}u\right)^2$
Joint Density Function (Normalization of pdf)	1	$\dfrac{1}{2}$	$\dfrac{3}{4}$	$\dfrac{\pi}{4}$	1	1
Main Lobe Factor (Λ)	$2\left[\text{sinc}\Psi - \left(\dfrac{1-\cos\Psi}{\Psi^2}\right)\right]$	$\text{sinc}\Psi$	$\dfrac{3}{\Psi^2}\left[\text{sinc}\Psi - \cos\Psi\right]$ $\equiv 3\dfrac{j_1(\Psi)}{\Psi} \equiv 3\text{tinc}\Psi$	$\dfrac{\pi^2\cos(\Psi)}{(\pi)^2 - (2\Psi)^2}$	$\text{sinc}\left(\dfrac{\Psi}{2}\right)^2$	$\text{sinc}(\Psi)\left[\dfrac{\pi^2}{\pi^2 - \Psi^2}\right]$
First Null (Rad) $\Psi = 2\pi\tilde{A}\sin\theta$ $\begin{cases}\phi=0°\ \text{E-plane}\\ \phi=90°\ \text{H-plane}\end{cases}$	$\sin^{-1}\left(\dfrac{.3711}{\tilde{A}}\right)$	$\sin^{-1}\left(\dfrac{.5}{\tilde{A}}\right)$	$\sin^{-1}\left(\dfrac{.7150}{\tilde{A}}\right)$	$\sin^{-1}\left(\dfrac{.75}{\tilde{A}}\right)$	$\sin^{-1}\left(\dfrac{1}{\tilde{A}}\right)$	$\sin^{-1}\left(\dfrac{1}{\tilde{A}}\right)$
3dB Beamwidth $\Psi = 2\pi\tilde{A}\sin\theta$ $\begin{cases}\phi=0°\ \text{E-plane}\\ \phi=90°\ \text{H-plane}\end{cases}$	$\dfrac{.3562}{\tilde{A}}$	$\dfrac{.4422}{\tilde{A}}$	$\dfrac{.5767}{\tilde{A}}$	$\dfrac{.5933}{\tilde{A}}$	$\dfrac{.6367}{\tilde{A}}$	$\dfrac{.7189}{\tilde{A}}$

Table 5 Continued
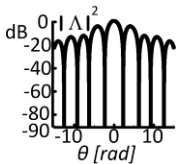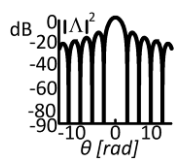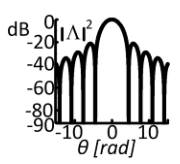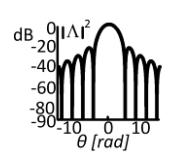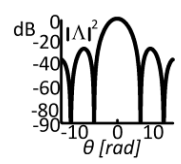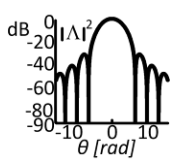
DISTRIBUTION	V	UNIFORM	PARABOLIC	COSINE	TRIANGULAR	COSINE-SQUARED
Nulls $$\Psi = 2\pi\tilde{A}\cos\phi$$ $$\{\theta = \theta_0 = 90°\}$$	$\approx\cos^{-1}\left(\pm\dfrac{q}{2\tilde{A}}\right)$	$\cos^{-1}\left(\pm\dfrac{q}{2\tilde{A}}\right)$	$\cos^{-1}\left(\dfrac{q+\frac{1}{2}}{2A}\right)$	$\cos^{-1}\left(\pm\left\|\dfrac{\left(\frac{3}{2}+q\right)}{2\tilde{A}}\right\|\right)$	$\cos^{-1}\left(\pm\dfrac{q}{\tilde{A}}\right)$	$\cos^{-1}\left(\pm\left(\dfrac{2+q}{2\tilde{A}}\right)\right)$
Peaks $$\Psi = 2\pi\tilde{A}\cos\phi$$ $$\{\theta = \phi = 90°\}$$	$\approx\cos^{-1}\left(\pm\left(m+\dfrac{1}{2}\right)\dfrac{1}{2\tilde{A}}\right)$	$\cos^{-1}\left(\dfrac{\pm\left(m+\frac{1}{2}\right)}{\frac{1}{2\tilde{A}}}\right)$	$\cos^{-1}\left(\dfrac{q+1}{2\tilde{A}}\right)$	$\cos^{-1}\left(\pm\left(\dfrac{1+q}{2\tilde{A}}\right)\right)$	$\cos^{-1}\left(\pm\left(q+\dfrac{1}{2}\right)\dfrac{1}{\tilde{A}}\right)$	$\cos^{-1}\left(\pm\left\|\dfrac{\left(\frac{3}{2}+q\right)}{2\tilde{A}}\right\|\right)$
Relative Gain	$(283)\to\lim\limits_{N\to\infty}(\Lambda)=$ .75	(284) $\to\lim\limits_{N\to\infty}(\Lambda)=$ 1	(285) $\to\lim\limits_{N\to\infty}(\Lambda)=$ .833	$\lim\limits_{N\to\infty}(\Lambda)=.8106$	$(286)\to\lim\limits_{N\to\infty}(\Lambda)=$ .75	$\lim\limits_{N\to\infty}(\Lambda)=$ .6667
Sidelobe Level $N\to\infty$	$\lim\limits_{N\to\infty}(\Lambda)=\text{-4.6}$	$\lim\limits_{N\to\infty}(\Lambda)=\text{-13.3}$	$\lim\limits_{N\to\infty}(\Lambda)=\text{-21.3}$	$\lim\limits_{N\to\infty}(\Lambda)=\text{-23.1}$	$\lim\limits_{N\to\infty}(\Lambda)=\text{-26.5}$	$\lim\limits_{N\to\infty}(\Lambda)=\text{-31.5}$
3 dB Sidelobe Level	$\approx\dfrac{\sqrt{(N-1)}}{\pi}-\dfrac{1}{2}$	$\dfrac{\sqrt{(N-1)}}{\pi}-\dfrac{1}{2}$	$\dfrac{\left(9(N-1)\right)^{\frac{1}{4}}}{\pi}-1$	$\dfrac{\sqrt{\sqrt{N-1}-\pi^2}}{2\pi}-1$	$\dfrac{1}{2}\left(-2+\sqrt{1+\sqrt{N-1}}\right)$	(282)
$\|\Lambda\|$						

Table 6. Random Array Taper Distributions (Cylindrical) $\zeta_x^r(\theta,\phi), \Psi_y = \zeta_y^r(\theta,\phi)\ \Psi_z = \zeta_z^r(\theta)$
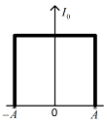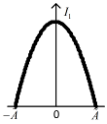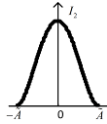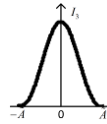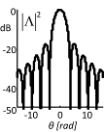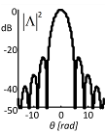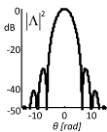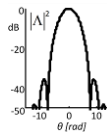
Distribution	Uniform	Radial Taper	Radial Taper Squared	Radial Taper Cubed
Element Distribution				
Distribution (graphical)	$I_0\left[1-\left(\dfrac{\rho_n}{\tilde{A}}\right)^2\right]^0$	$I_1\left[1-\left(\dfrac{\rho_n}{\tilde{A}}\right)^2\right]^1$	$I_2\left[1-\left(\dfrac{\rho_n}{\tilde{A}}\right)^2\right]^2$	$I_3\left[1-\left(\dfrac{\rho_n}{\tilde{A}}\right)^2\right]^3$
Joint Density Function	$\dfrac{1}{I_0\pi\tilde{A}^2}$	$\dfrac{2}{I_1\pi\tilde{A}^2}$	$\dfrac{3}{I_2\pi\tilde{A}^2}$	$\dfrac{4}{I_3\pi\tilde{A}^2}$
Main Lobe Factor (Λ)	$\dfrac{2J_1(\Psi)}{\Psi}$	$\dfrac{8J_2(\Psi)}{\Psi^2}$	$\dfrac{48J_3(\Psi)}{\Psi^3}$	$\dfrac{384J_2(\Psi)}{\Psi^4}$
$|\Lambda|^2$				

107

Table 7. Random Array Taper Distributions (Spherical) $\zeta_x^r(\theta,\phi), \Psi_y = \zeta_y^r(\theta,\phi)\ \Psi_z = \zeta_z^r(\theta)$
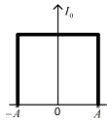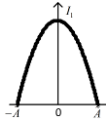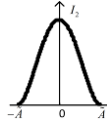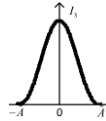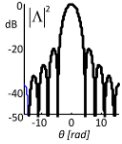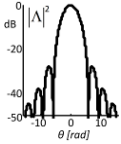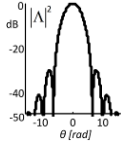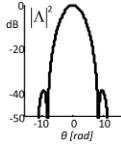
Distribution	Uniform	Radial Taper	Radial Taper Squared	Radial Taper Cubed
Element Distribution				
Distribution (Taper)	$I_0\left[1-\left(\dfrac{r_n}{\tilde{A}}\right)^2\right]^0$	$I_1\left[1-\left(\dfrac{r_n}{\tilde{A}}\right)^2\right]^1$	$I_2\left[1-\left(\dfrac{r_n}{\tilde{A}}\right)^2\right]^2$	$I_3\left[1-\left(\dfrac{r_n}{\tilde{A}}\right)^2\right]^3$
Joint Density Function	$\dfrac{1}{I_0\tilde{A}^3}\dfrac{3}{4\pi}$	$\dfrac{1}{I_1\tilde{A}^3}\dfrac{15}{8\pi}$	$\dfrac{1}{I_2\tilde{A}^3}\dfrac{105}{32\pi}$	$\dfrac{1}{I_3\tilde{A}^3}\dfrac{315}{64\pi}$
Main Lobe Factor (Λ)	$\dfrac{3\mathrm{j}_1(\Psi)}{\Psi}$	$\dfrac{15\mathrm{j}_2(\Psi)}{\Psi^2}$	$\dfrac{105\mathrm{j}_3(\Psi)}{\Psi^3}$	$\dfrac{945\mathrm{j}_4(\Psi)}{\Psi^4}$
$|\Lambda|^2$				

Distribution	Rectilinear	Antiphase Constant	Sine	Antiphase Sine Squared	Antiphase Triangular	Antiphase Triangular Squared
Element Distribution $\left|\tilde{A}\right| \le 1$						
Distribution (Taper)	$\tilde{A}$	± 1 $\tilde{A} \neq 0$	$\sin\left(\pi\tilde{A}\right)$	$\sin^2\left(\pi\tilde{A}\right)$	$\pm 1 - \tilde{A}$ $\left(\tilde{A} \neq 0\right)$	$\pm\left(\pm 1 - \tilde{A}\right)^2$ $\left(\tilde{A} \neq 0\right)$
Main Lobe Factor (Λ)	$\cdot \dfrac{-2\mathrm{j}}{\Psi^2}\left[\dfrac{\Psi\cos(\Psi)-}{\sin\Psi}\right]\cdot$	$2\mathrm{j}\left[\dfrac{1-\cos(\Psi)}{\Psi}\right]$	$2\pi\mathrm{j}\dfrac{\sin\Psi}{\left(\pi^2-\Psi^2\right)}$	$\mathrm{j}\left\{\dfrac{\left(\dfrac{1-\cos\Psi}{\Psi}\right)x}{\left(\dfrac{4\pi^2}{\pi^2-\Psi^2}\right)}\right\}$	$2\mathrm{j}\left(\dfrac{\Psi-\sin\Psi}{\Psi^2}\right)$	$2\mathrm{j}\left(\dfrac{\Psi^2+2\cos\Psi-2}{\psi^3}\right)$
First Peak $\Psi = 2\pi\tilde{A}\sin\theta$ $\begin{cases}\phi=0°\\ \text{E-plane}\\ \phi=90°\\ \text{H-plane}\end{cases}$	$\pm\sin^{-1}\left(\dfrac{.3314}{\tilde{A}}\right)$	$\pm\sin^{-1}\left(\dfrac{.3711}{\tilde{A}}\right)$	$\pm\sin^{-1}\left(\dfrac{.4186}{\tilde{A}}\right)$	$\pm\sin^{-1}\left(\dfrac{.4414}{\tilde{A}}\right)$	$\pm\sin^{-1}\left(\dfrac{.5}{\tilde{A}}\right)$	$\pm\sin^{-1}\left(\dfrac{.8808}{\tilde{A}}\right)$

Table 9. Random Array Gaussian and Truncated Gaussian Distributions $\zeta_x^r(\theta,\phi), \Psi_y = \zeta_y^r(\theta,\phi)\ \Psi_z = \zeta_z^r(\theta)$.
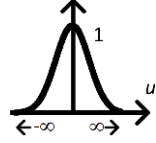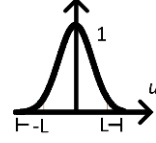
Distribution	Gaussian Distribution	Truncated Gaussian Distribution
Element Distribution $u = {Z_n}/{A}$	1	1
Distribution (Taper)	$\dfrac{1}{\sqrt{2\pi}\sigma}e^{\frac{-u^2}{2\sigma^2}}$ $-\infty < \vec{u} < \infty$	$\dfrac{1}{\sqrt{2\pi}\sigma}e^{\frac{-u^2}{2\sigma^2}}$ $-L < \vec{u} < L$
Main Lobe Factor (Λ)	$\left| e^{\frac{-\Psi^2\sigma^2}{2}} \right|$	$\left| \dfrac{1}{2}e^{-\frac{\Psi^2\sigma^2}{2}}\left[erf\left(\dfrac{L-j\Psi\sigma^2}{\sqrt{2}\sigma}\right) + erf\left(\dfrac{L+j\Psi\sigma^2}{\sqrt{2}\sigma}\right) \right] \right|$
3dB Beamwidth $\Psi = 2\pi\tilde{A}\sin\theta$ $\{\phi = 0°\ \text{E-plane},\quad \phi = 90°\,\text{H-plane}\}$	$\sin^{-1}\left(\dfrac{.1325}{\tilde{A}\sigma}\right)$	(Undefined due to L)
Relative Gain $\Psi = 2\pi\tilde{A}\sin\theta$ $\{\phi = 0°\ \text{E-plane},\quad \phi = 90°\,\text{H-plane}\}$	$(334) \rightarrow \lim_{N\to\infty}(\Lambda) = (335)$ $for\ \sigma = 1$ $\lim_{N\to\infty}(\Lambda) = .9803$	(Undefined due to L)
3 dB Sidelobe Level $\phi_{Sidelobe}$ $\{\phi = 0°\ \text{E-plane},\quad \phi = 90°\,\text{H-plane}\}$	$\sin^{-1}\left(\dfrac{\sqrt{2\ln(N-1)}}{2\pi\sigma}\right)$	(Undefined due to L)
	$|\Lambda|^2$	Figure 100

The directivity for select tapers of the planar, polar and spherical tapers shown in TABLE 5-Table 7 are shown in (282)-(291). From these expressions it is seen the gain will converge to N as $\tilde{A} \to \infty$. This is a result since $J_n(x), H_n(x)$ and $_m F_n(m;n;x)$ are damped sinusoids and converge to 0 as $x \equiv \tilde{A} \to \infty$. Thus, the gain will generally be less than N, but will be approached for large aperture sizes.[2]

$$\frac{3}{2} + \frac{\left(\frac{2\pi}{3}\right)^{\frac{1}{3}}}{\left(9\sqrt{N-1}+\sqrt{81N-12\pi^2-81}\right)^{\frac{1}{3}}} + \frac{\left(9\sqrt{N-1}+\sqrt{81N-12\pi^2-81}\right)^{\frac{1}{3}}}{(3)^{\frac{2}{3}}(2\pi)^{\frac{1}{3}}} \tag{282}$$

$$\frac{N}{\left(1+\frac{(N-1)}{3A^2\pi^3}\left(\begin{array}{l}2\pi\left(1+4\tilde{A}^2\pi^2\right)\left(J_0\left(2\pi\tilde{A}\right)-J_0\left(4\pi\tilde{A}\right)\right)+\left(1+2\tilde{A}^2\pi^2\right)\left(-2J_1\left(2\pi\tilde{A}\right)+J_1\left(4\pi\tilde{A}\right)\right)+\\4\pi^4A^3\left(\begin{array}{l}J_1\left(2\pi\tilde{A}\right)H_0\left(2\pi\tilde{A}\right)-J_1\left(4\pi\tilde{A}\right)H_0\left(4\pi\tilde{A}\right)-J_0\left(2\pi\tilde{A}\right)H_1\left(2\pi\tilde{A}\right)\\+J_0\left(4\pi\tilde{A}\right)H_1\left(4\pi\tilde{A}\right)\end{array}\right)\end{array}\right)\right)}$$

(283)

$$\frac{N}{1+\frac{(N-1)}{2\pi\tilde{A}}\left[4\tilde{A}J_0-J_1\left(4\tilde{A}\pi\right)+2\tilde{A}\pi^2J_1\left(4\tilde{A}\pi\right)H_0\left(4A\pi\right)-2\tilde{A}\pi^2J_0\left(4\tilde{A}\pi\right)H_1\left(4A\pi\right)\right]} \tag{284}$$

$$\frac{N}{\left(1+\frac{3(N-1)}{\left(80\tilde{A}^5\pi^5\right)}\left(J_1(x)\left(\begin{array}{l}-4+11\tilde{A}^2\pi^2-16\tilde{A}^4\pi^4+\\80\pi^4\tilde{A}^4-35A\pi^2\tilde{A}-\\4A\pi^4\tilde{A}\left(\begin{array}{l}5\tilde{A}+\\32\tilde{A}^3\pi^2\\-15A\end{array}\right)H_0(x)\end{array}\right)+AxJ_0(x)\left(\begin{array}{l}2-9\tilde{A}^2\pi^2-64\tilde{A}^4\pi^4+\\\tilde{A}\pi^2\left(\begin{array}{l}25\tilde{A}+\\\pi\left(\begin{array}{l}5\tilde{A}+\\32\tilde{A}^3\pi^2\\-15\tilde{A}\end{array}\right)H_1(x)\end{array}\right)\end{array}\right)\right)\right)} \tag{285}$$

$$x = 4\pi\tilde{A}$$

2 (287) is also provided in ([9], [81], [82]) and that of (288) in [81] and [82].

$$\frac{N}{1+\dfrac{(N-1)}{6\pi^3\tilde{A}^3}\begin{pmatrix} J_1\left(2\tilde{A}\pi\right)\left(4\left(-1+\tilde{A}^2\pi^2\right)+\tilde{A}\pi^2\left(3-4\tilde{A}^2\pi^2\right)H_0\left(2\tilde{A}\pi\right)\right)+ \\ J_1\left(4\tilde{A}\pi\right)\left(2-8\tilde{A}^2\pi^2+\tilde{A}\pi^2\left(-3+16\tilde{A}^2\pi^2\right)H_0\left(4\tilde{A}\pi\right)\right)+ \\ \tilde{A}\pi\,_0\tilde{F}_1\left(;1;-\tilde{A}^2\pi^2\right)\begin{pmatrix} 4-8\tilde{A}^2\pi^2+ \\ \pi\left(-3+4\tilde{A}^2\pi^2\right)H_1\left(2\tilde{A}\pi\right)\end{pmatrix}+ \\ \tilde{A}\pi\,_0\tilde{F}_1\left(;1;-4\tilde{A}^2\pi^2\right)\begin{pmatrix} -4+32\tilde{A}^2\pi^2+ \\ \pi\left(3-16\tilde{A}^2\pi^2\right)H_1\left(4\tilde{A}\pi\right)\end{pmatrix} \end{pmatrix}} \tag{286}$$

$$\frac{N}{1+(N-1)\,_2F_3\left(\dfrac{1}{2},\dfrac{3}{2};1,2,3;-\left(4\pi\tilde{A}\right)^2\right)} \tag{287}$$

$$\frac{N}{1+(N-1)\dfrac{1}{5}\left[6\,_1F_2\left(\dfrac{1}{2};3,\dfrac{7}{2};-\left(4\pi\tilde{A}\right)^2\right)-\,_1F_2\left(\dfrac{1}{2};4,\dfrac{7}{2};-\left(4\pi\tilde{A}\right)^2\right)\right]} \tag{288}$$

$$\frac{N}{1+e^{-2A^2\pi^2\sigma^2}(N-1)\,_0\tilde{F}_1\left(;1;A^4\pi^4\sigma^4\right)} \tag{289}$$

$$\frac{\left(2\pi^{1/2}\sigma^2*erf\left(\dfrac{\left(2^{1/2}\left(\dfrac{1}{\sigma^2}\right)^{(1/2)}\right)}{2}\right)^2*\left(\dfrac{1}{\sigma^2}\right)^{1/2}\right)}{2erf\left(\left(\dfrac{1}{\sigma^2}\right)^{1/2}\right)}\left\{\neg u=[-1,1]\right\} \tag{290}$$

$$\frac{N}{1+e^{-8\pi^2\sigma^2}(N-1)I_0\left(8\pi^2\sigma^2\right)} \tag{291}$$

In conclusion, the array tapers discussed in Chapter VII should be better known as the directive tapers. This is due since the tapers start with the uniform circular random array and taper outward, i.e. spreading the current distribution and as a consequence providing a more directive main beam. In this Chapter (VIII) the Gaussian tapers were discussed. Moreover, the Gaussain tapers are related to the *N*-sphere family of modes. Hencesofar, it is known that the 2-sphere is a regular sphere and any sphere higher than this it is seen that the solutions alternate from circular Bessel functions to spherical Bessel functinos. As a consequence, a 3-sphere (Glome) is suggested to a normal sphere that is able to move with per say velocity in a plane (circular plane) whereas a 4-sphere is available to move with a velocity in a volumetric or spherical space. Otherwise, the Hyperspherical Bessel Fourier transform may be appied in

Section 15.4 of which takes into account phase error. These descriptions present logical explanations whereas concepts of string theory are much more difficult to comprehend.

CHAPTER IX

MULTIPLE BEAMS

9.1 Anti-Modal Phasing

The beampatterns for the distributions shown in TABLE 4-Table 7 demonstrate even symmetry. These types of distributions use a cosine Fourier transform shown in (297) derived from the relations (292)-(296). However, for distributions of odd symmetry a main beam at broadside does not occur. For these types of distributions one uses the sine Fourier transform to obtain the main beam behavior as shown in (299) with derivation shown in (298). The sine Fourier transform creates a difference pattern with two main beams and examples of such are shown in Figure 61 and Table 8.

$$
\begin{aligned}
E_Z \left| U\left(\theta,\phi \middle| \vec{Z}\right)\right| &= \frac{1}{N^2}\sum_{m=1}^{N}\sum_{n=1}^{N}\int_{-\infty}^{0}\int_{-\infty}^{0} U\left(\theta,\phi \middle| \vec{Z}\right) f\left(Z_n\right) f\left(Z_m\right) dZ_n dZ_m + \\
&\quad \frac{1}{N^2}\sum_{m=1}^{N}\sum_{n=1}^{N}\int_{0}^{\infty}\int_{0}^{\infty} U\left(\theta,\phi \middle| \vec{Z}\right) f\left(Z_n\right) f\left(Z_m\right) dZ_n dZ_m \\
&= \int_{-\infty}^{0}\int_{-\infty}^{0}\left(\frac{1}{N}+\frac{1}{N^2}\sum_{m=1}^{N}\sum_{\substack{n=1\\n\neq m}}^{N} e^{j(Z_n(\theta,\phi)-Z_m(\theta,\phi))}\right) f\left(Z_n\right) f\left(Z_m\right) dZ_n dZ_m + \\
&\quad \int_{0}^{\infty}\int_{0}^{\infty}\left(\frac{1}{N}+\frac{1}{N^2}\sum_{m=1}^{N}\sum_{\substack{n=1\\n\neq m}}^{N} e^{j(Z_n(\theta,\phi)-Z_m(\theta,\phi))}\right) f\left(Z_n\right) f\left(Z_m\right) dZ_n dZ_m
\end{aligned}
\tag{292}
$$

For a spherical coordinate system (292) takes the form of (293).

$$
\begin{aligned}
&E_{\Upsilon,T}\left| U\left(\theta,\phi \middle| \vec{T},\vec{\Upsilon}\right)\right| = \\
&\int_{-\infty}^{0}\int_{-\infty}^{0}\int_{-\infty}^{0}\int_{-\infty}^{0}\left(\frac{1}{N}+\frac{1}{N^2}\sum_{m=1}^{N}\sum_{\substack{n=1\\n\neq m}}^{N} e^{j\zeta(\theta,\phi)(\Upsilon_n-\Upsilon_m)}e^{j\xi(\theta)(T_n-T_m)}\right) f\left(\Upsilon_n\right) f\left(\Upsilon_m\right) f\left(T_n\right) f\left(T_m\right) d\Upsilon_n d\Upsilon_m dT_n dT_m + \\
&\int_{0}^{\infty}\int_{0}^{\infty}\int_{0}^{\infty}\int_{0}^{\infty}\left(\frac{1}{N}+\frac{1}{N^2}\sum_{m=1}^{N}\sum_{\substack{n=1\\n\neq m}}^{N} e^{j\zeta(\theta,\phi)(\Upsilon_n-\Upsilon_m)}e^{j\xi(\theta)(T_n-T_m)}\right) f\left(\Upsilon_n\right) f\left(\Upsilon_m\right) f\left(T_n\right) f\left(T_m\right) d\Upsilon_n d\Upsilon_m dT_n dT_m
\end{aligned}
$$

$$\tag{293}$$

Interchanging integration with summation leads to (294) and it is observed that the term $1/N$ separates from the expression since the integration is done over the entire distribution space; or in other words the cumulative distribution over the entire space is equal to one. Now applying a summation identity [81] of (295) in succession provides (296).

$$E_{\Upsilon,T}\left|U\left(\theta,\phi\big|\vec{T},\vec{\Upsilon}\right)\right| = \frac{1}{N} + \sum_{m=1}^{N}\sum_{\substack{n=1\\n\neq m}}^{N}\int_{-\infty}^{\infty}\int_{-\infty}^{\infty}\int_{-\infty}^{\infty}\int_{-\infty}^{\infty}\left(\frac{1}{N^2}\left\{e^{j\zeta(\theta,\phi)(\Upsilon_n-\Upsilon_m)}e^{j\xi(\theta)(T_n-T_m)}\right\}\right)$$
$$f(\Upsilon_n)f(\Upsilon_m)f(T_n)f(T_m)d\Upsilon_n d\Upsilon_m dT_n dT_m$$

$$= \frac{1}{N} + \sum_{m=1}^{N}\sum_{\substack{n=1\\n\neq m}}^{N}\int_{0}^{\infty}\int_{0}^{\infty}\int_{0}^{\infty}\int_{0}^{\infty}\left(\frac{1}{N^2}\left\{\begin{matrix}e^{j\zeta(\theta,\phi)(\Upsilon_n-\Upsilon_m)}e^{j\xi(\theta)(T_n-T_m)}+\\e^{-j\zeta(\theta,\phi)(\Upsilon_n-\Upsilon_m)}e^{j\xi(\theta)(T_n-T_m)}\end{matrix}\right\}\right)$$
$$f(\Upsilon_n)f(\Upsilon_m)f(T_n)f(T_m)d\Upsilon_n d\Upsilon_m dT_n dT_m$$

$$= \frac{1}{N} + \sum_{m=1}^{N}\sum_{\substack{n=1\\n\neq m}}^{N}\int_{-\infty}^{\infty}\int_{-\infty}^{\infty}\int_{-\infty}^{\infty}\int_{-\infty}^{\infty}\left(\frac{1}{N^2}\left\{\cos\left(\begin{matrix}\zeta(\theta,\phi)(\Upsilon_n-\Upsilon_m)\\+\xi(\theta)(T_n-T_m)\end{matrix}\right)\right\}\right)$$
$$f(\Upsilon_n)f(\Upsilon_m)f(T_n)f(T_m)d\Upsilon_n d\Upsilon_m dT_n dT_m$$

$$= \int_{0}^{\infty}\int_{0}^{\infty}\int_{0}^{\infty}\int_{0}^{\infty}\sum_{m=1}^{N}\sum_{\substack{n=1\\n\neq m}}^{N}\left(\frac{1}{N^2}\left\{\cos\left(\begin{matrix}\zeta(\theta,\phi)(\Upsilon_n-\Upsilon_m)\\+\xi(\theta)(T_n-T_m)\end{matrix}\right)\right\}\right)$$
$$f(\Upsilon_n)f(\Upsilon_m)f(T_n)f(T_m)d\Upsilon_n d\Upsilon_m dT_n dT_m$$

$$= \frac{1}{N} + \int_{0}^{\infty}\int_{0}^{\infty}\int_{0}^{\infty}\int_{0}^{\infty}\left(\frac{1}{N^2}(N^2-N)\left\{\cos\left(\begin{matrix}\zeta(\theta,\phi)(\Upsilon_n-\Upsilon_m)\\+\xi(\theta)(T_n-T_m)\end{matrix}\right)\right\}\right)$$
$$f(\Upsilon_n)f(\Upsilon_m)f(T_n)f(T_m)d\Upsilon_n d\Upsilon_m dT_n dT_m \tag{294}$$

$$\sum_{m=1}^{N}\sum_{\substack{n=1\\n\neq m}}^{N}1 = N(N-1) \tag{295}$$

$$E_{\Upsilon,T}\left|U\left(\theta,\phi\big|\vec{T},\vec{\Upsilon}\right)\right| = \frac{1}{N} + \left(1-\frac{1}{N}\right)[\Lambda] \tag{296}$$

$$\Lambda = [\text{Main Lobe Factor}] = [\text{Characteristic Function}]^2$$

$$\Lambda_{\text{even mode}} = \int_{-\infty}^{\infty}\int_{-\infty}^{\infty}\left(\cos\left(Z_n(\theta,\phi)-Z_m(\theta,\phi)\right)\right)f(Z_n)f(Z_m)dZ_n dZ_m^2 \tag{297}$$
$$= [\text{Main Lobe Factor}] = [\text{Characteristic Function}]$$

For an anti-modal distribution the elements are not all excited isotroprically; that is half of the elements are provided with a current excitation $I_n = 1$ while the second half is $180°$ out of phase across a defined symmetry point $(I_n = -1)$. An illustration of these distribution types is shown in the bottom left hand corner of Figure 61.

$$E_{\Upsilon,\mathrm{T}}\left|U\left(\theta,\phi\,\middle|\,\vec{\mathrm{T}},\vec{\Upsilon}\right)\right| = \frac{1}{N} + \sum_{m=1}^{N}\sum_{\substack{n=1\\n\neq m}}^{N}\int_{0}^{\infty}\int_{0}^{\infty}\int_{0}^{\infty}\int_{0}^{\infty}\left(\frac{1}{N^{2}}\begin{Bmatrix}e^{j\zeta(\theta,\phi)(\Upsilon_n-\Upsilon_m)}e^{j\xi(\theta)(\mathrm{T}_n-\mathrm{T}_m)}-\\e^{-j\zeta(\theta,\phi)(\Upsilon_n-\Upsilon_m)}e^{j\xi(\theta)(\mathrm{T}_n-\mathrm{T}_m)}\end{Bmatrix}\right)$$
$$f\left(\Upsilon_n\right)f\left(\Upsilon_m\right)f\left(\mathrm{T}_n\right)f\left(\mathrm{T}_m\right)d\Upsilon_n d\Upsilon_m d\mathrm{T}_n d\mathrm{T}_m$$

$$=\frac{1}{N}+\sum_{m=1}^{N}\sum_{\substack{n=1\\n\neq m}}^{N}\int_{-\infty}^{\infty}\int_{-\infty}^{\infty}\int_{-\infty}^{\infty}\int_{-\infty}^{\infty}\left(\frac{1}{N^{2}}\left\{\sin\begin{pmatrix}\zeta(\theta,\phi)(\Upsilon_n-\Upsilon_m)\\+\xi(\theta)(\mathrm{T}_n-\mathrm{T}_m)\end{pmatrix}\right\}\right)$$
$$f\left(\Upsilon_n\right)f\left(\Upsilon_m\right)f\left(\mathrm{T}_n\right)f\left(\mathrm{T}_m\right)d\Upsilon_n d\Upsilon_m d\mathrm{T}_n d\mathrm{T}_m$$

$$=\int_{0}^{\infty}\int_{0}^{\infty}\int_{0}^{\infty}\int_{0}^{\infty}\sum_{m=1}^{N}\sum_{\substack{n=1\\n\neq m}}^{N}\left(\frac{1}{N^{2}}\left\{\sin\begin{pmatrix}\zeta(\theta,\phi)(\Upsilon_n-\Upsilon_m)\\+\xi(\theta)(\mathrm{T}_n-\mathrm{T}_m)\end{pmatrix}\right\}\right)$$
$$f\left(\Upsilon_n\right)f\left(\Upsilon_m\right)f\left(\mathrm{T}_n\right)f\left(\mathrm{T}_m\right)d\Upsilon_n d\Upsilon_m d\mathrm{T}_n d\mathrm{T}_m$$

$$=\frac{1}{N}+\int_{0}^{\infty}\int_{0}^{\infty}\int_{0}^{\infty}\int_{0}^{\infty}\left(\frac{1}{N^{2}}\left(N^{2}-N\right)\left\{\sin\begin{pmatrix}\zeta(\theta,\phi)(\Upsilon_n-\Upsilon_m)\\+\xi(\theta)(\mathrm{T}_n-\mathrm{T}_m)\end{pmatrix}\right\}\right)$$
$$f\left(\Upsilon_n\right)f\left(\Upsilon_m\right)f\left(\mathrm{T}_n\right)f\left(\mathrm{T}_m\right)d\Upsilon_n d\Upsilon_m d\mathrm{T}_n d\mathrm{T}_m$$

$$\tag{298}$$

$$\Lambda_{\text{odd mode}}=\int_{-\infty}^{\infty}\int_{-\infty}^{\infty}\left(\sin\left(Z_n\left(\theta,\phi\right)-Z_m\left(\theta,\phi\right)\right)\right)f\left(Z_n\right)f\left(Z_m\right)dZ_n dZ_m{}^2$$
$$=\left[\text{Main Lobe Factor}\right]=\left[\text{Characteristic Function}\right]$$

$$\tag{299}$$
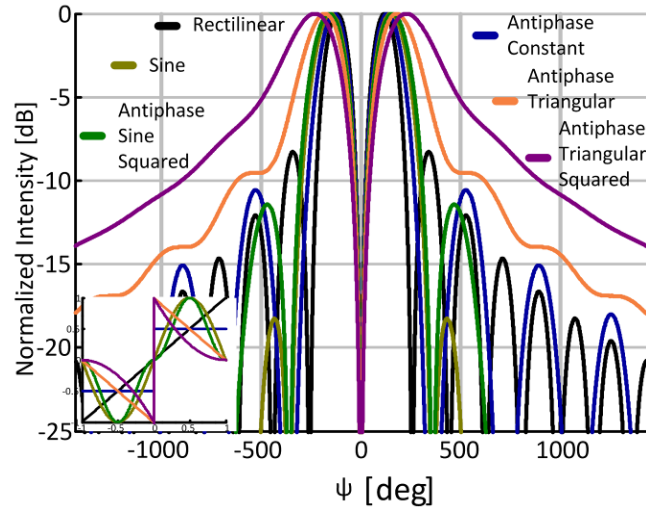
Figure 61. Characteristic functions (Table 8) comparison of odd distributions.

9.2 Complex Orthogonal (Perimeter and Filled) Anti-Modal Phasing Variations

It is possible to create patterns with multiple beams that become shifted, tapered and of multiple amplitudes using complex orthogonal phase variations. Figure 62-Figure 64 demonstrate that one may create one, two and four beams (300)-(302) of equal amplitude. This occurrence seems to be dependent upon the number of phase shifts applied to the topology and it is seen that these types of patterns also produce orthogonal symmetry across the axes. This orthogonal symmetry accounts for the symmetric interference of the waves across the axes of which is the cause of equal amplitude main beams. When orthogonal symmetry does not apply across the quadrants it is observed experimentally that one does not obtain equal amplitude main beams (303)-(311) as shown in Figure 65-Figure 75. More so these figures demonstrates it is possible to create numerous spatially independent main beams when the aperture contains many orthogonal phase multiples. In summary this discussion of multiple main beams is useful (theoretically and experimentally verified later in this paper) for random array theory since these characteristic functions can be steered in three dimensional space.

$$\Lambda^{Un-normalized} = \frac{4\sin(u)\sin(v)}{uv} \tag{300}$$

where

$$\{u,v\} \triangleq \{\alpha(\theta,\phi), \beta(\theta,\phi)\} \equiv \left\{ \frac{2\pi A}{\lambda} \frac{1}{A}(x_n \sin\theta\cos\phi, y_n \sin\theta\sin\phi) \right\}$$
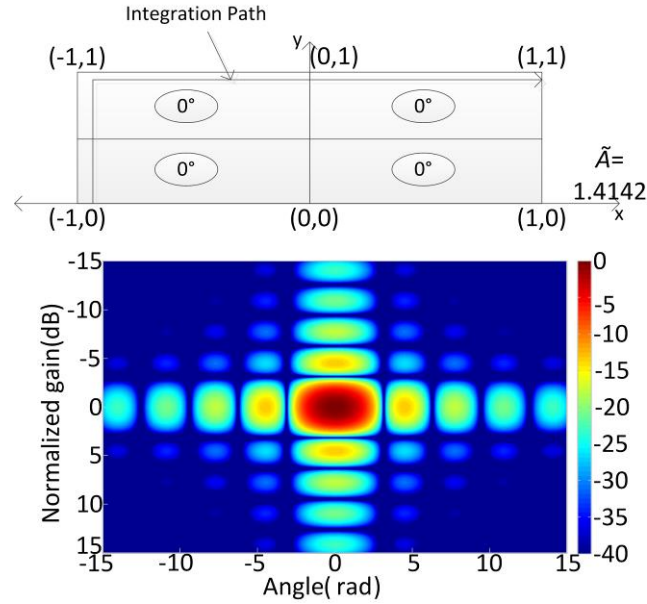
Figure 62. 3D pattern of even symmetry creating one main.

117

$$\Lambda = \frac{8j\sin(u)\sin\left(\dfrac{v}{2}\right)^2}{uv} \tag{301}$$
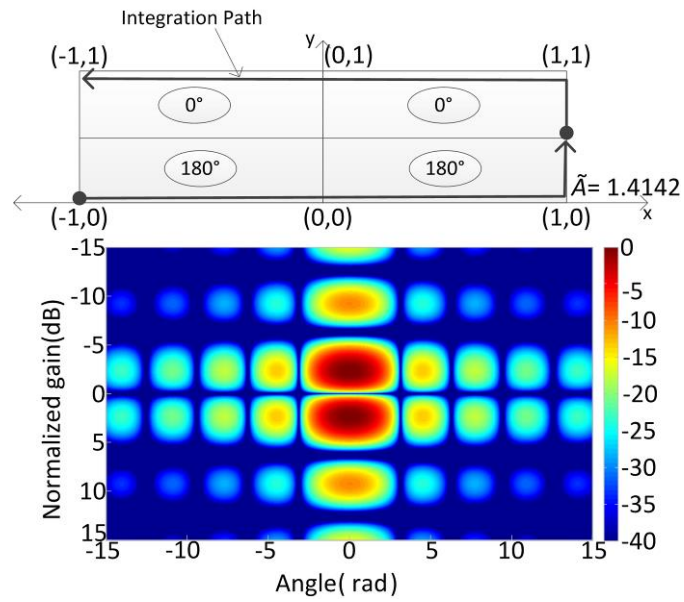
Figure 63. 3D pattern of odd symmetry creating two main beams.

$$\Lambda = \frac{(2+2j)(-1+\cos(v))\sin(u)+(4-4j)\sin\left(\dfrac{u}{2}\right)^2\sin(v)}{uv} \tag{302}$$

118
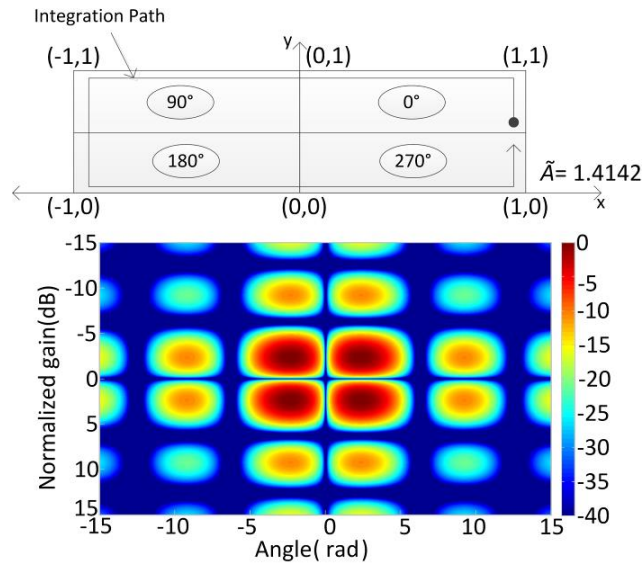
Figure 64. 3D pattern of odd symmetry creating four main beams.

$$\Lambda = \frac{2\left(-1+\cos(2u)+\sin(2u)\right)\left(-1+\cos(v)-\sin(v)\right)}{uv}$$ (303)
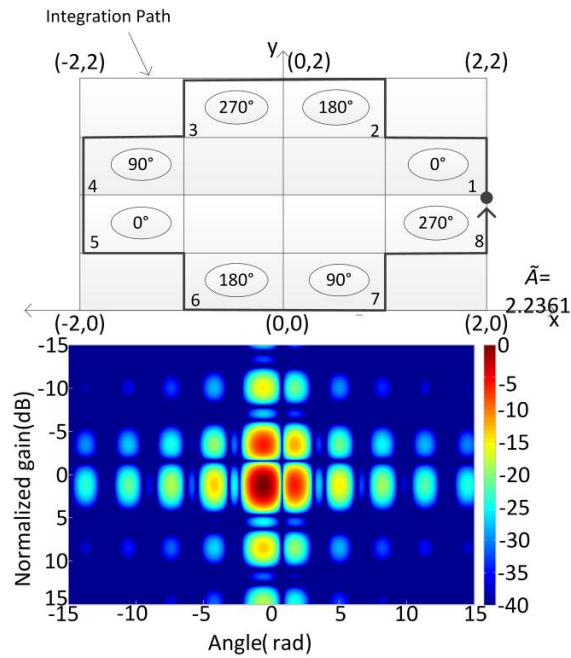
Figure 65. 3D pattern of skewed odd symmetry creating four main beams of unequal amplitude type 1.

119

$$\Lambda = \frac{16\sin\left(\frac{u}{2}\right)\sin(u)\sin\left(\frac{v}{2}\right)\left(j\sin\left(\frac{u-v}{2}\right)+\sin\left(\frac{u+v}{2}\right)\right)}{uv} \qquad (304)$$
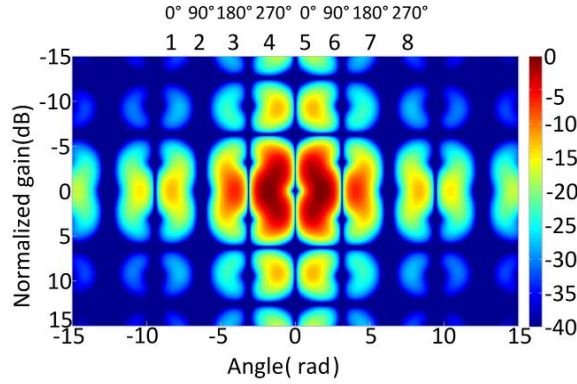
Figure 66. 3D pattern of skewed odd symmetry creating four main beams of unequal amplitude type 2.

$$\Lambda = \frac{(32-32j)\cos\left(\frac{u}{2}\right)\cos\left(\frac{u}{2}\right)-\sin\left(\frac{u}{2}\right)\sin\left(\frac{u}{2}\right)^2\sin\left(\frac{v}{2}\right)^2}{uv} \qquad (305)$$
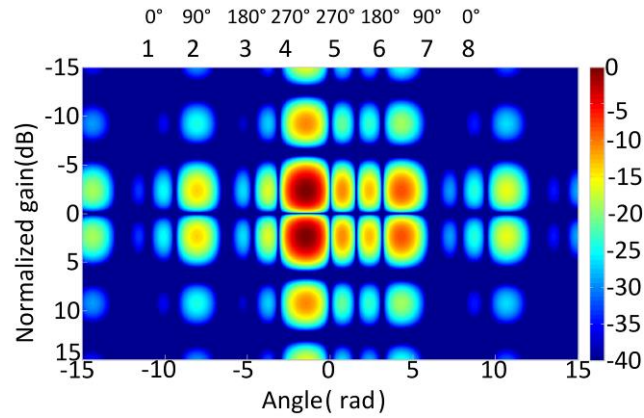
Figure 67. 3D pattern of skewed odd symmetry creating four main beams of unequal amplitude type 3.

$$\Lambda = \frac{(2+2j)\sin(u)\left(e^{ju}\left(-1+\cos(v)\right)+\left(2-(2-j)\cos(u)+\sin(u)\right)\sin(v)\right)}{uv} \qquad (306)$$
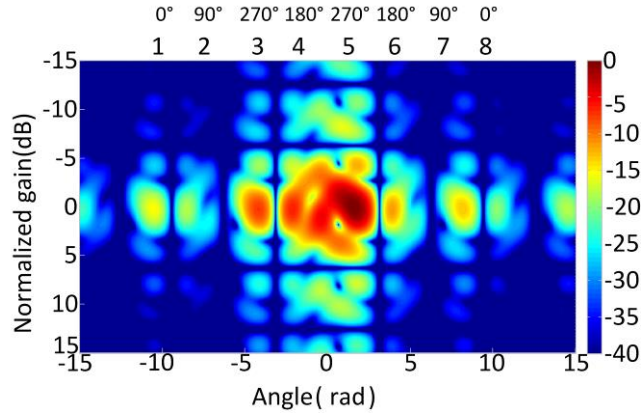
Figure 68. 3D pattern of skewed odd symmetry creating four main beams of unequal amplitude type 4.

$$\Lambda = \frac{(4+4j)\sin(u)\sin\left(\dfrac{v}{2}\right)\left(\begin{array}{c}(-1+j)\cos\left(u+\dfrac{v}{2}\right)+\cos\left(\dfrac{v}{2}\right)\\[2mm] -j\left((1+j)\sin\left(u-\dfrac{v}{2}\right)+\sin\left(\dfrac{v}{2}\right)\right)\end{array}\right)}{uv} \qquad (307)$$
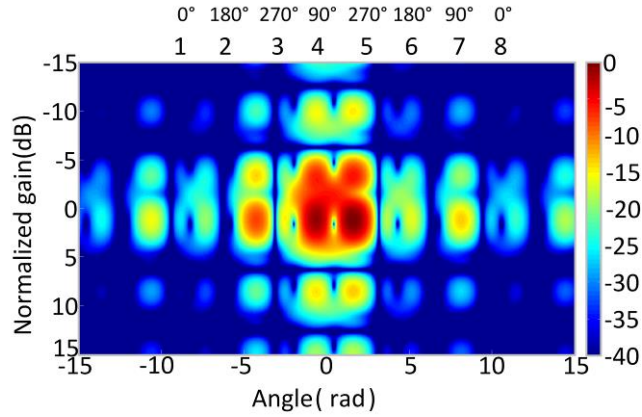
Figure 69. 3D pattern of skewed odd symmetry creating four main beams of unequal amplitude type 5.

$$\Lambda = \frac{e^{-i(2u+v)}\left(-1+e^{ju}\right)\left(-1+e^{jv}\right)\left(\begin{array}{c}je^{j(u+v)}\left(-1+e^{ju}\right)\left(-1+e^{jv}\right)+\\[2mm] \dfrac{1}{uv}\left(\begin{array}{c}1-e^{2ju}+je^{3ju}+e^{jv}\left(j+e^{3ju}\right)-\\[1mm] j\cos(u)+\sin(u)\end{array}\right)\end{array}\right)}{u^2v^2} \qquad (308)$$

121
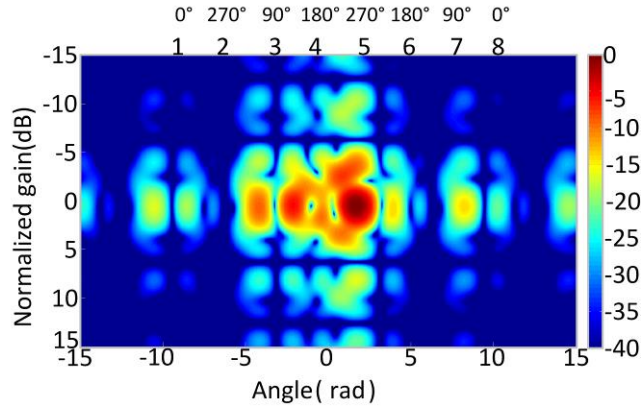
Figure 70. 3D pattern of skewed odd symmetry creating four main beams of unequal amplitude type 6.

$$\Lambda = \frac{e^{-j(2u+v)}\left(-1+e^{ju}\right)\left(-1+e^{jv}\right)\left(\begin{array}{l} -e^{j(u+v)}\left(-1+e^{ju}\right)\left(-1+e^{jv}\right) \\ +uv\left(\begin{array}{l} 1-e^{2ju}+je^{3ju} \\ +e^{jv}\left(1+e^{3ju}\right)-j\cos(u)+\sin(u) \end{array}\right) \end{array}\right)}{u^2 v^2} \qquad (309)$$
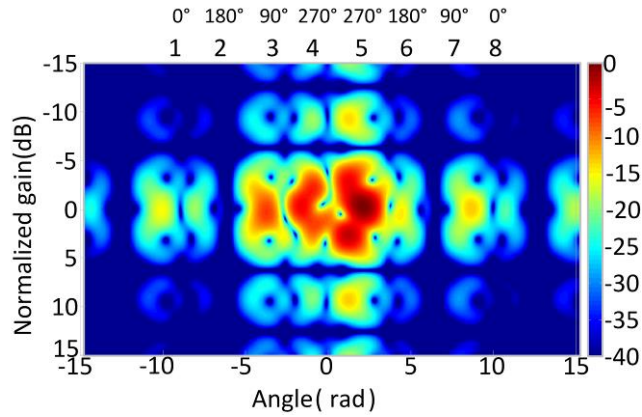
Figure 71. 3D pattern of skewed odd symmetry creating four main beams of unequal amplitude type 7.

$$\Lambda = \frac{8\sin\left(\dfrac{u}{2}\right)^2 \left(1+\cos(u)+\sin(u)\right)\left(1-\cos(v)+\sin(v)\right)}{uv} \qquad (310)$$
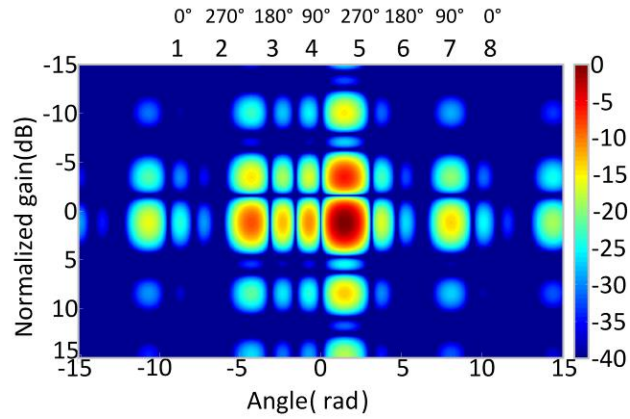
Figure 72. 3D pattern of skewed odd symmetry creating four main beams of unequal amplitude type 8.

$$\Lambda = \frac{16j\left(\sin\left(\frac{u}{2}\right) - \sin\left(\frac{3u}{2}\right)\right)\sin\left(\frac{v}{2}\right)\sin(v)\left(\sin\left(\frac{u-v}{2}\right) + j\sin\left(\frac{u+v}{2}\right)\right)}{uv} \tag{311}$$
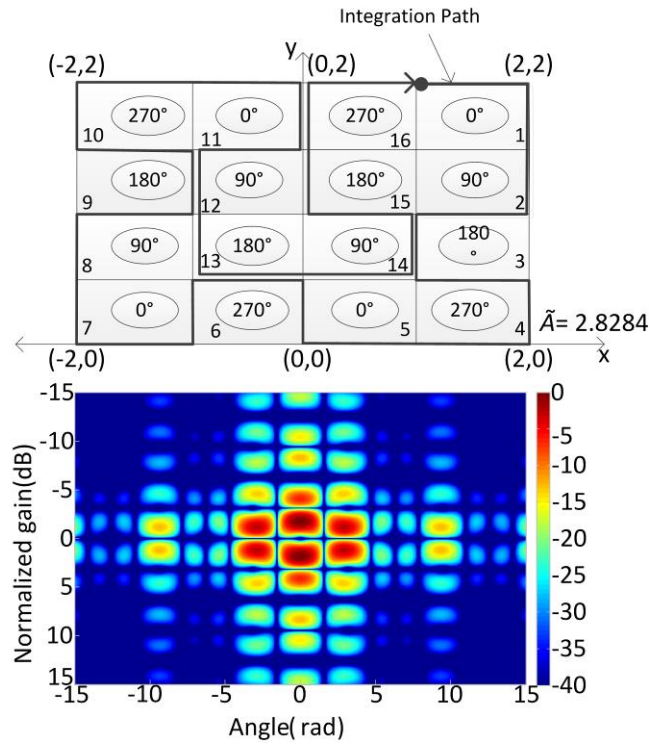
Figure 73. 3D pattern of skewed odd symmetry creating four main beams of unequal amplitude type 9.

123

$$\Lambda = \frac{1}{u^2 v^2} \mathrm{e}^{-j(2u+3v)} \left| \begin{array}{l} -j\mathrm{e}^{4ju}\left(-1+\mathrm{e}^{ju}\right)^2 - (1+j)uv\mathrm{e}^{4jv}\left(-1+\mathrm{e}^{4ju}\right) \\ +uv\mathrm{e}^{3jv}\left((-1-j)+je^{3ju}+\mathrm{e}^{4ju}\right)+ \\ \mathrm{e}^{i(u+v)}\left(-1+\mathrm{e}^{iu}\right)\left(uv+2je^{3ju}\left(-1+\mathrm{e}^{ju}\right)+2juv\cos(u)\right)+ \\ (2-2j)uv\mathrm{e}^{2ju+5jv}\left(-1+\sin(u)\right)\left(1-\cos(u)+\sin(u)\right)- \\ je^{2jv}\left(-1+\mathrm{e}^{ju}\right)\left(\binom{1}{j}uv\binom{1+}{2\cos(u)}\binom{-e^{4ju}+\mathrm{e}^{5ju}+}{-j\cos(u)}\right) \end{array} \right| \tag{312}$$
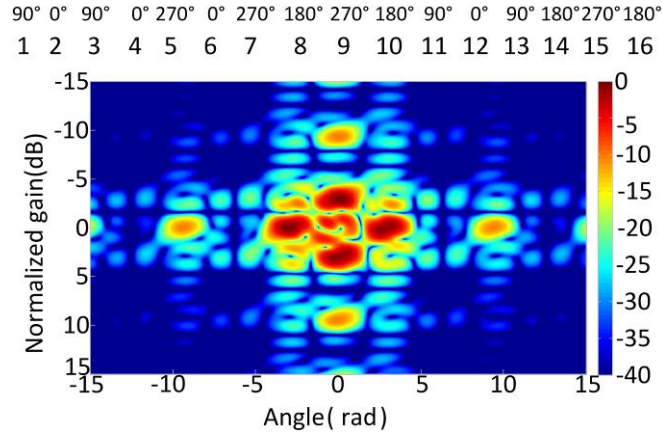
Figure 74. 3D pattern of skewed odd symmetry creating four main beams of unequal amplitude type 10.

$$\Lambda = \frac{(32-32j)\cos(u)\sin\left(\frac{u}{2}\right)^2 \sin\left(\frac{v}{2}\right)^2 \left(1+\cos(u)-\sin(v)\right)}{uv} \tag{313}$$
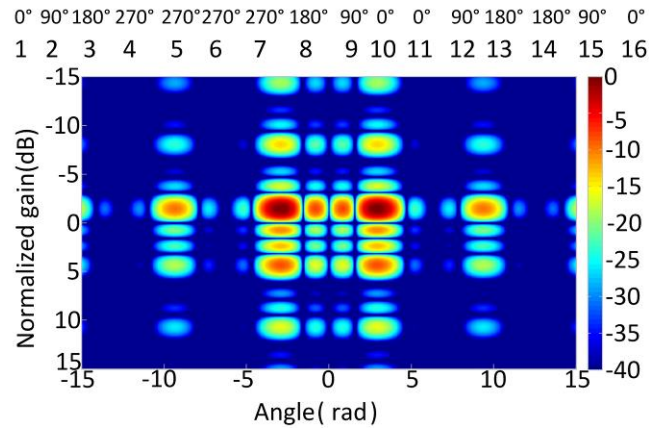
Figure 75. 3D pattern of skewed odd symmetry creating four main beams of unequal amplitude type 11.

9.3 Simulated Verification.

In order to validate that the results of the proposed shared aperture solutions are correct the following simulations are illustrated in Figure 76-Figure 84. For instance, as the element distribution is increased from 100 elements to 1000 elements it is seen that the analytical solution matches much more faithfully to the expected patter. Furthermore when the number of elements is increased even further up to 10000 elements it is seen that the simulated and expected pattern match almost exactly. The small discontinuity in the pattern can also be attributed since the code does not adjust element spacing. I.e. if two elements land in the same location no adjustments are made and will as a consequence offset the results by making an amplitude distribution at that location.
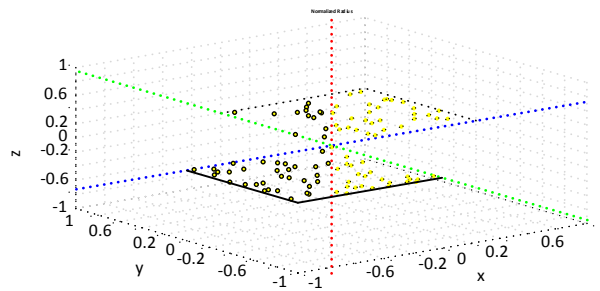
Figure 76. One hundred element anti modal distribution.
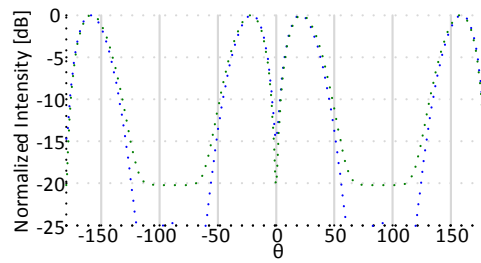
Figure 77. Rectangular plot of the expected value and simulated patterns for an anti-modal uniform distribution of *N*=100.
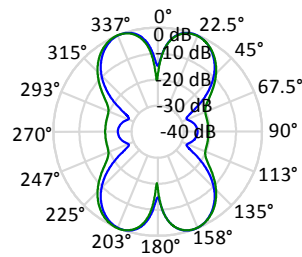
Figure 78. Polar plot of the expected value and simulated patterns for an anti-modal uniform distribution of *N*=100.
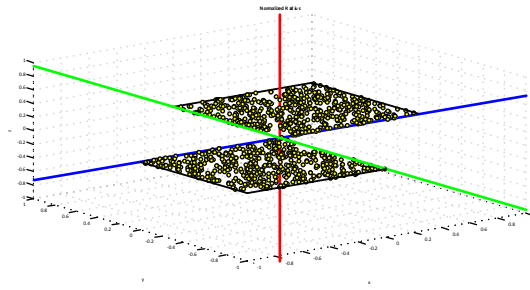
Figure 79. One thousand element anti modal distribution.
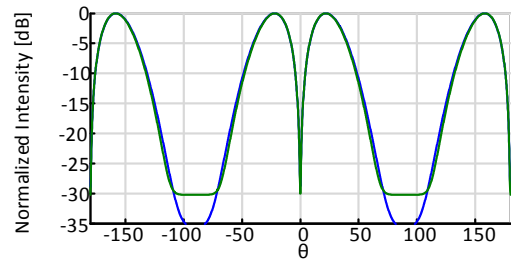
Figure 80. Rectangular plot of the expected value and simulated patterns for an anti-modal uniform distribution of *N*=1000.
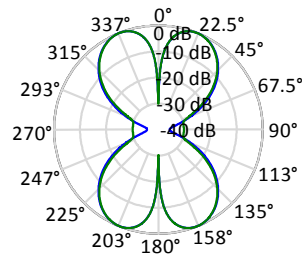
Figure 81. Rectangular plot of the expected value and simulated patterns for an anti-modal uniform distribution of *N*=1000.
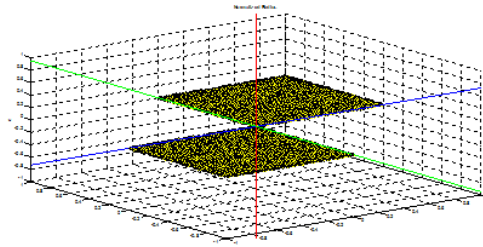
Figure 82. Ten thousand element anti-modal distribution.
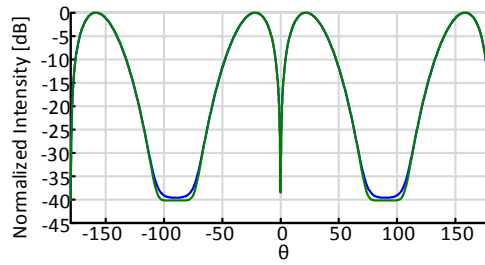
Figure 83. Rectangular plot of the expected value and simulated patterns for an anti-modal uniform distribution of N=10000.
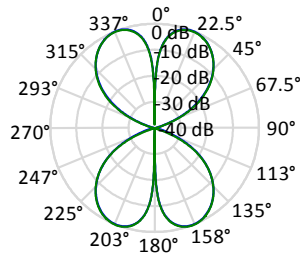
Figure 84. Polar plot of the expected value and simulated patterns for an anti-modal uniform distribution of N=10000.

9.3 Zernike Polynomials (Amplitude Orthogonality)

The Zernike polynomials are a common orthogonal set of polynomials used to express the aberrations in the eye. Moreover, these modes are composed of both even and odd modes and have orthogonal solutions in terms of its radial and angular solutions. These are similar in respect to the spherical harmonics used in the hydrogen like atoms and orbitals. Moreover, the complete set of Zernike polynomials is 35 solutions where the first ten modes are: piston, tilt x, tilt y, power, astig x, astig y, coma x, primary spherical, trefoil x, trefoil y. Independent solutions to these characteristic functions are found in the Appendix II with illustrations of their solutions. A complete graphical illustration of all 7 independent modal solutions (Figure 85) is found below in Figure 86 and Figure 87 where $X = (\hat{x} + \hat{y} + \hat{z}) \cdot (\hat{r}(\theta, \phi) - \hat{r}_o(\theta_o, \phi_o))$ (beamsteering coefficient).
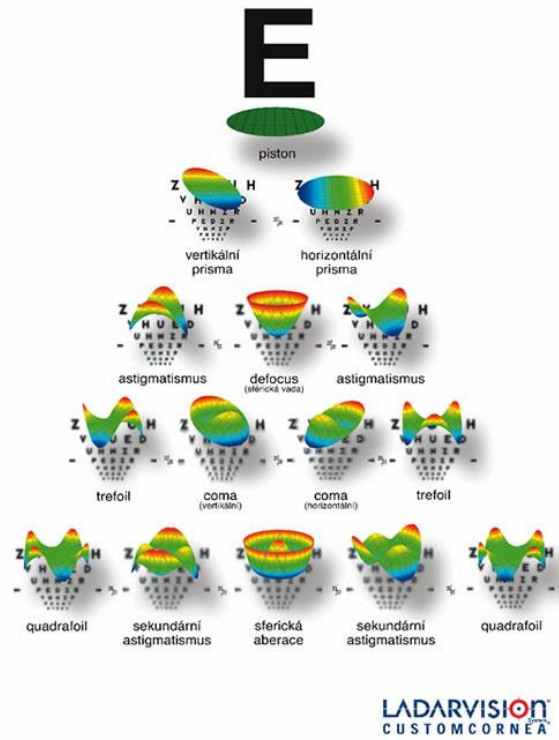
Figure 85. Chart of the Zernike polynomials or abberations typically encountered at the eye doctor. [144]
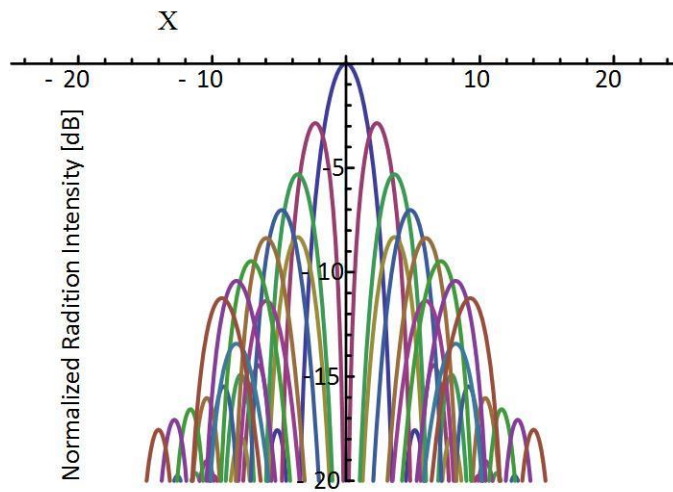
Figure 86. Seven independent solutions of the thirty five total *Zernike* polynomials.

X
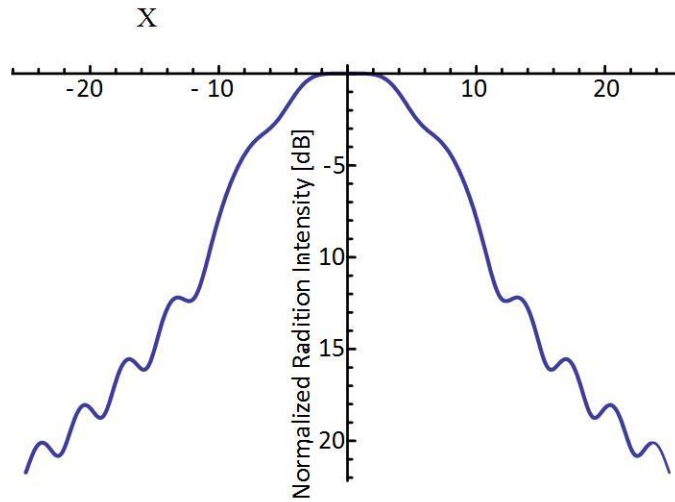
Figure 87. Aggregate of the seven independent solutions.

9.4 Physical Explanation (Multiple Beams)

The array factor of two isotropic sources located d/2 above the z axis and below the z axis is (314). By producing a progressive phase shift of pi *rad* ($180°$) one phases the upper half plane to be 0 degrees and the lower half plane to be $180°$. This is better shown this by the method of images for electric sources shown in Figure 88.

$$\sin\left(\frac{1}{2}\left(kd\cos\theta + \beta\right)\right)_{between\ 1\&3\ Quadrants} \tag{314}$$
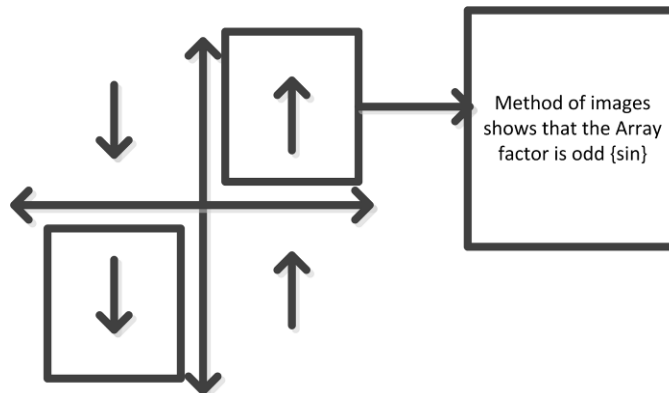
Figure 88. Multiple beams explanation using image theory.

130

Solving (315) for the null locations one obtains (316). Now since the distance between a positive charge and a negative charge is $\pm\lambda/2$ or some multiple thereof one obtains (317).

$$\sin\left(\frac{1}{2}\left(kd\cos\theta+\pi\right)\right)=0 \tag{315}$$

$$
\begin{aligned}
&\frac{1}{2}\left(kd\cos\theta+\pi\right)=\{0,\pi\}\\
&\frac{\pi d}{\lambda}\cos\theta=\left\{\frac{\pi}{2},-\frac{\pi}{2}\right\}\\
&\theta=\cos^{-1}\left\{\frac{-\lambda}{2d},\frac{\lambda}{2d}\right\}
\end{aligned}
\tag{316}
$$

$$
\begin{aligned}
&\theta=\cos^{-1}\left\{-1,1\right\}_{d=\frac{\lambda}{2}}\\
&\theta_n=0,\pm\pi
\end{aligned}
\tag{317}
$$

Similarly it can be shown that this odd mode has two peak locations at the locations given by (318) as shown in Figure 89.

$$\theta_p=\pm\frac{\pi}{2} \tag{318}$$
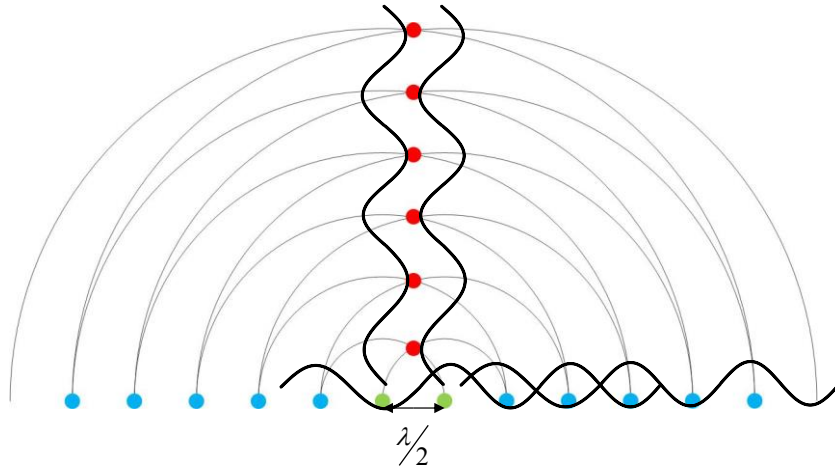
Figure 89. Interference pattern for two isotropic sources spaced half a wavelength apart.

This example illustrates the simple fact that an odd mode produces two main beams with a null at the center. However, this was done for the most simplest of cases being two isotropic point sources. Therefore when the sources are not point sources the physical process becomes much more difficult to comprehend and as a consequence we turn to the Fourier transform in order to understand the process.

Moreover, as we use more complicated source topologies we are essentially tapering the odd mode apertures such that we obtain two main beams with lower side lobe levels. These types are shown in descending order of side lobe levels in Table 8 and illustrated in Figure 61. For more complex structures we can observe the behavior in Figure 62-Figure 75 and also identify that the beamwidth is affected by the manner in which the current excitation is either clustered or dispersed; such that in general the beamwidth is broad when the current density is high near the center of the aperture and low toward the edges, and vice versa.

It also is noted that the beamwidth is affected by the manner in which the element population is either clustered or dispersed. The sidelobe level is determined by the abruptness of the change in the element distribution. I.e. the delta derivative model as illustrated below in Figure 90-Figure 92. For instance, if large impulses or large peaks appear in the nth derivative of the aperture excitation, then the sidelobe level is the order of -$10n$ dB. An analysis of this sidelobe behavior is provided in Table 10.

Table 10. Impulses in the Element Population (Aperture Excitation).

Aperture	Derivative in which impulses or large peaks are found	
Inferometer	0	0
Rectangle	1	-13.4
Circle	1-2	-17.5
Parabola	2	-22.0
Circle	2	-23.5
Triangle	2	-26.8
Raised Cosine	3	-32.0
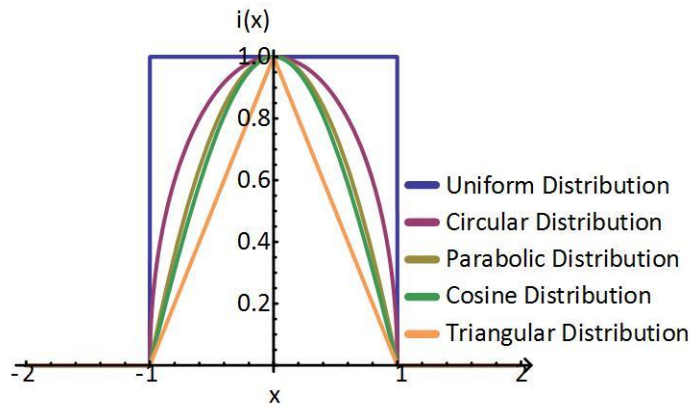
Figure 90. Element population (duality with current distribution *i(x)*).
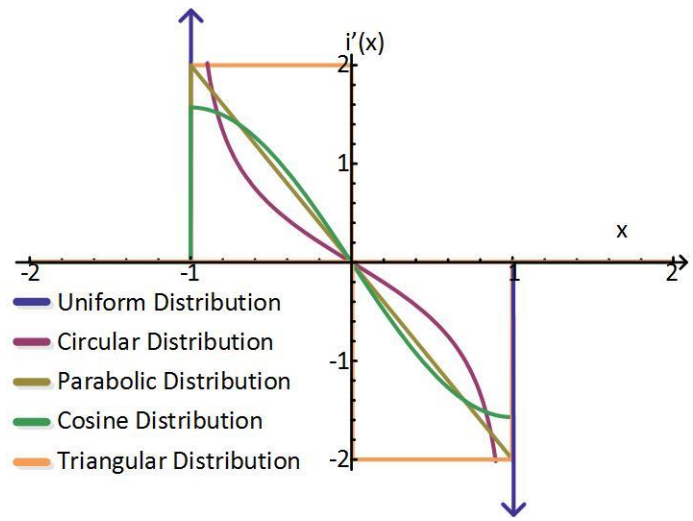
Figure 91. First derivative of the element population.
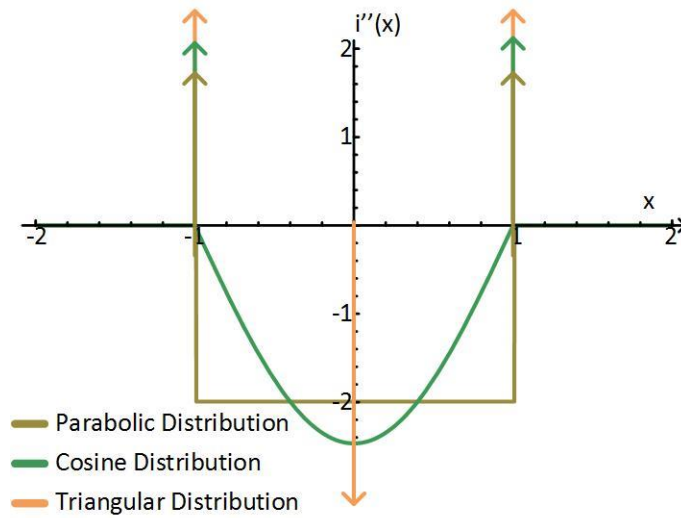
Figure 92. Second derivative of the element population.

9.5 Amplitude Monopulse Scanning

Amplitude comparison monopulse is similar to sequential lobing but instead the beams are created simultaneously as shown in Figure 93. For tracking purposes only the sum beam (addition of the two beams) is used for transmission, while both sum and difference beams (subtraction of the two beams) are used for reception with the objective of placing the target in the null of the difference pattern Figure 94.
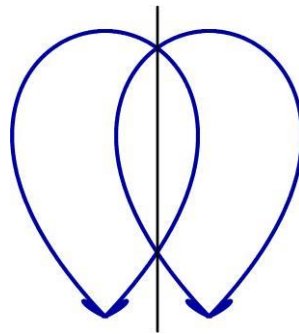
Figure 93. Two overlapping beams.
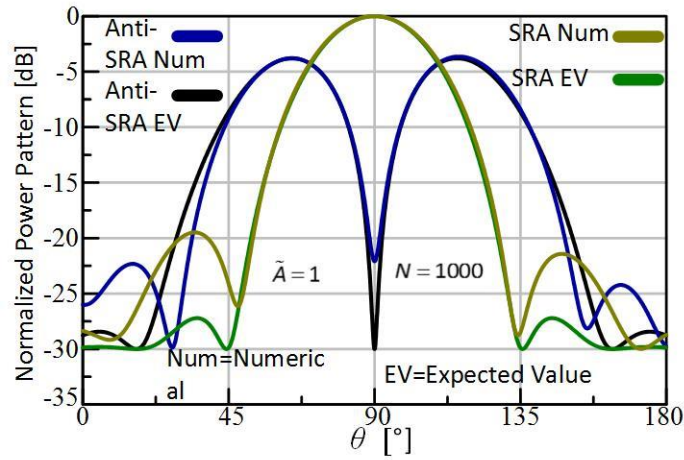
Figure 94. The sum and difference patterns of a spherical random antenna array.

The difference in the amplitudes received from these two beams (the difference beam) gives the angular error while the angular phase error is found from the ratio of the difference-to-sum voltage ratio(319). The real and imaginary components are given respectively by (320) and (321) where δ is the relative phase between sum and difference beams. A common rule of thumb is that the accuracy of a tenth of beamwidth can be achieved with an SNR of 10 dB.

$$\frac{\Delta}{\Sigma} = \frac{\text{difference voltage}}{\text{sum voltage}} \tag{319}$$

$$\text{Re}\left\{\frac{\Delta}{\Sigma}\right\} = \frac{|\Delta|}{|\Sigma|}\cos\delta \tag{320}$$

$$\text{Im}\left\{\frac{\Delta}{\Sigma}\right\} = \frac{|\Delta|}{|\Sigma|}\sin\delta \tag{321}$$

An example of this using a periodic digital phased array is shown in Figure 95. The phase shifting of each element is done using a progressive phase shift and is controlled by the DBF.

135
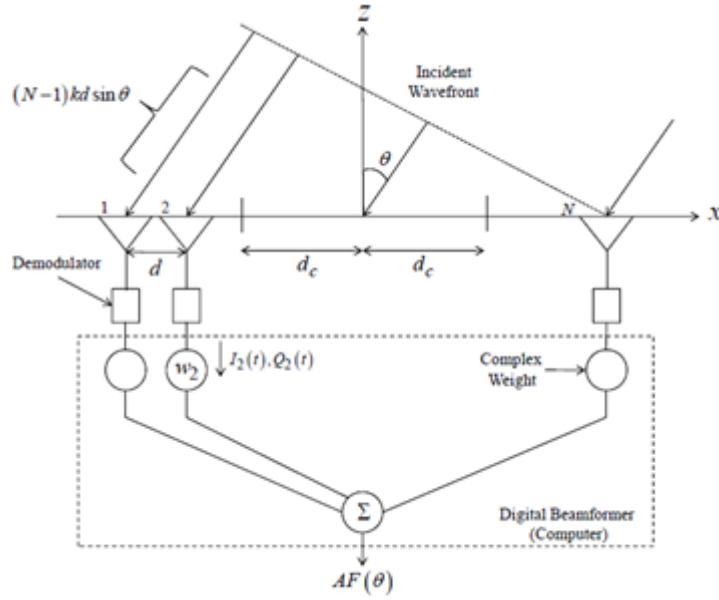
Figure 95. Digital phased array azimuth beamforming on reception. [104]

The element spacing d_n on the x-axis (n =1, 2,..., N) is centered along the origin with inter-element spacing d (322) and the one-dimensional uniformly distributed linear array factor is given by (323) (np) and ψ_n is the scan angle of the main beam (np)

$$d_n = \frac{2n-(N+1)}{2}d \tag{322}$$

$$AF(\theta) = \sum_{n=1}^{N} e^{j(kd_n \sin\theta - \psi_n)} \tag{323}$$

$$\psi_n = -kd_n \sin\theta_0 \tag{324}$$

For the application of monopulse tracking the digital beamforming is split into two azimuth subarrays with $N/2$ elements each. The subarrays are centered from the origin of the array given by (325). Thus, the individual subarray factor is (326)

$$d_c = \frac{N}{4}d \tag{325}$$

$$SF = \frac{\sin\left[\dfrac{Nkd(\sin\theta - \sin\theta_s)}{4}\right]}{\sin\left[\dfrac{kd(\sin\theta - \sin\theta_s)}{2}\right]} \tag{326}$$

Differently for a random array this architecture is shown below in Figure 96
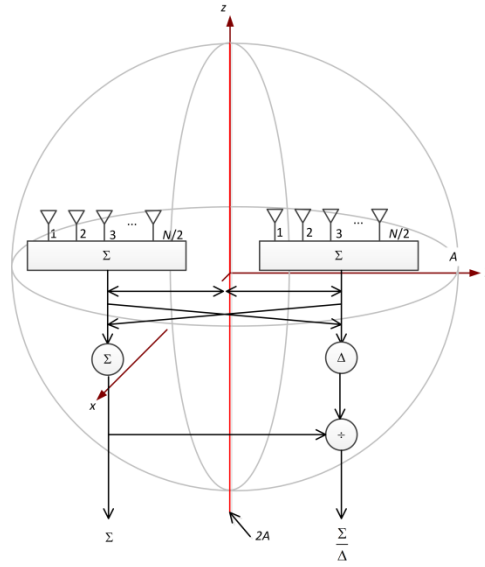
Figure 96. Sum and difference beamforming of monopulse amplitude tracking.

The usefulness of splitting an array into two subarrays is such that the sum and difference beams be formed respectively as (327) and(328).

$$\sum = SF\, e^{-jkd_c(\sin\theta - \sin\theta_s)} + SF\, e^{-jkd_c(\sin\theta - \sin\theta_s)}$$
$$= SF\, 2\cos\left[kd_c\left(\sin\theta - \sin\theta_s\right)\right] \tag{327}$$

$$\Delta = SF\, e^{-jkd_c(\sin\theta - \sin\theta_s)} - SF\, e^{-jkd_c(\sin\theta - \sin\theta_s)}$$
$$= SF\, 2j\sin\left[kd_c\left(\sin\theta - \sin\theta_s\right)\right] \tag{328}$$

Where the ratio of difference over the sum ratio is given to be that of(329).

$$\frac{\Delta}{\Sigma} = j\tan\left[kd_c\left(\sin\theta - \sin\theta_s\right)\right] \tag{329}$$

Furthermore, by assuming a small angle approximation for ($\theta - \theta_0$) one may simplify (329) by use of a first order Taylor approximation giving (330) where K is the monopulse slope constant.

$$\frac{\Delta}{\Sigma} \approx kd_c\left(\theta - \theta_s\right) = K\left(\theta - \theta_s\right) \tag{330}$$

The monopulse slope constant can be transformed to [118]

$$K \approx kd_c = \frac{2\pi}{\lambda}\frac{N}{4}d = \frac{N\pi}{2}\frac{d}{\lambda} = \frac{.88\lambda}{\theta_B}\left(\frac{\pi}{2\lambda}\right) = \frac{1.38}{\theta_B} \tag{331}$$

"Where $\theta_B \approx .88\lambda/D \approx .88\lambda/Nd$ and is accurate near broadside. However, at wide scan angles the slope decreases significantly due to a reduction in the array's projected aperture. To compensate, the constant can be modified by multiplying by $\cos\theta_s$ [26]."

The normalized ratio of (319) and (330) illustrates a linear region in the vicinity of the null of the difference pattern. "The plot of a typical Δ/Σ ratio is given by Figure 97. Also for clarity the example of the output voltages for sum and difference beams is shown in Figure 98 with application provided in Figure 99 .
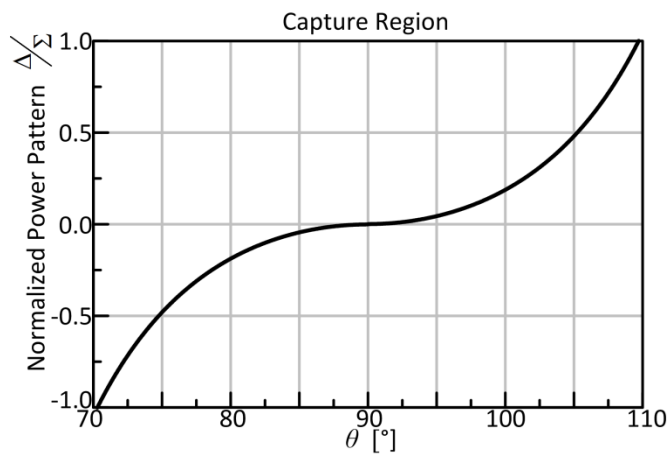
Figure 97. Normalized Δ/Σ vs. pattern angle.
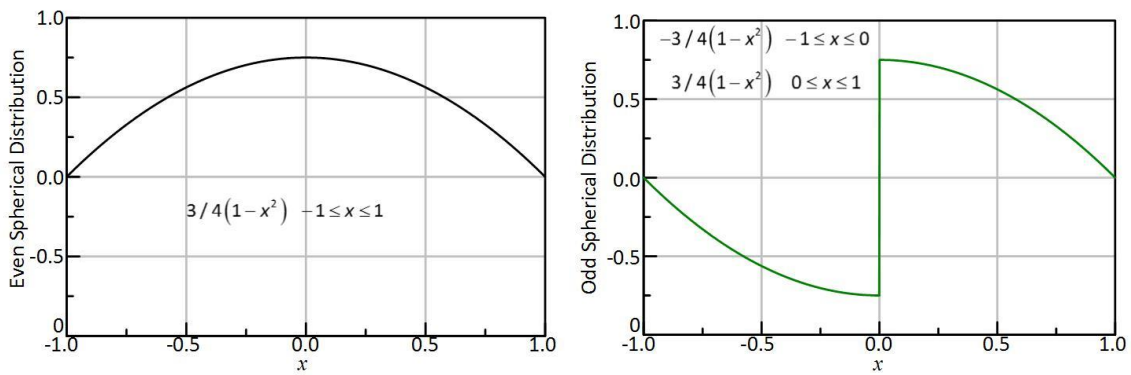
Figure 98. Sum and difference beam output voltages.

138
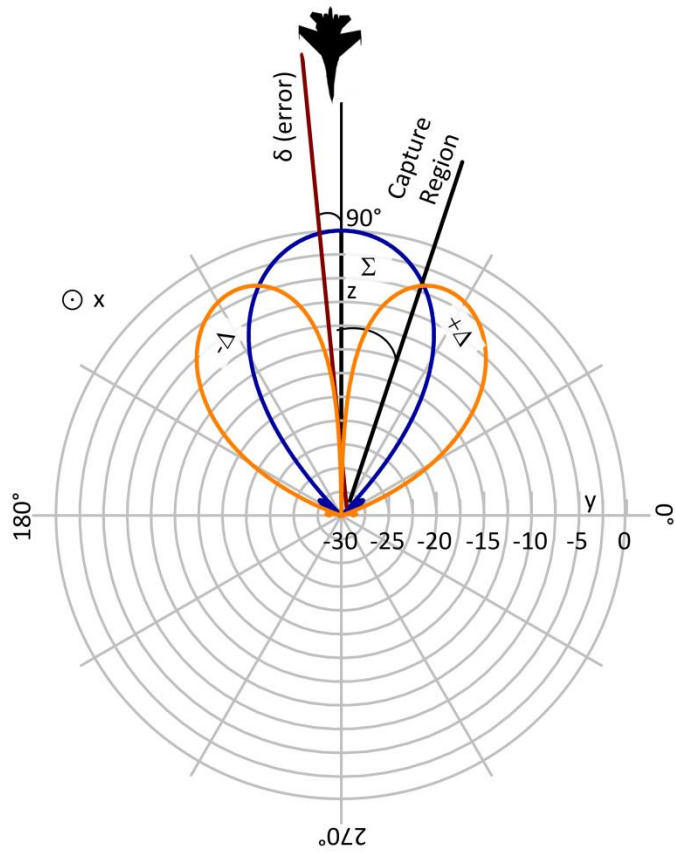
Figure 99. Illustration of azimuth sum and difference beams.

CHAPTER X

GAUSSIAN BEAMS

10.1 Compaision of Gaussian Beams

In many applications it is important to maintain low sidelobe levels such that the field strength is centralized in the target location and not wasted elsewhere. In other words removing energy from the main lobe places this energy elsewhere into the sidelobe region such that it may be picked up by unintended receivers, altered by interfering signals, increase clutter and the noise level in the receiver. Hence, it is important to remove these sidelobes and one such distribution that is able to completely remove all sidelobes is the Gaussian distribution. A comparison of the characteristic function for both Gaussian and truncated Gaussian distribution are shown in Figure 100 for a variety of truncated lengths and element populations. Moreover, it is seen that when L approaches the value of $\tilde{A}$ that the truncated Gaussian distribution becomes equivalent to the true Gaussian distribution.

A comparison of the results of the Gaussian distribution (Table 9) are similar to the results of the uniform distribution (TABLE 5), such that the 3dB azimuthal angle decreases with increasing $\tilde{A}$, however the 3dB beamwidth is seen to be larger for the same cluster area [9]. Hence, in order to compare the results of a Gaussian distribution to that of a uniform distribution, the standard deviation (332) is derived such that it can be comparable. The derivation is shown in [81]. However, in [12] the metric of comparison used was (333). The latter metric provides a 99.73% accuracy that all antennas are located within the disc of radius $\tilde{A}$ providing that the uniform coverage will be the same in both cases.

The directivity for a Gaussian taper in rectangular coordinates is given by that of (334) and is also shown in Table 9. The relative gain of the Gaussian distribution compared to that of the uniform distribution is given by that of (335). From these expressions it is seen the gain will converge to N as $\tilde{A} \to \infty$. In addition the directivity for a Gaussian taper in polar and spherical coordinates $(\theta = \theta_0 = \pi/2)$ is given by that of (336). Moreover, it is once again observed that $I_n(x)$ and $_mF_n(m;n;x)$ are damped sinusoids and converge to 0 as $x \equiv \tilde{A} \to \infty$. Thus, the gain will generally be less than N, but will be approached for large aperture size. Lastly it should be noted that a Gaussian distribution is nothing more than the convolution of any regular distribution with itself over and over again to infinity. The exception to this rule is irregular distributions such as a pulse train. More so the radial tapers of both spherical and polar distributions shown in Table 6 and Table 7 arise from ongoing multiplication with each other. So for example, convolution of a square and a square produces a triangular distribution. In the Fourier transform space the transform of a square is a sinc function and the Fourier transform of a triangle is a sinc squared function. Furthermore convolution of a square with a triangle will produce some sort of more bell shaped

distribution but will end up causing a sinc cubed transform. Hence, since a Gaussian distribution transforms into a Gaussian beam then one can either create a taper function by continuous multiplication of the distribution or continuous convolution with itself. Last of all these radial and polar tapers are related to the Fourier transform of an *n-sphere*. For example, if one finds the probability distribution of a circle and then for a glome one will find the pdf of the glome is the square of circle. In conclusion, the radial and polar tapers of circles and spheres are related to an *n*-sphere. Furthermore a glome may be thought of as a sphere of which moves with circular motion. The higher form of a glome being a 3 sphere would be a sphere that move with three dimensional motion. Otherwise these *n-sphere* models can be used to derive error models, which will be shown in Section 15.4.

$$\sigma = \frac{A}{2\sqrt{3}} \tag{332}$$

$$\sigma = \frac{A}{3} \tag{333}$$

$$\frac{N}{1 + e^{-2A^2\pi^2\sigma^2}(N-1)\,_0\tilde{F}_1\left(;1;A^4\pi^4\sigma^4\right)} \tag{334}$$

$$\frac{\left(2\pi^{1/2}\sigma^2 * erf\left(\frac{\left(2^{1/2}\left(\frac{1}{\sigma^2}\right)^{(1/2)}\right)}{2}\right)\right)^2 * \left(\frac{1}{\sigma^2}\right)^{1/2}}{2erf\left(\left(\frac{1}{\sigma^2}\right)^{1/2}\right)} \left\{\neg u = [-1,1]\right\} \tag{335}$$

$$\frac{N}{1 + e^{-8\pi^2\sigma^2}(N-1)I_0\left(8\pi^2\sigma^2\right)} \tag{336}$$

Other Gaussian beam appear to come from the distributions listed in the representation of characteristic functions provided in Figure 101 and are referenced from Appendix XV [192]. The exception to these beams is the arctangent distribution of which provides a beam similar to the superposition of modes seen previously by the Zernike polynomials in Figure 87.
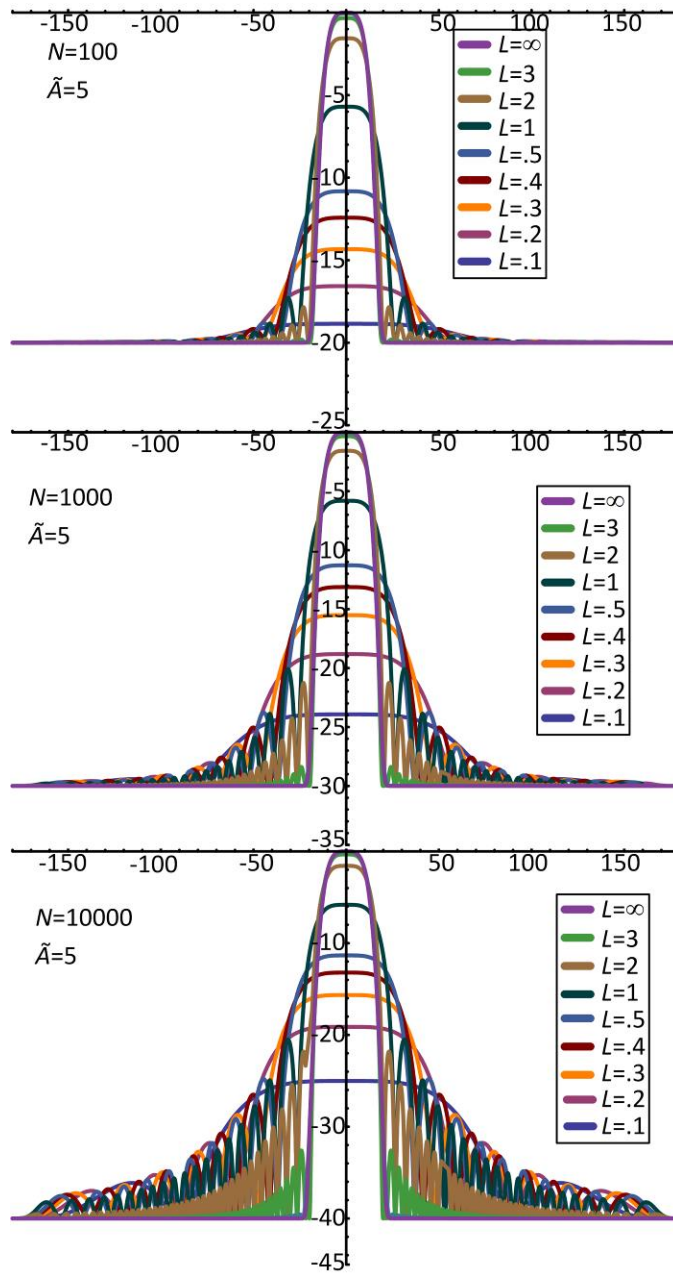
Figure 100. Gaussian and truncated Gaussian characteristic function comparison for $N= \{100, 1000, 10,000\}$.
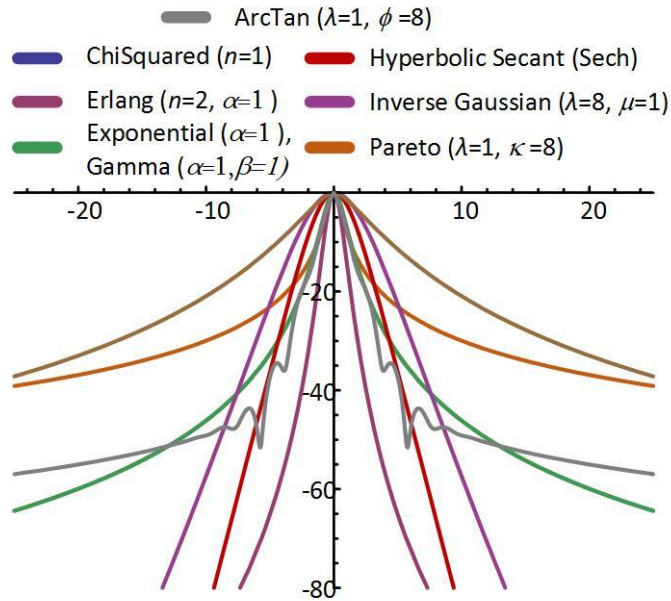
Figure 101. Other common distributions providing Gaussian like beams.

10.2 Explanation of the N-Sphere Taper

As can be seen from TABLE 5-Table 9 is that the radial tapers of the polar and spherical forms are essentially converging to the nth power. As it was explained previously the convolution of a rectangle and a rectangle is a triangle. In the Fourier domain this is the multiplication of a sinc function by a sinc function. Then a rectangle convolved with a triangle is some form of shape, but in the Fourier domain is a sinc function to the third power (sinc x $sinc^2$). This process continues until essentially one arrives at $sinc^N$, which will appear as a Gaussian beam. Thus, on the other side of the space this Gaussian beam is found by convolving a shape by itself over and over again (as long as it is not something that convolves into itself like a pulse train). Analogously the n-sphere tapers are seen to grow to the Nth, which means they are also a Gaussian taper family, which also implies some form of convolution with one shape over and over again. I.e. convolution of a circle (circle by a circle is a sphere; sphere convolved with a circle is a glome etc.) However, the negative solutions are seen to diverge this is a consequence of negative curvature illustrated in Figure 102. In fact the negative solutions are related to the Ricatti-Bessel functions such that the solutions of (337) are found.

$$C_0(x) = (-xy_0(x))\,(n = -1\;sphere)$$
$$xC_1(x) = x(-xy_1(x))\,(n = -3\;sphere)$$
$$x^2C_2(x) = x(-xy_2(x))\,(n = -5\;sphere)$$

(337)

143
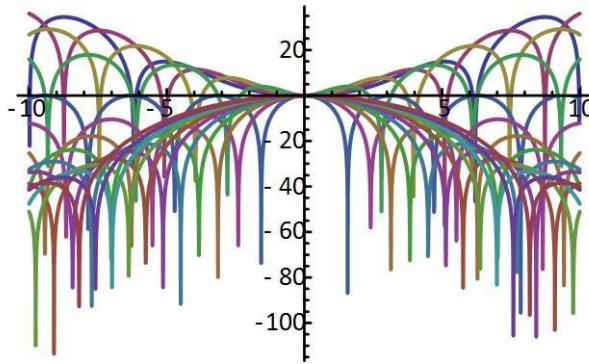
Figure 102. Example of the *N*-shere tapers and the negative *N*-sphere (odd solutions) tapers.

These diverging waves are perfectly described by negative n-sphere curvature as shown in Figure 103. As it can be seen here the isotropic radiatior expand outward isotropically and due to the negative curvature and ignoring path, loss, and absorption it is seen that mutual coupling has the ability to enhance the beams gain above the normailized gain found in positive curvature of the *N*-sphere. Mathematically it is considered that the differing equation behind these positive and negative *N*-spheres are shown by (338). These solution are modified from a 2-sphere as shown to a 1-sphere by setting *z*=0. Then to a 0-sphere by setting *y*=0 and essentially taking the derivative to excite the delta functions or end points of the line otherwise you would have a one ball. An example of the negative 2 sphere as shown by (338) is illustrated in Figure 104.

$$x^2 + y^2 + z^2 = 1 \; (positive \; sphere)$$

$$x^2 + y^2 - z^2 = 1 \begin{pmatrix} negative \; sphere \\ hyperboloids \; of \; one \; sheet \end{pmatrix}$$

(338)
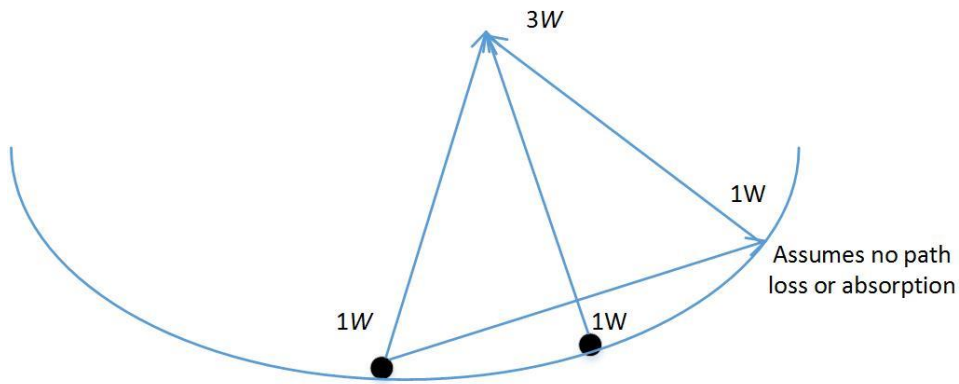
Figure 103. Negative *N*-sphere topology.
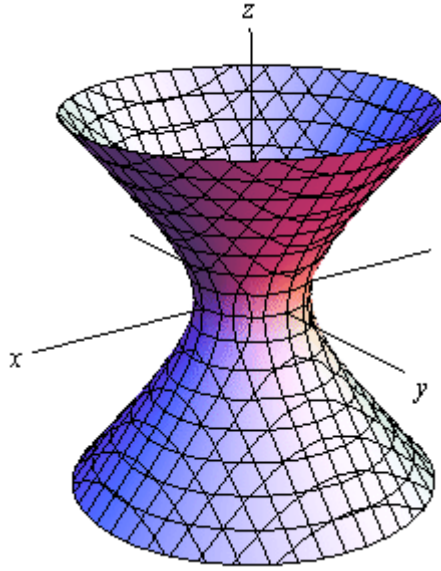
Figure 104. Example of a hyperboloid of one sheet.

Another theory of why the even negative modes do not exist is perhaps the negative *N*-spheres alternate by quadrics such that $N=-1$ is a hyperboloid of two sheets (339) and $N=-2$ is a degenerate quadric (cone) being (340) or possibly a degernerate hyperbolic cylinder (341).

$$x^2 + y^2 - z^2 = -1 \tag{339}$$

$$x^2 + y^2 - z^2 = 0 \tag{340}$$

$$x^2 - y^2 = 1 \tag{341}$$

Spherical neuman functions relating to the ricatti Bessel functions shown above can be formulated by Bessel functions of the second type (342) and spherical Bessel functions of the second type by (343). Moreover, there are a handful of meaningful interpretations of these expressions that are still considered questionable. Hence, it is left upon the reader or future investigator to make the necessary contributions as to what these negative spheres mean and how the probability density functions are generated. More thoughtful analysis of Ricatti Bessel functions should be researched in Mie scattering.

$$Y_n(t) = \frac{2\left(\frac{1}{2}t\right)^n}{\pi^{\frac{1}{2}}\Gamma\left(n+\frac{1}{2}\right)} \left(\int_0^1 \left(1-x^2\right)^{n-\frac{1}{2}} \sin(xt)\,dx - \int_0^\infty e^{-xt}\left(1+x^2\right)^{n-\frac{1}{2}}\,dx \right) \tag{342}$$

$$y_n(t) = \sqrt{\frac{\pi}{2t}} \frac{2\left(\frac{1}{2}t\right)^{n+\frac{1}{2}}}{\pi^{\frac{1}{2}}\Gamma(n+1)} \left(\int_0^1 \left(1-x^2\right)^n \sin(xt)dx - \int_0^\infty e^{-xt}\left(1+x^2\right)^n dx \right) \tag{343}$$

CHAPTER XI

EXPERIMENTAL AND SIMULATED RESULTS

The antenna pattern is taken based upon the reciprocity theorem. Other methods exists, but the reciprocity method is simple and consist of comparing the power received by a reference antenna $\left(P_{ref} \right)$ to the power received by the random array $\left(P_{RandArr} \right)$ operating at 2.45 GHz. The reference antenna used in this case is a standard gain horn and are standard for calibrating other antennas. Moreover, the gain of the reference antenna is known Figure 105 and is used to reference the antenna under test by the formula:" Furthermore in the context of setting up the chamber to take the desired measurements the horn is normalized in both the E-plane and H-plane as illustrated in Figure 106 and Figure 107 respectively. This is useful since the reference gain can be added at the end of the test during the post processing as illustrated in Figure 108. Also for completeness the simulated HFSS patch element pattern is provided in Figure 109.

$$G_{Test} = \frac{P_{Test}}{P_{ref}} G_{Ref}$$

$$G_{Test(dB)} = P_{Test(dB)} - P_{ref(dB)} + G_{Ref(dB)}$$

(344)
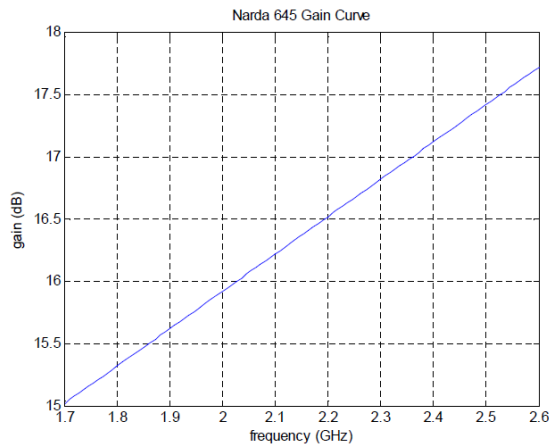
Figure 62.   Gain of reference antenna (After [25])

Figure 105. Gain of the reference antenna. [193]
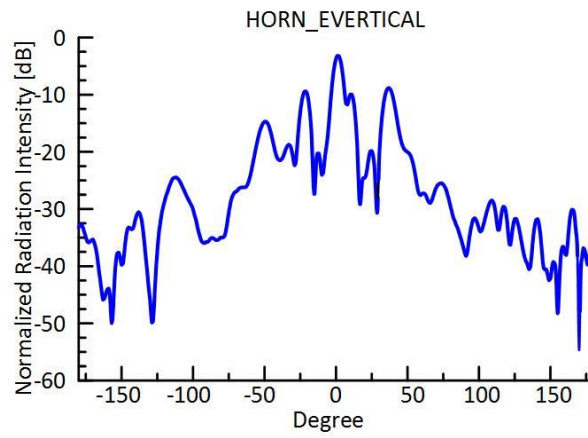
Figure 106. Normalized *E-plane* horn gain.
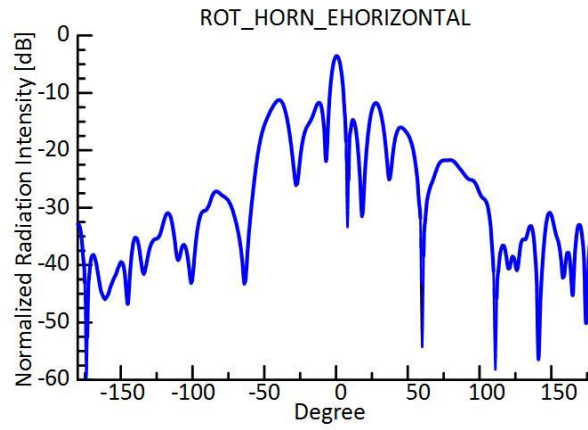
Figure 107. Normalized horn *H-plane* horn gain.
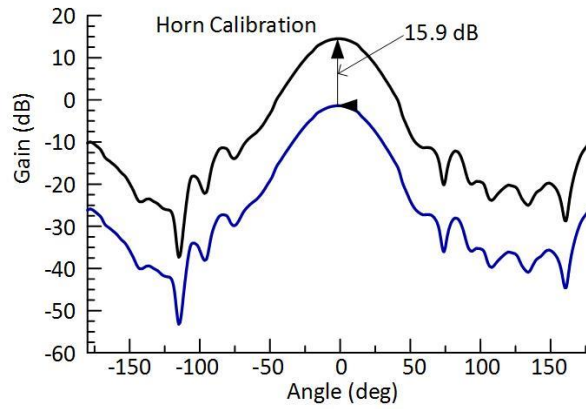
Figure 108. Horn calibration from the gain reference table with patch element radiation pattern.
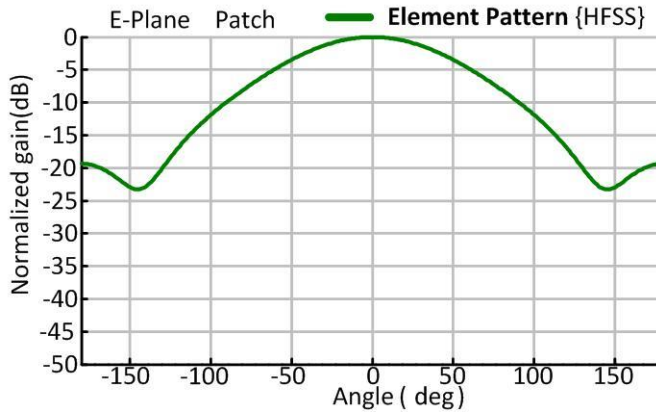
Figure 109. Element pattern of a single patch antenna element simulated in HFSS.

Now once the antenna is reference to that of a standard gain horn one takes the patterns in the desired polarization (horizontal or vertical), and starts the test program is started. The system begins to rotate the antenna under test (AUT) located on a pedestal through the angles specified in the program. Moreover, Figure 110 shows a notional example of the reference antenna installed on the rotating pedestal. The actual measurement was taken at the anechoic chamber at Texas A&M university and displays form reference antenna in Figure 111. Moreover, the communication link between the two antennas is notionally demonstrated by that in Figure 112.
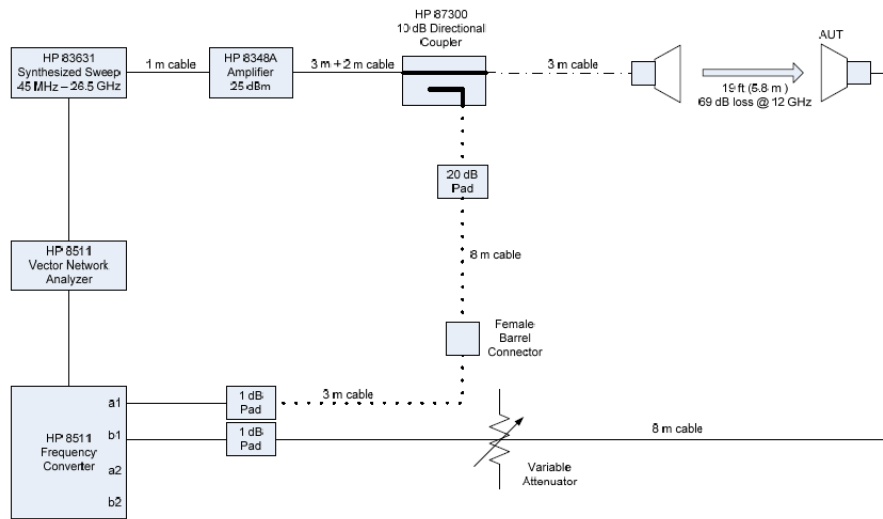
Figure 63.   Measurement setup of the anechoic chamber

Figure 110. Notional example of the anechoic chamber setup at Texas A&M University. [193]

Figure 111. Anechoic chamber at Texas A&M University.

Capable of Measuring Angle

Array   Horn
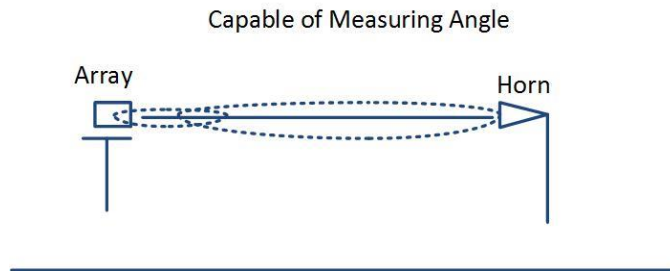
Figure 112. Measurement of the array pattern.

The full design of the random array used in this research was designed following the works of [194]-[199] and is illustrated in Figure 113. Only a brief description of the system will be reviewed and a more complete description can be found in [198]. The elements used in the array were a standard microstrip patch designed in the ISM band (2.45 GHz) with coax feed. The design parameters are W = 39.75 mm, L = 40 mm, d = $\lambda/2$, ε_r = 2.2 (Rogers 5880) with an illustration shown in Figure 114. The phase shifter is a commercial off the shelf Hittie Figure 115. This type of phase shifter uses a range of input voltages in order to produce a full 360 degree phase shift as shown in Figure 116. Moreover, the experimental verification of this phase shifter showed a slight variation at the higher frequencies. Hence a voltage equation was used in control to adjust for this small variation as shown in Figure 117. Next the power divider is shown in Figure 118 with manufacturer specifications of 1.0 dB (max) 10 degree (max) of phase offset. The experimental verification validating these claims are shown in Figure 119 and Figure 120. Last of all the phase shifts are coded and controlled using a smart phone, which sends in the required packets delegating the required phase shifted needed at each element in the array Figure 121. Lastly, a view of the complete system is shown in Figure 122.

Figure 113. Random array system overview.
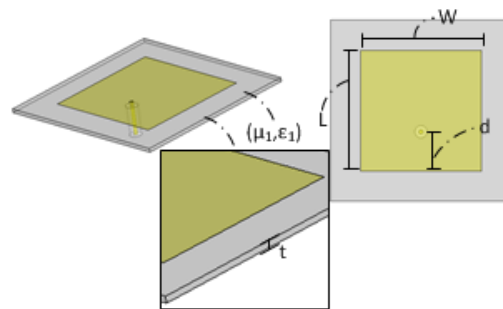
Figure 114. Patch element design parameters.

Figure 115. Hittite phase shifter.

152
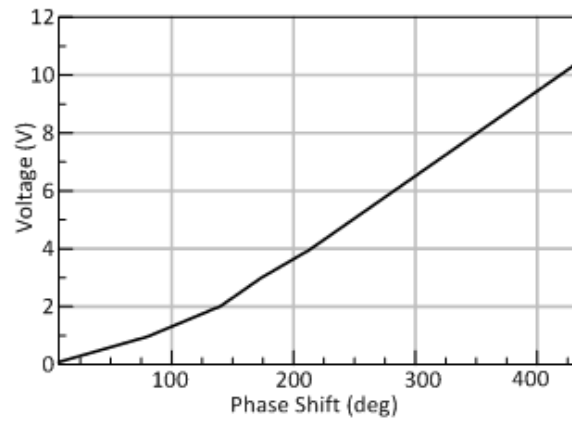
Figure 116. Phase shifter output vs. input voltage.
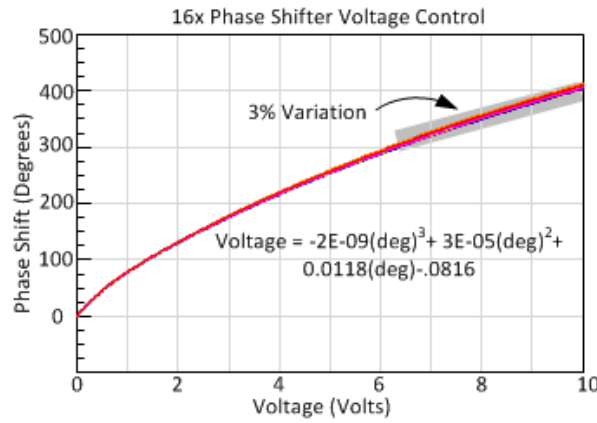
Figure 117. Phase shifter experimental verification.
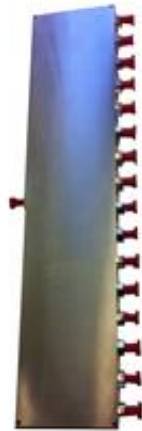
Figure 118. One to sixteen power divider.
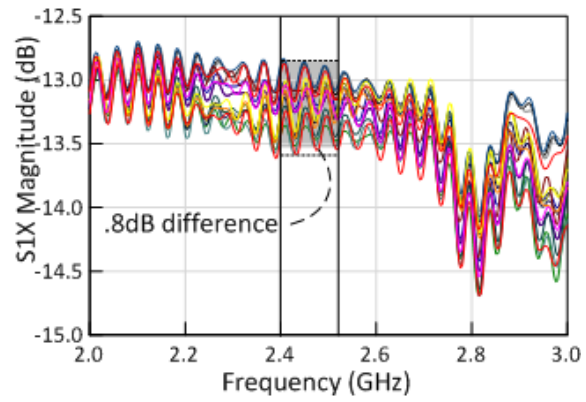
Figure 119. Amplitude tolerance of the 1:16 power divider.
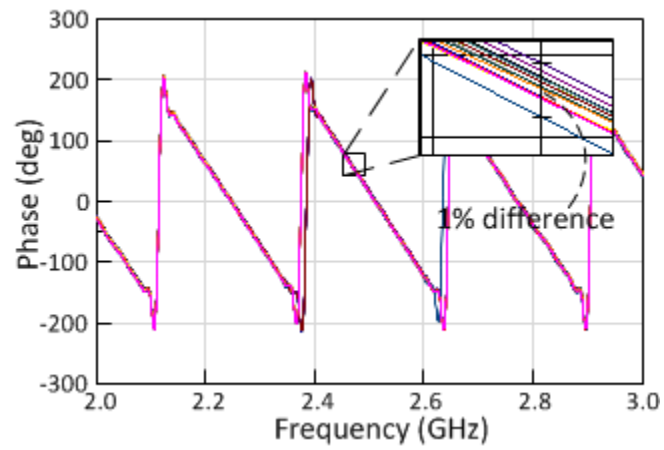
Figure 120. Phase tolerance of the 1:16 power divider.
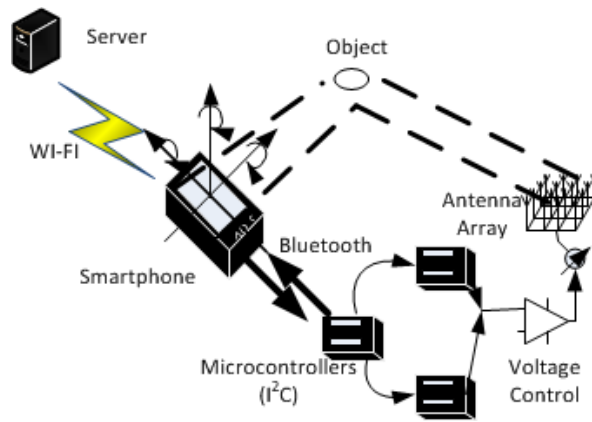
Figure 121. Random array communication and phase shifting system overview.
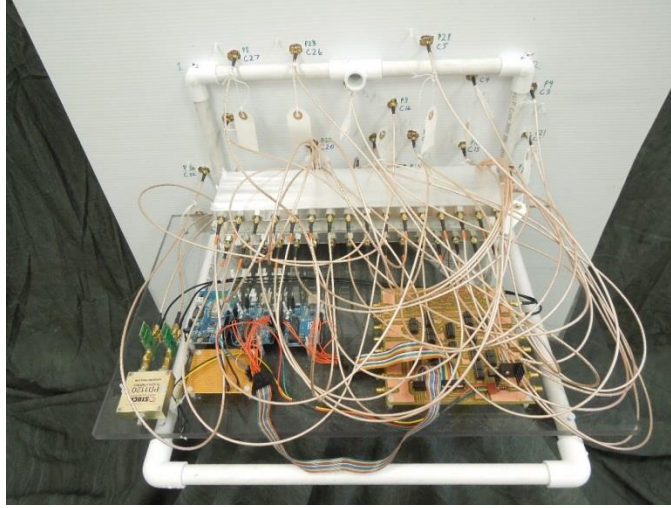
Figure 122. Complete system.

11.1 Planar Periodic Array

To avoid grating lobes in a periodic array under all conditions of beam steering the array must satisfy the spacing criteria of $d \leq \lambda/2$. Otherwise grating lobes can be avoided over a desired scan interval by satisfying the requirement $d \leq \lambda/\left(1 + |\sin\theta_o|\right)$. Thus, the total aperture size of N periodic elements is $A \equiv L = N \times d \approx N\lambda/2$. Also the gain of the linear periodic linear array may be calculated as

$$D = \frac{1}{\dfrac{a_0}{N} + \dfrac{2}{N^2} \displaystyle\sum_{m=1}^{N-1} \dfrac{N-m}{m\beta d}\left(a_1 \sin(mkd) + a_2 \cos(mkd)\right)\cos(m\alpha)} \tag{345}$$

The parameter α is the inter element phase shift (zero at broadside) and the factor $a_0, a_1,$ and a_2 provided in Table 11. Also the addition of the ground plane increases the gain of (345) by 3dB. Also similarly to the random array the maximum gain of an isotropic periodic linear array with no grating lobes is approximated as $D \approx 2\dfrac{L}{\lambda} \equiv 2\tilde{A} = 2\dfrac{Nd}{\lambda}$. Hence, for half wavelength spacing this reduces as N as illustrated in Figure 123. Also combining the results of the number of elements and scan angle provides the best angular resolution of a periodic array as $N \approx 2/\theta_{3dB}$ where θ_{3dB} is the 3dB beamwidth. In other words "the cost of a linear and periodic phased array increases as the reciprocal of the desired angular resolution. In a two-dimensional array, both the number of elements and the cost will increase as the square of the desired angular resolution." [102] As a result the cost of these large periodic arrays can be very expense and prohibitive. Thus, it makes economic sense to study and explore the use of random

arrays, thinned or other types of arrays "as a means of reducing costs (and weight) vis-à-vis large periodic arrays." [102]

Table 11. Parameters Used for Calculating the Gain of (345).

Element Type	$\left\|g_a\left(\theta,\phi\right)\right\|^2$	a_0	a_1	a_2
Isotropic	1	1	1	0
Collinear short dipoles	$\sin^2\left(\theta\right)$	$\dfrac{2}{3}$	$\dfrac{2}{\left(mkd\right)^2}$	$\dfrac{-2}{mkd}$
Parallel short dipoles	$1-\sin^2\theta\cos^2\phi = \sin^2\gamma$	$\dfrac{2}{3}$	$1-\dfrac{1}{\left(mkd\right)^2}$	$\dfrac{1}{mkd}$
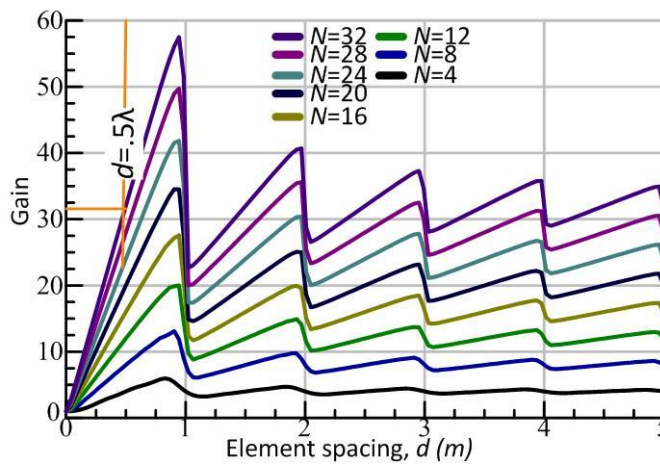
Figure 123. Gain for an isotropic periodic linear array vs. element spacing (broadside scan) (345).

To verify the beamsteering capability of a periodic linear array the design of a 16 element patch array was designed and simulated in HFSS with illustration in Figure 124. The results of both the simulation and experiment are shown (normalized) in Figure 125 at the forty five degree cut plane. Here it is seen that there is excellent agreement between the simulated (theoretical) results to that of the actual measurement. A complete scan of the measured sixteen element periodic patch element array is provided in Figure 126-Figure 127. The scan interval of –45° to 45° with a 7.5° incremental scan was chosen since the field of view of the patch elements radiation pattern attenuates strongly outside of this window as seen by Figure 108 or Figure 137.
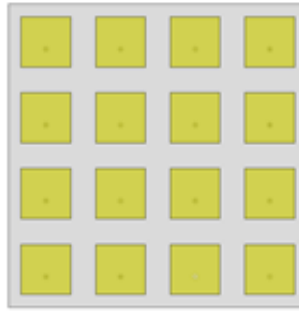
Figure 124. Sixteen element patch element antenna array.
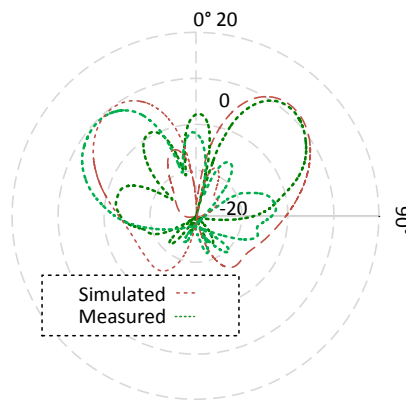
Figure 125. Forty-five degree simulated and measured pattern comparison.
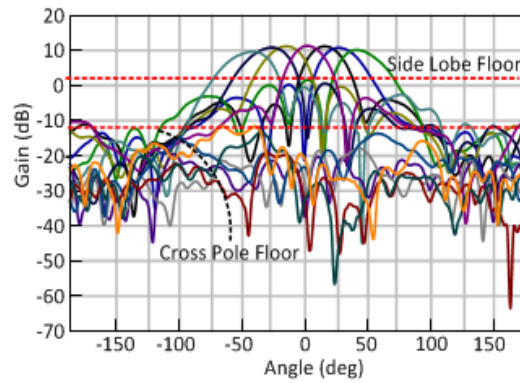
Figure 126. Beamsteering E-Plane periodic planar periodic array measurement (rectangular).
($-45°$ to $45°$ with $15°$ incremental span).
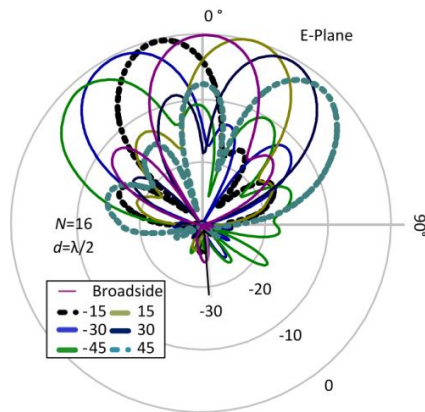
Figure 127. Beamsteering E-Plane periodic planar periodic array measurement (polar).
($-45°$ to $45°$ with $15°$ incremental span).

11.2 Planar Random Array

The geometry of a aperiodic random array in HFSS is shown by that in Figure 128. Next the HFSS simulations shown in Figure 129-Figure 132 demonstrate the effectiveness towards beamsteering a planar random array with an effective aperture of $\tilde{A} = 3.3493$; using a 16 element population with locations provided in Table 12. Experimental results of a planar array are shown in Figure 133-Figure 136 with a comparison of a periodic planar array measurement as given in Figure 137. A detailed design process of this experiment can be found in the works [194]-[199]. A broadside comparison of the ideal conditioned analytical solution, ideal conditioned expected value solution, HFSS non-ideal conditioned simulation, and measured result is shown for both E and H planes in Figure 137-Figure 138. Moreover, from these it is seen that there is excellent theoretical agreement of all the methods applied. The main beam region is demonstrated to be deterministic whereas the sidelobe region is totally random yet maintained 10dB below the average sidelobe level (1/N).
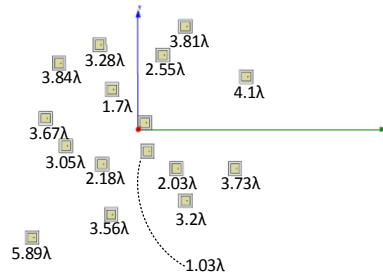
Figure 128. Simulated example of the element locations of a planar random array (does not match table below).

Table 12. Element Locations in a Planar Random Array.

Frequency=2.44Ghz, Element 1 → (0,0) (Distance in wavelengths) $\tilde{A} = 3.3493$

Element	(x,y)	Element	(x,y)	Element	(x,y)
2	(-1.22,-2.44)	7	(-1.18,1.18)	12	(-2.74,1.72)
3	(0.098,-1.01)	8	(.65,2.4)	13	(2.78,-.066)
4	(-.35,-2.83)	9	(-.244,2.52)	14	(-2.66,-1.04)
5	(-.79,-.715)	10	(2.44,-2.52)	15	(-2.86,259)
6	(1.14,-1.63)	11	(-2.33,-2.67)	16	(1.73,1.39)
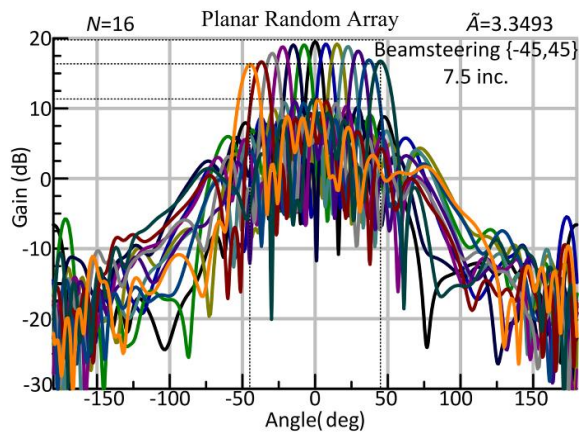
Figure 129. Beamsteering HFSS planar random array simulation ($-45°$ to $45°$ with $7.5°$ incremental span).
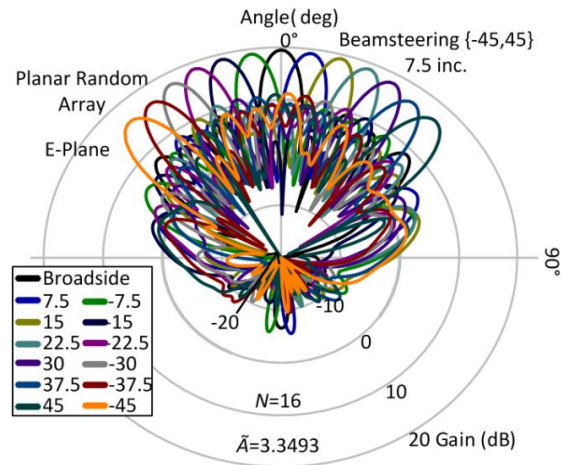
Figure 130. Beamsteering polar HFSS planar random array simulation (−45° to 45° with 7.5° incremental span).
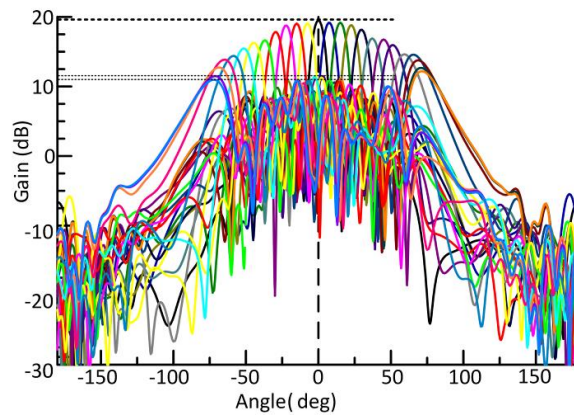
Figure 131. Beamsteering HFSS planar random array simulation (−90° to 90° with 7.5° incremental span).
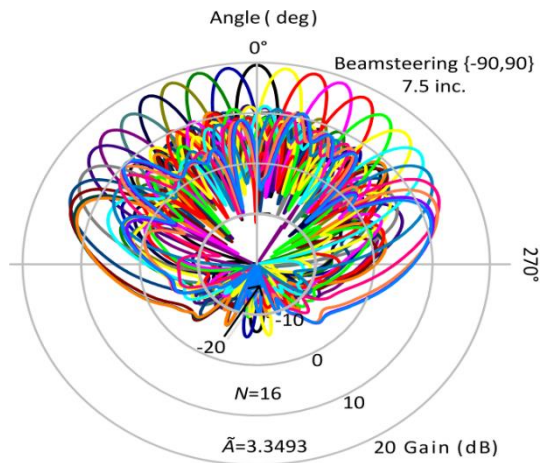
Figure 132. Beamsteering planar random array HFSS polar simulation (−90°to 90° with an 7.5° incremental span).
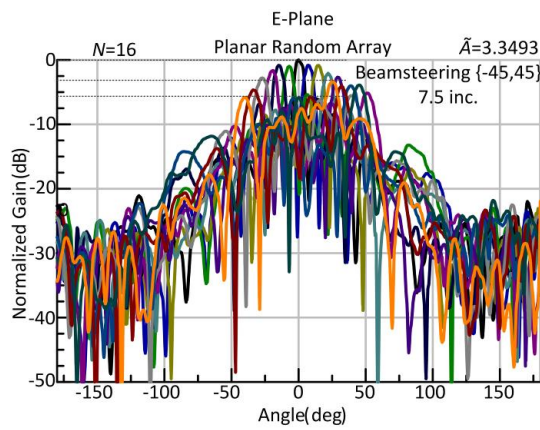
Figure 133. Beamsteering E-Plane planar random array measurement (−45°to 45° with an 7.5° incremental span).
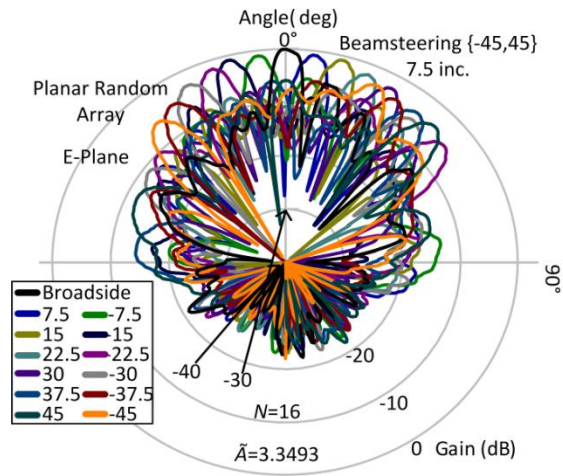
Figure 134. Beamsteering E-Plane planar random array measurement (polar) (−45°to 45° with 7.5° incremental span).
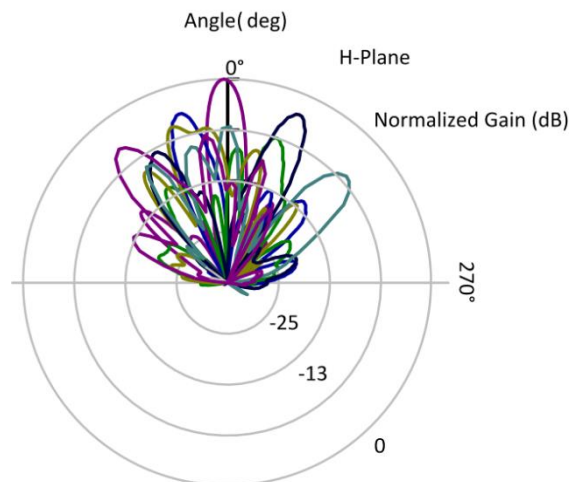
Figure 135. Beamsteering H-Plane planar random array measurement (polar).
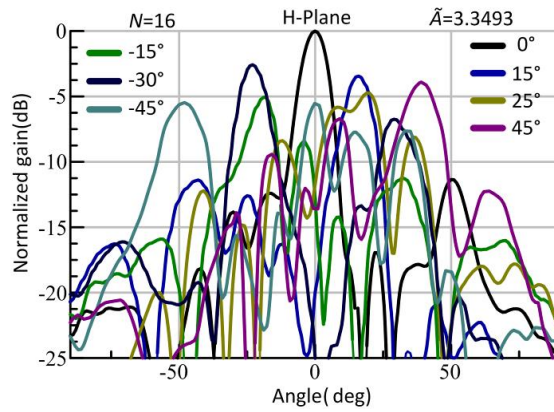
Figure 136. Beamsteering H-Plane planar random array measurement (−45°to 45° with 7.5° incremental span).
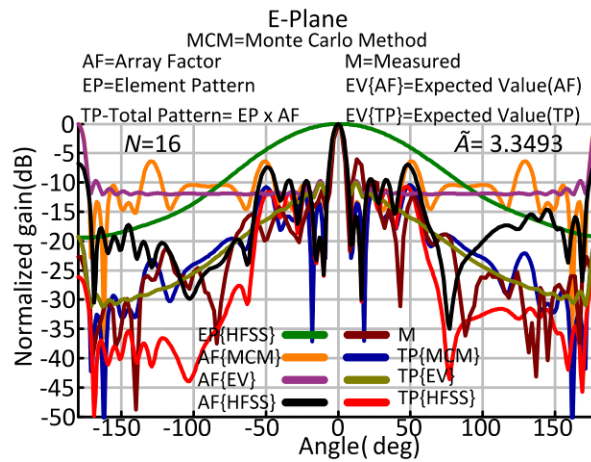
Figure 137. E-Plane broadside comparison of the planar random array {HFSS, measured and analytical}.
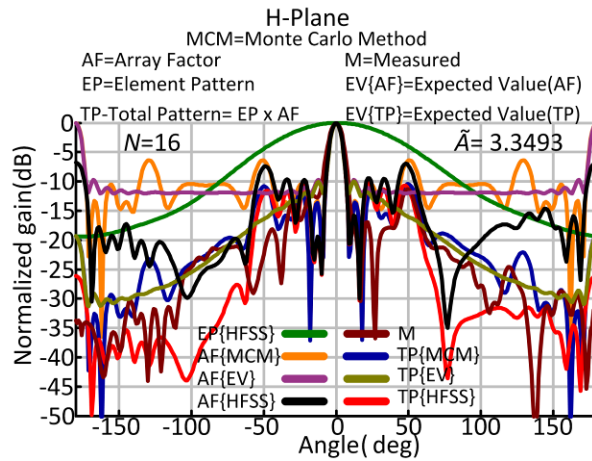
Figure 138. H-Plane broadside comparison of the planar random array {HFSS, measured and analytical}.

11.3 Planar Random Array (Anti-Modal Phasing)

An anti-modal constant comparison is made for the planar random array. A comparison is shown in Figure 139 for the ideal conditioned analytical solution, ideal conditioned expected value solution, and non-ideal HFSS simulation. Also a thirty two element patch antenna array was constructed Figure 140 using two one to sixteen power dividers such that half the elements used a zero degree phase shift and the other sixteen used a one hundred eighty degree phase shift. Furthermore a shared aperture approach was also utilized by illustrated in Figure 141 where the inner elements were 180 degrees out of phase from the perimeter elements. The results of the shared aperture method are illustrated in Figure 142 and overall the results of are also seen to match up very well to the theoretical analysis as well as illustrated in Figure 143.
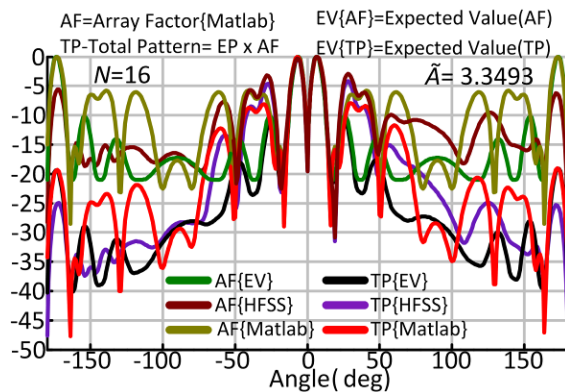
Figure 139. E-Plane anti-phase constant of the anti-modal planar random array broadside comparison {HFSS, and analytical}.

165

Figure 140. Thirty two element square patch random antenna array.
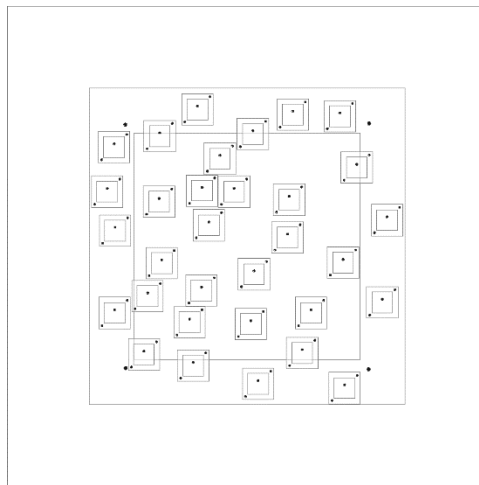
Figure 141. Shared aperture of a square patch random antenna array.
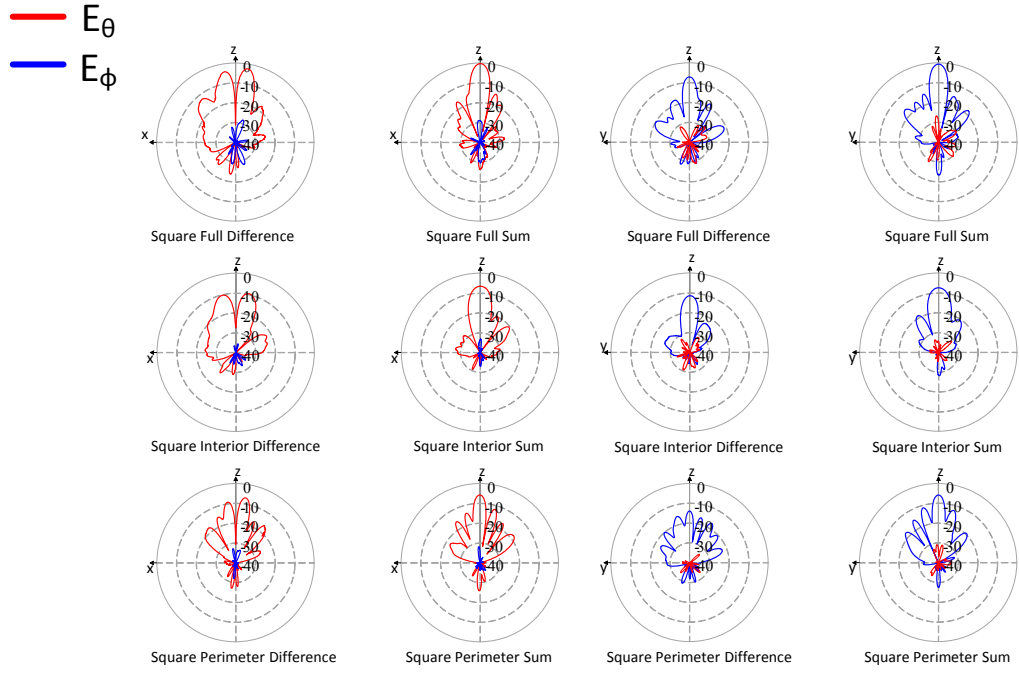
Figure 142. Measured odd and shared aperture modes of a square planar random array.
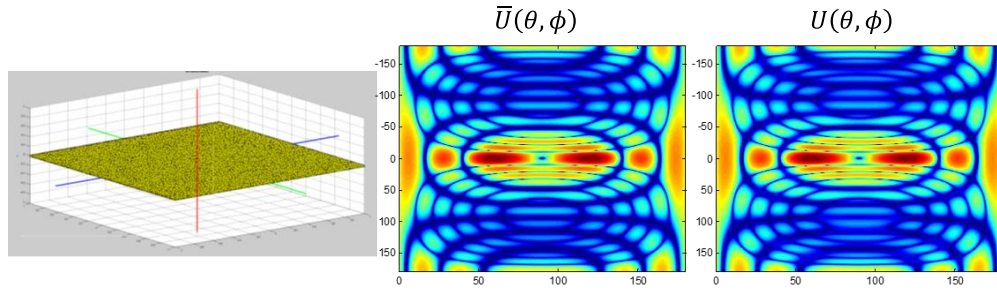
Figure 143. Analytical beampattern and mean valued beam pattern convergence as the number of elements goes to infinity.

The characteristic function of the anti-modal planar random array is calculated as

$$\Lambda(u,v) = \left(\int_{-1}^{0} e^{-jxu} \left(-\frac{1}{2} \right) dx + \int_{0}^{1} e^{-jxu} \left(\frac{1}{2} \right) dx \right) \int_{-1}^{1} e^{-jvy} \left(\frac{1}{2} \right) dy = -\frac{j\left(-1 + \cos(u) \right)}{u} \left(\frac{\sin(v)}{v} \right) \qquad (346)$$

11.4 Cosine Random Array

HFSS simulations shown in Figure 144-Figure 147 demonstrate the effectiveness towards beamsteering a co-sinusoidal random array with an effective aperture of $\tilde{A} = 2.6840$ and 16 element locations given in Table 13.

Table 13. Element Locations of a Co-Sinusoidal Distributed Random Array

Frequency=2.44Ghz, Element $1 \rightarrow (0,0)$ (Distance in millimeters) $\tilde{A} = 2.6840$

Element	(x,y)	Element	(x,y)	Element	(x,y)
2	(0,-2.928)	7	(1.139,0.732)	12	(2.44,0)
3	(0.163,-1.46)	8	(0.325,.732)	13	(0.325,1.55)
4	(-.325,-2.115)	9	(0,2.44)	14	(1.789,0.24)
5	(0.813,0.163)	10	(.935,-.6913)	15	(1.22,1.464)
6	(1.138,-1.63)	11	(0.325,-1.30)	16	(1.545,.488)
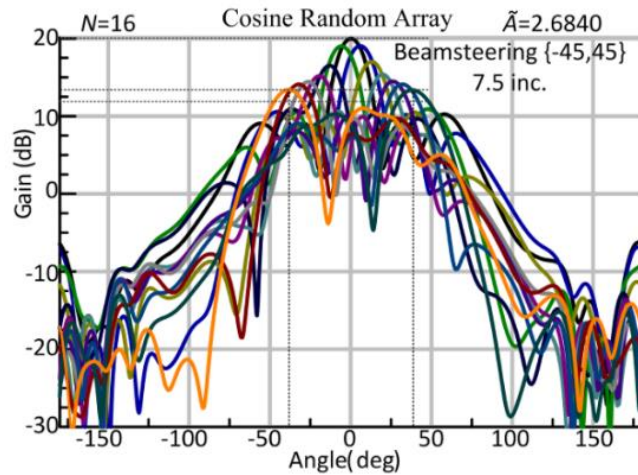
Figure 144. Beamsteering HFSS simulation (cosine random array).
($-45°$to $45°$ with $7.5°$ incremental span).
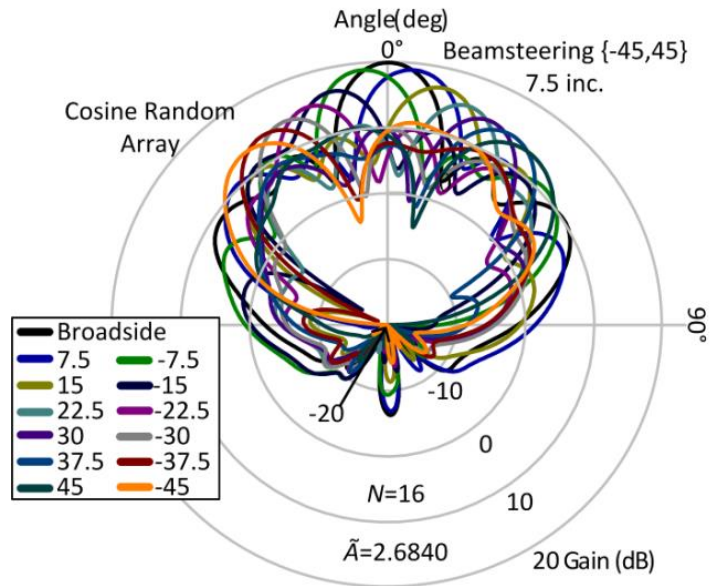
Figure 145. Beamsteering polar HFSS cosine random array simulation ($-45°$ to $45°$ with $7.5°$ incremental span).
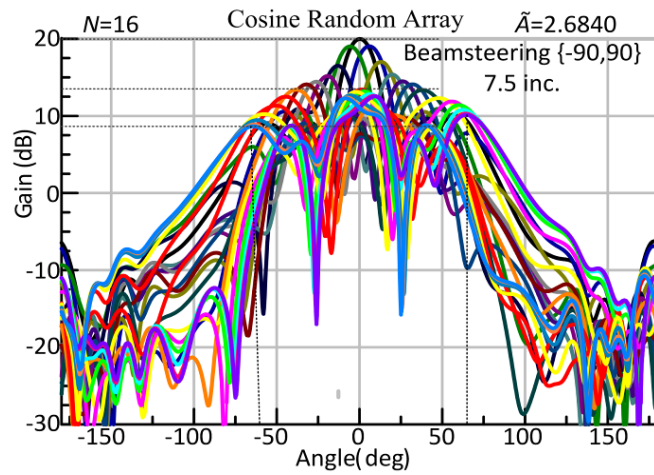
Figure 146. Beamsteering HFSS cosine random array simulation ($-90°$ to $90°$ with $7.5°$ incremental span).
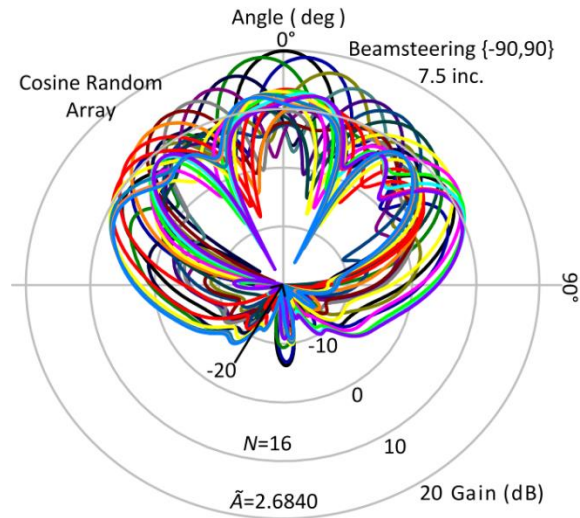
Figure 147. Beamsteering polar HFSS cosine random array simulation ($-90°$to $90°$ with $7.5°$ incremental span).

11.5 Triangular Random Array

HFSS simulations shown in Figure 149-Figure 152 demonstrate the effectiveness towards beamsteering a triangular random array with an effective aperture of $\tilde{A} = 2.6840$ and 16 element locations given in Table 14 and illustrated in Figure 148. Experimental results of a triangular random array are shown in Figure 153-Figure 156. An anti-modal experimental campaign was also done similar to the planar square random array and is illustrated in Figure 157-Figure 159.
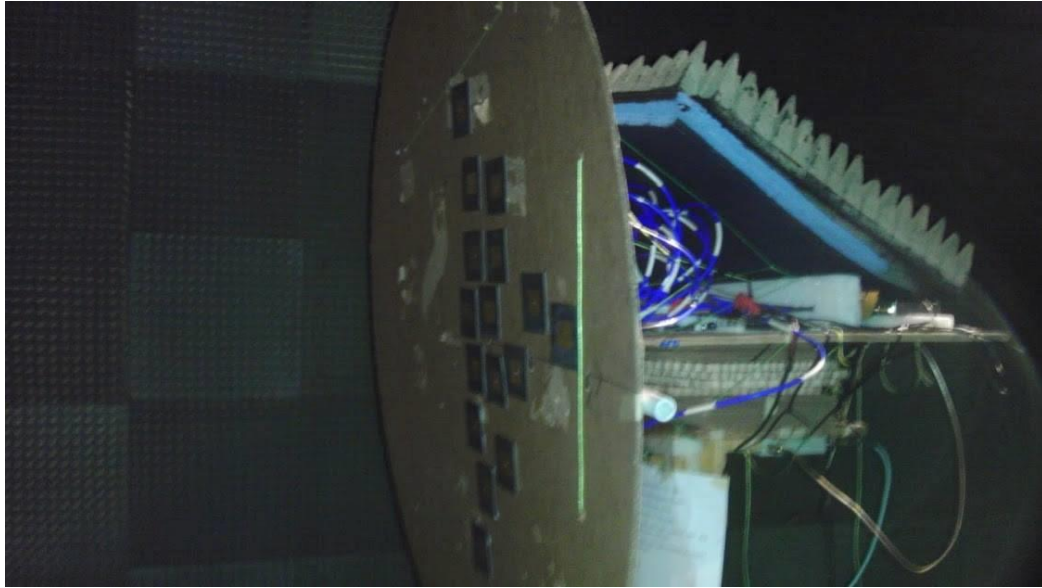
Figure 148. Triangular random array experiment.

Table 14. Element Placement of a Cosine Distributed Random Array.

Frequency=2.44Ghz, Element 1 → (0,0) (Distance in millimeters) $\tilde{A} = 3.3493$

Element	(x,y)	Element	(x,y)	Element	(x,y)
2	(0,-2.928)	7	(1.139,0.732)	12	(2.44,-.244)
3	(0.163,-.651)	8	(0.325,.732)	13	(0.325,1.55)
4	(1.627,-2.27)	9	(0,2.44)	14	(.81333,0)
5	(2.277,0.732)	10	(2.03,-1.301)	15	(1.22,1.952)
6	(1.138,-1.63)	11	(0,-1.627)	16	(1.545,.488)
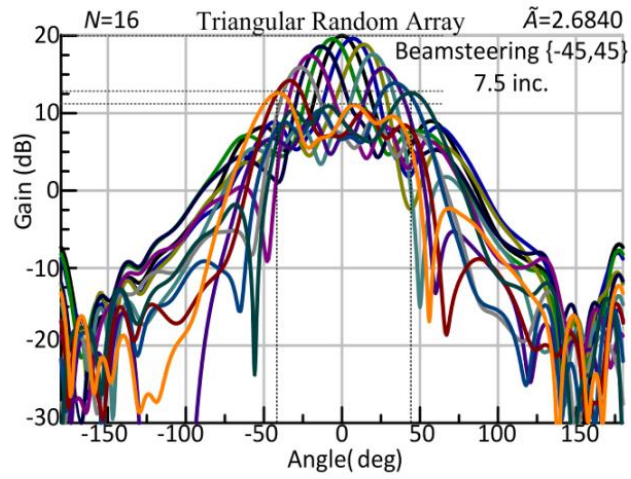
Figure 149. Beamsteering HFSS simulation (triangular random array).
($-45°$ to $45°$ with $7.5°$ incremental span).
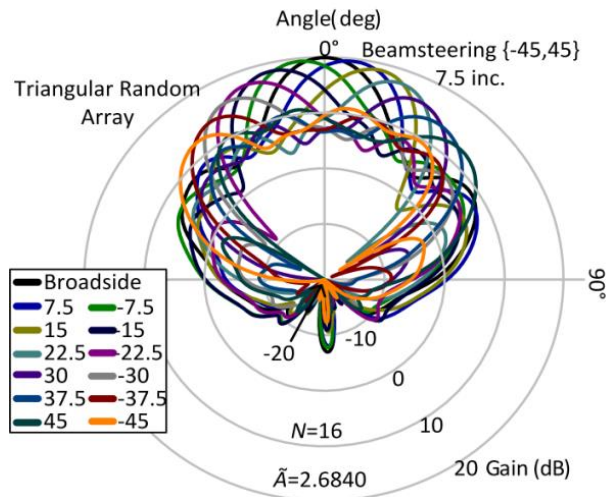
Figure 150. Beamsteering polar HFSS simulation (triangular random array).
($-45°$ to $45°$ with $7.5°$ incremental span).
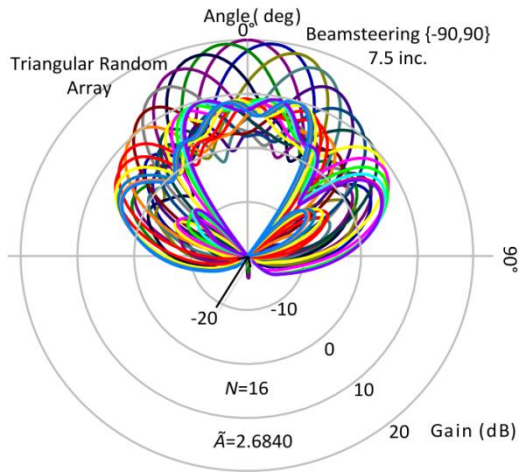
Figure 151. Beamsteering polar HFSS simulation (triangular random array).
($-90°$ to $90°$ with $7.5°$ incremental span).
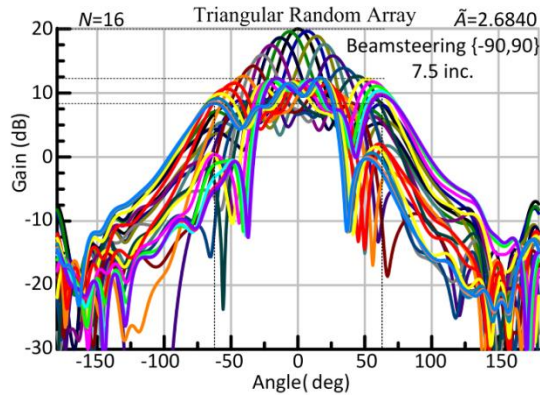
Figure 152. Beamsteering HFSS simulation ($-90°$ to $90°$ with $7.5°$ incremental span).
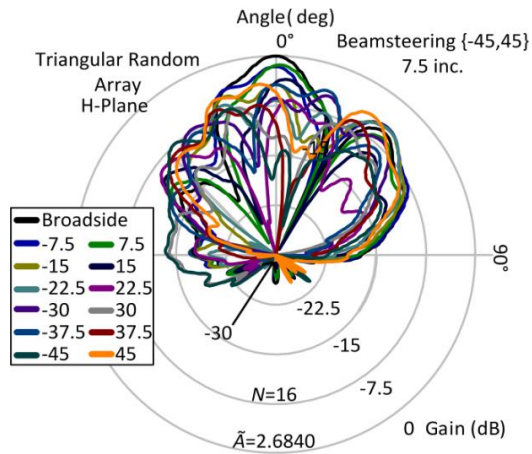
Figure 153. Beamsteering polar measurement triangular random array H-plane ($-45°$ to $45°$ with $7.5°$ incremental span).
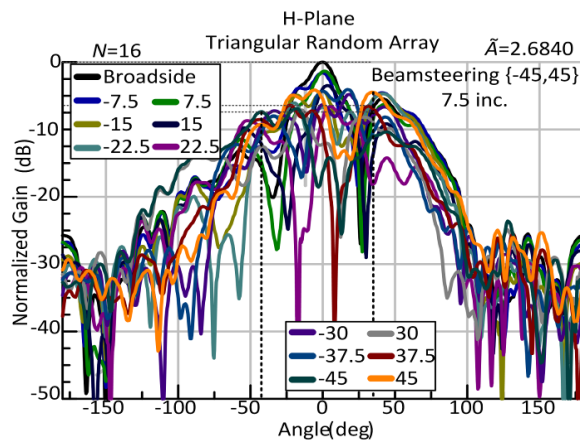
Figure 154. Beamsteering measurements triangular random array H-plane ($-45°$ to $45°$ with $7.5°$ incremental span).

174
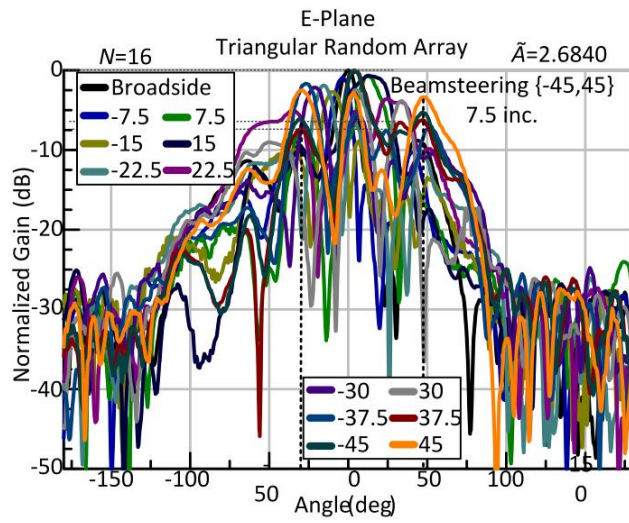
Figure 155. Beamsteering measurement E-Plane (–45° to 45° with an 7.5° incremental span).
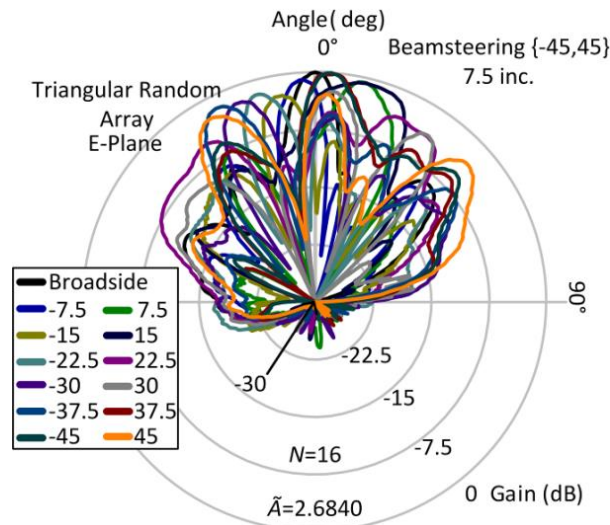
Figure 156. Beamsteering measurements E-Plane (–45° to 45° with an 7.5° incremental span).
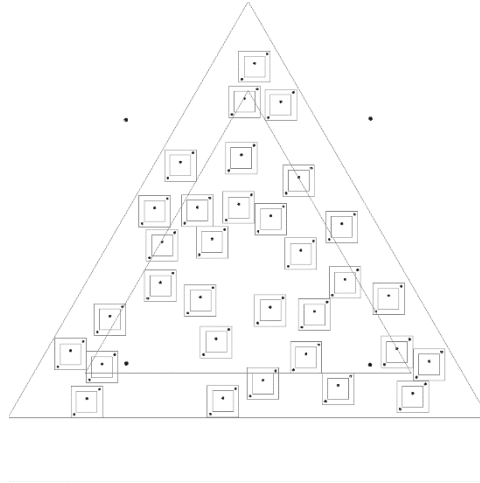
Figure 157. Shared aperture of a patch element triangularly distributed random antenna array.
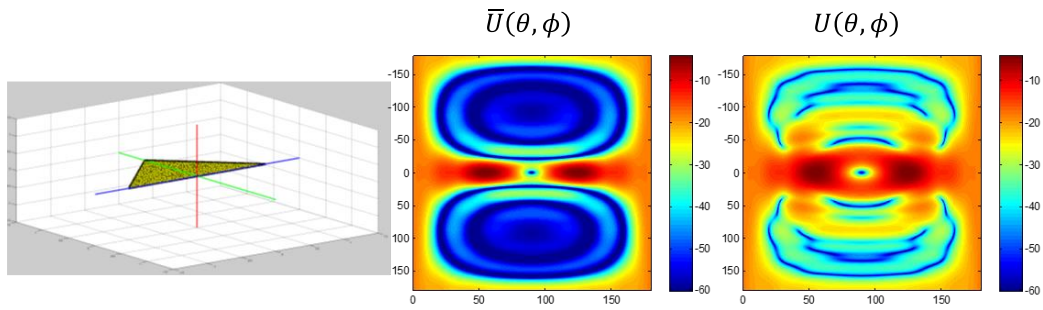
Figure 158. Analytical beampattern and mean valued beam pattern convergence as the number of elements goes to infinity for a triangular random array.

The characteristic function of the anti-modal triangular random array is calculated as

$$\Lambda(u,v) = \left(\int_{-1}^{0} e^{-jxu} \left(-(1-|x|) \right) dx + \int_{0}^{1} e^{-jxu} \left((1-|x|) \right) dx \right) \int_{0}^{1} e^{-jvy} dy = \frac{2j(u-\sin(u))}{u^2} \left(\frac{\sin(v)}{v} \right) \quad (347)$$
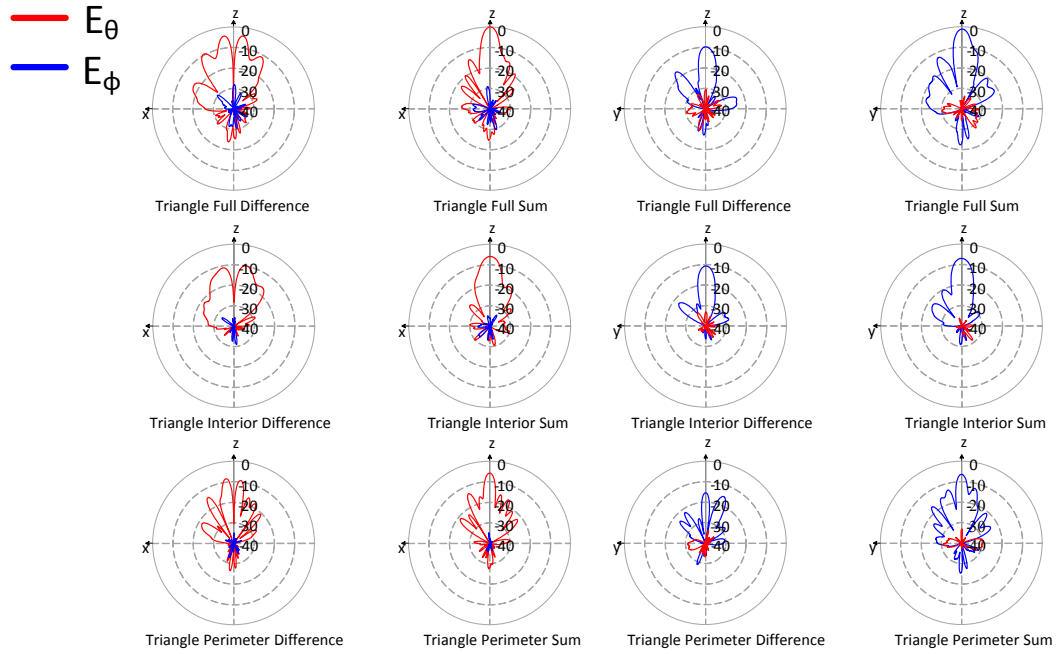
Figure 159. Measured odd and shared aperture modes of a triangularly distributed random patch element antenna array.

11.6 Circular Random Array

Experimental results of a circular random array with an effective aperture of $\tilde{A} = 2.6840$ and 16 elements uniformly distributed in the aperture are shown in Figure 160-Figure 163. An anti-modal experimental campaign was also done similar to the planar square random array and is illustrated in Figure 164-Figure 166.
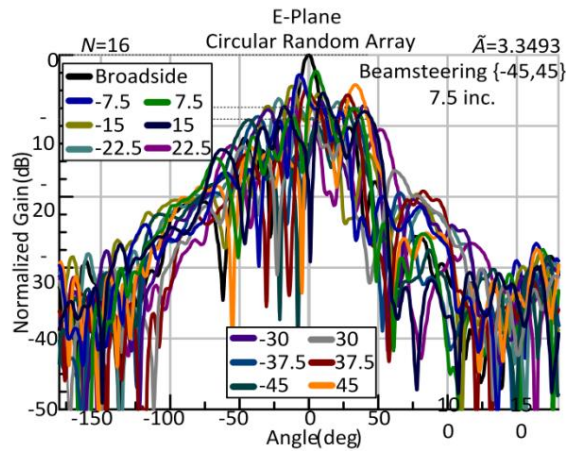
Figure 160. Beamsteering measurements E-Plane (circular random array).
($-45°$ to $45°$ with $7.5°$ incremental span).
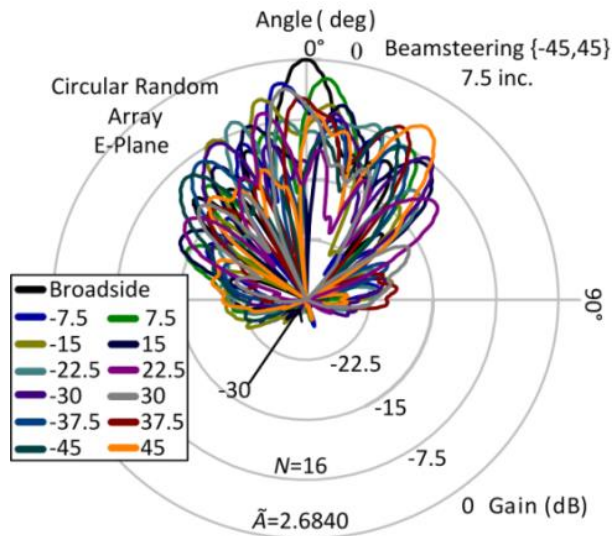
Figure 161. Beamsteering polar measurements E-Plane (circular random array).
($-45°$ to $45°$ with $7.5°$ incremental span).
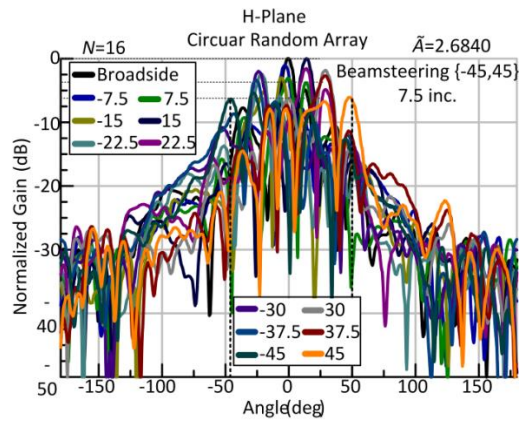
Figure 162. Beamsteering measurements H-Plane (circular random array).
(−45°to 45° with 7.5° incremental span).
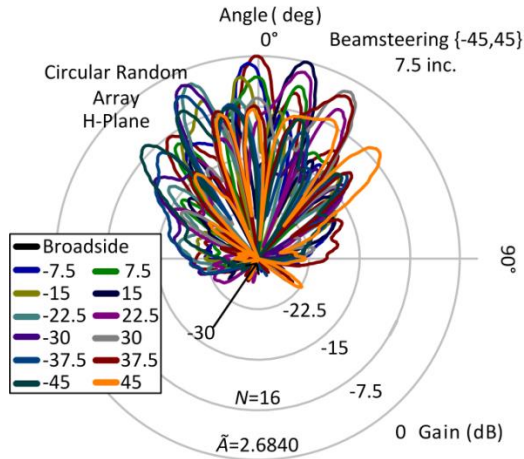
Figure 163. Beamsteering polar measurements H-Plane (circular random array).
(−45°to 45° with 7.5° incremental span).

179
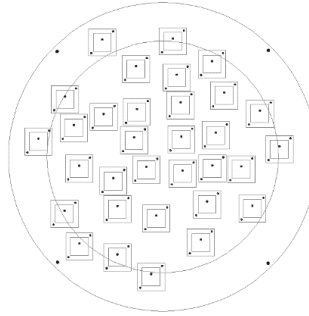
Figure 164. Shared aperture of a circularly distributed patch random antenna array.
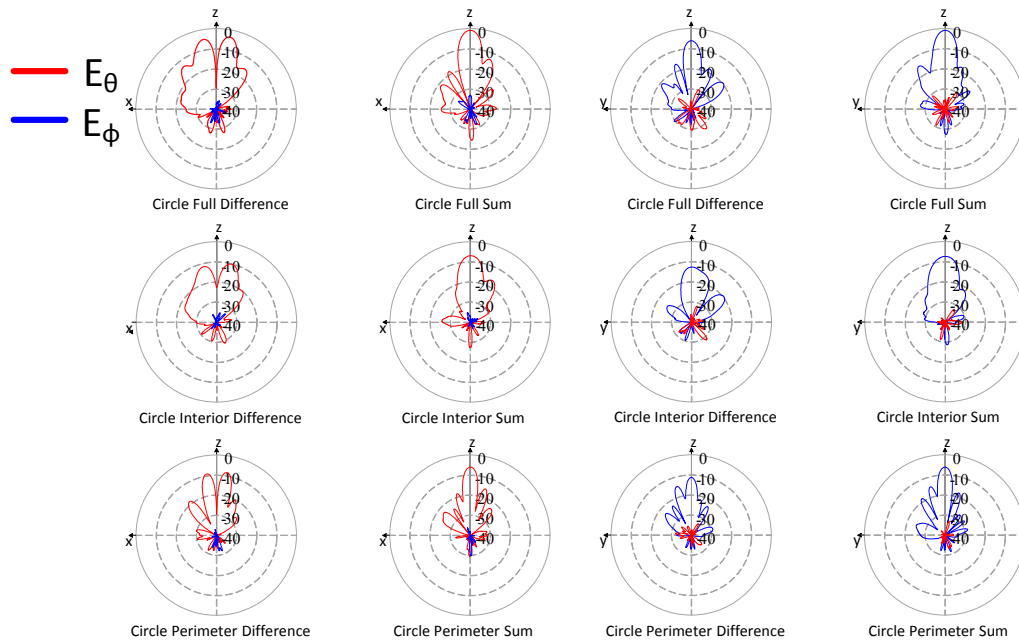
Figure 165. Measured odd and shared aperture modes of a circularly distributed random patch element antenna array.
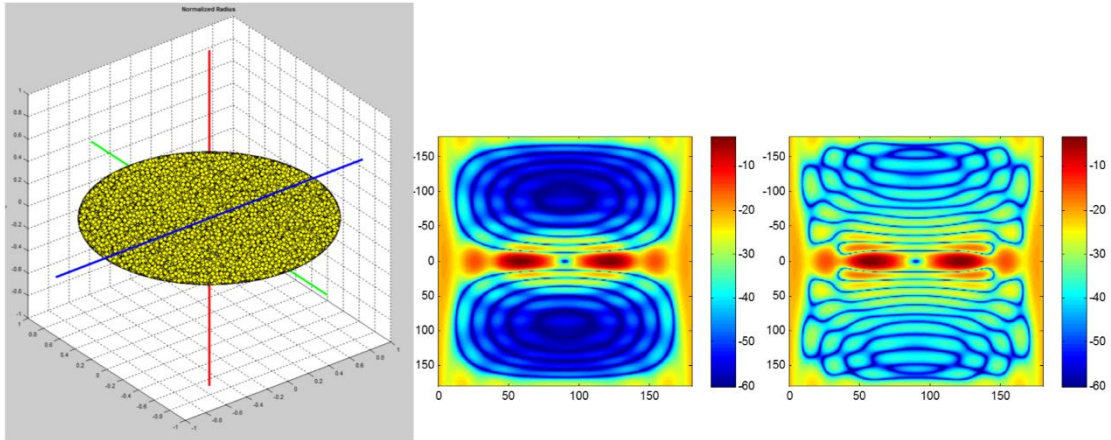
Figure 166. Analytical beampattern and mean valued beam pattern convergence as the number of elements goes to infinity for a circular random array.

The characteristic function of the anti-modal circular random array is calculated as

$$\Lambda(u,v) = \left(\int_{-1}^{0} e^{-jxu} \left(-\frac{2}{\pi}\sqrt{1-x^2} \right) dx + \int_{0}^{1} e^{-jxu} \left(\frac{2}{\pi}\sqrt{1-x^2} \right) dx \right) \int_{-1}^{1} e^{-jvy} \left(\frac{2}{\pi}\sqrt{1-y^2} \right) dy =$$
$$2j\frac{H_1(u)}{u} \left(2\mathrm{jinc}(v) \right)$$

(348)

Where H_1 is the Struve function of the first kind. In other words the Struve function is like having two subwoofers per say in a car where one is on and the other is off; then immediately when one quits the other turns on. This would be the radiation pattern of this kind of element distribution.

For brevity the cross pol measurements for both E and H-planes for planar, triangular and circular random arrays are shown in Figure 167 (Note all measurements are normalized to their respective topology).
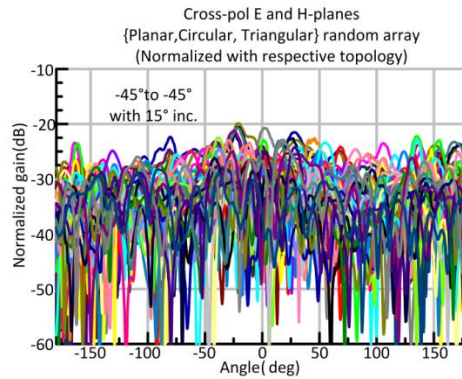
Figure 167. Beamsteering cross-pol measurements (E,H) -Plane (planar random array, triangular random array and circular random array). (−45°to 45° with 15° incremental span).

11.7 Spherical Random Array

For the spherical random antenna array an HFSS simulation was completed using 32 patch elements uniformly distributed in a spherical volume as shown in Figure 168. The effective aperture of the spherical geometry is $\tilde{A} = 2.777$ and interestingly the results of Figure 169 show that the spherical geometry is capable of beamsteering. However though the maximum gain of the main beam is no longer located at broadside and instead is located at seven and a half degrees from the elevation plane. In other words this location presents less mutual coupling than at broadside and as a consequence is the strongest of the main beams shown. Also the degradation of the main beam at broadside compared to at its strongest location (7.5 degrees) is very small yet more studies of shadowing and mutual coupling should be done to verify that this is not too problematic.
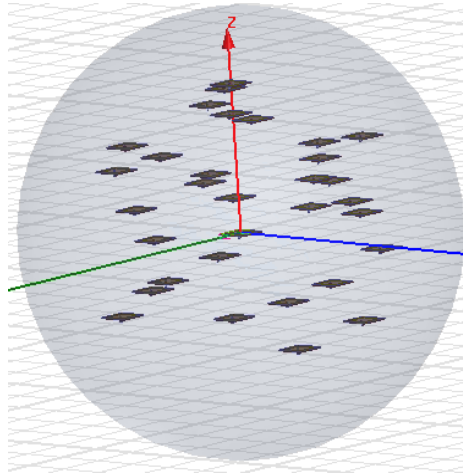
Figure 168. HFSS uniform distribution of thirty two elements in a spherical topology.
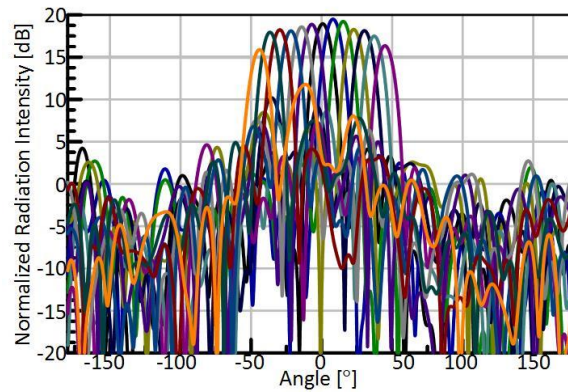
Figure 169. HFSS simulation of a thirty two element spherical random array with patch elements.
($-45°$ to 45° with an 7.5° incremental span).

11.8 Comparison of the Circular and Spherical Random Array Patterns and their Effective

Aperture

The beam pattern of a random array may be shown in a variety of spaces such as the actual angular space Θ and ϕ. Another representation may be the *u, v,* and *w* or *kz, kz, kz* space. For example one defines these spaces by the relations $u = kz = \sin\theta\cos\phi$, $v = kz = \sin\theta\sin\phi$ and $w = kz = \cos\theta$. The problem with these translations is that the pattern shape becomes invariant as it is scanned. Otherwise in terms of the physical angular space Θ, and ϕ, the shape of the radiation pattern and the beamwidth do vary with scan angle. To observe that the pattern is variant in the angular space take for example a linear

183

random array along the x-cut plane $\phi = 0$. Then the defining relation $u = \sin \theta$, and the beamwidth Δu in the variable u is related to the beamwidth $\Delta \theta$ in the real angular variable θ by (349) where θ_0 is the beam-steering angle. For large apertures the relation of (349) is well approximated by (350). Furthermore the 3dB beamwidth of a linear random array is approximated such that $\Delta u = \dfrac{.88}{\tilde{A}} \approx \dfrac{1}{\tilde{A}}$. A more in detail explanation can be found in [101] such that it was determined most distributions are confined to a beamwidth in error no greater or smaller than 25%. Now equating Δu with $\tilde{A}$ the beamwidth of the pattern is provided by that of (351).

$$\Delta u = \sin\left(\theta_0 + \frac{\Delta\theta}{2}\right) - \sin\left(\theta_0 - \frac{\Delta\theta}{2}\right) = 2\cos\theta_0 \sin\frac{\Delta\theta}{2} \tag{349}$$

$$\Delta u \approx \Delta\theta \cos\theta_0 \quad \Delta\theta \ll 1 \tag{350}$$

$$\Delta\theta(\theta_0) = \frac{1}{D(\theta_0)} = \frac{1}{2\tilde{A}\cos\theta_0} = \frac{1}{\tilde{A}\cos\theta_0} \tag{351}$$

From the relation of (351) it is obvious that $\Delta\theta$ grows inversely proportional to the effective aperture $1/\tilde{A}$ going from a minimum at broadside ($\theta_0 = 0°$) with growth followed by the secant of the scan angle. The physical reason for the increase in beamwidth is a consequence of the lost line of sight the source has with the target. The projected aperture transverse to the target is reduced as the scan angle increases as shown in Figure 170. Yet the problem with the relation of (351) is that as the beam is steered towards the end fire $(\theta_0 = \pi/2)$ location, $\sec\theta_0$ grows without limit. Also one should notice that the effective aperture is perpendicular (shown in red Figure 170) to the steering vector. "The beamwidth increases, following (351), but at some angle the growth ceases to follow this trigonometric law." [101] So far the best reason to describe this is due to the approximation made in (350) such that there becomes some point in the beam scan that the approximation breaks down. It is also likely that when the effective depth of the aperture supersedes the effective length of the aperture that the beamwidth that the approximation $\Delta\theta \ll 1$ does not hold otherwise the beamwidth keeps on growing. Or in other words "as the end-fire steering position is approached, the depth dimension of the aperture provides a greater effective aperture than the projected length $D\cos\theta_0$. The beamwidth reaches a limiting size that is called the end-fire beamwidth." [101]

In order to calculate the effective aperture size of the end-fire beamwidth consider the geometry shown in Figure 171. In this situation the phase slope required to steer the main beam to the end-fire location is $\cos\psi_{n0} = \hat{x}\cdot\left(-\hat{r}_o\left(\theta_o,\phi_o\right)\right)\Big|_{\phi_0=0°} = -\sin\theta_o \rightarrow u_0 = -1$. Furthermore for a isotropic aperture excitation, the far field radiation pattern is given by (354), in terms of u and has the linear random array

solution of (355). Moreover, to find the end fire beamwidth we first replace θ with its complement β (the scan angle measured from end-fire), which is used to find the 3 dB half beamwidth in (356), approximated as (352) and solved by that of (353).

$$f(u) = \int e^{-jkx(1-u)} \tag{354}$$

$$f(\theta) = \frac{\sin\left(2\pi\tilde{A}(1-\sin\theta)\right)}{2\pi\tilde{A}(1-\sin\theta)} \tag{355}$$

$$2\pi\tilde{A}\left(1-\cos\beta_{1/2}\right) = 1.4 \tag{356}$$

$$\cos\beta_{1/2} \approx 1 - \frac{\beta_{1/2}^2}{2} \tag{357}$$

$$\beta_{1/2} = \sqrt{\frac{1.4}{\pi\tilde{A}}} \tag{358}$$

Hence, the 3 dB total beamwidth is twice that of (359) and given by

$$\Delta\theta = 2\beta_{1/2} = 2.8\sqrt{\frac{\lambda}{A}} = 2.8\sqrt{\frac{1}{\tilde{A}}} \tag{360}$$

Finally it is observed that the end-fire beamwidth varies as square root of the effective aperture. This means if one were to solve for the effective aperture size one would observe that for small 3 dB beamwidths $\Delta\theta \ll 1$ that the effective aperture size grows by the square of $\Delta\theta$ in fact causing the beamwidth to grow. This is in dramatic contrast to the linear variation of beamwidth with aperture size when the array is scanned at broadside. Finally it should not be left without noting that "arrays with reflectors and plane arrays with ground planes avoid this peculiarity." [101]
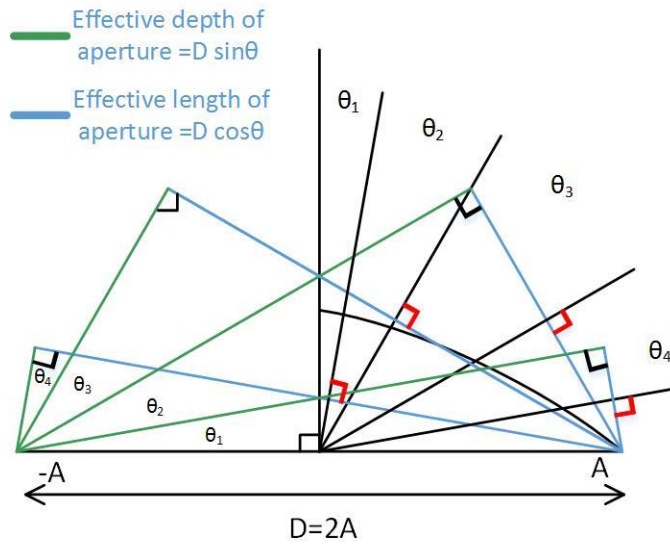
Figure 170. Effective aperture length reduced to D cosθ.
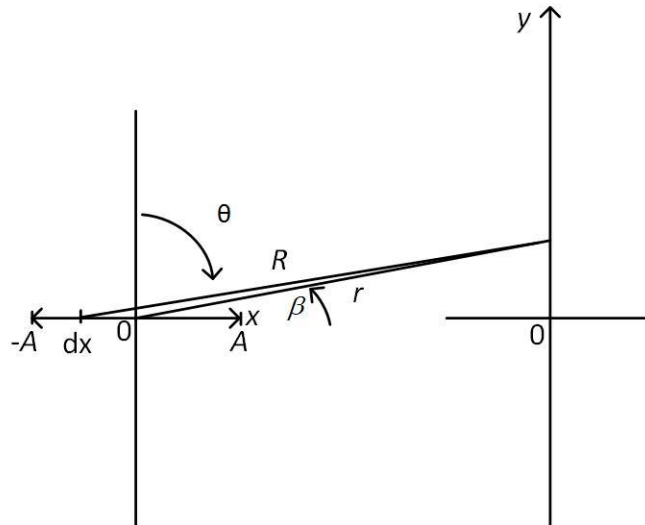
Figure 171. End-fire geometry.

In order to verify the claims of the effective aperture size a small blade antenna with resonant frequency $\left(f_0 = 3GHz \right)$ was designed as shown in Figure 172. At its resonant frequency it is observed that the pattern is omnidirectional in the x-z cut plane and varies in the y-z cut plane Figure 173. By this the x-z plane is sufficient toward demonstrating the effective aperture of a circular random array, but will also be used to demonstrate that the effective aperture of a spherical random array is constant.
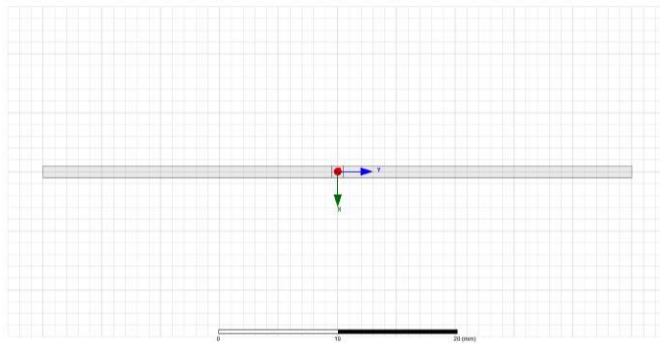
Figure 172. Blade antenna (omnidirectional in *x-z* plane).
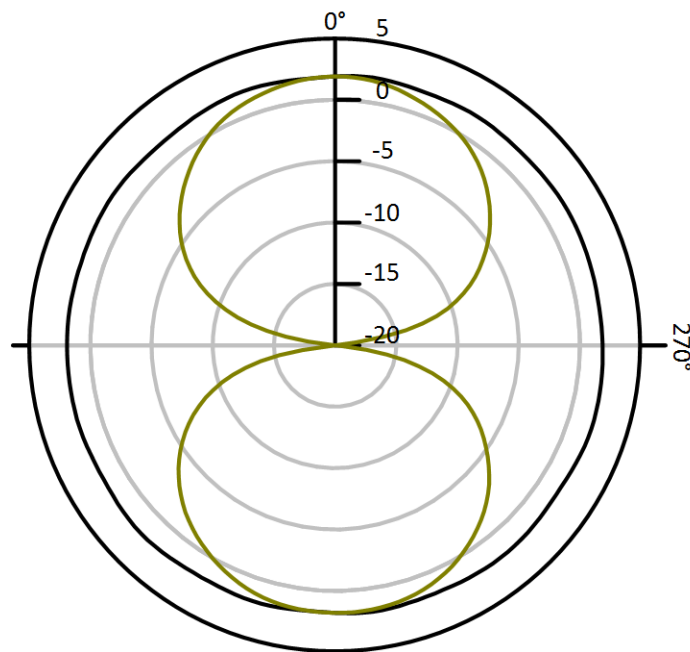
Figure 173. Blade antenna radiation pattern (black curve *x-z* plane, brown curve *y-z* plane).

To begin this demonstration observe the aggregate pattern of thirty two elements (blade antennas) phased in a spherical volume of $\tilde{A} = 2$ as shown in Figure 174. Here it is observed that there is a distinctive main beam at the normal with low sidelobe level. Next a comparison of its broadside and endfire patterns are demonstrated by those in Figure 175 and it is seen that the overall main beamwidth is unaffected by scan angle. A complete comparison of the spherical random arrays scan capability is provided in polar format by Figure 176 or in rectangular by Figure 177 verifying the spherical random array main beamwidth invariance with scan angle.

187
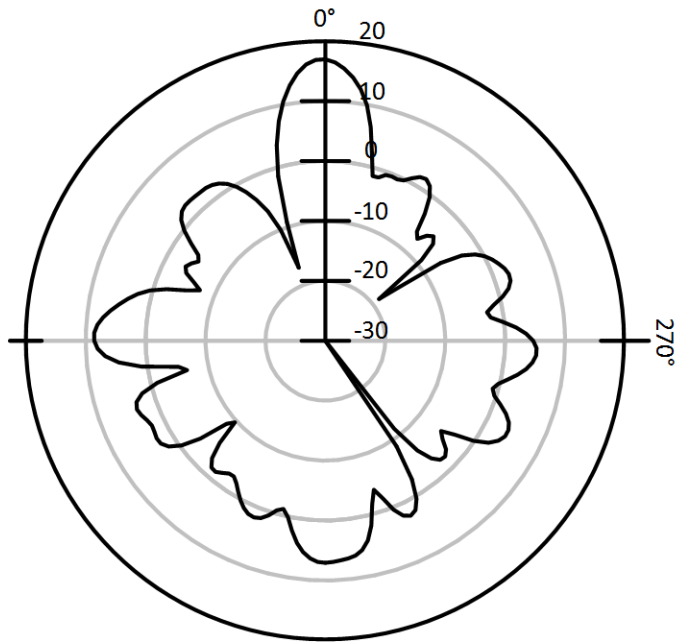
Figure 174. Thirty two element spherical random array broadside gain pattern (blade antenna).
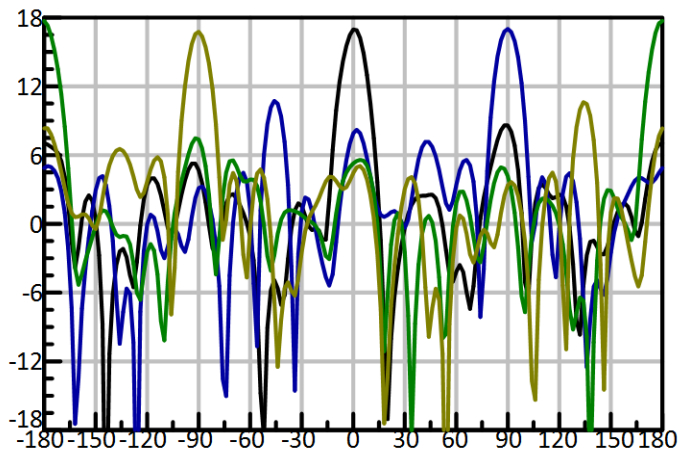
Figure 175. Thirty two element spherical random array broadside (theta=[0, 180] deg) and in the plane (theta=[90, -90] deg) gain patterns.
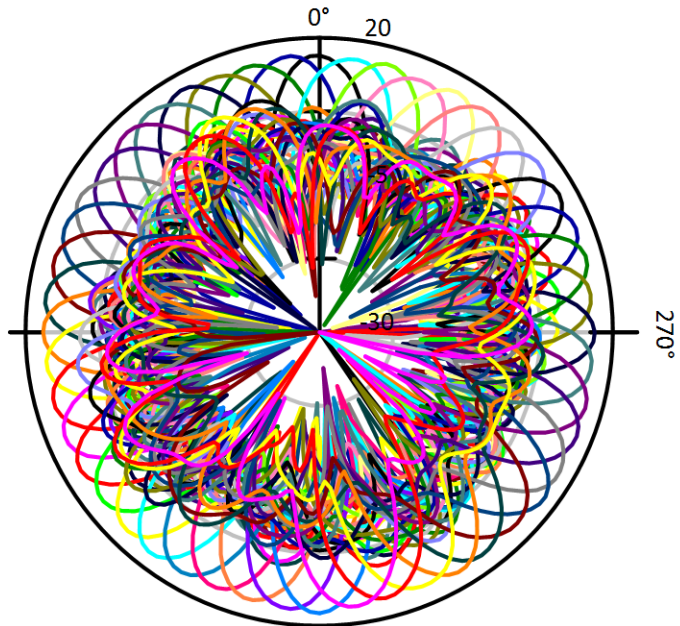
Figure 176. Thirty two element spherical random array beamsteering along theta with 7.5 deg increments (polar).
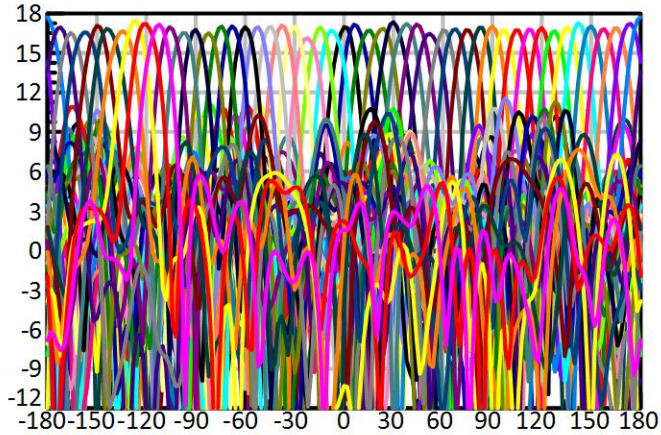
Figure 177. Thirty two element spherical random array beamsteering along theta with 7.5 deg increments (rectangular).

Differently the aggregate pattern of thirty two elements (blade antennas) phased in a circular volume of $\tilde{A} = 2$ is shown in Figure 178. Here it is observed that there is a distinctive main beam at the normal with low sidelobe level, but at the endfire location the main beam pattern is enlarged. More so the main lobe pattern is essentially in the shape of a duck bill, which verifies that the effective aperture varies

for planar topology with scan angle. A complete comparison of the circular random arrays scan capability is provided in polar format by Figure 179 or in rectangular by Figure 180. Last of all it should be noticed that the planar random array topologies suffer from aliasing. I.e. for a beampattern phased at θ_0 in the upper half plane $\theta_0 \leq 90°$ there is a symmetrical pattern in the lower half plane $\theta_0 \geq 90°$. In other words as the pattern is scanned toward endfire the patterns tend to superimpose upon one another and can be used as another explanation as to why the beamwidth is enlarged with scan angle.
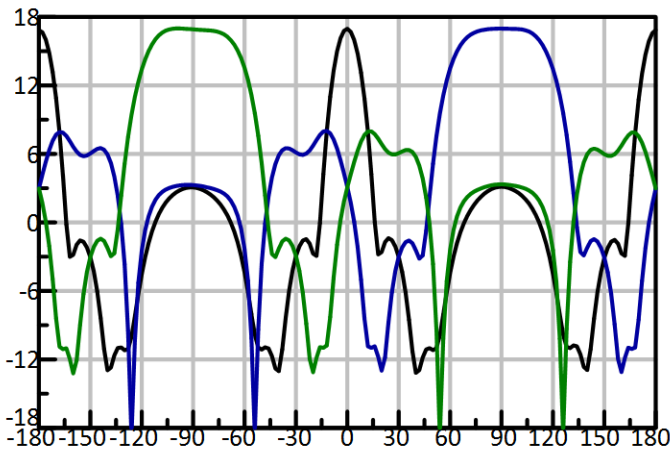
Figure 178. Thirty two element circular random array broadside (theta=0 deg) and in the plane (theta=[90, -90] deg) gain patterns.
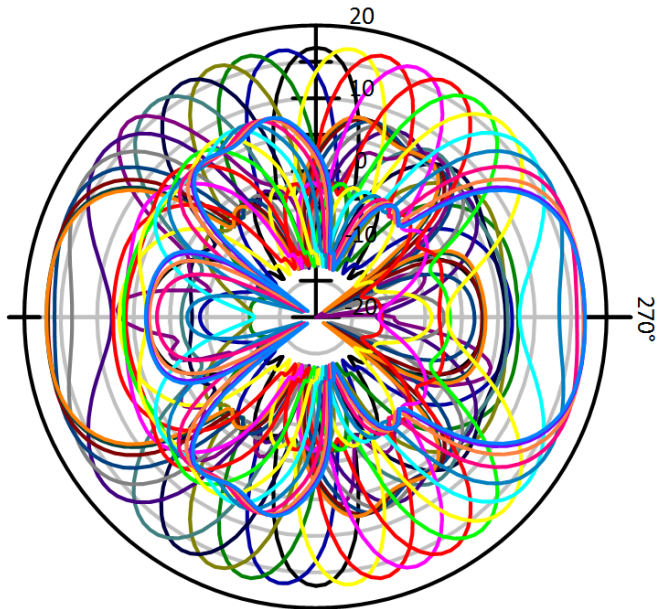
Figure 179. Thirty two element circular random array beamsteering along theta with 7.5 deg increments (polar).
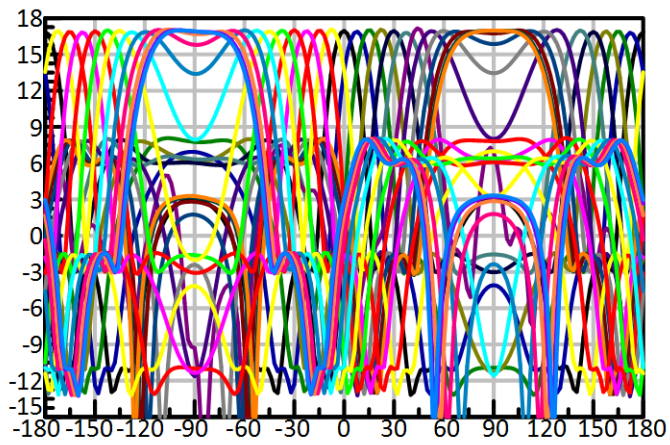
Figure 180. Thirty two element circular random array beamsteering along theta with 7.5 deg increments (polar).

CHAPTER XII

ELEMENT CORRECTION

Antenna located randomly within a spherical topology originates a localized field intensity at an observed point *P'* identified in Figure 181. The local coordinate system of this radiator is centered at the point *P'* with axis *x'*, *y'* and *z'*, forming an orthogonal coordinate system shown in Figure 182. The *z'* axis is normal to the point *P'* with *x'* and *y'* axis located coplanar to the element.

12.1 Element Pattern from a Local Source Position

The radiation pattern (361) of an antenna randomly located within a spherical topology of radius *A* is determined at its relative origin $P'(r_n, \theta_n, \phi_n)$. Now shifting the local origin *P'* of the local coordinate system Figure 181 to a global coordinate system located at the point *O* (true origin) in Figure 182, one may rewrite (361) as (362) where $\overrightarrow{OP'} = r_n \hat{a}_{r'}$ (363). This describes a vector originating at the origin *O* and ending at the point *P'*.

$$
\begin{aligned}
\vec{E}\left(r', \theta', \phi' \middle| r_n, \theta_n, \phi_n\right) &= \hat{a}_{\theta'} E_{\theta'_{\theta_n, \phi_n}} + \hat{a}_{\phi'} E_{\phi'_{\theta_n, \phi_n}} \\
&= \left[\hat{a}_{\theta'} f_1\left(\theta', \phi'\right) \frac{e^{j(wt - kr' - \cos\psi_0)}}{r'} + \hat{a}_{\phi'} f_2\left(\theta', \phi'\right) \frac{e^{j(wt - kr' - \cos\psi_0 - \delta)}}{r'} \right]
\end{aligned}
\tag{361}
$$

Where $\hat{a}_{\theta'}, \hat{a}_{\phi'}$ are the unit vectors in the θ' and ϕ' directions. The parameter δ is the phase difference between the two components of the field and $f_1(\theta', \phi')$, and $f_2(\theta', \phi')$ are the pattern factors of the two components of the field distribution.

$$
\begin{aligned}
\vec{E}\left(r, \theta', \phi' \middle| r_n, \theta_n, \phi_n\right) &= \\
\sum_{n=1}^{N} &\left[\hat{a}_{\theta'} f_1\left(\theta', \phi'\right) + \hat{a}_{\phi'} f_2\left(\theta', \phi'\right) \right] e^{j\left(k\overrightarrow{OP'} \cdot a_r - \cos\psi_0\right)} \frac{e^{j(wt - kr)}}{r},
\end{aligned}
\tag{362}
$$

$$
r_n \cos\theta' = \overrightarrow{OP'} \cdot \hat{a}_r = r_n \left(\sin\theta_n \sin\theta \cos(\phi - \phi_n) + \cos\theta_n \cos\theta \right)
\tag{363}
$$
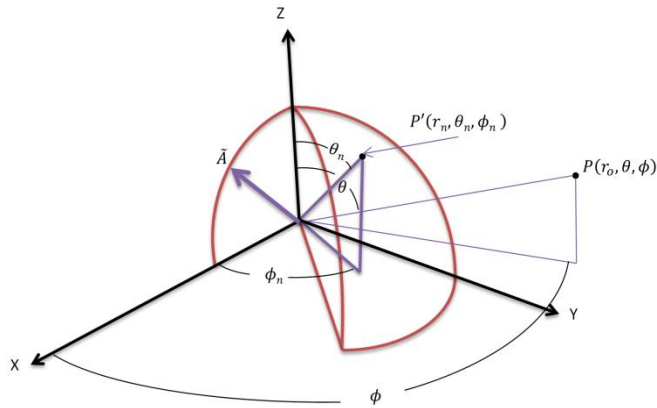
Figure 181. Geometry of a periodic spherical array referenced to the element.
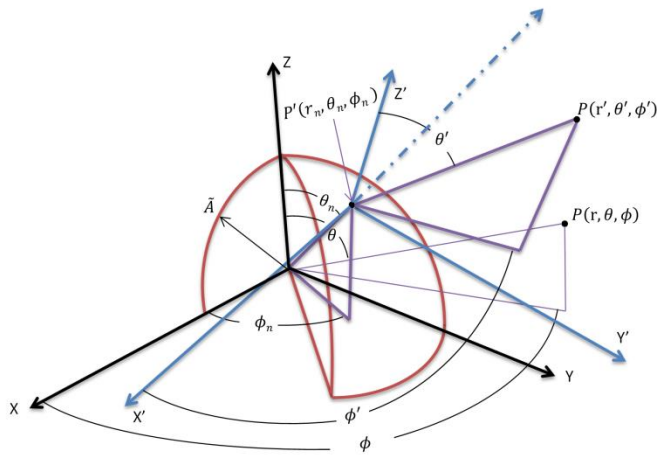
Figure 182. Geometry of a periodic spherical array rotated about the element in order to be referenced to the origin.

12.2 Coordinate Transformation Relationships in Spherical Coordinates

Equation (362) represents field intensity in terms of primed spatial angles; however it is traditionally more accepted to represent filed intensity in terms of unprimed spatial angles. Accordingly, a transformation going from primed to unprimed coordinates is obtained by using a general method of orthogonal transformation of coordinates [200]. Other notable spherical array literature is found in [201]-[204].

The transformation between primed and unprimed unit vector coordinates are related by a rotation matrix Φ such that

$$\begin{bmatrix} \hat{a}_x \\ \hat{a}_y \\ \hat{a}_z \end{bmatrix} = \Phi \begin{bmatrix} \hat{a}_x \\ \hat{a}_y \\ \hat{a}_z \end{bmatrix} \tag{364}$$

This is a consequence of Euler's rotation theorem [141], which states any rotation can be described using three angles. For example, in an "x y z convention," rotation about θ defines the pitch, ψ defines the roll, and ϕ provides the amount of yaw. Using a mathematical context these rotation angles are described such that

$$\Phi = \begin{bmatrix} 1 & 0 & 0 \\ 0 & \cos\psi & \sin\psi \\ 0 & -\sin\psi & \cos\psi \end{bmatrix}, \begin{bmatrix} \cos\gamma & 0 & -\sin\gamma \\ 0 & 1 & 0 \\ \sin\gamma & 0 & \cos\gamma \end{bmatrix}, \begin{bmatrix} \cos\beta & \sin\beta & 0 \\ -\sin\beta & \cos\beta & 0 \\ 0 & 0 & 1 \end{bmatrix} \tag{365}$$

$$\text{Roll about X axis} \qquad \text{Pitch about Y axis} \qquad \text{Yaw about Z axis}$$

and the substitution of unit vectors into the former equations (366) and (367) gives (368) and (369).

It is important to observe that the coplanar axes in the first and third rotations are identical. Consequently, one rotates the global coordinate system of Figure 182 with just pitch and yaw matrices (excluding the roll matrix) to generate the necessary rotation matrix Φ used for going from unprimed to primed coordinates. The angles θ' and ϕ' are found by taking the gradient of (368) and (369) in spherical coordinates. Applied to (368) one obtains (370) and likewise applied to (369) one obtains (371). However, to make these equations symmetric one may assume $\phi' = \phi - \phi_n$ and $\theta' = \theta$ giving (372) [200].

$$\cos\theta' = (\hat{a}_r \cdot \hat{a}_{Z'}) \tag{366}$$

$$\cot\phi' = \left(\frac{\hat{a}_r \cdot \hat{a}_{X'}}{\hat{a}_r \cdot \hat{a}_{Y'}} \right) \tag{367}$$

$$\cos\theta' = \sin\theta_n \sin\theta \cos(\phi - \phi_n) + \cos\theta_n \cos\theta \tag{368}$$

$$\cot\phi' = \frac{\cos\theta_n \sin\theta \cos(\phi - \phi_n) - \sin\theta_n \cos\theta}{\sin\theta \sin(\phi - \phi_n)} \tag{369}$$

$$\hat{a}_{\theta'} = -\hat{a}_\theta \frac{\cos\theta \sin\theta_n \cos(\phi - \phi_n) - \cos\theta_n \sin\theta}{\sin\theta'} + \hat{a}_\phi \frac{\sin\theta_n \sin(\phi - \phi_n)}{\sin\theta'}. \tag{370}$$

$$\hat{a}_{\phi'} = -\frac{\sin\theta'}{\csc^2\phi'} \frac{\sin\theta_n \sin(\phi - \phi_n)}{(\sin\theta \sin(\phi - \phi_n))^2} \hat{a}_\theta$$
$$-\frac{\sin\theta'}{\csc^2\phi'} \left[\frac{\cos\theta \sin\theta_n \cos(\phi - \phi_n) - \sin\theta \cos\theta_n}{\sin^2\theta \sin^2(\phi - \phi_n)} \right] \hat{a}_\phi \tag{371}$$

$$\hat{a}_{\phi'} = -\frac{\sin\theta_n \sin(\phi - \phi_n)}{\sin\theta'} \hat{a}_\theta - \left[\frac{\cos\theta \sin\theta_n \cos(\phi - \phi_n) - \sin\theta \cos\theta_n}{\sin\theta'} \right] \hat{a}_\phi \tag{372}$$

Finally, suppressing the time dependence, free space greens function e^{-jkr}/r and substituting (372) and (370) into (362) one obtains the radiation intensity of a spherical random array with rotated offset parameters given by (373).

$$U\left(\theta,\phi|\vec{Z}\right)\triangleq\left|E\left(\theta,\phi|r_n,\gamma_n,\beta_n\right)\right|^2 =$$

$$\frac{1}{N^2}\sum_{m=1}^{N}\sum_{n=1}^{N}\left(\begin{bmatrix}\begin{bmatrix}\dfrac{\cos\theta\sin\theta_n\cos\left(\phi-\phi_n\right)-\cos\theta_n\sin\theta}{\sin\theta'}f_1\left(\theta',\phi'\right)+\\\dfrac{\sin\theta_n\sin\left(\phi-\phi_n\right)}{\sin\theta'}f_2\left(\theta',\phi'\right)e^{-j\delta}\end{bmatrix}\hat{a}_\theta\\+\begin{bmatrix}\dfrac{\sin\theta_n\sin\left(\phi-\phi_n\right)}{\sin\theta'}f_1\left(\theta',\phi'\right)\\-\dfrac{\cos\theta\sin\theta_n\cos\left(\phi-\phi_n\right)-\cos\theta_n\sin\theta}{\sin\theta'}f_2\left(\theta',\phi'\right)e^{-j\delta}\end{bmatrix}\hat{a}_\phi\\e^{j\xi(\theta)(\mathrm{T}_n-\mathrm{T}_m)}e^{j\zeta(\theta,\phi)(\Upsilon_n-\Upsilon_m)}\end{bmatrix}\right)^2 \quad (373)$$

CHAPTER XIII

FREQUENCY RESPONSE OF A SPHERICAL RANDOM ARRAY

The frequency response of a spherical random array, was examined by [60] in the late 70's, but does not contain closed form expressions. An attempt was made to solve the necessary integrations although the attempt was overall unsuccessful. Nevertheless it is interesting to note [60] assumed a uniform probability density function for element distribution; the main effort for finding an average pattern of a random array. Yet, a year earlier a closed form integration for the uniformly distributed spherically bound random array was published by [59], and is disguised as the oscillatory tinc function (374) or (96), introduced by [82]. Likewise it has been shown by [59] that when such a closed form expression is used the average 3dB beamwidth (375) will demonstrate bandwidth characteristics independent of the center frequency, which makes logical sense; since the averaging of the array was done about its center frequency. This does not limit the analysis exclusively to the arrays center frequency [59]. The substitution $c = \lambda f$ can be substituted into (375) and its relative bandwidth is shown in (376)-(377).

$$AF(u) = \frac{3}{u}\frac{u\sin u - u^2 \cos u}{u^3} = 3\frac{j_1(u)}{u} = 3\text{tinc}(u) \tag{374}$$

$$B = 2(\Delta f)_o = .578\frac{c}{R} \tag{375}$$

$$\delta = .578\frac{\lambda}{R} \tag{376}$$

$$u = \frac{2\pi}{c}\Delta f d \tag{377}$$

The results given by [59] are close to the results of [82] for a spherically bound random array for the special case for which the beam is pointed at the meridian angle $\theta = \theta_o = \pi/2$ and $u = 4\pi \sin(\phi/2)d$. Moreover, upon substitution of the former (374)-(377) are redefined as those in (378)-(382).

$$E_u\left|AF\left(\phi|\vec{u}\right)\right| = \left|3\frac{j_1(\alpha(\phi))}{\alpha(\phi)}\right| = \left|3\text{tinc}(\alpha(\phi))\right| \tag{378}$$

$$\frac{4\pi R f}{c}\sin\left(\frac{\phi_{av}^{3dB}}{2}\right) = 1.815 \tag{379}$$

$$\phi_{av}^{3dB} = 2\arcsin\left(\frac{.1444\lambda_o}{R}\right) = 2\arcsin\left(\frac{.1444c}{Rf_o}\right) \tag{380}$$

$$\alpha(\phi) = 4\pi \frac{Rf}{c} \sin\left(\frac{\phi}{2}\right) \tag{381}$$

$$BW_{\text{relative}} = \frac{\phi_{av}^{3dB}}{f} = \frac{2\arcsin\left(\frac{.1444c}{Rf_o}\right)}{f} \infty \tag{382}$$

Now to finally expand [59], [60] and [180] the analysis uses a receiving spherical random array and claims a bandwidth. In actuality these references are changing what has been defined as *A* the radius of the random array in this series and essentially has integrated (616) for different values of *A*, but using the same bandwidth. The proper solution of the frequency independence is shown in Figure 183-Figure 186 for three different radius sizes.
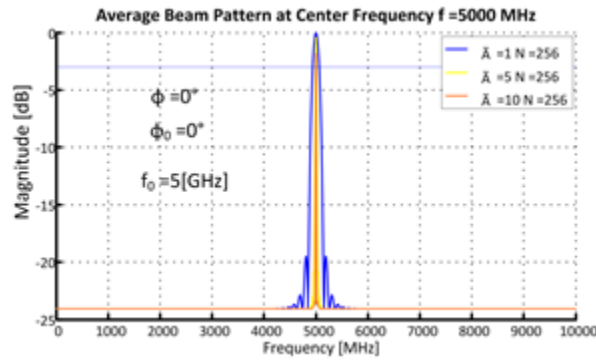
Figure 183. Radiation intensity of a spherical random array $\theta = \theta_0 = \pi/2$ made for operation at 5 GHz and spatially unphased.
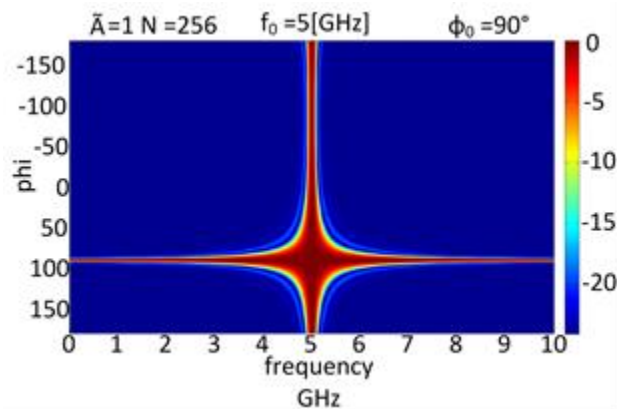
Figure 184. Radiation intensity of a spherical random array $\theta = \theta_0 = \pi/2$ of the above Figure in 3d for $\tilde{A} = 1$. At this steering location the beampattern is frequency independent.

197
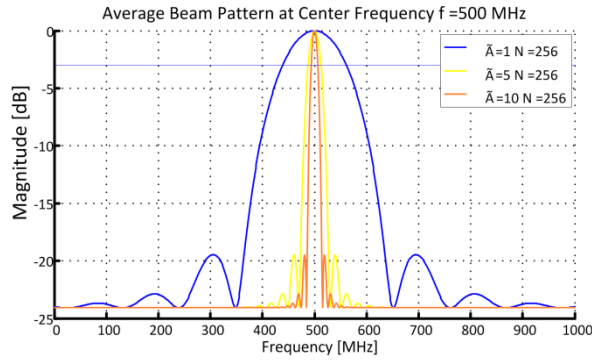
Figure 185. Radiation intensity of a spherical random array $\theta = \theta_0 = \pi/2$ made for operation at 5 GHz and is spatially unphased.
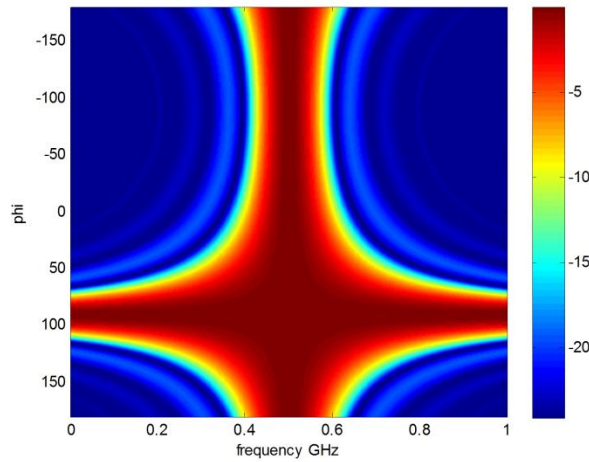
Figure 186. Illustration that the beampattern is frequency independent at the meridian location of operation of a spherical random array $\tilde{A} = 1$.

For brevity it is seen that in the far field at the meridian elevation angle $\theta = \theta_o = \pi/2$ a spherical random array is frequency independent. It should be noted though that a random array is band limited due to the element pattern. Being the *EP x AF*. Furthermore this result of frequency independence can be expanded to any random array. Thus, it is noted that now to finally expand [59], [60] and [180] were essentially plotting the array factor as given. Moreover, it is seen that at the beamsteering the random array becomes frequency independent.

CHAPTER XIV

STATISTICAL ANALYSIS ON THE IMPACT OF SIDELOBE BEHAVIOR ON

RANDOM ARRAYS

The sidelobe behavior of circular and spherical random arrays with uniform and Gaussian distributions are analyzed statistically to identify regions with deterministic, transitional, and random behavior. Isotropic radiators are preferred in this analysis since they provide relevant information on the fundamental behavior, which can be applied to provide practical estimates of the maximum peaking sidelobe located in the totally random or three dB sidelobe region since it behaves non-deterministically. The mathematical process required for this analysis includes a statistical formulation of the array factor, including the mean, or expected value, and the variance. This is examined in the context of prior work on random arrays, but simplified analytically to now provide an accurate estimate for the maximum peaking sidelobe behavior in a volumetric scan region. Numerical results are included to illustrate scanning from zenith to meridian elevation angles to evaluate the theory and compare the behavior of both circular and spherical arrays.

The theory of random arrays is considered non-deterministic and because of this no unified theory exists. Yet, curiously enough an adequate theory has been developed for the random array. This is because the mathematics of stochastic systems and processes, that is, statistics, can be applied in order to determine the system probabilistically. As a random array can only be described statistically, it is logical to develop its properties in a probabilistic manner. Such an approach yields important statistical averages of the radiation pattern: mainbeam behavior, three dB beamwidth, and sidelobe mean null and peak locations. Of these, particular interest resides in the maximum peaking sidelobe behavior especially to the extent and concern of the array designers. A fortiori, since the discrepancy between the peak sidelobe and average sidelobe can be significant; an estimator of the peak is a necessity of these random arrays confining the sidelobes in terms of a probability, or confidence interval, of which some predicted value will not be exceeded. This is a pertinent characteristic of the design and is developed in this paper.

First a historical analysis is followed in order to determine the maximum peaking sidelobe. A statistical analysis of this process was initially followed by [31] for linear random arrays and was followed in the same year by its sequel [34]. Improvements to this work were added by numerous investigators [32]-[33], [85], [101], [186] and [205]-[206] with more complete and recent examples applied to: planar (circular random array) topology in [7]-[14] and volumetric [6], [81]-[82] and [191] (spherically bound random array) herein.

14.1 Random Variables

Often, one takes two random variables X and Y and solves for each variable independently. Otherwise one needs to convolve the two together to create a new random variable to simplify the mathematics. Normally this new random variable is named Z, but still correct if named $X*Y$. Now for two random variables the properties (383)-(386) of the expectation operator imply that:

$$m_Z = E(Z) = m_{X*Y} = E(X) + E(Y) = m_X + m_Y \tag{383}$$

$$\sigma_{X+Y}^2 = \sigma_X^2 + \sigma_Y^2 + 2Cov_{XY} \tag{384}$$

$$Cov_{XY} = E[XY] - E[X]E[Y] \tag{385}$$

$$\mathrm{Var}\left(\sum_{i=1}^{n} X_i\right) = \sum_{i=1}^{n} Var(X_i) \tag{386}$$

Thus, if one were to find the variance of a random array one could not just look at the variance of the distribution alone. For example the variance of the Wigner semicircle distribution is given by (387) and the derivation (388)-(390) is also shown below for completeness. Variance of a circular random array differs because there are actually two random variables composing the circular random array shown in (391). Thus, the correct form of the variance is shown in (398) given by the addition of (394) and (396). This type of method used to find the variance is similar to applications such as I-Q modulation, the study of noise and radar imaging where the joint pdf is given by (399).

$$\sigma^2 = \frac{R^2}{4} \tag{387}$$

$$\sigma^2 = E\left[x^2\right] - E\left[x\right]^2 \tag{388}$$

$$E\left[x^2\right] = \int_{-1}^{1} x^2 \frac{2}{\pi}\sqrt{R^2 - x^2}\, dx = \frac{R}{4} \tag{389}$$

$$E[x] = \int_{-1}^{1} x \frac{2}{\pi}\sqrt{R^2 - x^2}\, dx = 0 \tag{390}$$

$$F(\theta,\phi|\vec{\upsilon}) = \frac{1}{N}\sum_{n=1}^{N} e^{j\upsilon_{n,x}^r \zeta_x^r(\theta,\phi) + \upsilon_{n,y}^r \zeta_y^r(\theta,\phi)} = \frac{1}{N}\sum_{n=1}^{N} (\tilde{x}_n + j\tilde{y}_n) = (X + jY)$$

where $\tag{391}$

$$\tilde{x}_n = \cos\left(\upsilon_{n,x}^r \zeta_x^r(\theta,\phi) + \upsilon_{n,y}^r \zeta_y^r(\theta,\phi)\right), \quad \tilde{y}_n = \sin\left(\upsilon_{n,x}^r \zeta_x^r(\theta,\phi) + \upsilon_{n,y}^r \zeta_y^r(\theta,\phi)\right)$$

$$E\left[X(\theta,\phi|\vec{\upsilon}^r)\right] = \sum_{n=1}^{N} \frac{1}{N}\int_{-1}^{1} \frac{2}{\pi}\sqrt{1 - \upsilon_n^{r\,2}}\cos\left(\upsilon_n \zeta^r(\theta,\phi)\right) d\upsilon_n^r = 2\,\mathrm{jinc}\left(\zeta_x^r(\theta,\phi)\right) 2\,\mathrm{jinc}\left(\zeta_y^r(\theta,\phi)\right) \tag{392}$$

$$E\left[X^2\left(\theta,\phi\middle|\vec{\upsilon}^{\vec{r}}\right)\right] = \sum_{n=1}^{N} \frac{1}{N} \int_{-1}^{1} \frac{2}{\pi} \sqrt{1-\upsilon_n^{\vec{r}2}} \cos^2\left(\upsilon_n \zeta^{\vec{r}}\left(\theta,\phi\right)\right) d\upsilon_n^{\vec{r}} =$$

$$\frac{1}{2}\left(1 + \frac{J_1\left(2\zeta_x^r\left(\theta,\phi\right)\right)}{\zeta_x^r\left(\theta,\phi\right)} \frac{J_1\left(2\zeta_y^r\left(\theta,\phi\right)\right)}{\zeta_y^r\left(\theta,\phi\right)}\right) = \frac{1}{2}\left(1 + {}_0\bar{F}_1\left(;2;-\zeta_x^r\left(\theta,\phi\right)^2\right){}_0\bar{F}_1\left(;2;-\zeta_y^r\left(\theta,\phi\right)^2\right)\right) \tag{393}$$

$$\sigma_x^2 = \frac{1}{2}\left(1 + \frac{J_1\left(2\zeta_x^r\left(\theta,\phi\right)\right)}{\zeta_x^r\left(\theta,\phi\right)} \frac{J_1\left(2\zeta_y^r\left(\theta,\phi\right)\right)}{\zeta_y^r\left(\theta,\phi\right)}\right) - \left(\frac{2J_1\left(\zeta_x^r\left(\theta,\phi\right)\right)}{\zeta_x^r\left(\theta,\phi\right)} \frac{2J_1\left(\zeta_y^r\left(\theta,\phi\right)\right)}{\zeta_y^r\left(\theta,\phi\right)}\right)^2 \tag{394}$$

$$E[XY] = \sum_{n=1}^{N}\sum_{m=1}^{N} \frac{1}{N} \int_{-1}^{1}\int_{-1}^{1} \frac{1}{\pi} \cos\left(\upsilon_n^{\vec{r}}\zeta^{\vec{r}}\left(\theta,\phi\right)\right)\sin\left(\upsilon_m^{\vec{r}}\zeta^{\vec{r}}\left(\theta,\phi\right)\right) d\upsilon_n^{\vec{r}} d\upsilon_m^{\vec{r}}$$

$$= E[X]E[Y] = 0 \tag{395}$$

Similarly,

$$\sigma_y^2 = \frac{1}{2}\left(1 - \frac{J_1\left(2\zeta_x^r\left(\theta,\phi\right)\right)}{\zeta_x^r\left(\theta,\phi\right)} \frac{J_1\left(2\zeta_y^r\left(\theta,\phi\right)\right)}{\zeta_y^r\left(\theta,\phi\right)}\right) - 0 \tag{396}$$

$$E_{X+Y} = 2\operatorname{jinc}\left(\zeta_x^r\left(\theta,\phi\right)\right) 2\operatorname{jinc}\left(\zeta_y^r\left(\theta,\phi\right)\right) \tag{397}$$

$$\sigma_{x+y}^2 = 1 - \left(\frac{2J_1\left(\zeta_x^r\left(\theta,\phi\right)\right)}{\zeta_x^r\left(\theta,\phi\right)} \frac{2J_1\left(\zeta_y^r\left(\theta,\phi\right)\right)}{\zeta_y^r\left(\theta,\phi\right)}\right)^2 \tag{398}$$

$$f_{X,Y}\left(x,y\right) = \frac{1}{2\pi\sigma_x\sigma_y} e^{\left(-\frac{(x-m_x)^2}{2\sigma_x^2} - \frac{y^2}{2\sigma_y^2}\right)} \tag{399}$$

14.2 Steering Functions at the Meridian and Zenith Angles

Two beamforming scenarios are covered to find the maximum peaking sidelobe; broadside and endfire since overwhelming simplicity exists in their analysis. Steering at these regions will be utilized first at the meridian elevation angle $\zeta_{endfire}^{\vec{r}}\left(\phi\right) = \left\langle \zeta_m^r\left(\theta = \theta_0 = \pi/2, \phi_0 = 0, \phi\right)\right\rangle_{m=x,y,z}$ and also $\zeta_{endfire}^{\vec{r}}\left(\theta\right) = \left\langle \zeta_m^r\left(\theta_0 = \pi/2, \phi_0 = \phi = 0\right)\right\rangle_{m=x,y,z}$. This in turn simplifies the steering vector (400) to $\zeta_{endfire}^{\vec{r}}\left(\phi\right) = 2\pi\tilde{A}\left\langle \cos\phi - 1, \sin\phi, 0\right\rangle$ or $\zeta_{endfire}^{\vec{r}}\left(\theta\right) = 2\pi\tilde{A}\left\langle \sin\theta - 1, 0, 0\right\rangle$ for either spherical or circular random array. Next at the zenith elevation angle $\zeta_{broadside}^{\vec{r}}\left(\theta\right) = \left\langle \zeta_m^{\vec{r}}\left(\phi_0 = \phi = \theta_0 = 0, \theta\right)\right\rangle_{m=x,y,z}$ and also $\zeta_{broadside}^{\vec{r}}\left(\phi\right) = \left\langle \zeta_m^{\vec{r}}\left(\phi_0 = \theta = \theta_0 = 0, \phi\right)\right\rangle_{m=x,y,z}$ the steering vector similarly simplifies as $\zeta_{broadside}^{\vec{r},sph}\left(\theta\right) = 2\pi\tilde{A}\left\langle \sin\theta, 0, \cos\theta - 1\right\rangle$ and $\zeta_{broadside}^{\vec{r},sph}\left(\phi\right) = 2\pi\tilde{A}\left\langle 0,0,0\right\rangle$ for a spherical random array and as $\zeta_{broadside}^{\vec{r},cir}\left(\theta\right) = 2\pi\tilde{A}\left\langle \sin\theta, 0\right\rangle$ for a circular random array.

$$\zeta_x^r(\theta,\phi) = \cos(\delta)\zeta(\theta,\phi), \zeta_y^r(\theta,\phi) = \sin(\delta)\zeta(\theta,\phi)$$

$$\zeta_z^r(\theta) = \cos(\gamma)\zeta(\theta,\phi), \zeta(\theta,\phi) \triangleq 2\pi\tilde{A}\rho_o, \tilde{A} = A/\lambda$$

$$\rho_o = \sqrt{\left(\frac{\sin\theta\cos\phi-}{\sin\theta_o\cos\phi_o}\right)^2 + \left(\frac{\sin\theta\sin\phi-}{\sin\theta_o\sin\phi_o}\right)^2}$$

$$\delta = \tan^{-1}\left[\frac{\sin\theta\sin\phi - \sin\theta_0\sin\phi_0}{\sin\theta\cos\phi - \sin\theta_0\cos\phi_0}\right]$$

$$\gamma = \cos^{-1}\left(\rho_0^{-1}(\cos\theta - \cos\theta_0)\right)$$

(400)

14.3 Uniform Distribution at the Meridian Elevation Angle

As stated by [9] the exact evaluation of the complementary cumulative distribution function (CCDF) is computationally demanding especially when there is a need for high precision accuracy. A different approach is to consider the aggregate sum of a large element population of N (i.i.d.) random variables. This approach satisfies conditions of the Lindeberg–Lévy central limit theorem. As a consequence, one expects the constituents of the complex array factor U and V, to approach a complex Gaussian distribution given in (401), except for the deterministic angles $\theta_0 = \theta = 90°$ and $\phi_0 = \phi = 0°$. The distributions of U and V (402) at the direction $\pi \geq |\phi| > 0$ will yield supporting Gaussian statistical measures given in (403)-(406) for the spherical and circular random array. Furthermore these results are equivalent at the zenith steering direction such that the steering vector $\zeta_{endfire}^r(\phi)$ is replaced by $\zeta_{zenith}^r(\theta)$.

$$F\left(\phi|\vec{\Upsilon}\right) = \frac{1}{\sqrt{N}}(U + jV)$$

(401)

$$U = \frac{1}{\sqrt{N}}\sum_{n=1}^{N}\cos(X), \quad V = \frac{1}{\sqrt{N}}\sum_{n=1}^{N}\sin(X)$$

$$X_{spherical} = \Upsilon_n\zeta_{endfire}^r(\phi), \quad X_{circular} = \upsilon_n\zeta_{endfire}^r(\phi)$$

(402)

$$\bar{U}^{Sph} = \sqrt{N}\left\langle\frac{3j_1\left(\zeta_{endfire}^{\vec{r}}(\phi)\right)}{\zeta_{endfire}^{\vec{r}}(\phi)}\right\rangle = \sqrt{N}\left\langle 3\text{Tinc}\left(\zeta_{endfire}^{\vec{r}}(\phi)\right)\right\rangle$$

$$\bar{U}^{Cir} = \sqrt{N}\left\langle\frac{2J_1\left(\zeta_{endfire}^{\vec{r}}(\phi)\right)}{\zeta_{endfire}^{\vec{r}}(\phi)}\right\rangle = \sqrt{N}\left\langle 2\text{Jinc}\left(\zeta_{endfire}^{\vec{r}}(\phi)\right)\right\rangle$$

(403)

$$\left\langle 3\text{Tinc}\left(\zeta_{endfire}^{\vec{r}}(\phi)\right)\right\rangle = 3\text{Tinc}\left(\zeta_x^r(\phi)\right)3\text{Tinc}\left(\zeta_y^r(\phi)\right)$$

$$\left\langle 2\text{Jinc}\left(\zeta_{endfire}^{\vec{r}}(\phi)\right)\right\rangle = 2\text{Jinc}\left(\zeta_x^r(\phi)\right)2\text{Jinc}\left(\zeta_y^r(\phi)\right)$$

$$\bar{V}_{Sph|Cir} = E\left[V\left(\phi|\vec{\Upsilon}^{\vec{r}}\right)\right] = E\left[V\left(\phi|\vec{\upsilon}^{\vec{r}}\right)\right] = 0$$

(404)

$$\sigma_U^2 \overset{Sph}{=} \frac{1+\left\langle 3\mathrm{Tinc}\left(2\zeta_{endfire}^{\vec{r}}\left(\phi\right)\right)\right\rangle}{2} - \left\langle 3\mathrm{Tinc}\left(\zeta_{endfire}^{\vec{r}}\left(\phi\right)\right)\right\rangle^2$$

$$\sigma_U^2 \overset{Cir}{=} \frac{1+\left\langle 2\mathrm{Jinc}\left(2\zeta_{endfire}^{\vec{r}}\left(\phi\right)\right)\right\rangle}{2} - \left\langle 2\mathrm{Jinc}\left(\zeta_{endfire}^{\vec{r}}\left(\phi\right)\right)\right\rangle^2 \tag{405}$$

$$\sigma_V^2 \overset{Sph}{=} \frac{1}{2}\left(1+\left\langle 3\mathrm{Tinc}\left(2\zeta_{endfire}^{r}\left(\phi\right)\right)\right\rangle\right)-0$$

$$\sigma_V^2 \overset{Cir}{=} \frac{1}{2}\left(1+\left\langle 2\mathrm{Jinc}\left(2\zeta_{endfire}^{r}\left(\phi\right)\right)\right\rangle\right)-0 \tag{406}$$

14.4 Gaussian Distribution at the Meridian Elevation Angle

(a) Standard deviation

In the work of [12] a standard deviation metric $\sigma = \tilde{A}/3$ is utilized, which provides 99.73% accuracy that all antennas are located within the circular disc of radius $\tilde{A}$. A different value is derived in [81] given by (407) and is used in this analysis.

$$\sigma = \frac{\tilde{A}}{2\sqrt{3}} \tag{407}$$

(b) Steering functions

Once again the *Lindeberg–Lévy central limit theorem* is assumed to hold true. As a consequence, one expects a complex Gaussian distribution given in (401), with supporting Gaussian statistical measures specified in (408)-(411) for both the spherical and circular random array. The underlying difference from the previous section exists in the fact that Gaussian distributed pdfs are used to calculate the supporting statistical measures [6], [12], [81]-[82].

$$\bar{U}_{Sph|Cir} = \sqrt{N}\left\langle e^{\frac{-\zeta_{endfire}^{\vec{r}}(\phi)^2 \sigma^2}{2}}\right\rangle = \sqrt{N} e^{\frac{-\zeta_x^{r}(\phi)^2 \sigma^2}{2}} e^{\frac{-\zeta_y^{r}(\phi)^2 \sigma^2}{2}} \tag{408}$$

$$\bar{V}_{Sph|Cir} = 0 \tag{409}$$

$$\sigma_{U_{Sph|Cir}}^2 = \frac{1}{2}\left(1+\left\langle e^{-2\zeta_{endfire}^{\vec{r}}(\phi)^2 \sigma^2}\right\rangle\right)-\left\langle e^{-\zeta_{endfire}^{\vec{r}}(\phi)^2 \sigma^2}\right\rangle \tag{410}$$

$$\sigma_{V_{Sph|Cir}}^2 = \frac{1}{2}\left(1-\left\langle e^{-2\zeta_{endfire}^{\vec{r}}(\phi)^2 \sigma^2}\right\rangle\right) \tag{411}$$

This time it is interesting to notice that the results of (408)-(411) are the same for both the circular and spherical random array. This is a result of the similarities circles and spheres share from symmetries at this unique angle. Otherwise when derived outside of the meridian elevation angle (zenith) the results are not the same since $\zeta_{broadside}^{\vec{r},sph}\left(\theta\right)$ changes for circular and spherical arrays. Previous results of this nature are also provided from the derivation of [12] for a Gaussian distributed circular random array,

using the standard deviation $\sigma = \tilde{A}/3$, in addition to the incorrect array factor provided in [6]-[14], [81]-[82] and [191].

14.5 Relation to Previous Work

The calculation of the variance formulations (405)-(406), and (410)-(411) have been derived in recent developments by [9], [12], and [81], but are quite similar to the general result of equation (5) in the historical work provided by [31] for one dimensional topologies. Moreover this work provides the even (412) and odd (413) modes such that the spatial parameter $X(\theta,\phi)$ is defined to represent the angular beamsteering function (utilized in the characteristic function); similar to $\zeta^{\tilde{r}}(\theta,\phi)$. However, the biggest difference in the relations from [31] exists with the variance. This earlier analysis performed a linear transformation on the variance following the Bienaymé formula (414) by dividing by the number of elements. In other words the variance of (405)-(406), and (410)-(411) are considered to be the individual variances of each radiator whereas the total variance of all radiators is to be given by (415), which also matches the results of other previous works specified by (415) [17]-[18]. .The results of (405)-(406), and (410)-(411) demonstrate that the (412)-(415) can be expanded up to a three dimensional topology using the vector $\langle x, y, z \rangle$.

$$\sigma_U^2 = \frac{1}{2N}\left[1+\Lambda\left(2X(\theta,\phi)\right)\right]-\frac{1}{N}\Lambda\left(X(\theta,\phi)\right)^2 \qquad (412)$$

$$\sigma_V^2 = \frac{1}{2N}\left[1-\Lambda\left(2X(\theta,\phi)\right)\right] \qquad (413)$$

$$\text{Var}\left(\bar{X}\right) = \text{Var}\left(\frac{1}{N}\sum_{n=1}^{N}X_n\right) = \frac{1}{N^2}\sum_{n=1}^{N}\text{Var}\left(X_n\right) = \frac{\sigma^2}{N} \qquad (414)$$

$$\sigma_{U+V}^2 = \frac{1}{N}\left[1-\left|\Lambda\left(X(\theta,\phi)\right)\right|^2\right] \qquad (415)$$

A proof of the variance relations of (412)-(415) is provided in below such that; the total variance of any random array is computed as (416). However, if one is to solve for the variance of the complex radiation pattern of (391) then one finds the variance of the total pattern by taking the sum of the quadrature components of the pattern as provided in (417).

$$
\begin{aligned}
\sigma^2 &= \overline{\left(F\left(\phi|Z_n\right)-\bar{F}\left(\phi|Z_n\right)\right)\left(F\left(\phi|Z_n\right)-\bar{F}\left(\phi|Z_n\right)\right)^*}, Z_n = x_n, y_n, z_n \\
&= \overline{\left[F\left(\phi|Z_n\right)F\left(\phi|Z_n\right)^* - F\left(\phi|Z_n\right)\bar{F}\left(\phi|Z_n\right)^* - \bar{F}\left(\phi|Z_n\right)F\left(\phi|Z_n\right)^* + \bar{F}\left(\phi|Z_n\right)\bar{F}\left(\phi|Z_n\right)^*\right]} \\
&= \overline{F\left(\phi|Z_n\right)F\left(\phi|Z_n\right)^*} - \overline{F\left(\phi|Z_n\right)\bar{F}\left(\phi|Z_n\right)^*} - \overline{\bar{F}\left(\phi|Z_n\right)F\left(\phi|Z_n\right)^*} + \overline{\bar{F}\left(\phi|Z_n\right)\bar{F}\left(\phi|Z_n\right)^*} \\
&= \overline{F\left(\phi|Z_n\right)F\left(\phi|Z_n\right)^*} - \bar{F}\left(\phi|Z_n\right)\bar{F}\left(\phi|Z_n\right)^* = \left|E[Z_n]\right|^2\left(1-\frac{1}{N}\right)+\frac{1}{N}-\left|E[Z_n]\right|^2 = \frac{1}{N}\left(1-\left|E[Z_n]\right|^2\right)
\end{aligned}
\qquad (416)
$$

$$\sigma^2 = \overline{\left(\begin{array}{l}F_a(\phi|Z_n)+\\ jF_b(\phi|Z_n)\end{array}\right)\left(\begin{array}{l}F_a(\phi|Z_n)-\\ jF_b(\phi|Z_n)\end{array}\right)} - \left(\begin{array}{l}\overline{F}_a(\phi|Z_n)+\\ j\overline{F}_b(\phi|Z_n)\end{array}\right)\left(\begin{array}{l}\overline{F}_a(\phi|Z_n)-\\ j\overline{F}_b(\phi|Z_n)\end{array}\right) = \left(\begin{array}{l}\overline{F_a(\phi|Z_n)^2} + \overline{F_b(\phi|Z_n)^2} -\\ \left|\overline{F}_a(\phi|Z_n)\right|^2 - \left|\overline{F}_b(\phi|Z_n)\right|^2\end{array}\right)$$

$$= \left(\overline{F_a(\phi|Z_n)^2} - \left|\overline{F}_a(\phi|Z_n)\right|^2\right) + \left(\overline{F_b(\phi|Z_n)^2} - \left|\overline{F}_b(\phi|Z_n)\right|^2\right) = \sigma_a^2 + \sigma_b^2 \qquad (417)$$

Here it is seen that the total variance decreases when N increases, and for $N \to \infty$ the standard error of the sample mean almost surely approaches the expected value since the $\mathrm{Var}(\overline{X}) \to 0$. Moreover, this appropriately matches the definition of the central limit theorem and is depicted below in Figure 187-Figure 188 for a linear random array.

Overall when one doesn't consider the variance of all radiators it is seen the variance always begins at zero, which defines the mainbeam region (i.e. deterministic region), but converges to ½, which defines the sidelobe region (i.e. non-deterministic region). Again this means the beampattern is completely deterministic at the mainlobe region, but completely random in the sidelobe region.
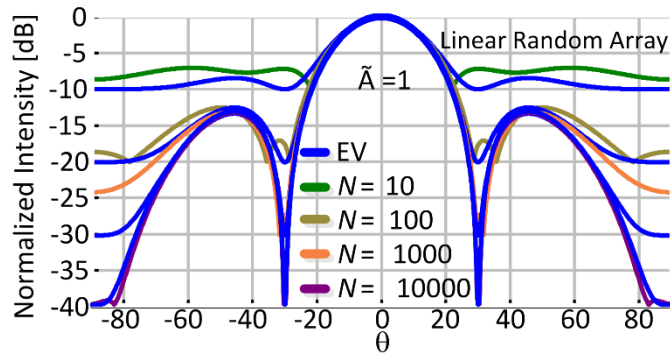
Figure 187. Analytical convergence of the beampattern to its expected value (*EV* i.e. continuous distribution).
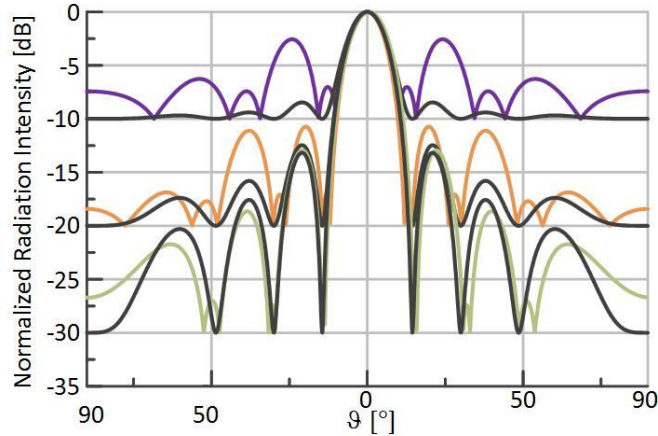
Figure 188. Analytical beampattern (Monte Carlo Method) is deterministic at the mainlobe, but completely random in the sidelobe region; unless for large *N* the entire pattern is deterministic.

14.6 CCDF of the Maximum Peaking Sidelobe

At this point the required information being the first moment (mean), and second moment (variance and covariance) is now obtained (where the covariance can easily be shown to equal zero; since *U* and *V* are orthogonal they are of course statistically uncorrelated). These parameters are useful in setting up the joint probability distribution function (JPDF) of (418) which is suitable for defining confidence intervals in the random array beampatterns (noted if the variables were correlated the covariance matrix (419) would have been used for calculation). Last of all, it is interesting to note that the JPDF of the CCDF of each random variable is independent from one another and will be covered in more detail in the following section.

$$f_{U,V}(u,v) = \frac{1}{2\pi\sigma_u\sigma_v} e^{\left(\frac{-|u-\bar{u}|^2}{2\sigma_u^2} - \frac{v^2}{2\sigma_v^2}\right)} \tag{418}$$

$$f_{U,V}(u,v) = \frac{1}{2\pi\sigma_u\sigma_v(1-\rho^2)} e^{\left(\frac{-|u-\bar{u}|^2}{2\sigma_u^2} - \frac{v^2}{2\sigma_v^2} - \frac{2\rho(u-\bar{u})v}{\sigma_u\sigma_v}\right)} \tag{419}$$

(a) CCDF at the zenith elevation angle

Two steps are now needed to approximate the Complementary Cumulative Distribution Function (CCDF) of U_0. First the result of (418) is converted to polar coordinates (420). Next the spatial constraint $\zeta(\theta) \gg 1$ is assumed since this condition causes the variances of each radiator to rapidly decrease and approach $\sigma_U^2 \approx \sigma_v^2 \approx 1/2$ (independent of the spatial angular parameter θ). More so, since the variances converge equally the distribution can be simplified such that it follows the Nakagami-Rice distribution

206

(also achieved by integrating with respect to ϑ) and is provided by (421) (written compactly by a first-order Marcum-Q function). The term I_n is the nth order modified Bessel function of the first kind for non-negative n.

$$\Pr\left[U(\theta) > U_o\right] = \Pr\left[\sqrt{U^2 + V^2} > \sqrt{NU_o}\right]$$
$$= \int_{\sqrt{NU_o}}^{\infty} \int_{-\pi}^{\pi} \frac{r}{2\pi\sigma_u\sigma_v} e^{\left(\frac{-|r\cos\vartheta - \bar{u}|^2}{2\sigma_u^2} - \frac{r^2\sin^2\vartheta}{2\sigma_v^2}\right)} d\vartheta dr \tag{420}$$

$$\Pr\left[U(\theta) > U_o\right] = Q\left(\frac{\bar{U}}{\sigma_u}, \frac{\sqrt{NU_o}}{\sigma_v}\right) = Q\left(\sqrt{2\bar{U}}, \sqrt{2NU_o}\right) \tag{421}$$

A third and final step may be applied to this analysis following similar to the historical work done in [31]-[34], [85], [101], [186] and [205]-[206], but is not absolutely necessary. This last step gives further simplification in the process, but at the expense a reduced accuracy in the estimator of the maximum peaking sidelobe is incurred; though as a caveat it provides one of the most convenient and easiest expressions utilized for practical use. To apply this step one assumes that the mean approaches zero, hence the region of interest is outside of the main beam region, or far enough away such that one is operating entirely in the sidelobe region. As a consequence the CCDF is simplified as a Rayleigh distribution (due to converging variances and a zero mean assumption) provided by (422) [31]-[32], [34], [186] and [205]. The surprising observation of this result is the pdf of the element population plays no effect on the pdf of the amplitude of the array factor. This happens because the element population is assumed to be sufficiently large. Therefore, the peaking sidelobe in the random sidelobe region becomes submerged by taking the Fourier transform of the array factor.

$$\Pr\left[U(\theta) > U_o\right] = e^{-NU_o} \tag{422}$$

A comparison of the results of (420) and (419) are shown in Figure 189 using the mean and variance characteristics provided in (403)-(406) and (408)-(411). In fact, Figure 189 is also the same at the meridian elevation angle for a spherical random array since the pattern is symmetric as was shown in Figure 17. Secondly Figure 189 indicates that for large values of N the zero mean approximation does not hold. This is because the angle $\theta = 45°$ is not within the 3dB sidelobe region, but in between this sidelobe and mainlobe region [9], [12] and [81]. An example of the three dB sidelobe region is shown in Figure 190 [82]. Hence, based upon observations thus far random arrays may be broken up into three regions as illustrated in Figure 191. The first region is to be called the controlled or mainlobe region. The second region is the transition region, in which the sidelobe pattern degenerates yet closely matches the design pattern (i.e. the first sidelobe and sometimes second and on occasion tertiary lobes). The third and final portion is the random portion (three dB sidelobe region) in which the sidelobe statistics applied in this section closely approximate to those of the random array.
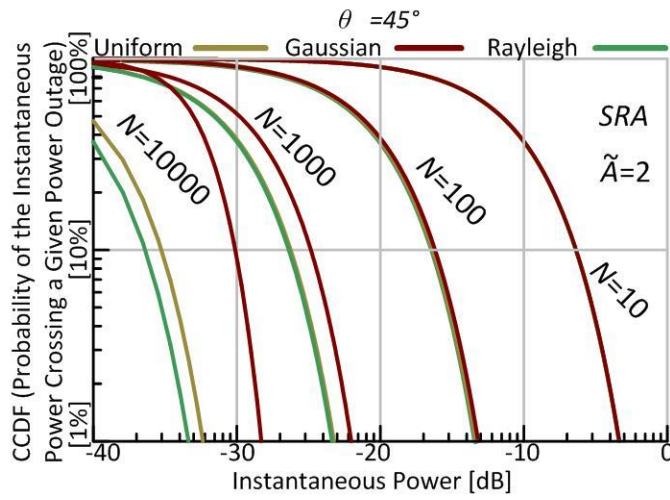
Figure 189. CCDF of the maximum peaking side lobe at the spatial location $\theta = 45°$ and phased at the zenith angle.
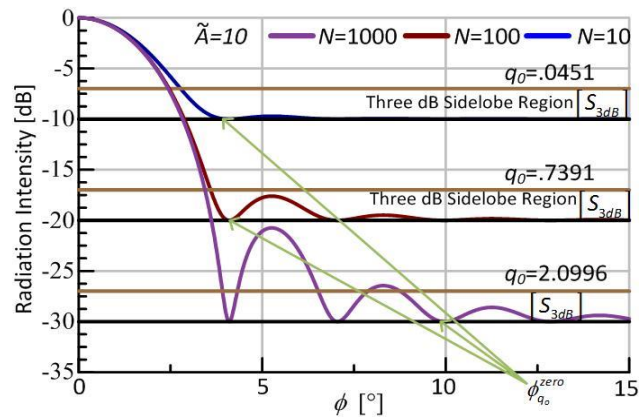
Figure 190. Example of the 3 dB sidelobe region.
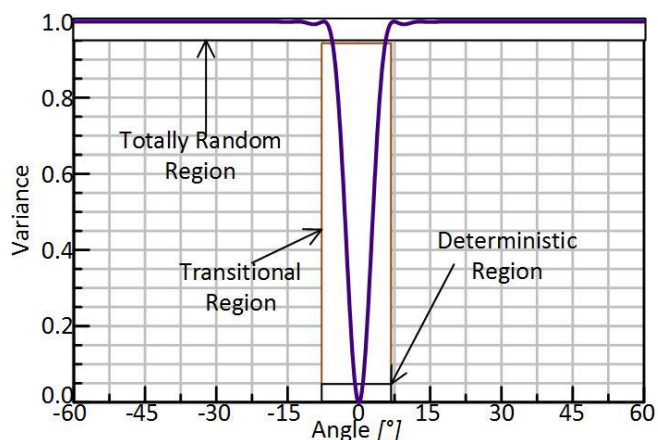
Figure 191. Individual variance of each radiator.

A. 3dB sidelobe region

The simplified distribution becomes readily tractable for the spatial region in which the mean value of the array factor is assumed zero. This is greatly dependent upon the number of antennas present and if N increases the mean value increases. Ideally, this would be the case, but in practice a low number of elements might persist. Since, this may very well hold true the *3dB sidelobe region* is re-examined in order to redefine the necessary confidence interval.

In [9], [81] the 3dB sidelobe region is defined to satisfy the condition (423). This term can be rewritten as (424) by adding the variance of the corresponding random variables U and V.

$$NU_{av}(\phi) \leq 2 \tag{423}$$

$$Var(U) + Var(V) + |E[U]|^2 + |E[V]|^2 \leq NU_{av}(\phi) \leq 2 \tag{424}$$

Given the inequality of (424) the average power pattern is bounded to that of (425). This shows the square of the mean 3dB sidelobe region is bounded by unity when N is large. Additionally the result also shows the mean does not grow unbounded with the number of antenna N similar to [9].

$$|E[U]|^2 \leq \frac{1}{\left(1 - \frac{1}{N}\right)} \tag{425}$$

B. Peaking sidelobe bounds in the 3dB sidelobe region

To prove a random array is free of grating lobes, (given a sufficient number of radiators) one must find a distribution relating to the maximum output power of the sidelobes. This type of work is provided in papers from [9] and [12] for planar circular arrays and dates back to a very classic paper from Donovito [186]-[205] for linear random arrays. Additional classical texts discussing the distribution of

peak sidelobes for linear random arrays have arisen from these earlier works and can be found in [9], [12], [31]-[32], [34], and [81]-[82] which include situations of non-isotropic elements or non-stationarity [16], [17], [85], and [207]. For clarity, this section follows similarly to the work presented by [9], [12] and [186] in setting up the fundamental limits of a uniformly distributed spherical random array with isotropic elements, behaving stationary.

The average representation of the number of upward crossings at a given power level say $v(a)$ [9], [12], and [81] is prepared under the assumption U and V are uncorrelated zero-mean Gaussian processes with variance $\sigma_U^2 = \sigma_V^2 = 1/2$. This calculation of the average representation of crossings will be referred to as the *outage probability* denoted by U_{out}. To define this outage probability one takes the autocorrelation function of U at two differently located spatial instants $u_1 = 2\pi\tilde{A}\langle\cos\phi_1, \sin\phi_1 - 1, 0\rangle$ and u_2, providing (426) under stationary conditions (where $\Upsilon_n \triangleq \Upsilon_n^{\vec{r}}$). This result is simplified to (427) since weak-sense stationarity can be applied as the mean valued radiation pattern and covariance matrix of this process are independent of time. A more detailed explanation of this is found in [81]. Or in other words imagine the autocorrelation functions is taken such that $u_1 = 10°\,\pi/180 = \pi/18$ and $u_2 = -10°\,\pi/180 = -\pi/18$. Then $u_1 + u_2 = 0$ and $u_1 - u_2 = \pi/9 = 20°$. Hence, we are operating in the random region and not in the deterministic region.

$$
\begin{aligned}
K_{\Upsilon\Upsilon}(u_1, u_2) &= E_\Upsilon\left\{\cos\left(\Upsilon_n 2\pi\tilde{A}u_1\right)\cos\left(\Upsilon_n 2\pi\tilde{A}u_2\right)\right\} \\
&= R_{\Upsilon\Upsilon}(u_1 - u_2) - \mu^2
\end{aligned}
\tag{426}
$$

$$
R_\Upsilon(\Theta) = \frac{1}{2}E_\Upsilon\left\{\left(\cos\left(\Upsilon 2\pi\tilde{A}\Theta\right)\right)\right\}, \; \Theta = (u_1 - u_2)
\tag{427}
$$

For a zero mean Gaussian process one should find the variance U' by differentiating (427) with respect to Θ twice, followed by setting $\Theta = 0$ in addition to taking the negative of the statistical average giving (428) and (429) for the uniformly distributed spherical and circular random array [9] and (430) for the Gaussian distribution.

$$
\sigma_{U'_{Sph,Uniform}}^2 = \frac{4}{5}\pi^2\tilde{A}^2
\tag{428}
$$

$$
\sigma_{U'_{Cir,Uniform}}^2 = \pi^2\tilde{A}^2
\tag{429}
$$

$$
\sigma_{U'_{Cir|Sph\;Gaussian}}^2 = 4\pi^2\tilde{A}^2\sigma^2
\tag{430}
$$

In a similar manner, it can be shown that $\sigma_{u'}^2 = \sigma_{v'}^2$. Hence, the joint pdf of *U, U', V, V'* at the meridian elevation angle gives the joint pdf (431) and is simplified by converting the coordinates from Cartesian to polar such that $U = \Omega\cos\Theta$, $V = \Omega\cos\Theta$ (432). Integrating out the terms θ, θ' one obtains

(433) aiding to the average representation of the number of upward crossings at a given power level $v(a)$ resulting with (434). This expression like [9] represents the number of upward crossings at a given power level a, per interval in the *3dB sidelobe region* S_{3dB}. The associated average value of the number of upward crossing is given by (435) (since the 3dB sidelobe region is symmetric in the region $-\theta_{q_0}^{zero} \rightarrow -\pi$ or $-\phi_{q_0}^{zero} \rightarrow -\pi$). Resulting is the associated average value of the number of upward crossing given by (436)-(441) (where $\vartheta = \{\text{zenith}, \text{endfire}\} = \{\theta, \phi\}$ is the angular dependence) for the spherical and circular distributions derived previously by the primed variances in (428)-(430).

It is important to note the function unfolding the average number of maximum peaking sidelobes includes the term e^{-a^2} and decreases monotonically only for $a \geq 1/\sqrt{2}$. Hence, the outage probability exceeding a power level of $a = \sqrt{NU_0}$ can be simplified by a small argument approximation such that $\cos x \approx 1$ and $\sin x \approx x$ simplifying the results of (438)-(441). An illustration of the results are shown in Figure 192 using a small argument approximation for either ϑ_{q_o} as a function of the aperture size for a given number of elements. This is useful since the maximum peaking sidelobe appears to be contained no greater than 12 dB above the average sidelobe level for aperture sizes less than $\tilde{A} = 100$.

$$f_{U',V'}^{U,V}\left(\begin{smallmatrix} u',v' \\ u,v \end{smallmatrix}\right) = \frac{e^{\left(-\frac{u^2+v^2}{2\sigma_u^2} - \frac{u'^2+v'^2}{2\sigma_u^2}\right)}}{(2\pi)^2 \sigma_u \sigma_{u'}} \tag{431}$$

$$f_{\Omega,\Omega'}^{\Theta,\Theta'}(\omega,\omega',\theta,\theta') = \frac{\omega^2}{(2\pi)^2 \sigma_u^2 \sigma_{u'}^2} e^{\left(-\frac{\omega^2}{2\sigma_u^2} - \frac{\omega'^2+\omega^2\theta'^2}{2\sigma_{u'}^2}\right)} \tag{432}$$

$$f_{\Omega,\Omega'}(\omega,\omega') = \frac{\omega}{\sqrt{2\pi}\sigma_u^2\sigma_{u'}} e^{\left(-\frac{\omega^2}{2\sigma_u^2} - \frac{\omega'^2}{2\sigma_{u'}^2}\right)} \tag{433}$$

$$v(a)\|du\| = \|du\| \int_0^\infty w' f_{\Omega,\Omega'}(a,\omega')d\omega'$$
$$= \int_0^\infty \frac{a\|du\|w'}{\sqrt{2\pi}\sigma_u^2\sigma_{u'}} e^{\left(-\frac{\omega^2}{2\sigma_u^2} - \frac{\omega'^2}{2\sigma_{u'}^2}\right)} = \frac{ae^{-a^2}\|du\|}{\sqrt{2\pi}\sigma_u^2}[\sigma_{u'}] \tag{434}$$

$$v(a)\left[du_{\Upsilon_x^r} + du_{\Upsilon_y^r} + du_{\Upsilon_z^r}\right] = \frac{ae^{-a^2}}{\sqrt{2\pi}} \frac{\lfloor \sigma_{u_\Upsilon} \rfloor}{\sigma_{u_\Upsilon}^2}[du_\Upsilon]$$
$$[du_\Upsilon] = \left[du_{\Upsilon_x^r} + du_{\Upsilon_y^r} + du_{\Upsilon_z^r}\right] \tag{435}$$

211

$$E\left\{v\left(a\left(\phi\right)\right)\right\}\overset{Sra,\text{Unif}}{\underset{endfire}{=}}ae^{-a^2}\sqrt{\frac{2}{\pi}}\left(-1-\cos\vartheta_{q_{0-}}^{zero}-\sin\vartheta_{q_0}^{zero}\right)\left[\pm\sigma_{\mathbf{u}_{\Upsilon}'}\right]+A$$

$$E\left\{v\left(a\left(\theta\right)\right)\right\}\overset{Sra,\text{Unif}}{\underset{endfire}{=}}ae^{-a^2}\sqrt{\frac{2}{\pi}}\left(-\sin\vartheta_{q_0}^{zero}\right)\left[\pm\sigma_{\mathbf{u}_{\Upsilon}'}\right]+B$$

$$E\left\{v\left(a\left(\theta\right)\right)\right\}\overset{zenith}{\underset{SRA}{=}}ae^{-a^2}\sqrt{\frac{2}{\pi}}\left(-1-\cos\theta_{q_0}^{zero}-\sin\theta_{q_0}^{zero}\right)\left[\pm\sigma_{\mathbf{u}_{\Upsilon}'}\right]+C$$

$$E\left\{v\left(a\left(\phi\right)\right)\right\}\overset{Sra,\text{Unif}}{\underset{Zenith}{=}}0+D$$

A,B,C,D are constants of integration

$$\left(\begin{array}{l} B=\sqrt{\dfrac{2}{\pi}}a\left[\pm\sigma_{\mathbf{u}_{\Upsilon}'}\right]e^{-a^2}\left(-1-\cos\theta_{q_0}^{zero}\right) \text{ to make the results match a Rayleigh Distribution}\\[3ex] \text{of amplitude } \sqrt{\dfrac{2}{\pi}}a\left[\pm\sigma_{\mathbf{u}_{\Upsilon}'}\right]\left(-1-\cos\theta_{q_0}^{zero}\right) \text{ which for a spherical random array should}\\[3ex] \text{be independent of scan angle} \end{array}\right)$$

$$A=C=D=0 \qquad\qquad (436)$$

$$E\left\{v\left(a\left(\phi\right)\right)\right\}\overset{Cra,\text{Unif}}{\underset{endfire}{=}}ae^{-a^2}\sqrt{\frac{2}{\pi}}\left(-1-\cos\vartheta_{q_{0-}}^{zero}-\sin\vartheta_{q_0}^{zero}\right)\left[\pm\sigma_{\mathbf{u}_{\Upsilon}'}\right]+A$$

$$E\left\{v\left(a\left(\theta\right)\right)\right\}\overset{Cra,\text{Unif}}{\underset{endfire}{=}}ae^{-a^2}\sqrt{\frac{2}{\pi}}\left(-\sin\vartheta_{q_0}^{zero}\right)\left[\pm\sigma_{\mathbf{u}_{\Upsilon}'}\right]+B$$

$$E\left\{v\left(a\left(\theta\right)\right)\right\}\overset{Cra,Unif}{\underset{Zenith}{=}}ae^{-a^2}\sqrt{\frac{2}{\pi}}\left(-\sin\theta_{q_0}^{zero}\right)\left[\pm\sigma_{\mathbf{u}_{\Upsilon}'}\right]+C$$

$$E\left\{v\left(a\left(\phi\right)\right)\right\}\overset{Cra,\text{Unif}}{\underset{Zenith}{=}}0+D$$

A,B,C,D are constants of integration

$$\left(\begin{array}{l} B=\sqrt{\dfrac{2}{\pi}}a\left[\pm\sigma_{\mathbf{u}_{\Upsilon}'}\right]e^{-a^2}\left(-1\right) \text{ to make the results match a Rayleigh Distribution}\\[3ex] \text{of amplitude } \sqrt{\dfrac{2}{\pi}}a\left[\pm\sigma_{\mathbf{u}_{\Upsilon}'}\right]\left(-1\right) \text{ which should be dependent of scan angle}\\[3ex] C=\sqrt{\dfrac{2}{\pi}}a\left[\pm\sigma_{\mathbf{u}_{\Upsilon}'}\right]e^{-a^2}\left(-1-\cos\vartheta_{q_{0-}}^{zero}\right) \text{ since it is expected one will have a}\\[2ex] \text{more directive beam in the zentith allowing more energy or higher peaking}\\[1ex] \text{sidelobes in the totally random region} \end{array}\right)\qquad(437)$$

$$A=D=0$$

$$E\left\{\nu\left(a\left(\phi\right)\right)\right\}_{endfire}^{Sra,\text{Unif}} = \sqrt{\frac{8\pi}{5}}\tilde{A}ae^{-a^2}\left(1+\cos\vartheta_{q_0}^{zero}+\sin\vartheta_{q_0}^{zero}\right)$$

$$E\left\{\nu\left(a\left(\theta\right)\right)\right\}_{endfire}^{Sra,\text{Unif}} = \sqrt{\frac{8\pi}{5}}\tilde{A}ae^{-a^2}\left(1+\cos\vartheta_{q_0}^{zero}+\sin\vartheta_{q_0}^{zero}\right)$$

$$E\left\{\nu\left(a\left(\theta\right)\right)\right\}_{Zenith}^{Sra,\text{Unif}} = \sqrt{\frac{8\pi}{5}}\tilde{A}ae^{-a^2}\left(1+\cos\vartheta_{q_0}^{zero}+\sin\vartheta_{q_0}^{zero}\right)$$

$$E\left\{\nu\left(a\left(\phi\right)\right)\right\}_{Zenith}^{Sra,\text{Unif}} = 0$$

(438)

$$E\left\{\nu\left(a\left(\phi\right)\right)\right\}_{endfire}^{Sra,Gaus} = 2\sqrt{2\pi}\tilde{A}\sigma ae^{-a^2}\left(1+\cos\vartheta_{q_0}^{zero}+\sin\vartheta_{q_0}^{zero}\right)$$

$$E\left\{\nu\left(a\left(\theta\right)\right)\right\}_{endfire}^{Sra,Gaus} = 2\sqrt{2\pi}\tilde{A}\sigma ae^{-a^2}\left(1+\cos\vartheta_{q_0}^{zero}+\sin\vartheta_{q_0}^{zero}\right)$$

$$E\left\{\nu\left(a\left(\theta\right)\right)\right\}_{Zenith}^{Sra,Gaus} = 2\sqrt{2\pi}\tilde{A}\sigma ae^{-a^2}\left(1+\cos\vartheta_{q_0}^{zero}+\sin\vartheta_{q_0}^{zero}\right)$$

$$E\left\{\nu\left(a\left(\phi\right)\right)\right\}_{Zenith}^{Sra,Gaus} = 0$$

(439)

$$E\left\{\nu\left(a\left(\phi\right)\right)\right\}_{endfire}^{Cra,\text{Unif}} = \sqrt{2\pi}\tilde{A}ae^{-a^2}\left(1+\cos\vartheta_{q_0}^{zero}+\sin\vartheta_{q_0}^{zero}\right)$$

$$E\left\{\nu\left(a\left(\theta\right)\right)\right\}_{endfire}^{Cra,\text{Unif}} = \sqrt{2\pi}\tilde{A}ae^{-a^2}\left(1+\sin\vartheta_{q_0}^{zero}\right)$$

$$E\left\{\nu\left(a\left(\theta\right)\right)\right\}_{zenith}^{Cra,\text{Unif}} = \sqrt{2\pi}\tilde{A}ae^{-a^2}\left(1+\cos\vartheta_{q_0}^{zero}+\sin\vartheta_{q_0}^{zero}\right)$$

$$E\left\{\nu\left(a\left(\phi\right)\right)\right\}_{zenith}^{Cra,\text{Unif}} = 0$$

(440)

$$E\left\{\nu\left(a\left(\phi\right)\right)\right\}_{endfire}^{Cra,Gaus} = 2\sqrt{2\pi}\tilde{A}\sigma ae^{-a^2}\left(1+\cos\vartheta_{q_0}^{zero}+\sin\vartheta_{q_0}^{zero}\right)$$

$$E\left\{\nu\left(a\left(\theta\right)\right)\right\}_{endfire}^{Cra,Gaus} = 2\sqrt{2\pi}\tilde{A}\sigma ae^{-a^2}\left(1+\sin\vartheta_{q_0}^{zero}\right)$$

$$E\left\{\nu\left(a\left(\theta\right)\right)\right\}_{Zenith}^{Cra,Gaus} = 2\sqrt{2\pi}\tilde{A}\sigma ae^{-a^2}\left(1+\cos\vartheta_{q_0}^{zero}+\sin\vartheta_{q_0}^{zero}\right)$$

$$E\left\{\nu\left(a\left(\phi\right)\right)\right\}_{Zenith}^{Cra,Gaus} = 0$$

(441)

Figure 192. Maximum peaking sidelobe bound (normalized *N*) for beamsteering at the zenith elevation angle.

The results of (438)-(441) illustrate that the maximum peaking sidelobe remains the same for a spherically bound uniformly or Gaussian distributed random array regardless of whether it is scanned toward endfire or broadside. However, for the circularly bound random array it is seen that the maximum peaking sidelobe is likely to be twice the magnitude at endfire relative to the peaking sidelobe at broadside. This is different from the spherical array, which has already been shown to have symmetric patterns at these angles. Furthermore for the CRA there becomes a superposition of the sidelobes adding in phase in both upper and lower half planes of the array at endfire causing this beamsteering angle to probabilistically have greater sidelobe levels. In addition at the endfire steering location $\theta_0 = \pi/2$ there remains two beamsteering functions $\zeta_x^r(\theta,\phi)$ and $\zeta_y^r(\theta,\phi)$ for both CRA and SRA. Yet for the broadside condition $\theta_0 = 0$ there only remains two beamsteering functions $\zeta_x^r(\theta,\phi)$ and $\zeta_z^r(\theta,\phi)$ for the SRA. For this reason the results of the spherical bound random array will remain the same whether it is steered at the zenith or endfire while that of a circularly bound random array will change in turn causing sidelobe maximum to be different at the zenith and meridian angles. Finally numerical solutions of the results of the CRA and SRA are illustrated in Figure 193-Figure 202 for completeness. Furthermore as illustrated in Chapter 11 section 8 it was described that the radiation pattern shape is invariant as it is scanned when using the angular variables u, v and w or ($kz = u = \sin\theta\cos\phi$, $kz = v = \sin\theta\sin\phi$ and $kz = w = \cos\theta$), which is shown in Figure 193-Figure 202. Otherwise if the pattern is scanned using the physical angles θ, and ϕ, the shape of the radiation pattern and beamwidth do in fact vary with scan angle as illustrated in the examples of Figure 203-Figure 220. Thus, it is easy to observe that the beampattern of the spherical random array is invariant to scan angle since the effective aperture remain constant Figure 203-Figure 211.

Whereas for the circular random array its pattern is variant to scan angle as shown in Figure 212-Figure 220.
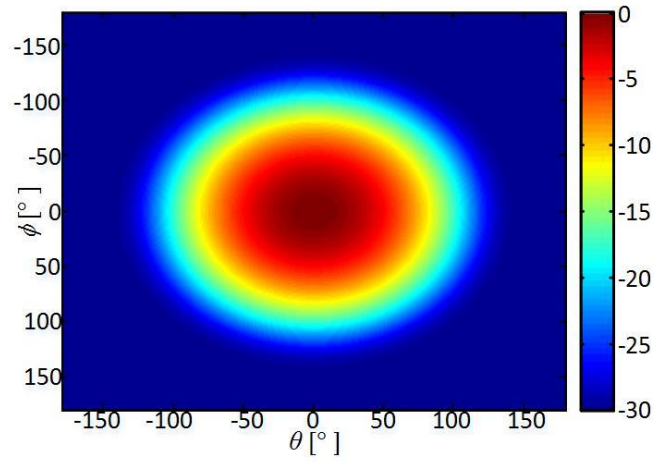
Figure 193. SRA (96), *N=1000*, $\tilde{A} = 1, \theta = 0°$.
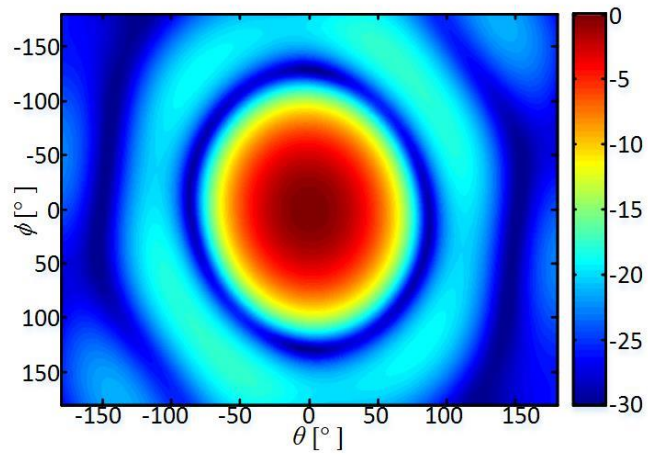
Figure 194. SRA (96) analytical solution, *N=1000*, $\tilde{A} = 1, \theta = 0°$.
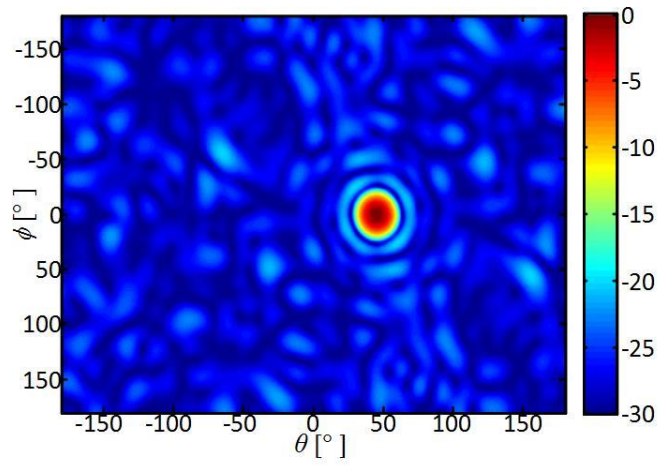
Figure 195. SRA (96) analytical sol., *N=1000*, $\tilde{A} = 1, \theta = 45°$.
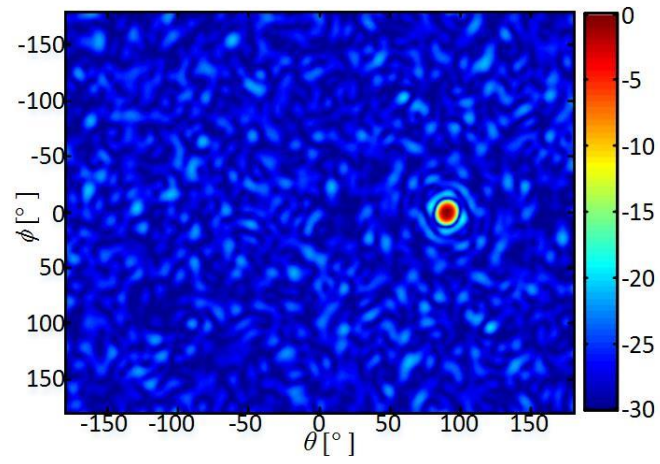
Figure 196. SRA (96) analytical sol., *N=1000*, $\tilde{A} = 10, \theta = 90°$.
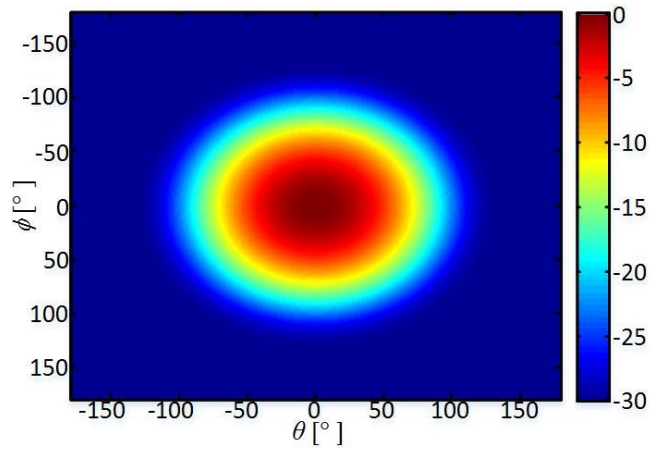
Figure 197. CRA (97), *N=1000*, $\tilde{A} = 1, \theta = 0°$.
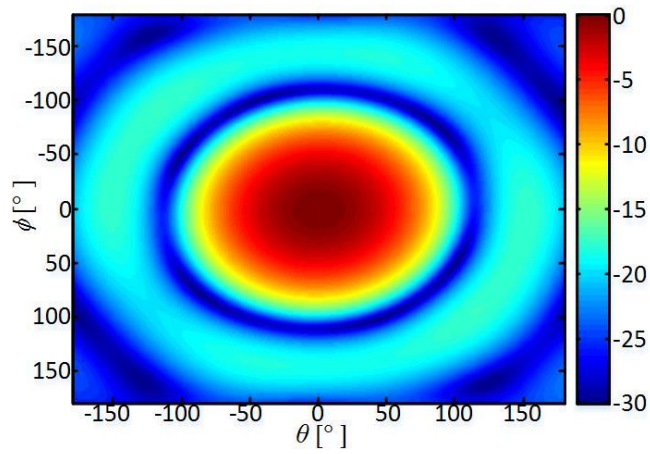
Figure 198. CRA (97) analytical sol., *N=1000*, $\tilde{A} = 1, \theta = 0°$.
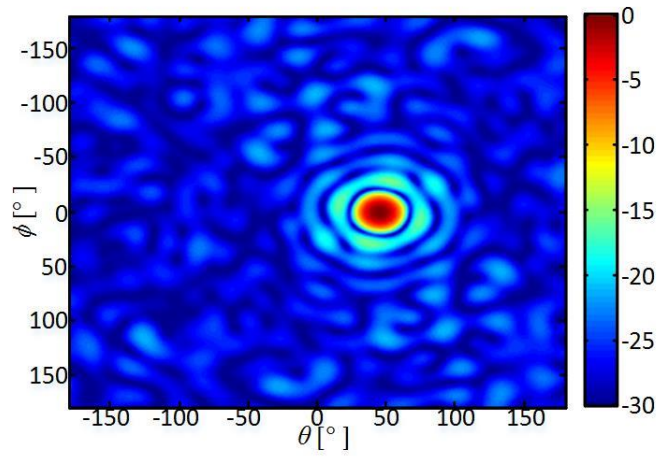
Figure 199. CRA (97) analytical sol., *N=1000*, $\tilde{A} = 5, \theta = 45°$.
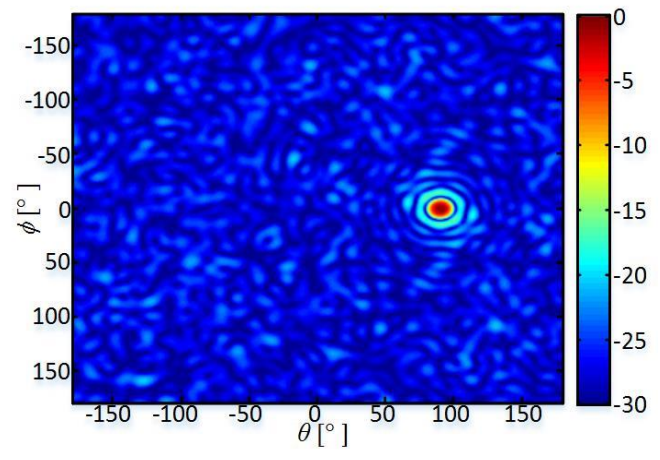
Figure 200. CRA (97) analytical sol., *N=1000*, $\tilde{A} = 10, \theta = 90°$.
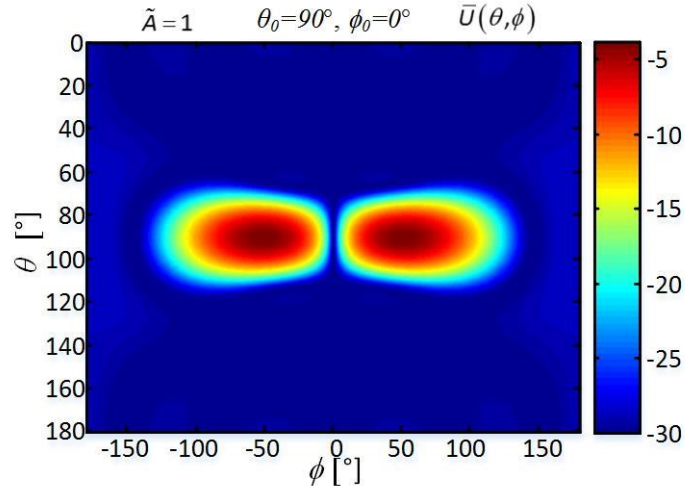
Figure 201. Odd mode of a SRA, $N=1000, \ \tilde{A} = 1, \theta = 90°$.
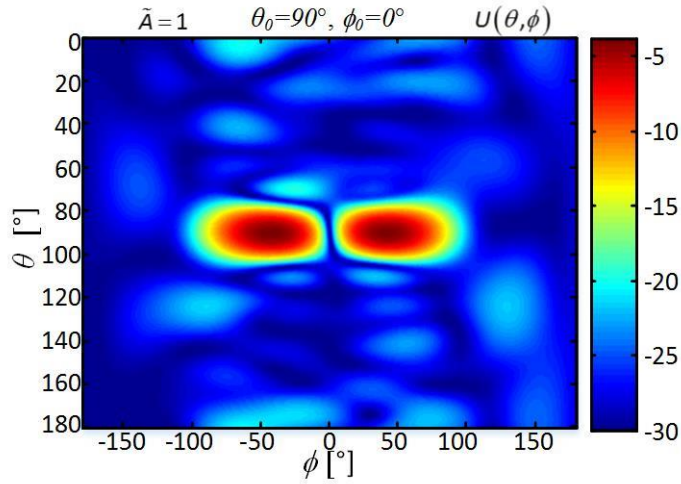
Figure 202. Odd SRA analytical sol., $N=1000, \tilde{A} = 1, \theta = 90°$.

The solution to the characteristic function of an anti-modal spherical random array is given as

$$\Lambda(u,v,w) = \left(\int_{-1}^{0} \frac{3}{4}\left(1-z^2\right)e^{-jwz} + \int_{0}^{1} \frac{3}{4}\left(1-z^2\right)e^{-jwz} \right)\left(\int_{-1}^{1} \frac{3}{4}\left(1-x^2\right)e^{-jxu} \right)\left(\int_{-1}^{1} \frac{3}{4}\left(1-y^2\right)e^{-jyv} \right)$$

$$= \frac{3j\left(2+w^2 - 2\cos(w) - 2w\sin(w)\right)}{2w^3} 3\mathrm{tinc}(u)3\mathrm{tinc}(v)$$

(442)

Here it is more than likely the odd mode with w is a spherical Struve function of the first kind since there is so much duality between circles and spheres (348). The only problem is the literature does

not say anything about spherical Struve functions. Yet it is obvious it contains properties of Bessel and Struve functions.
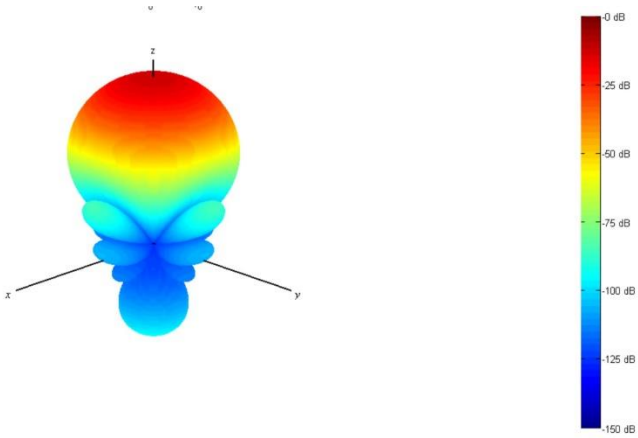
Figure 203. SRA characteristic function broadside $\tilde{A} = 1$.
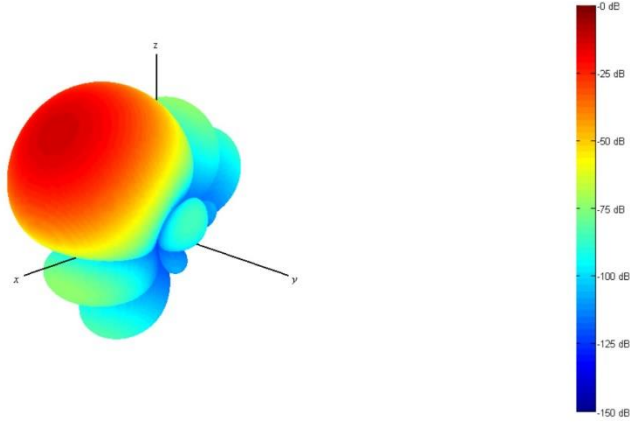
Figure 204. SRA characteristic function 45 degrees $\tilde{A} = 1$.
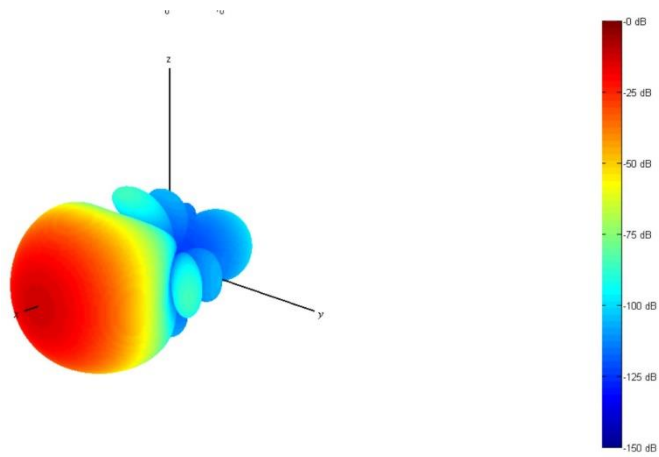
Figure 205. SRA characteristic function endfire $\tilde{A} = 1$.
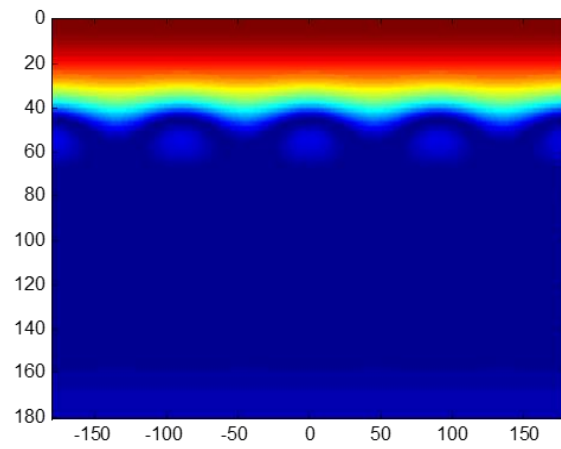
Figure 206. SRA mean pattern., $N=1000$, $\tilde{A} = 1$, $\theta = 0°$.
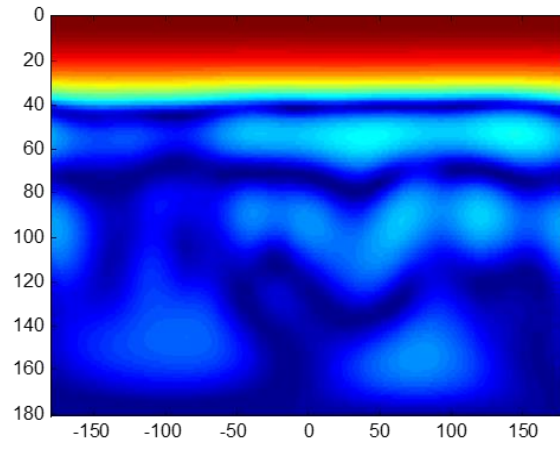
Figure 207. SRA analytical sol., $N{=}1000$, $\tilde{A} = 1, \theta = 0°$.
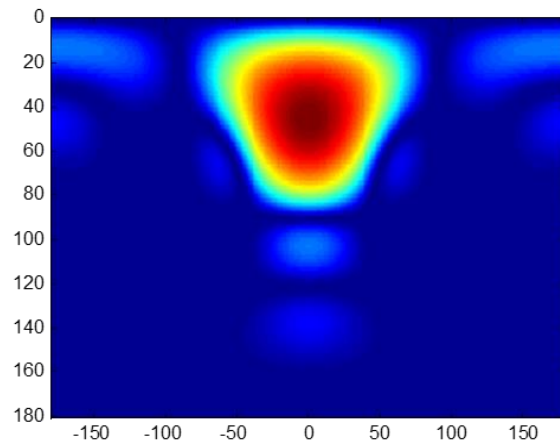
Figure 208. SRA mean pattern., $N{=}1000$, $\tilde{A} = 1, \theta = 45°$.
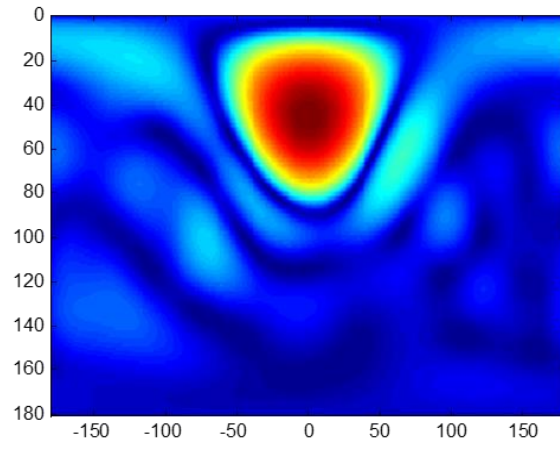
Figure 209. SRA analytical sol., *N=1000*, $\tilde{A} = 1, \theta = 45°$.
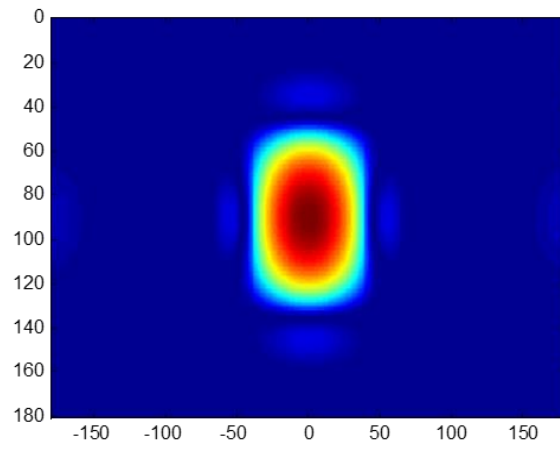
Figure 210. SRA mean pattern., *N=1000*, $\tilde{A} = 1, \theta = 90°$.
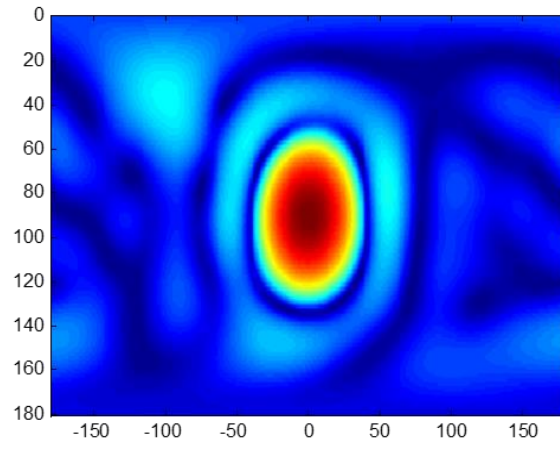
Figure 211. SRA analytical sol., *N=1000*, $\tilde{A} = 1, \theta = 90°$.
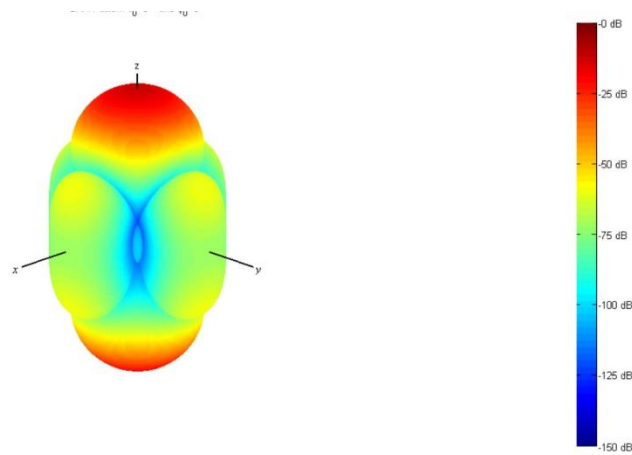
Figure 212. CRA characteristic function broadside $\tilde{A} = 1$.
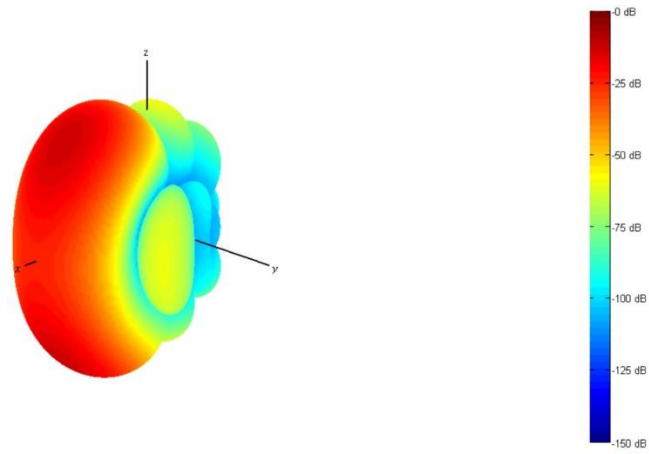
Figure 213. CRA characteristic function 45 degrees $\tilde{A} = 1$.
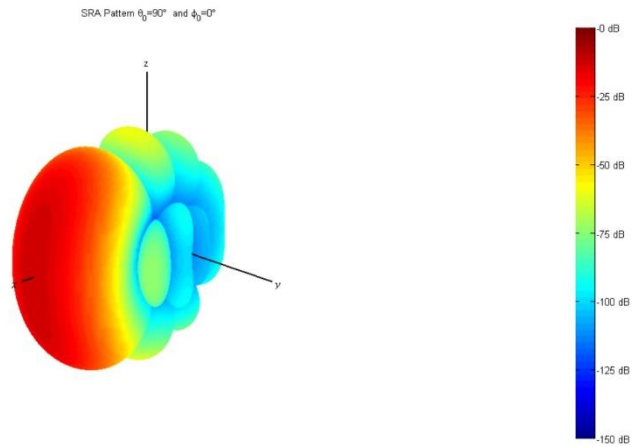
Figure 214. CRA characteristic function endfire $\tilde{A} = 1°$.
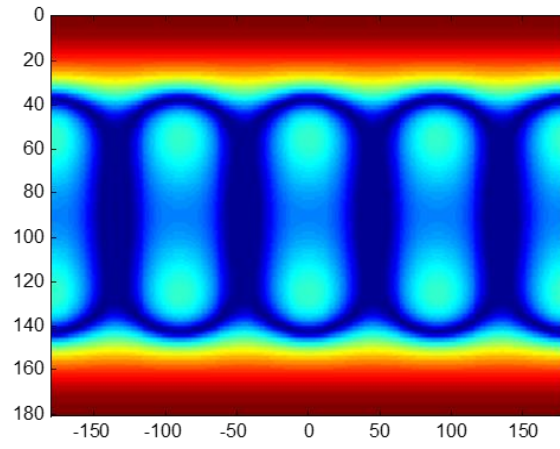
Figure 215. CRA mean pattern, *N=1000*, $\tilde{A} = 1, \theta = 0°$.
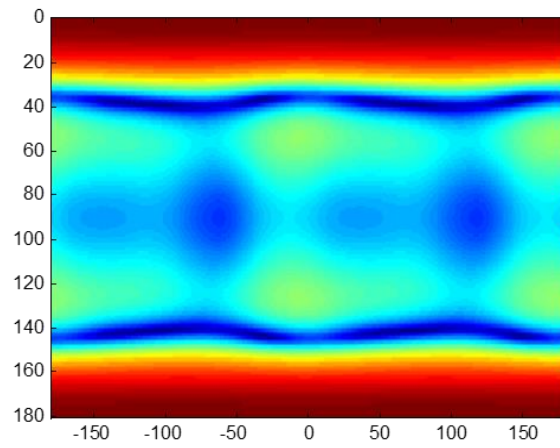
Figure 216. CRA analytical sol., *N=1000*, $\tilde{A} = 1, \theta = 0°$.
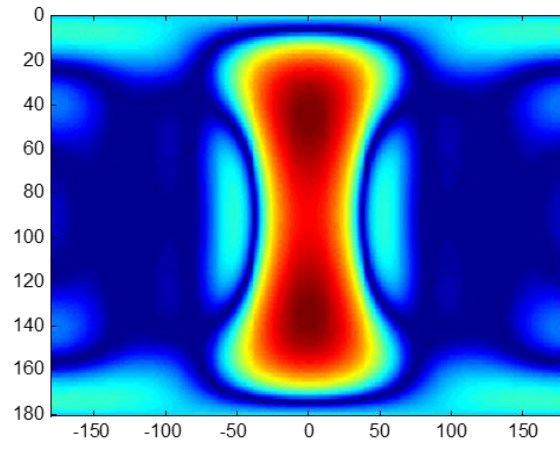
Figure 217. CRA mean pattern, *N=1000*, $\tilde{A} = 1, \theta = 45°$.
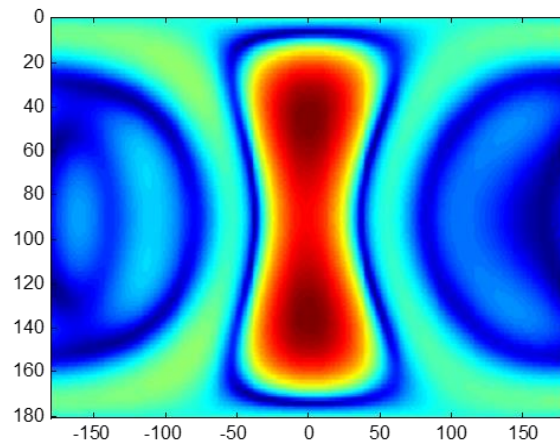
Figure 218. CRA (97) analytical sol., *N=1000*, $\tilde{A} = 1, \theta = 45°$.
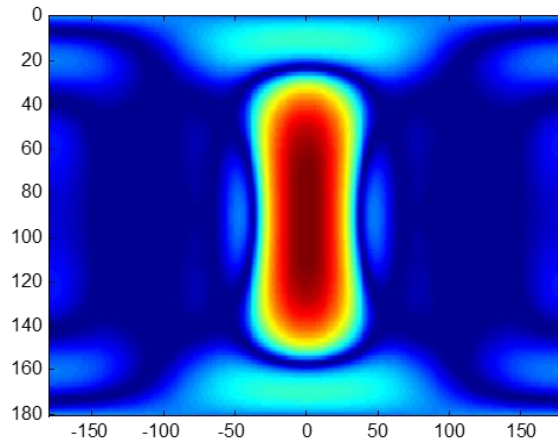
Figure 219. CRA mean pattern, *N=1000*, $\tilde{A} = 1, \theta = 90°$.
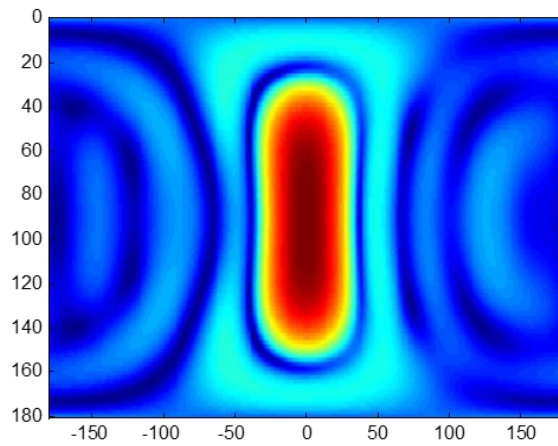
Figure 220. CRA analytical sol., *N=1000*, $\tilde{A} = 1, \theta = 90°$.

14.7 Skewness and Kurtosis

The raw moments of the characteristic function are calculated as (443)-(444) where the total is given by (445).

$$\mu'_{n,U} = \int_{-1}^{1} \cos^{n}(XU) f(U) dU \tag{443}$$

$$\mu'_{n,V} = \int_{-1}^{1} \cos^{n}(XV) f(V) dV \tag{444}$$

$$\mu'_n = \mu'_{n,U} + \mu'_{n,V} \tag{445}$$

For a spherical random array the first four moments come out to be those of (446)-(449).

$$\mu'_{1,U} = \int_{-1}^{1} \cos(XU) \frac{3}{4}(1-U^2) dU = 3\text{tinc}(X)$$

$$\mu'_{1,V} = \int_{-1}^{1} \sin(XV) \frac{3}{4}(1-V^2) dV = 0 \tag{446}$$

$$\mu'_1 = \mu'_{1,U} + \mu'_{1,V} = 3\text{tinc}(X)$$

$$\mu'_{2,U} = \int_{-1}^{1} \cos^2(XU) \frac{3}{4}(1-U^2) dU = \frac{1}{2}(1+3\text{tinc}(2X))$$

$$\mu'_{2,V} = \int_{-1}^{1} \sin^2(XV) \frac{3}{4}(1-V^2) dV = \frac{1}{2}(1-3\text{tinc}(2X)) \tag{447}$$

$$\mu'_2 = \mu'_{2,U} + \mu'_{2,V} = 1$$

$$\mu'_{3,U} = \int_{-1}^{1} \cos^3(XU) \frac{3}{4}(1-U^2) dU = \frac{1}{4}(3\text{tinc}(3X)+9\text{tinc}(t))$$

$$\mu'_{3,V} = \int_{-1}^{1} \sin^3(XV) \frac{3}{4}(1-V^2) dV = 0 \tag{448}$$

$$\mu'_3 = \mu'_{3,U} + \mu'_{3,V} = \frac{1}{4}(3\text{tinc}(3X)+9\text{tinc}(t))$$

$$\mu'_{4,U} = \int_{-1}^{1} \cos^4(XU) \frac{3}{4}(1-U^2) dU = \frac{1}{8}(3+12\text{tinc}(2X)+3\text{tinc}(4X))$$

$$\mu'_{4,V} = \int_{-1}^{1} \sin^4(XV) \frac{3}{4}(1-V^2) dV = \frac{1}{8}(3-12\text{tinc}(2X)+3\text{tinc}(4X)) \tag{449}$$

$$\mu'_4 = \mu'_{4,U} + \mu'_{4,V} = \frac{1}{4}(3+3\text{tinc}(4X))$$

Now the next step in the calculation is to calculate the central moments these are calculated as (450)-(453).

$$\mu_1 = 0 \tag{450}$$

$$\mu_2 = \mu'_2 - \mu'^2_1 \tag{451}$$

$$\mu_3 = 2\mu'^3_1 - 3\mu'_1\mu'_2 + \mu'_3 \tag{452}$$

$$\mu_4 = -3\mu'^4_1 + 6\mu'^2_1\mu'_2 - 4\mu'_1\mu'_3 + \mu'_4 \tag{453}$$

Hence, upon calculating these moments one may find the skewness (454), kurtosis and excess kurtosis (456) by the relations shown below.

$$\gamma_1 = \frac{\mu_3}{\mu_2^{3/2}} \tag{454}$$

$$\beta_2 = \frac{\mu_4}{\mu_2^2} \tag{455}$$

$$\gamma_2 = \frac{\mu_4}{\mu_2^2} - 3 \tag{456}$$

Furthermore it can be shown that the skewness, kurtosis and excess kurtosis can be further generalized in terms of the characteristic function $\Lambda(\mathrm{X})$ by the relations in (457)-(459). Moreover, examples of these moments are shown in Figure 221-Figure 223. What is not illustrated in these figures is that the kurtosis blows up to infinity near the origin meaning there is a sharp peak, i.e. the mainlobe region. The settlement of the kurtosis is likely to mean that the pattern converges similarly to a uniform distribution in the 3dB sidelobe region as illustrated in the example patterns of Figure 224. Alternatively the skewness of the characteristic function is oppositely defined as the expected array factor. For example when the mean array factor is positive the skewness is negative and vice versa.

$$\gamma_1 = \frac{1}{4}\left[\Lambda(3\mathrm{X}) + 3\Lambda(\mathrm{X})\right] \tag{457}$$

$$\beta_2 = \frac{1}{4}\left[3 + \Lambda(4\mathrm{X})\right] \tag{458}$$

$$\gamma_2 = \frac{1}{4}\left[\Lambda(4\mathrm{X})\right] \tag{459}$$
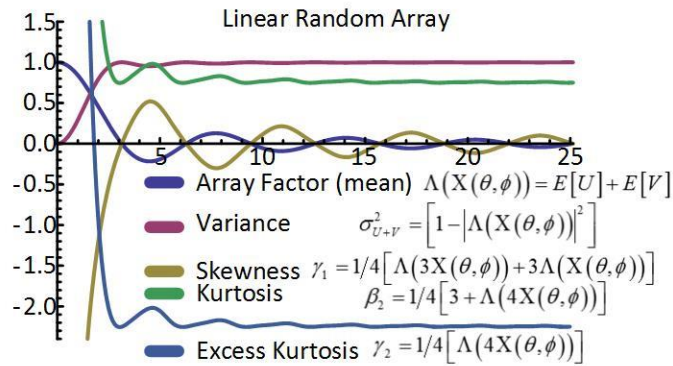
Figure 221. First four moments of the characteristic function of a linear random array.
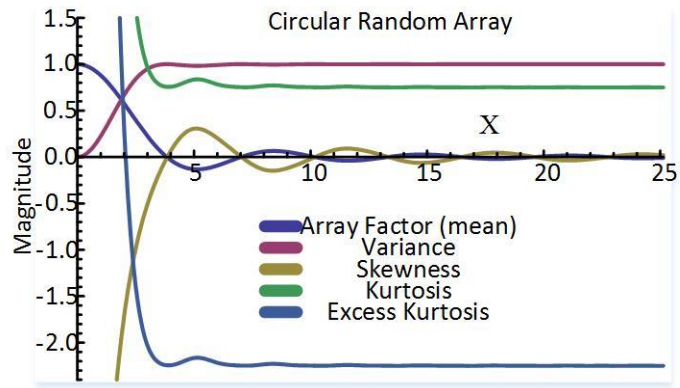
Figure 222. First four moments of the characteristic function of a circular random array.
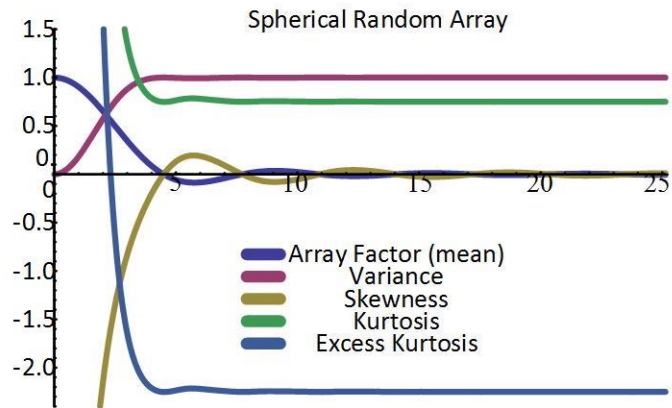
Figure 223. First four moments of the characteristic function of a spherical random array.

Canonical Random Arrays
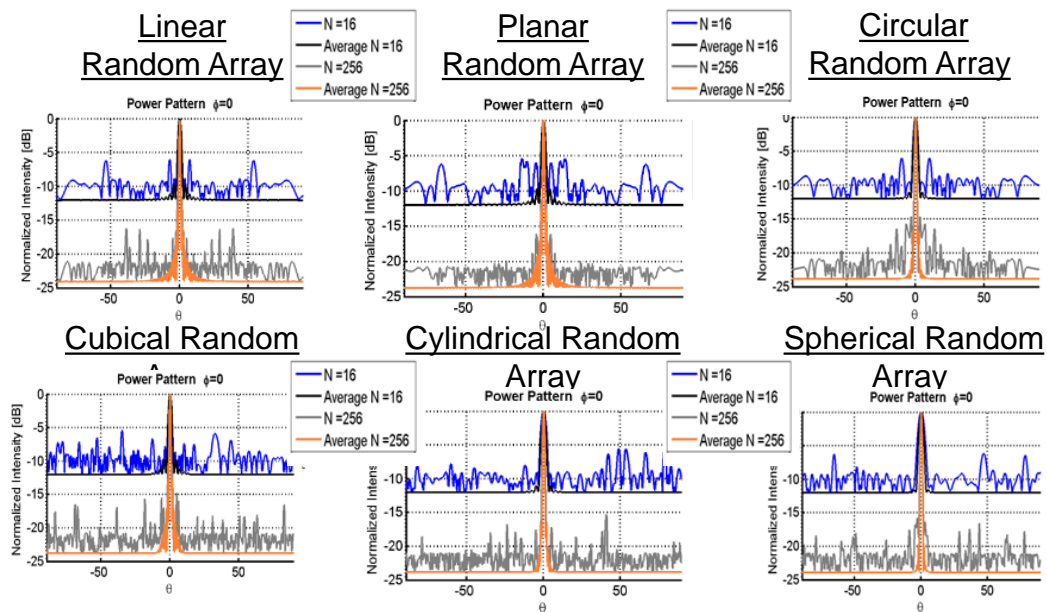
Figure 224. Example of the beampattern of six canonical random arrays.

14.8 Section Conclusion

This section has analyzed the maximum peaking sidelobe in a rigorous statistical sense applicable for beamsteering in either the meridian elevation angle (endfire) or zenith elevation angle (broadside). Results of this method appear to be very accurate when applied far enough away from the main beam such that characteristic function has monotonically decayed into the three dB sidelobe region. Moreover, it was seen that this theory provides greater accuracy than the popular Rayleigh approximation; since inaccuracy occurs for large element populations. Last of all Figure 192 has provided a limiting bound for the maximum peaking sidelobe such that the maximum peaking sidelobe is contained no greater than 12 dB above the average sidelobe level out to aperture sizes spanning $\tilde{A} = 100$. This differs by other work in [101] such that through a rigorous process it is determined that the peak side lobe level is generally unlikely to exceed the average side lobe level by 10 dB.

CHAPTER XV

METHODS OF DETERMINING PHASE ERROR DISTRIBUTIONS

15.1 Linear, Quadratic and Cubic Phase Error

The probability density function is equivalent to an amplitude distribution and thus far it has assumed a uniform phase variation throughout the extent of the random array. However, practical radiators located within a random array are likely to have non-uniform phase fronts caused by one or more of the following:

-First: Displacement of the feed location

-Second: Feeds whose wave fronts that are not ideally cylindrical or spherical as assumed

-Third: Distortion

-Fourth: Physical geometry of the radiator.

The previous criteria give rise to phases errors, and they are more evident in radiators with tilted beams.

Conventional means typically simplify these formulations by assuming phase fronts with either linear, quadratic, or cubic variations. These phase distributions are then associated with its respective amplitude distribution and add an additional phase represented as (460). With an excitation coefficient shown in (461). The distribution $\phi(Z)$ represents a probability distribution of the phase error given by one of the following phase distributions (462)-(464) (linear, quadratic or cubic).

$$E_{\Upsilon^{\vec{r}}}\left|U\left(\theta,\phi\left|\vec{\Upsilon}^{\vec{r}}\right.\right)\right| = \frac{1}{N} + \left(1-\frac{1}{N}\right)\int_{-\infty}^{\infty}\int_{-\infty}^{\infty}\left(\cos\left(\zeta^{\vec{r}}\left(\theta,\phi\right)\left(\Upsilon_n^{\vec{r}}-\Upsilon_m^{\vec{r}}\right)+\phi(Z)\right)\right)f\left(\Upsilon_n^{\vec{r}}\right)f\left(\Upsilon_m^{\vec{r}}\right)d\Upsilon_n^{\vec{r}}d\Upsilon_m^{\vec{r}} \quad (460)$$

$$f_{no}\left(r_n,\theta_{no},\phi_{no}\right) = I_n e^{-jkr_n\cos\psi_{no}+\phi(Z)} \quad (461)$$

linear: $\quad \phi_1(Z) = \beta_1\frac{2}{\ell}Z = \frac{2\pi}{\lambda_1}\frac{1}{\tilde{A}}Z = \frac{2\pi f_1}{c}\frac{1}{A}\lambda Z = 2\pi\frac{f_1}{f}\frac{Z}{A} \quad (462)$

quadratic: $\phi_2(Z) = \beta_2\left(\frac{2}{\ell}Z\right)^2 \quad (463)$

cubic: $\quad \phi_3(Z) = \beta_3\left(\frac{2}{\ell}Z\right)^3 \quad (464)$

$$\ell = 2\tilde{A}$$

The representation of the quadratic term in (463) is analogous to representing a phase variation at the aperture of a horn or that of a defocused (along the symmetry of the axis) reflector and lens antennas [65].

In general the analytical formulations of (462)-(464) can be used to obtain (93), however it should be noted that the analytical formulations become lengthy and complex, especially for the quadratic and cubic distributions and numerical integration of which it may deem almost impossible to obtain closed form solutions and numerical integration should be chosen as an alternative.

Linear phase distributions given by (462) will have a tendency to tilt the main beam of an antenna by an angle θ_0 (given a linear array along the z-axis) and form an symmetrical pattern [65] shown in Figure 225.

$$1/2\int_{-1}^{1} e^{-j(x\phi_{error}+\psi_x)}dx \tag{465}$$

$$\frac{\sin(\phi_{error}+\psi_x)}{\phi_{error}+\psi_x} \tag{466}$$
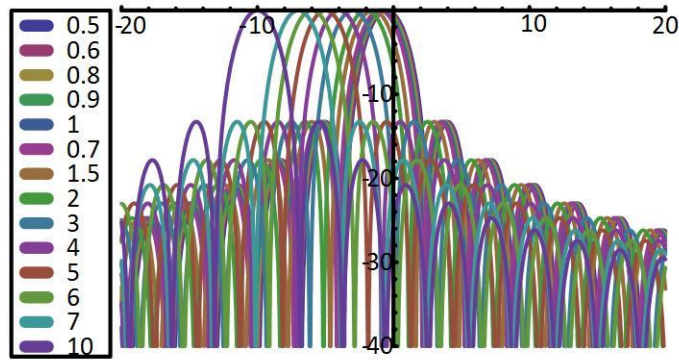
Figure 225. First order phase error.

Quadratic phase errors maintain symmetry of the original problem, but primarily lead to reductions of directivity and increases in sidelobe level on either side of the main lobe. In addition, for moderate phase variations, ideal nulls in the patterns tend to disappear causing minor lobes to blend into each other and even into the main beam. This causes shoulders in the main beam instead of appearing as separate lobes as seen in Figure 226.

$$1/2\int_{-1}^{1} e^{-j(x^2\phi_{error}-\psi_x)}dx \tag{467}$$

$$\frac{(-1)^{3/4} e^{\frac{j\psi_x^2}{4\phi_{error}}} \sqrt{\pi}\left(Erf\left[\frac{(-1)^{1/4}(-2\phi_{error}+\psi_x)}{2\sqrt{\phi_{error}}}\right] - Erf\left[\frac{(-1)^{1/4}(2\phi_{error}+\psi_x)}{2\sqrt{\phi_{error}}}\right]\right)}{4\sqrt{\phi_{error}}} \tag{468}$$

234
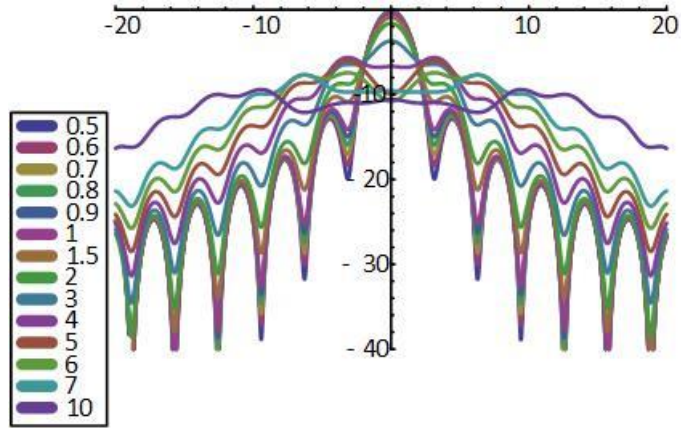
Figure 226. Second order phase error.

Additional analysis of this type of behavior can be found in quadratic phase error on horn antennas [65].

Cubic phase distributions introduce not only a tilt in the beam but also decrease the directivity. The newly formed patters are symmetrical. The minor lobes on one side are increased in magnitude and those on the other side are reduced in intensity as seen in Figure 227.
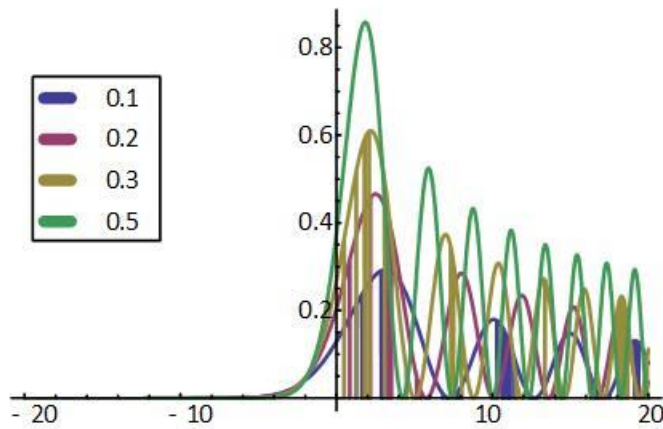
Figure 227. Third order phase error.

$$\int_{-Infinity}^{Infinity} e^{-j(x^3/\phi_{error} - x\psi_x)} dx, \left(\phi_{error} \in Reals \, \& \, \psi_x \in Reals\right) \tag{469}$$

235

$$\frac{1}{9}\pi\left(\begin{array}{l}\sqrt{j\phi_{error}}\sqrt{j\psi_x}\,J\left(-\frac{1}{3},\frac{2\sqrt{j\phi_{error}}\,(j\psi_x)^{3/2}}{3\sqrt{3}}\right)-j\sqrt{\phi_{error}}\sqrt{\psi_x}\,J\left(-\frac{1}{3},-\frac{2\sqrt{\phi_{error}}\,\psi_x^{3/2}}{3\sqrt{3}}\right)-\\[2mm]\sqrt{j\phi_{error}}\sqrt{j\psi_x}\,J\left(\frac{1}{3},\frac{2\sqrt{j\phi_{error}}\,(j\psi_x)^{3/2}}{3\sqrt{3}}\right)+j\sqrt{\phi_{error}}\sqrt{j\psi_x}\,J\left(\frac{1}{3},-\frac{2\sqrt{\phi_{error}}\,Psi^{3/2}}{3\sqrt{3}}\right)\end{array}\right) \qquad (470)$$

15.2 Phase Error Relation to Horn Antennas

To illustrate the effects of phase error the simple horn antenna is analyzed. For simplicity this analysis focuses upon a rectangular E-plane horn illustrated in Figure 228.

The type of horn used, direction and amount of taper (flare) can have a profound effect on the overall performance of the element as a radiator. Moreover, since this paper has demonstrated that the analytical method of random arrays relates almost identically to the theory of aperture antennas. By this means it is well known that one assumes an infinite plane that coincides with the aperture of the horn such that the fields just outside of the aperture are zero. This method is better known as using equivalent principle techniques. Whereas the fields inside the horn are not TEM and propagate in terms of cylindrical TE and TM wave functions which include Hankel functions. These are found by treating the horn as a radial waveguide [152]-[154].

The well-known first order mode of a waveguide can be shown if the fields of the waveguide are those of its dominant TE_{10} mode and secondly when the horn length is large compared to the aperture dimensions. The parameter E_1 is a constant and the primes designate fields at the aperture of the horn. Thus, these fields represent the fields for a rectangular aperture with dimensions of a and $b_1\left(b_1 > a\right)$, but with the exception of a complex exponential term used to represent the quadratic phase variations of the field over the aperture of the horn.

The necessity of the quadratic phase variations is illustrated geometrically in Figure 229. Also for completeness the mathematics for this phase correction are shown in (476)-(477) where (477) is referred as a spherical phase term.

$$E'_{z'} = E'_{x'} = H'_{y'} = 0 \qquad (471)$$

$$E'_y\left(x',y'\right) \simeq E_1 \cos\left(\frac{\pi}{a}x'\right)e^{-j\left[ky'^2/(2\rho_1)\right]} \qquad (472)$$

$$H'_z\left(x',y'\right) \simeq jE_1\left(\frac{\pi}{ka\eta}\right)\sin\left(\frac{\pi}{a}x'\right)e^{-j\left[ky'^2/(2\rho_1)\right]} \qquad (473)$$

$$H'_x\left(x',y'\right) \simeq -\frac{E_1}{\eta}\cos\left(\frac{\pi}{a}x'\right)e^{-j\left[ky'^2/(2\rho_1)\right]} \qquad (474)$$

$$\rho_1 = \rho_e \cos\psi \qquad (475)$$

$$\left[\rho_1 + \delta(y') \right]^2 = \rho_1^2 + (y')^2 \qquad (476)$$

$$\delta(y') = -\rho_1 + \rho_1\sqrt{\rho_1^2 + y'^2} = -\rho_1 + \rho_1\sqrt{1 + \left(\frac{y'}{\rho_1}\right)^2} \qquad (477)$$

Expanding using the binomial expansion gives (478) and when multiplying (478) by a phase factor k, one obtains the result to the phase term in (472)-(474).

$$\delta(y') \simeq -\rho_1 + \rho_1\left[1 + \frac{1}{2}\left(\frac{y'}{\rho_1}\right)^2\right] = \frac{1}{2}\left(\frac{y'}{\rho_1}\right)^2 \qquad (478)$$
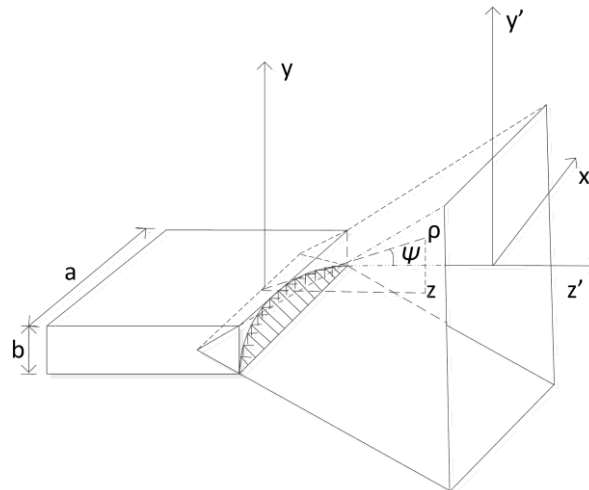
Figure 228. Horn antenna.
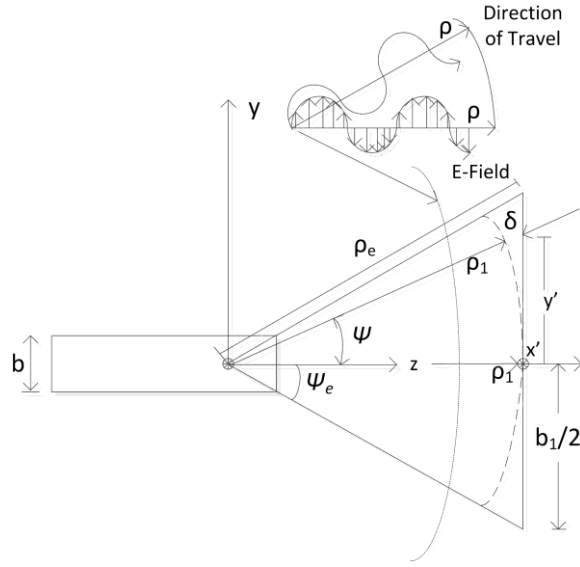
Figure 229. Horn antenna side (cut plane).

15.3 Random Array Phase Error Relation to Horn Antennas

Inserting the phase correction term (478) for a uniformly distributed and normalized (a=1,b1=2) square planar random array given in the x-y plane with uniform tapers such that $A_n(x) = 1$ and $A_n(y) = 1$ into the random array space factor (479) gives (480).

$$\text{RASF}(\theta, \phi) = \Lambda = \int_{-1}^{1} \int_{-1}^{1} \Re e \left[\begin{array}{c} e^{j\alpha(\theta,\phi)(\tilde{x}_n)} e^{j\beta(\theta,\phi)(\tilde{y}_n)} e^{j\varsigma_n(x',y')} \\ f(x,y) A_n(x) A_n(y) d\tilde{x}_n d\tilde{y}_n \end{array} \right] \tag{479}$$

$$\text{RASF}(\theta, \phi) = \Lambda = \frac{1}{4} \int_{-1}^{1} \int_{-1}^{1} \Re e \left[\begin{array}{c} e^{j\alpha(\theta,\phi)(\tilde{x}_n)} e^{j\beta(\theta,\phi)(\tilde{y}_n)} e^{j\frac{1}{2}\left(\frac{\tilde{y}_n}{\rho_1}\right)^2} \\ d\tilde{x}_n d\tilde{y}_n \end{array} \right] \tag{480}$$

The parameter ρ_1 in the case of the RASF will serve as a tuning factor. Thus, for large values (480) will be analogous to measuring fields in the far field such that the quadratic error term (478) decays and rapidly approaches zero. Otherwise when the factor is small the wave appears as a cylindrical wavefront across the aperture and critically damps the performance of the main beam as seen in Figure 226.

15.4 Estimating Phase Error Using the Hyperspherical Bessel Fourier Transform

An *n-sphere* [155], [156] is an *n* dimensional manifold in Euclidean space. Also sometimes called a hypersphere for *n>2* and a glome for *n=3*. To define its coordinate system in an *n* dimensional Euclidean space it is analogous to a spherical coordinate system defined for 3-diemensional Euclidean space, but

with n dimensions. This type of coordinate system is shown below with a few examples of the first few specific spheres: (482) is the 2-vol of the surface of a 2-sphere (ordinary 2D surface area), (483) is the 3-vol of the E3 embedding space enclosed by a 2-sphere (ordinary 3D sphere volume), (484) is the 3-vol of the surface of a 3-sphere, (485) is the 4-vol of the E4 embedding space enclosed by a 3-sphere. General formulas relating the volume of an n-sphere are given in (486)-(488). Thus, these formulations should serve as a corollary in helping the reader understand the next part of this section.

$$
\begin{aligned}
x_1 &= r\cos(\phi_1) \\
x_2 &= r\sin(\phi_1)\cos(\phi_2) \\
x_3 &= r\sin(\phi_1)\sin(\phi_2)\cos(\phi_3) \\
&\vdots \\
x_{n-1} &= r\sin(\phi_1)\ldots\sin(\phi_{n-2})\cos(\phi_{n-1}) \\
x_n &= r\sin(\phi_1)\ldots\sin(\phi_{n-1})\cos(\phi_n)
\end{aligned}
\tag{481}
$$

$$
(s2,2) = \iint (rd\theta)(r\sin\theta d\phi) = 4\pi r^2
\tag{482}
$$

$$
(s2,3) = \iiint dr(rd\theta)(r\sin\theta d\phi) = \frac{4}{3}\pi r^3
\tag{483}
$$

$$
(s3,3) = \iiint (rd\theta)(r\sin\theta d\phi)(r\sin\theta\sin\phi d\varphi) = 2\pi^2 r^3
\tag{484}
$$

$$
(s3,3) = \iiiint (dr)(rd\theta)(r\sin\theta d\phi)(r\sin\theta\sin\phi d\varphi) = \frac{1}{2}\pi^2 r^4
\tag{485}
$$

$$
V_n(R) = C_n R^n
\tag{486}
$$

$$
C_n = \frac{\pi^{n/2}}{\Gamma(n/2 + 1)}
\tag{487}
$$

$$
V_5(R) = \frac{15\pi^3}{8}
\tag{488}
$$

When errors are present in the location parameters one may redefine the initial phase as (489).

$$
\begin{aligned}
\cos(\breve{\psi}_n)^+ &= k\breve{r}_n \sin\breve{\theta}_n \sin\theta \cos(\phi - \breve{\phi}_n) + \cos\breve{\theta}_n \cos\theta \\
&= \begin{bmatrix} k(r_n + \delta r_n)\sin(\theta_n + \delta\theta_n)\sin(\theta)\cos(\phi - (\phi_n + \delta\phi_n)) + \\ \cos(\theta_n + \delta\theta_n)\cos(\theta) \end{bmatrix} \\
&= \begin{bmatrix} kr_n \sin(\theta_n + \delta\theta_n)\cos(\phi - (\phi_n + \delta\phi_n)) + \\ k\delta r_n \sin(\theta_n + \delta\theta_n)\sin(\theta)\cos(\phi - (\phi_n + \delta\phi_n)) + \\ \cos(\theta_n + \delta\theta_n)\cos(\theta) \end{bmatrix}
\end{aligned}
\tag{489}
$$

$$F\left(\phi\,\middle|\,\vec{r}_n,\vec{\phi}_n,\vec{\theta}_n,\delta\vec{r}_n,\delta\vec{\phi}_n,\delta\vec{\theta}_n\right)$$

$$=\frac{1}{N}\sum_{k=1}^{N}e\left[jk\left[\left(r_n+\delta r_n\right)\left[\sin\left(\theta_n+\delta\theta_n\right)\begin{Bmatrix}\cos\left(\phi-\left(\phi_n+\delta\phi_n\right)\right)\sin\theta\\-\cos\left(\phi_0-\left(\phi_n+\delta\phi_n\right)\right)\sin\theta_0\end{Bmatrix}\right]\\+\left(r_n+\delta r_n\right)\cos\left(\delta\theta_n+\theta_n\right)\left[\left(\cos\theta_o-\cos\theta\right)\right]\right]\right] \tag{490}$$

$$=\frac{1}{N}\sum_{k=1}^{N}e^{j\zeta(\theta,\phi)(\delta\Upsilon_n)}e^{j\xi(\theta)(\delta\Upsilon_n)}$$

$$\delta=\tan^{-1}\left[\frac{\sin\theta\sin\phi-\sin\theta_0\sin\phi_0}{\sin\theta\cos\phi-\sin\theta_0\cos\phi_0}\right]$$

$$\rho_0=\sqrt{\begin{aligned}\left(\sin\theta_0\cos\phi_0-\sin\theta\cos\phi\right)^2+\\\left(\sin\theta_0\sin\phi_0-\sin\theta\sin\phi\right)^2\end{aligned}} \tag{491}$$

$$\Upsilon_n=\left(r_n\right)\sin\left(\theta_n\right)\cos\left(\delta-\left(\phi_n\right)\right)$$

$$\delta\Upsilon_n=\left(r_n+\delta r_n\right)\sin\left(\theta_n+\delta\theta_n\right)\cos\left(\delta-\left(\phi_n+\delta\phi_n\right)\right)$$

$$\delta\Upsilon_n=\left(r_n+\delta r_n\right)\cos\left(\delta\theta_n+\theta_n\right) \tag{492}$$

Variables $\left\{\delta r_n,\delta\phi_n,\delta\theta_n\right\}$ are characterizing the corresponding error in location, jitter, noise of the environment etc. and are assumed to be i.i.d. and independent of r_n,ϕ_n and θ_n for simplicity (i.e. correlation amongst the variables is zero). To base the analysis on a compound random variable with no coupling the random variables $\delta\Upsilon_n,\delta\Upsilon_n$ are uncoupled such that

$$\delta\Upsilon_n=\left(r_n+\delta r_n\right)\sin\left(\theta_n+\delta\theta_n\right)\cos\left(\phi-\left(\phi_n+\delta\phi_n\right)\right)$$

$$=\begin{bmatrix}\cos\theta_n\cos\phi_n\delta r_n\sin\delta\theta_n\cos\delta\phi_n\cos\delta+r_n\cos\theta_n\cos\phi_n\sin\delta\theta_n\cos\delta\phi_n\cos\delta+\\\cos\theta_n\cos\phi_n\delta r_n\sin\delta\theta_n\sin\delta\phi_n\sin\delta+r_n\cos\theta_n\cos\phi_n\sin\delta\theta_n\sin\delta\phi_n\sin\delta-\\\cos\theta_n\sin\phi_n\delta r_n\sin\delta\theta_n\sin\delta\phi_n\cos\delta-r_n\cos\theta_n\sin\phi_n\sin\delta\theta_n\sin\delta\phi_n\cos\delta+\\\cos\theta_n\sin\phi_n\delta r_n\sin\delta\theta_n\cos\delta\phi_n\sin\delta+r_n\cos\theta_n\sin\phi_n\sin\delta\theta_n\cos\delta\phi_n\sin\delta+\\\sin\theta_n\cos\phi_n\delta r_n\cos\delta\theta_n\cos\delta\phi_n\cos\delta+r_n\sin\theta_n\cos\phi_n\cos\delta\theta_n\cos\delta\phi_n\cos\delta+\\\sin\theta_n\cos\phi_n\delta r_n\cos\delta\theta_n\sin\delta\phi_n\sin\delta+r_n\sin\theta_n\cos\phi_n\cos\delta\theta_n\sin\delta\phi_n\sin\delta-\\\sin\theta_n\sin\phi_n\delta r_n\cos\delta\theta_n\sin\delta\phi_n\cos\delta-r_n\sin\theta_n\sin\phi_n\cos\delta\theta_n\sin\delta\phi_n\cos\delta+\\\sin\theta_n\sin\phi_n\delta r_n\cos\delta\theta_n\cos\delta\phi_n\sin\delta+r_n\sin\theta_n\sin\phi_n\cos\delta\theta_n\cos\delta\phi_n\sin\delta\end{bmatrix} \tag{493}$$

$$\delta\Upsilon_n \approx$$

$$= \begin{bmatrix}
+\cos\theta_n\cos\phi_n\delta r_n\left(\delta\theta_n\right)\left(1-\dfrac{\delta\phi_n^2}{2}\right)\cos\delta + r_n\cos\theta_n\cos\phi_n\left(\delta\theta_n\right)\left(1-\dfrac{\delta\phi_n^2}{2}\right)\cos\delta \\
+\cos\theta_n\cos\phi_n\delta r_n\left(\delta\theta_n\delta\phi_n\right)\sin\delta + r_n\cos\theta_n\cos\phi_n\left(\delta\theta_n\delta\phi_n\right)\sin\delta \\
-\cos\theta_n\sin\phi_n\delta r_n\left(\delta\theta_n\delta\phi_n\right)\cos\delta - r_n\cos\theta_n\sin\phi_n\left(\delta\theta_n\delta\phi_n\right)\cos\delta \\
+\cos\theta_n\sin\phi_n\delta r_n\left(\delta\theta_n\right)\left(1-\dfrac{\delta\phi_n^2}{2}\right)\sin\delta + r_n\cos\theta_n\sin\phi_n\left(\delta\theta_n\right)\left(1-\dfrac{\delta\phi_n^2}{2}\right)\sin\delta \\
+\sin\theta_n\cos\phi_n\delta r_n\left(1-\dfrac{\delta\theta_n^2}{2}\right)\left(1-\dfrac{\delta\phi_n^2}{2}\right)\cos\delta + r_n\sin\theta_n\cos\phi_n\left(1-\dfrac{\delta\theta_n^2}{2}\right)\left(1-\dfrac{\delta\phi_n^2}{2}\right)\cos\delta \\
+\sin\theta_n\cos\phi_n\delta r_n\left(1-\dfrac{\delta\theta_n^2}{2}\right)\left(\delta\phi_n\right)\sin\delta + r_n\sin\theta_n\cos\phi_n\left(1-\dfrac{\delta\theta_n^2}{2}\right)\left(\delta\phi_n\right)\sin\delta \\
-\sin\theta_n\sin\phi_n\delta r_n\left(1-\dfrac{\delta\theta_n^2}{2}\right)\left(\delta\phi_n\right)\cos\delta - r_n\sin\theta_n\sin\phi_n\left(1-\dfrac{\delta\theta_n^2}{2}\right)\left(\delta\phi_n\right)\cos\delta \\
+\sin\theta_n\sin\phi_n\delta r_n\left(1-\dfrac{\delta\theta_n^2}{2}\right)\left(1-\dfrac{\delta\phi_n^2}{2}\right)\sin\delta + r_n\sin\theta_n\sin\phi_n\left(1-\dfrac{\delta\theta_n^2}{2}\right)\left(1-\dfrac{\delta\phi_n^2}{2}\right)\sin\delta
\end{bmatrix} \quad (494)$$

$$\delta\Upsilon_n \approx\approx$$

$$= \begin{bmatrix}
+\cos\theta_n\cos\phi_n\delta r_n\left(\delta\theta_n\right)(1)\cos\delta + r_n\cos\theta_n\cos\phi_n\left(\delta\theta_n\right)(1)\cos\delta \\
+\cos\theta_n\cos\phi_n\delta r_n\left(\delta\theta_n\delta\phi_n\right)\sin\delta + r_n\cos\theta_n\cos\phi_n\left(\delta\theta_n\delta\phi_n\right)\sin\delta \\
-\cos\theta_n\sin\phi_n\delta r_n\left(\delta\theta_n\delta\phi_n\right)\cos\delta - r_n\cos\theta_n\sin\phi_n\left(\delta\theta_n\delta\phi_n\right)\cos\delta \\
+\cos\theta_n\sin\phi_n\delta r_n\left(\delta\theta_n\right)(1)\sin\delta + r_n\cos\theta_n\sin\phi_n\left(\delta\theta_n\right)(1)\sin\delta \\
+\sin\theta_n\cos\phi_n\delta r_n(1)(1)\cos\delta + r_n\sin\theta_n\cos\phi_n(1)(1)\cos\delta \\
+\sin\theta_n\cos\phi_n\delta r_n(1)\left(\delta\phi_n\right)\sin\delta + r_n\sin\theta_n\cos\phi_n(1)\left(\delta\phi_n\right)\sin\delta \\
-\sin\theta_n\sin\phi_n\delta r_n(1)\left(\delta\phi_n\right)\cos\delta - r_n\sin\theta_n\sin\phi_n(1)\left(\delta\phi_n\right)\cos\delta \\
+\sin\theta_n\sin\phi_n\delta r_n(1)(1)\sin\delta + r_n\sin\theta_n\sin\phi_n(1)(1)\sin\delta
\end{bmatrix} \quad (495)$$

$$\delta\Gamma_n = \left(r_n+\delta r_n\right)\cos\left(\delta\theta_n+\theta_n\right)$$
$$= \cos\theta_n\delta r_n\cos\delta\theta_n - \sin\theta_n\delta r_n\sin\delta\theta_n + r_n\cos\theta_n\cos\delta\theta_n - r_n\sin\theta_n\sin\delta\theta_n \quad (496)$$

$$\delta\Gamma_n \approx \cos\theta_n\delta r_n\cos\delta\theta_n - \sin\theta_n\delta r_n\sin\delta\theta_n + r_n\cos\theta_n\cos\delta\theta_n - r_n\sin\theta_n\sin\delta\theta_n$$

$$\cos\theta_n = \frac{x_n}{r_n} = \frac{x_n}{\sqrt{x_n^2+y_n^2}} \quad (497)$$

since $x_n = r_n\cos\theta_n$

In terms of Hyperspherical coordinates the joint density (498) and marginal density (499) necessary for finding the error in one of the five parameter compound random variables can be calculated in the following fashion.

$$f\left(x,y,z,w,v\right) = \frac{8\pi^2}{15} \quad (498)$$

$$f(x) = \left| \int_{-\sqrt{(1+\phi_{\max})^2-x^2}}^{\sqrt{(1+\phi_{\max})^2-x^2}} \int_{-\sqrt{(1+\phi_{\max})^2-x^2-y^2}}^{\sqrt{(1+\phi_{\max})^2-x^2-y^2}} \int_{-\sqrt{(1+\phi_{\max})^2-x^2-y^2-z^2}}^{\sqrt{(1+\phi_{\max})^2-x^2-y^2-z^2}} \int_{-\sqrt{(1+\phi_{\max})^2-x^2-y^2-z^2-w^2}}^{\sqrt{(1+\phi_{\max})^2-x^2-y^2-z^2-w^2}} \frac{15}{8\pi^2} \, dv \, dw \, dz \, dy \right|$$

$$= \frac{4}{15}(-1+x^2)^2 \Big|_{\phi_{\max}=0}$$

(499)

However, a simpler and more tractable method of finding random error is done in [9] for a circular random array and will be done in this section for a spherical random array. To do this procedure one simplifies the array factor at the meridian angle $\theta = \theta_0 = \pi/2$ and follows the method shown in (500)-(507) the following manner.

$$U\left(\phi \big| \vec{r}_n, \vec{\theta}_n, \vec{\phi}_n, \delta\vec{r}_n, \delta\vec{\theta}_n, \delta\vec{\phi}_n\right)$$
$$= \frac{1}{N} + \frac{1}{N^2} \sum_{m=1}^{N} \sum_{\substack{n=1 \\ m \neq n}}^{N} e^{j4\pi\tilde{A}\left(\Upsilon_n \sin\left(\frac{\phi_o-\phi-\delta\phi_n}{2}\right) - \Upsilon_m \sin\left(\frac{\phi_o-\phi-\delta\phi_m}{2}\right)\right)} e^{j(k(u_n-u_m))}$$

(500)

$$u_n \triangleq \delta r_n \sin\tilde{\theta}_n \cos\left(\phi_n + \delta\phi_n - \phi_o\right)$$

(501)

$$f_u(u) = \frac{2}{r_{\max}^2 \pi} \sqrt{r_{\max}^2 - u^2}, \quad -r_{\max} \leq u \leq r_{\max}$$

(502)

$$f_{\delta\phi}(\delta\phi) = \frac{1}{2}, \quad -\phi_{\max} \leq \phi \leq \phi_{\max}$$

(503)

$$U_{av}(\phi) = \frac{1}{N} + \left(1 - \frac{1}{N}\right) \left|A_{\Upsilon_n}(\phi)\right|^2 \left|A_{u_n}\right|^2$$

(504)

$$A_{u_n} \triangleq E_u\left[e^{jk(u_k-u_l)}\right] = \left|3\mathrm{tinc}(kr_{\max})\right|^2$$

(505)

$$A_{\Upsilon_n}(\phi) = E_{\delta\phi}\left[3\mathrm{tinc}\left(4\pi\tilde{A}\sin\left(\frac{\phi-\delta\phi_n}{2}\right)\right)\right]$$

(506)

$$A_{\Upsilon_n}(\phi) = \frac{1}{2}\left(1 - \frac{\phi}{\phi_{\max}}\right) {}_1F_2\left(\frac{1}{2};\frac{3}{2},2;-\left(\pi\tilde{A}(\phi-\phi_{\max})\right)^2\right)$$
$$+ \frac{1}{2}\left(1 + \frac{\phi}{\phi_{\max}}\right) {}_1F_2\left(\frac{1}{2};\frac{3}{2},2;-\left(\pi\tilde{A}(\phi+\phi_{\max})\right)^2\right)$$

(507)

The solutions here give a hypergeometric function ${}_1F_2\left(\frac{1}{2};\frac{3}{2},2;-(x)^2\right)$ which produces a maximum when $-\left(\pi\tilde{A}(\phi-\phi_{\max})\right)^2 = 0$ or $-\left(\pi\tilde{A}(\phi+\phi_{\max})\right)^2 = 0$ and happens when $\phi = \phi_{\max}$ or $\phi = -\phi_{\max}$

. This is also assuming the value of $\tilde{A} \neq 0$, which would be trivial. Consequently, this expression is independent of $\tilde{A}$, and produces two symmetric peaks about the mainbeam at $\phi = \pm\phi_{\max}$, which is known as a pointing error therefore, causing the mainbeam to spread over a factor of $|\phi_{\max}|$ [9]. For example, when $\phi = 0$, one obtains

$$A_{v_k}(0) = {}_1F_2\left(\frac{1}{2};\frac{3}{2},2;-\left(\pi\tilde{A}\phi_{\max}\right)^2\right) \tag{508}$$

Also, the terms $\left|A_{u_k}\right|^2, \left|A_{\Upsilon_n}(\phi)\right|^2$ correspondingly have different connotations in respect to how the mainbeam is affected.

The term $\left|A_{u_k}\right|^2$ represents degradation of the mainbeam. When the term $\left|3\mathrm{tinc}\left(kr_{\max}\right)\right|^2$ is evaluated with $r_{\max} = 0$ as shown in (509), the main beam suffers no degradation yet degradation occurs $r_{\max} \neq 0$.

$$\left|3\mathrm{tinc}\left(kr_{\max}\right)\right|^2\bigg|_{r_{\max}=0} = 1 \tag{509}$$

Alternatively $\left|A_{\Upsilon_n}(\phi)\right|^2$ represents a pointing error, in addition to mainbeam degradation error. To suppress this degradation error below 3dB one should observe the inequality in (510) yielding (511). It follows that by observing the inequality for large $\tilde{A}$; the requirement of minimum angle ambiguity becomes severe. Therefore very accurate phase information should be sought for very large random arrays.

$$\frac{\pi A\phi_{n_{\max}}}{\lambda} \leq \frac{1}{2} \tag{510}$$

$$\phi_{n_{\max}} \leq \frac{1}{2}\frac{\lambda}{\pi A} = \frac{1}{2\pi\tilde{A}} \tag{511}$$

15.5 Random Array on Receive

It has been shown by [157] that if the local oscillators (LO) of the elements are not synchronized correctly, or if the phase corrections are in error due to position uncertainty that a common LO reference is not possible for the exact phase shifts to be maintained such that all transmitters are focused at the receive antenna. Moreover it has been shown by [157] the power at the receiver antenna output from multiple transmit signals as a function of random phase error of the type that would occur with imperfect phase synchronization as that given by

$$P_L = \frac{P_t G_t G_r \lambda^2}{(4\pi R)^2}\left[N^2 e^{-\delta^2} + \left(1 - e^{-\delta^2}\right)N\right]$$
$$\Rightarrow \frac{P_L}{N^2} = \frac{P_t G_t G_r \lambda^2}{(4\pi R)^2}\left[\frac{1}{N} + \left(1 - \frac{1}{N}\right)e^{-\bar{\delta}^2}\right] \tag{512}$$

243

"The first term in the brackets is the coherent part which increases as N^2, whereas the second term is the noncoherent part which increases as N. This is analogous to the result derived by Ruze [208] for the effect of random errors on antenna patterns." [157] The term δ encapsulates the error occurred in the transmitters and it is explained that this term should be defined by its variance $\bar{\delta}^2$. This makes it convenient since the Fourier transform of a Gaussian is a Gaussian such that

$$E\left(e^{j\bar{\delta}^2}\right) = e^{-j\bar{\delta}^2} \tag{513}$$

Thus, this is equivalent to modeling a random array with second order phase error, which has been explained previously.

15.6 Array Factor (Time Independent with Location Error)

Assuming imperfect spatial position independent of time we obtain (514).

$$F\left(\theta,\phi \middle| \delta\vec{\Upsilon}^{\vec{x},\vec{y},\vec{z}}\right) = \frac{e^{-jkr_0}}{N} \sum_{n=1}^{N} e^{j\left(\delta r_n^{\vec{x},\vec{y},\vec{z}}\right)2\pi\tilde{A}\rho_0} \tag{514}$$

$$\delta\Upsilon_n^{\vec{x},\vec{y},\vec{z}} = (r_n + \delta r_n)\sin(\theta_n + \delta\theta_n)\cos\big((\phi_n + \delta\phi_n) - \delta\big) + (r_n + \delta r_n)\cos(\delta\theta_n + \theta_n)\cos\gamma \tag{515}$$

The total random variable (515) is decomposed into three spatial compound random variables (516)-(518) in accordance to the product of directional sine and cosine factors (519)-(522). These relations provide a simplified imperfectly spatial and phase synchronized array factor of (523).

$$\begin{aligned}
\delta\Upsilon_n^{\vec{x}} &= (r_n + \delta r_n)\sin(\theta_n + \delta\theta_n)\cos\big((\phi_n + \delta\phi_n)\big) \\
&= \begin{bmatrix} (r_n + \delta r_n)\cos\theta_n \cos\phi_n \sin\delta\theta_n \cos\delta\phi_n - (r_n + \delta r_n)\cos\theta_n \sin\phi_n \sin\delta\theta_n \sin\delta\phi_n + \\ (r_n + \delta r_n)\sin\theta_n \cos\phi_n \cos\delta\theta_n \cos\delta\phi_n - (r_n + \delta r_n)\sin\theta_n \sin\phi_n \cos\delta\theta_n \sin\delta\phi_n \end{bmatrix}
\end{aligned} \tag{516}$$

$$\begin{aligned}
\delta\Upsilon_n^{\vec{y}} &= (r_n + \delta r_n)\sin(\theta_n + \delta\theta_n)\sin(\phi_n + \delta\phi_n) \\
&= \begin{bmatrix} (r_n + \delta r_n)\cos\theta_n \cos\phi_n \sin\delta\theta_n \sin\delta\phi_n + (r_n + \delta r_n)\cos\theta_n \sin\phi_n \sin\delta\theta_n \cos\delta\phi_n + \\ (r_n + \delta r_n)\sin\theta_n \cos\phi_n \cos\delta\theta_n \sin\delta\phi_n + (r_n + \delta r_n)\sin\theta_n \sin\phi_n \cos\delta\theta_n \cos\delta\phi_n \end{bmatrix}
\end{aligned} \tag{517}$$

$$\delta\Upsilon_n^{\vec{z}} = (r_n + \delta r_n)\cos\theta_n \cos\delta\theta_n - (r_n + \delta r_n)\sin\theta_n \sin\delta\theta_n \tag{518}$$

$$\zeta(\theta,\phi) = 2\pi\tilde{A}\rho_0 \tag{519}$$

$$\zeta_x^r(\theta,\phi) = \cos(\delta)\zeta(\theta,\phi) \tag{520}$$

$$\zeta_y^r(\theta,\phi) = \sin(\delta)\zeta(\theta,\phi) \tag{521}$$

$$\zeta_z^r(\theta) = \cos(\gamma)\zeta(\theta,\phi) \tag{522}$$

$$F\left(\theta,\phi \middle| \delta\vec{\Upsilon}^{\tilde{x},\tilde{y},\tilde{z}}\right) = \frac{e^{-jkr_0}}{N}\sum_{n=1}^{N}e^{j\left(\delta\Upsilon_n^{\tilde{x},\tilde{y},\tilde{z}}\right)2\pi\tilde{A}\rho_0} = \frac{e^{-jkr_0}}{N}\sum_{n=1}^{N}e^{j\left(\delta\Upsilon_n^{\tilde{x}}\cos(\delta)+\delta\Upsilon_n^{\tilde{y}}\sin(\delta)+\delta\Upsilon_n^{\tilde{z}}\cos(\gamma)\right)2\pi\tilde{A}\rho_0}$$
$$= \frac{e^{-jkr_0}}{N}\sum_{n=1}^{N}e^{j\left(\delta\Upsilon_n^{\tilde{x}}\zeta^{x,r}(\theta,\phi)+\delta\Upsilon_n^{\tilde{y}}\zeta^{y,r}(\theta,\phi)+\delta\Upsilon_n^{\tilde{z}}\zeta^{z,r}(\theta)\right)}$$

(523)

The three imperfectly synchronized compound random variables (516)-(518) are simplified by grouping the range error in (524) giving (525)-(534). Next the common uniform compound random Υ_n variable is grouped with the associated range error emerging the relations (525)-(534) with compound random variable T_n. This separates the angular erred random variables $\delta\theta_n$ and $\delta\phi_n$. This type of separation is common and convenient since the products of radial terms $r(x,y,z) = \{\delta\tilde{r}_n\sin\theta_n\cos\phi_n, \delta\tilde{r}_n\sin\theta_n\sin\phi_n, \delta\tilde{r}_n\cos\theta\}$ and functions of angles $g(\varphi) = \{\delta\theta_n, \delta\phi_n\}$ is separated. Moreover, the newly defined compound random variable T_n is similar to the spatially perfect random variable Υ_n, but takes into account range error and is free of angular phase error $\delta\theta_n$ and $\delta\phi_n$. Last of all a first order small argument simplification is applied for each $\delta\theta_n$ and $\delta\phi_n$ simplifying the expression of (525)-(534).

$$\delta\tilde{r}_n = \frac{\left(\tilde{r}_n + \delta\tilde{r}_n\right)}{\left(\tilde{A}\right)} \qquad \left|\delta\tilde{r}\right| \le 1 + \tilde{r}_{err}$$

(524)

$$\delta\Upsilon_n^{r,x_1} = T_n^{x,\theta}\sin\delta\theta_n\cos\delta\phi_n \approx T_n^{x,\theta}\delta\theta_n \qquad -\left(1+\tilde{r}_{err}\right) \le \delta\Upsilon_n^{r,x_1} \le \left(1+\tilde{r}_{err}\right)$$
$$\delta\Upsilon_n^{r,x_1} \approx T_n^{x,\theta}\delta\theta_n \qquad for \qquad -1 \le \delta\theta_n \le 1$$
$$T_n^{x,\theta} = \delta\tilde{r}_n\cos\theta_n\cos\phi_n \qquad -\left(1+\tilde{r}_{err}\right) \le T_n^{x,\theta} \le \left(1+\tilde{r}_{err}\right)$$

(525)

$$\delta\Upsilon_n^{r,y_1} = T_n^{x,\theta}\sin\delta\theta_n\sin\delta\phi_n \approx T_n^{x,\theta}\delta\theta_n\delta\phi_n \qquad \left|\delta\Upsilon_n^{r,y_1}\right| \le \left(1+\tilde{r}_{err}\right)$$
$$T_n^{x,\theta} = \delta\tilde{r}_n\cos\theta_n\cos\phi_n \qquad \left|T_n^{x,\theta}\right| \le \left(1+\tilde{r}_{err}\right)$$

(526)

$$\delta\Upsilon_n^{r,x_2} = -T_n^{y,\theta}\sin\delta\theta_n\sin\delta\phi_n \approx -T_n^{y,\theta}\delta\theta_n\delta\phi_n \qquad \left|\delta\Upsilon_n^{r,x_2}\right| \le \left(1+\tilde{r}_{err}\right)$$
$$T_n^{y,\theta} = \delta\tilde{r}_n\cos\theta_n\sin\phi_n \qquad \left|T_n^{y,\theta}\right| \le \left(1+\tilde{r}_{err}\right)$$

(527)

$$\delta\Upsilon_n^{r,y_2} = T_n^{y,\theta}\sin\delta\theta_n\cos\delta\phi_n \approx T_n^{y,\theta}\delta\theta_n \qquad \left|\delta\Upsilon_n^{r,y_2}\right| \le \left(1+\tilde{r}_{err}\right)$$
$$T_n^{y,\theta} = \delta\tilde{r}_n\cos\theta_n\sin\phi_n \qquad \left|T_n^{y,\theta}\right| \le \left(1+\tilde{r}_{err}\right)$$

(528)

$$\delta\Upsilon_n^{r,x_3} = T_n^{x,r}\cos\delta\theta_n\cos\delta\phi_n \approx T_n^{x,r} \qquad \left|\delta\Upsilon_n^{r,x_3}\right| \le \left(1+\tilde{r}_{err}\right)$$
$$T_n^{x,r} = \delta\tilde{r}_n\sin\theta_n\cos\phi_n \qquad \left|T_n^{x,r}\right| \le \left(1+\tilde{r}_{err}\right)$$

(529)

$$\delta\Upsilon_n^{r,y_3} = T_n^{x,r}\cos\delta\theta_n\sin\delta\phi_n \approx T_n^{x,r}\delta\phi_n \qquad \left|\delta\Upsilon_n^{r,y_3}\right| \le \left(1+\tilde{r}_{err}\right)$$
$$T_n^{x,r} = \delta\tilde{r}_n\sin\theta_n\cos\phi_n \qquad \left|T_n^{x,r}\right| \le \left(1+\tilde{r}_{err}\right)$$

(530)

$$\delta\Upsilon_n^{r,x_4} = -T_n^{y,r}\cos\delta\theta_n\sin\delta\phi_n \approx -T_n^{y,r}\delta\phi_n \qquad \left|\delta\Upsilon_n^{r,x_4}\right| \le \left(1+\tilde{r}_{err}\right)$$
$$T_n^{y,r} = \delta\tilde{r}_n\sin\theta_n\sin\phi_n \qquad \left|T_n^{y,r}\right| \le \left(1+\tilde{r}_{err}\right)$$

(531)

$$\delta\Upsilon_n^{r,y_4} = T_n^{y,r}\cos\delta\theta_n\cos\delta\phi_n \approx T_n^{y,r} \qquad \left|\delta\Upsilon_n^{r,y_4}\right| \le \left(1+\tilde{r}_{err}\right)$$
$$T_n^{y,r} = \delta\tilde{r}_n\sin\theta_n\sin\phi_n \qquad \left|T_n^{y,r}\right| \le \left(1+\tilde{r}_{err}\right)$$

(532)

$$\delta\Upsilon_n^{r,z_1} = T_n^{z,r}\cos\delta\theta_n \approx T_n^{z,r} \qquad \left|\delta\Upsilon_n^{r,z_1}\right| \le \left(1+\tilde{r}_{err}\right)$$
$$T_n^{z,r} = \delta\tilde{r}_n\cos\theta_n \qquad \left|T_n^{z,r}\right| \le \left(1+\tilde{r}_{err}\right)$$

(533)

$$\delta\Upsilon_n^{r,z_2} = T_n^{z,\theta}\sin\delta\theta_n \approx T_n^{z,\theta}\delta\theta_n \qquad \left|\delta\Upsilon_n^{r,z_2}\right| \le \left(1+\tilde{r}_{err}\right)$$
$$T_n^{z,\theta} = -\delta\tilde{r}_n\sin\theta_n \qquad \left|T_n^{z,\theta}\right| \le \left(1+\tilde{r}_{err}\right)$$

(534)

The probability density functions (pdfs) of $T_n^{x,r}$ and $T_n^{y,r}$ are found in (536) normalized to the joint probability density function (*jpdf*) of (535). This procedure is analogous to finding the (*pdfs*) of $f_T\left(T^{\theta,y}\right)$ and $f_T\left(T^{\theta,x}\right)$ will not be repeated, but one finds the (*pdfs*) of .
$f_T\left(T_n^{x,r}\right) = f_T\left(T_n^{y,r}\right) = f_T\left(T_n^{x,\theta}\right) = f_T\left(T_n^{y,\theta}\right) = f_T\left(T_n^{z,r}\right) = f_T\left(T_n^{z,\theta}\right)$ Thus a compact *pdf* independent of coordinate is provided in (537) for simplification.

$$\int_{-\sqrt{\left(1+\tilde{r}_{err}\right)^2-x^2-y^2}}^{\sqrt{\left(1+\tilde{r}_{err}\right)^2-x^2-y^2}} f_T\left(T^{r,x},T^{r,y},T^{r,u}\right)dz = 1$$

$$\int_{-\sqrt{\left(1+\tilde{r}_{err}\right)^2-x^2}}^{\sqrt{\left(1+\tilde{r}_{err}\right)^2-x^2}} f_T\left(T^{r,x},T^{r,y},T^{r,u}\right)2\sqrt{\left(1+\tilde{r}_{err}\right)^2-x^2-y^2}\,dy = 1$$

(535)

$$\int_{-\left(1+\tilde{r}_{err}\right)^2}^{\left(1+\tilde{r}_{err}\right)^2} f_T\left(T^{r,x},T^{r,y},T^{r,u}\right)\pi\left(1+\tilde{r}_{err}-x\right)\left(1+\tilde{r}_{err}+x\right)dx = 1$$

$$f_T\left(T^{r,x},T^{r,y},T^{r,u}\right) = \dfrac{1}{\dfrac{4\pi}{3}+4\pi\tilde{r}_{err}+4\pi\tilde{r}_{err}^2+\dfrac{4\pi\tilde{r}_{err}^2}{3}}$$

$$f_{\delta\Upsilon}\left(\mathrm{T}^{r,x},\mathrm{T}^{r,y}\right)=\int_{-\sqrt{1^2-x^2-y^2}}^{\sqrt{1^2-x^2-y^2}}f_{\mathrm{T}}\left(\mathrm{T}^{r,x},\mathrm{T}^{r,y},\mathrm{T}^{r,u}\right)dz=\frac{1}{\dfrac{4\pi}{3}+4\pi\tilde{r}_{err}+4\pi\tilde{r}_{err}^2+\dfrac{4\pi\tilde{r}_{err}^2}{3}}\int_{-\sqrt{1^2-x^2-y^2}}^{\sqrt{1^2-x^2-y^2}}dz$$

$$f_{\mathrm{T}}\left(\mathrm{T}^{r,x}\right)=\int_{-\sqrt{1^2-x^2}}^{\sqrt{1^2-x^2}}f_{\mathrm{T}}\left(\mathrm{T}^{r,x},\mathrm{T}^{r,y}\right)dz=\frac{1}{\dfrac{4\pi}{3}+4\pi\tilde{r}_{err}+4\pi\tilde{r}_{err}^2+\dfrac{4\pi\tilde{r}_{err}^2}{3}}\int_{-\sqrt{1^2-x^2-y^2}}^{\sqrt{1^2-x^2-y^2}}2\sqrt{1^2-x^2-y^2}\,dy$$

$$f_{\mathrm{T}}\left(\mathrm{T}^{r,x}\right)=f_{\mathrm{T}}\left(\mathrm{T}^{r,y}\right)=f_{\mathrm{T}}\left(\mathrm{T}^{r,z}\right)=\frac{\displaystyle\int_{-\sqrt{1^2-x^2}}^{\sqrt{1^2-x^2}}\int_{-\sqrt{1^2-x^2-y^2}}^{\sqrt{1^2-x^2-y^2}}dzdy}{\displaystyle\int_{-(1+\tilde{r}_{err})}^{(1+\tilde{r}_{err})}\int_{-\sqrt{(1+\tilde{r}_{err})^2-x^2}}^{\sqrt{(1+\tilde{r}_{err})^2-x^2}}\int_{-\sqrt{(1+\tilde{r}_{err})^2-x^2-y^2}}^{\sqrt{(1+\tilde{r}_{err})^2-x^2-y^2}}dzdydx}=\frac{\pi-\pi x^2}{\dfrac{4\pi}{3}+4\pi\tilde{r}_{err}+4\pi\tilde{r}_{err}^2+\dfrac{4\pi\tilde{r}_{err}^2}{3}}$$

(536)

$$f_{\mathrm{T}}\left(\mathrm{T}_n^{x,y,z}\right)\triangleq f_{\mathrm{T}}\left(\mathrm{T}_n^{x,r}\right)=f_{\mathrm{T}}\left(\mathrm{T}_n^{x,\theta}\right)=f_{\mathrm{T}}\left(\mathrm{T}_n^{y,r}\right)=f_{\mathrm{T}}\left(\mathrm{T}_n^{y,\theta}\right)=f_{\mathrm{T}}\left(\mathrm{T}_n^{z,r}\right)=f_{\mathrm{T}}\left(\mathrm{T}_n^{z,\theta}\right) \qquad (537)$$

To understand these newly defined random variables first assume the expected value of $\vec{\mathrm{T}}^x$ is taken such that $\vec{\mathrm{T}}^y=\vec{\mathrm{T}}^z=0$. This assumption gives (538) normalized to the associated range error. Now in the limit the associated range error goes to zero it is seen that the expected value reduces to the familiar mean valued radiation pattern of the perfect spatial random variable Υ^x (539).

$$\bar{U}\left(\theta,\phi\big|\delta\vec{\theta},\delta\vec{\phi}\right)_{\substack{\vec{\mathrm{T}}^y=0,\\\vec{\mathrm{T}}^z=0}}=E_{\mathrm{T}^{x,r}}\left(U\left(\theta,\phi\big|\vec{\mathrm{T}}^x,\delta\vec{\theta},\delta\vec{\phi}\right)\right)$$

$$=\frac{1}{N}+\left(1-\frac{1}{N}\right)\left|\int_{(1+\tilde{r}_{err})}^{-(1+\tilde{r}_{err})}e^{j\mathrm{T}_n^x x}\frac{\pi-\pi x^2}{\dfrac{4\pi}{3}+4\pi\tilde{r}_{err}+4\pi\tilde{r}_{err}^2+\dfrac{4\pi\tilde{r}_{err}^2}{3}}d\mathrm{T}_n^x\right|^2 \qquad (538)$$

$$=\frac{1}{N}+\left(1-\frac{1}{N}\right)\left|-\frac{6\left(1+\tilde{r}_{err}\right)x\cos\left(\left(1+\tilde{r}_{err}\right)x\right)+3\left(-2+\tilde{r}_{err}\left(2+\tilde{r}_{err}\right)x^2\right)\sin\left(\left(1+\tilde{r}_{err}\right)x\right)}{2\left(1+\tilde{r}_{err}\right)^3 x^3}\right|^2$$

$$x=\zeta_x^r\left(\theta,\phi\right)\left(1+\delta\theta_n+\delta\phi_n+\delta\theta_n\delta\phi_n\right)$$

$$\lim_{\tilde{r}_{err}\to 0}E_{\mathrm{T}}\left(U\left(\theta,\phi\big|\vec{\mathrm{T}},\delta\vec{\theta},\delta\vec{\phi}\right)\right)=3tinc(x) \qquad (539)$$

The problem with this formulation is the imperfectly phased random variables $\delta\theta_n$ and $\delta\phi_n$ become embedded within a complex expression. This causes difficulty when trying to applying a (pdf) and taking the expected value due to the complexity of the expression. An alternative to this situation is to reduce the (pdfs) of T_n to those of (540)-(542). Doing so one may interchange the expected value of T_n with taking the expected value of $\delta\theta_n$ and $\delta\phi_n$ first (543).

$$\delta\Upsilon_n^x\approx\mathrm{T}_n^x\left(1+\delta\theta+\delta\phi+\delta\theta\delta\phi\right) \qquad\qquad \left|\delta\Upsilon_n^{r,x}\right|\le\left(1+\tilde{r}_{err}\right) \qquad (540)$$

$$\delta\Upsilon_n^y \approx \mathrm{T}_n^y \left(1 + \delta\theta + \delta\phi + \delta\theta\delta\phi\right) \qquad\qquad \left|\delta\Upsilon_n^{\mathrm{r,y}}\right| \leq \left(1 + \tilde{r}_{err}\right) \tag{541}$$

$$\delta\Upsilon_n^z \approx \mathrm{T}_n^z \left(1 + \delta\theta\right) \qquad\qquad \left|\delta\Upsilon_n^{\mathrm{r,z}}\right| \leq \left(1 + \tilde{r}_{err}\right) \tag{542}$$

$$E_{\delta\theta,\delta\phi}\left[E_{\mathrm{T}}\left[e^{j\left(\delta\Upsilon_n^{\tilde{x}}\zeta_x^r(\theta,\phi) + \delta\Upsilon_n^{\tilde{y}}\zeta_y^r(\theta,\phi) + \delta\Upsilon_n^{\tilde{z}}\zeta_z^r(\theta,\phi)\right)} \right] \right] = E_{\mathrm{T}}\left[E_{\delta\theta,\delta\phi}\left[e^{j\left(\delta\Upsilon_n^{\tilde{x}}\zeta_x^r(\theta,\phi) + \delta\Upsilon_n^{\tilde{y}}\zeta_y^r(\theta,\phi) + \delta\Upsilon_n^{\tilde{z}}\zeta_z^r(\theta,\phi)\right)} \right] \right] \tag{543}$$

The issue now is formulating a pdf of $\delta\theta_n$ and $\delta\phi_n$. To due this one must assume that the error of each random variable will typically tend to be concentrated near the spatial angles $\left(\theta_0, \phi_0\right)$ and hence a von Mises distribution will be derived for each random variable. First, since the random variables $\delta\theta_n$ and $\delta\phi_n$ are assumed small and concentrated about the beamsteering location the product with each $\mathrm{T}_n^{x,y,z}$ is also assumed small such that the compound random variables of (544)-(546) are considered.

$$\Xi_n = \left\|\mathrm{T}_n^x \delta\theta_n \zeta_x^r(\theta,\phi) + \mathrm{T}_n^y \delta\theta_n \zeta_y^r(\theta,\phi) + \mathrm{T}_n^z \delta\theta_n \zeta_z^r(\theta)\right\| \approx \mathrm{T}_n \delta\theta_n \left\|\zeta_{x,y,z}^r(\theta,\phi)\right\|$$
$$\text{for } \mathrm{T}_n \delta\theta_n \approx \mathrm{T}_n^x \delta\theta_n \approx \mathrm{T}_n^y \delta\theta_n \approx \mathrm{T}_n^z \delta\theta_n \tag{544}$$

$$\mathrm{X}_n = \left\|\mathrm{T}_n^x \delta\phi_n \zeta_x^r(\theta,\phi) + \mathrm{T}_n^y \delta\phi_n \zeta_y^r(\theta,\phi) + \mathrm{T}_n^z \delta\phi_n \zeta_z^r(\theta)\right\| \approx \mathrm{T}_n \delta\phi_n \left\|\zeta_{x,y,z}^r(\theta,\phi)\right\|$$
$$\text{for } \mathrm{T}_n \delta\phi_n \approx \mathrm{T}_n^x \delta\phi_n \approx \mathrm{T}_n^y \delta\phi_n \approx \mathrm{T}_n^z \delta\phi_n \tag{545}$$

$$\mathrm{E}_n = \left\|\mathrm{T}_n^x \delta\phi_n \delta\theta_n \zeta_x^r(\theta,\phi) + \mathrm{T}_n^y \delta\phi_n \delta\theta_n \zeta_y^r(\theta,\phi) + \mathrm{T}_n^z \delta\phi_n \delta\theta_n \zeta_z^r(\theta)\right\| \approx \mathrm{T}_n \delta\theta_n \delta\phi_n \left\|\zeta_{x,y,z}^r(\theta,\phi)\right\|$$
$$\text{for } \mathrm{T}_n \delta\theta_n \delta\phi_n \approx \mathrm{T}_n^x \delta\theta_n \delta\phi_n \approx \mathrm{T}_n^y \delta\theta_n \delta\phi_n \approx \mathrm{T}_n^z \delta\theta_n \delta\phi_n \tag{546}$$

The problem with (544)-(546) is that they are not easily measured as a function of angular error. Hence, in order to provide additional insight in the use of the von Mises distribution these random variables are rewritten as those of (547)-(551).

$$\tilde{\Xi}_n = \pi \mathrm{T}_n \delta\tilde{\theta}_n \qquad\qquad \left|\pi \mathrm{T}_n \delta\tilde{\theta}_n\right| \simeq \leq \pi \tag{547}$$

$$\tilde{\mathrm{X}}_n = \pi \mathrm{T}_n \delta\tilde{\phi}_n \qquad\qquad \left|\pi \mathrm{T}_n \delta\tilde{\phi}_n\right| \simeq \leq \pi \tag{548}$$

$$\tilde{\mathrm{E}}_n = \pi \mathrm{T}_n \delta\tilde{\phi}_n \delta\tilde{\theta}_n \qquad\qquad \left|\pi \mathrm{T}_n \delta\tilde{\phi}_n \delta\tilde{\theta}_n\right| \simeq \leq \pi \tag{549}$$

$$\mathrm{T}_n \qquad\qquad \left|\mathrm{T}_n\right| \simeq \leq 1 \tag{550}$$

$$\delta\tilde{\theta}_n = \frac{\delta\theta_n}{\theta_{\max}} \qquad -1 \leq \delta\tilde{\theta}_n \leq 1 \tag{551}$$

Next in order to use the von Mises distribution a function describing the mean location (beamsteering) and concentration parameter must be defined. In order to define each of these functions the magnitude of the spatial coefficient $\left\|\zeta_{x,y,z}^r(\theta,\phi)\right\|$ is found in (552) where variations of $\Theta(\theta,\phi)$ will be used to define the beamsteering or mean location in the von Mises distribution and another variation of the parameter $\left(2\tilde{A}\theta_{\max}\right)$ will be found to fulfill the concentration parameter. These variations are found in (553) such that the ratio of the inverse of the sectoral area is given to be the concentration parameter.

However, at the beamsteering location the inverse of the concentration parameter will provide minimal impact against the mean location.

$$\left\|\zeta_{x,y,z}^{r}\left(\theta,\phi\right)\right\|=\sqrt{\left(2\pi\tilde{A}\rho_{0}\cos\delta\right)^{2}+\left(2\pi\tilde{A}\rho_{0}\sin\delta\right)^{2}+\left(2\pi\tilde{A}\rho_{0}\cos\gamma\right)^{2}}$$
$$=2\pi\tilde{A}\sqrt{\rho_{0}^{2}\left(1+\cos^{2}\gamma\right)}=2\pi\tilde{A}\ \Theta\left(\theta,\phi\right) \tag{552}$$

$$\Theta\left(\theta,\phi\right)=\sqrt{\rho_{0}^{2}\left(\theta,\phi\right)+\left(\cos\theta-\cos\theta_{0}\right)^{2}}\left\{\rho_{0}=\sqrt{\begin{array}{c}\left(\sin\theta_{0}\cos\phi_{0}-\sin\theta\cos\phi\right)^{2}+\\ \left(\sin\theta_{0}\sin\phi_{0}-\sin\theta\sin\phi\right)^{2}\end{array}}\right\}$$

$$\mathrm{T}_{n}\delta\tilde{\theta}_{n}\left\|\zeta_{x,y,z}^{r}\left(\theta,\phi\right)\right\|=\left(\mathrm{T}_{n}\delta\tilde{\theta}_{n}\pi\right)_{comp.\,random\,variable}\left\lfloor\frac{1}{\left(\tilde{A}2\theta_{\max}\right)}\right\rfloor_{\substack{k=concentration\\parameter}}\left(\tilde{A}2\theta_{\max}\right)^{2}\Theta\left(\theta,\phi\right)_{\mu=mean\,location}$$

$$=\left(\mathrm{T}_{n}\delta\tilde{\theta}_{n}\pi\right)_{comp.\,random\,variable}\left[\frac{1}{\left(\tilde{A}\Delta\theta_{\max}\right)}\right]_{\substack{k=concentration\\parameter}}\left(\tilde{A}\Delta\theta_{\max}\right)^{2}\Theta\left(\theta,\phi\right)_{\mu=mean\,location} \tag{553}$$

$$\Delta\theta_{\max}=2\theta_{\max} \tag{554}$$

$$\frac{1}{\tilde{A}\Delta\theta_{\max}}\le 2$$
$$\frac{1}{\tilde{A}2}=\frac{1}{D}\le\Delta\theta_{\max} \tag{555}$$

$$f_{\Xi}\left(\vec{\Xi}\middle|\theta_{0},\kappa_{\theta}\right)=\frac{e^{\kappa_{\theta}\cos\left(\Xi_{n}-\left(\tilde{A}\Delta\theta_{\max}\right)^{2}\Theta\left(\theta_{0},\phi\right)\right)}}{2\pi I_{0}\left(\kappa_{\theta}\right)}$$
$$\kappa_{\theta}=\frac{1}{\tilde{A}\Delta\theta_{\max}} \tag{556}$$

$$f_{X}\left(\vec{X}\middle|\phi_{0},\kappa_{\phi}\right)=\frac{e^{\kappa_{\phi}\cos\left(X_{n}-\left(\tilde{A}\Delta\phi_{\max}\right)^{2}\Theta\left(\theta,\phi_{0}\right)\right)}}{2\pi I_{0}\left(\kappa_{\phi}\right)}$$
$$\kappa_{\phi}=\frac{1}{\tilde{A}\Delta\theta_{\max}\Delta\phi_{\max}} \tag{557}$$

$$f_{E}\left(\vec{E}\middle|\theta_{0},\phi_{0},\kappa_{\theta,\phi}\right)=\frac{e^{\kappa_{\theta,\phi}\cos\left(E_{n}-\left(\tilde{A}\Delta\theta_{\max}\right)^{2}\Theta\left(\theta_{0},\phi_{0}\right)\right)}}{2\pi I_{0}\left(\kappa_{\theta,\phi}\right)}$$
$$\kappa_{\theta,\phi}=\frac{1}{\tilde{A}\theta_{\max}\Delta\phi_{\max}} \tag{558}$$

Hence, the expected value of the $\delta\theta_{n}$ and $\delta\phi_{n}$ is found by the creation of the compound random variables Ξ_{n}, X_{n} and E_{n} for the process provided in (559).

$$\bar{U}\left(\theta,\phi\,\middle|\,\vec{T}^{x,y,z}\right)=E_{\delta\theta,\delta\phi}\left(U\left(\theta,\phi\,\middle|\,\vec{T}^{x,y,z},\delta\vec{\theta},\delta\vec{\phi}\right)\right)$$

$$=\frac{1}{N}+\left(1-\frac{1}{N}\right)e^{j\left(T_n^x\zeta_x^r(\theta,\phi)+T_n^y\zeta_y^r(\theta,\phi)+T_n^z\zeta_z^r(\theta,\phi)\right)}\left|E_\Xi\left[e^{j(\Xi_n)}\right]\right|^2\left|E_X\left[e^{j(X_n)}\right]\right|^2\left|E_E\left[e^{j(E_n)}\right]\right|^2 \tag{559}$$

$$\left[E_\Xi\right]=\left|\frac{I_1\left(\kappa_\theta\right)}{I_0\left(\kappa_\theta\right)}e^{j\left(\tilde{A}\Delta\theta_{max}\right)^2\Theta(\theta_0,\phi)}\right| \tag{560}$$

$$\left[E_X\right]=\left|\frac{I_1\left(\kappa_\phi\right)}{I_0\left(\kappa_\phi\right)}e^{j\left(\tilde{A}\Delta\phi_{max}\right)^2\Theta(\theta,\phi_0)}\right| \tag{561}$$

$$\left[E_E\right]=\left|\frac{I_1\left(\kappa_{\theta,\phi}\right)}{I_0\left(\kappa_{\theta,\phi}\right)}e^{j\left(2\tilde{A}\phi_{max}\theta_{max}\right)^2\Theta(\theta_0,\phi_0)}\right|\approx1$$

$$\text{since}\quad\kappa_{\theta,\phi}=\frac{1}{\tilde{A}\theta_{max}\Delta\phi_{max}}\approx\infty\Rightarrow\frac{I_1\left(\infty\right)}{I_0\left(\infty\right)}=1 \tag{562}$$

For $\phi_{max}\approx\theta_{max}$

$$\frac{1}{2\tilde{A}\theta_{max}\phi_{max}}\leq2\Rightarrow\frac{1}{4\tilde{A}}\leq\theta_{max}^2$$

$$\sqrt{\frac{1}{4\tilde{A}}}=\frac{1}{2}\sqrt{\frac{1}{\tilde{A}}}\leq\theta_{max} \tag{563}$$

$$\sqrt{\frac{1}{\tilde{A}}}=\sqrt{\frac{2}{D}}\leq\Delta\theta_{max}$$

Hence the mean valued imperfect phased spherical random array is given by that of (564) and reduces to the perfectly phased spherical random array pattern for $\tilde{r}_{err}=0$ and $\kappa_\theta=\kappa_\phi=\infty$ as expected in (565).

$$\bar{U}(\theta,\phi) \approx \frac{1}{N} +$$

$$\left(1-\frac{1}{N}\right)\left\{ \left| -\frac{6\left(\dfrac{1+}{\tilde{r}_{err}}\right)\zeta_x^r(\theta,\phi)\cos\left(\left(\dfrac{1+}{\tilde{r}_{err}}\right)\zeta_x^r(\theta,\phi)\right)+3\left(\dfrac{-2+}{\tilde{r}_{err}}\left(\dfrac{2+}{\tilde{r}_{err}}\right)\zeta_x^r(\theta,\phi)^2\right)\sin\left(\left(\dfrac{1+}{\tilde{r}_{err}}\right)\zeta_x^r(\theta,\phi)\right)}{2\left(1+\tilde{r}_{err}\right)^3 \zeta_x^r(\theta,\phi)^3} \right|^2 \right.$$

$$\left| -\frac{6\left(\dfrac{1+}{\tilde{r}_{err}}\right)\zeta_y^r(\theta,\phi)\cos\left(\left(\dfrac{1+}{\tilde{r}_{err}}\right)\zeta_y^r(\theta,\phi)\right)+3\left(\dfrac{-2+}{\tilde{r}_{err}}\left(\dfrac{2+}{\tilde{r}_{err}}\right)\zeta_y^r(\theta,\phi)^2\right)\sin\left(\left(\dfrac{1+}{\tilde{r}_{err}}\right)\zeta_y^r(\theta,\phi)\right)}{2\left(1+\tilde{r}_{err}\right)^3 \zeta_y^r(\theta,\phi)^3} \right|^2$$

$$\left| -\frac{6\left(\dfrac{1+}{\tilde{r}_{err}}\right)\zeta_z^r(\theta)\cos\left(\left(\dfrac{1+}{\tilde{r}_{err}}\right)\zeta_z^r(\theta)\right)+3\left(\dfrac{-2+}{\tilde{r}_{err}}\left(\dfrac{2+}{\tilde{r}_{err}}\right)\zeta_z^r(\theta)^2\right)\sin\left(\left(\dfrac{1+}{\tilde{r}_{err}}\right)\zeta_z^r(\theta)\right)}{2\left(1+\tilde{r}_{err}\right)^3 \zeta_z^r(\theta)^3} \right|^2$$

$$\left.\left|\frac{I_1(\kappa_\theta)}{I_0(\kappa_\theta)}\right|^2 \left|\frac{I_1(\kappa_\phi)}{I_0(\kappa_\phi)}\right|^2 \right\}$$

$$(564)$$

for $\quad \vec{T}^{r,z} \approx \vec{Y}^{r,z}$

$$\bar{U}(\theta,\phi) \approx \frac{1}{N} + \left(1-\frac{1}{N}\right)\left\{ \left|3\,\mathrm{tinc}\left(\zeta^{x,r}(\theta,\phi)\right)\right|^2 \left|3\,\mathrm{tinc}\left(\zeta^{y,r}(\theta,\phi)\right)\right|^2 \left|2\,\mathrm{jinc}\left(\zeta^{z,r}(\theta)\right)\right|^2 \right\}_{\substack{\tilde{r}_{err}=0,\\ \kappa_\theta=\kappa_\phi=\infty}} \quad (565)$$

Examination of the range error in the expected value of either T_n^x or T_n^y can be evaluated in a simpler fashion by assuming $\delta=0$ and $\theta_{MaxErr}=\phi_{MaxErr}=0$. These conditions provide $\sin\delta=0$ causing $T_n^y\big|_{\delta=0}$ to be irrelevant. Instead, $\cos\delta=1$ and hence, $\zeta_x^r(\theta,\phi)\big|_{\delta=0}=2\pi\tilde{A}\rho_0$ with the given relations of (566)-(569). Hence this reduces (564) to that of

$$\rho_0\big|_{\delta=0} = \left(\sin\theta_0\cos\phi_0 - \sin\theta\cos\phi\right) \quad (566)$$

$$\delta = \tan^{-1}\left[\frac{\sin\theta\sin\phi - \sin\theta_0\sin\phi_0}{\sin\theta\cos\phi - \sin\theta_0\cos\phi_0}\right] \xrightarrow{\ \delta=0\ } \left(\sin\theta\sin\phi - \sin\theta_0\sin\phi_0\right) = 0 \quad (567)$$

$$\cos\gamma = \rho_0^{-1}\left(\cos\theta_0 - \cos\theta\right) = \frac{\left(\cos\theta_0 - \cos\theta\right)}{\left(\sin\theta_0\cos\phi_0 - \sin\theta\cos\phi\right)} \quad (568)$$

$$\bar{U}(\theta,\phi)\Big|_{\delta=\theta_{MaxErr}=\phi_{MaxErr}=0} \approx \frac{1}{N} +$$

$$\left(1-\frac{1}{N}\right)\left\{ \left| -\frac{6\left(\dfrac{1+}{\tilde{r}_{err}}\right)\zeta_x^r(\theta,\phi)\cos\left(\left(\dfrac{1+}{\tilde{r}_{err}}\right)\zeta_x^r(\theta,\phi)\right)+3\left(\dfrac{-2+}{\tilde{r}_{err}}\left(\dfrac{2+}{\tilde{r}_{err}}\right)\zeta_x^r(\theta,\phi)^2\right)\sin\left(\left(\dfrac{1+}{\tilde{r}_{err}}\right)\zeta_x^r(\theta,\phi)\right)}{2\left(1+\tilde{r}_{err}\right)^3\zeta_x^r(\theta,\phi)^3} \right|^2 \right.$$

$$\left. \left| -\frac{6\left(\dfrac{1+}{\tilde{r}_{err}}\right)\zeta_z^r(\theta)\cos\left(\left(\dfrac{1+}{\tilde{r}_{err}}\right)\zeta_z^r(\theta)\right)+3\left(\dfrac{-2+}{\tilde{r}_{err}}\left(\dfrac{2+}{\tilde{r}_{err}}\right)\zeta_z^r(\theta)^2\right)\sin\left(\left(\dfrac{1+}{\tilde{r}_{err}}\right)\zeta_z^r(\theta)\right)}{2\left(1+\tilde{r}_{err}\right)^3\zeta_z^r(\theta)^3} \right|^2 \right\} \tag{569}$$

Now the range estimate can be found by assuming the target location resides in the beamsteering location $\zeta^{x,r}(\theta)=\zeta^{z,r}(\theta)=0$. Or that is $\cos\gamma=0$ when $\theta=\theta_0$ and $\rho_0=0$ when $\phi=\phi_0$ reducing (569) to (570). Last assuming $R_{max}=0$ simplifies the error free mean valued pattern at the target location to (571) as expected.

$$\bar{U}(\theta,\phi)\Big|_{\substack{\delta=\theta_{MaxErr}=\phi_{MaxErr}=0,\\(\theta_0,\phi_0)=(\theta,\phi)}} \approx$$

$$\lim_{\zeta_x^r(\theta_0,\phi_0),\zeta_y^r(\theta_0,\phi_0)\to 0,} \frac{1}{N}+\left(1-\frac{1}{N}\right)\left\{ \left| -\frac{\begin{bmatrix}6\left(1+\tilde{r}_{err}\right)\zeta_x^r(\theta_0,\phi_0)\cos\left(\left(1+\tilde{r}_{err}\right)\zeta_x^r(\theta_0,\phi_0)\right)+\\ 3\left(-2+\tilde{r}_{err}\left(2+\tilde{r}_{err}\right)\zeta_x^r(\theta_0,\phi_0)^2\right)\sin\left(\left(1+\tilde{r}_{err}\right)\zeta_x^r(\theta_0,\phi_0)\right)\end{bmatrix}}{2\left(1+\tilde{r}_{err}\right)^3\zeta_x^r(\theta_0,\phi_0)^3} \right|^2 \right\} \tag{570}$$

$$=\frac{1}{N}+\left(1-\frac{1}{N}\right)\left| -\frac{-2+2Rmax+Rmax^2}{2\left(1+Rmax\right)^2} \right|^2$$

$$\bar{U}(\theta,\phi)\Big|_{\substack{\delta=\theta_{MaxErr}=\phi_{MaxErr}=R_{max}=0,\\(\theta_0,\phi_0)=(\theta,\phi)}} = \frac{1}{N}+\left(1-\frac{1}{N}\right)|1|^2 \tag{571}$$

For perfect elevation phasing $\zeta^{x,r}(\theta,\phi)=\zeta^{x,r}(\theta_0,\phi)$ and $\zeta^{z,r}(\theta_0)=0$ (569) reduces to (572). A plot of (572) is shown in

$$\left. \bar{U}\left(\theta_0,\phi\right)\right|_{\substack{\delta=\theta_{MaxErr}=\phi_{MaxErr}=0, \\ \left(\theta_0,\phi\right)=\left(\theta,\phi\right)}} \approx \frac{1}{N} +$$

$$\left(1-\frac{1}{N}\right)\left\{-\left\|\left[\frac{\left[\begin{array}{l}6\left(1+\tilde{r}_{err}\right)\zeta_x^r\left(\theta_0,\phi\right)\cos\left(\left(1+\tilde{r}_{err}\right)\zeta_x^r\left(\theta_0,\phi\right)\right)+ \\ 3\left(-2+\tilde{r}_{err}\left(\frac{2+}{\tilde{r}_{err}}\right)\right)\zeta_x^r\left(\theta_0,\phi\right)^2\sin\left(\left(\frac{1+}{\tilde{r}_{err}}\right)\zeta_x^r\left(\theta_0,\phi\right)\right)\end{array}\right]}{2\left(1+\tilde{r}_{err}\right)^3\zeta_x^r\left(\theta_0,\phi\right)^3}\right]\right\|^2\right\} \tag{572}$$

Hence, it is determined that the 3dB point (half power loss) of the radiation pattern is given to be $.115\lambda$ as shown in Figure 230-Figure 231.
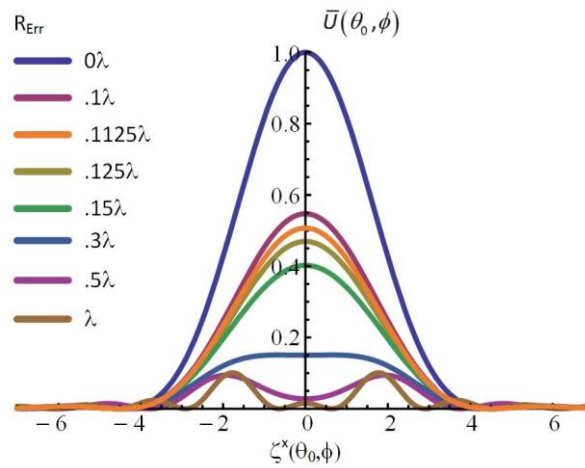
Figure 230. Mean valued radiation intensity with range error.
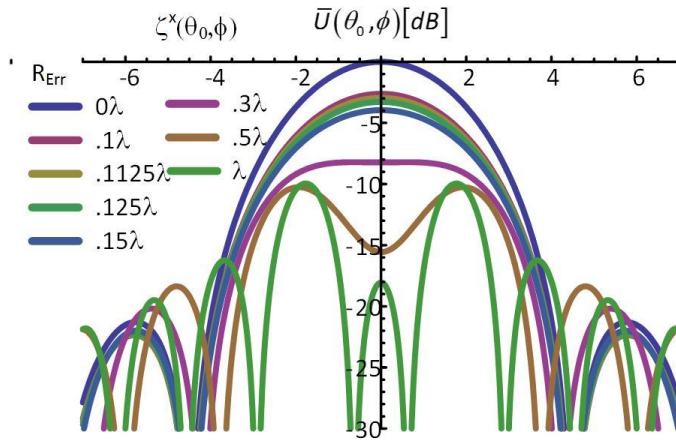
Figure 231. Mean valued radiation intensity with range error [dB].

A plot of (559) is provided differently in Figure 232-Figure 233 under the assumption no range error is present, but phase error exists. Hence, this time it is analytically determined that the phase shifter accuracy must be greater than twice the total diameter $\left(D = 2\tilde{A} = 2Af/c\right)$ of the array. Under a brute force technique, a 4 bit phase shifter will provide accuracy up to $11.25°$. Thus, the largest diameter *(D)* possible for beamforming with less than 3dB of power loss is 2.5465. Improvements in diameter are obtained to 40.7437 and 10417 respectively for 8 and 16 bit phase shifters. Hence, phase accuracy becomes critical in the design for low bit phase shifters.
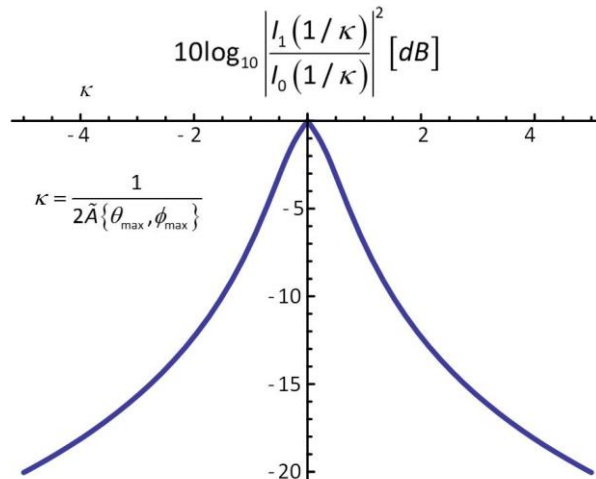
Figure 232. Plot of the effective phase error including the aperture size. (also known as a circular or Tikahnov distribtuion).

254
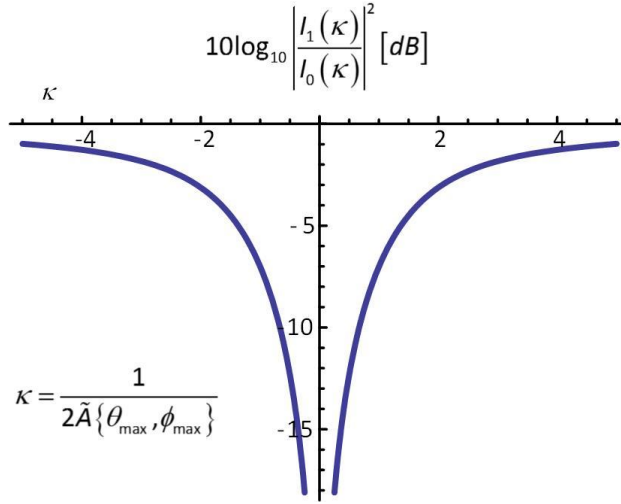
Figure 233. Plot of the effective phase error when not plotted as the Tikanhov Distribution.

Last of all if one introduces time and information error into the array then the array is addressed by using the relations in (573)-(582)

$$\delta\zeta^{x,r}(\theta,\phi) = 2\pi\left(\tilde{A} + \tilde{r}_{err}\right)\rho_0 \cos\delta \tag{573}$$

$$\delta\zeta^{y,r}(\theta,\phi) = 2\pi\left(\tilde{A} + \tilde{r}_{err}\right)\rho_0 \sin\delta \tag{574}$$

$$\delta\zeta^{z,r}(\theta) = 2\pi\left(\tilde{A} + \tilde{r}_{err}\right)\rho_0 \cos\gamma \tag{575}$$

$$\delta\zeta^{x,t}(\theta,\phi) = 2\pi\left(T + t_{err}\right)W\rho_0 \cos\delta \tag{576}$$

$$\delta\zeta^{y,t}(\theta,\phi) = 2\pi\left(T + t_{err}\right)W\rho_0 \sin\delta \tag{577}$$

$$\delta\zeta^{z,t}(\theta) = 2\pi\left(T + t_{err}\right)W\rho_0 \cos\gamma \tag{578}$$

$$\delta\varpi^{x,t}(\theta,\phi) = 2\pi\left(T + t_{err}\right)\left(W - W_{err}\right)\rho_0 \cos\delta \tag{579}$$

$$\delta\varpi^{y,t}(\theta,\phi) = 2\pi\left(T + t_{err}\right)\left(W - W_{err}\right)\rho_0 \sin\delta \tag{580}$$

$$\delta\varpi^{z,t}(\theta) = 2\pi\left(T + t_{err}\right)\left(W - W_{err}\right)\rho_0 \cos\gamma \tag{581}$$

255

$$U\left(T,W\theta,\phi\middle|\vec{\Upsilon}^r,\delta\vec{\Upsilon}^t,\delta\vec{\tilde{\omega}}\right) = \frac{\left|F\left(T,W,\theta,\phi\middle|\delta\vec{\Upsilon}^r,\delta\vec{\Upsilon}^t,\delta\vec{\tilde{\omega}}\right)F^*\left(T,W,\theta,\phi\middle|\delta\vec{\Upsilon}^r,\delta\vec{\Upsilon}^t,\delta\vec{\tilde{\omega}}\right)\right|}{\eta}$$

$$e^{-j\left(\delta\Upsilon_n^{x,t}\cos\delta+\delta\Upsilon_n^{y,t}\sin\delta+\delta\Upsilon_n^{z,t}\cos\gamma\right)2\pi(T+t_{err})W\rho_0}$$

$$[\text{time synchronization with error}]$$

$$F\left(T,W,\theta,\phi\middle|\vec{\Upsilon}^r,\delta\vec{\Upsilon}^t,\delta\vec{\tilde{\omega}}\right) = \frac{e^{j[\omega t_0 - kr_0]}}{N}\sum_{n=1}^{N}e^{-j\delta\tilde{\omega}_n\left(\delta\Upsilon_n^{x,t}\cos\delta+\delta\Upsilon_n^{y,t}\sin\delta+\delta\Upsilon_n^{z,t}\cos\gamma\right)2\pi(T+t_{err})(W-W_{err})\rho_0}\ [\text{information error with time synchronization error}]$$

$$e^{j\left(\Upsilon_n^{x,r}\cos\delta+\Upsilon_n^{y,r}\sin\delta+\Upsilon_n^{z,r}\cos\gamma\right)2\pi\tilde{A}\rho_0}$$

$$[\text{perfect spatial synchronization}]$$

$$\overset{Normalized}{=}\ \frac{1}{N}+\frac{1}{N^2}\sum_{n=1}^{N}\sum_{\substack{m=1\\m\neq n}}^{N}e^{\substack{j\delta\zeta^{x,r}(\theta,\phi)\left(\delta\Upsilon_n^{x1,2,3,4,r}-\delta\Upsilon_m^{x1,2,3,4,r}\right)}e^{j\delta\zeta^{y,r}(\theta,\phi)\left(\delta\Upsilon_n^{y1,2,3,4,r}-\delta\Upsilon_m^{y1,2,3,4,r}\right)}e^{j\delta\zeta^{z,r}(\theta)\left(\delta\Upsilon_n^{z1,2,r}-\delta\Upsilon_n^{z1,2,r}\right)}}$$

$$e^{j\delta\zeta^{x,t}(\theta,\phi)\left(\delta\Upsilon_n^{x,t}-\delta\Upsilon_m^{x,t}\right)}e^{j\delta\zeta^{y,t}(\theta,\phi)\left(\delta\Upsilon_n^{y,t}-\delta\Upsilon_m^{y,t}\right)}e^{j\delta\xi^{z,t}(\theta)\left(\delta\Upsilon_n^{z,t}-\delta\Upsilon_m^{z,t}\right)}$$

$$e^{j\delta\varpi^{x,t}(\theta,\phi)(\delta\tilde{\omega}_n-\delta\tilde{\omega}_m)\left(\delta\Upsilon_n^{x,t}-\delta\Upsilon_m^{x,t}\right)}e^{j\delta\varpi^{y,t}(\theta,\phi)(\delta\tilde{\omega}_n-\delta\tilde{\omega}_m)\left(\delta\Upsilon_n^{y,t}-\delta\Upsilon_m^{y,t}\right)}e^{j\delta\varpi^{z,t}(\theta)(\delta\tilde{\omega}_n-\delta\tilde{\omega}_m)\left(\delta\Upsilon_n^{z,t}-\delta\Upsilon_m^{z,t}\right)}$$

$$T=\frac{r_{n0}+A/2}{c}\frac{[m]}{\left[m\middle/s\right]}$$

$$\tilde{t}_{n0}=\frac{t_{n0}}{T}\qquad\qquad -1\leq\tilde{t}_{n0}\leq 1$$

$$\delta\tilde{\omega}_n=\frac{\delta\omega_n}{(W-W_{err})}\qquad -1\leq\delta\tilde{\omega}_n\leq 1$$

$$\omega_n=\omega_0+\delta\omega_n=2\pi\left(f_0+\delta f_n\right)=(W-W_{err})$$

$$(582)$$

{attributed to modulation, since the random array is frequency independent}

CHAPTER XVI

NEAR FIELD ANALYSIS OF CIRCULAR AND SPHERICAL RANDOM ARRAYS

A near field derivation of the array factor is demonstrated in this section for a uniformly distributed volumetric random array with perfect phase information bound to a Euclidean domain. It begins by examining the normalized electric field E in (41) of the array at an observation point $P(r,\theta,\phi)$ for randomly spaced elements at locations $P_n(r_n,\theta_n,\phi_n)$. The element distance $R_n(\theta,\phi)$ in (43) provides the Euclidean distance between P_n and P.

$$E(R_n,\theta,\phi) = \frac{1}{N}\sum_{n=1}^{N} f_{no}(R_{no},\theta_{no},\phi_{no})\frac{e^{-jkR_n}}{R_n} \tag{583}$$

$$R_n(\theta,\phi|r_n,\theta_n,\phi_n) = |r - r_n| = r\sqrt{1 + \left(\frac{r_n}{r}\right)^2 - \frac{2r_n\cos\psi_n}{r}}$$
$$= r - r_n\cos\psi_n + \frac{1}{r}\left(\frac{r_n^2}{2}\sin^2\psi_n\right) + \frac{1}{r^2}\left(\frac{r_n^3}{2}\cos\psi_n\sin^2\psi_n\right) + \dots \tag{584}$$

If P is assumed to reside in the near field of the array, the common approximations are a first order approximation for the magnitude $R_n \approx r$ and third order approximation for phase $R_n \approx r - r_n\cos\psi_n + \frac{1}{r}\left(\frac{r_n^2}{2}\sin^2\psi_n\right)$ [65]. These contributions can be made by linking the direction vectors $\hat{r}$ from the origin (46) and $\hat{r}_n$ from P_n (47) to P through the direction cosine in (48).

$$\hat{r} = \hat{x}\sin\theta\cos\phi + \hat{y}\sin\theta\sin\phi + \hat{z}\cos\theta \tag{585}$$

$$\hat{r}_n = \hat{x}\sin\theta_n\cos\phi_n + \hat{y}\sin\theta_n\sin\phi_n + \hat{z}\cos\theta_n \tag{586}$$

$$\cos\psi_n = \hat{r}_n\cdot\hat{r} = \sin\theta_n\sin\theta\cos(\phi-\phi_n) + \cos\theta_n\cos\theta$$
$$\sin\psi_n = |\hat{r}_n\times\hat{r}| = \sqrt{1-\cos^2\psi_n} \tag{587}$$

It should be further noted that neglecting a third order approximation with antennas greater than $(l > \lambda)$ produces a maximum phase error of $(22.5°)$ [65]. Thus, this can be critical and perhaps detrimental in the hopes of collaborative beamforming applications. However, the exception here is that by neglecting a third order phase approximation one considerably simplifies the math leading to mathematical insight on the behavior of these random array structures. Moreover, being that a third order approximation is not neglected in this section it will be seen that the math is considerably more involved.

With (48) and by inserting an excitation coefficient $f_{no}(r_n,\theta_{no},\phi_{no}) = I_n e^{jkr_n\cos\psi_{no}}$ where amplitude I_n and phase $\cos\psi_{no}$ information for the nth element gives a rewritten electric field expression of (49).

$$E\left(r,\theta,\phi\big|\vec{r}_n,\vec{\theta}_n,\vec{\phi}_n\right)=\frac{1}{N}\frac{e^{-jkr}}{r}\sum_{n=1}^{N}I_n e^{jk\left(r_n\left(\cos\psi_n-\cos\psi_{no}\right)+\frac{\frac{r_n^2}{2}\left(\sin^2\psi_n-\sin^2\psi_{no}\right)}{r}\right)}$$
(588)

Using the definition of the array factor $F\left(\theta,\phi\big|r_n,\theta_n,\phi_n\right)$ the electric field distribution simplifies to (50) and to (51) for a uniform amplitude distribution $I_n = I_o = 1$. The approximation symbol has been included to show a far field approximation has been made; the exact expression is calculated using (41).

$$E\left(r,\theta,\phi\big|r_n,\theta_{no},\phi_{no}\right)=F\left(\theta,\phi\big|r_n,\theta_{no},\phi_{no}\right)\frac{e^{-jkr}}{r}$$
(589)

$$F\left(\theta,\phi\big|r_n,\theta_{no},\phi_{no}\right)\approx\frac{1}{N}\sum_{n=1}^{N}e^{jk\left(r_n\left(\cos\psi_n-\cos\psi_{no}\right)+\frac{\frac{r_n^2}{2}\left(\sin^2\psi_n-\sin^2\psi_{no}\right)}{r}\right)}$$
(590)

16.1 Radiation Intensity and Beamforming

The array factor in (590) will be analyzed throughout the rest of this paper. It can be rewritten by expanding the angular information (587) in the exponential term of (590) according to (592) using (593)-(596) to give(597). It is important to note that (592) provides a compact expression for the azimuthal and elevation information while maintaining the integrity of each random variable $\{r_n,\theta_n,\phi_n\}$.

$$\left(\cos\psi_n-\cos\psi_{no}\right)=\left\{\begin{array}{l}\sin\theta_n\left(\cos\phi_n\left(\sin\theta\cos\phi-\sin\theta_0\cos\phi_0\right)-\sin\phi_n\left(\sin\theta\sin\phi-\sin\theta_0\sin\phi_0\right)\right)+\\\cos\theta\cos\theta_n-\cos\theta_0\cos\theta_n\end{array}\right\}$$
$$=\rho_o^{(-)}\left(\cos\left(\phi_n-\delta^{(-)}\right)+\cos\theta_n\cos\gamma\right)=\rho_o^{(-)}\left(\cos\left(\phi_n\right)\cos\left(\delta^{(-)}\right)+\sin\left(\phi_n\right)\sin\left(\delta^{(-)}\right)+\cos\theta_n\cos\gamma\right)$$
(591)

$$\rho_o^{(-)}=\left[\left(\sin\theta\cos\phi-\sin\theta_o\cos\phi_o\right)^2+\left(\sin\theta\sin\phi-\sin\theta_o\sin\phi_o\right)^2\right]^{\frac{1}{2}}$$
(592)

$$\cos\delta=\rho_0^{-1}\left(\sin\theta\cos\phi-\sin\theta_o\cos\phi_o\right)$$
(593)

$$\sin\delta=1-\cos^2\delta=1-\frac{A^2}{A^2+B^2}=\frac{B^2}{A^2+B^2}=\rho_0^{-1}\left(\sin\theta\sin\phi-\sin\theta_o\sin\phi_o\right)$$
(594)

$$\delta^{(-)}=\tan^{-1}\left[\frac{\sin\theta\sin\phi-\sin\theta_o\sin\phi_o}{\sin\theta\cos\phi-\sin\theta_o\cos\phi_o}\right]$$
(595)

$$\cos\gamma=\rho_0^{-1}\left(\cos\theta-\cos\theta_o\right)$$
(596)

$$F\left(\theta,\phi\big|r_n,\phi_n,\theta_n\right)=\frac{1}{N}\sum_{n=1}^{N}e^{jk\left(r_n\rho_o^{(-)}\left(\sin\theta_n\left(\cos(\phi_n)\cos\left(\delta^{(-)}\right)+\sin(\phi_n)\sin\left(\delta^{(-)}\right)\right)+\cos\theta_n\cos\gamma\right)+\frac{\frac{r_n^2}{2}\left(\sin^2\psi_n-\sin^2\psi_{no}\right)}{r}\right)}$$
(597)

To simplify the second order term expand the directional sin term as shown in (598). From this term we observe the spatial solution to $(\cos\psi_n - \cos\psi_{no})$ defined in (591). For a compaction of the term $(\cos\psi_n + \cos\psi_{no})$ one only needs to redefine (592) as(599) and (595) as(600) such that $(\cos\psi_n + \cos\psi_{no})$ becomes that of (601). Finally the array factor of (597) is re-expressed as that of

$$\sin^2\psi_n - \sin^2\psi_{no} = \sqrt{1-\sin^2\psi_n}^2 - \sqrt{1-\sin^2\psi_{n0}}^2 = -\left(\cos^2\psi_n - \cos^2\psi_{no}\right)$$
$$= -\left(\cos\psi_n - \cos\psi_{no}\right)\left(\cos\psi_{no} + \cos\psi_n\right) \tag{598}$$

$$\rho_o^{(+)} = \left[\left(\sin\theta\cos\phi + \sin\theta_o\cos\phi_o\right)^2 + \left(\sin\theta\sin\phi + \sin\theta_o\sin\phi_o\right)^2\right]^{\frac{1}{2}} \tag{599}$$

$$\delta^{(+)} = \tan^{-1}\left[\frac{\sin\theta\sin\phi + \sin\theta_o\sin\phi_o}{\sin\theta\cos\phi + \sin\theta_o\cos\phi_o}\right] \tag{600}$$

$$\left(\cos\psi_n + \cos\psi_{no}\right) = \rho_o^{(+)}\left(\cos\left(\phi_n - \delta^{(+)}\right) + \cos\theta_n\cos\gamma\right)$$
$$= \rho_o^{(+)}\left(\cos\left(\phi_n\right)\cos\left(\delta^{(+)}\right) + \sin\left(\phi_n\right)\sin\left(\delta^{(+)}\right) + \cos\theta_n\cos\gamma\right) \tag{601}$$

$$F\left(\theta,\phi|\vec{r}_n,\vec{\theta}_n,\vec{\phi}_n\right) =$$

$$\frac{\sum_{n=1}^{N} e^{jk\left[r_n\rho_o\left(\sin\theta_n\left(\cos\phi_n\cos\delta^{(-)} + \sin\phi_n\sin\delta^{(-)}\right) + \cos\theta_n\cos\gamma\right) + \frac{\frac{r_n^2}{2}\left[\rho_o^{(-)}\left(\sin\theta_n\left(\cos\phi_n\cos\delta^{(-)} + \sin\phi_n\sin\delta^{(-)}\right) + \cos\theta_n\cos\gamma\right)\right]}{r}\right]}}{N} \tag{602}$$

The radiation intensity in a given direction (604) is defined as the power radiated from the antenna per unit solid angle. This is obtained by multiplying the radiation density (603) by the square of the distance. Normalized radiation intensity is given by (605) and will also be used throughout this paper where the parameter Z holds as a placeholder for an appropriate set of random variables dependent upon the coordinate system i.e. (spherical, Cartesian, and polar).

$$W_{rad} = \frac{1}{2\eta}\left|\vec{E}\left(r,\theta,\phi|\vec{r}_n,\vec{\theta}_n,\vec{\phi}_n\right)\right|^2 \simeq \frac{1}{2\eta}\left[\begin{array}{c}\left|E_\theta\left(r,\theta,\phi|\vec{r}_n,\vec{\theta}_n,\vec{\phi}_n\right)\right|^2 \\ + \left|E_\phi\left(r,\theta,\phi|\vec{r}_n,\vec{\theta}_n,\vec{\phi}_n\right)\right|^2\end{array}\right]$$
$$= \frac{1}{\eta}\left[\left|\frac{F\left(\theta,\phi|\vec{r}_n,\vec{\theta}_n,\vec{\phi}_n\right)}{r}\right|^2\right]\left(\text{For an isotropic radiator}\right) \tag{603}$$

$E_\theta, E_\phi =$ Far-zone electric field of the antenna $\left(\textit{Element Factor}\right)$

$= \left(1\text{ for an isotropic radiator}\right)$

$$U\left(\theta,\phi\big|\vec{Z}\right)=\frac{\left|F\left(\theta,\phi\big|\vec{Z}\right)\right|^{2}}{\eta} \tag{604}$$

$$U\left(\theta,\phi\big|\vec{Z}\right)^{Normalized}=\left|F\left(\theta,\phi\big|\vec{Z}\right)\right|^{2} \tag{605}$$

The radiation intensity (power pattern or beampattern) for a spherical coordinate system is defined by (609), using the relations in (606)-(608) and normalizing $\tilde{A}=A/\lambda$ and $\tilde{r}_{n}=r_{n}/A$. Notice that unlike [82] that (606) is now redefined in terms of its plus and minus definition due to the third order approximation taken in the binomial expansion. This formulation introduces randomness into the array, and in most circumstances for a random environment it is favorable to express the array factor as this. Last of all, an orthonormal steering vector will be defined as $\zeta^{\vec{r}(+,-)}\left(\theta,\phi\right)\triangleq\left(\zeta_{x}^{r(+,-)}\left(\theta,\phi\right),\zeta_{y}^{r(+,-)}\left(\theta,\phi\right),\zeta_{z}^{r}\left(\theta\right)^{(+,-)}\right)$ for simplicity in analysis when referring to the beamsteering functions. Second the random variables Υ_{n} and T_{n} utilized in [82] have been replaced by the correctly defined orthonormal random variable (610).

$$\zeta\left(\theta,\phi\right)^{(+,-)}=2\pi\tilde{A}\rho_{o}^{(+,-)} \tag{606}$$

$$\zeta_{x}^{r(+,-)}\left(\theta,\phi\right)=\cos\left(\delta^{(+,-)}\right)\zeta\left(\theta,\phi\right)^{(+,-)},$$

$$\zeta_{y}^{r(+,-)}\left(\theta,\phi\right)=\sin\left(\delta^{(+,-)}\right)\zeta\left(\theta,\phi\right)^{(+,-)},$$

$$\zeta_{z}^{r(+,-)}\left(\theta\right)=\cos\gamma^{(+,-)}\zeta\left(\theta,\phi\right)^{(+,-)}, \tag{607}$$

$$\cos\gamma^{(+)}=\rho_{o}^{-1}\left(\cos\theta+\cos\theta_{o}\right),$$

$$\cos\gamma^{(-)}=\rho_{o}^{-1}\left(\cos\theta-\cos\theta_{o}\right)$$

$$\Upsilon_{n}^{x}=\tilde{r}_{n}\sin\theta_{n}\cos\phi_{n},\ -1\leq\Upsilon_{n}^{x}\leq1$$

$$\Upsilon_{n}^{y}=\tilde{r}_{n}\sin\theta_{n}\sin\phi_{n},\ -1\leq\Upsilon_{n}^{y}\leq1$$

$$\Upsilon_{n}^{z}=\tilde{r}_{n}\cos\theta_{n},\qquad -1\leq\Upsilon_{n}^{z}\leq1 \tag{608}$$

$$\Upsilon_{n}^{\vec{r}}\triangleq\left\langle\Upsilon_{n}^{x},\Upsilon_{n}^{y},\Upsilon_{n}^{z}\right\rangle$$

$$U\left(\theta,\phi\big|\vec{\Upsilon}^{\vec{r}}\right)^{Normalized}=\frac{1}{N}+$$

$$\frac{1}{N^{2}}\sum_{n=1}^{N}\sum_{\substack{m=1\\m\neq n}}^{N}e^{j\zeta(\theta,\phi)^{-}\left(\Upsilon_{n}^{\vec{r}}-\Upsilon_{m}^{\vec{r}}\right)}e^{j\frac{\zeta(\theta,\phi)^{-}\zeta(\theta,\phi)^{+}}{2r}\left(\Upsilon_{n}^{\vec{r}}-\Upsilon_{m}^{\vec{r}}\right)^{2}} \tag{609}$$

$$\Upsilon_{n}^{\vec{r}}\triangleq\left\{\begin{array}{l}\Upsilon_{n}^{x}=\tilde{r}_{n}\sin\theta_{n}\cos\phi_{n}\Upsilon_{n}^{y}=\tilde{r}_{n}\sin\theta_{n}\sin\phi_{n},\\ \Upsilon_{n}^{z}=\tilde{r}_{n}\cos\theta_{n}\end{array}\right\} \tag{610}$$

16.2 Characteristics of a Spherical Uniformly Distributed Random Array Near Field Solution

(a) Expected power-patterns

The expected (long-run average, or mean) power-pattern of a random array is formulated in (611) similar to [9], [12], and [82] by taking the expected value of (74) at the meridian elevation angle $\theta = \theta_0 = \pi/2$. Taking the expectation of the power pattern develops (613). This term is characterized compactly by the oscillatory *tinc* function [68], which decreases rapidly with increase of the spatial function $\zeta(\theta,\phi)$, but instead is a much more involved function including the range *r*.

$$U_{av}(\phi) = E_\Upsilon \left| U\left(\phi|\vec{\Upsilon}\right) \right| = \int_{-1}^{1} U\left(\phi|\vec{\Upsilon}\right) f_\Upsilon(\Upsilon) d\Upsilon$$

$$= \frac{1}{N} + \left(1 - \frac{1}{N}\right) \left| \int_{-1}^{1} U\left(\phi|\vec{\Upsilon}\right) \frac{3\left(1-\Upsilon^2\right)}{4} d\Upsilon \right|^2$$

$$(611)$$

Since $\left(\Upsilon_n - \Upsilon_m\right)^{(-)} \left(\Upsilon_n - \Upsilon_m\right)^{(+)}$ is a multiplication of i.i.d. random variables assume that the random variable can be made such that

$$\left(\Upsilon_n - \Upsilon_m\right)^2 = \left(\Upsilon_n - \Upsilon_m\right)^{(-)} \left(\Upsilon_n - \Upsilon_m\right)^{(+)}$$

$$(612)$$

Thus, we now re-express

$$U_{av}(\theta,\phi) = \frac{1}{N} + \left(1 - \frac{1}{N}\right) \begin{bmatrix} \left|\Lambda\left(\zeta_x^r(\theta,\phi)\right)\right|^2 \\ \left|\Lambda\left(\zeta_y^r(\theta,\phi)\right)\right|^2 \\ \left|\Lambda\left(\zeta_z^r(\theta)\right)\right|^2 \end{bmatrix} = \left\langle \left|\Lambda\left(\zeta^{\vec{r}}(\theta,\phi)\right)\right|^2 \right\rangle,$$

$$\langle \Lambda \rangle = \left\langle \int_{-1}^{1} e^{j\left(\frac{\zeta^{\vec{r}}(\theta,\phi)\left(\Upsilon^{\vec{r}}\right)+}{\zeta^{\vec{r}}(\theta,\phi)^- \zeta^{\vec{r}}(\theta,\phi)^+}{2r}\left(\Upsilon^{\vec{r}}\right)^2\right)} \frac{3\left(1-\left(\Upsilon^{\vec{r}}\right)^2\right)}{4} d\Upsilon^{\vec{r}} \right\rangle$$

$$\Lambda = \left\langle \left. \left(3/8 + 3j/8\right) + e^{\frac{-jru}{2v}} \sqrt{r} \begin{pmatrix} (-1-j)e^{\frac{ju(r-v)^2}{2rv}} \sqrt{r}\sqrt{u}\left(-r + e^{j2u}(r-v)-v\right)\sqrt{v} + \\ \sqrt{\pi}\left(-jr^2 u + rv + juv^2\right) \\ erfi\left[\frac{(1/2+j/2)\sqrt{u}(r-v)}{\sqrt{r}\sqrt{v}}\right] - \\ erfi\left[\frac{(1/2+j/2)\sqrt{u}(r+v)}{\sqrt{r}\sqrt{v}}\right] \end{pmatrix} \right/ \left(u^{3/2} v^{5/2}\right) \right\rangle.$$

$$u = \zeta(\theta,\phi)^{\vec{r}-}, v = \zeta(\theta,\phi)^{\vec{r}+}$$

$$(613)$$

In order to verify the result of (613) the $\lim_{r \to \infty}$ the mean valued radiation pattern becomes

$\Lambda = \left\langle 3\text{tinc}\left(\zeta\left(\theta,\phi\right)^{\bar{r}-}\right)\right\rangle$ [81]-[82]. Moreover it is seen that for $3\text{tinc}\left(\zeta_x^r\left(\phi\right)\right)3\text{tinc}\left(\zeta_y^r\left(\phi\right)\right)$ the

beampattern is expressed by $3\text{tinc}\left(\zeta_x^r\left(\phi\right)\right)3\text{tinc}\left(\zeta_y^r\left(\phi\right)\right)$ and is expected. Whereas for $\lim_{u \to 0}\Lambda$ the

beampattern should approach a maximum where beamforming is expected and a minimum at $\lim_{v \to 0}\Lambda$,

which does. Lastly, the law of large numbers describes this expected power pattern as a convergence

resembling the definition of an average defined from the context of probability as $N \to \infty$.

(b) Comments on the previous section

The representation of (613) was derived in order to compare against the analytical expression

derived in [180]. For [31], [59], [60], [68], [179] and [180] the analysis uses a receiving spherical random

array. This is why in [180] the result for the near field being a normalized tinc function is the same result

as that of a spherical random array evaluated at the meridian angle.

In (eq. 4 [59] and 1 [180]) the attempt is to evaluate the integral of a sphere. The difference in the

formulations presented in this series is that the simplification of the Euclidian distance R_n is taken to be a

second order approximation for phase and has been expanded to a third order in this paper in order to help

compare to previous analysis. Moreover the simplification of the Euclidean distance given in [59] and

[180] is equivalent to the following.

$$R_n\left(\theta,\phi\middle|r_n,\theta_n,\phi_n\right) = \left|r - r_n\right| =$$
$$r\sqrt{1+\left(\frac{r_n}{r}\right)^2 - \frac{2r_n\cos\psi_n}{r}} \equiv r\sqrt{1+x^2 - 2x\cos\psi_n} \tag{614}$$
$$x \triangleq \left(\frac{r_n}{r}\right)$$

Also since r is not a part of the integration it is placed into the β given in (eqn. [180]). Such that

$\beta = \dfrac{2\pi\Delta f}{c}r$. Also since the integration is done over a sphere the following integration is done similar

again to [59] and [180]. Moreover, due to the change of variables being $x \triangleq \left(\dfrac{r_n}{r}\right)$ one obtains as a

consequence the multiplication of $R_A^{\ 3}$ in (616). Hence,

$$\int_0^{r_n}\int_0^\pi\int_0^{2\pi}\exp\left[-j\beta\sqrt{1+x^2-2x\cos\theta}\right]x^2\sin\theta d\theta d\phi$$
$$= \int_0^{r_n}\int_0^\pi\exp\left[-j\beta\sqrt{1+x^2-2x\cos\theta}\right]x^2\sin\theta d\theta d\phi \tag{615}$$

$$2\pi\left\{R_A^{\ 3}\right\}\int_0^{x'}\int_0^{\pi}\exp\left[-j\beta\sqrt{1+x^2-2x\cos\theta}\right]\left\{x^2 dx\right\}\sin\theta d\theta d\phi$$

$$x = r_n/r \to rx = r_n \tag{616}$$

$$dx = 1/r dr_n \to r dx = dr_n$$

$$r \equiv R_A$$

Moreover, the integration of (616) in the near field for a receiving array as in [59], [60] and [180] or as in this analysis the far field for a transmit array produces a mainlobe factor being that of a

$$\Lambda = \frac{-3u\cos(u)+3\sin(u)}{u^3} = 3\text{tinc}(u) \tag{617}$$

What is odd about this solution is the lack of multiplication of pattern multiplication. The reason why there is no pattern multiplication is due to the following. A sphere is composed of two types of symmetry a ball containing the interior of the sphere and a rings composing the outer shell of the sphere. Therefore (617) is the solution to a spherical random array in the far field, but yet is missing the information about the surface area of the sphere. Therefore the total solution to a spherical random array in the far field for transmit is given by pattern multiplication.

$$\Lambda = \left\langle 3\text{tinc}\left(\zeta(\theta,\phi)^{\bar{r}-}\right)\right\rangle \tag{618}$$

This new method of using compound random variables has helped to unleash the total solution to a spherical random array, which is actually a product of pattern multiplication of the symmetries encountered in three dimensions. The difference in the results of eqn. 5 of [180] and (617) compared to that of (618) may at first seem difficult to comprehend, but with a little though becomes undeniable.

CHAPTER XVII

CONCLUSION

This paper has clarified the Fourier transform relation in random arrays and has added a significant contribution to the literature. It has been shown how compound random variables simplify the process in terms of determining characteristics functions. The addition of the discrete Fourier transform was added for finding the characteristic modes of discrete distributions. This type of distribution is likely to give better clarity and resolution of a radiation pattern for a real world scenario. The difficulty however is limited by the available knowledge on discrete distributions and their respective characteristic functions. Other common techniques of shared aperture partitions, adaptive nulling and tapering was found to be applicable to random arrays. Also it was found that the range error of the radiators must be less than lambda over ten and also that the phase shifter has a big impact on the overall effective aperture size of the random array.

In addition the theoretical analysis of this dissertation was shown to have big impacts on the opportunistic array design being worked on in [103]-[125]. For instance, the opportunistic nature, allows for enhanced "stealth, multifunction capabilities and high survivability of these arrays [that] can be exploited by the Army and Air Force to deploy radar networks within urban centers in crisis areas – quickly and covertly."[102]

Also it has been shown under ideal conditions the directivity of aperiodic array are capable of achieving directivity of order N with narrow beams, as long as the antenna are located sparsely enough. In addition, it has been shown a volumetric array is independent of scan angle where as a circular random arrays pattern changes. Most importantly the derivations of a random array are explicitly shown such that the topic traces back to its origins effortlessly.

Lastly, a number of open issues remain, such that beamforming from a destination in rapid motion creates challenges causing channel suffering and severe multipath fading. Consequently, algorithms ought to be developed for frequency offset correction as well as methods for initial phase or location estimation. Also genetic algorithms may have added benefits to random arrays as they may eventually be applied to enhance optimizations schemes of which arrange optimal traits in the topology to assist in the radiation characteristics of these random arrays.

REFERENCES

[1] I. Kocaman, "Distributed beamforming in a swarm UAV network," M.S. thesis, Dept. Elect. Eng., Naval Postgraduate School, Monterey, CA, 2008.

[2] Y. Loke, "Sensor synchronization, geolocation and wireless communication in a shipboard opportunistic array," M.S. thesis, Dept. Elect. Eng., Naval Postgraduate School, Monterey, CA, 2006.

[3] C. M. Chan, "Distributed beamforming in man portable communication networks," M.S. thesis, Dept. Elect. Eng., Naval Postgraduate School, Monterey, CA, 2007.

[4] E. C. Yeo, "Wirelessly networked opportunistic digital phased array: System analysis and development of a 2.4 GHZ Demonstrator," M.S. thesis, Dept. Elect. Eng., Naval Postgraduate School, Monterey, CA, 2006.

[5] W. F. Young, "Measurements of randomly placed wireless transmitters used as an array for receivers located within the array volume with application to emergency responders," *IEEE Trans. Antennas Propag. Mag.*, vol. 57, pp. 241-247, Jan. 2009.

[6] K. Buchanan and G. Huff, "A comparison of geometrically bound random arrays in Euclidean space," in *IEEE Antennas and Propag. Soc. Int. Symp.,* Spokane, WA, July 2011, pp. 3-8.

[7] H. Ochiai, "On the effects of phase estimation errors on collaborative beamforming in wireless ad hoc networks," in *Proc. of Acoustics, Speech, and Signal Proc.*, vol. 53, Nov. 2005, pp. 4110-4124.

[8] H. Ochiai, "Variable-rate two-phase collaborative communication protocols for wireless networks," *IEEE Trans. on Inf. Theory*, vol. 52, pp. 4299, Sept. 2006.

[9] H. Ochiai, "Collaborative beamforming for distributed wireless ad hoc sensor networks," *IEEE Trans. Signal Process.*, vol. 53, pp. 4110, Nov. 2005.

[10] M. F. A. Ahmed and S. A. Vorobyov, "Performance characteristics of collaborative beamforming for wireless sensor networks with Gaussian distributed sensor nodes," in *Proc. 33st*

IEEE Inter. Conf. on Acoustics, Speech, and Signal Processing (ICASSP '08) , Las Vegas, Nevada, USA, Mar. 30-Apr. 4, 2008, pp. 3249-3252.

[11] M. F. A. Ahmed and S. A. Vorobyov, "Beampattern random behavior in wireless sensor networks with Gaussian distributed sensor nodes," in *Proc. Canadian Conference on Electrical and Computer Engineering (CCECE '08)* , Niagara Falls, ON, Canada, May. 4-7, 2008, pp. 257-260.

[12] M. F. A. Ahmed and S. A. Vorobyov, "Collaborative beamforming for wireless sensor networks with Gaussian distributed sensor nodes," *IEEE Trans. on Wireless Commun.*, vol. 8, pp. 638-643, Feb. 2009.

[13] M. F. A. Ahmed and S. A. Vorobyov, "Node selection for sidelobe control in collaborative beamforming for wireless sensor networks," in *Signal Processing Advances in Wireless Communications (SPAWC '09)*, Perugia, Italy, June 2009, pp. 519-523.

[14] M. F. A. Ahmed and S. A. Vorobyov, "Sidelobe control in collaborative beamforming via node selection," *IEEE Trans. on Signal Proc.*, vol. 58, pp. 6168-6180, Dec. 2010.

[15] J. T. Bernhard, "Wideband random phased arrays: theory and design," in *Wideband and Multi-band Antennas and Arrays, 2005. IEE* (Ref. No. 2005/11059), Birmingham, UK, Sept. 2005, pp. 89-93.

[16] K. C. Kerby and J. T. Bernhard, "Sidelobe level and wideband behavior of arrays of random subarrays," *IEEE Trans. Antennas Propag.*, vol. 54, pp. 2253, Aug. 2006.

[17] K. C. Kerby and J. T. Bernhard, "Correction to sidelobe level and wideband behavior of arrays of random subarrays," *IEEE Trans. Antennas Propag*, vol. 55, pp. 250, Jan. 2007.

[18] Z. Huseyin-Arslan and M. D. Benedetto, *Ultra Wideband Wireless Communication,* London, UK: Wiley, 2005.

[19] M. Lanne, "Wideband Array Antenna System Development," in *Phased Array Syst. and Technology Int. Symp.*, Waltham, MA, Oct. 2010, pp. 789.

[20] W. Liu, *Wideband Beamforming Concepts and Technique,* London, UK: Wiley, 2010.

[21] B. Svensson and Y. Jensen, "Verification of a large broadband electronically scanned array aperture," in *Proc. of the Fourth European Conf. in Antennas and Propag.*, Spain, Apr. 2010, pp. 1-3.

[22] S. W. Ellingson, "Beamforming and interference canceling with very large wideband arrays," *IEEE Trans. Antennas Propag.*, vol. 51, pp. 1338-1346, Jun. 2003.

[23] P. Saengudomlert and V. W. S. Chan, "Hybrid optical and electronic signal processing for ultra-wideband RF antenna arrays," in *IEEE Int. Conf. in Communications*, Seoul, KR, May 2005, pp. 2063-2069.

[24] L. C. Godara, "Application of antenna arrays to mobile communications, part II: Beam-forming and direction-of-arrival considerations," *Proc. IEEE*, vol. 85, pp. 1195, Apr. 1997.

[25] L. C. Godara, "Applications of antenna arrays to mobile communications. I. Performance improvement, feasibility, and system considerations," *Proc. IEEE*, vol. 85, pp. 1031, Jul. 1997.

[26] M. Andreasen, "Linear arrays with variable interelement spacings," *IEEE Trans. Antennas Propag.*, vol. 10, pp. 137, Mar. 1962.

[27] F. Anderson, "Ultra-wideband beamforming in sparse arrays," *Proc. IEE Proceedings-H*, vol. 138, pp. 342-346, Aug. 1991.

[28] Y. Lo, "A spacing weighted antenna array," in *IRE Int. Conv. Record*, pt. 1, Urbana, IL., 1962, pp. 191-195.

[29] Y. Lo, "Sidelobe level in nonuniformly spaced antenna arrays," *IEEE Trans. Antennas Propag.*, vol. 11, pp. 511-512, Mar. 1963.

[30] Y. Lo, "A probabilistic approach to the design of large antenna arrays," *IEEE Trans. Antennas Propag.*, vol. 11, pp. 95-96, Jan. 1963.

[31] Y. Lo, "A mathematical theory of antenna arrays with randomly spaced elements," *IEEE Trans. Antennas Propag.*, vol. 12, pp. 257-268, May 1964.

[32] V. Agrawal and L. Yuen, "Mutual coupling in phased arrays of randomly spaced antennas," *IEEE Trans. Antennas Propag.*, vol. 20, pp. 288-295, May 1972.

[33] V. D. Agrawal and Y. T. Lo, "Distribution of sidelobe level in random arrays," *Proc. of the IEEE*, vol. 57, pp. 1764-1765, Oct. 1969.

[34] A. Maffett, "Array factors with nonuniform spacing parameter*," IRE Trans. Antennas and Propag.*, vol. 10, pp. 131-136, Mar. 1962.

[35] D. King, R. Packard, and R. Thomas, "Unequally-spaced, broad-band antenna arrays," *IEEE Trans. Antennas Propag.*, vol. 8, pp. 380-384, Jul. 1960.

[36] G. Swenson, Jr. and Y. Lo, "The University of Illinois radio telescope," *IEEE Trans. Antennas Propag.*, vol. 9, pp. 9-16, Jan. 1961.

[37] Y. Lo and R. Simcoe, "An experiment on antenna arrays with randomly spaced elements," *IEEE Trans. Antennas Propag.*, vol. 15, pp. 231-235, Mar. 1967.

[38] K. C. Kerby and J. T. Bernhard, "Wideband periodic array of random subarrays," in *IEEE Antennas and Propag. Society Int. Symp.*, Singapore, July 2006, pp. 555-558.

[39] J. T. Bernhard, "Development of wideband random phased arrays composed of modified canted sector antennas," in *Wireless Commun. and Appl. Comp. Electromagnetics Int. Conf*, Honolulu, HI, Apr. 2005, pp. 229-232.

[40] G.H. Huff and T.L. Roach, "Stripline-based spiral antennas with integrated feed structure, impedance transformer, and Dyson-style balun," in *Antennas and Propag. Int. Symp.,* Honolulu, HI, June 2007, pp. 2698-2701.

[41] J. Dyson, "The equiangular spiral antenna," in *Proc. of Antenna Applications Symp.*, Monticello, IL, Oct. 1955, pp. 1–12.

[42] J. A. Kaiser, "The Archimedean two-wire spiral antenna," *IRE Trans. Antennas and Propag.*, vol. 8, pp. 312–323, May 1960.

[43] P. E. Mayes, "Frequency-independent antennas and broad-band derivatives thereof," *Proc. IEEE*, vol. 80, pp. 103–112, Jan. 1992.

[44] R. Gunnarsson, T. Martin, A. Ouacha, "Wide-band circular antenna arrays consisting of bicone, semi bicone or bowtie elements," in *APMC Microw. Conf.,* Yokohama, JP, Dec. 2006, pp.2074-2077.

[45] M. C. Vigano, G. Toso, P. Angeletti, I. E. Lager, A. Yarovoy, D. Caratelli, "Sparse antenna array for earth-coverage satellite applications," in *Proc. of the Fourth European Conf. on Antennas and Propag.,* Barcelona, SP, 2010, pp. 1-4.

[46] M. C. Viganò, G. Caille, G. Toso, C. Mangenot, I. E. Lager, "Sparse planar array synthesis technique for satellite applications," in *Antennas and Propag. Soc. Int. Symp.,* Toronto, ON, Canada, July 2010, pp. 1-4.

[47] P. Steinmann; J. M. R. Weaver, "Nanometer-scale gaps between metallic electrodes fabricated using a statistical alignment technique," *Applied Phys. Letters*, vol.86, pp.63104-63104, Feb. 2005.

[48] M. Rattan, M. Patterh, B.S. Sohi (2008, Jan.). *Antenna Array Optimization Using Evolutionary Approaches* [Online]. Available: http://redshift.vif.com

[49] H. Wheeler, "The radiation resistance of an antenna in an infinite array or waveguide," *Proc. IRE*, vol.36, pp. 478- 487, Apr. 1948.

[50] H. Wheeler, "Simple relations derived from a phased-array antenna made of an infinite current sheet," *IEEE Trans. Antennas Propag*, vol.13, pp. 506- 514, July 1965.

[51] D. Pozar, "General relations for a phased array of printed antennas derived from infinite current sheets," *IEEE Trans. Antennas Propag.*, vol.33, pp. 498- 504, May 1985.

[52] J. A. Kasemodel, C. Chen, J. L. Volakis, "Low-cost, planar and wideband phased array with integrated balun and matching network for wide-angle scanning," in *Antennas and Propag. Society Int. Symp.* Toronto, ON, Canada, July 2010, pp.1-4.

[53] Y. Chen, S. Yang, Z. Nie, "The role of ground plane plays in wideband phased array antenna," in *IEEE Int. Conference Ultra-Wideband (ICUWB)*, Nanjing, China, Sept. 2010, pp.1-4.

[54] L. M. Hilliard, et al., "Lightweight linear broadband antennas enabling small UAV wing systems and space flight nanosat concept," in *Proc. IEEE Int. Geosci. and Remote Sensing Symp.*, Anchorage, AK., Sept. 2004, pp. 3577-3580.

[55] Y. Bar-Ness and A. Haimovich, "Synthesis of random antenna array patterns with prescribed nulls," *IEEE Trans. Antennas Propag.,* vol. 32, pp. 1298-1307, Dec. 1984.

[56] A. Trucco and F. Repetto, "A stochastic approach to optimizing the aperture and the number of elements of an aperiodic array," in *OCEANS Prospects for the 21st Century*, Fort Lauderdale, FL, Sept. 1996, pp. 1510-1515.

[57] C. Wai, "Distributed beamforming in wireless sensor networks" M.S. thesis, Dept. Elect. Eng., Naval Postgraduate School, Monterey, CA, 2004.

[58] A. Panicali and L. Yuen, "A probabilistic approach to large circular and spherical arrays," *IEEE Trans. Antennas Propag.,* vol. 17, pp. 514-522, Jul. 1969.

[59] T. A. Dzekov and R. S. Berkowitz, "Parameters of a spherical random antenna array," *Electronics Lett.*, vol. 14, pp. 495-496, Aug 1978.

[60] D. Yavuz, "Frequency response and bandwidth of a spherical random array," *Electronics Lett.*, vol. 15, pp. 314-315, May 1979.

[61] D. Yavuz, "Frequency and focal region properties of random sparse arrays," *IEEE Trans. Antennas Propag*, vol. 32, pp. 456-465, May 1984.

[62] A. Fereidountabar, "Wide-band beamformer with integrated antennas," *WSEAS Trans. Commun., vol.* 8, pp. 279-289, Feb. 2009.

[63] M. Hussain, A. S. Al-Zayed, "Aperture-sparsity analysis of ultrawideband two-dimensional focused array," *IEEE Trans. Antennas Propag.,* vol. 56, pp.1908-1918, July 2008.

[64] P. K. Weber, "Optimization of random sparse 2-D transducer arrays for 3-D electronic beam steering and focusing," in *IEEE Ultrasonics Symp.*, Cannes, France, Nov. 1994, pp. 1503-1506.

[65] C. A. Balanis, *Antenna Theory: Analysis and Design 3 ed*, New York: John Wiley & Sons, Inc., 2005.

[66] B. I. Raju and C. S. Hall, "Space-filling, aperiodic array ultrasonic therapy transducers," in *IEEE Ultrasonics Symposium*, Beijing, China, Nov. 2008, pp. 463-466.

[67] N. K. Nikolova. (2012) *Introduction into the Theory of Radiation* [Online]. Available: https://www.ece.mcmaster.ca/faculty/nikolova.pdf

[68] R. E. Blahut, *Theory of Remote Image Formation*, New York: Cambridge University Press, 2004.

[69] L. C. Andrews, *Special Functions for Engineers and Applied Mathematicians,* New York: MacMilan, 1986.

[70] Y. L. Luke, *the Special Functions and Their Approximations vol. 1*, New York: Academic Press, 1969.

[71] W. N. Bailey, *Generalized Hypergeometric Series*, New York: Stechert-Hafner Service Agency, 1964.

[72] I. S. Gradshteyn, *Table of Integrals Series and Products* vol. *7*, New York: Academic Press, 2007.

[73] Q. Cao, "Generalized Jinc functions and their application to focusing and diffraction of circular apertures," *Opt. Soc. Am. A*, vol. 20, pp. 661-667, Apr. 2003.

[74] L. Sorensen. (2011) *Two-Dimensional Diffraction* [Online]. Available: https://faculty.washington.edu/seattle/physics575/pdf/optical%20diffraction%20goals.pdf

[75] G. J. Gbur, *Mathematical Methods for Optical Physics and Engineering,* New York: Cambridge University Press, 2011.

[76] G. Urcid and A. Padilla, "Far-field diffraction patterns of circular sectors and related apertures," *Appl. Optics*, vol. 44, pp. 7677-7696, Dec. 2005

[77] Brown, C.L. Zoubir, A.M., "A new approach to testing Gaussianity with the characteristic function," in *Proc. Inform. Commun. and Signal Process Int. Conf. ICICS.,* Singapore, Sept. 1997, pp.1198-1202.

[78] J. Liu, Y. Zhu; , "A new definition of characteristic function for random fuzzy variable," in *Fifth Int. Conf. on Fuzzy Systems and Knowledge Discovery*, Washington D.C., USA, Oct. 2008, pp.132-136.

[79] Wolfram. (2007). *Characteristic Function*. [Online]. Available: http://mathworld.wolfram.com/CharacteristicFunction.html

[80] P. Kim, P T. Kim, "On the characteristic function of the von Mises-Fisher matrix distribution" in *High Dimensional Probability II*, Boston, MA, 2000, pp.475–490.

[81] K. R. Buchanan, "A study of aperiodic (random) arrays of various geometries," M.S. thesis, Dept. Elect. & Com. Eng., Texas A&M University, TX, 2011.

[82] K. Buchanan and G. Huff, "Spherically bound random arrays," *IEEE Trans. Antennas Propag., 2014 (to be published).*

[83] Wolfram Research, Inc., Mathematica, Version 8.0, Champaign, IL (2010).

[84] Wolfram Research Inc. (2012). *Jinc Function* [Online] Available: http://mathworld.wolfram.com/JincFunction.html

[85] B. D. Steinberg, "The peak sidelobe of the phased array having randomly located elements," *IEEE Trans. Antennas Propag.*, vol. 20, pp. 129-136, Mar. 1972.

[86] A. Ishimaru, "Theory of unequally-spaced arrays," *Proc. IRE Antennas and Propag.*, vol. 10, pp. 691-702, Nov. 1962.

[87] S. Holm, B. Elgetun, & G. Dahl, "Properties of the beampattern of weight- and layout-optimized sparse arrays," *IEEE Trans. Ultrason. Ferroelect. and Freq. Contr.,* vol. 44, pp. 983-991, Sept. 1997.

[88] J. S. Petko, D. H. Werner, "Analysis and design optimization of robust micro-UAV swarm based antenna arrays," *IEEE Trans. Antennas Propag.,* vol. 60, pp. 2295-2308, May 2012.

[89] Jenkins, J., "Some properties and examples of random listening arrays," in *IEEE Int. Conf. on Eng. in the Ocean Environment*, Seattle, WA, 25-28 Sept. 1973, pp.466-469.

[90] Haupt, R.L., "Optimized element spacing for low sidelobe concentric ring arrays," *IEEE Trans. Antennas Propag.*, vol.56, pp.266-268, Jan. 2008.

[91] F. D. Tolba, D. Magoni, and P. Lorenz, "Connectivity, energy and mobility driven clustering algorithm for mobile ad hoc networks," in *Proc. IEEE GLOBECOM*, Washington, DC, Nov. 2007, pp. 2786–2790.

[92] C. Taylor, "Terrestrial communication between wireless sensor networks using beamforming and space division multiple access," M.S. thesis, Dept. Elect. Eng., Naval Postgraduate School, Monterey, CA, 2008

[93] G. Galati, S. Perna, and M. Abbati, "Quasibistatic random arrays," *IEE Proc. F Radar and Signal Process.*, vol.139, pp.193-198, Jun 1992.

[94] W.J. Hendricks, "The totally random versus the bin approach for random arrays," *IEEE Trans. Antennas Propag.*, vol.39, pp.1757-1762, Dec 1991

[95] O. Younis and S. Fahmy, "HEED: A hybrid, energy-efficient, distributed clustering approach for ad hoc sensor networks" *IEEE Trans. on Mobile Computing*, vol. 3, pp. 660-669, Oct. 2004.

[96] D. L. Jaggard, A. Jaggard, and O. Manuar. (1999). *Fractal Random Arrays* [Online]. Available: http://www.seas.upenn.edu/sunfest/docs/papers/Dimas.pdf

[97] W. Richards and L. Yuen, "Antenna pattern synthesis based on optimization in a probabilistic sense," *IEEE Trans. Antennas Propag.*, vol. 23, pp. 165-172, Mar. 1975.

[98] C. Walker (2007, Jan.). *The Use of Broadband Antenna Technology in Modern Communication Systems* [Online]. Available: http://digital-transmissions.co.uk/2007-01defencebroadband.html

[99] H. Kook, P. Davies, and J. S. Bolton, "Statistical properties of random sparse arrays," *Journal of Sound and Vibration*, vol. 255 pp. 819-848, Aug. 2002.

[100] R. M. Leahy, and B. D. Jeffs, "On the design of maximally sparse beamforming arrays". *IEEE Trans. Antennas Propag*, vol. 39, pp. 1178-1187, Aug. 1991.

[101] B. D. Steinberg, *Principles of Aperture & Array System Design*, New York: Wiley, 1976.

[102] M. Tong, "System study and design of broad-band u-slot microstrip patch antennas for aperstructures and opportunistic arrays," M.S. thesis, Dept. Elect. Eng., Naval Postgraduate School, Monterey, CA, 2005.

[103] Y. Yong, "Receive channel architecture and transmission system for digital array radar," M.S. thesis, Dept. Elect. Eng., Naval Postgraduate School, Monterey, CA, 2005.

[104] B. Gezer, "Multi-Beam digital antenna for radar communications and uav tracking based on off-the-shelf wireless technologies," M.S. thesis, Dept. Elect. Eng., Naval Postgraduate School, Monterey, CA, 2006.

[105] H. Edmund, "Digital tracking array for fm signals based on off-the-shelf wireless technologies," M.S. thesis, Dept. Elect. Eng., Naval Postgraduate School, Monterey, CA, 2007.

[106] University of Hamburg. (2014) *HF Radar Home Page* [Online]. Available: http://ifmaxp1.ifm.uni-hamburg.de/ANT_PET_1_100DPI.shtml

[107] Raytheon. (2014) *Relocatable Over-the-Horizon Radar* [Online]. Available: http://www.mobileradar.org/Documents/ROTHR.pdf

[108] A. Denk, "Detection and jamming low probability of intercept (lpi) radars," M.S. thesis, Dept. Elect. Eng., Naval Postgraduate School, Monterey, CA, 2006.

[109] D. Jenn, "Microwave devices and radar," in *Lecture Notes (distance learning)*, vol. 1, ver. 4.7, Naval Postgraduate School, Monterey, CA, 2005.

[110] Tikalon. (2014) *Scientific Consulting and Intellectual Property Creation* [Online]. Available: http://tikalon.com/blog/2013/mm_wave_absorption.png

[111] G. Ong and K. Teng, "Digital LPI radar detector," M.S. thesis, Dept. Elect. Eng., Naval Postgraduate School, Monterey, CA, 2001.

[112] G. Burgstaller, "Wirelessley networked digital phased array: design and analysis of a 2.4 ghz demonstrator," M.S. thesis, Dept. Elect. Eng., Naval Postgraduate School, CA, 2006.

[113] J. Bartee, "Genetic algorithms as a tool for phased array radar design," M.S. thesis, Dept. Elect. Eng., Naval Postgraduate School, Monterey, CA, 2002.

[114] F. Kaya, "Development of a receiver processor for uav video signal acquisition and tracking using digital phased array antenna," M.S. thesis, Dept. Elect. Eng., Naval Postgraduate School, Monterey, CA, 2010.

[115] N. Paepolshiri, "Extending the unambiguous range of cw polyphase radar systems using number theoretic transforms," M.S. thesis, Dept. Elect. Eng., Naval Postgraduate School, Monterey, CA, 2011.

[116] A. Kaptan, "Net-Centric controlled distributed stand-in-jamming using uavs-transmission losses and range limitations due to geo-localization problem over turkish geography," M.S. thesis, Dept. Elect. Eng., Naval Postgraduate School, Monterey, CA, 2012.

[117] M. Batson, "Enhanced radio frequency (rf) collection with distributed wireless sensor networks," M.S. thesis, Dept. Elect. Eng., Naval Postgraduate School, Monterey, CA, 2007.

[118] S. Yeh, "Development of a digital tracking array with single-channel rsns and monopulse digital beamforming," M.S. thesis, Dept. Elect. Eng., Naval Postgraduate School, Monterey, CA, 2010.

[119] T. Yen-Chang, "Development of the Phase Synchronization Circuit for Wirelessley Distributed Digital Phase Array," M.S. thesis, Dept. Elect. Eng., Naval Postgraduate School, Monterey, CA, 2009.

[120] E. Shin, "Digital antenna architectures using commercial off the shelf hardware," M.S. thesis, Dept. Elect. Eng., Naval Postgraduate School, Monterey, CA, 2003.

[121] W. Cheng, "Cancellation circuit for transmit-receive isolation," M.S. thesis, Dept. Elect. Eng., Naval Postgraduate School, Monterey, CA, 2010.

[122] J. Noris, "Wireless networks for beamforming in distributed phased array radar," M.S. thesis, Dept. Elect. Eng., Naval Postgraduate School, Monterey, CA, 2007.

[123] Online Notes. (2014) *Radar Fundamentals by D. Jenn* [Online]. Available: http://www.nps.navy.mil/faculty/jenn

[124] D. Jenn, Loke Y, Chin M., Choon Y., Siang O. and Yam Y., "Distributed phased arrays and wireless beamforming networks," *Intl. Jour of Distributed Sensor Networks*, vol. 5: July 2009, pg. 283-302.

[125] P. Djerf, "Development of a distributed digital array radar (DDAR)," M.S. thesis, Dept. Elect. Eng., Naval Postgraduate School, Monterey, CA, 2008.

[126] J. Uher, T. Wysocki and B. Wysocki, "Review of distributed beamforming," *J. of Telecommun. and Inform. Technology*, University of Nebraska-Lincoln, Omaha, Mar. 2011.

[127] C. Wehner. (2014) *Euler's Identity and the Eucalculus* [Online]. Available: http://wehner.org/euler/

[128] S. Haykin and B. V. Veen, *Signals and Systems.* New York, NY: John Wiley & Sons, Inc., 2005.

[129] R. N. Bracewell and J. D. Villasenor, "Fraunhofer diffraction by a spiral slit," *Opt. Soc. Am. A., vol.* 7, pp. 21-25, Jan. 1990.

[130] W. Cochran, F.H. Crick and V. Vand, "The structure of synthetic polypeptides. I. The transform of atoms on a helix." *Acta Crystallographica*, vol. 5, pg. 581-586, Sept. 1952.

[131] F.H. Crick and J. D. Watson, "Molecular structure of nucleic acids," *Nature*, vol. 171, pg. 737-738, Apr. 1953.

[132] D. Harker, and J. S. Kasher, "Phases of Fourier coefficients directly from the crystal diffraction data," *Acta Cystallographia*, vol. 1, pg. 70–5, May 1948.

[133] J. Karle, and H. Hauptman., "The phases and magnitudes of the structure factors," *Acta Crystallographia,* vol. 3, pg. 181-187, May 1950.

[134] D. Sayre, "Some implications of a theorem due to Shannon," *Acta Crystallographia*, vol. 5, pg. 843, 1952.

[135] D. Sayre, "The squaring method: a new method for phase determination," *Acta Crystallographia*, vol. 5, pg. 60–65, Nov. 1952.

[136] J. Ruze, "The effect of aperture errors on the antenna radiation pattern," *Nouvo Cimento,* vol. 3, 9, pp. 364-380, Mar. 1952.

[137] E. N. Gilbert, and S. P. Morgan, "Optimum design of directive antenna arrays subject to random variations," *Bell Syst. Tech. J.*, vol. 23, pp. 637-663, May 1955.

[138] M. Grahn, "Wirelessley networked digital phased array: analysis and development of a phase synchronization concept," M.S. thesis, Dept. Elect. Eng., Naval Postgraduate School, Monterey, CA, 2007.

[139] K. Yao, R. E. Hudson, C. W. Reed, D. C. Chen, and F. Lorenzelli, "Blind beamforming on a randomly distributed sensor array system," *IEEE J. Select. Areas Commun.*, vol. 16, pp. 1555-1567, Oct. 1998.

[140] H. Ochiai, and H. Imai, "On the distribution of the peak-to-average power ratio in OFDM signals," *IEEE Trans on Commun.*, vol. 49, pp. 282-289, Feb. 2001.

[141] Wolfram Research Inc. (2012). *Euler Angles* [Online]. Available:
http://mathworld.wolfram.com/EulerAngles.html

[142] Y. Lo and S. W. *Lee, Antenna Handbook vol. II Antenna Theory*. New York, NY: Van Nostrand Reinhold, 1993.

[143] S. Stanislav. (2014) *K-Space Images of n-Dimensional Spheres and Generalized Sinc Functions* [Online]. Available: http://www.ebyte.it/library/docs/math07/SincN.html

[144] Astro-foren. (2014) *Optik* [Online]. Available: http://astro-foren.de/index.php/Thread/6556-Es-ist-ein-Jammer/

[145] P. Nelson, F. Fazi, K. Holland, T. Takeuchi, "Inverse problems and sound reproduction," in *ISVR Abisonics Symposium*, Paris FR, Mar. 2010.

[146] Wolfram Research Inc. (2012). *Lambda function* [Online]. Available:
http://mathworld.wolfram.com/LambdaFunction.html

[147] G. Francis, J. M. Sullivan, "Visualizing a sphere eversion," *IEEE Trans. Visualization and Comput. Graph.*, vol.10, pp.509-515, Sept.-Oct. 2004.

[148] J.M. Sullivan, "Sphere eversions: from smale through the optiverse," *Math. and Art: Math. Visualization in Art and Education*, pp. 201-212, 311-313, 2002.

[149] Wolfram Research Inc. (2012). *Radon Transform* [Online]. Available:
http://mathworld.wolfram.com/RadonTransform.html

[150] Wikipedia. (2014) *Radon Transform* [Online]. Available:
http://en.wikipedia.org/wiki/Radon_transform

[151] Wikipedia. (2014) *Tomographic Reconstruction* [Online]. Available:
http://en.wikipedia.org/wiki/Tomographic_reconstruction

[152] C. A. Balanis, *Advanced Engineering Electromagnetics*. New York, NY: John Wiley & Sons, 2nd Edition, 2012.

[153] R. F. Harrington, *Time-Harmonic Electromagnetic Fields*. New York, NY: McGraw-Hill, 1961.

[154] S. Silver (ed.), *Microwave Antenna Theory and Design MIT Radiation Laboratory Series, vol. 12*. New York, NY: McGraw-Hill, 1949.

[155] H. Foundalis. (2014) *What Does a 4-Dimensional Sphere Look Like?* [Online]. Available: http://www.foundalis.com/phy/4Dsphere.htm

[156] Wikipedia. (2014) *N-sphere* [Online]. Available: http://en.wikipedia.org/wiki/N-sphere

[157] D. Jenn, "Transmission Equation for Multiple Cooperative Transmitters and Collective Beamforming," *IEEE Trans. Antennas Wireless Propag.*, vol. 7, pp. 606- 608. Dec. 2008.

[158] K. Zarifi, A. Ghrayeb and S. Affes "Collaborative beamforming for wireless sensor networks with improved graph connectivity and energy efficiency," *IEEE Trans. Signal Process.,* vol., 58, pp. 1904-1921, Mar. 2010.

[159] L. Dong, A. P. Petropulu, and H. V. Poor, "A cross-layer approach to collaborative beamforming for wireless ad hoc networks," *IEEE Trans. Signal Process.,* vol. 56, pp. 2981–2993, Jul. 2008.

[160] R. Mudumbai, G. Barriac, and U. Madhow, "On the feasibility of distributed beamforming in wireless sensor networks," *IEEE Trans. Wireless Commun.,* vol. 6, pp. 1754–1763, Apr. 2007.

[161] A. G. Marques, X. Wang, and G. B. Giannakis, "Minimizing transmit power for coherent communications in wireless sensor networks with finite-rate feedback," *IEEE Trans. Signal Process.,* vol. 56, pp.4446–4457, Sep. 2008.

[162] V. Havary-Nassab, S. Shahbazpanahi, A. Grami, and Z.-Q. Luo, "Distributed beamforming for relay networks based on second-order statistics of the channel state information," *IEEE Trans. Signal Process.,* vol. 56, pp. 4306–4316, Sep. 2008.

[163] Y. Jing and H. Jafarkhani, "Network beamforming using relays with perfect channel information," *IEEE Trans. Inf. Theory*, vol. 55, pp. 2499–2517, Jun. 2009.

[164] A. El-Keyi and B. Champagne, "Collaborative uplink transmit beamforming with robustness against channel estimation errors," *IEEE Trans. Veh. Technol.,* vol. 58, pp. 126–139, Jan. 2009.

[165] R. Mudumbai, D. R. Brown, U. Madhow, and H. V. Poor, "Distributed transmit beamforming: Challenges and recent progress," *IEEE Commun. Mag.,* vol. 47, pp. 102–110, Feb. 2009.

[166] S. Boyd, A. Ghosh, B. Prabhakar, and D. Shah, "Randomized gossip algorithms," *IEEE Trans. Inf. Theory*, vol. 52, pp. 2508–2530, Jun. 2006.

[167] T. C. Aysal, M. J. Coates, and M. G. Rabbat, "Distributed average consensus with dithered quantization," *IEEE Trans. Signal Process*., vol. 56, pp. 4905–4918, Oct. 2008.

[168] R. Karp, C. Schindelhauser, S. Shenker, and B. Vöking, "Randomized rumor spreading," in *Proc. Symp. Found. of Comput. Sci.*, Redondo Beach, CA, Nov. 2000, pp. 564–574.

[169] D. R. Brown, III and H. V. Poor, "Time-slotted round-trip carrier synchronization for distributed beamforming," *IEEE Trans. Signal Process.,* vol. 56, pp. 5630–5643, Nov. 2008.

[170] P. Gupta and P. R. Kumar, "Critical power for asymptotic connectivity in wireless networks," in *Stochastic Analysis, Control, Optimization and Applications: A Volume in Honor of W. H. Fleming, W. M. McEneany, G. Yin, and Q. Zhang, Eds,* Boston, MA, Dec. 1998, pp. 547–566.

[171] C. Bettstetter, "On the connectivity of ad hoc networks," *Computer J.*, vol. 47, pp. 432–447, Jul. 2004.

[172] M. Haenggi, "On distances in uniformly random networks," *IEEE Trans. Inf. Theory*, vol. 51, pp. 3584–3586, Oct. 2005.

[173] S. Mukherjee, D. Avidor, and K. Hartman, "Connectivity, power, and energy in a multihop cellular-packet system," *IEEE Trans. Veh. Technol.,* vol. 56, pp. 818–836, Mar. 2007.

[174] W. Ye, J. Heidemann, and D. Estrin, "Medium access control with coordinated adaptive sleeping for wireless sensor networks," *IEEE/ACM Trans. Netw.,* vol. 12, pp. 493–506, Jun. 2004.

[175] M. Desai and D. Manjunath, "On the connectivity in finite ad hoc networks," *IEEE Commun. Lett.,* vol. 6, pp. 437–439, Oct. 2002.

[176] C. Bettstetter and C. Hartmann, "Connectivity of wireless multihop networks in a shadow fading environment," *ACM/Springer Wireless Netw.,* vol. 11, pp. 571–579, Sept. 2005.

[177] O. Younis and S. Fahmy, "HEED: A hybrid, energy-efficient, distributed clustering approach for ad hoc sensor networks," *IEEE Trans. Mob. Comput.,* vol. 3, pp. 366–379, Oct. 2004.

[178] F. D. Tolba, D. Magoni, and P. Lorenz, "Connectivity, energy and mobility driven clustering algorithm for mobile ad hoc networks," in *Proc. GLOBECOM'07*, Washington D.C., USA, Nov. 2007, pp. 2786–2790.

[179] D. Sengupta, et al., "Radiation characteristics of a spherical array of circularly polarized elements," *IEEE Trans. Antennas Propag.,* vol. 16, pp. 2-7, Jan. 1968.

[180] L. Lewin, "Comment analytic expression for the frequency response and bandwidth of a spherical random array," *Electronics Lett.,* vol. 15, pp. 585-586, Sept. 1979.

[181] G. N. Watson, *A Treatise on the Theory of Bessel Functions*. London: Cambridge University Press, 1922.

[182] Wolfram. (2007). *Generalized Cases for Powers of Spherical Bessel* [Online]. Available: http://functions.wolfram.com/Bessel-TypeFunctions/SphericalBesselJ/26/02/20/

[183] I. S. Eduardo, I. Guendelman, G. Cantatore, and K. Zioutas, "Photon production from the scattering of axions out of a solenoidal magnetic field," *J. of Cosmology and Astroparticle Physics*, vol. 1, pp. 1-19, June 2010.

[184] J. N. Newman and W. Frank, "An integral containing the square of a Bessel function," *Amer. Math. Soc.*, vol. 17, pp. 64-70, Jan. 1963.

[185] C. W. Qiu, "On the integral identities consisting of two spherical Bessel functions," *IEEE Trans. Antennas Propag*, vol. 55, pp. 240-244, Jan. 2007.

[186] M. Donvito and S. Kassam, "Characterization of the random array peak sidelobe," *IEEE Trans. Antennas Propag.,* vol. 27, pp. 379-385, May 1979.

[187] Thorn, J.; Booth, N.O.; Lockwood, J., "Directivity index of partially random sonobuoy arrays," in *OCEANS '79* , San Diego, CA, Sept. 1979, pp.40-43.

[188] H. Tan, "The effect of mutual coupling on the performance of adaptive arrays," M.S. thesis, Naval Postgraduate School, Monterey, CA, 1999.

[189] R. Haupt, "Unit circle representation of aperiodic arrays," *IEEE Trans. Antennas Propag.,* vol. 43, pp. 1152-1155, Oct. 1995.

[190] Y. Bar-Ness, and A. M. Haimovich, "Synthesis of random antenna array patterns with prescribed nulls," *IEEE Trans. Antennas and Propag.*, vol. 32, 1298-1307, Dec. 1984.

[191] K. Buchanan and G. Huff, "Statistical confined sidelobe behavior for circular and spherically bound random arrays," *IEEE Trans. Antennas Propag.*, 2014. (in review)

[192] L. Leemis and J. McQueston, "Univariate distribution relationships," *American Statistician*, vol. 62, pp. 45-53, Feb. 2008.

[193] I. Tan and D. Pandya, "UAV digital tracking array design, development and testing," M.S. thesis, Dept. Elect. Eng., Naval Postgraduate School, Monterey, CA, 2009.

[194] J. Jensen, G. H. Huff, and J.-F. Chamberland-Tremblay, "Cognitive Motion-Dynamic Tethering of a Phased Array to an Android Smartphone," *IEEE Trans. Antennas Propag*., vol. 62, pp. 1093-1101, Mar. 2014.

[195] G. H. Huff, J.-F. Chamberland, S. Shakkottai, H. Waterman, J. Hanson-Daisa, A. McDonald, and N. M. Morales, "An Android controlled phased array," in *IEEE Int. Symp. Antennas Propag. USNC/URSI Nat. Radio Sci. Meeting*, Spokane, WA, USA, Jul. 2011.

[196] J. Jensen, J.-F. Chamberland, and G. H. Huff, "Smart phone enabled cognitive control of a phased array," in *USNC/URSI Nat. Radio Sci. Meeting, Boulder, CO, USA*, Jan. 2012

[197] J. S. Jensen, J.-F. Chamberland, and G. H. Huff, "Development of a smart phone enabled cognitive controlled phased array," in *IEEE Int. Symp. on Antennas and Propag. and USNC/URSI Nat. Radio Sci. Meeting,* Chicago, IL, USA, Jul. 2011.

[198] J. S. Jensen, "A cognitive phased array using smart phone control," M.S. thesis, Dept. Elect. Comput. Eng., Texas A&M Univ., College Station, TX, 2012.

[199] J. Jensen, J.-F. Chamberland, and G. H. Huff, "Beamsteering, tracking, phasing using an android smart phone," in *Proc. Antenna Applicat. Symp.*, Monticello, IL, USA, Sep. 2012, pp. 112–124.

[200] D. L. Sengupta, "Azimuth and elevation direction finder study," Fort Monmouth United States Army Electronics Command, Fort Monmouth, NJ, 1965.

[201] B. Tomasic, "Spherical arrays - design considerations," in *18th Int. Conference Appl. Electromagnetics and Commun ICECom,* Dubrovnik, Croatia, Oct. 2005, pp. 487-493.

[202] R. Goossens, "Phase-mode processing for spherical antenna arrays with a finite number of antenna elements and including mutual coupling," *IEEE Trans. Antennas Propag.*, vol. 57, pp. 3783-3790, Dec. 2009.

[203] L. Marantis, "Comparison of various spherical antenna array element distributions," in *3rd European Conference on Antennas and Propag. EuCAP*, Berlin, Germany, Mar. 2009, pp. 2980-2984.

[204] G. D. Ouderkirk, "Geodesic dome phased array radars," in *IEEE Radar Conference*, Waltham, MA, Apr. 2007, pp. 431-436.

[205] V. Agrawal, and Y. T. Lo, "Comments on "Characterization of the random array peak sidelobe", *IEEE Trans. Antennas Propag*., vol.28, pp.946-948, Nov. 1980.

[206] B. D. Steinberg, "Comparison between the peak sidelobe of the random array and algorithmically designed aperiodic arrays," *IEEE Trans. Antennas Propag.*, vol.21, pp.366-370, May 1973.

[207] B. D. Steinberg, "Sidelobe reduction of random arrays by element position and frequency diversity," *IEEE Trans. Antennas Propag.*, vol. 31, pg. 922-931, Nov. 1983.

[208] J. Ruze, "Physical limitations on antennas mit research laboratory of electronics," Research Lab MIT, Cambridge, MA, Tech. Rep. 248, Oct. 1952.

[209] Mostly Missile Defense. (2014) *Ballistic Missile Defense* [Online], Available: http://mostlymissiledefense.com/2012/09/21/ballistic-missile-defense-radar-range-calculations-for-the-antpy-2-x-band-and-nas-proposed-gbx-radars-september-21-2012/

[210] Modern Era FM Handheld Portables. (2014) *H4855* [Online], Available: http://www.greenradio.de/e_h4855.htm

[211] Mathworks Phased Array System Toolbox. (2014) *Radarvcd* [Online], Available: http://www.mathworks.com/help/phased/ref/radarvcd.html#bttpxb0-2

[212] M. Hall. (2014) *Great Geophysists #5: Huygens* [Online], Available: http://www.agilegeoscience.com/journal/2012/9/10/great-geophysicists-5-huygens.html

[213] B. Crandall, Nanotechnology Molecular Speculations on Golbal Abundance. Massachusetts: Library of Congress Cataloging in Publication Data, 1996.

[214] Wikipedia. (2014) *Interference.* [Online], Available: http://en.wikipedia.org/wiki/Interference_%28wave_propagation%29

[215] H2physics. (2014) *Chapter 5: Diffraction Grating* [Online]. Available: http://h2physics.org/?cat=49

[216] Eric Weisstein's. (2014) *Diffraction Grating* [Online]. Available: http://scienceworld.wolfram.com/physics/DiffractionGrating.html

[217] Hyperphysics. (2014) *Single Slit Diffraction* [Online]. Available: http://hyperphysics.phy-astr.gsu.edu/hbase/phyopt/mulslid.html#c1

[218] J. Pearson. (2014) *Electrodynamics.* [Online]. Available: http://www.jpoffline.com/physics_docs/y3s6/electrodynamics_ln.pdf

[219] C. Baker, R. Anandakrishnan and A. Onufriev, "Optimal Physical Multipoles," Virginia Tech, Blacksburg, VA, Dec. 2013.

[220] K. Milton. (2014) *Chapter 12 Green's Functions* [Online]. Available: http://nhn.nhn.ou.edu/~milton/p5013/chap12.pdf

[221] Wolfram Research Inc. (2012). *Spherical Bessel Differential Equation* [Online]. Available: http://mathworld.wolfram.com/EulerAngles.html

[222] K. Howell. (2014) *Power Series and Differential Equations: the Method of Frobenius* [Online]. Available: http://www.math.uah.edu/howell/MAPH/Notes/Series/Frob.pdf

[223] C. Gundlach. (2014) *Partial Differential Equations* [Online]. Available: http://www.southampton.ac.uk/~cjg/teaching/math3024/lecturenotes.pdf

[224] Wikipedia. (2014) *Hydrogen-like Atom* [Online], Available: http://en.wikipedia.org/wiki/Hydrogen-like_atom

[225] WebElements Nexum. (2014) *Orbitron Atomic Orbitals Poster* [Online], Available: https://www.webelements.com/nexus/content/orbitron-atomic-orbitals-poster

APPENDIX I

APPLICATIONS

I.1 Radar Equation

In radar the range R of a target is given by (619) where C_p is the velocity of propagation relative to the medium and the factor of 1/2 is the result of the round trip time Figure 234. Its transmitted signal voltage equation is given by that of (620) where ϕ_0 is the initial phase at t=0.

$$R = \frac{1}{2}\tau C_p \tag{619}$$
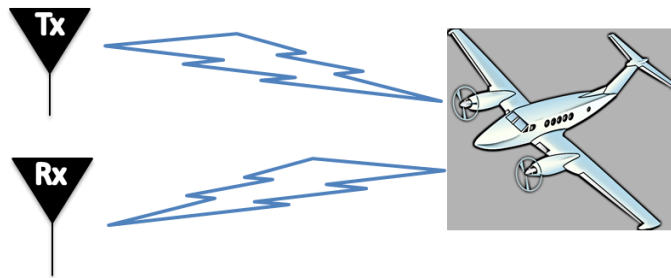
Figure 234. Round trip time of the signal.

$$v_T(t) = \sin\left(2\pi f_T t + \phi_0\right) \tag{620}$$

For a moving point target the equivalent range is given by (621) where R_0 is the range at t=0 and given that higher order range derivatives are considered negligible (relativistic, acceleration, jerk, etc...). Also neglecting attenuation, the same signal that was transmitted τ seconds earlier given by (622) with delay τ rewritten since the signal travel time $\dot{R} \ll C$.

$$R(t) = R_0 + \dot{R}t \tag{621}$$

$$v_R(t) = v_T(t - \tau) = \sin\left[2\pi f_T(t - \tau) + \phi_0\right] \tag{622}$$

$$\tau = \frac{2R(t)}{C} = \frac{2(R_0 + \dot{R}t)}{C} \tag{623}$$

Also given a moving target it is possible for a difference between the received and transmitted frequency known as a Doppler frequency shift to occur given by that of. Thus, (622) is rewritten as (625),

but if a Doppler shifted frequency defined by (626) it is again rewritten as (627). This expression provides a received frequency given by (628).

$$f_D = f_R - f_T \tag{624}$$

$$v_R(t) = \sin\left[2\pi f_T\left(t - \frac{2(R_0 + \dot{R}t)}{C}\right) + \phi_0\right] = \sin\left[2\pi f_T t - 2\pi f_T \frac{2\dot{R}}{C}t - 4\pi f_T \frac{R_0}{C} + \phi_0\right] \tag{625}$$

$$f_D = -f_T \frac{2\dot{R}}{C} = -\frac{2\dot{R}}{\lambda} \tag{626}$$

$$v_R(t) = \sin\left[2\pi(f_T + f_D)t - 4\pi f_T \frac{R_0}{C} + \phi_0\right] \tag{627}$$

$$f_R = f_T + f_D \tag{628}$$

It is important to note that transmitted frequency of a signal generally contains a finite bandwidth. Hence (627) is appropriate for narrow-band signals, whereas for wide-band signals more complicated measures, involving Doppler broadening, are necessary. For ease of analysis it is assumed a given target velocity provides the same Doppler shift for the entire signal bandwidth making (627) sufficient in calculation.

The signal-to-noise-ratio is a key parameter used for determining a targets range, velocity and bearing information. One method used for calculating SNR is typically by means of the radar equation.

The power density is specified by (629), and assumes a pulsed output power P_T, lossless environment, isotropic *Tx* and *Rx* antenna and range separation *R*. Otherwise if the transmit antenna is not isotropic, but has a gain of *G* and points in the direction of the target then the power density is to be multiplied by *G*.

$$\mathrm{P}_{rad} = \mathrm{P}_T = \text{Power density} = \oiint_S W_0 \cdot \vec{ds}\,d = W_0 \int_0^{2\pi}\int_0^{\pi}\left[\hat{a}_r r^2 \sin\theta\, d\theta\, d\phi\right] = 4\pi r^2 W_0$$

$$\therefore \vec{W}_0 = W_0 \hat{a}_r = \hat{a}_r\left(\frac{\mathrm{P}_T}{4\pi R^2}\right) \tag{629}$$

Now assume the same situation for the antenna. Therefore, if the target antenna is isotropic and reflects back all the power intercepted from its effective area (630) then the power will be received back at the radar isotroprically and given by (631) and shown in Figure 235.
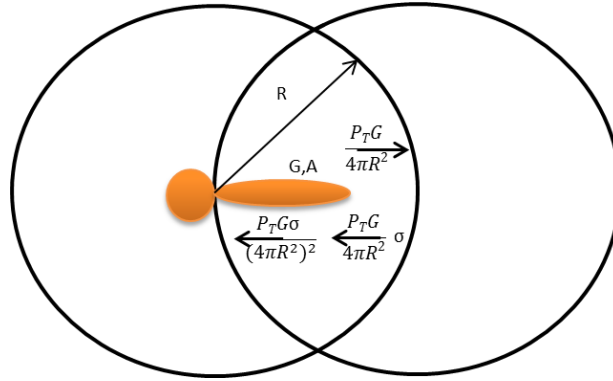
Figure 235. Overlapping coverage patterns of two antennas.

$$\text{Reflected power} = \frac{P_T G \sigma}{4\pi R^2} \tag{630}$$

$$\text{Reflected power} = \frac{P_T G \sigma}{\left(4\pi R^2\right)^2} \tag{631}$$

The radar equation given in (631) was developed from assuming ideal features to include a target with area σ using an isotropic reflection pattern. In reality though most targets are not isotropic and to find σ one typically needs to calibrate the system by replacing the physical target with that of either an ideal isotropic target or otherwise known (calibrated) target with known σ value. Hence, this value of σ will be modified until the calculated power matches the measured amount of power as the original target. Hence, σ is found and is defined as the area of a target that reflects back either isotroprically or to some form of calibrated value.

If the receiving antenna was not isotropic then the collected power at the target will be given as (632) where A is a measure of the effective area. Hence, (631) is rewritten as (633).

$$P_r = W_r A_r = \frac{P_t D_t A_r}{4\pi R^2}$$

or (632)

$$D_t A_r = \frac{P_r}{P_t}\left(4\pi R^2\right)$$

$$P_R = \frac{P_T G A \sigma}{\left(4\pi R^2\right)^2} \tag{633}$$

The problem with the above expression is that we used the parameter A in order to convert the transmitted power density to a form of collected power. Instead, why wasn't this expression written in terms of the receiver gain as it was done for the transmitter? This though is very much possible and will be shown through the following derivation.

288

Applying reciprocity to the system we rewrite (632) as (634) and equating the two gives

$$D_r A_t = \frac{P_r}{P_t}\left(4\pi R^2\right) \tag{634}$$

$$\frac{D_t}{A_t} = \frac{D_r}{A_r} \tag{635}$$

The physical area of a real target will be quite different from its radar cross section (σ). Plus to make matters worse most targets exhibit different $\sigma's$ at different aspect angles and at different frequencies illustrated by the additional path length of Figure 236.
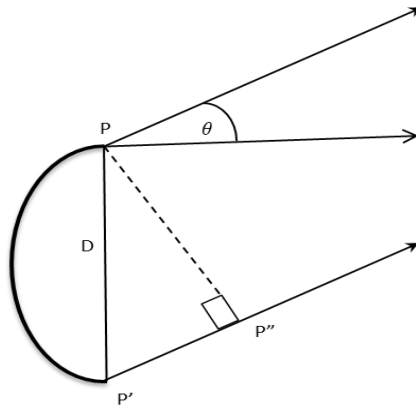
Figure 236. Additional path length.

To relate antenna gain *G* in terms of effective area we first assume two parabolic antennas face each other shown in Figure 237. The feed point is generally located at the focal point of the parabolic reflect and emits a wavefront that is parallel to the vertical line PP'. Like a phased array the path length assumes an additional distance in the angle θ or path $P'P'' = D\sin\theta \approx D\theta$.

This is important to consider because if this additional distance is equal to $\lambda/2$ the radiation from the two edges of the parabola will tend to cancel each other by being out of phase. For that reason setting $D\theta = \lambda/2$ one obtains the critical angle given in (636). At this angle the radiated power is evenly distributed evenly over the equivalent circular diameter as given in (637).

$$\theta_1 = \lambda/(2D) \tag{636}$$

$$2R\theta_1 = \frac{R\lambda}{D_T} \tag{637}$$

The next step is to rewrite (635) as A_r/A_T and note that the ratio of received power to transmit power will be proportional (638). This assumes a receiving parabola with diameter D_R placed a distance R away

$$\frac{P_R}{P_T} \approx \frac{\pi \left(\frac{D_R}{2}\right)^2}{\pi \left[\frac{\left(R\lambda / (D_T)\right)}{2}\right]^2} = \frac{D_R^2 D_T^2}{(R\lambda)^2} \tag{638}$$

Converting from diameter to area this is rewritten as (639) where the factor 1.62 is the result of various simplifying assumptions. However the exact factor is 1 giving (640).

$$\frac{P_R}{P_T} = \frac{D_R^2 D_T^2}{(R\lambda)^2} = \frac{16 A_R A_T}{\pi^2 (R\lambda)^2} = 1.62 \frac{A_R A_T}{(R\lambda)^2}$$

since $\tag{639}$

$$D^2 = \frac{4A}{\pi}$$

$$\frac{P_R}{P_T} = \frac{A_R A_T}{(R\lambda)^2} \tag{640}$$

Received (and reflected) power from an area $A_R = \sigma$ is given by (641) and equating to (640) (dropping the subscript T) provides (642).

$$\frac{P_R}{P_T} = \frac{A_R G_T}{4\pi R^2} \tag{641}$$

$$\frac{P_R}{P_T} = \frac{A_R A_T}{(R\lambda)^2} = \frac{A_R G_T}{4\pi R^2} \Rightarrow A = \frac{G\lambda^2}{4\pi} \tag{642}$$

As a simple check it's well-known that a dipole has gain G=1.5 and $A = .119\lambda^2$ where indeed, $1.5/(4\pi) = .119$.
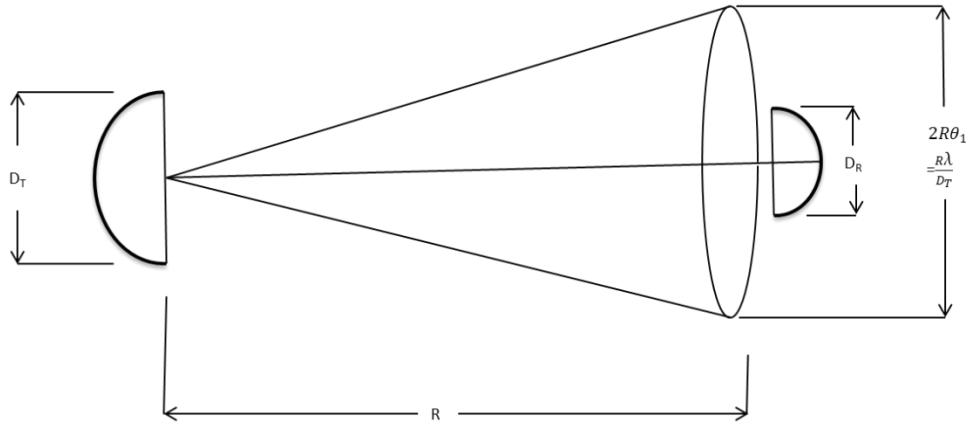
Figure 237. Effective area of the receiver in relation to the affective area of the transmitter.

I.1.1 Signal to Noise Ratio

To develop the signal to noise ratio we first assume a signal. This time around it is to be a train of coherent RF pulses, at the carrier frequency f_c. Then a rectangular response with bandwidth f_B (in hertz) is given by (643), which is seen to be inversely proportional to a single pulse of duration.

$$f_B = \frac{1}{t_P}$$ (643)

The thermal noise power of this pulse type is given by

$$N = FKT_E f_B = N_p f_B$$ (644)

Where

F is the receiver noise figure,
K is Boltzmann's constant ($=1.38 \times 10^{-23} W \cdot s/°K$),
T_E is the temperature in degrees Kelvin,
N_0 is the noise (one-sided) spectral power density in watts per hertz.

Therefore the radar equation in terms of signal-to-noise ratio is (645) provided that this ratio defines only one pulse returned from the target.

$$SNR_P = \frac{P_T G^2 \lambda^2 \sigma}{\left(4\pi\right)^3 R^4 N_0 f_B}$$ (645)

Normally the target is illuminated for a relatively long period of time T_1. Hence, for a pulse repetition frequency f_R the number of coherent pulses used is given by (646). Coherent integration of M pulses increases the overall SNR to that of (647) or rewritten to that of (648) using an average transmit power defined in (649).

$$M = T_I f_R \tag{646}$$

$$SNR = M \ SNR_P \tag{647}$$

$$SNR = \frac{P_{AVE} T_I G^2 \lambda^2 \sigma}{(4\pi)^3 R^4 N_0} \tag{648}$$

$$P_{AVE} = P_T t_P f_R = P_T \frac{M}{f_B T_I} \tag{649}$$

A synchronous detector is used for the coherent integration of the M pulses. This is done by maintaining phase information [through the in-phase (I) and the quadrature (Q) components], which is further discussed in [109]-[125].

For a CW signal the SNR is that of (650) where $P_T = P_{AVE}$ with pulse of duration T_I given by (651).

$$SNR_P = SNR \tag{650}$$

$$f_B = \frac{1}{T_I} \tag{651}$$

The illumination time of a point target by scanning radar is a function of the antenna scan rate and the antenna beamwidth in the scan plane. The antenna beamwidth is obviously related to the antenna gain. A simple relationship can be deduced from realizing that there are $4\pi \left(\frac{180}{\pi}\right)^2 = 41,253$ square degrees in a sphere. An antenna with 3-dB beamwidths θ_H and θ_V, in the two principal planes, radiates into $\theta_H \theta_V$ square degrees out of a total of 41,253. The antenna efficiency ρ_A is usually about 0.5. Thus

$$G \approx \frac{41,253}{\theta_H \theta_V} \rho_A \approx \frac{20,000}{\theta_H \theta_V} \tag{652}$$

Where θ_H and θ_V are in radians,

$$G \approx \frac{4\pi}{\theta_H \theta_V} \rho_A \tag{653}$$

Another form of the radar equation is suitable for surveillance radar, which scans a two-dimensional angular region of Ω square radians. If the total scan time is t_s, then the target illumination time is given by,

$$t_I \approx t_S \frac{\theta_H \theta_V}{\Omega} \approx t_S \frac{4\pi \rho_A}{\Omega G} \tag{654}$$

And hence the signal to noise ratio is given by,

$$SNR = \frac{P_{AVE} A \sigma \rho_A}{4\pi R^4 N_0} \frac{t_s}{\Omega} \tag{655}$$

A few nominal examples of traditional SNR are provided from [209] or Figure 238.

Model	Frequency Range (MHz)	σ_{TDOAv}(s)	Receiver 3 dB Bandwidth (MHz)	Signal-to-Noise Ratio (dB)
AD 8347 Direct Conversion Quadrature Demodulator	800 – 2700	1e-9	90	15.7
AD 8348 Quadrature Demodulator	50 – 1000	1e-9	500	0.8278
DRT 4011 Wideband Tuner	10 – 3000	1e-9	30	25.3
TeamSentinel Signal Acquisition Frontend (V/UHF)	30 – 300	1e-9	40	22.8

Table 15.   Required received signal-to-noise rations (SNR) for a few commercially available receivers.

Figure 238. Common SNR examples from [209].

I.2. FRIIS TRANSMISSION EQUATIONS OF FOR PERSONAL ROLE RADIO (PRR)

I.2.1 H4855 Personal Role Radio (PRR)

Personal Role Radio Figure 239 operates in the UHF/ISM band at 2.4 GHz and uses a modified 802.11b protocol. The radio has a short transmission range of 500 meters in rural terrain and is capable of transmitting through three floors in an urban setting. With such short range its main purpose is to eliminate the need for shouting during battle. The radio employs Direct Sequence Spread Spectrum (DSSS) with voice coding (CVSD) modulation and is considered low probability intercept (LPI). Hence due to its small size and low power output this radio, is promising for future Network Centric Warfare applications. Collaborative beamforming amongst the network will provide the capability of both pushing and pulling relevant information up the chain of command. [3]

Figure 239. Personal role radio (PRR). [210]

I.2.2 Flat Earth Reflections (Horizontal Polarization)

The power radiated from an antenna is provided by that of (656) with directivity and gain relations provided in (657)-(658).

$$W = \frac{P_t}{4\pi r^2} = \frac{|E|^2}{2\eta_0} \tag{656}$$

$$D = \frac{4\pi}{\Omega_A} = \frac{1}{\frac{1}{4\pi}\iint_{4\pi}|E_{norm}(\theta,\phi)|^2\,d\Omega}$$

$$D \approx \frac{4\pi}{\theta_{HPBW}\phi_{HPBW}} \tag{657}$$

$$G = \varepsilon D = \frac{4\pi A_e}{\lambda^2}$$

$$\varepsilon = \frac{P_{radiated}}{P_{input}} \tag{658}$$

For higher frequency such as 2.45 GHz it's first important to realize what distance is to be considered the far field. For example if the length of the PRR antenna is $\lambda/4$ and its image is another $\lambda/4$ long then the total nominal length is half a wavelength $\lambda/2$. This gives a far field region very close to the antenna as shown in (659). On the other hand, if there are two PRRs in use of which they are utilized in the form of an array of length *L (A or D)*. Then *L* is their separation, and in order to beamform coherently in the far field they must be separated by 10m as shown in (660)

294

$$r_{ff} \geq \frac{2(.0625)^2}{.122} = .064m \tag{659}$$

$$f = 2.45GHz, \quad \lambda = .122m$$

$$r_{ff} \geq 2\frac{(10)^2}{.122} = 1639m \tag{660}$$

Following the idealistic parameters provided in this dissertation and the set up given in [3] one is able to derive the received signal at element n from a cluster of N distributed PRR elements. The subscript b is to be the signal of which was sent from the base station toward the cluster of elements.

$$P_{r_n} = \frac{P_{t_b} G_b(\theta_n)}{4\pi R_n^2}\left[\frac{\lambda^2 G_n(\theta_n)}{4\pi}\right]\left|F_n(\theta_n)\right|^2 (PLF_n)^2 \tag{661}$$

The bracketed term in (661) is denoted as the effective area $\left(A_{e_n}(\theta_n) = \lambda^2 G_n(\theta_n)/4\pi\right)$ for each PRR_n antenna in the direction of the base station. The term denoted *PLF* is the polarization loss factor or mismatch error for each PRR_n antenna and $F_n(\theta_n)$ is the path gain factor between the base station and each PRR_n of which will be covered in greater detail in the following subsection.

I.2.3 Path Gain Factor

For simplicity a single bounce multipath (flat earth model) signal is developed in this section, which provides a simple expression for F_n and is shown in Figure 240.
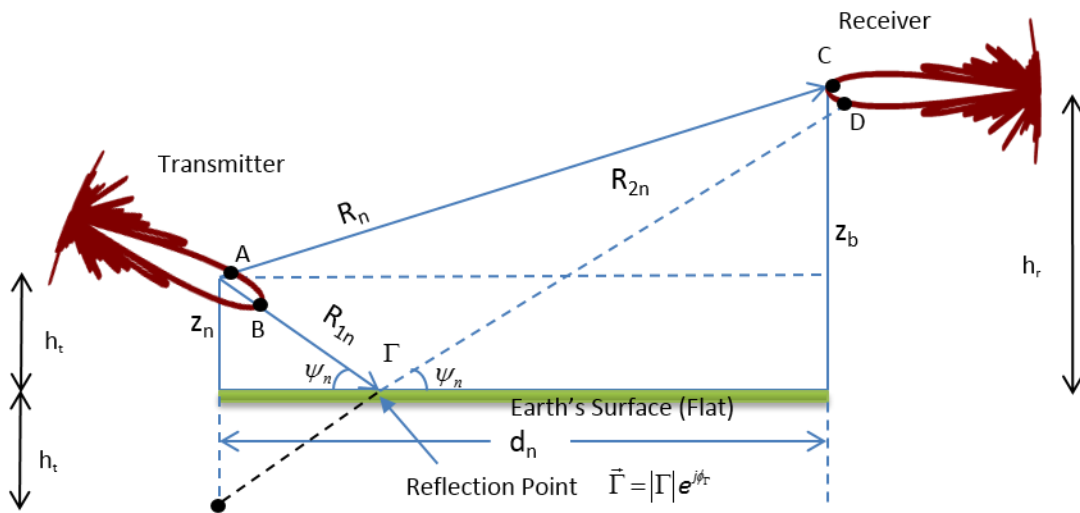
Figure 240. Multipath between transmitter and receiver.

Superposition of the direct and reflected paths is given by (662).

$$F_n = \frac{E_{d_n} + E_{r_n}}{E_{d_n}} = 1 + \Gamma e^{-jk\Delta R_n} \tag{662}$$

The difference in path length (665) is given by the subtraction of (664) and (663). Also if attenuation is included over the entire length of the paths and assuming $\Gamma \approx -1$ and $\alpha_{d_n} = \alpha_{r_n}$ for simplicity we obtain (666).

$$R_0 = \sqrt{d^2 + (h_r - h_t)} \approx d + \frac{1}{2} \frac{(h_r - h_t)^2}{d} \tag{663}$$

$$R_1 + R_2 = \sqrt{d^2 + (h_r + h_t)} \approx d + \frac{1}{2} \frac{(h_r + h_t)^2}{d} \tag{664}$$

$$\Delta R \approx \frac{2 h_r h_t}{d} \tag{665}$$

This provides the pattern propagation factor (PPF) as

$$F_n = e^{-\alpha_{d_n} R_n} + \Gamma e^{-\alpha_{r_n}(R_n + \Delta R_n)} \approx e^{-\alpha_{d_n} R_n} \left(1 - e^{-jk\frac{2z_n z_b}{d_n}} \right)$$

$$= e^{-\alpha_{d_n} R_n} e^{-jk\frac{z_n z_b}{d_n}} \left(e^{jk\frac{z_n z_b}{d_n}} - e^{-jk\frac{z_n z_b}{d_n}} \right) \tag{666}$$

$$= e^{-\alpha_{d_n} R_n} e^{-jk\frac{z_n z_b}{d_n}} 2\sin\left(k \frac{z_n z_b}{d_n} \right)$$

Hence the one way voltage gain factor is given by

$$|F_n|^2 = e^{-2\alpha_{d_n}} 4\sin\left(\frac{k z_b z_n}{d_n} \right)^2 \approx e^{-2\alpha_{d_n}} 4\left(\frac{k z_b z_n}{d_n} \right)^2 \tag{667}$$

I.2.4 Coverage Diagram

Another common approach or form of the argument frequently encountered is derived assuming the transmitter to be near the ground $h_t \approx 0$. Hence, the elevation angle ψ can be given by (668). Thus, the PPF can be expressed in terms of ψ as

$$\tan\psi = \frac{h_r - h_t}{d} = \frac{\Delta h}{d} \approx \frac{h_r}{d} \tag{668}$$

$$|F| = 2\sin(kh_t \tan\psi) \tag{669}$$

The minima of the PPF are located at:

$$kh_t \tan\psi = n\pi \quad (n = 0, 1, \ldots, \infty) \tag{670}$$

$$\frac{2\pi}{\lambda}h_t \tan\psi = n\pi \tag{671}$$

$$\tan\psi = \frac{n\lambda}{h_t} \tag{672}$$

And maxima occur at

$$kh_t \tan\psi = m\frac{\pi}{2} \quad (m = 1,3,5,\infty) \tag{673}$$

$$\frac{2\pi}{\lambda}h_t \tan\psi = \frac{2n+1}{2}\pi \quad (n = 0,1,\ldots,\infty) \tag{674}$$

$$\tan\psi = \frac{(2n+1)\lambda}{4h_t} \tag{675}$$

Lastly, plots of $|F|$ are called a coverage diagram where the horizontal axis is typically distance and the vertical axis is the receiver height. An example is provided below similar to that shown in Figure 241.
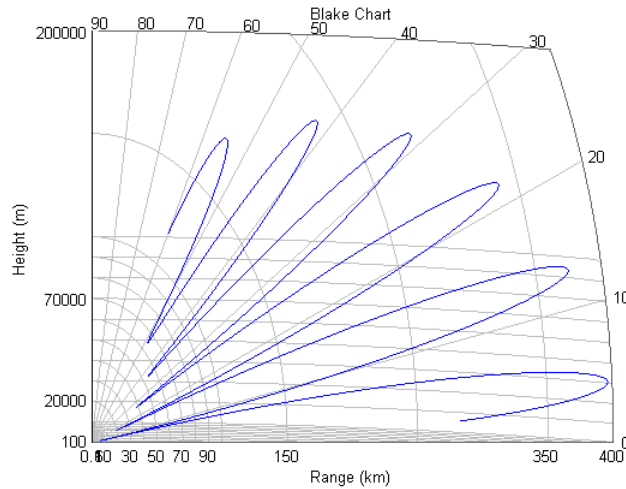
Figure 241. Notional example of a coverage diagram. [211]

Last of all the reflected and direct paths reaching a receiver create what is called the Fresnel zones when their phases differs by an amount of $180°$; or by integer multiples of $\lambda/2$, i.e $\Delta R = n\lambda/2$ where n=0,1,... etc. Moreover the collection of points with excess path length $n\lambda/2$ is called the nth Fresnel zone and are ellipsoids centered on the direct path between the transmitter and receiver as shown below in Figure 242.

LOCUS OF REFLECTION
POINTS (SURFACES OF
REVOLUTION)

DIRECT
PATH (LOS)

$n = 2$

$n = 1$

RECEIVER

TRANSMITTER

h_t

h_r

REFLECTING SURFACE
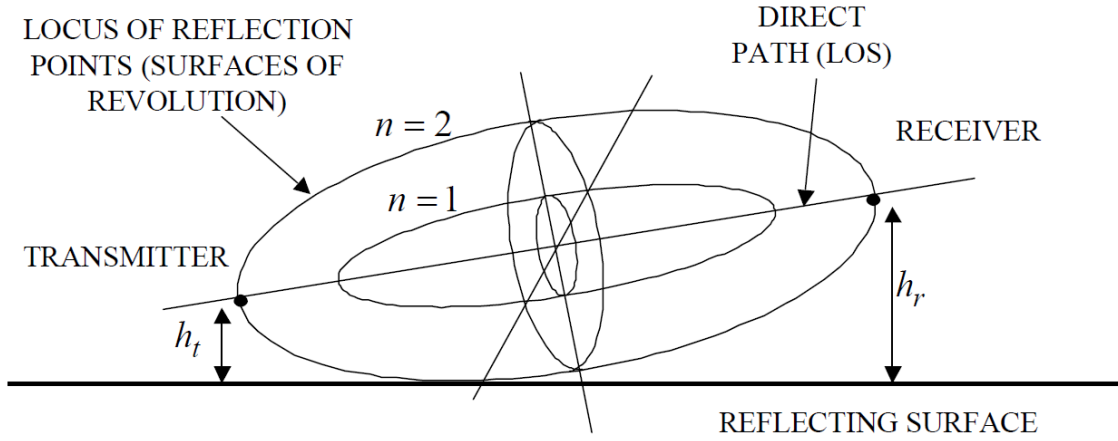
Figure 242. n^{th} Fresnel zones. [109]

I.2.5 Element Voltage

The peak electric filed intensity at PRR_n can be found from rewriting the power density of (676) to that of (677). The complex value (678) is obtained from multiplying and adding the phase's terms.

$$\left| \vec{W}_{i_n} \right| = \frac{\left| \vec{E}_{i_n} \right|^2}{2\eta_0} = \frac{P_{t_b} G_b}{4\pi R_n^2} \left| F_n(\theta_n) \right|^2 \tag{676}$$

$$\left| \vec{E}_{i_n} \right| = \sqrt{\frac{2\eta_0 P_{t_b} G_b}{4\pi R_n^2}} \left| F_n(\theta_n) \right| \tag{677}$$

$$\left| \vec{E}_{i_n} \right| = \left| \vec{E}_{i_n} \right| e^{-jkR_n} e^{j\Phi_b} \hat{e}_i \tag{678}$$

For simplicity the phase of only the direct path $\left| F_n(\theta_n) \right| = 1$ was shown, in addition to the phase Φ_b, representing the arbitrary initial phase of the transmitter. The unit vector $\hat{e}_i$ is the direction of electric field vector.

Once the beam is transmitted an array can be used to receive the beam collectively using *N* PRRs. Each antenna collects samples of the complex electric field and sends this data to a central node for processing. More importantly, the collection of these complex voltages is maximized when measured at the antenna terminals linearly related to the incident electric fields at the antennas. I.e. the voltage can be obtained by either of two methods: Case 1: effective height or Case 2: effective area. Both cases can be represented in the form of an equivalent circuit shown in Figure 243.

298
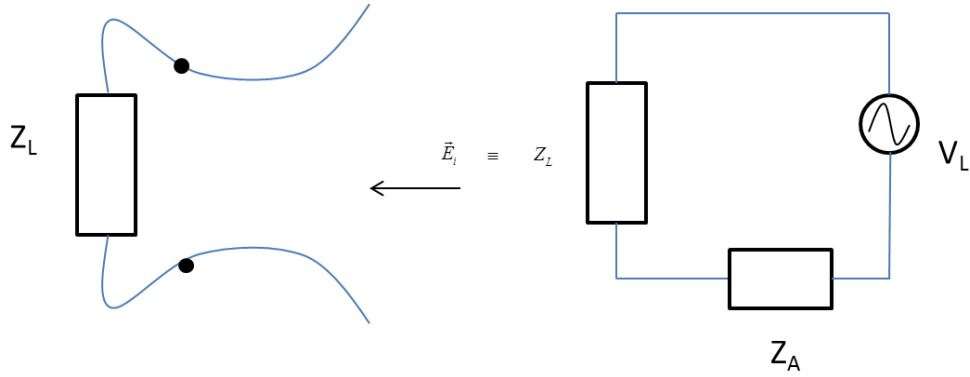
Figure 243. Effective height.

(a) Case 1: effective height

The effective height is nothing more than taking the simple dot product of the incident electric field and with the polarization of the antenna. In other words the voltage at the antenna terminal is measured directly from the dot product given by (679), where $\vec{h}_e$ is the effective height of the PRR antenna.

$$V_n = \vec{E}_{i_n} \cdot \vec{h}_e \tag{679}$$

(b) Case 2: effective area

The received power is given by (680) and it can be rewritten in terms of the load R_L in(681).

$$P_{r_n} = \left|W_{i_n}\right| A_{e_n} = \left|W_{i_n}\right| \frac{\lambda^2 G_n}{4\pi} \tag{680}$$

$$P_{r_n} = \frac{1}{2}\mathrm{Re}\left\{V_L I_L^*\right\} = \frac{1}{2}\frac{|V_L|^2}{R_L} \tag{681}$$

The power can also be rewritten by finding the current through the load impedance given by (682), and using this parameter to find the available power given by (683). With a conjugate matched load this reduces to (684)

$$I = \frac{V_L}{\sqrt{\left(R_A + R_L\right)^2 + \left(X_A + X_L\right)^2}} \tag{682}$$

$$P_R = \frac{V_L^2 R_L}{\sqrt{\left(R_A + R_L\right)^2 + \left(X_A + X_L\right)^2}} \tag{683}$$

$$P_R = \frac{V_A^2}{2R_L} \tag{684}$$

Next we rewrite the power as (685) and solve for the effective area in (686) when $Z_L = Z_A^*$.

$$P_R = W(\theta,\phi)A_e(\theta,\phi) \tag{685}$$

$$A_{e_n} = \frac{V_n^2}{W_{r_n}(\theta,\phi)}\frac{R_L}{|Z_A + Z_L|^2} = \frac{V_n^2}{W_{r_n}(\theta,\phi)}\frac{R_L}{(2R_A)^2} \tag{686}$$

Next the magnitude of the effective height h_e is to be calculated from using (687) and (688).

$$V_A = E(\theta,\phi)h_e(\theta,\phi) \tag{687}$$

$$W(\theta,\phi) = \frac{E(\theta,\phi)^2}{\eta} \tag{688}$$

Substituting the previous two equations into (686) gives

$$h_e = 2\sqrt{\frac{A_e(\theta_{bn})R_A}{\eta_0}} \tag{689}$$

Knowing the effective height is useful since we now have enough information to calculate the maximum effective aperture

$$A_{e_n} = \frac{h_e^2\eta_0}{4R_r} \tag{690}$$

Also for the conjugate matched condition $R_A = R_L$ and $X_A = -X_L$, we can rewrite (686) as

$$V_n^2 = \frac{W_{r_n}(\theta,\phi)A_{e_n}(2R_A)^2}{R_L} = W_{r_n}(\theta,\phi)A_{e_n}(4R_A) \tag{691}$$

$$\frac{V_n^2}{4R_A} = W_{r_n}(\theta,\phi)A_{e_n} \tag{692}$$

Now assuming that there is no ohmic loss, then $R_A = R_r$ (all radiation resistance) and multiplying by the phase exponentials gives the complex voltage for each PRR_n

$$V_n = \sqrt{4W_{r_n}(\theta,\phi)A_{e_n}R_r}\,e^{-jkR_n}e^{j\Phi_n} \tag{693}$$

Where the RMS values is

$$V_n = \sqrt{2W_{r_n}(\theta,\phi)A_{e_n}R_r}\,e^{-jkR_n}e^{j\Phi_n} \tag{694}$$

Where in this cases each PRR is designed to have a $\lambda/4$ monopole antenna with 50Ω impedance such that

$D = 3.2$ and $A_e = \frac{\lambda^2 D}{4\pi} = .255\lambda^2$ making the voltage at each PRR equal to

$$V_n = .87\sqrt{W_{r_n}(\theta,\phi)}e^{-jkR_n}e^{j\Phi_n} \tag{695}$$

These voltages after demodulation are written in phase and quadrature ($I_n + jQ_n$) components.

$$V_n = I_n + jQ_n \tag{696}$$

In conclusion, if one were to beamform utilizing "three PRR elements, there is a gain increase of 9.5 dB in the received power" [3]

$$10\log_{10}\left(N^2\right) = 10\log_{10}\left(3^2\right) = 9.5dB \tag{697}$$

I.2.6 Total Signal Strength at the Base Station to all PRR_n

The total field at the base station for antenna polarization defined by the vector $\hat{h}_b$ is given by (698) with a total power in (699) where $A_{e_b} = \dfrac{G_b \lambda^2}{4\pi}$.

$$
\begin{aligned}
E_b &= \sum_{n=1}^{N} \vec{E}_{b_n} \cdot \hat{h}_b = \sum_{n=1}^{N} E_{b_n} \hat{e}_n \cdot \hat{h}_b \\
&= \sum_{n=1}^{N} \sqrt{\frac{2\eta_0 P_{t_n} G_n\left(\theta_n\right)\left|F_n\left(\theta_n\right)\right|^2}{4\pi R_n^2}} e^{-jkR_n} e^{j\Phi_n} \hat{e}_n \cdot \hat{h}_b
\end{aligned}
\tag{698}
$$

$$P_{r_b} = \frac{1}{2}\frac{\left|E_b\right|^2}{\eta_0} A_{e_b} \tag{699}$$

Therefore

$$P_{r_b} = \frac{G_b \lambda^2}{\left(2\eta_0\right)4\pi}\left|\sum_{n=1}^{N} \sqrt{\frac{2\eta_0 P_{t_n} G_n\left(\theta\right)\left|F_n\left(\theta\right)\right|^2}{4\pi R_n^2}} e^{-jkR_n} e^{j\Phi_n} \hat{e}_n \cdot \hat{h}_b\right|^2 \tag{700}$$

This summation considerably reduces from assuming the following conditions

- No multipath exists such that $F_n = 1$ (LOS only)

- Amplitude differences in incident waves are neglected, $\left|\vec{R}_n\right| = \left|\vec{r}_b\right|$

- All elements are phase synchronized for coherent beamforming, $kR_n + \Phi_n$ is constant for all n.

- Equal PRR gain $G_n = G_0$ and $P_{t_n} = P_{t_0}$ transmitted power for all elements

- No polarization loss (all antennas are parallel $\hat{e}_n \cdot \hat{h}_b \approx 1$)

- There is a localized distribution meeting the condition $\left|\vec{r}_n\right| \ll d$

to

$$
\begin{aligned}
P_{r_b} &= \left|\sum_{n=1}^{N} \sqrt{\frac{P_{t_0} G_0}{4\pi r_b^2}}\right|^2 = \frac{P_{t_0} G_0}{\left(r_b\right)^2}\left|\sum_{n=1}^{N}\left(1\right)\right|^2 \\
&= \frac{\left(NP_{t_0}\right)\left(NG_0\right)G_b \lambda^2}{\left(4\pi r_b\right)^2} = \left(N^2 P_{t_0}\right)\frac{G_0 \lambda^2 G_b}{\left(4\pi r_b\right)^2}
\end{aligned}
\tag{701}
$$

301

The term NP_{t_0} is the total transmitted power from the array and is also called the total effective radiative power (ERP). NG_0 is the total gain of the array when coherently phased. Thus, it is seen that main advantage of using multiple transmitters is an overall increase in power by N^2.

I.2.7 Attenuation

Attenuation of the signal is often attributed to environments that are not free space, such as urban, forests or desert. Moreover, in regions with high vegetation it is found that the branches from trees and its leaves will provide a significant amount of attenuation to especially to UHF and microwave signals (since the wavelength is small). Moreover, this signal attenuation is mainly caused from foliage absorption and scattering from discrete scatters such as; from branches and leaves. "Foliage attenuation is considered one of the dominant effects for rural and suburban areas of operation" [3] and can typically be predicted by that of (702)

$$\alpha = af^b \tag{702}$$

where α is differential attenuation in decibels per meter, a and b are constant from different seasonal characteristics, and f is the frequency expressed in GHz. Moreover, examples of the parameters of a and b are provided in Table 15 such that the total excess path loss can be expressed using the exponential decay model by

$$L_e = \alpha d_f \tag{703}$$

Where d_f is denoted as the depth of a deciduous tree.

Table 15. Foliage Parameters. [3]

Season	Summer			Winter		
Parameters	Median	50%	90%	Median	50%	90%
a	.57	.71	.78	.36	.52	.59
b	.60	.47	.42	.43	.29	.25

I.3. FRIIS TRANSMISSION EQUATIONS FOR UAV SWARMS

I.3.1 Single UAV Model

The assumptions for a single UAV element are considered very similar those provided for PRR in the prior chapter such that: it is assumed each UAV is small enough to be hand launched. Second every UAV has its own digital transmit receive (T/R) module. Third, each UAV's (T/R) module has its own

local oscillator. Fourth, there is some capability or algorithm provided to synchronize all local oscillators to a common "master" clock. Fifth, the UAV antennas have an isotropic radiation pattern. Last, the wireless network connecting all UAVs data and commands are connected with negligible latency.

I.3.2 The Swarm

Collaborative beamforming amongst a UAV swarm will only be realized if they can operate autonomously: "able to fly, adapt, communicate, negotiate, and carry out missions with no human in the loop." [1] Next defining the swarm and swarm behavior will make the concept of future research methods more understandable.

(a) Swarming and swarm behavior

"Many technological inventions and concepts are motivated by the natural behavior of animals. Any collective behavior of these animals, flock of birds, a school of fish, and a colony of bees has been of interest for some time now." [116] Furthermore after numerous observations, it's become quite obvious that there is some sort of learning intelligence amongst these collections. For instance, local sensing from the elements induces small interacting contributions to the overall global behavior and is regarded as reactive behaviors since they're dynamic processes of which do not require a plan. This collection of entities forms the underlying autonomy to be considered a swarm. This type of ability will be important in future stages of research and algorithms requiring efficient means of autonomy.

Similar in relation to the collaborative beamforming ability of PRR, a micro-UAV swarm distribution will be analyzed in this chapter in a similar fashion. The analysis assumes the swarm is above a given terrain, where major application intent is for the enhancement of SNR capability in order to effectively conduct electronic attack (EA).

(b) Swarm control

Autonomy of the UAV swarm during the flight is important in application to UAV swarming. Several different emerging strategies are considered in [1] for UAV swarm control such as:

1. *Baseline strategy*- All UAVs fly in a straight line until they reach a known set of boundary points, at which time they turn to avoid exiting the area.
2. *Random strategy*-Similar to baseline except each UAV may change its heading by a small arbitrary angle during each time step.
3. *Repulsion strategy*-UAVs maneuver to keep out of each other's repulsion radius.
4. *Pheromone strategy*-An indicator is left over every terrain cell during a flyover indicating whether the cell has been visited. These markers are used to notify other UAVs whether the cells have been visited or not and can service the flight pattern in order to fly over unexplored cells.
5. *Global strategy*-A search space is divided into a number of large, square regions where a central controller monitors the level of coverage and UAVS within each region. [1]

From [1] it was determined that the *pheromone strategy* is to be the most effective to control a UAV swarm in general cases and is considered the method of choice in this dissertation. Though these are only a few of the general cases advantageous mainly for searching applications it should be noted that other applications may exist. For example, once a swarm finds a target such as victim radar, the swarm control objectives change. For an EA attack scenario as in this case the elements may go into a pre-designated attack mode as they arrange themselves geometrically in order to maximize their lethality (e.g., maximum jamming power) and survivability.

I.3.3 Transmission Equations for Swarm UAVs

The geometry of the UAV swarm is presented in Figure 244 and is utilized for the derivation of the free space transmission equations.
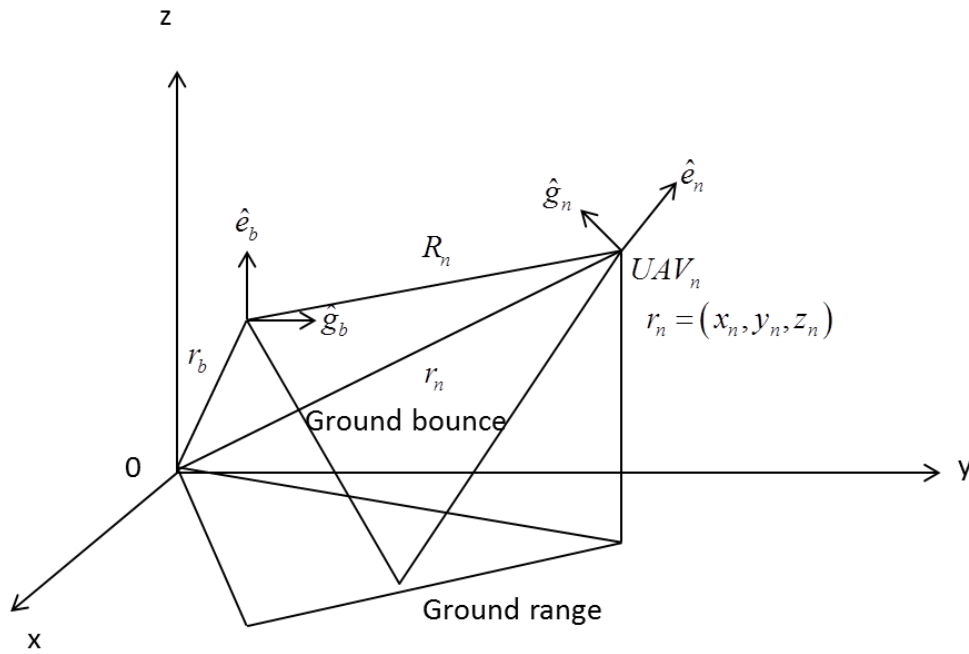
Figure 244. Geometry of the UAV swarm.

The location of the bases station and n^{th} UAV are:

Base station: $\vec{r}_b = \hat{x}x_b + \hat{y}y_b + \hat{z}z_b$

n^{th} UAV: $\vec{r}_n = \hat{x}x_n + \hat{y}y_n + \hat{z}z_n$

The polarization references for each are:

Base station: $\hat{e}_b$

n^{th} UAV: $\hat{e}_n$

Maximum antenna gain:

Base station: $\hat{g}_b$

n^{th} UAV: $\hat{g}_n$

For ease of analysis the path gain factor is ignored, but could be analyzed quite similar to the analysis covered in the PRR chapter. Utilizing the Friis transmission equation the *nth* UAV signal received at the base station $\left(P_{bn} \right)$ (downlink) can be expressed as (704) where the polarization loss factor between the UAV_n and the base station antenna is given by (705).

$$P_{bn} = \frac{P_{tn} G_n \left(\theta_n, \phi_n \right) G_b \left(\theta_{bn}, \phi_{bn} \right) \lambda^2}{\left(4\pi R_n \right)^2} \left| PLF_n \right|^2 \tag{704}$$

$$\left| PLF_n \right|^2 = \left| \hat{e}_b \cdot \hat{e}_n \right|^2 \tag{705}$$

Like the analysis covered in the PRR chapter it is convenient to use the antenna concept of effective height (also called effective length) (706), since it gives the open circuit voltage directly (707).

$$\vec{h}_b = h_b \hat{e}_b \tag{706}$$

$$V_{oc_n} = \vec{h}_b \cdot \vec{E}_{bn} \tag{707}$$

The equivalent base station receiving circuit is shown in Figure 245 and is identical to the circuit used for PRR.
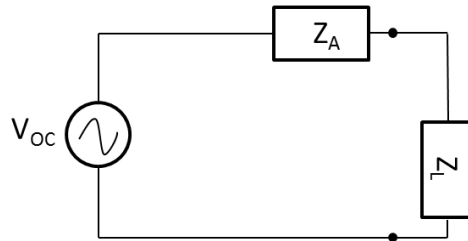
Figure 245. Circuit representation of the receiving circuit (base station).

The antenna impedance is given by (708) with real part given by(709).

$$Z_A = R_A + jX_A \tag{708}$$

$$R_A = R_r + R_l \tag{709}$$

305

Where R_r is the radiation resistance and R_l is the loss resistance; assumed to be zero for simplicity. For a conjugate matched load $Z_L = Z_A^*$ and Figure 245 is simplified to Figure 246.
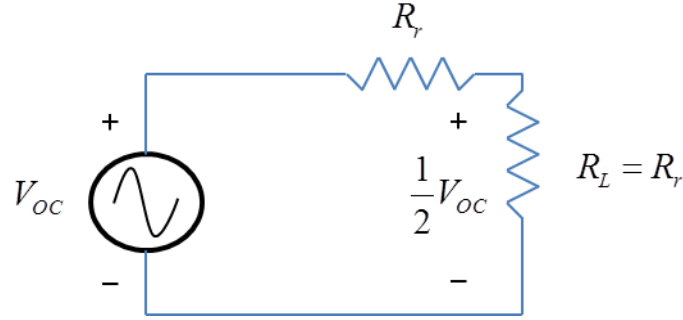
Figure 246. Conjugate matched receiver.

For a matched load $(R_r = R_L = R_A)$ the $V_L = \dfrac{1}{2}V_{OC}$ and thus, the power across the load can be written as;

$$P_L = \frac{V_{OC}^2}{4R_L} \tag{710}$$

Once again the effective height of the base station antenna is related to its effective area(711), which is also related to the gain of the antenna given in (712). Hence, (711) is rewritten as(713).

$$h_b\left(\theta_{bn}\right) = 2\sqrt{\frac{A_e\left(\theta_{bn},\phi_{bn}\right)R_A}{\eta_0}} \tag{711}$$

$$G_b\left(\theta_{bn},\phi_{bn}\right) = \frac{4\pi A_e\left(\theta_{bn},\phi_{bn}\right)}{\lambda^2} \tag{712}$$

$$h_b\left(\theta_{bn},\phi_{bn}\right) = 2\sqrt{\frac{R_A G_b\left(\theta_{bn},\phi_{bn}\right)\lambda^2}{4\pi\eta_0}} = \sqrt{\frac{R_A G_b\left(\theta_{bn},\phi_{bn}\right)}{\pi\eta_0}}\,\lambda \tag{713}$$

Now we are interested in finding the electric field. This can be easily found from the power density W_{bn} (W/m²) at the base station from UAV_n (714). Hence, solving to obtain the electric field intensity $|E_{bn}|$ (715).

$$W_{bn} = \frac{1}{2\eta_0}|E_b|^2 = \frac{P_{tn}G_n\left(\theta_n\right)}{4\pi R_n^2} \tag{714}$$

$$|E_{bn}| = \sqrt{\frac{2\eta_0 P_{tn}G_n\left(\theta_n\right)}{4\pi R_n^2}} \tag{715}$$

Adding the path phase shift/length e^{-jkR_n} and all other phases (such as synchronization, antenna, transmitter etc.) represented by $e^{j\phi_n}$ give the complex vector form given by (716).

$$\vec{E}_{bn} = \hat{e}_n \left| E_{bn} \right| e^{-jkR_n} e^{j\phi_n} \tag{716}$$

The voltage at the base station can finally be expressed as

$$V_{bn} = \frac{\vec{E}_{bn} \cdot \vec{h}_b \left(\theta_{bn}, \phi_{bn}\right)}{2} = \frac{1}{2} \sqrt{\frac{2\eta_0 P_{tn} G_n \left(\theta_n, \phi_n\right)}{4\pi R_n^2}} e^{-jkR_n} e^{j\phi_n} \hat{e}_n \cdot \vec{h}_b$$

$$= \left[\frac{2 P_{tn} G_n \left(\theta_n, \phi_n\right) G_{bn} \left(\theta_{bn}, \phi_{bn}\right) \lambda^2 R_A}{\left(4\pi R_n\right)^2} \right]^{1/2} e^{-jkR_n} e^{j\phi_n} \hat{e}_n \cdot \hat{e}_b \tag{717}$$

Now the complex voltage of the nth UAV transmitter at the output of the base station antenna is found by (718) assuming no ohmic loss $R_A = R_r$ (all radiation resistance), in addition to adding in the phase shift for PRR_n.

$$V_n = \sqrt{2 W_{r_n} \left(\theta, \phi\right) A_{e_n} R_r} \, e^{-jkR_n} e^{j\Phi_n} \tag{718}$$

(a) Total signal at the base station due to all UAV's

Again similar to the conditions for the PRR we assume the following conditions in order to derive the expression for the total signal strength at the base station due to all the UAVs transmitting simultaneously:

(1) All UAVs are perfectly phased synchronized.

(2) No polarization mismatch $\hat{e}_n \cdot \hat{e}_b = 1$.

(3) All UAVs have equal transmitter power and gain $G_n \equiv G_t, G_{tn} \equiv G_t$.

(4) All UAVs are pointed in the same direction $G_b \left(\theta_{bn}, \phi_{bn}\right) \equiv G_b$.

(5) All UAVs are approximately at the same range $\left(R_n \equiv R\right)$

The total voltage (719) at the base station from all of the UAVs is given by the summation of the individual UAV antenna voltages at the base station (across R_L in Figure 246). Yet, for the ideal conditions listed above, this summation reduces considerably to (720).

$$V_{tot} = \sum_n V_n = \sum_n \vec{h}_b \left(\theta_{bn}\right) \cdot \frac{1}{2} \vec{E}_{bn}$$

$$V_{tot} = \sum_n V_{bn} = \frac{\sqrt{2\lambda^2 R_A}}{4\pi} \sum_n \sqrt{P_{tn} G_n \left(\theta_n\right) G_b \left(\theta_{bn}\right)} \frac{e^{-jkR_n}}{R_n} e^{j\phi_n} \hat{e}_n \cdot \hat{e}_b \tag{719}$$

$$V_{tot} = \sum_n V_{bn} = \frac{\sqrt{2\lambda^2 R_A P_t G_t G_b}}{4\pi R} N \tag{720}$$

Once again we see that the power at the load for N identical coherent sources has increased by a factor of N^2.

$$P_L = \frac{1}{2}\frac{|V_{tot}|^2}{R_A} = \frac{P_t G_t G_b \lambda^2}{(4\pi R)^2} N^2 \tag{721}$$

(b) Base station signal at UAV$_n$ (uplink)

The received signal at UAV_n from the base station illustrated in Figure 247 can be expressed similarly as shown in (722) and its base station field is given by (723) , where the phase term ψ_n is included for phase synchronization.
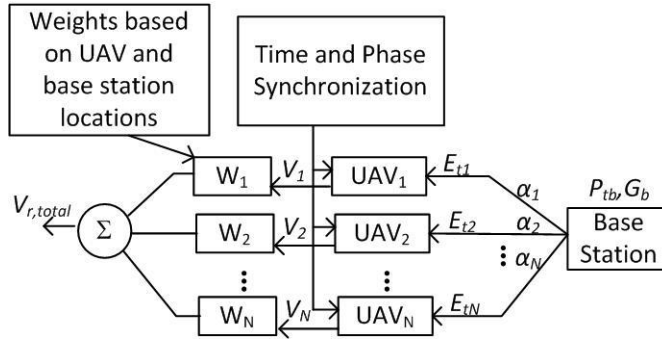
Figure 247. Collective beamforming for the uplink. [116]

$$P_{rn} = \frac{P_{tb} G_b(\theta_{bn}) G_n(\theta_n)\lambda^2}{(4\pi R_n)^2}|PLF_n|^2 \tag{722}$$

$$\vec{E}_n = \sqrt{\frac{2\eta_0 P_{tb} G_b(\theta_{bn})}{4\pi R_n^2}} e^{-jkR_n} e^{j\psi_n}\hat{e}_b \tag{723}$$

The voltage at the UAV_n antenna terminal is obtained directly using the effective height of the UAV antenna $\vec{h}_{en}$ as follows:

$$V_n = \vec{E}_n \cdot \vec{h}_{en} \tag{724}$$

$$V_{bn} = \sqrt{\frac{P_{tb} G_n(\theta_n) G_b(\theta_{bn}) R_A}{2}} \frac{\lambda}{\pi R_n} e^{-jkR_n} e^{j\psi_n}\hat{e}_n \cdot \hat{h}_{en} \tag{725}$$

(c) Phase coherence analysis

The expected power at the base station can be written as (726) for an element swarm of i.i.d. random variables. From this the coherent and non-coherent transmission will be derived as a special case of the downlink.

$$E[P_L] = \frac{1}{2}\frac{E\left[V_{tot}V_{tot}^*\right]}{R_A} \tag{726}$$

Now if one considers the random variable ϕ_n in (726) as a uniformly distributed variable over $[-\pi, \pi]$, the variance of ϕ_n will be:

$$\mathrm{var}(\phi_n) = \frac{(2\pi)^2}{12} \tag{727}$$

While it's mean will be equal to zero, $E[\phi_n] = 0$

Now rewriting (726) as

$$E[P_L] = \frac{P_t G_t G_b \lambda^2}{(4\pi)^2}\sum_m \sum_n \frac{e^{-jk(R_n - R_m)}}{R_n R_m}E\left[e^{j(\phi_n - \phi_m)}\right] \tag{728}$$

Once can redefine the phase term as one new random variable with variance $\bar{\Delta}^2$ as follows:

$$\Delta = \phi_n - \phi_m \tag{729}$$

Which, can also be separated using Euler's identity as

$$E\left[e^{j\Delta}\right] = E[\cos\Delta] + jE[\sin\Delta] \tag{730}$$

Now similar to taking the mean valued radiation intensity of a random array we assume that for m=n that $E[\cos\Delta] = 1$ and $E[\sin\Delta] = 0$. Otherwise for $m \neq n$ then $E[\cos\Delta] = e^{-\bar{\Delta}^2}$ and $E[\sin\Delta] = 0$. Now assuming that the UAVs are concentrated at a long range $(R_n \approx R_m \equiv R)$, (728) can be written as follows:

$$\langle P_L \rangle = \frac{P_t G_t G_b \lambda^2}{(4\pi R)^2}\left[e^{-\bar{\Delta}^2}N^2 + \left(1 - e^{-\bar{\Delta}^2}\right)N\right] \tag{731}$$

Where $e^{-\bar{\Delta}^2}N^2$ indicates coherent transmission and $\left(1 - e^{-\bar{\Delta}^2}\right)N$ indicates random (noncoherent) transmission. This result is derived in [116] and differs from the work in this dissertation such that the mean valued radiation intensity $\bar{U}(\theta, \phi)$ represents coherent transmission at the location $\bar{U}(\theta_0, \phi_0)$ where as non-coherent transmission is further away from the mean valued radiation pattern or in the 3 dB sidelobe region.

For example, coherent transmission from [116] assumes no phase differences so $\bar{\Delta}^2 \approx 0$ and hence,

$$\langle P_L \rangle = \frac{P_t G_t G_b \lambda^2}{(4\pi R)^2}N^2 \tag{732}$$

For non-coherent transmission, the phase differences are large, so $\bar{\Delta}^2 \to \infty$ is assumed and Equation (2.32) yields

$$\langle P_{L} \rangle = \frac{P_t G_t G_b \lambda^2}{(4\pi R)^2} N \tag{733}$$

More importantly, the result of (733) portrays an important result about the mean valued radiation intensity. The mean power of a random array does not go to zero from total randomness of the array, but yet grows by a magnitude of N. This is why the normalized mean valued radiation intensity is at 0 dB with average side lobe level $1/N$. Hence, a random array applied with no modulation will work as either a noise jammer with non-coherent strength N or with coherent strength N^2. An illustration of this is provided below in Figure 248 from [116].
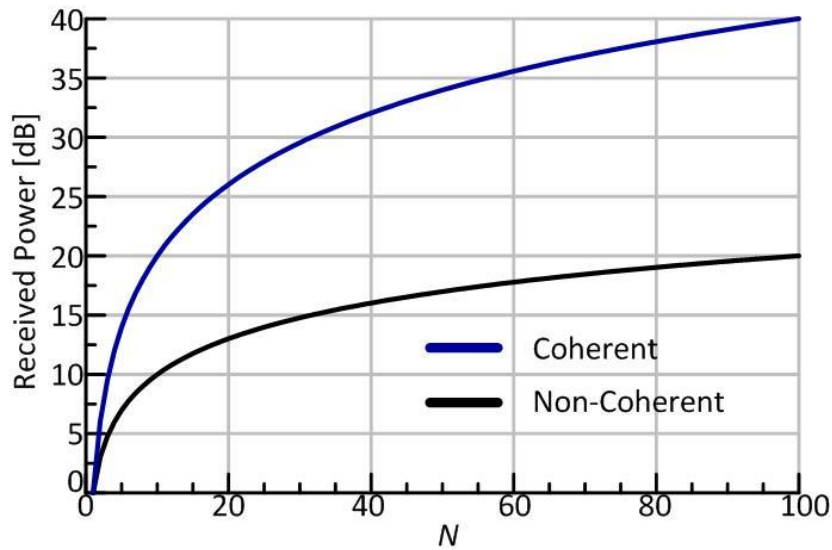
Figure 248. Coherent vs. non-coherent jamming.

I.4. ELEMENT SYNCHRONIZATION

Difficulty arises from attempting to acquire exact spatial information from a mobile antenna and attempting to estimate the location will trigger random error into the system. This leads to inaccuracy in the geometric information acquired. Since it is nearly impossible for every local oscillator to be synchronized with perfect precision. Two solutions to cope with these impairments are: closed-loop and open loop beamforming. In closed-loop each antenna receives a beacon from the destination antenna (such as a base station) and adjusts its initial phase accordingly. This is referred to as self-phasing and it is effective for systems using Time-Division Duplex (TDD). The open-loop consideration assumes the antenna ping a relative location from a nearby reference point or cluster head.

The proposed method in this dissertation for element synchronization in closed-loop beamforming as the locations of the nodes are considered to be "known exactly or at least to an acceptable level of accuracy such that location errors are less than a fraction of the wavelength ($\lambda/10$)." [2], [117] In general a desired lattice structure for many aperiodic arrangements is difficult to achieve in situations where dynamic and potentially uncoordinated movement is desired from platforms that host radiating elements. Constraints from the host platform require an accurate estimation of position and location information along with adequate synchronization. The ability to acquire the location parameters is assumed ideal in the theoretical framework proposed here, but certainly play a major role in the use (and usefulness) of random array techniques for platforms such as micro air vehicles (MAVs), portable communications networks (PCNs), unattended ground sensors (UGSs) and unpiloted aerial vehicles (UAVs) [54]. Moreover in practive "there is a wide variety of commercially available position location systems for navigation, communication, and asset tracking applications. They generally apply one or combination of TOF [Time of Flight], TDOA [Time Difference of Arrival], AOA [Angle of Arrival], and RSS [Received Signal Strength (Indicator)] to measure an object's distance from three or more reference points." [2] In addition for the random array the most fitting location algorithm is to utilize the fairly new Spatial Division Multiple Access (SDMA) algorithms. This technique spatially separates received signals using Direct Sequence Spread Spectrum (DSSS) techniques and is analogous to a code division multiple access (CDMA) receiver. Moreover, the method introduces a virtual receiver array in computer memory that expects I directions of arrival such that it chips the phase of these received signals at each of the array element with individual spreading sequences. Meanwhile in the physical array the received signals are summed together and a quadrature correlation is performed amongst the received signal and each of the I expected DOA virtual signals. From the correlation values R_i a determined threshold is set such that exceeding values identify the signal from an expected DOA_i. The information of the signal is also recovered from the phase of the correlation R_i,. The only problematic issues of concern is that interfering signals will not be well correlated and as a consequence minimized (this is similar in concept to a matched filter bank in a code division multiplexing receiver). [92]

The synchronization challenges arise from the mobile structure of the application and can be improved based upon the overall (random array) network topology. Moreover, in the random array the array elements need to be synchronized in both time and phase. Hence, for time synchronization, one must ensure that the transmitted or received radar signals overlap at the target or array output respectively. Alternatively, for phase synchronization, "the phases of the transmitted or received radar signals should be adjusted so that they arrive in phase at the target or at the output of the receiver." [2]

I.4.1 Beamforming Circuitry (Brute Force)

The beamforming circuitry for a random array is followed in this section using the architecture utilized in [2] and [117] for the wirelessly networked digital distributed phased array (opportunistic array)

311

shown in Figure 249. This type of design uses a central controller which is used to send the necessary synchronization signals to each transmit receive module (antenna element) containing its own synchronization block shown in in Figure 249. This block encompasses a modem and controller connected to a phase shifter and a switch with two modes of operation. The first mode of these modes is positioned for synchronization operation (as shown) such that the Local Oscillator (LO) signal is passed through a circulator, low-noise amplifier (LNA), phase shifter and then retransmitted back and compared to a reference signal at the central controller. In the second mode of operation (normal operation and the switch opposite as shown), the LO signal is sent out to the modulator and demodulator for coherent beamforming. [2]. Last of all when incorporating this design to a swarm of UAVs it should be understood that each UAV is mobile and sensor synchronization and element geolocation problems will tend to be more complicated than a single platform design. These types of environments will typically require fast synchronization times and Doppler compensation techniques. Furthermore "with PIN diode phase shifters, switching of two bits can be done between 1 ns to 2 ns per element." [2] Hence, for a large 1000 element random array population, synchronization can be done with a sixteen bit phase shifter in about $16\mu s$ to $32\mu s$ and with a 4 bit phase shifter in about $4\mu s$ $8\mu s$. Therefore it will be critical to design electronic steering capability algorithms to compensate for large mobile random arrays in motion. Secondly, phase correction or synchronization at a single frequency may also be insufficient since; a single frequency is sufficient for simple waveforms such as continuous wave (CW) or narrow band pulsed CW operation. "For more complicated wide band waveforms that employ frequency modulation, frequency hopping or pulse compression techniques, synchronization may have to be carried out at several frequencies or at the center of a band of frequencies. This will add more complexity to the synchronization hardware and software requirements. Further investigations will have to be carried out in this area." [2], [117]

Last of all as a practical example, in relation to PRR if one was interested in bounding the phase error due to placement error θ_e to within $\delta\theta$, where $\delta\theta$ implies that placement error distance $|d_e(n)| \leq \dfrac{\lambda\delta\theta}{2\pi}$. Then since PRR operates at 2.45 GHz and for an arbitrary tolerance on the placement error of $30°$ $|d_e| \leq .122\dfrac{30°}{2\pi}\dfrac{\pi}{180°} = 10mm$. This is about the best achievable in the most favorable conditions by GPS and consequently, better location finding equipment will be of paramount importance to the random array.
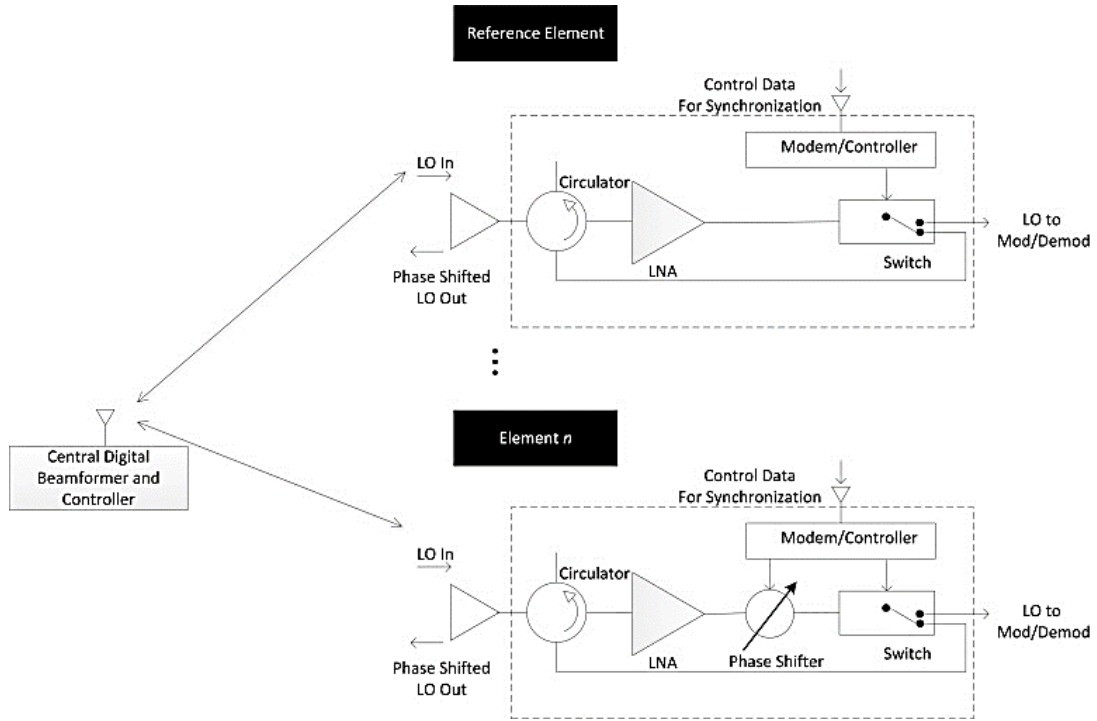
Figure 249. Illustration of the beamforming circuitry for phase shifting (top is the phase shifting circuitry for the reference element).

(a) Synchronization independent of path loss amplitudes

The start of the synchronization cycle begins with the central controller sending out each element's address in turn to begin its synchronization cycle. Once the element is selected the switch is moved to the synchronization position and the process begins. I.e. first the LO signal from the central controller arrives at each element at a different phase, given by e^{-jkr_n}, where k is the wave number and r_n is the distance from the central controller to the element n. Following this, one element of the formation is selected as the reference node and as a consequence it receives the corresponding LO signal $e^{-jkr_{ref}}$. Next the objective is to synchronize the remaining elements to the reference element (by adjusting the phase shifter ϕ_n to correct for the difference in path length $(r_{ref} - r_n)$). Hence, the combined field at the central controller is given by (assuming the amplitudes are suitably compensated by signal amplifiers)

$$E_{difference} = E_n - E_{ref} = e^{-j(2kr_n + \phi_n)} - e^{-j(2kr_{ref})} \tag{734}$$

Here it is obvious that when ϕ_n is known, the difference in path length $(r_{ref} - r_n)$ can be corrected and all the elements can be synchronized. In other words the applied phase shifts ϕ_n are continuously updated in

element n until the two signals cancel, $\phi_n = 2k\left(r_{ref} - r_n\right)$. "This method will also correct for any phase variation due to differences in the propagation channels (e.g., walls with different insertion phases))" [117]

However, discrete phase steps, using a bit phase shifter will not be able to achieve complete cancellation. Therefore a threshold value is necessary to detect when the minima of the two signals will cancel sufficiently. For example, assuming equal amplitudes and a 4 bit phase shifter provides (360/2^4) 22.5° steps of phase correction such that, the final phase error is $\pm 11.25°$. Hence, "the minimum field can be computed using phasor geometry." [117]

$$
\begin{aligned}
\min\left(\left|E_{difference}\right|\right) &= \left|E_{ref}\, e^{-j(11.25°)} - E_{ref}\right| \\
&= 2\sin\left(11.25°/2\right) \\
&= 0.196
\end{aligned}
\tag{735}
$$

Therefore a 4 bit phase shifter will provide for a field threshold of 0.2 (−14 dB) error. In addition since there is 16 phase steps between 0 and 360 there will be on average eight iterations (half the quantization levels) required to synchronize each element, because the required phase shift is unknown. "This is then repeated for the rest of the elements. Four-bit digitization was deemed satisfactory for digital phase shifter quantization based on the required sidelobe level." [117] Hence, for a large 1000 element random array population, synchronization can be done with a sixteen bit phase shifter in about $2^4 \mu s$ x $2^{15}=0.52428s$ to $2^5 \mu s$ x $2^{15}=1.048576s$ and with a 4 bit phase shifter in about $2^2 \mu s$ x $2^4=64\mu s$ to $2^3 \mu s$ x $2^4=128\mu s$.

$$
\begin{aligned}
& 2^{\sqrt{\# bits}}\, ns \ \text{ or } \ 2^{\sqrt{\# bits+1}}\, ns \ x \ \left(mean\ iterations\right)2^{\# bits-1}\, ns\left(1+RTT\right) \\
& \text{-Round trip time}\left(RTT\right) = \\
& 2x\left(\frac{A}{2}\right)/c = 667ns\Big|_{A=100\,meters}
\end{aligned}
\tag{736}
$$

Hence, a -16 bit phase shifter has accuracy up to 0.00225° and can phase synchronize (excluding transceiver throughput and processing) in 0.35s - .70s for 1000 elements Figure 251. Alternatively, a 4 bit phase shifter has accuracy up to 11.25° and will synchronize (excluding transceiver throughput and processing) in 21.4ms - 42.8ms for 1000 elements Figure 252.

The phase error of each element is displayed in Figure 250 for the reference element plotted against the number of iterations necessary to synchronize. Each change in color denotes a new element being synchronized and the example shown is for 20 randomly located elements. Hence, the average number of iterations necessary is 20x8 =160 and was done in 157 iterations as shown. A frequency of 300 MHz, was chosen for convenience, i.e. lambda =1.
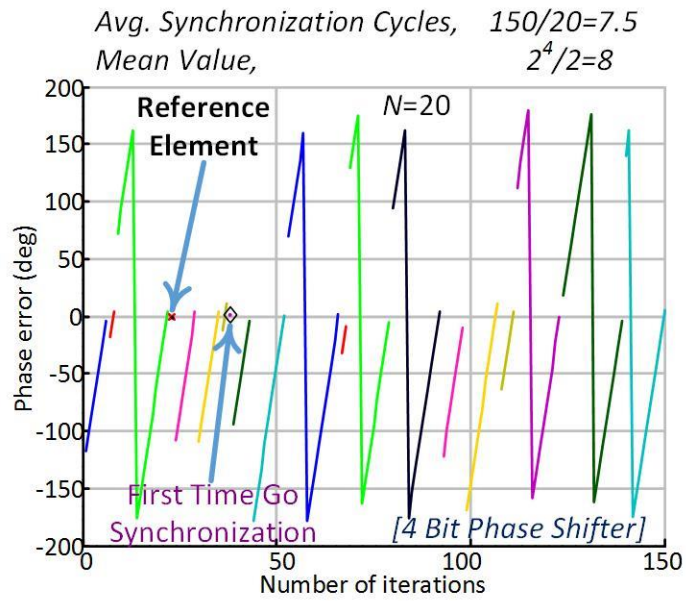
Figure 250. Twenty element phase synchronization example of the brute force algorithm.
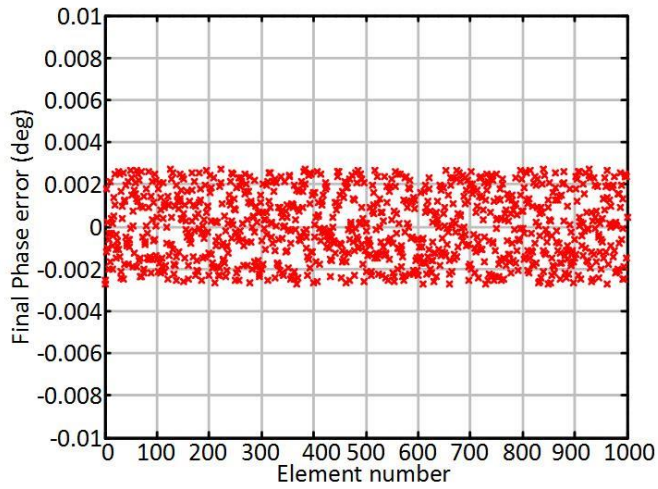
Figure 251. Phase error is bound to $\pm.003°$ for a sixteen bit phase shifter.
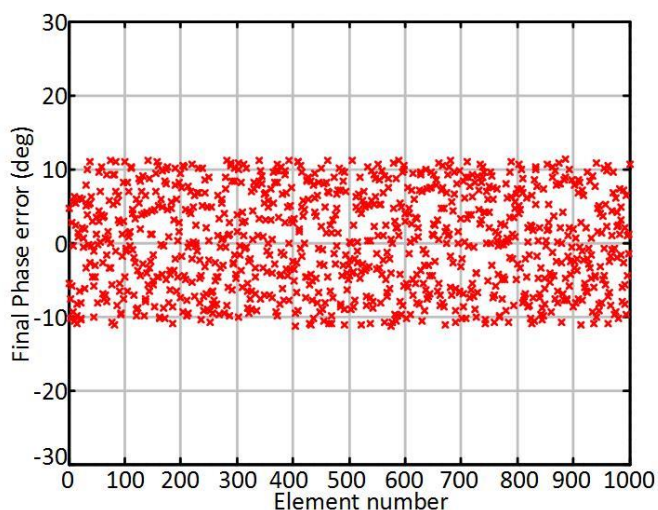
Figure 252. Phase error with a 4 bit phase shifter is bound to $\pm 11.25°$.

(b) Synchronization with varying path loss amplitudes

In a real environment the synchronization (LO) signals are subject to geometrical spreading, i.e. path loss ($4\pi r^2$, denominator of the Friss transmission equation in a sphere or $2\pi r$ in a plane). Hence to take the effect of varying path loss amplitudes (734) is replaced by

$$E_{difference} = \frac{1}{2r_n} e^{-j(2kr_n + \phi_n)} - \frac{1}{2r_{ref}} e^{-j(2kr_{ref})} \qquad (737)$$

The factor of $2r$ is used as the round trip time to go to the synchronization circuit and back. More accurate approaches should use the square of the denominator of the Friis Transmission equation. Moreover, the effect of varying signal amplitude is significant for elements located far away from the reference element. For example if a distribution of elements has a minimum distance of 17 m, and a maximum distance of 88.8 m then the relative signal amplitude could vary up to five times.

I.4.2 Beam Tagging

This research does not focus upon the beam tagging algorithm, however the architecture is show in [117] Beside the point, in summary [2] "concluded that even though the "beam tagging" technique was faster on the order of *2* to *3μs*, the more simple "brute force" technique is preferred for the wireless radar." [117] However though contradictory to [117], it is known that more sufficient synchronization schemes will need to be investigate further, because the brute force" technique will be too slow and inefficient for large mobile random arrays.

316

I.4.3 Data Rate

The data rate required for a random array is shown in the table below

Table 16. Suggested Data Rate for the Random Array.

Description	From	Data Rate
Waveform Control	Beam Controller	2 bits/second
Synchronization control	Beam Controller	1 bi/s synchronization command 1 bit/t for phase correction command
Phase Weights control	Beam Controller	4 bit/s
Received radar signals	T/R module	16 bit x 2 x 100 kS/s =3,200,000=3.2 Mb/s

Two bits will be sufficient to choose between four possible waveforms, such as continuous sinusoid, pulsed sinusoid and possibly linear frequency modulated waveforms. Then for the wireless distribution of the LO used, two bits are required for synchronization control. One bit is used to send a synchronization command for the T/R module to go into synchronization mode. Another bit is used to send phase correction command for the T/R module to step its phase shifter by 22.5°

On RX, a high data rate is needed because the performance of the ADC affects the resolution of the received digitized signal [3]. The sampling rate of the ADC must meet the Nyquist condition, which is at least twice the intermediate frequency (IF) bandwidth (in a super heterodyne receiver) or twice the baseband frequency (in a homodyne system). The approximate data rate requirement is given by [24]:

$$R_b = N_c x N_b x R_s$$

$R_b = $ data rate

$N_c = $ data channels per array element (738)

$N_b = $ ADC bits of resolution

$R_s = $ ADC sampling rate (samples per second)

Therefore, if a two-channel ADC is simultaneously sampled with 100 MS/s for each element and the resolution is eight bits, then for each element in the wireless network, the required data rate is approximately 2 8 100 MS/s 1.6 Gb/s Rb. For an *N*-element full-scale array, the total required data rate is 1.6 Gb/s. Above all it is 2 x 16 x 100 MS/s=3.2 Mb/s. In Loke's work [2] the data rate needed for *N* elements is 3.2 Mb/s *N*. For a 1200 element array as in the Chang's work [119] it requires 3.2 Mb/s

*1200=3840 Mb/s and 3840 Mb/s * (1Gb/s) / (1024Mb/s) 3.75 Gb/s. Otherwise for a 16 bit phase shifter you would need a 20 bit circuit at minimum, so assuming a 24 bit system. This comes out to be 2x24x100kS/s=4800kS/s = 4.8 mS/s. In [119] you need 2*8*100MS/s=1.6 Gb/s and for N elements 1.6*N Gb/s are needed. Thus for 1200 elements this is 1.6 Gb/s *1200 = 1920 Gb/s *1Tb/s / 1024 Gb/s =1.875 Tb/s. For a 16 bit phase shifter you would need (assuming 24 bit architecture) this comes out to be 2*24*100mS/s = 48 mS/s

I.4.4 Conclusion

Last of all for the two modes of operation being synchronization and date mode it was investigated in [2] such that 5.8 GHz was utilized for the data communication and 2.4 GHz for the LO and phase synchronization. "The different frequency bands were chosen to minimize interference, and indeed there was no observable interference between them. A number of phase synchronization tests were done with different positions of the LO antenna, symbolizing different T/R module positions, and the measurements verified the concept." ([138])

In essence, for applications of stationary electronic random arrays of which there will be less difficulty involved in the process when there is no moving parts and there will be no suffrage from vibration and as a consequence will be inherently better stabilized contrary to ship or aircraft motion, as "the electronic array simply steers the main beam counter to the detected motion." [105] As a consequence, elements located far away will incur unrealistic requirements in terms of accuracy to reach the destination with collaborative structure. On the other hand, decreasing the effective aperture size allows for greater bandwidth, in exchange for a small growth in sidelobe level. Thus, sophisticated phase algorithms and high resolution phase shifters will be necessary in order to realize and make possible these large mobile random arrays.

I.5. SDMA

Spatial Division Multiple Access (SDMA) was first patented by Chris Elam in 2004 with an example by Frank Gross in the book Smart Antennas in 2005. Moreover, the method is similar in respect to code division multiple access (CDMA) techniques such that SDMA separates received signals using direct sequence spread spectrum (DSSS) techniques. The method utilizes a virtual array in computer memory such that identically chipped virtual signals are searched for in I expected directions of arrival. It looks in these locations by utilizing spreading sequences and chipping the phase of the signals received by each array element. The aggregate of the received signals is correlated between the I expected directions of arrival (DOA) virtual signals. Any correlation (R_i) value exceeding a threshold value is identified as a signal coming from the expected location DOA_i. Next the message of the signal can be extracted from the phase of the correlation Ri. Thus, far the only problematic issue is that "interfering signals are not well correlated and thus minimized. This is similar in concept to a matched filter bank in a code division multiplexing receiver. [92]

The received signals are samples with length T such that the received signals are exploited at each receive element using M pseudorandom chips. Independent separate pseudorandom noise (*pn*) spreading codes are applied to each receive element and can be thought of as pseudorandom array weights. In other words, during the time period T, the array has been "steered" by M sets of pseudo-random weights. An example of the physical receiver is shown in Figure 253 and will be described in greater detail in the following section.
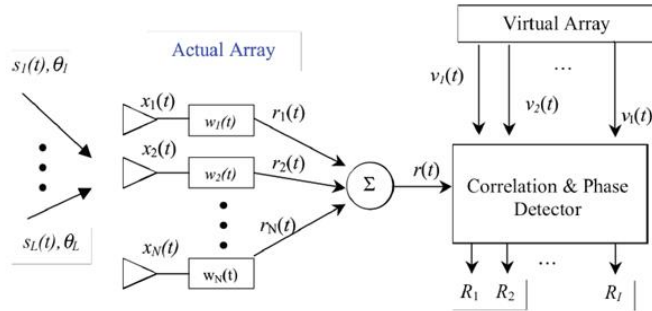
Figure 253. Example of the SDMA receiver.

I.5.1 The Actual Array

A group of L phase shift keyed (PSK) signals $s_l(t) = e^{j\zeta_l(t)}$ are assumed to arrive at the array and form the received signal $x_n(t)$ at each of the N antenna elements. More so the more random these N elements helps the performance the architecture by helping to improve independent phases at each element for the expected angle of arrivals. Thus, the spread signal $r(t)$ is created from the sum of received signals $x_n(t)$ spread or chipped with a pseudorandom noise (pn) code associated with that antenna element, producing. In mathematical form the received signal is given by (739). Afterwards the signal is chipped with an orthogonal spreading sequence $\vec{w}(t)$ producing the pn chipped signal $r(t)$ provided in (741)

$$\vec{x}(t) = \begin{bmatrix} 1 & 1 & \cdots & 1 \\ e^{jkd\sin\theta_1} & e^{jkd\sin\theta_2} & \cdots & e^{jkd\sin\theta_L} \\ \vdots & & \ddots & \\ e^{jkd(N-1)\sin\theta_1} & & & e^{jkd(N-1)\sin\theta_L} \end{bmatrix} \begin{bmatrix} e^{j\zeta_1(t)} \\ e^{j\zeta_2(t)} \\ \vdots \\ e^{j\zeta_L(t)} \end{bmatrix} \tag{739}$$

$$\vec{w}(t) = \begin{bmatrix} w_0(t) & w_1(t) & \cdots & w_{N-1}(t) \end{bmatrix} \tag{740}$$

$$r(t) = \vec{w}(t)\vec{x}(t) \tag{741}$$

319

Since the received signals are samples with length T then vector $w_n(t)$ should contain M chips of length τ, chosen such that the length of the vector is $M\tau = T$, the sample time. In other words "the number of chips M should be chosen such that it is greater than the Nyquist rate of the received baseband signal modulation. This implies the phase modulation of the received baseband signal is nearly constant over T. The time-bandwidth product of the sample time T and the message signal bandwidth B should be $TB \leq .25$." [92] Last of all there are numerous pseudorandom noise spreading codes that can be applied. I.e. Gold codes, Goday codes, Walsh-Hadamard and Welti codes can all be used where Walsh-Hadamard is utilized in the following section similar to [92] for simplicity. However, Welti codes have been identified to produce the best results [92]. An example of the spreading codes on a sin modulated signal is shown in Figure 254. Hence, it is seen that the real part of the chipped signal $r_n(t)$ is unique and is repeated at each of the N elements.
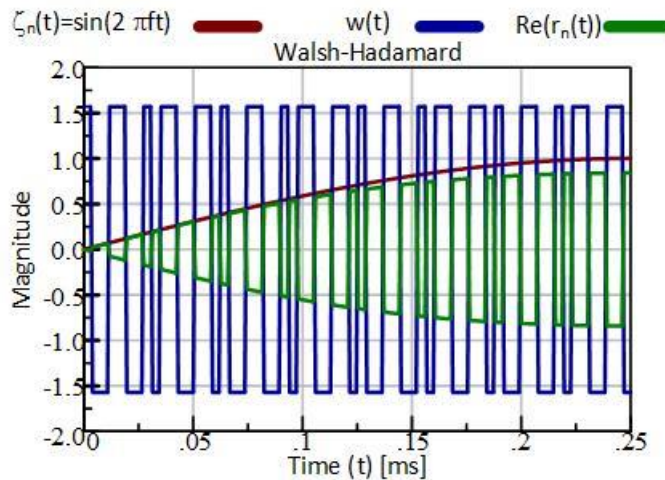
Figure 254. Example of the modulated message with Walsh-Hadamard spreading.

I.5.2 The Virtual Array

The expected direction θ_I is equivalent to the beam steering angle θ_o by reciprocity (742). Therefore the array factor for each of the N elements is chipped with the *identical spreading codes* as the physical array (743). The process is repeated and stored in memory for each of the I expected directions of arrival θ_I where the steering vector (743) for each expected direction is given by the $N \times 1$ column vector. Furthermore, prior knowledge of the incoming signals, multipath can be beneficial since the I

expected directions can be chosen to avoid known interfering directions. However, the "expected directions cannot be chosen any finer than physically allowed by the actual array." [92]

$$\vec{a}_i^v(\theta_i) = \begin{vmatrix} 1 \\ e^{jkd\sin\theta_1} \\ \vdots \\ e^{jkd(N-1)\sin\theta_i} \end{vmatrix} \tag{742}$$

$$v_i(t) = \vec{w}(t)\vec{a}_i^v(\theta_i) \tag{743}$$

I.5.3. Signal and Phase Correlator

The correlation of the received and virtual signal is calculated as:

$$R_i = \int_t^{t+T} r(t)v_i^*(t)dt \tag{744}$$

where R_i is the complex correlation value for each direction θ_i. "The magnitude of R_i will be plotted for each angle θ_i becoming the array factor for the signals present. The threshold detector depicted compares the magnitude of R_i against a predetermined value and declares a signal present or not at this angle. If a signal is present, the data is extracted as explained in the next subsection. This is similar to a matched filter or correlation detector operation." [92]

To understand how this works, we first examine the received signal (745) and virtual signals (746) and substitute these into (744) to give (747).

$$r(t) = \sum_{n=1}^{N} e^{j(n-1)kd\sin\theta_0} e^{j\zeta(t)} e^{j\frac{\pi}{2}w_n(t)} \tag{748}$$

$$v_i(t) = \sum_{m=1}^{N} e^{j(m-1)kd\sin\theta_i} e^{j\frac{\pi}{2}w_m(t)} \tag{749}$$

$$R_i = \int_t \sum_{n=1}^{N} e^{j(n-1)kd\sin\theta_0} e^{j\zeta(t)} e^{j\frac{\pi}{2}w_n(t)} \sum_{m=1}^{N} e^{-j(m-1)kd\sin\theta_i} e^{-j\frac{\pi}{2}w_m(t)} \tag{750}$$

Now rearranging the element summation yields (752) and (751) since the phase $\zeta(t)$ of the signal *s(t)* is approximately constant over the sample period and can be approximated as its average $\bar{\zeta}$.

$$R_i = \int_t \sum_{n=1}^{N}\sum_{m=1}^{N} e^{j(n-1)kd\sin\theta_0} e^{j\zeta(t)} e^{j\frac{\pi}{2}w_n(t)} e^{-j(m-1)kd\sin\theta_i} e^{-j\frac{\pi}{2}w_m(t)} \tag{752}$$

$$R_i = \int_t \sum_{n=1}^{N}\sum_{m=1}^{N} e^{j(n-1)kd\sin\theta_0} e^{-j(m-1)kd\sin\theta_i} e^{j\bar{\zeta}(t)} \underbrace{\int_t e^{j\frac{\pi}{2}w_n(t)} e^{-j\frac{\pi}{2}w_m(t)}}_{\delta(n-m)\begin{cases} 1 \ if \ n=m \\ 0 \ if \ n\neq m \end{cases}} \tag{753}$$

As a consequence, of the orthogonality between w_n and w_m the correlation yields a delta function $\delta(n-m)$ and reduces as

$$R_i = \sum_{n=1}^{N} e^{j(n-1)kd(\sin\theta_0 - \sin\theta_i)} e^{j\bar{\zeta}} \qquad (754)$$

This solution is equivalent to the array factor, but multiplied by the constant phase of the received signal. Therefore in vector format the correlation is expressed as (755) where the magnitude contains the DOA information and the phase term contains the message information."

$$R_i = |R_i| e^{j\rho_i} \qquad (755)$$

Examples of the spatial division multiple access technique are provided below in Figure 255-Figure 259.
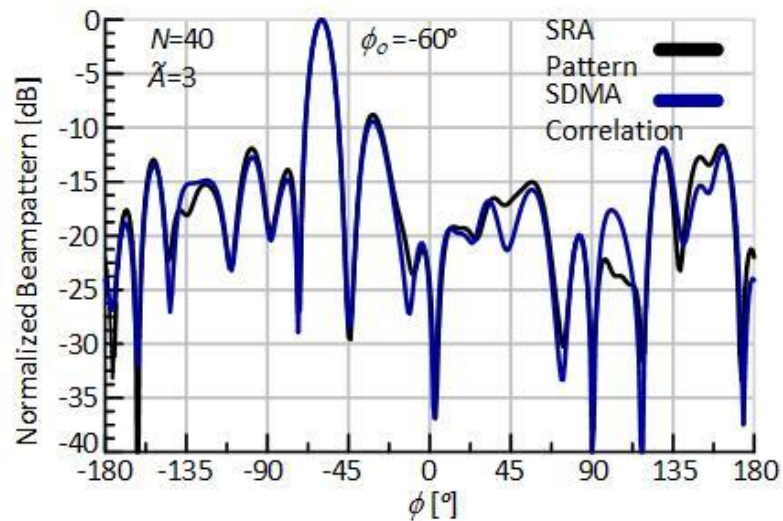
Figure 255. SDMA correlation of a spherical random array with incoming signal $\theta_{0,1} = -60°$.
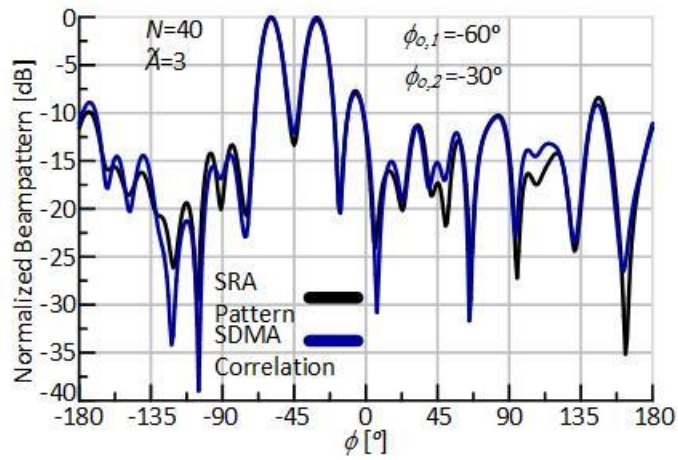
Figure 256. SDMA correlation of a spherical random array with two incoming signals $\theta_{0,1} = -60°$ and $\theta_{0,2} = -30°$.
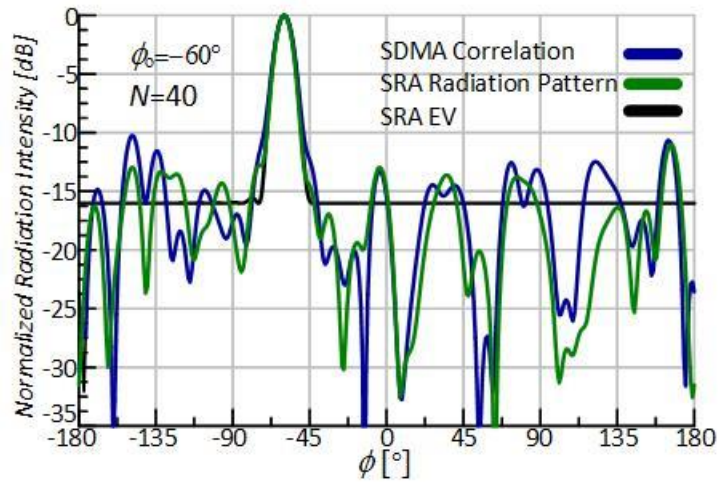
Figure 257. SDMA correlation of a spherical random array with incoming signal $\theta_{0,1} = -60°$ with comparison to the expected value.
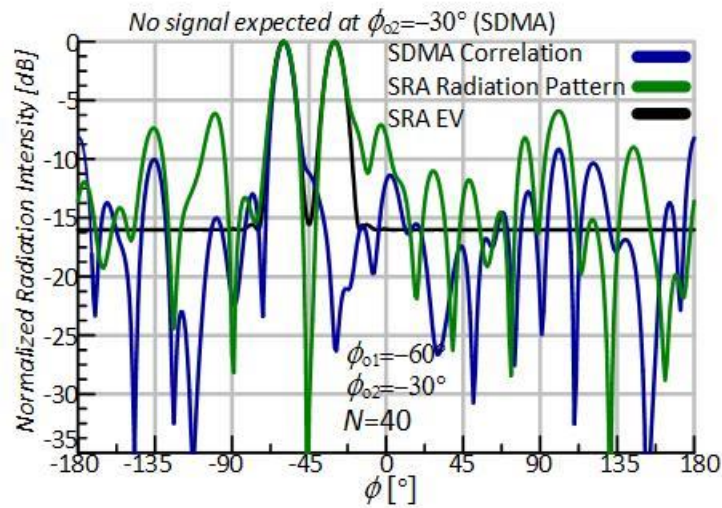
Figure 258. SDMA correlation of a spherical random array with two incoming signals $\theta_{0,1} = -60°$ and $\theta_{0,2} = -30°$ with comparison to the superposition of the expected value of two signals.
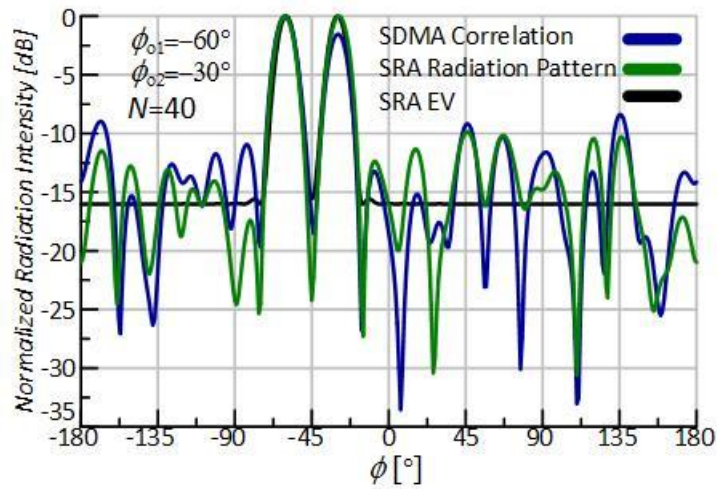
Figure 259. SDMA correlation of a spherical random array with two incoming signals $\theta_{0,1} = -60°$ and $\theta_{0,1} = -30°$, but with only one look angle at $\theta_{0,1} = -60°$ and comparison to the superposition of the expected value of two signals.

4. Message Extraction

To extract the message data of the received signal the correlation integral averages the received signal phase over T [92]

$$\rho_i \simeq \bar{\zeta} = \frac{1}{T} \int\limits_{t}^{t+T} \zeta_i(t) dt \qquad (756)$$

where $\bar{\zeta}$ is the average signal modulation during the time period T at θ_i. This means that one can simultaneously extract more than one message signal from the correlation data by calculating ρ_i at each angle where a signal has been determined. [92] A few examples of the message extraction ability of spatial division multiple access are provided in Figure 260-Figure 262.
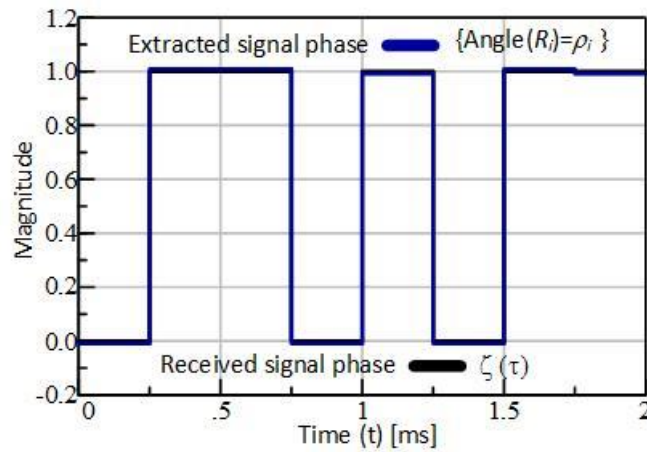
Figure 260. SNR =80dB.
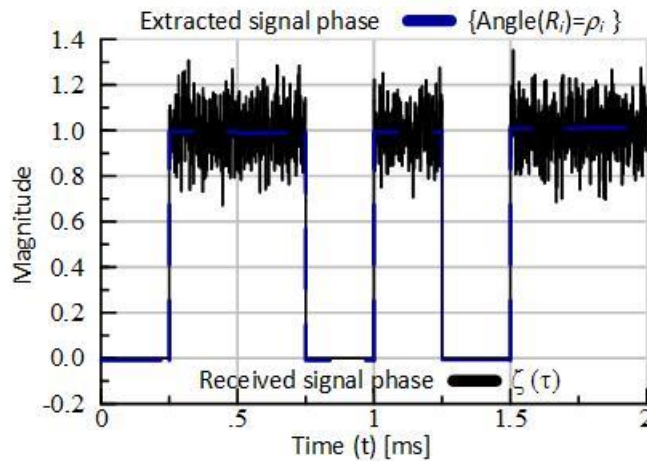
Figure 261. SNR =20dB.
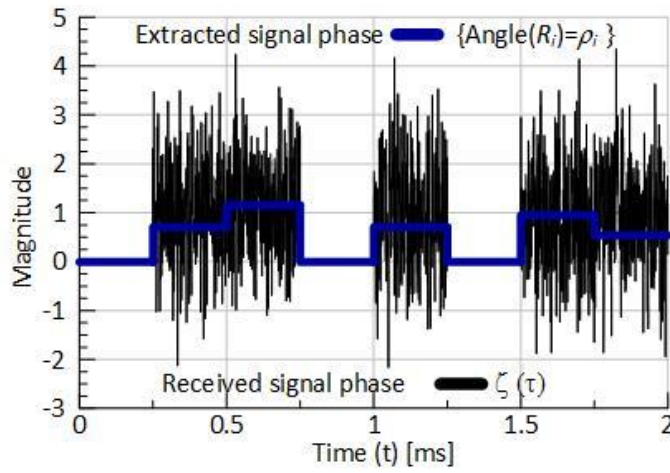
Figure 262. SNR =0dB.

Overall SDMA provides numerous advantages compared to other DOA techniques. Its ability to create a set of virtual signals in memory, decreases the computational cost significantly compared to the traditional methods of conjugate gradient and other iterative matrix solution methods. "Additionally, the technique provides a processing gain of $\sqrt{N_{chips}}$." [92]

APPENDIX II

EXPLANATION OF THE PHYSICAL PROCESS

II.1 Helmholtz Differential Equation - Spherical Eigenfunction Expansion

The Helmholtz equation in spherical coordinates is provided by (757) for a spherically symmetric source (758). Field (e.g. from a point monopole), solutions are of the form (759) where B and C are the amplitudes of outward and inward traveling waves respectively (Appendix).

$$\frac{1}{r^2}\frac{\partial}{\partial r}\left(r^2\frac{\partial A}{\partial r}\right)+\frac{1}{r^2\sin\theta}\frac{\partial}{\partial\theta}\left(\sin\theta\frac{\partial A}{\partial\theta}\right)+\frac{1}{r^2\sin^2\theta}\frac{\partial^2 A}{\partial\phi^2}+k^2 A=0 \tag{757}$$

$$\frac{\partial A}{\partial\theta}=\frac{\partial A}{\partial\phi}=0 \tag{758}$$

$$A=B\frac{e^{jkr}}{r}+C\frac{e^{-jkr}}{r} \tag{759}$$

Alternatively we may express this solution using the *method of separation of variables* to change the partial differential equation into a number of independent ordinary differential equations (770). First it is assumed that

$$A(r,\theta,\phi)=R(r)\Theta(\theta)\Phi(\phi) \tag{760}$$

Where $A(r,\theta,\phi)$ are the complex pressure and the harmonic time dependence of the form $e^{-j\omega t}$ has been assumed. Separating variables yields three *ordinary differential equations* (ODE) (761)-(763). These equations give independent dependence of pressure on r, θ, and ϕ.

$$\frac{d}{dr}\left(r^2\frac{dR}{dr}\right)+\left[k^2 r^2-n(n+1)\right]R=0 \tag{761}$$

$$\frac{1}{\sin\theta}\frac{d}{d\theta}\left(\sin\theta\frac{d\Theta}{d\theta}\right)+\left[n(n+1)-\frac{m^2}{\sin^2\theta}\right]\Theta=0 \tag{762}$$

$$\frac{d^2\Phi}{d\phi^2}+m^2\Phi=0 \tag{763}$$

The solutions to these ODEs are shown in (764) with derivations given in the Appendix.

$$\boxed{\begin{aligned}
&\Phi(\phi) = De^{jm\phi} + EDe^{-jm\phi} \quad [m \in \mathfrak{I}] \\
&\Theta(\phi) = FP_n^m(\cos(\theta)) + GQ_n^m(\cos(\theta)) \\
&R(r) = H_{nm}\frac{e^{jkr}}{r} + I_{nm}\frac{e^{-jkr}}{r} = J_{nm}h_n^{(1)}(kr) + K_{nm}h_n^{(2)}(kr) \\
&\text{where} \\
&\text{D,E,F,G are the amplitudes and} \\
&H_{nm}, I_{nm}, J_{nm}, K_{nm} \text{ are the complex amplitudes of outgoing and incoming} \\
&\text{waves respecitively with angular order n and m}
\end{aligned}}$$

(764)

The expression $P_n^m(x)$ is the *associated Legendre functions* of the first kind. Also of importance is noting that the *spherical Hankel function* of the *2nd* kind is simply the complex conjugate of the *1st* kind, and that h_0 represents the spherically symmetric wave field, which will be of importance later on. Hence, another familiar solution for the radial dependence can also be rewritten as a linear combination of these *spherical Hankel functions*.

$$\begin{aligned}
R(r) &= J_{nm}h_n^{(1)}(kr) + K_{nm}h_n^{(2)}(kr) \\
&= J_{nm}\left(j_n(kr) + jy_n(kr)\right) + K_{nm}\left(j_n(kr) - jy_n(kr)\right) \\
h_n^{(1)}(kr) &= j_n(kr) + jy_n(kr) \\
h_n^{(2)}(kr) &= j_n(kr) - jy_n(kr)
\end{aligned}$$

(765)

Solutions of the angular dependence on θ and ϕ can also be combined and expressed in terms of *spherical harmonics* given as

$$Y_n^m = \sqrt{\frac{(2n+1)(n-m)!}{4\pi(n+m)!}}P_n^m(\cos(\theta))e^{jm\phi}$$

(766)

Thus, the angular dependence is expressed as a combination (weighted sum) of spherical harmonics. A visual representation of the angular dependence of the spherical harmonics is shown below where each order of *spherical harmonic* is associated with the outgoing wave generated by elemental source types as shown in Figure 263.
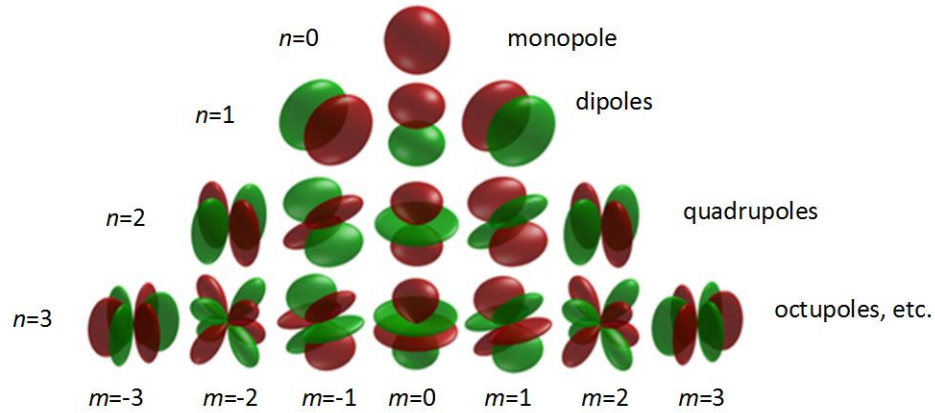
Figure 263. Spherical harmonics three dimensional representations.

Now combining the angular and radial functions any solution of the wave equation, can be written

$$A(r,\theta,\phi) = \sum_{n=0}^{\infty} \sum_{m=-n}^{n} \left(J_{nm} h_n^{(1)}(kr) + K_{nm} h_n^{(1)}(kr) \right) Y_n^m(\theta,\phi) \tag{767}$$

Or an alternative form of the solution, using the definition of the Hankel functions can be written as

$$A(r,\theta,\phi) = \sum_{n=0}^{\infty} \sum_{m=-n}^{n} \left((J_{nm} + K_{nm}) j_n(kr) + j(J_{nm} - K_{nm}) y_n(kr) \right) Y_n^m(\theta,\phi)$$
$$= \sum_{n=0}^{\infty} \sum_{m=-n}^{n} \left(A_{nm} j_n(kr) + jB_{nm} y_n(kr) \right) Y_n^m(\theta,\phi) \tag{768}$$

Lastly since the $y_n(kr)$ is infinite at $r=0$ and if the region is source free we rewrite our solution in its final form as

$$A(r,\theta,\phi) = \sum_{n=0}^{\infty} \sum_{m=-n}^{n} A_{nm} j_n(kr) Y_n^m(\theta,\phi) \tag{769}$$

From this result it can be shown that the n*ormalized Greens' function* is given as:

$$\frac{e^{jk|\vec{r}_1 - \vec{r}_2|}}{4\pi |\vec{r}_1 - \vec{r}_2|} = jk \sum_{l=0}^{\infty} \left\{ \begin{array}{l} j_l(kr_1) h_l^{(1)}(kr_2) \ \ [r_1 < r_2] \\ j_l(kr_2) h_l^{(1)}(kr_1) \ \ [r_1 > r_2] \end{array} \right\} \sum_{m=-l}^{l} Y_l^m(\theta_1,\phi_1) Y_l^{m*}(\theta_2,\phi_2) \tag{770}$$

II.2 Plane Wave Expansion- A Sum of Spherical Waves

The *Jacobi-Anger expansion* is a method used in order to show that a plane wave can be expressed in terms of a series of spherical harmonics of infinite order. Thus, a plane wave can be expressed as a sum of spherical waves as

329

$$e^{j\vec{k}\cdot\vec{r}} = \sum_{l=0}^{\infty} j^l (2l+1) j_l(kr) P_l \cos(\psi) = 4\pi \sum_{n=0}^{\infty} j^n j_n(kr) \sum_{m=-n}^{n} Y_n^m(\theta_r,\phi_r) Y_n^m(\theta_k,\phi_k)^*$$

$$e^{-j\vec{k}\cdot\vec{r}} = \sum_{l=0}^{\infty} j^{-l} (2l+1) j_l(kr) P_l \cos(\psi) \tag{771}$$

ψ -angle between $\vec{k}$ & $\vec{r}\,'$

An illustration of this superposition of these modes truncated at l=10 is shown below such that an increasing good representation of a plane wave exists for more modes illustrated in Figure 264.
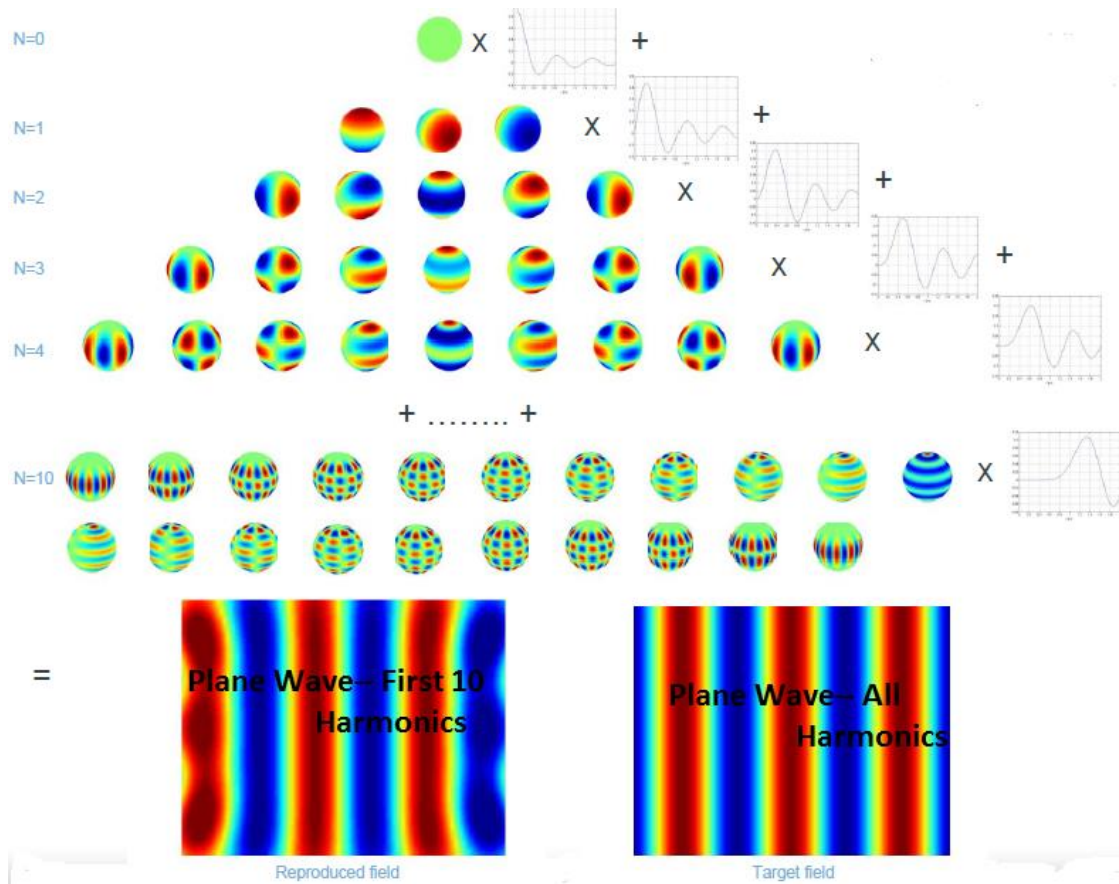
Figure 264. Summation of Spherical Harmonics Leads to a Plane Wave in the Far Field. [143]

The addition of spherical harmonic modes in the plane wave solution is also equivalent to a Fourier series as shown in Figure 265-Figure 266 below.
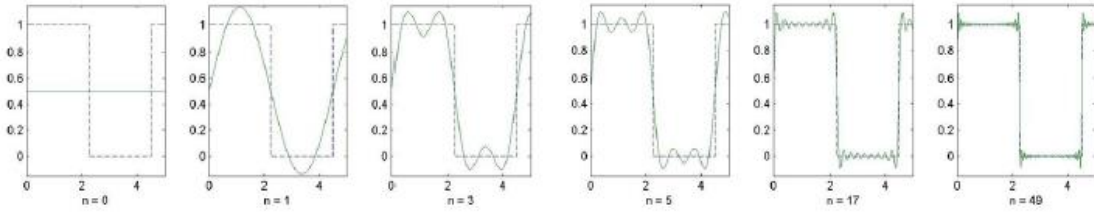
Figure 265. Illustration of the Fourier series of a square wave. [143]
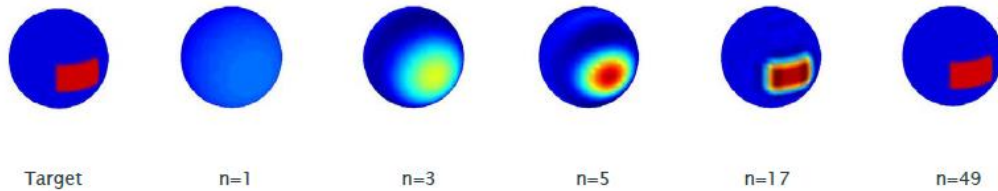
Figure 266. Illustration of the spherical harmonic expansion (generalized Fourier series). [143]

II.3 Wave-Particle Duality {Huygens' Principle}

II.3.1 Transformation of a spherical wavefront to a plane wavefront

Shown in the previous sections is that there are two basic types of waves: spherical and plane waves. This detail was discovered some two hundred years ago by Christian Huygens, a Dutch mathematician. He discovered a surface examined containing spherical wave sources some distance away appeared like a flat wave surface; a plane wave front, but composed of the superposition of spherical wavelets. An example of such wave fronts are spherical surfaces of constant phase from a point source. These rays are lines that are normal to these wavefronts, and show the direction of energy flow at one particular point illustrated in Figure 267. This basic process occurs for as the duality property waves serve. In other words in essence all the particles in the universe and such examples are "spherical waves emanating from every point in a light source, such as a candle's flame illustrated in Figure 268. The sum of these manifold wavefronts predicts the distribution of the wave everywhere and at all times in the future (since sources continue to combine and form a new plane wave front). It's a sort of infinitesimal calculus for waves." [211]
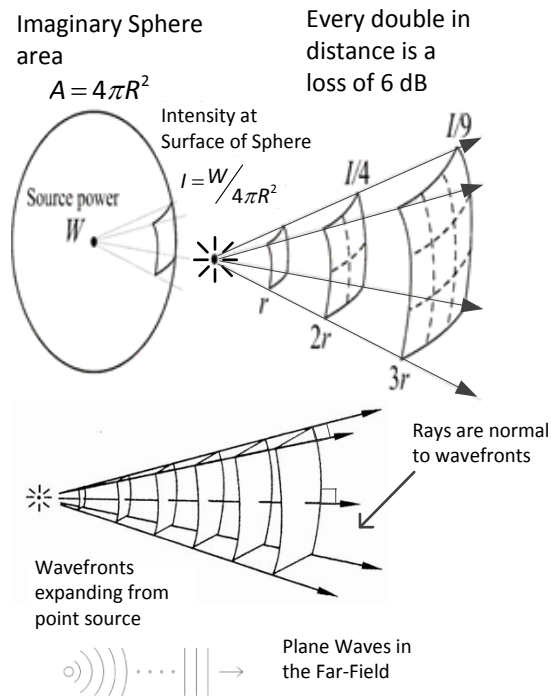
Figure 267. Expansion of the wave front (geometrical spreading power loss). [212]
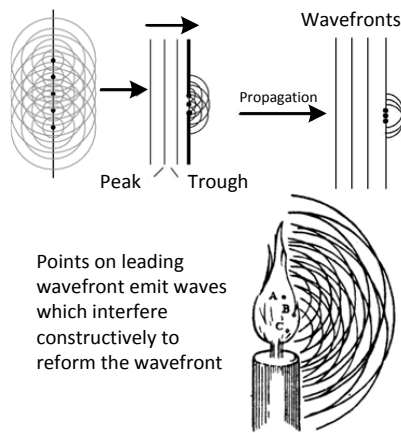
Figure 268. Examples of Huygen's principle in everyday life. [213]

If for any reason one section of a wavefront has to slow down, the orientation of the wavefront has to rotate in the direction of that part that has slowed, leading to a change in direction of the wave, according to Huygens' Principle. The simplest case is that of a plane wave. Imagine that one side of the wave slows down momentarily. Then the wavelets at a given point on that part of the wavefront produces

a wavefront that will be retarded compared to those produced on a part that is not slowed as indicated in Figure 269. Therefore, the direction of propagation will change accordingly. Differently, the result of interference is approximately what is seen on the right; a somewhat oval-shaped wavefront that propagates away from the gap. This happens because a lot of the wavefront has been blocked by the barrier; the points on the edges of the hole emit waves that bend round the edges. Before the wavefront strikes the barrier the wavefront generates another forward moving wavefront (applying Huygens 'Principle). Once the barrier blocks most of the wavefront you can see that the forward moving wavefront bends around the slit because the secondary waves interfere and do not create a straight wavefront due to the blockage by the barrier. Thus, by employing Huygens 'Principle you can see the effect is that the wavefronts are no longer straight lines. The easiest place to see such an effect is by observing waves in bodies of water large enough for something like plane waves to occur, rolling in toward shore as illustrated in Figure 269. From an elevated position you will see the wavefronts "bending around" obstacles such as man-made structures extending out into the water. Other examples of the discrete superposition between two point sources for different wavelengths and source separations are shown in. Thus, the four main types of wavefronts are shown below Figure 269. Other illustrations of wave interference for two sources are shown in Figure 270.

Plane Wave-
Waves Emanting from Discrete Sources in a Phased Array Interfere to Create a Plane Wave that Appears to come from a Distant Source behind the Array

Beamsteering
Emitting Waves with Different Phase Relationships, the Array Sources are able to Create a Plane Wave that Propagates at an Angle to the Array Surfce

Spherical Wave-
A Different Combination of Phase Relationships Produces a Spherical Wave that Appears to Come from a Point Near the Array Surface

Apparent source

Plane Wave Entering an Aperture- Wave Emerges as Discrete Sources (Spherical Waves) and the Associated Interference Pattern of the Waves (Superposition) Induces the Diffraction Pattern observed in the Far-Field

Figure 269. Examples of different ways of steering the wavefront. [213]
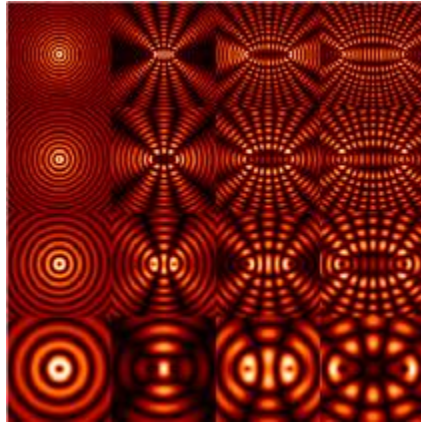
Figure 270. Optical interference between two point sources for different wavelengths and source separations. [214]

II.3.2 Diffraction

(a) Single slit

The expected value is almost surly the limit of a sample mean as the sample size grows to infinity (by the law of large numbers). Equation (93) represents this sensation mathematically by showing that a summation of all possible source locations in a linear random array provides a beampattern equivalent to a continuous line source as N approaches infinity illustrated in Figure 271-Figure 273. This is explained in better detail using wave particle duality suggesting that all particles exhibit both wave and particle properties. Here demonstrates this perception showing a constructive and destructive interference behavior amongst a discrete number of particles whereas Figure 276 shows the same phenomena for a continuous distribution of sources. Essentially outgoing waves propagate from the aperture distribution in all radial directions such that the superposition of all the waves' result in the observed pattern or characteristic function of wave propagation seen in TABLE 4 (Huygens' Principle). Moreover, characteristic functions of constructive and destructive interference measured some distance away from the source are a consequence of two properties of waves, diffraction and interference where it is common for these characteristic functions to be interchangeably called an interference pattern or a diffraction pattern. Both names are correct and both properties are required for the pattern to be observed, but for consistency these patterns will be identified as a *diffraction pattern* relating the characteristic function, mean valued power pattern and expected power pattern used throughout the rest of this dissertation. Supplementary examples of the illustrious process are provided in Figure 274-Figure 278.

For the limit N does not approach infinity the aperture is no longer continuous; a common solution to this problem is the periodic solution. For the random scenario a permutation of the possible source positions induces a superposition of the waves' such that some closely related subset of the

334

aggregate characteristic function is produced as shown in TABLE 4. For this reason a uniform distribution will present a steerable main beam at the expense of higher sidelobe levels, which is verified in Chapter XIV and for that reason it is suggested that at least a few hundred elements be utilized for the outmost effective probability of low sidelobe control.
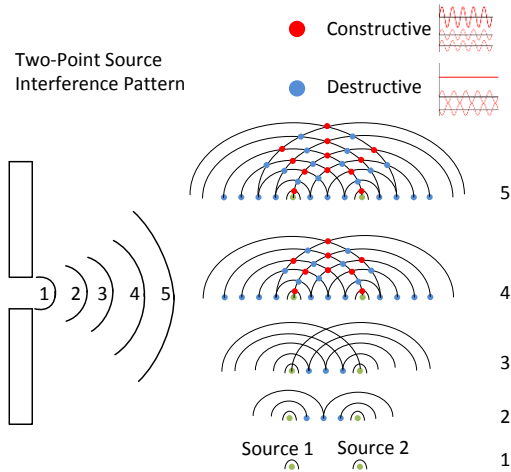
Figure 271. Representation of constructive and destructive interference in waves.
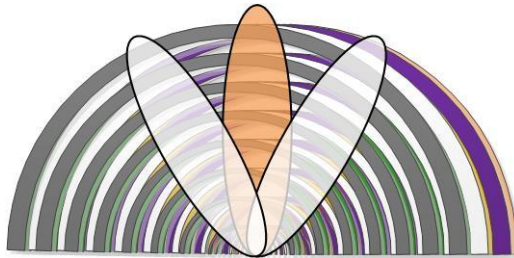
Figure 272. Sources spaced continuously along a line of length *L (even distribution).*
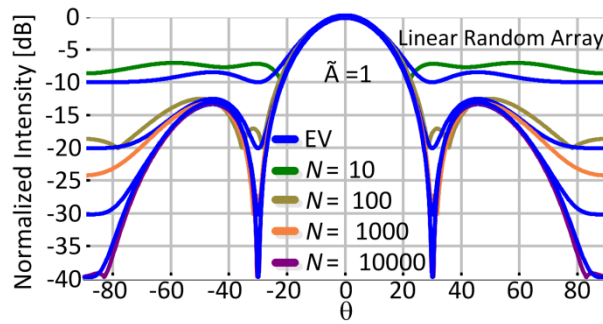
Figure 273. Analytical convergence of the beampattern to its expected value (EV).

These are also the same principles as to how a camera works
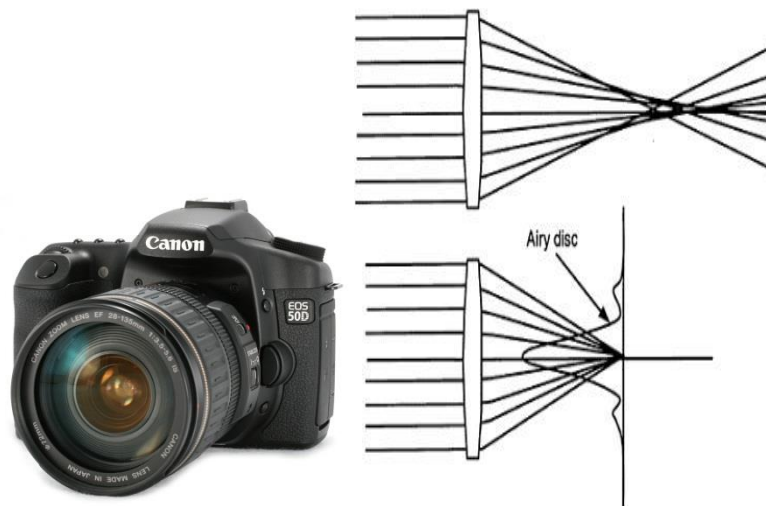
Figure 274. Same principles apply to cameras (aperture [lens] takes a Fourier transform of the particle nature of the wave.

More intuitive insight in regard to these characteristic functions can also be obtained by applying Huygens 'Principle further. A visual representation of the beampattern can be observed by simply observing two point sources either close together or far apart (operating at the same wavelength and frequency). Therefore a series of diagrams label where places of constructive interference (peak meets a peak or trough meets a trough [red dot]) takes place and places where destructive interference (trough meets a peak [blue dot]) takes place for a series of separation lengths of the two sources relative to wavelength. Finally it is noted that troughs will enhance troughs, peaks will enhance peaks, and troughs and peaks will tend to cancel as shown.
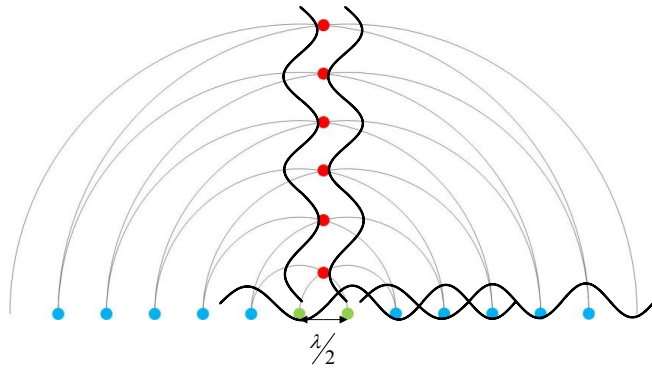
Figure 275. Two sources spaced by half a wavelength apart.
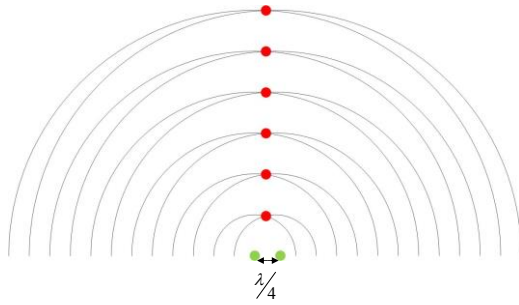
Figure 276. Two sources spaced by a quarter wavelength apart.

The amount that the waves diffract depends on the wavelength. The case where the wavelength is smaller results in larger angles between the lines of constructive and destructive interference.
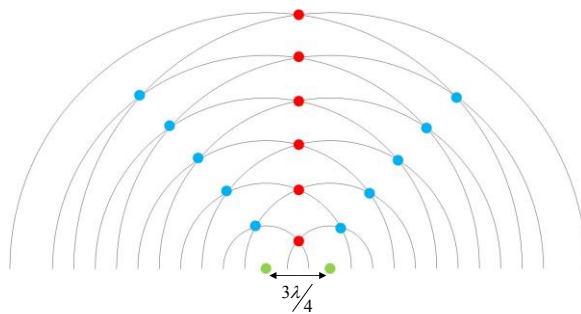
Figure 277. Two sources spaced by a three quarters of a wavelength apart.
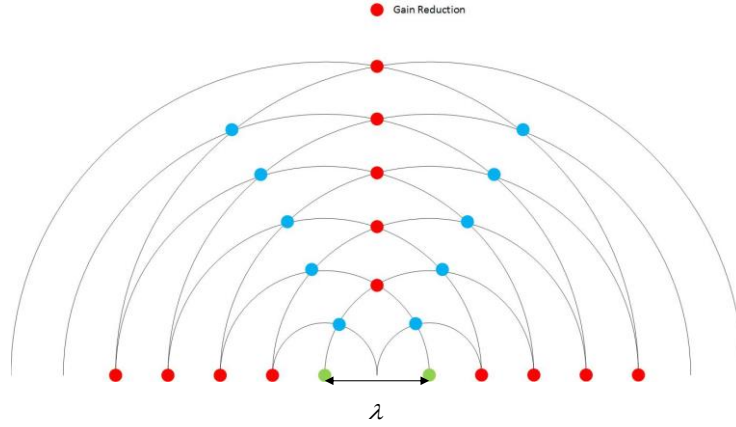
Figure 278. Two sources spaced by a wavelength apart.

Using the illustrations of Figure 275-Figure 278 shows that the narrower the separation is, the less diffraction there is and the larger the wavelength the more diffraction there is. It is also visually identified that the maximum directivity occurs for spacing $d \approx 3\lambda/4$.

Differently this process may be described as follows: first one samples the inhomogeneous wave equation with point sources.

$$\nabla^2 \psi + k^2 \psi = \sum \delta\left(\vec{r} - \vec{r}_n^{'}\right) \tag{772}$$

The solution of this equation at the origin is provided as

$$\psi = \frac{e^{-jkr}}{4\pi r} \tag{773}$$

Otherwise when the source is not located at the origin the solution is

$$\psi = \sum_{n=1}^{N} \frac{e^{-jk|r-r_n|}}{4\pi |r-r_n|} \tag{774}$$

Now approximating the solution not at the origin by the binomial expansion and assuming equal path loss (i.e. this is assumed to be compensated for during the post processing phase) the solution becomes

$$\psi \simeq \left(\frac{e^{-jkr}}{4\pi r}\right) \sum_{n=1}^{N} e^{jkr_n(\cos\psi_n)}, \cos\psi_n = \hat{r}_n \cdot \left(\hat{r}(\theta,\phi)\right) \tag{775}$$

Now the element is out of phase by the angle $\psi = \sum_{n=1}^{N} e^{jkr_n(\cos\psi_n)}$. Thus, if we ignore the common factor i.e. (reference element) for simplification and now steer the beam by imposing the linear steering factor $\cos\psi_{n0}$ we obtain $e^{jkr_n\left(\hat{r}_n \cdot \left(\hat{r}(\theta,\phi) - \hat{r}(\theta_0,\phi_0)\right)\right)}$. Hence, the sources are now isotropic and in phase; they intersect at alternating maxima and minima. For multiple beams we phase half the aperture positive and half the

338

aperture 180 degrees out of phase (negative) causing the nulls and main beam to switch. Hence, the Fourier Transform is the superposition of the constructive destructive interference of the particle nature of the wave; easy to visualize in the Fraunhofer region. Also the expected value is the aggregate over all possible realizations of the aperture (with applicable convergence factor to a continuous distribution).

Last of all an odd distribution implies the odd Fourier transform such that the maxima and minima locations are interchanged as illustrated in Figure 279.
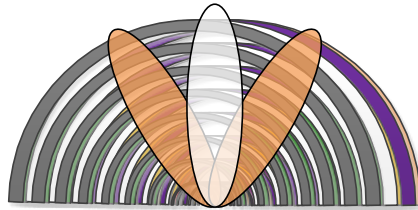
Figure 279. Sources spaced continuously along a line of length *L (odd distribution)*.

(b) Double slit (diffraction gratings)

A diffraction grating is a set of parallel slits used to disperse light using Fraunhofer diffraction. If a plane wave of uniform amplitude feeds multiple slits a diffraction grading pattern is formed as Figure 280.
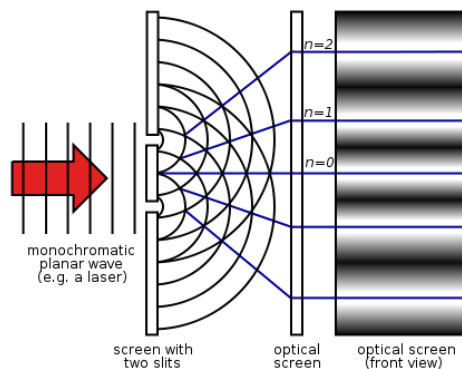
Figure 280. Example of the diffraction grating out of multiple slits.

Notice that at each order, there will be a spectrum containing the range of wavelength of the source, as each wavelength is deviated by a slightly different angle. Note that the *zeroth order*, $m = 0$ has no wavelength dependence, and so no separation of wavelengths occurs. Another view of this is provided

in Figure 281 and is a basic example of the periodic array solution with spacing greater than a wavelength producing multiple beams.
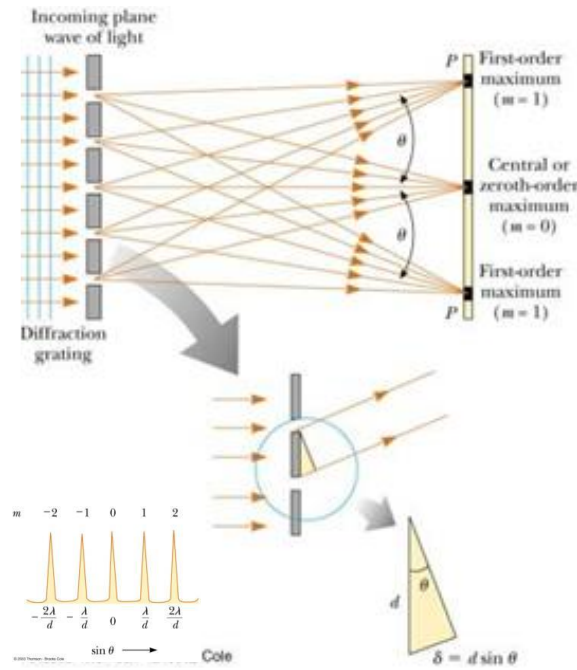
Figure 281. Diffraction of a monochromatic source out of two slits. [215]

This is also familiar to how a prism separates light. I.e. higher orders produce greater spreads in wavelength. These orders will overlap for example $\sin\theta_{peak}$ will be the same for $m=1$ and $\lambda=800nm$ as for $m=2$ and $\lambda=400nm$. At higher orders, spectra will overlap as illustrated in Figure 282!
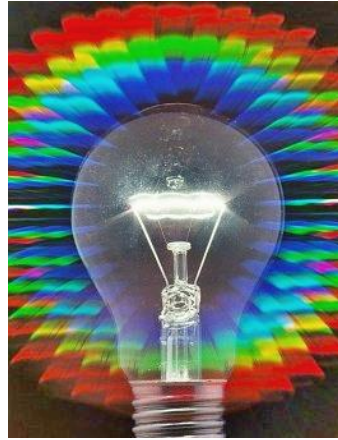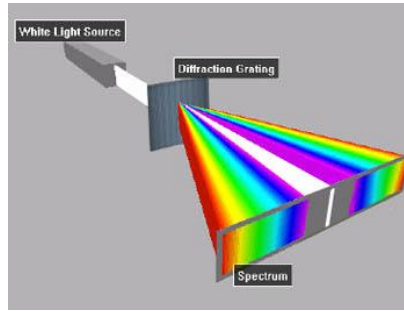
Figure 282. Another example of the diffraction gratings of a monochromatic source. Essentially each mode off from broadside is lowered in intensity and follows the envelope of the linear random array characteristic function (sinc(X)). [215]

Hence, the results of a double slit are analogous to the effects of slit width and diffraction patterns as described. The further the point sources are separated the more diffraction gratings are seen to occur.

(c) Single slit feeding *N* slits

As described above a diffraction grating is a set of parallel slits used to disperse light using Fraunhofer diffraction. Now let there be *N* slits of width 2a, of which are centered at the origin and separated by a distance *d*. Thus, the wave function ψ of scalar diffraction theory is given by (776) [216] and simplified to a one dimensional traveling wave in the x direction by (777).

$$\psi = C\iiint e^{-jk\hat{r}\cdot\vec{r}'}r'^2\sin\theta' d\theta' d\phi' \tag{778}$$

$$\psi = C\int e^{-jk\hat{x}\cdot\vec{x}'}dx' \tag{779}$$

Now for *N* slits of width 2a we can rewrite this as

$$\psi = C\int e^{-jk\hat{x}\cdot\vec{x}'}dx' = C\sum_{n=0}^{N-1}\int_{2nd-a}^{2nd+a} e^{-jk\frac{x}{A}x'}dx' \tag{780}$$

Now we define the length parameter

$$q = \frac{kx}{A} \tag{781}$$

Then

$$\begin{aligned}
\psi &= C\sum_{n=0}^{N-1}\int_{2nd-a}^{2nd+a} e^{-jqx'}dx' \\
&= -2C\sum_{n=0}^{N-1} e^{-2jqnd}\frac{e^{jqa}-e^{-jqa}}{2jq} \\
&= 2aC\frac{\sin(qa)}{qa}\sum_{n=0}^{N-1}e^{-2jqnd}
\end{aligned} \tag{782}$$

Now using

$$\sum_{n=0}^{N-1}r^n = \frac{1-r^N}{1-r} \tag{783}$$

$$\begin{aligned}
\sum_{n=0}^{N-1}e^{-2jqnd} &= \frac{1-e^{-2jNqd}}{1-e^{-2jqd}} = \frac{e^{-jNqd}\left(e^{jNqd}-e^{-jqd}\right)}{e^{-jqd}\left(e^{jqd}-e^{-jqd}\right)} \\
&= \frac{\sin(Nqd)}{(qd)}e^{-jqd(N-1)}
\end{aligned} \tag{784}$$

Gives

$$\psi = 2aC\frac{\sin(qa)}{qa}\frac{\sin(Nqd)}{\sin(qd)}e^{-jqd(N-1)} \tag{785}$$

So the resulting intensity function is given by

$$\Lambda = |\psi|^2 = 4a^2C^2\left|\frac{\sin(qa)}{qa}\right|^2\left|\frac{\sin(Nqd)}{\sin(qd)}\right|^2 \tag{786}$$

Thus, this can be seen as pattern multiplication of a random array pattern multiplied by a periodic array pattern. This is the result of a single slit diffraction pattern feeding N periodic slits, of which induces a periodic array pattern. In other words the single slit diffraction pattern is identical to that of a random array since the wave is identical to say the slit is composed of an infinite number of sources whose pattern becomes the mean valued radiation pattern from the expected value. For the periodic slits each slit can also be thought of interchanging the wave with an infinite number of particles, but is separated by a periodic discontinuity in the field. The result is thus given by that of (786) and illustrated in Figure 283.
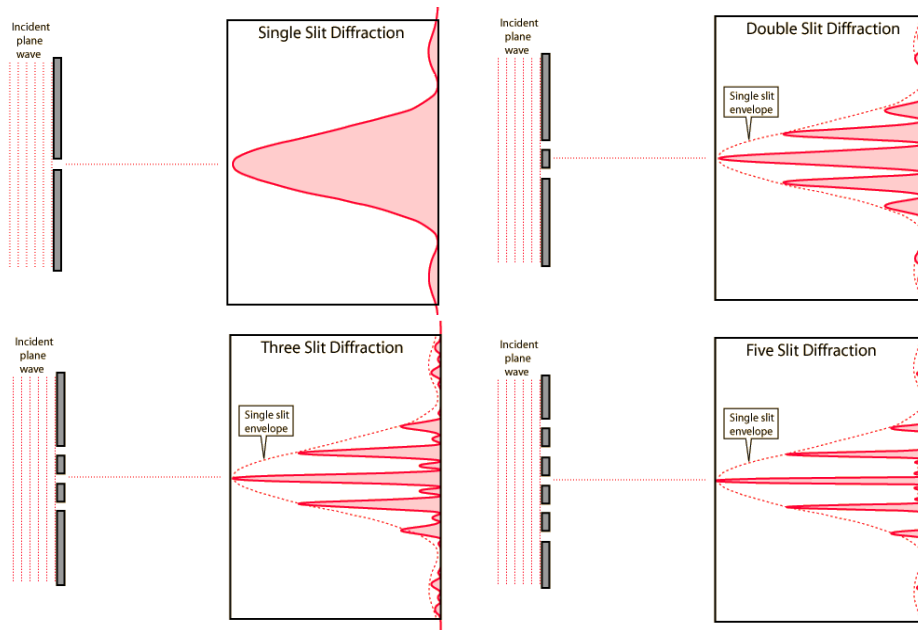
Figure 283. Exmample of the linear random array characteristic function multiplied by the periodic linear array characteristic function. [217]

Last of all it should be noted for all of the patterns shown in this chapter it's been assumed the conditions for interference are held true, but this is not always the case. Conditions for interference must be met such that: the sources must be coherent such that they maintain constant phase with respect to each other. Second the waves must have identical wavelengths (operate at the same frequency, i.e. be monochromatic sources).

APPENDIX III

MULTIPOLES

III.1 Multipole Moment Expansion

The goal of this section will be to introduce the theory of multipoles. Multipoles expansions are useful in exploiting the monopole, dipole, quadrupole, hexadecapole and higher order behaviors of radiation patterns.

To start this we will re-evaluate (43) and rewrite the inverse of (43) as follows

$$|r - r'| = r\sqrt{1 + \left(\frac{r'}{r}\right)^2 - \frac{2r'}{r}\cos\psi} = r\sqrt{1 + \delta}$$

$$\text{where } \delta \doteq \left(\frac{r'}{r}\right)^2 - \frac{2r'}{r}\cos\psi \qquad (787)$$

$$\text{thus}$$

$$\frac{1}{|r - r'|} = \frac{1}{r}(1 + \delta)^{-\frac{1}{2}}$$

Using the binomial expansion this is expanded as such

$$(1 + x)^n = 1 + nx + \frac{n(n-1)}{2!}x^2 + \frac{n(n-1)(n-2)}{3!}x^3 + \dots$$

$$\therefore$$

$$(1 + \delta)^{-\frac{1}{2}} = 1 - \frac{1}{2}\delta + \frac{\left(-\frac{1}{2}\right)\left(-\frac{3}{2}\right)}{2}\delta^2 + \frac{\left(-\frac{1}{2}\right)\left(-\frac{3}{2}\right)\left(-\frac{5}{2}\right)}{6}\delta^3 + \dots \qquad (788)$$

$$= 1 - \frac{1}{2}\delta + \frac{3}{8}\delta^2 - \frac{5}{16}\delta^3 + \dots$$

This can also be rewritten as

$$\frac{1}{|r - r'|} = \frac{1}{r}\left[1 - \frac{1}{2}\left(\frac{r'}{r}\right)\left(\frac{r'}{r} - 2\cos\psi\right) + \frac{3}{8}\left(\frac{r'}{r}\right)^2\left(\frac{r'}{r} - 2\cos\psi\right)^2 - \frac{5}{16}\left(\frac{r'}{r}\right)^3\left(\frac{r'}{r} - 2\cos\psi\right)^3 + \dots\right] \qquad (789)$$

And after collecting terms this can be rewritten as (790) and in terms of Legendre polynomial as [218]

$$\frac{1}{|r - r'|} = \frac{1}{r}\left[1 + \left(\frac{r'}{r}\right)\cos\psi + \left(\frac{r'}{r}\right)^2\left(\frac{3\cos^2\psi - 1}{2}\right) + \left(\frac{r'}{r}\right)^3\left(\frac{5\cos^3\psi - 3\cos\psi}{2}\right) + \dots\right] \qquad (790)$$

In compact notation this is written as

$$\frac{1}{|r - r'|} = \frac{1}{r}\sum_{l=0}^{\infty}\left(\frac{r'}{r}\right)^l P_l(\cos\psi) = \sum_{l=0}^{\infty}\frac{(r')^l}{r^{l+1}}P_l(\cos\psi) \qquad (791)$$

$$\frac{1}{|r-r'|}=\frac{1}{r}\left[P_0\left(\cos\psi\right)-\left(\frac{r'}{r}\right)P_1\left(\cos\psi\right)+\left(\frac{r'}{r}\right)^2 P_2\left(\cos\psi\right)-\left(\frac{r'}{r}\right)^3 P_3\left(\cos\psi\right)+\ldots\right]$$

$$\infty \tag{792}$$

$$P_0\left(\cos\psi\right)=1,\ P_1\left(\cos\psi\right)=\cos\psi,\ P_2\left(\cos\psi\right)=\frac{3\cos^2\psi-1}{2},\ P_3\left(\cos\psi\right)=\frac{5\cos^3\psi-3\cos\psi}{2}$$

This can also be rewritten using the Legendre addition theorem.

$$\frac{1}{|r-r'|}=\frac{4\pi}{2l+1}\sum_{l=0}^{\infty}\sum_{m=-l}^{l}\frac{\left(r'\right)^l}{r^{l+1}}P_l\left(\cos\psi\right)Y_{lm}\left(\theta,\phi\right)Y_{lm}^*\left(\theta',\phi'\right) \tag{793}$$

Therefore the electrostatic potential (voltage) can be calculated as follows

$$V(\vec{r})=\frac{1}{4\pi\varepsilon_0}\sum_{l=0}^{\infty}\frac{1}{r^{l+1}}\int\left(r'\right)^l P_l\left(\cos\psi\right)\rho(\vec{r}')d^3\vec{r}'^{3}$$

$$=\frac{1}{4\pi\varepsilon_0}\sum_{l=0}^{\infty}\frac{4\pi}{\left(2l+1\right)}\frac{1}{r^{l+1}}\sum_{m=-l}^{l}Y_{lm}\left(\theta,\phi\right)\int\left(r'\right)^l Y_{lm}^*\left(\theta',\phi'\right)\rho(\vec{r}')d^3\vec{r}'^{3} \tag{794}$$

In order to clean up this notation we defined

$$C_{lm}\left(\theta,\phi\right)=\sqrt{\frac{4\pi}{2l+1}}Y_{lm}\left(\theta,\phi\right) \tag{795}$$

And

$$C_{lm}^*\left(\theta',\phi'\right)=\sqrt{\frac{4\pi}{2l+1}}Y_{lm}^*\left(\theta',\phi'\right) \tag{796}$$

$$Q_{lm}=\int r'^l C_{lm}^*\left(\theta',\phi'\right)\rho(\vec{r}')d^3\vec{r}' \tag{797}$$

$$V(\vec{r})=\frac{1}{4\pi\varepsilon_0}\sum_{lm}\frac{1}{r^{l+1}}C_{lm}\left(\theta,\phi\right)Q_{lm} \tag{798}$$

Or

$$V(\vec{r})=\frac{1}{4\pi\varepsilon_0}\sum_{lm}\frac{\rho_l}{r^{l+1}}$$

$$\rho_l=\int r'^l P_l\left(\cos\psi\right)\rho(\vec{r}')d^3\vec{r}' \tag{799}$$

It should be noted "if we have some axially-symmetric charge distribution at $\vec{r}'$; with observation point $\vec{r}$, then, we are able to expand the distribution in terms of multipoles, so that the scalar potential may be written:

$$V(\vec{r})=\frac{1}{4\pi\varepsilon_0}\sum_{lm}\frac{\rho_l}{r^{l+1}}$$

$$\rho_l=\int r'^l P_l\left(\cos\psi\right)\rho(\vec{r}')d^3\vec{r}' \tag{800}$$

If; however, the charge distribution is not axially-symmetric, then we must appeal to a sum over spherical harmonics, as opposed to Legendre polynomials."

$$V(\vec{r}) = \frac{1}{4\pi\varepsilon_0}\sum_{lm}\frac{1}{r^{l+1}}C_{lm}(\theta,\phi)Q_{lm} \tag{801}$$

To make this solution more apparent in Cartesian coordinates one may show the path length using a Taylor expansion

$$\frac{1}{|r-r'|} = e^{-\vec{r}'\cdot\vec{\nabla}\frac{1}{r}} \tag{802}$$

$$e^{-\vec{r}'\cdot\vec{\nabla}\frac{1}{r}} = \frac{1}{r} - (\vec{r}'\cdot\vec{\nabla})\frac{1}{r}\Big|_{\vec{r}'=0} + \frac{1}{2}(\vec{r}'\cdot\vec{\nabla})^2\frac{1}{r}\Big|_{\vec{r}'=0} + \ldots \frac{(-1)^n}{n!}(\vec{r}'\cdot\vec{\nabla})\frac{1}{r}\Big|_{\vec{r}'=0}$$

$$\frac{1}{|\vec{r}-\vec{r}'|} = \frac{1}{r} + \frac{\vec{r}'\cdot\hat{r}}{r^2} + \frac{3(\vec{r}'\cdot\hat{r})^2 - r'^2}{2r^3} + \frac{5(\vec{r}'\cdot\hat{r})^3 - r'^2(\vec{r}'\cdot\hat{r})}{2r^4}\ldots \tag{803}$$

$$\frac{1}{|r-r'|} = \frac{1}{r}\left[P_0(\cos\psi) - \left(\frac{r'}{r}\right)P_1(\cos\psi) + \left(\frac{r'}{r}\right)^2 P_2(\cos\psi) - \left(\frac{r'}{r}\right)^3 P_3(\cos\psi) + \ldots\right]$$

In Cartesian coordinates each power of $(\vec{r}'\cdot\hat{r})$ can be expanded as

$$
\begin{aligned}
(\vec{r}'\cdot\hat{r}) &= (\hat{x}x' + \hat{y}y' + \hat{z}z')\cdot(\hat{x}+\hat{y}+\hat{z}) = (x'+y'+z') \\
(\vec{r}'\cdot\hat{r})^2 &= (x'+y'+z')(x'+y'+z') = (x'+y'+z')^2 \\
&= x'^2 + y'^2 + z'^2 + (x'y'+y'x') + (x'z'+z'x') + (z'y'+y'z') \\
&= x'^2 + y'^2 + z'^2 + 2x'y' + 2x'z' + 2z'y' \\
(\vec{r}'\cdot\hat{r})^3 &= x'^3 + y'^3 + z'^3 + 3x'^2 y' + 3x'^2 z' + 3y'^2 x' + 3y'^2 z' + 3z'^2 x' + 3z'^2 y' + 6x'y'z'
\end{aligned}
\tag{804}
$$

$$\frac{1}{|\vec{r}-\vec{r}'|} = \frac{1}{r} + \frac{\vec{r}'\cdot\hat{r}}{r^2} + \frac{3\hat{r}\cdot(\vec{r}'\otimes\vec{r}')\cdot\hat{r} - r'^2}{2r^3} + \frac{5((\hat{r}\cdot(\vec{r}'\otimes\vec{r}')\cdot\hat{r})\otimes\vec{r}'\cdot\hat{r}) - 3r'^2(\vec{r}'\cdot\hat{r})}{2r^4}\ldots \tag{805}$$

Where

$$
\vec{r}'\otimes\vec{r}' = \vec{r}'\vec{r}'^{\mathrm{T}} = \begin{bmatrix} x'\hat{x} \\ y'\hat{y} \\ z'\hat{z} \end{bmatrix}\begin{bmatrix} x'\hat{x} & y'\hat{y} & z'\hat{z} \end{bmatrix} = \begin{vmatrix} x'\hat{x}\begin{bmatrix} x'\hat{x} & y'\hat{y} & z'\hat{z} \end{bmatrix} \\ y'\hat{y}\begin{bmatrix} x'\hat{x} & y'\hat{y} & z'\hat{z} \end{bmatrix} \\ z'\hat{z}\begin{bmatrix} x'\hat{x} & y'\hat{y} & z'\hat{z} \end{bmatrix} \end{vmatrix}
$$

$$
= \begin{bmatrix} x'x'\hat{x}\hat{x} & x'y'\hat{x}\hat{y} & x'z'\hat{x}\hat{z} \\ y'x'\hat{y}\hat{x} & y'y'\hat{y}\hat{y} & y'z'\hat{y}\hat{z} \\ z'x'\hat{z}\hat{x} & z'y'\hat{z}\hat{y} & z'z'\hat{z}\hat{z} \end{bmatrix}
\tag{806}
$$

And

$$\hat{r} \cdot (\vec{r}\,' \otimes \vec{r}\,') \cdot \hat{r} = \begin{bmatrix} \hat{x}^* & \hat{y}^* & \hat{z}^* \end{bmatrix} \cdot (\vec{r}\,' \otimes \vec{r}\,') \cdot \begin{vmatrix} \hat{x} \\ \hat{y} \\ \hat{z} \end{vmatrix}$$

$$= \begin{bmatrix} \hat{x} & \hat{y} & \hat{z} \end{bmatrix} \cdot \begin{bmatrix} x'x'\hat{x}\hat{x} & x'y'\hat{x}\hat{y} & x'z'\hat{x}\hat{z} \\ y'x'\hat{y}\hat{x} & y'y'\hat{y}\hat{y} & y'z'\hat{y}\hat{z} \\ z'x'\hat{z}\hat{x} & z'y'\hat{z}\hat{y} & z'z'\hat{z}\hat{z} \end{bmatrix} \begin{bmatrix} \hat{x} \\ \hat{y} \\ \hat{z} \end{bmatrix}$$

(807)

$$= \begin{bmatrix} \hat{x}(x'x'+y'x'+z'x') & (x'y'+y'y'+z'y')\hat{y} & (x'z'+y'z'+z'z')\hat{z} \end{bmatrix} \cdot \begin{bmatrix} \hat{x} \\ \hat{y} \\ \hat{z} \end{bmatrix}$$

$$= x'^2 + y'^2 + z'^2 + 2x'y' + 2x'z' + 2z'y'$$

$$(\vec{r}\,' \otimes \vec{r}\,') \otimes \vec{r}\,' = (\vec{r}\,' \otimes \vec{r}\,')\vec{r}\,'^{\mathrm{T}} = \begin{vmatrix} x'x'\hat{x}\hat{x} & x'y'\hat{x}\hat{y} & x'z'\hat{x}\hat{z} \\ y'x'\hat{y}\hat{x} & y'y'\hat{y}\hat{y} & y'z'\hat{y}\hat{z} \\ z'x'\hat{z}\hat{x} & z'y'\hat{z}\hat{y} & z'z'\hat{z}\hat{z} \end{vmatrix} \begin{bmatrix} x'\hat{x} & y'\hat{y} & z'\hat{z} \end{bmatrix}$$

$$= \begin{bmatrix} x'x'\hat{x}\hat{x}[x'\hat{x} \ y'\hat{y} \ z'\hat{z}] & x'y'\hat{x}\hat{y}[x'\hat{x} \ y'\hat{y} \ z'\hat{z}] & x'z'\hat{x}\hat{z}[x'\hat{x} \ y'\hat{y} \ z'\hat{z}] \\ y'x'\hat{y}\hat{x}[x'\hat{x} \ y'\hat{y} \ z'\hat{z}] & y'y'\hat{y}\hat{y}[x'\hat{x} \ y'\hat{y} \ z'\hat{z}] & y'z'\hat{y}\hat{z}[x'\hat{x} \ y'\hat{y} \ z'\hat{z}] \\ z'x'\hat{z}\hat{x}[x'\hat{x} \ y'\hat{y} \ z'\hat{z}] & z'y'\hat{z}\hat{y}[x'\hat{x} \ y'\hat{y} \ z'\hat{z}] & z'z'\hat{z}\hat{z}[x'\hat{x} \ y'\hat{y} \ z'\hat{z}] \end{bmatrix} \{3x3x3\} \, Matrix$$

(808)

$$= \begin{bmatrix} x'x'x'\hat{x}\hat{x}\hat{x} & x'x'y'\hat{x}\hat{x}\hat{y} & x'x'z'\hat{x}\hat{x}\hat{z} & x'y'x'\hat{x}\hat{y}\hat{x} & x'y'y'\hat{x}\hat{y}\hat{y} & x'y'z'\hat{x}\hat{y}\hat{z} & x'z'x'\hat{x}\hat{z}\hat{x} & x'z'y'\hat{x}\hat{z}\hat{y} & x'z'z'\hat{x}\hat{z}\hat{z} \\ y'x'x'\hat{y}\hat{x}\hat{x} & y'x'y'\hat{y}\hat{x}\hat{y} & y'x'z'\hat{y}\hat{x}\hat{z} & y'y'x'\hat{y}\hat{y}\hat{x} & y'y'y'\hat{y}\hat{y}\hat{y} & y'y'z'\hat{y}\hat{y}\hat{z} & y'z'x'\hat{y}\hat{z}\hat{x} & y'z'y'\hat{y}\hat{z}\hat{y} & y'z'z'\hat{y}\hat{z}\hat{z} \\ z'x'x'\hat{z}\hat{x}\hat{x} & z'x'y'\hat{z}\hat{x}\hat{y} & z'x'z'\hat{z}\hat{x}\hat{z} & z'y'x'\hat{z}\hat{y}\hat{x} & z'y'y'\hat{z}\hat{y}\hat{y} & z'y'z'\hat{z}\hat{y}\hat{z} & z'z'x'\hat{z}\hat{z}\hat{x} & z'z'y'\hat{z}\hat{z}\hat{y} & z'z'z'\hat{z}\hat{z}\hat{z} \end{bmatrix}$$

or $\{3x9\}$ *Matrix*

$$\left(\hat{r} \cdot (\vec{r}\,' \otimes \vec{r}\,') \cdot \hat{r}\right) \otimes \vec{r}\,' \cdot \hat{r} = x'^3 + y'^3 + z'^3 + 3x'^2y' + 3x'^2z' + 3y'^2x' + 3y'^2z' + 3z'^2x' + 3z'^2y' + 6x'y'z'$$

since

$$\left(x'^2 + y'^2 + z'^2 + 2x'y' + 2x'z'\right) \otimes \vec{r}\,'$$

$$= \left(x'^2 + y'^2 + z'^2 + 2x'y' + 2x'z'\right)\begin{bmatrix} x'\hat{x} & y'\hat{y} & z'\hat{z} \end{bmatrix}$$

(809)

$$= \begin{bmatrix} x'^3\hat{x} + x'^2y'\hat{x} + x'^2z'\hat{x} + & \left(x'^2+y'^2+z'^2+2x'y'+2x'z'\right)y'\hat{y} & \left(x'^2+y'^2+z'^2+2x'y'+2x'z'\right)z'\hat{z} \end{bmatrix}$$

We can also write this as

$$\frac{1}{\left|\vec{r}-\vec{r}\,'\right|}=\frac{1}{r}+\frac{1}{r^2}\sum_{i=x,y,z}\vec{r}_i\,'\cdot\hat{r}+\frac{1}{2!r^3}\sum_{i=x,y,z}\hat{r}_i\hat{r}_j\cdot Q_{ij}+\frac{1}{3!r^4}\sum_{i,j,k=x,y,z}\hat{r}_i\hat{r}_j\hat{r}_k\cdot O_{ijk}$$

expanding

$$Q_{ij}=3\left(\vec{r}\,'\cdot\hat{r}\right)^2-r\,'^2=3\left(\vec{r}\,'\cdot\frac{\vec{r}}{r}\right)^2-\left(\frac{\vec{r}}{r}\cdot\frac{\vec{r}}{r}\right)r\,'^2=3\sum_{i=x,y,z}\frac{r_i}{r}r_i\,'\sum_{j=x,y,z}\frac{r_j}{r}r_j\,'-\sum_{i=x,y,z}\frac{r_i}{r}\frac{r_i}{r}r\,'^2$$

$$=\sum_{i,j=x,y,z}\frac{r_i}{r}\frac{r_j}{r}\left(3r_i\,'r_j\,'-r\,'^2\,\delta_{ij}\right)=\frac{r_i}{r}\left[\sum_{i,j=x,y,z}\left(3r_i\,'r_j\,'-r\,'^2\,\delta_{ij}\right)\right]\frac{r_j}{r}=\hat{r}_i\hat{r}_j\left[\sum_{i,j=x,y,z}\left(3r_i\,'r_j\,'-r\,'^2\,\delta_{ij}\right)\right] \qquad (810)$$

$$\vec{r}=\begin{bmatrix}r\sin\theta\cos\phi\\r\sin\theta\sin\phi\\r\cos\theta\end{bmatrix}=r\sin\theta\cos\phi\hat{x}+r\sin\theta\sin\phi\hat{y}+r\cos\theta\hat{z}$$

Similarly

$$O_{ijk}=\sum_{i=x,y,z}\left(15r_ir_jr_k-3r^2\left(r_i\delta_{jk}+r_j\delta_{ik}+r_k\delta_{ij}\right)\right)$$

In terms of the electrostatic potential this can be generalized as

$$\frac{q}{4\pi\varepsilon_0\left|\vec{r}-\vec{r}\,'\right|}=\frac{1}{4\pi\varepsilon_0}\left[\frac{q}{r}+\frac{\displaystyle\sum_{i=x,y,z}\vec{\rho}_i\cdot\hat{r}}{r^2}+\frac{\displaystyle\sum_{i=x,y,z}\hat{r}_i\hat{r}_j\cdot Q_{ij}}{2!r^3}+\frac{\displaystyle\sum_{i,j,k=x,y,z}\hat{r}_i\hat{r}_j\hat{r}_k\cdot O_{ijk}}{3!r^4}+\ldots\right] \qquad (811)$$

where

$$q=\sum_{n=1}^{N}q_n$$

$$\vec{\rho}_i=\sum_{n=1}^{N}q_n r_{n,i}$$

$$Q_{ij}=\hat{r}_i\hat{r}_j\sum_{n=1}^{N}q_n\left[\sum_{i,j=x,y,z}\left(3r_{n,i}\,'r_{n,j}\,'-r_n\,'^2\,\delta_{ij}\right)\right]$$

$$O_{ijk}=\hat{r}_i\hat{r}_j\hat{r}_k\sum_{n=1}^{N}q_n\left[\sum_{i=x,y,z}\left(15r_{n,i}\,'r_{n,j}\,'r_{n,k}\,'-3r_n\,'^2\left(r_{n,i}\,'\delta_{jk}+r_{n,j}\,'\delta_{ik}+r_{n,k}\,'\delta_{ij}\right)\right)\right]$$

Where q, $\vec{\rho}$, Q, O are known as a monopole, dipole, quadrupole and octupole moments respectively, and δ_{ij} is the Kronecker delta. "The multipole moments are symmetric tensors where the lowest order non-vanishing multipole is origin independent." [219]-[224] It can also be seen that the quadrupole tensor is symmetric, real-valued and traceless thereby providing three real eigenvalues.

III.2 Multipole Moments and the Real Spherical Harmonics

To compare the spherical multipole harmonics with the Cartesian multipole harmonics, we'll look at the expressions for the spherical harmonic first.

$$q_{00}=\sqrt{\frac{4\pi}{2l+1}}\int\rho(\vec{x}\,')Y_{00}^*(\theta',\phi')d^3x'=\sqrt{4\pi}\frac{1}{\sqrt{4\pi}}\int\rho(\vec{x}\,')d^3x'=q \qquad (812)$$

$$V(\vec{r}) = \frac{q}{4\pi\varepsilon_0 r} \tag{813}$$

This can also be found from the first term in the expression (811). Now with l=1 (1/r^2 term) there are three contributions with $m = \pm 1$ and 0. However, noting that

$$
\begin{aligned}
q_{l,-m} &= \int \rho(\vec{x}')(r')^l Y_{l,-m}^*(\theta',\phi')d^3x' \\
&= (-1)^m \int \rho(\vec{x}')(r')^l Y_{lm}(\theta',\phi')d^3x' \\
&= (-1)^m q_{lm}^*
\end{aligned}
\tag{814}
$$

As a consequence, there are only two values to calculate. With l=1, m=0

$$
\begin{aligned}
q_{10} &= \sqrt{\frac{4\pi}{2+1}} \int \rho(\vec{x}')r'Y_{10}^*(\theta',\phi')d^3x' = \sqrt{\frac{4\pi}{3}} \int \rho(\vec{x}')r'\sqrt{\frac{3}{4\pi}}\cos\theta'd^3x' \\
&= \int \rho(\vec{x}')z'd^3x' = p_z
\end{aligned}
\tag{815}
$$

In this formulation only the z-component of (811) was necessary. With l=1, m=1

$$
\begin{aligned}
q_{11} &= \sqrt{\frac{4\pi}{3}} \int \rho(\vec{x}')r'Y_{11}^*(\theta',\phi')d^3x' = \sqrt{\frac{4\pi}{3}} \int \sqrt{\frac{3}{8\pi}}\sin\theta'e^{-j\phi'}\rho(\vec{x}')r'd^3x' \\
&= \sqrt{\frac{1}{2}} \int \sin\theta'(\cos\phi'-j\sin\phi')\rho(\vec{x}')r'd^3x' \\
&= \sqrt{\frac{1}{2}}(jp_y - p_x)
\end{aligned}
\tag{816}
$$

Thus the corresponding term for the potential is

$$
\begin{aligned}
V(\vec{r}) &= \frac{1}{4\pi\varepsilon_0 r^2}\sum_{m=-1}^{1}C_{lm}(\theta,\phi)Q_{lm} = \frac{1}{4\pi\varepsilon_0 r^2}\left(q_{11}Y_{11}(\theta,\phi)+q_{10}Y_{10}(\theta,\phi)+q_{1,-1}^*Y_{1,-1}(\theta,\phi)\right) \\
&= \frac{1}{4\pi\varepsilon_0 r^2}\left(q_{11}Y_{11}(\theta,\phi)+q_{10}Y_{10}(\theta,\phi)+(-1)q_{11}^*(-1)Y_{11}^*(\theta,\phi)\right) \\
&= \frac{1}{4\pi\varepsilon_0 r^2}\left(\frac{1}{2}(jp_y - p_x)(-\sin\theta)e^{j\phi}+p_z\cos\theta+\frac{1}{2}(jp_y + p_x)(\sin\theta)e^{-j\phi}\right) \\
&= \frac{1}{4\pi\varepsilon_0 r^2}\left(\frac{1}{2}(jp_y - p_x)(-\sin\theta)(\cos\phi+j\sin\phi)+p_z\cos\theta+\frac{1}{2}(jp_y + p_x)(\sin\theta)(\cos\phi-j\sin\phi)\right) \\
&= \frac{1}{4\pi\varepsilon_0 r^2}\begin{pmatrix} -\frac{1}{2}jp_y\sin\theta\cos\phi+\frac{1}{2}p_y\sin\theta\cos\phi+\frac{1}{2}p_x\sin\theta\cos\phi_x+\frac{1}{2}jp_x\sin\theta\sin\phi_x \\ +p_z\cos\theta \\ +\frac{1}{2}jp_y\sin\theta\cos\phi+\frac{1}{2}p_y\sin\theta\cos\phi+\frac{1}{2}p_x\sin\theta\cos\phi_x-\frac{1}{2}jp_x\sin\theta\sin\phi_x \end{pmatrix} = \frac{\vec{p}\cdot\hat{r}}{4\pi\varepsilon_0 r^2} \\
&= \frac{1}{4\pi\varepsilon_0 r^2}\left(p_x\sin\theta\cos\phi + p_y\sin\theta\sin\phi + p_z\cos\theta\right)
\end{aligned}
\tag{817}
$$

Thus, we see that this solution consists of three independent values. These values are proportional to the real spherical harmonics of which are calculated as:

$$d_z = C_{10} Y_1^0 = \sqrt{\frac{4\pi}{3}} \sqrt{\frac{3}{4\pi}} \frac{z}{r} = \frac{z}{r}$$

$$d_y = C_{11} j \frac{1}{\sqrt{2}} \left(Y_1^{-1} + Y_1^1 \right) = \sqrt{\frac{4\pi}{3}} \sqrt{\frac{3}{4\pi}} \frac{y}{r} = \frac{y}{r}$$

(818)

$$d_x = C_{11} \frac{1}{\sqrt{2}} \left(Y_1^{-1} - Y_1^1 \right) = \sqrt{\frac{4\pi}{3}} \sqrt{\frac{3}{4\pi}} \frac{x}{r} = \frac{x}{r}$$

With l=2 $\left(\dfrac{1}{r^3} \right)$ term we have m=2, 1 and 0. The multiple moment q_{20} is

$$q_{20} = \sqrt{\frac{4\pi}{2l+1}} \int \rho(\vec{x}')(r')^2 Y_{20}^* d^3 x'$$

$$= \frac{1}{2} \int \rho(\vec{x}')(r')^2 \left(3\cos^2 \theta' - 1 \right) d^3 x'$$

(819)

$$= \frac{1}{2} Q_{33}$$

Where Q represents a discrete system of point charges each with charge q_l with position $\vec{r} = \left(r_{xl}, r_{yl}, r_{z.} \right)$, which define $Q_{ij} = q_l \sum_l \left(3 r_{il} \cdot r_{jl} - r_l^2 \delta_{ij} \right)$. Hence, this is the explanation as to why we used the (3, 3) component. Similarly

$$q_{21} = \sqrt{\frac{4\pi}{2l+1}} \int \rho(\vec{x}')(r')^2 Y_{21}^* d^3 x'$$

$$= \sqrt{\frac{4\pi}{5}} \int \rho(\vec{x}')(r')^2 \left(-\sqrt{\frac{15}{8\pi}} \right) e^{-j\phi} \sin\theta \cos\theta d^3 x' = -\sqrt{\frac{3}{2}} \int \rho(\vec{x}')(r')^2 e^{-j\phi} \sin\theta \cos\theta d^3 x'$$

(820)

$$= \sqrt{\frac{3}{2}} \frac{1}{3} \left(j Q_{23} - Q_{13} \right) = \sqrt{\frac{1}{6}} \left(j Q_{23} - Q_{13} \right)$$

And

$$q_{22} = \sqrt{6} \frac{1}{\sqrt{12}} \frac{1}{\sqrt{12}} \left(Q_{11} - Q_{22} - 2 j Q_{12} \right)$$

$$= \frac{1}{\sqrt{24}} \left(Q_{11} - Q_{22} - 2 j Q_{12} \right)$$

(821)

Up to this point there are three independent solutions of the charges q_{2m} being q_{20}, q_{21} and q_{22}. Furthermore, each unique solution has a real and imaginary part and only provides five real numbers, but yet there are six independent values Q_{ij} in general symmetric rank two tensor. Nonetheless, in this circumstance not all six values are independent Q_{ij} is traceless, hence leaving only five independent solutions.

$$V(\vec{r}) = \frac{1}{4\pi\varepsilon_0 r^3} \sum_{m=-1}^{1} C_{lm}(\theta,\phi) Q_{lm} = \frac{1}{4\pi\varepsilon_0 r^2}\sqrt{\frac{4\pi}{2l+1}} \left(\begin{array}{c} q_{22} Y_{22}(\theta,\phi) + q_{21} Y_{21}(\theta,\phi) + q_{20} Y_{20}(\theta,\phi) \\ + q_{2,-1}^* Y_{2,-1}(\theta,\phi) + q_{2,-2}^* Y_{2,-2}(\theta,\phi) \end{array} \right) \tag{822}$$

$$= \frac{1}{4\pi\varepsilon_0 r^3}\sqrt{\frac{4\pi}{2l+1}} \left(\begin{array}{c} q_{22} Y_{22}(\theta,\phi) + q_{21} Y_{21}(\theta,\phi) + q_{20} Y_{20}(\theta,\phi) \\ + (-1)q_{21}^*(-1)Y_{21}^*(\theta,\phi) + (-1)q_{22}^*(-1)Y_{22}^*(\theta,\phi) \end{array} \right)$$

$$= \frac{1}{4\pi\varepsilon_0 r^3}\sqrt{\frac{4\pi}{5}} \left(\begin{array}{c} \frac{1}{\sqrt{24}}(Q_{11} - Q_{22} - 2jQ_{12})\frac{1}{4}\sqrt{\frac{15}{2\pi}} e^{j2\phi}\sin^2\theta + \frac{1}{\sqrt{24}}(Q_{11} - Q_{22} + 2jQ_{12})\frac{1}{4}\sqrt{\frac{15}{2\pi}} e^{-j2\phi}\sin^2\theta + \\ \sqrt{\frac{1}{6}}(jQ_{23} - Q_{13})\left(-\frac{1}{2}\sqrt{\frac{15}{2\pi}} e^{j\phi}\sin\theta\cos\theta\right) + \sqrt{\frac{1}{6}}(-jQ_{23} - Q_{13})\left(-\frac{1}{2}\sqrt{\frac{15}{2\pi}} e^{-j\phi}\sin\theta\cos\theta\right) + \\ \frac{1}{2}Q_{33}\frac{1}{4}\sqrt{\frac{5}{\pi}}(3\cos^2\theta - 1) \end{array} \right)$$

$$= \frac{1}{4\pi\varepsilon_0 r^3} \left(\begin{array}{c} \frac{1}{4\sqrt{4}}\sin^2\theta\left(Q_{11}\left[e^{j2\phi} + e^{-j2\phi}\right] - Q_{22}\left[e^{j2\phi} + e^{-j2\phi}\right] - 2jQ_{12}\left[e^{j2\phi} - e^{-j2\phi}\right]\right) + \\ -\frac{1}{2}\sin\theta\cos\theta\left(jQ_{23}\left[e^{j\phi} - e^{-j\phi}\right] - Q_{13}\left[e^{j\phi} + e^{-j\phi}\right]\right) + \\ \frac{1}{4}Q_{33}(3\cos^2\theta - 1) \end{array} \right)$$

$$= \frac{1}{4\pi\varepsilon_0 r^3} \left(\begin{array}{c} \frac{1}{8}\sin^2\theta\left(2\cos(2\phi)Q_{11} - 2\cos(2\phi)Q_{22} - \sin(2\phi)Q_{12}\right) + \\ -\frac{1}{2}\sin\theta\cos\theta\left(2\sin\phi Q_{23} - 2Q_{13}\cos\phi\right) + \\ \frac{1}{4}Q_{33}(3\cos^2\theta - 1) \end{array} \right)$$

$$= \frac{1}{4\pi\varepsilon_0 r^3} \left(\begin{array}{c} \frac{1}{8}\sin^2\theta\left(2(\cos^2\phi - \sin^2\phi)Q_{11} - 2(\cos^2\phi - \sin^2\phi)Q_{22} - 2\sin\phi\cos\phi Q_{12}\right) + \\ -\frac{yz}{r^2}[Q_{23}] + \frac{xz}{r^2}[Q_{13}] \\ \frac{1}{4}Q_{33}\left(3\frac{z^2}{r^2} - \frac{x^2+y^2+z^2}{r^2}\right) \end{array} \right)$$

$$= \frac{1}{4\pi\varepsilon_0 r^3} \left(\begin{array}{c} \frac{1}{4}\left(\frac{x^2-y^2}{r^2}\right)[Q_{11} - Q_{22}] - \frac{1}{4}\frac{xy}{r^2}[Q_{12}] \\ -\frac{yz}{r^2}[Q_{23}] + \frac{xz}{r^2}[Q_{13}] \\ \frac{1}{4}\left(\frac{2z^2 - x^2 - y^2}{r^2}\right)[Q_{33}] \end{array} \right)$$

Thus, we see that this solution consists of five independent values. These values are proportional to the real spherical harmonics of which are calculated as:

$$d_{z^2} = C_{20}Y_2^0 = \sqrt{\frac{4\pi}{5}}\frac{1}{4}\sqrt{\frac{5}{\pi}}\frac{2z^2-x^2-y^2}{r^2} = 2\frac{2z^2-x^2-y^2}{r^2}$$

$$d_{yx} = \sqrt{\frac{4\pi}{5}}j\sqrt{\frac{1}{2}}\left(Y_2^{-1}+Y_2^1\right) = \sqrt{\frac{4\pi}{5}}\frac{1}{2}\sqrt{\frac{15}{\pi}}\frac{yz}{r^2} = \frac{\sqrt{6}}{2}\frac{yz}{r^2}$$

$$d_{xz} = \sqrt{\frac{4\pi}{5}}\sqrt{\frac{1}{2}}\left(Y_2^{-1}-Y_2^1\right) = \frac{\sqrt{6}}{2}\frac{xz}{r^2} \qquad (823)$$

$$d_{xy} = \sqrt{\frac{4\pi}{5}}j\sqrt{\frac{1}{2}}\left(Y_2^{-2}-Y_2^2\right) = \frac{\sqrt{6}}{2}\frac{xy}{r^2}$$

$$d_{x^2-y^2} = \sqrt{\frac{4\pi}{5}}\sqrt{\frac{1}{2}}\left(Y_2^{-2}+Y_2^2\right) = \frac{\sqrt{6}}{4}\frac{x^2-y^2}{r^2}$$

III.3 Multipole Moment Summary

The Potential $V(\vec{r})$ of the charge distribution $\rho(\vec{r}')$ can be written as by the Coulomb kernel as

$$V(\vec{r}) = \int d\vec{r}\, T(\vec{r}-\vec{r}')\rho(\vec{r}') \qquad (824)$$

This can be expanded in further by a Taylor series around $\vec{r}'=0$ $(|\vec{r}'|<\vec{r})$. Taylor expansion of the Coulomb kernel

$$T(\vec{r}-\vec{r}') = \frac{1}{r} - \vec{r}'_\alpha \vec{\nabla}_\alpha\left(\frac{1}{r}\right) + \frac{1}{2!}\vec{r}'_\alpha \vec{r}'_\beta \vec{\nabla}_\alpha \vec{\nabla}_\beta\left(\frac{1}{r}\right) - \frac{1}{3!}\vec{r}'_\alpha \vec{r}'_\beta \vec{r}'_\gamma \vec{\nabla}_\alpha \vec{\nabla}_\beta \vec{\nabla}_\gamma\left(\frac{1}{r}\right)+\ldots \qquad (825)$$

Now the Cartesian Coulomb interaction tensors are found as

$$T(\vec{r}) = \frac{1}{r} \qquad (826)$$

$$T_\alpha(\vec{r}) = \vec{\nabla}_\alpha\left(\frac{1}{\vec{r}}\right) \qquad (827)$$

$$T_{\alpha\beta}(\vec{r}) = \vec{\nabla}_\alpha \vec{\nabla}_\beta\left(\frac{1}{\vec{r}}\right) \qquad (828)$$

$$T_{\alpha\beta\gamma}(\vec{r}) = \vec{\nabla}_\alpha \vec{\nabla}_\beta \vec{\nabla}_\gamma\left(\frac{1}{\vec{r}}\right) \qquad (829)$$

$$T_{\alpha\beta\gamma\ldots\upsilon}(\vec{r}) = \vec{\nabla}_\alpha \vec{\nabla}_\beta \vec{\nabla}_\gamma \ldots \vec{\nabla}_\upsilon\left(\frac{1}{\vec{r}}\right) \qquad (830)$$

Where the electrostatic potential now takes the form

$$V(\vec{r}) = T(\vec{r})\int d\vec{r}\,\rho(\vec{r}') - T_\alpha(\vec{r})\int d\vec{r}\,r_\alpha \rho(\vec{r}') + \frac{1}{2!}T_{\alpha\beta}(\vec{r})\int d\vec{r}\,r_\alpha r_\beta \rho(\vec{r}') - \frac{1}{3!}T_{\alpha\beta\gamma}(\vec{r})\int d\vec{r}\,r_\alpha r_\beta r_\gamma \rho(\vec{r}')+\ldots \qquad (831)$$

This sets up the derivation of the multipole moments of the charge distribution as

$$q = \int d\vec{r}\,\rho(\vec{r}) \qquad (832)$$

$$m_\alpha = \int d\vec{r}\,r_\alpha \rho(\vec{r}) \qquad (833)$$

$$Q_{\alpha\beta} = \int d\vec{r} \, r_\alpha r_\beta \rho(\vec{r})$$

(834)

$$O_{\alpha\beta\gamma} = \int d\vec{r} \, r_\alpha r_\beta r_\gamma \rho(\vec{r})$$

(835)

$$\xi_{\alpha\beta\gamma\ldots\upsilon} = \int d\vec{r} \, r_\alpha r_\beta r_\gamma \ldots r_\upsilon \rho(\vec{r})$$

(836)

Where in Cartesian coordinates the multipole expansion of the potential is written as

$$V(\vec{r}) = qT(\vec{r}) \int d\vec{r} \, \rho(\vec{r}') - m_\alpha T_\alpha(\vec{r}) + \frac{1}{2!} Q_{\alpha\beta} T_{\alpha\beta}(\vec{r}) - \ldots + \frac{(-1)^n}{n!} \xi_{\alpha\beta\ldots\upsilon} T_{\alpha\beta\ldots\upsilon}(\vec{r})$$

(837)

Thus, the details of the charge distribution in the volume are encoded into the multipoles Q_{lm}, such that: L=0 is the monopole moment (2^0=1 charges), L=1 is the dipole moment (2^1=2charges), L=2 is the quadrupole moment (2^2=4 charges), L=3 is the Octupole moment (2^3=8 charges). Moreover, the far field potential is dominated by the first non-zero moment and represents the typical region of interest, i.e. the Fraunhofer region of the antenna pattern measurement. Last of all visual representation of the permutations of monopole, dipole, and quadrupole moments are shown below in Figure 284.
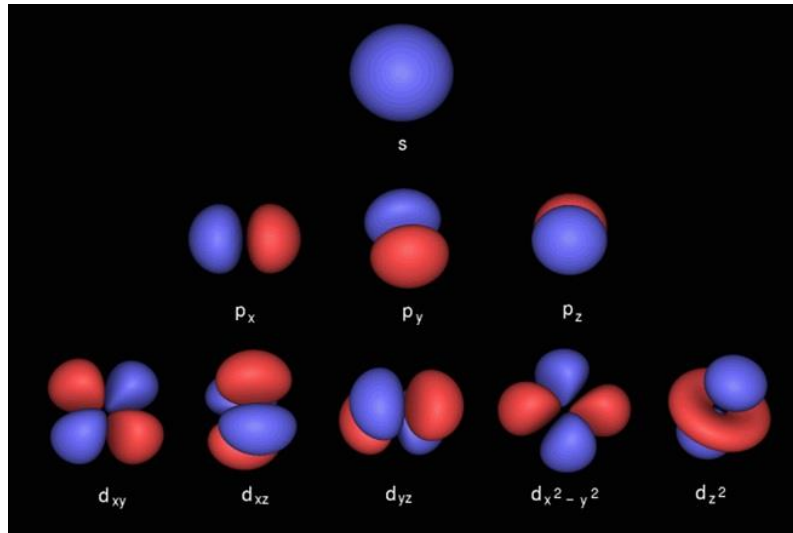
Figure 284. Example of the multipole moments.

SPHERICAL RANDOM ARRAY MOMENTS

Integration of a plane wave over a spherically symmetric volume can be expressed as an integration of the sum of spherical waves as

$$\frac{1}{V}\int_0^1\int_0^{2\pi}\int_0^{\pi}e^{j\vec{k}\cdot\vec{r}} = \frac{1}{V}\sum_{l=0}^{\infty}\int_0^1\int_0^{2\pi}\int_0^{\pi}(j)^l(2l+1)j_l(kr)P_l(\cos\psi)r^2\sin\theta d\theta d\phi \tag{838}$$

Furthermore, it was previously shown that the spherical Hankel function of order zero h_0 represents the spherically symmetric wave field. Therefore upon integrating the zeroth order mode one obtains

$$3\text{Tinc}(k) = \frac{3}{4\pi}\int_0^1\int_0^{2\pi}\int_0^{\pi}e^{j\vec{k}\cdot\vec{r}} = \frac{3}{4\pi}\int_0^1\int_0^{2\pi}\int_0^{\pi}(j)^0(2l+1)j_0(kr)P_0(\cos\psi)r^2\sin\theta d\theta d\phi \tag{839}$$

The Greens function of a finite spherical point source is calculated as

$$\frac{e^{-jk|\vec{r}-\vec{r}_n|}}{|\vec{r}-\vec{r}_n|} = jk\sum_{l=0}^{\infty}j_l(kr')h_l^{(1)}(kr)\sum_{m=-l}^{l}Y_l^m(\theta,\phi)Y_l^{m*}(\theta',\phi'),\ [r>r'] \tag{840}$$

For a theoretical point source we can calculate its far-field distribution by keeping the dominant term n=0

$$\frac{e^{-jk|\vec{r}-\vec{r}_n|}}{|\vec{r}-\vec{r}_n|} = jk\sum_{l=0}^{\infty}j_l(kr')h_l(kr)\sum_{m=-l}^{l}Y_{lm}(\theta,\phi)Y_{lm}^*(\theta',\phi')$$

$$\approx jkj_0(kr')h_0(kr)Y_{00}(\theta,\phi)Y_{00}^*(\theta',\phi') = \frac{jk}{4\pi}\left(\frac{\sin(kr')}{kr'}\left(-j\frac{e^{jkr}}{kr}\right)\right) \tag{841}$$

$$= \left.\frac{e^{jkr}}{4\pi r}\right|_{r'=0} \quad\{\text{point source}\}$$

And for multiple sources or sources offset from the origin we use a second order approximation for phase (43) and a first order approximation for path loss such that

$$\frac{e^{-jk|\vec{r}-\vec{r}_n|}}{|\vec{r}-\vec{r}_n|} \approx \frac{e^{-jkr}}{4\pi r}e^{jkr'\cos\psi} \tag{842}$$

This result is the mathematical description of a plane wave. It can be expanded by the Jacobi-Anger expansion which is useful in converting an expansion of plane waves into a series of cylindrical waves.

$$e^{jz\cos\psi} = \sum_{n=-\infty}^{\infty}J_n(z)e^{jn\psi} \tag{843}$$

And for integer *n* the expansion becomes

$$e^{jz\cos\psi} = J_0(z) + 2\sum_{n=1}^{\infty}j^nJ_n(z)\cos(n\theta) \tag{844}$$

Therefore, we have seen that the monopole moment of a point source Greens function is given to be the familiar plane wave function of which can be transformed/expanded as a superposition of cylindrical waves. From this result we observe the far-field diffraction pattern composed of its cylindrical wave basis functions as:

$$
\begin{aligned}
&\frac{e^{-jkr}}{4\pi r}\int_0^{2\pi}\int_0^1\left[J_0\left(kr'\right)+2\sum_{l=1}^{\infty}j^l J_l\left(kr'\right)\cos\left(l\psi'\right)\right]r'dr'\\
&=\frac{e^{-jkr}}{4\pi r}\int_0^{2\pi}\left(\frac{J_1(k)}{k}+\sum_{l=1}^{\infty}2^{-l}e^{jn\frac{\pi}{2}}k^l\cos\left(l\psi\right)\Gamma\left(1+\frac{l}{2}\right){}_1F_2\left[\left\{1+\frac{l}{2}\right\},\left\{2+\frac{l}{2},1+l\right\},-\frac{k^2}{4}\right]\right)d\psi'\\
&=\frac{e^{-jkr}}{4\pi r}\left(\frac{J_1(k)}{k}2\pi+\sum_{l=1}^{\infty}2^{-l-1}e^{jn\frac{\pi}{2}}k^l\cos\left(l\psi\right)\Gamma\left(\frac{l}{2}\right){}_1F_2\left[\left\{1+\frac{l}{2}\right\},\left\{2+\frac{l}{2},1+l\right\},-\frac{k^2}{4}\right]\left(\sin 2l\pi\right)\right)\\
&=\frac{e^{-jkr}}{2r}\frac{J_1(k)}{k}\left\{\text{since }l\in\Im\ \rightarrow\sin 2l\pi=0\right\}
\end{aligned}
\tag{845}
$$

Interestingly we see that the diffraction pattern of the $n=0$ mode is equivalent to that diffraction pattern of a circular random array. This is also true since the term is also angled independently. Consequently, this represents a uniform plane wave incident upon a circular aperture.

Alternatively, a plane wave can be expressed as a sum of spherical waves. This time (246) is expanded by the by converting an expansion of plane waves into a series of spherical waves.

$$
e^{jkr'\cos\psi}=4\pi\sum_{l,m}\left(j\right)^l j_l\left(kr'\right)Y_{lm}\left(\theta,\phi\right)Y_{lm}^*\left(\theta',\phi'\right)
$$

or for a axially symmetric term

$$
e^{jkr'\cos\psi}=\sum_{l=0}^{\infty}\left(j\right)^l\left(2l+1\right)j_l\left(kr'\right)P_l\left(\cos\psi\right)
\tag{846}
$$

And for $l=0$ (250) reduces to

$$
e^{jkr'\cos\psi}\underset{\substack{l=0\\ \text{monopole moment}}}{\doteq}j_0\left(kr'\right)
\tag{847}
$$

Now integrating the monopole moment over a spherical volume one obtains

$$
\frac{e^{-jkr}}{4\pi r}\int_0^1\int_0^{2\pi}\int_{-\pi}^{\pi}j_0\left(kr'\right)r'^2\sin\theta'd\theta'd\phi'dr'=\frac{J_1(k)}{k}\frac{e^{-jkr}}{r}
\tag{848}
$$

The associated diffraction pattern is shown below in Figure 285.
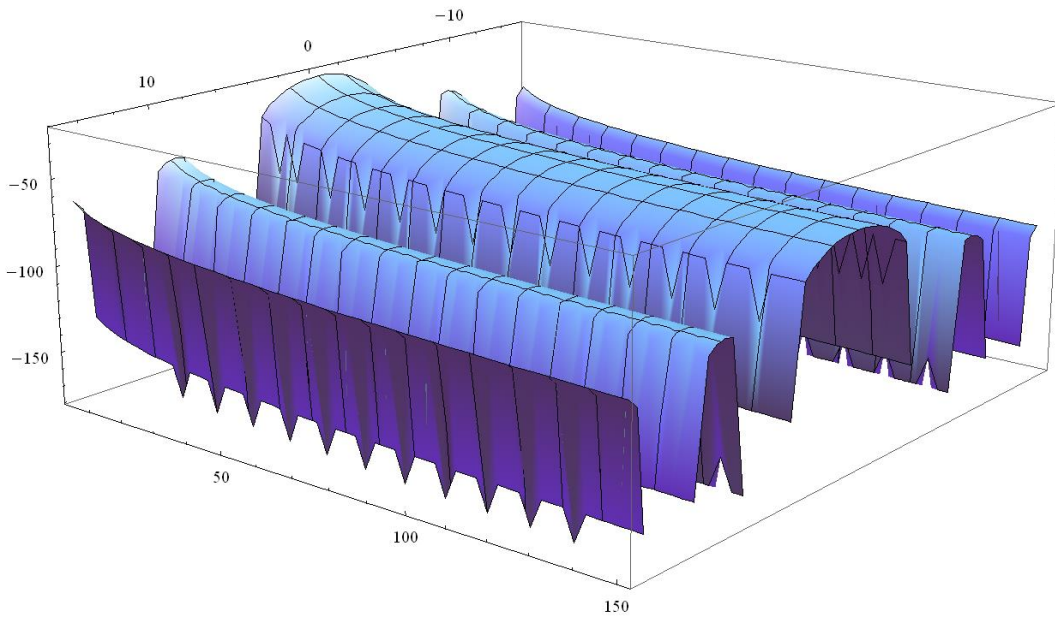
Figure 285. Diffraction pattern of the monopole moment.

Again we see that the diffraction pattern of the n=0 mode is equivalent to that diffraction pattern of a spherical random array. This is also true since the term is angle independent. This consequently represents a uniform plane wave incident upon a spherical aperture.

This time keeping the monopole (l=0) and dipole (l=1) terms the approximation becomes

$$\frac{e^{-jk|\vec{r}-\vec{r}_n|}}{|\vec{r}-\vec{r}_n|} = jk\sum_{l=0}^{\infty} j_l(kr')h_l(kr)\sum_{m=-l}^{l} Y_{lm}(\theta,\phi)Y_{lm}^*(\theta',\phi')$$

$$= jk\left[\begin{array}{l} j_0(kr')h_0(kr)Y_{00}(\theta,\phi)Y_{00}^*(\theta',\phi')+ \\ jkj_1(kr')h_1(kr)\left[\begin{array}{l} Y_{1,-1}(\theta,\phi)Y_{1,-1}^*(\theta',\phi')+ \\ Y_{10}(\theta,\phi)Y_{10}^*(\theta',\phi')+Y_{11}(\theta,\phi)Y_{11}^*(\theta',\phi') \end{array}\right] \end{array}\right]$$

$$= jk\left(\begin{array}{l} \left(\frac{\sin(kr')}{kr'}\right)\left(-j\frac{e^{jkr}}{kr}\right)Y_{00}(\theta,\phi)Y_{00}^*(\theta',\phi')+ \\ \left(\frac{\sin(kr')}{(kr')^2}-\frac{\cos(kr')}{kr'}\right)\left(jk\frac{e^{jkr}}{(kr)^2}(-kr-j)\right)\left[\begin{array}{l} Y_{1,-1}(\theta,\phi)Y_{1,-1}^*(\theta',\phi')+ \\ Y_{10}(\theta,\phi)Y_{10}^*(\theta',\phi')+ \\ Y_{11}(\theta,\phi)Y_{11}^*(\theta',\phi') \end{array}\right] \end{array}\right)$$

$$\approx \frac{e^{jkr}}{r}\left(1Y_{00}(\theta,\phi)Y_{00}^*(\theta',\phi')+\frac{r'}{3r}(kr+j)\left[\begin{array}{l} Y_{1,-1}(\theta,\phi)Y_{1,-1}^*(\theta',\phi')+ \\ Y_{10}(\theta,\phi)Y_{10}^*(\theta',\phi')+ \\ Y_{11}(\theta,\phi)Y_{11}^*(\theta',\phi') \end{array}\right]\right)\{\text{dipole source}\}$$

$$= \frac{e^{jkr}}{r}e^{jkr'\cos\psi}\left(1Y_{00}(\theta,\phi)Y_{00}^*(\theta',\phi')+\frac{r'}{3r}(kr+j)\left[\begin{array}{l} Y_{1,-1}(\theta,\phi)Y_{1,-1}^*(\theta',\phi')+ \\ Y_{10}(\theta,\phi)Y_{10}^*(\theta',\phi')+ \\ Y_{11}(\theta,\phi)Y_{11}^*(\theta',\phi') \end{array}\right]\right)$$

where $J_\alpha \approx \frac{1}{\Gamma(\alpha+1)}\left(\frac{z}{2}\right)^\alpha$ is used to simplify

$$\left(\frac{\sin(kr')}{kr'}\right)\approx 1$$

$$\left(\frac{\sin(kr')}{(kr')^2}-\frac{\cos(kr')}{kr'}\right)\approx \frac{kr'}{3}$$

(849)

$$j_n(x) = \sqrt{\frac{\pi}{2x}}J_{n+1/2}(x)$$

$$j_1(x) = \sqrt{\frac{\pi}{2x}}J_{3/2}(x) \approx \sqrt{\frac{\pi}{2x}}\frac{1}{\Gamma(3/2+1)}\left(\frac{x}{2}\right)^{3/2} = \frac{x}{3}$$

$$\Gamma(5/2) = \frac{3\sqrt{\pi}}{4}$$

$$j_2(x) = \sqrt{\frac{\pi}{2x}}J_{5/2}(x) \approx \sqrt{\frac{\pi}{2x}}\frac{1}{\Gamma(5/2+1)}\left(\frac{x}{2}\right)^{5/2} = \sqrt{\frac{\pi}{2x}}\frac{8}{15\sqrt{\pi}}\left(\frac{x}{2}\right)^{5/2} \approx \frac{x^2}{15}$$

$$\Gamma(7/2) = \frac{15\sqrt{\pi}}{8}$$

Now expanding a plane wave in into cylindrical harmonics and finding its far field contribution is calculated as:

$$\frac{e^{-jk|\vec{r}-\vec{r}_n|}}{|\vec{r}-\vec{r}_n|} \approx \frac{e^{jkr}}{r}e^{jkr'\cos\psi}\left(\begin{array}{l} 1Y_{00}(\theta,\phi)Y_{00}^*(\theta',\phi')+\\ \frac{r'}{3r}(kr+j)\left[\begin{array}{l} Y_{1,-1}(\theta,\phi)Y_{1,-1}^*(\theta',\phi')+\\ Y_{10}(\theta,\phi)Y_{10}^*(\theta',\phi')+\\ Y_{11}(\theta,\phi)Y_{11}^*(\theta',\phi') \end{array}\right] \end{array}\right)$$

$$=\frac{e^{jkr}}{r}\left[J_0(kr')+2\sum_{l=1}^{\infty}j^lJ_l(kr')\cos(l\phi')\right]\left(\begin{array}{l}\frac{1}{4\pi}P_0(\cos(\phi'))+\\ \frac{r'}{3r}(kr+j)\left(\frac{3}{4\pi}\right)P_1(\cos(\phi'))\end{array}\right)$$

$$\Rightarrow \frac{1}{4\pi}\frac{e^{jkr}}{r}\int_0^{2\pi}\int_0^{\pi}\int_0^1\left[J_0(kr')+2\sum_{l=1}^{\infty}j^lJ_l(kr')\cos(l\phi')\right]\left(1+\frac{r'}{r}(kr+j)\cos(\phi')\right)r'dr'd\phi'd\theta'$$

$$\frac{1}{4\pi}\frac{e^{jkr}}{r}\left[\begin{array}{l}\int_0^{2\pi}\int_0^{\pi}\int_0^1 J_0(kr')r'dr'd\phi'd\theta'+\frac{(kr+j)}{r}\int_0^{2\pi}\int_0^{\pi}\int_0^1 J_0(kr')\cos(\phi')r'^2\,dr'd\phi'd\theta'+\\ 2\sum_{l=1}^{\infty}\int_0^{2\pi}\int_0^{\pi}\int_0^1 j^lJ_l(kr')\cos(l\phi')r'dr'd\phi'd\theta'+\\ \frac{2(kr+j)}{r}\sum_{l=1}^{\infty}\int_0^{2\pi}\int_0^{\pi}\int_0^1 j^lJ_l(kr')\cos(l\phi')\cos(\phi')r'^2\,dr'd\phi'd\theta'\end{array}\right]$$

$$=\frac{e^{jkr}}{4\pi r}\left[\begin{array}{l}4\pi\frac{J_1(k)}{k}+2\frac{(kr+j)}{r}\left(\frac{2kJ_1(k)-\pi J_1(k)H_0(k)+\pi J_0(k)H_1(k)}{2k^2}\right)\int_0^{2\pi}(\cos(\phi'))d\phi'\\ +0+\frac{4\pi j}{r}(kr+j)\int_0^1 J_1(kr')r'^2\,dr'\end{array}\right]$$

$$+=\frac{e^{jkr}}{4\pi r}\left[4\pi\frac{J_1(k)}{k}+\frac{4\pi}{r}(krj-1)\frac{J_2(k)}{k}\right] \qquad (850)$$

$$=\frac{e^{jkr}}{r}\left[\frac{J_1(k)}{k}+\frac{(krj-1)}{r}\frac{J_2(k)}{k}\right]$$

Alternatively for a spherical wave this result is calculated

$$\left|\frac{e^{-jk|\vec{r}-\vec{r}_n|}}{|\vec{r}-\vec{r}_n|} \approx \frac{e^{jkr}}{r}e^{jkr'\cos\psi}\left(1Y_{00}(\theta,\phi)Y_{00}^*(\theta',\phi') + \frac{r'}{3r}(kr+j)\begin{bmatrix}Y_{1,-1}(\theta,\phi)Y_{1,-1}^*(\theta',\phi')+\\Y_{10}(\theta,\phi)Y_{10}^*(\theta',\phi')+\\Y_{11}(\theta,\phi)Y_{11}^*(\theta',\phi')\end{bmatrix}\right)\right.$$

$$= \frac{e^{jkr}}{r}\left(4\pi\begin{pmatrix}j_0(kr')\left(Y_{00}(\theta,\phi)Y_{00}^*(\theta',\phi')\right)+\\ j_1(kr')j\begin{pmatrix}j_0(kr)Y_{1,-1}(\theta,\phi)Y_{1,-1}^*(\theta',\phi')+\\Y_{10}(\theta,\phi)Y_{10}^*(\theta',\phi')+\\Y_{1,1}(\theta,\phi)Y_{1,1}^*(\theta',\phi')\end{pmatrix}\end{pmatrix}\right)\begin{pmatrix}Y_{00}(\theta,\phi)Y_{00}^*(\theta',\phi')+\\ \frac{r'}{3r}(kr+j)\begin{bmatrix}Y_{1,-1}(\theta,\phi)Y_{1,-1}^*(\theta',\phi')+\\Y_{10}(\theta,\phi)Y_{10}^*(\theta',\phi')+\\Y_{11}(\theta,\phi)Y_{11}^*(\theta',\phi')\end{bmatrix}\end{pmatrix}$$

$$= \frac{4\pi e^{jkr}}{r}\int_0^{2\pi}\int_0^{\pi}\int_0^1\begin{pmatrix}j_0(kr')Y_{00}(\theta,\phi)Y_{00}^*(\theta',\phi')Y_{00}(\theta,\phi)Y_{00}^*(\theta',\phi')+\\ j_0(kr')Y_{00}(\theta,\phi)Y_{00}^*(\theta',\phi')\frac{r'}{3r}(kr+j)\begin{bmatrix}Y_{1,-1}(\theta,\phi)Y_{1,-1}^*(\theta',\phi')+\\Y_{10}(\theta,\phi)Y_{10}^*(\theta',\phi')+\\Y_{11}(\theta,\phi)Y_{11}^*(\theta',\phi')\end{bmatrix}+\\ j_1(kr')jY_{00}(\theta,\phi)Y_{00}^*(\theta',\phi')\frac{r'}{3r}(kr+j)\begin{bmatrix}Y_{1,-1}(\theta,\phi)Y_{1,-1}^*(\theta',\phi')+\\Y_{10}(\theta,\phi)Y_{10}^*(\theta',\phi')+\\Y_{11}(\theta,\phi)Y_{11}^*(\theta',\phi')\end{bmatrix}+\\ j_1(kr')j\begin{pmatrix}j_0(kr)Y_{1,-1}(\theta,\phi)Y_{1,-1}^*(\theta',\phi')+\\Y_{10}(\theta,\phi)Y_{10}^*(\theta',\phi')+\\Y_{1,1}(\theta,\phi)Y_{1,1}^*(\theta',\phi')\end{pmatrix}\frac{r'}{3r}(kr+j)\begin{bmatrix}Y_{1,-1}(\theta,\phi)Y_{1,-1}^*(\theta',\phi')+\\Y_{10}(\theta,\phi)Y_{10}^*(\theta',\phi')+\\Y_{11}(\theta,\phi)Y_{11}^*(\theta',\phi')\end{bmatrix}\end{pmatrix}$$

$$\left.r'^2\,dr'\sin\theta'd\theta'd\phi'\right| \tag{851}$$

$$\left|= \frac{4\pi e^{jkr}}{r}\int_0^{2\pi}\int_0^{\pi}\int_0^1\left(\begin{pmatrix}j_0(kr')Y_{00}(\theta,\phi)Y_{00}^*(\theta',\phi')Y_{00}(\theta,\phi)Y_{00}^*(\theta',\phi')+\\ j_1(kr')j\frac{r'}{3r}(kr+j)Y_{10}(\theta,\phi)Y_{10}^*(\theta',\phi')Y_{10}(\theta,\phi)Y_{10}^*(\theta',\phi')\end{pmatrix}\right)r'^2\,dr'\sin\theta'd\theta'd\phi'\right.$$

$$= \frac{e^{jkr}}{r}\int_0^1\left(j_0(kr')+j\frac{(kr+j)\cos^2\theta}{r}r'j_1(kr')\right)r'^2\,dr'$$

$$= \frac{e^{jkr}}{r}\frac{1}{4\pi}\int_0^1\left(j_0(kr')+j_1(kr')\frac{r'}{r}(krj-1)\cos^2\theta\right)r'^2\,dr' \tag{852}$$

$$= \frac{e^{jkr}}{r}\left(\frac{j_1(k)}{k}+\frac{(krj-1)}{r}\left(-\frac{3k\cos k+(-3+k^2)\sin k}{k^4}\right)\cos^2\theta\right)$$

$$\left.= \frac{e^{jkr}}{r}\left(\frac{j_1(k)}{k}+\frac{(krj-1)}{r}\frac{j_2(k)}{k}\cos^2\theta\right)\right|$$

The associated diffraction pattern is shown below in Figure 286.
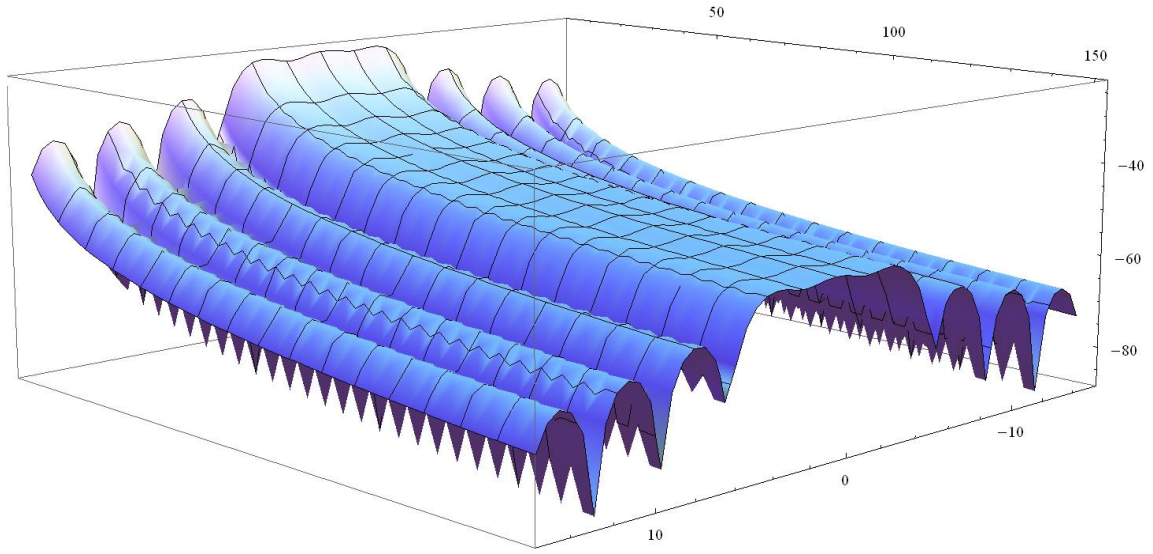
Figure 286. Diffraction pattern of the dipole moment.

Isolating the dipole moment such that

$$
\begin{aligned}
&\int_{0}^{2\pi}\int_{0}^{\pi}Y_{00}\left(\theta,\phi\right)Y_{00}^{*}\left(\theta',\phi'\right)Y_{00}\left(\theta,\phi\right)Y_{00}^{*}\left(\theta',\phi'\right)\sin\theta'd\theta'd\phi'=\frac{1}{4\pi}\\
&\int_{0}^{2\pi}\int_{0}^{\pi}Y_{1,0}\left(\theta,\phi\right)Y_{1,0}^{*}\left(\theta',\phi'\right)Y_{1,0}\left(\theta,\phi\right)Y_{1,0}^{*}\left(\theta',\phi'\right)\sin\theta'd\theta'd\phi'=\frac{3\cos^{2}\theta}{4\pi}\\
&\int_{0}^{2\pi}\int_{0}^{\pi}Y_{00}\left(\theta,\phi\right)Y_{00}^{*}\left(\theta',\phi'\right)Y_{1,-1}\left(\theta,\phi\right)Y_{1,-1}^{*}\left(\theta',\phi'\right)\sin\theta d\theta d\phi=0\\
&\int_{0}^{2\pi}\int_{0}^{\pi}Y_{00}\left(\theta,\phi\right)Y_{00}^{*}\left(\theta',\phi'\right)Y_{1,0}\left(\theta,\phi\right)Y_{1,0}^{*}\left(\theta',\phi'\right)\sin\theta d\theta d\phi=0\\
&\int_{0}^{2\pi}\int_{0}^{\pi}Y_{00}\left(\theta,\phi\right)Y_{00}^{*}\left(\theta',\phi'\right)Y_{1,1}\left(\theta,\phi\right)Y_{1,1}^{*}\left(\theta',\phi'\right)\sin\theta d\theta d\phi=0\\
&\int_{0}^{2\pi}\int_{0}^{\pi}Y_{1,-1}\left(\theta,\phi\right)Y_{1,-1}^{*}\left(\theta',\phi'\right)Y_{1,-1}\left(\theta,\phi\right)Y_{1,-1}^{*}\left(\theta',\phi'\right)\sin\theta d\theta d\phi=0\\
&\int_{0}^{2\pi}\int_{0}^{\pi}Y_{1,-1}\left(\theta,\phi\right)Y_{1,-1}^{*}\left(\theta',\phi'\right)Y_{1,0}\left(\theta,\phi\right)Y_{1,0}^{*}\left(\theta',\phi'\right)\sin\theta d\theta d\phi=0\\
&\int_{0}^{2\pi}\int_{0}^{\pi}Y_{1,-1}\left(\theta,\phi\right)Y_{1,-1}^{*}\left(\theta',\phi'\right)Y_{1,1}\left(\theta,\phi\right)Y_{1,1}^{*}\left(\theta',\phi'\right)\sin\theta d\theta d\phi=0
\end{aligned}
$$

(853)

$$\frac{e^{-jk|\vec{r}-\vec{r}_n|}}{|\vec{r}-\vec{r}_n|} = jk\sum_{l=0}^{\infty} j_l(kr')h_l(kr)\sum_{m=-l}^{l}Y_{lm}(\theta,\phi)Y_{lm}^*(\theta',\phi')$$

$$= \begin{bmatrix} j_0(kr')h_0(kr)Y_{00}(\theta,\phi)Y_{00}^*(\theta',\phi') + \\[2mm] jkj_1(kr')h_1(kr)\begin{bmatrix} Y_{1,-1}(\theta,\phi)Y_{1,-1}^*(\theta',\phi') + \\ Y_{10}(\theta,\phi)Y_{10}^*(\theta',\phi') + \\ Y_{11}(\theta,\phi)Y_{11}^*(\theta',\phi') \end{bmatrix} + \\[4mm] j^2k^2 j_2(kr')h_2(kr)\begin{bmatrix} Y_{2,-2}(\theta,\phi)Y_{2,-2}^*(\theta',\phi') + \\ Y_{2,1}(\theta,\phi)Y_{2,1}^*(\theta',\phi') + Y_{2,0}(\theta,\phi)Y_{2,0}^*(\theta',\phi') + \\ Y_{2,-1}(\theta,\phi)Y_{2,-1}^*(\theta',\phi') + Y_{2,-2}(\theta,\phi)Y_{2,-2}^*(\theta',\phi') \end{bmatrix} \end{bmatrix}$$

$$\approx \frac{e^{jkr}}{r}\left(\begin{array}{l} 1Y_{00}(\theta,\phi)Y_{00}^*(\theta',\phi') + \frac{r'}{3r}(kr+j)\begin{bmatrix} Y_{1,-1}(\theta,\phi)Y_{1,-1}^*(\theta',\phi') + \\ Y_{10}(\theta,\phi)Y_{10}^*(\theta',\phi') + \\ Y_{11}(\theta,\phi)Y_{11}^*(\theta',\phi') \end{bmatrix} \\[6mm] + j^2k^2\frac{k^2 r'^2}{15}j\frac{1}{k^3 r^2}\left(-3+3j(kr)+(kr)^2\right)\begin{bmatrix} Y_{2,-2}(\theta,\phi)Y_{2,-2}^*(\theta',\phi') + \\ Y_{2,1}(\theta,\phi)Y_{2,1}^*(\theta',\phi') + \\ Y_{2,0}(\theta,\phi)Y_{2,0}^*(\theta',\phi') + \\ Y_{2,-1}(\theta,\phi)Y_{2,-1}^*(\theta',\phi') + \\ Y_{2,-2}(\theta,\phi)Y_{2,-2}^*(\theta',\phi') \end{bmatrix} \end{array}\right) \quad \{\text{dipole source}\}$$

$$= \frac{e^{jkr}}{r}e^{jkr'\cos\psi}\left(\begin{array}{l} 1Y_{00}(\theta,\phi)Y_{00}^*(\theta',\phi') + \frac{r'}{3r}(kr+j)\begin{bmatrix} Y_{1,-1}(\theta,\phi)Y_{1,-1}^*(\theta',\phi') + \\ Y_{10}(\theta,\phi)Y_{10}^*(\theta',\phi') + \\ Y_{11}(\theta,\phi)Y_{11}^*(\theta',\phi') \end{bmatrix} + \\[6mm] + - jk\frac{r'^2}{15r^2}\left(-3+3j(kr)+(kr)^2\right)\begin{bmatrix} Y_{2,-2}(\theta,\phi)Y_{2,-2}^*(\theta',\phi') + \\ Y_{2,1}(\theta,\phi)Y_{2,1}^*(\theta',\phi') + \\ Y_{2,0}(\theta,\phi)Y_{2,0}^*(\theta',\phi') + \\ Y_{2,-1}(\theta,\phi)Y_{2,-1}^*(\theta',\phi') + \\ Y_{2,-2}(\theta,\phi)Y_{2,-2}^*(\theta',\phi') \end{bmatrix} \end{array}\right)$$

$$
\begin{aligned}
&= \frac{4\pi e^{jkr}}{r} \int_0^{2\pi}\int_0^{\pi}\int_0^{1} \left(\begin{pmatrix} j_0(kr')Y_{00}(\theta,\phi)Y_{00}^*(\theta',\phi')Y_{00}(\theta,\phi)Y_{00}^*(\theta',\phi')+ \\ j_1(kr')j\dfrac{r'}{3r}(kr+j)Y_{10}(\theta,\phi)Y_{10}^*(\theta',\phi')Y_{10}(\theta,\phi)Y_{10}^*(\theta',\phi')+ \\ j_2(kr')j^2-jk\dfrac{r'^2}{15r^2}\begin{pmatrix}-3+\\3j(kr)\\+(kr)^2\end{pmatrix}Y_{20}(\theta,\phi)Y_{20}^*(\theta',\phi')Y_{20}(\theta,\phi)Y_{20}^*(\theta',\phi') \end{pmatrix} \right) r'^2\,dr'\sin\theta'd\theta'd\phi' \\[10pt]
&= \frac{e^{jkr}}{r}\int_0^{1}\left(j_0(kr')+j\frac{(kr+j)\cos^2\theta}{r}r'j_1(kr')-jk\frac{r'^2}{15r^2}\begin{pmatrix}-3+\\3j(kr)\\+(kr)^2\end{pmatrix}5\frac{(1+3\cos(2\theta))^2}{64\pi}j_2(kr')\right)r'^2\,dr' \\[10pt]
&= \frac{e^{jkr}}{r}\frac{1}{4\pi}\int_0^{1}\left(\begin{array}{l} j_0(kr')+ \\ j_1(kr')\dfrac{r'}{r}(krj-1)\cos^2\theta- \\ \dfrac{jk}{r^2}\left(-3+3j(kr)+(kr)^2\right)\dfrac{(1+3\cos(2\theta))^2}{192\pi}r'^2 j_2(kr') \end{array}\right)r'^2\,dr' \\[10pt]
&= \frac{e^{jkr}}{r}\left(\begin{array}{l} \dfrac{j_1(k)}{k}+\dfrac{(krj-1)}{r}\left(-\dfrac{3k\cos k+(-3+k^2)\sin k}{k^4}\right)\cos^2\theta \\ -\dfrac{jk}{r^2}\left(-3+3j(kr)+(kr)^2\right)\dfrac{(1+3\cos(2\theta))^2}{192\pi}\dfrac{\left(k(-15+k^2)\cos k+3(5-2k^2)\sin k\right)}{k^5} \end{array}\right) \\[10pt]
&= \frac{e^{jkr}}{r}\left(\frac{j_1(k)}{k}+\frac{(krj-1)}{r}\frac{j_2(k)}{k}\cos^2\theta-\frac{jk}{r^2}\left(-3+3j(kr)+(kr)^2\right)\frac{(1+3\cos(2\theta))^2}{192\pi}\frac{j_3(k)}{k}\right)
\end{aligned}
$$

$$
\int_0^{2\pi}\int_0^{\pi}Y_{2,0}(\theta,\phi)Y_{2,0}^*(\theta',\phi')Y_{2,0}(\theta,\phi)Y_{2,0}^*(\theta',\phi')\sin\theta'd\theta'd\phi'=5\frac{(1+3\cos(2\theta))^2}{64\pi} \tag{854}
$$

However, instead of truncating this series for solely a plane wave it can be used to allow for all modes such that

$$\int_0^{2\pi} \int_{-\infty}^{\infty} \int_{-\pi}^{\pi} \sum_{l=0}^{\infty} \sum_{m=-l}^{l} jkj_l(kr')h_l^{(1)}(kr)Y_l^m(\theta,\phi)Y_l^{m*}(\theta',\phi')\sin\theta' d\theta' d\phi'$$

$$= \sum_{l=0}^{\infty} \int_{-\infty}^{\infty} jkj_l(kr')h_l^{(1)}(kr) \sum_{m=-l}^{l} \int_0^{2\pi} \int_{-\pi}^{\pi} Y_l^m(\theta,\phi)Y_l^{m*}(\theta',\phi')\sin\theta' d\theta' d\phi'$$

$$= \sum_{l=0}^{\infty} h_l^{(1)}(kr) \sum_{m=-l}^{l} \frac{4\pi}{2l+1}\delta_{l,l'}\delta_{m,m'} \int_0^1 jkj_l(kr')r'^2 \, dr'$$ (855)

$$= 4\pi \sum_{l=0}^{\infty} h_l^{(1)}(kr) \int_0^1 jkj_l(kr')r'^2 \, dr'$$

where

$$\int_0^{2\pi} \int_{-\pi}^{\pi} Y_l^m(\theta,\phi)Y_l^{m*}(\theta',\phi')\sin\theta d\theta' d\phi' = \frac{4\pi}{2l+1}\delta_{l,l'}\delta_{m,m'}$$

Thus,

$$\int_0^{2\pi} \int_{-\infty}^{\infty} \int_{-\pi}^{\pi} \sum_{l=0}^{\infty} \sum_{m=-l}^{l} \begin{matrix} jkj_l(kr')h_l^{(1)}(kr) \\ Y_l^m(\theta,\phi)Y_l^{m*}(\theta',\phi') \\ \sin\theta' d\theta' d\phi' \end{matrix}$$

$$= \frac{j2^{-\frac{5}{2}-l}k^{1+l}\pi\Gamma\left[\frac{3+l}{2}\right]h_{\frac{1}{2}+l}^{(1)}[kr]\,_1\tilde{F}_2\left[\left\{\frac{3+l}{2}\right\};\left\{\frac{5+l}{2},\frac{3}{2}+l\right\};\left\{-\frac{k^2}{4}\right\}\right]}{\sqrt{kr}}$$ (856)

The results of this are equivalent in explanation to the multipole moments. The l=0 moment is the monopole, m=1 (dipole), m=2 (quadrupole), m=3 (octupole), m=4 (hexadecapole). The monopole moment is calculated as follows.

For l=0 then m must equal 0:

$$\int_0^1 4\pi jkj_0(kr')h_0^{(1)}(kr)r'^2 \, dr' = \int_0^1 jk\left(-j\frac{e^{jkr}}{kr}\right)j_0(kr')r'^2 \, dr' = \frac{4\pi e^{jkr}}{r}\int_0^1 j_0(kr')r'^2 \, dr'$$

$$= 4\pi\frac{e^{ikr}}{r}\frac{(-k\cos k+\sin k)}{k^3} = 4\pi\frac{e^{ikr}}{r}\frac{j_1(k)}{k} = 4\pi\frac{e^{ikr}}{r}tinc(k)$$ (857)

where

$$j_1(k) = \frac{\sin k}{k^2} - \frac{\cos k}{k}$$

Normalizing this we obtain

$$\frac{4\pi}{V}\frac{e^{ikr}}{r}tinc(k) = \frac{e^{ikr}}{r}3tinc(k)$$ (858)

The dipole moment:

For l=1 then *m* can be -1, 0 and 1. Therefore

$$\int_0^1 jkj_1(kr')h_1^{(1)}(kr)\sum_{m=-l}^{l}\frac{4\pi}{2+1}\delta_{1,1'}\delta_{m,m'}r'^2\,dr' = \frac{4\pi}{3}\int_0^1 jkj_1(kr')h_1^{(1)}(kr)(1+1+1)r'^2\,dr'$$

$$= 4\pi\int_0^1 jkj_1(kr')h_1^{(1)}(kr)r'^2\,dr'$$

$$= 4\pi\int_0^1 jkj_1(kr')e^{jkr}\frac{kr+j}{(kr)^2}r'^2\,dr' \qquad (859)$$

$$= 4\pi\frac{e^{jkr}(1-ikr)}{kr^2}\int_0^1 j_1(kr')r'^2\,dr'$$

$$= \frac{e^{jkr}(-1+jkr)(-2+2\cos k+k\sin k)}{k^4 r^2}$$

Normalizing this we obtain

The quadrupole moment:

For l=2 then *m* can be -2, -1, 0, 1 and 2. Therefore

$$\int_0^1 jkj_2(kr')h_2^{(1)}(kr)\sum_{m=-l}^{l}\frac{4\pi}{4+1}\delta_{2,2'}\delta_{m,m'}r'^2\,dr' = \frac{4\pi}{5}\int_0^1 jkj_2(kr')h_2^{(1)}(kr)(1+1+1+1+1)r'^2\,dr'$$

$$= 4\pi\int_0^1 jkj_2(kr')h_2^{(1)}(kr)r'^2\,dr' = 4\pi\int_0^1 jkj_2(kr')e^{-jkr}\frac{kr+j}{(kr)^2}r'^2\,dr'$$

$$= 4\pi\frac{e^{jkr}(3-kr(3j+kr))}{k^2 r^3}e^{-jkr}\int_0^1 j_2(kr')r'^2\,dr' \qquad (860)$$

$$= -\frac{e^{jkr}(-3+kr(3j+kr))(k\cos k-4\sin k+3\mathrm{Si}(k))}{k^5 r^3}$$

where

$$\mathrm{Si}(k) = \int_0^k \frac{\sin x}{x}\,dx$$

APPENDIX V

GREEN'S FUNCTION OF A POINT SOURCE

The Green's Function for the Helmholtz' Equation satisfies the following PDE solution: Where $\vec{x}$ denotes the set of variables, e.g., $\vec{x} = (x, y, z)$.

$$L\Phi(\vec{x}) = f(\vec{x}) \tag{861}$$

$$\text{where}$$
$$L = \nabla^2 + \beta^2,$$
$$\Phi(\vec{x}) = \vec{A},$$
$$f(\vec{x}) = -\mu\vec{J}$$

Suppose also that a Green's functions it allows for the integral solution (Appendix)

$$\Phi(\vec{x}) = \iiint_{v'} G(\vec{x}, \vec{x}') \cdot f(\vec{x}') dv' \quad \text{or}$$
$$A_z(P) = \iiint_{V_Q} G(P, Q) \cdot \left[-\mu\vec{J}(Q) \right] dv_Q \tag{862}$$

Applying the operator L to both sides of (862), leads to

$$L\Phi(\vec{x}) = \iiint_{v'} L\left[G(\vec{x}, \vec{x}') \right] \cdot f(\vec{x}') dv' = f(\vec{x})$$
$$\left(\nabla^2 + \beta^2 \right)\vec{A} = \iiint_{v'} \left(\nabla^2 + \beta^2 \right)\left[G(P, Q) \right] \cdot -\mu\vec{J}(Q) dv' = -\mu\vec{J}(P) \tag{863}$$

From (863), we conclude that the Green's function must satisfy the same PDE as Φ with a point source described by Dirac's delta condition:

$$LG(\vec{x}, \vec{x}') = \delta(\vec{x} - \vec{x}') \quad \text{or}$$
$$\left(\nabla^2 + \beta^2 \right)\left[G(P, Q) \right] = \delta(P - Q)$$
$$\text{such that}$$
$$\delta(P - Q)_{Q=P} = 1$$
$$\delta(P - Q)_{Q \neq P} = 0 \tag{864}$$

Such that

Here, $\delta(\vec{x} - \vec{x}')$ is Dirac's delta function in 3-D space, e.g., $\delta(\vec{x} - \vec{x}') = \delta(x - x')\delta(y - y')\delta(z - z')$. If the Green's function of the problem is known, the construction of an integral is possible via (862).

Now the Green's function for the Helmholtz equation in open space must satisfy

$$\nabla^2 G + \beta^2 G = \delta(x - x')\delta(y - y')\delta(z - z') \tag{865}$$

Together with the scalar radiation condition (see *Appendix*)

$$\lim_{r\to\infty}\left(\frac{\partial G}{\partial r}+j\beta G\right)=0 \tag{866}$$

If the source is centered at the origin of the coordinate system i.e., $x'=y'=z'=0$. Integrate (865) within a sphere with its center at $(0,0,0)$ and a radius R as shown in Figure 287:
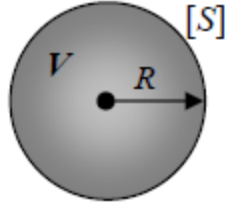
Figure 287. Example of a source with volume V bounded by surface area $[S]$.

$$\iiint_{v}\nabla^{2}Gdv+\iiint_{v}\beta^{2}Gdv=1 \tag{867}$$

The function G is due to a point source and thus has a spherical symmetry, i.e; it depends on r only. The Laplacian ∇^{2} in spherical coordinates is reduced to derivatives with respect to r only:

$$\frac{d^{2}G}{dr^{2}}+\frac{2}{r}\frac{dG}{dr}+\beta^{2}G=\delta(x)\delta(y)\delta(z) \tag{868}$$

Everywhere except at the point (x,y,z) , G must satisfy the homogeneous equation

$$\frac{d^{2}G}{dr^{2}}+\frac{2}{r}\frac{dG}{dr}+\beta^{2}G=0 \tag{869}$$

Whose solution for outgoing waves is well known (Appendix):

$$G(r)=C\frac{e^{-jkr}}{r}$$

Here, C is a constant to be determined. Consider first the integral from (867)

$$I_{1}=\iiint_{v}\beta^{2}C\frac{e^{-j\beta r}}{r}dv=\int_{0}^{R}\int_{0}^{2\pi}\int_{0}^{\pi}\beta^{2}C\frac{e^{-j\beta r}}{r}r^{2}\sin\theta d\theta d\phi dr \tag{870}$$

$$\Rightarrow I_{1}(R)=j4\pi\beta C\left(\mathrm{Re}^{-j\beta R}+\frac{e^{-j\beta R}}{j\beta}-\frac{1}{j\beta}\right) \tag{871}$$

366

To evaluate the integral in the point of singularity $(0,0,0)$, we let $R \to 0$, i.e., we let the sphere collapse into a point. We see that

$$\lim_{R \to 0} I_1(R) = 0 \tag{872}$$

Secondly, consider the other integral in (867),

$$I_2 = \iiint_v \nabla^2 G \, dv = \iiint_v \vec{\nabla} \cdot (\vec{\nabla} G) dv = \oiint_s \vec{\nabla} G \cdot d\vec{s} \tag{873}$$

Here $d\vec{s} = R^2 \sin\theta d\theta d\phi dr \cdot \hat{r}$ is a surface element on S, and

$$\vec{\nabla} G = \frac{\partial G}{\partial r} \hat{r} = -C \left(jk \frac{e^{-jkr}}{r} + \frac{e^{-jkr}}{r^2} \right) \hat{r} \tag{874}$$

$$\Rightarrow I_2(R) = -C \left(jkR \cdot e^{-jkR} + e^{-jkR} \right) \int_0^\pi \int_0^{2\pi} \sin\theta d\phi d\theta$$

$$\lim_{R \to 0} I_2(R) = -\frac{1}{4\pi} \tag{875}$$

Finally,

$$G(r) = -\frac{e^{-jkr}}{4\pi r} \tag{876}$$

It is not difficult to show that in the general case when the source is at a point $Q(x',y',z')$,

$$\nabla^2 G + \beta^2 G = \delta(x-x')\delta(y-y')\delta(z-z') \tag{877}$$

$$G(P,Q) = -\frac{e^{-jkR_{PQ}}}{4\pi R_{PQ}} \tag{878}$$

Where R_{PQ} is the distance between the observation point P and the source point Q.

$$R_{PQ} = \sqrt{(x-x')^2 + (y-y')^2 + (z-z')^2} \tag{879}$$

The solution of (876) is also shown in the form of the Green's function is shown as a series of orthonormal functions. The most appropriate orthonormal functions would be those that satisfy the boundary conditions by using the Sturm-Liouville operator.

APPENDIX VI

GENERALIZED GREEN'S FUNCTION METHOD

The presentation of Green's first and second identities in the previous section provide enough information for us to develop a generalized Green's function method of ϕ and the partial differential equation (861) whose Green's function $G(\vec{r},\vec{r}')$ satisfies (865).

"Let us multiply (861) by $G(\vec{r},\vec{r}')$ and (865) by $\vec{A}(\vec{r})$. Doing this leads to

$$G(\vec{r},\vec{r}')\nabla^2 A(\vec{r}) + \beta^2 A(\vec{r})G(\vec{r},\vec{r}') = A(\vec{r})G(\vec{r},\vec{r}') \tag{880}$$

$$A(\vec{r})\nabla^2 G(\vec{r},\vec{r}') + \beta^2 A(\vec{r})G(\vec{r},\vec{r}') = A(\vec{r})\delta(\vec{r}-\vec{r}') \tag{881}$$

Subtracting (880) from (881) and integrating over the volume *V*, we can write that

$$\iiint_V A(\vec{r})\delta(\vec{r}-\vec{r}')d\upsilon - \iiint_V A(\vec{r})G(\vec{r},\vec{r}')d\upsilon = \iiint_V \left(A(\vec{r})\nabla^2 G(\vec{r},\vec{r}') - G(\vec{r},\vec{r}')\nabla^2 A(\vec{r})\right)d\upsilon \tag{882}$$

"Or" [152]

$$A(\vec{r}=\vec{r}') = A(\vec{r}') = \iiint_V A(\vec{r})G(\vec{r},\vec{r}')d\upsilon + \iiint_V \left(A(\vec{r})\nabla^2 G(\vec{r},\vec{r}') - G(\vec{r},\vec{r}')\nabla^2 A(\vec{r})\right)d\upsilon \tag{883}$$

Applying Green's second identity (*Appendix*) (894) reduces (883) to

$$A(\vec{r}=\vec{r}') = A(\vec{r}') = \iiint_V A(\vec{r})G(\vec{r},\vec{r}')d\upsilon + \oiint_S \left[A(\vec{r})\nabla G(\vec{r},\vec{r}') - G(\vec{r},\vec{r}')\nabla A(\vec{r})\right]\cdot ds \tag{884}$$

Since $\vec{r}'$ is an arbitrary point within *V* and $\vec{r}$ is a dummy variable, we can also write (884) as

$$A(\vec{r}) = \iiint_V A(\vec{r}')G(\vec{r},\vec{r}')d\upsilon + \oiint_S \left[A(\vec{r}')\nabla' G(\vec{r},\vec{r}') - G(\vec{r},\vec{r}')\nabla' A(\vec{r}')\right]\cdot ds' \tag{885}$$

Or by the reciprocity theorem

$$G(\vec{r},\vec{r}') = G(\vec{r}',\vec{r}) \tag{886}$$

where $\vec{\nabla}'$ indicates differentiation with respect to the prime coordinates.

Equation (885) is a generalized formula for the development of the Green's function for a three-dimensional scalar Helmholtz equation. It can be simplified depending on the boundary conditions of $\vec{A}$ and $\vec{G}$, and their derivatives on *S*. The objective then will be to judiciously choose the boundary conditions on the development of G, once the boundary conditions on $\vec{A}$ are stated, so as to simplify, if not eliminate, the surface integral contribution in (885). We will demonstrate here some combinations of boundary conditions on $\vec{A}$ and $\vec{G}$, and the simplifications of (885), based on those boundary conditions." [152]

VI.1 Green's First and Second Identities

"Within a volume *V*, conducting bodies with surfaces S_1, S_2, S_3, …,S_n are contained, as shown in Figure 15-6. By introducing appropriate cuts, the volume *V* is bounded by a regular surface *S* that consists of surfaces $S_1 - S_n$, the surfaces along the cuts, and the surface S_a of an infinite radius sphere that encloses all the conducting bodies. A unit vector $\hat{n}$ normal to *S* is directed inward to the volume *V*, as shown in Figure 288.

Let us introduce within *V,* two scalar functions ϕ and ψ, which, along with their first and second derivatives, are continuous within *V* and on the surface *S*. To the vector $\phi\vec{\nabla}\psi$, we apply the divergence theorem,
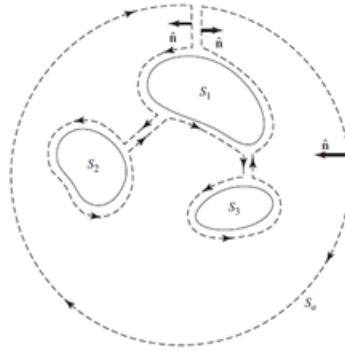
Figure 288. "Conducting surfaces and appropriate cuts for application of Green's theorem." [152]

$$\oiint_S \left(\phi\vec{\nabla}\psi\right)\cdot d\vec{s} = \oiint_S \left(\phi\vec{\nabla}\psi\right)\cdot\hat{n}\,da = \iiint_V \vec{\nabla}\cdot\left(\phi\vec{\nabla}\psi\right)d\upsilon \qquad (887)$$

When expanded, the integrand of the volume integral can be written as

$$\vec{\nabla}\cdot\left(\phi\vec{\nabla}\psi\right) = \phi\vec{\nabla}\cdot\left(\vec{\nabla}\psi\right)+\vec{\nabla}\phi\cdot\vec{\nabla}\psi = \phi\nabla^2\psi+\vec{\nabla}\phi\cdot\vec{\nabla}\psi \qquad (888)$$

Thus (887) can be expressed as

$$\oiint_S \left(\phi\vec{\nabla}\psi\cdot d\vec{s}\right) = \iiint_V \left(\phi\nabla^2\psi\right)d\upsilon + \iiint_V \left(\vec{\nabla}\phi\cdot\vec{\nabla}\psi\right)d\upsilon \qquad (889)$$

Which, is referred to as *Green's first identity*. Since

$$\left(\vec{\nabla}\psi\right)\cdot\hat{n} = \frac{\partial\psi}{\partial n} \qquad (890)$$

where the derivative $\partial\psi/\partial n$ is taken in the direction of positive normal, (889) can also be written as

369

$$\oiint_S \left(\phi \frac{\partial \psi}{\partial n} \right) = \iiint_V \left(\phi \nabla^2 \psi \right) dv + \iiint_V \left(\vec{\nabla} \phi \cdot \vec{\nabla} \psi \right) dv \tag{891}$$

which is an alternate form of Green's first identity.

If we repeat the procedure but apply the divergence theorem (887) to the vector $\psi \vec{\nabla} \phi$, then we can write, respectively, Green's first identity (889) and its alternate form (891) as

$$\oiint_S \left(\psi \vec{\nabla} \phi \cdot d\vec{s} \right) = \iiint_V \left(\psi \nabla^2 \phi \right) dv + \iiint_V \left(\vec{\nabla} \psi \cdot \vec{\nabla} \phi \right) dv \tag{892}$$

and

$$\oiint_S \left(\psi \frac{\partial \phi}{\partial n} \right) = \iiint_V \left(\psi \nabla^2 \phi \right) dv + \iiint_V \left(\vec{\nabla} \psi \cdot \vec{\nabla} \phi \right) dv \tag{893}$$

Subtracting (889) from (892), we can write that

$$\oiint_S \left(\phi \vec{\nabla} \psi - \psi \vec{\nabla} \phi \right) \cdot d\vec{s} = \iiint_V \left(\phi \nabla^2 \psi - \psi \nabla^2 \phi \right) dv \tag{894}$$

which is referred to as *Green's second identity*. Its alternate form

$$\oiint_S \left(\phi \frac{\partial \psi}{\partial n} - \psi \frac{\partial \phi}{\partial n} \right) = \iiint_V \left(\phi \nabla^2 \psi - \psi \nabla^2 \phi \right) dv \tag{895}$$

is obtained by subtracting (891) from (893)." [152]

(a) Nonhomogeneous partial differential equation with homogeneous dirichlet boundary conditions

A Dirichlet boundary condition in the Laplace equation imposes the restriction that the potential is some value at some location. A common case of Dirichlet boundary conditions are surfaces of perfectly conductive electrodes. Free charges in such a conductor will rearrange themselves over the conductive surfaces so that the potential will be uniform over the entire conductor. Typically, electrodes are held to some known potential by attaching them to a power supply or ground, so the Dirichlet condition is known directly, but conductive surfaces may alternately be floating.

The Dirichlet boundary conditions refer to specifying the function on the surface such that the nonhomogeneous form of the partial differential equation of (861) satisfies the homogeneous Dirichlet boundary condition

$$A(\vec{r}_s) = 0 \quad \text{where } \vec{r}_s \text{ is on S} \tag{896}$$

then it is reasonable to construct a Green's function with the same boundary condition

$$G(\vec{r}_s, \vec{r}') = 0 \quad \text{where } \vec{r}_s \text{ is on S} \tag{897}$$

so as to simplify the surface integral contributions in (885).

For these boundary conditions on A and G, both terms in the surface integral of (885) vanish, so that (885) reduces to

$$A(\vec{r}) = \iiint_V A(\vec{r}')G(\vec{r},\vec{r}')d\upsilon' \qquad (898)$$

Here, the Green function $G(\vec{r},\vec{r}')$ is assumed to satisfy the following boundary conditions1 on $S = \partial V$, such that

$$A(\vec{r})\hat{n}\cdot\vec{\nabla}G(\vec{r},\vec{r}') + B(\vec{r})\vec{\nabla}G(\vec{r},\vec{r}') = 0 \ ^3 \qquad (899)$$

The Green's function $G(\vec{r},\vec{r}')$ needed in (898) can be obtained using any of the previous methods developed thus far. In many cases, the bilinear form (15-61) or (15-94) or its equivalent, in the desired coordinate system and number of space variables, is appropriate for forming the Green's function. Its existence will depend upon the eigenvalues of the homogeneous partial differential equation, as discussed in previously. A sphere of radius R illustrating these conditions is provided in Figure 289.
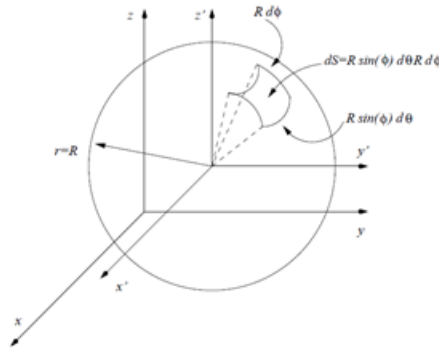
Figure 289. Sphere of radius R. [223]

---

3 $A(\vec{r}) = 0$ is called Dirichlet condition, whereas $B(\vec{r}) = 0$ is called Neumann condition. For acoustic waves, $B(\vec{r}) = 0$ corresponds $\psi = 0$, i.e. hard surface, $A(\vec{r}) = 0$ corresponds $\phi = 0$, i.e. soft surface, and $\dfrac{A(\vec{r})}{B(\vec{r})} = \text{const}$ corresponds to impedance surface

THE HELMHOLTZ DIFFERENTIAL EQUATION IN SPHERICAL COORDINATES

Take the Helmholtz differential equation

$$\nabla^2 F + k^2 F = 0 \tag{900}$$

In spherical coordinates this is simply Laplace's equation in spherical coordinates with the additional term, [221]

$$\frac{1}{r^2}\frac{\partial}{\partial r}\left(r^2\frac{\partial \psi}{\partial r}\right) + \frac{1}{r^2\sin\theta}\frac{\partial}{\partial \theta}\left(\sin\theta\frac{\partial \psi}{\partial \theta}\right) + \frac{1}{r^2\sin\theta}\frac{\partial \psi}{\partial \phi^2} + k^2\psi = 0 \tag{901}$$

Now substituting,

$$\psi(r,\theta,\phi) = R(r)\Theta(\theta)\Phi(\phi) \tag{902}$$

Multiplying the resulting equation by $r^2\sin^2\theta$, and dividing by ψ gives

$$\frac{\sin^2\theta}{R}\frac{d}{dr}\left(r^2\frac{dR}{dr}\right) + \frac{\sin\theta}{\Theta}\frac{d}{d\theta}\left(\sin\theta\frac{d\Theta}{d\theta}\right) + \frac{1}{\Phi}\frac{d^2\Phi}{d\phi} + k^2 r^2 \sin^2\theta = 0 \tag{903}$$

Now by letting,

$$\frac{1}{\Phi}\frac{d^2\Phi}{d\phi^2} = -m^2 \tag{904}$$

Upon substituting and dividing by $\sin^2\theta$ gives

$$\frac{1}{R}\frac{d}{dr}\left(r^2\frac{dR}{dr}\right) + \frac{1}{\Theta\sin\theta}\frac{d}{d\theta}\left(\sin\theta\frac{d\Theta}{d\theta}\right) - \frac{m^2}{\sin^2\theta} + k^2 r^2 = 0 \tag{905}$$

Now we separate the θ equation

$$\frac{1}{\Theta\sin\theta}\frac{d}{d\theta}\left(\sin\theta\frac{d\Theta}{d\theta}\right) - \frac{m^2}{\sin^2\theta} = -n(n+1) \tag{906}$$

Where the strange constant $-n(n+1)$ is chosen because the form of $\Theta(\theta)$ depends on whether or not $n \in \mathbb{Z}$. Thus, the equation is now rewritten as

$$\frac{1}{R}\frac{d}{dr}\left(r^2\frac{dR}{dr}\right) - n(n+1) + k^2 r^2 = 0 \tag{907}$$

Thus after separation we are left with three separated spherical equations.

$$\frac{d}{dr}\left(r^2\frac{dR}{dr}\right) + \left[k^2 r^2 - n(n+1)\right]R = 0 \tag{908}$$

$$\frac{1}{\sin\theta}\frac{d}{d\theta}\left(\sin\theta\frac{d\Theta}{d\theta}\right)+\left[n(n+1)-\frac{m^2}{\sin^2\theta}\right]\Theta=0 \tag{909}$$

$$\frac{d^2\Phi}{d\phi^2}+m^2\Phi=0 \tag{910}$$

It is important to note that there is no separation equation since two of the independent variables refer to angles.

VII.1 Method of Frobenius and Applied to Bessel's Differential Equation of Integer Order

The Bessel differential is one of the most important non-elementary differential equations.

$$x^2y''+xy'+\left(x^2-m^2\right)y=0 \tag{911}$$

Here it is seen that the leading coefficient $p(x)=x^2$ is nonzero except for $x=0$. Thus, all points except the origin are regular points. Therefore for points $x_0\neq0$ the standard power series construction can be used to generate the power series solutions of the Bessel differential equation. For our application, we need to know the solution to the equation at the singular point $x_0=0$. Therefore we rewrite this equation as

$$y''=-\frac{1}{x}y'+\left(\frac{m^2}{x^2}-1\right)y \tag{912}$$

One can use the method of Frobenius in order to find an infinite series solution for a second order ordinary differential equation of the form

$$x^2y''+p(x)xy'+q(x)y=0 \tag{913}$$

However, by isolating y'' (914)we see that there is a regular singular point $x=0$.

$$y''+\frac{p(x)}{x}y'+\frac{q(x)}{x^2}y=0 \tag{914}$$

This equation is not solvable using regular power series methods if either $\dfrac{p(x)}{x}$ or $\dfrac{q(x)}{x^2}$ are not analytic at $x=0$.

This now allows us to seek a solution in the form of a Frobenius expansion such that we define the Ansatz $y(x)$ and its derivatives as

$$y(x)=\sum_{k=0}^{\infty}x^{r+k}A_k \quad \left(A_0\neq0\right) \tag{915}$$

$$y'(x) = (k+r)\sum_{k=0}^{\infty} x^{r+k-1} A_k \qquad (916)$$

$$y''(x) = (k+r-1)(k+r)\sum_{k=0}^{\infty} x^{r+n-2} A_k \qquad (917)$$

Now substituting (915)-(917) into (914) gives

$$x^2 \sum_{k=0}^{\infty}(k+r-1)(k+r)A_k y^{k+r-2} + xp(x)\sum_{k=0}^{\infty}(k+r)A_k y^{k+r-1} + q(x)\sum_{k=0}^{\infty} A_k y^{k+r}$$

$$= \sum_{k=0}^{\infty}(k+r-1)(k+r)A_k y^{k+r} + p(x)\sum_{k=0}^{\infty}(k+r)A_k y^{k+r} + q(x)\sum_{k=0}^{\infty} A_k y^{k+r}$$

$$= \sum_{k=0}^{\infty}\left[(k+r-1)(k+r)A_k y^{k+r} + p(x)(k+r)A_k y^{k+r} + q(x)A_k y^{k+r}\right] \qquad (918)$$

$$= \sum_{k=0}^{\infty}\left[(k+r-1)(k+r) + p(x)(k+r) + q(x)\right]A_k y^{k+r}$$

$$= \left[r(r-1) + p(x)(r) + q(x)\right]A_0 y^r + \sum_{k=1}^{\infty}\left[(k+r-1)(k+r) + p(x)(k+r) + q(x)\right]A_k y^{k+r}$$

In (918) the term

$$\left\lfloor r(r-1) + p(0)(r) + q(0) \right\rfloor = I(r) \qquad (919)$$

Is the indicial equation and quadratic in r. The importance of the indicial equation is that it provides the allowed values of r in the series expansion.

For the Bessel differential equation

$$I(r) = \left\lfloor r(r-1) + r + -m^2 \right\rfloor = r^2 - m^2$$
$$= (r+m)(r-m) \qquad (920)$$

Thus, there we see that there are two solutions $r = \pm m$. Here we will ignore the negative solution and consider only the positive solution such that $r = m$ (and additionally avoiding the special case such that $m \neq 1/2$). This gives

$$r = 1$$
$$(m+1)(m+1-1)a_1 x^{r+1} + (m+1)a_1 x^{r+1} - m^2 a_1 x^{r+1} = 0$$
$$(m^2 + 2m + 1 - m^2)a_1 x^{r+1} = 0 \qquad (921)$$
$$(2m+1)a_1 = 0$$

$$(m+n)(m+n-1)a_1 x^{r+1} + (m+n)a_1 x^{r+1} - m^2 a_1 x^{r+n} + a_{n-2} x^{r+n} = 0$$
$$(m^2 + mn - m + mn + n^2 - n + m + n - m^2)a_1 + a_{n-2} = 0$$
$$n(2m+n)a_n + a_{n-2} = 0 \qquad (922)$$
$$a_n = -\frac{1}{n(2m+n)}a_{n-2}$$

This is the solution for n>1 where it can be shown by rearranging and simplifying that the series solutions are defined as the Bessel function of the first kind $J_m(x)$. The second solution for $m=-k$ proceeds analogously in the solution $J_{-m}(x)=(-1)^m J_m(x)$.

$$a_n = -\frac{1}{n(2m+n)}a_{n-2} = -\frac{1}{(m+n)^2 - m^2}a_{n-2} = \frac{a_{n-4}}{n(n-2)(n+2m)(n+2m-2)}$$

$$\Rightarrow a_{2p} = (-1)^m \frac{a_0}{2^{2m}p!}\frac{\Gamma(1+m)}{\Gamma(p+m+1)}$$

$$a_0 = \frac{1}{2^p\Gamma(1+p)}(\text{arbitrary choice})$$

$$J_p \equiv \sum_{m=0}^{\infty}\frac{(-1)^m}{\Gamma(1+m)\Gamma(m+p+1)}\left(\frac{x}{2}\right)^{2m+p}$$

(923)

VII.2 Spherical Bessel Differential Equation

The radial equation is of the form

$$r^2\frac{d^2R}{dr^2}+2r\frac{dR}{dr}+\left[k^2r^2-n(n+1)\right]R=0$$

(924)

This is the spherical Bessel differential equation. It is convenient to change variables to $x=kr$. The equation for $R\left(\frac{x}{k}\right)$ becomes

$$\frac{x^2}{k^2}\frac{d^2R}{d\left(\frac{x}{k}\right)^2}+\frac{2x}{k}\frac{dR}{d\left(\frac{x}{k}\right)}+\left[x^2-n(n+1)\right]R=0$$

$$=x^2\frac{d^2R}{d\left(\frac{x}{k}\right)^2}+2x\frac{dR}{d\left(\frac{x}{k}\right)}+\left[x^2-n(n+1)\right]R=0$$

(925)

Now dividing by x^2 we obtain

$$\frac{d^2R}{dx^2}+\frac{2}{x}\frac{dR}{dx}+\left|1-\frac{n(n+1)}{x^2}\right|R=0$$

(926)

This has a regular singular point at r=0.

In order to solve (908), we can look for a solution of the form $A(x)x^{-\frac{1}{2}}$. Then taking the second derivative of x we obtain

$$R'=A'x^{1/2}-\frac{1}{2}Ax^{-3/2}$$

(927)

$$R''=A''x^{1/2}-A'x^{-3/2}+\frac{3}{4}Ax^{-5/2}$$

(928)

Thus,

$$x^2 \left(A''x^{-1/2} - A'x^{-3/2} + \frac{3}{4}A^{-5/2} \right) + 2\left(A'x^{-1/2} - \frac{1}{2}Ax^{-3/2} \right) + \left[x^2 - n(n+1) \right]Ax^{-1/2} = 0 \qquad (929)$$

$$x^2 \left(A''- A'x^{-1} + \frac{3}{4}A^{-2} \right) + 2\left(A'- \frac{1}{2}Ax^{-1} \right) + \left[x^2 - n(n+1) \right]A = 0 \qquad (930)$$

$$x^2 A'' + (-x+2x)A' + \left[\frac{3}{4} - 1 + x^2 - n(n+1) \right]A = 0 \qquad (931)$$

$$x^2 A'' + xA' + \left[x^2 - n\left(n + \frac{1}{2} \right) \right]A = 0 \qquad (932)$$

This is seen to be Bessel's Differential equation of half-integer order and the normalized solutions to this equation are of the form:

$$R(r) = A'j_n(kr) + B'n_n(kr) \qquad (933)$$

These solutions can also be written in terms of spherical Hankel functions such that

$$R(r) = C'h_n^{(1)}(kr) + D'h_n^{(2)}(kr)$$
$$h_n^{[1,2]} = j_n \pm jy_n \qquad (934)$$

(a) Bessel function derivation

The Bessel equation of order $\frac{1}{2}$ is

$$\frac{d^2 y}{dx^2} + \frac{1}{x}\frac{dy}{dx} + \left[1 - \frac{1}{4x^2} \right]y = 0 \qquad (935)$$

Now expanding this in a power series

$$y(x) = \sum_{k=0}^{\infty} x^{r+k} A_k \quad (A_0 \neq 0) \qquad (936)$$

$$y'(x) = (k+r)\sum_{k=0}^{\infty} x^{r+k-1} A_k \qquad (937)$$

$$y''(x) = (k+r-1)(k+r)\sum_{k=0}^{\infty} x^{r+n-2} A_k \qquad (938)$$

We first right the differential equation in the desired form (multiplying by x^2), in order to remove fractions and simplify computation we obtain,

$$4x^2 \frac{d^2 y}{dx^2} + 4x\frac{dy}{dx} + \left[4x^2 - 1 \right]y = 0 \qquad (939)$$

Substituting,

$$0 = 4x^2 y'' + 4xy' + \left\lfloor 4x^2 - 1 \right\rfloor y = 0$$

$$= 4x^2 \sum_{k=0}^{\infty} a_k (k+r)(k+r-1) x^{k+r-2} + 4x \sum_{k=0}^{\infty} a_k (k+r) x^{k+r-1} + \left[4x^2 - 1 \right] \sum_{k=0}^{\infty} a_k x^{k+r}$$

$$= \sum_{k=0}^{\infty} 4a_k (k+r)(k+r-1) x^k + \sum_{k=0}^{\infty} ra_k (k+r) x^k + \sum_{k=0}^{\infty} 4a_k x^{k+2} - \sum_{k=0}^{\infty} a_k x^k \tag{940}$$

$$= \underbrace{\sum_{n=0}^{\infty} 4a_n (n+r)(n+r-1) x^n}_{n=k} + \underbrace{\sum_{n=0}^{\infty} ra_n (n+r) x^n}_{n=k} + \underbrace{\sum_{n=2}^{\infty} 4a_{n-2} x^n}_{n=k+2} - \underbrace{\sum_{n=0}^{\infty} a_n x^n}_{n=k}$$

Now since one of the series begins with n=2 we will separate the n=0 and n=1 terms and combine terms into one big series

$$0 = a_0 \left(4r^2 - 1 \right) x^0 + a_1 \left(4r^2 + 8r + 3 \right) x^1 + \sum_{n=2}^{\infty} \left[a_n 4(n+r)^2 + 4a_{n-2} \right] x^n \tag{941}$$

Now solving the indicial equation for r with the convention $r_2 \le r_1$

$$4r^2 - 1 = 0$$

$$r_1 = \frac{1}{2} \tag{942}$$

$$r_2 = -\frac{1}{2}$$

Now using the larger of the solutions

$$0 = a_0 \left(4\left(\frac{1}{2}\right)^2 - 1 \right) x^0 + a_1 \left(4\left(\frac{1}{2}\right)^2 + 8\left(\frac{1}{2}\right) + 3 \right) x^1 + \sum_{n=2}^{\infty} \left[a_n 4\left(n + \left(\frac{1}{2}\right)\right)^2 + 4a_{n-2} \right] x^n$$

$$= a_0 0 x^0 + a_1 8 x^1 + \sum_{n=2}^{\infty} \left[a_n 4n(n+1) + 4a_{n-2} \right] x^n \tag{943}$$

Now solving the recursion formula

$$a_n = \frac{-1}{n(n+1)} a_{n-2} \quad \text{for n=2, 3, 4, ...} \tag{944}$$

Now converting back to the trivial index $k = n$ gives

$$a_k = \frac{-1}{k(k+1)} a_{k-2} \quad \text{for k=2, 3, 4, ...} \tag{945}$$

Now we find the formulas for the lower order terms that is

$$0a_0 = 0 \Rightarrow a_0 \text{ is arbitrary}$$
$$8a_1 = 0 \Rightarrow a_1 = 0 \tag{946}$$

Now we observe the values for $k = 2,3,4,5,6,\cdots$

$$a_2 = \frac{-1}{2(2+1)}a_{2-2} = \frac{-1}{2(3)}a_0$$

$$a_3 = \frac{-1}{3(3+1)}a_{3-2} = \frac{-1}{3(4)}a_1 = \frac{-1}{3(4)}0 = 0$$

$$a_4 = \frac{-1}{4(4+1)}a_{4-2} = \frac{-1}{4(5)}a_2 = \frac{-1}{(5)4}\frac{-1}{(3)2}a_0 = \frac{(-1)^2}{5!}a_0$$

(947)

$$a_5 = \frac{-1}{5(5+1)}a_{5-2} = \frac{-1}{5(6)}0 = 0$$

$$a_6 = \frac{-1}{6(6+1)}a_{6-2} = \frac{-1}{6(7)}a_4 = \frac{-1}{6(7)}\frac{-1}{(5)4}\frac{-1}{(3)2}a_0 = \frac{(-1)^3}{7!}a_0$$

$$\vdots$$

Therefore we observe the obvious patterns

$$a_k = 0 \qquad \text{for } k=1, 3, 5, 7, \ldots$$

$$a_k = \frac{(-1)^{k/2}}{(k+1)!}a_0 \qquad \text{for } k=2, 4, 6, 8, \ldots$$

(948)

Then applying the substitution $k = 2m$, this can be written as

$$a_{2m} = \frac{(-1)^m}{(2m+1)!}a_0 \qquad \text{for } m=1, 2, 3, 4, \ldots$$

(949)

Now using the formulas just derived we can write out the resulting series for y

$$y = x^r \sum_{k=0}^{\infty} a_k x^k$$

$$= x^r \left[\sum_{\substack{k=0, \\ k=odd}}^{\infty} a_k x^k + \sum_{\substack{k=0, \\ k=even}}^{\infty} a_k x^k \right]$$

$$= x^{1/2} \left[\sum_{\substack{k=0, \\ k=odd}}^{\infty} 0x^k + \sum_{m=0}^{\infty} (-1)^m \frac{a_0}{(2m+1)!}x^{2m} \right]$$

(950)

$$= a_0 x^{1/2} \sum_{m=0}^{\infty} \frac{(-1)^m}{(2m+1)!}x^{2m}$$

Now repeating the process for $r = r_2$

$$0 = a_0 \left[4r^2 - 1 \right] x^0 + a_1 \left[4r^2 + 8r + 3 \right] x^1 + \sum_{n=2}^{\infty} \left[a_n \left[4(n+r)^2 - 1 \right] + 4a_{n-2} \right] x^n$$

$$= a_0 \left[4\left(\frac{-1}{2} \right) - 1 \right] x^0 + a_1 \left[4\left(\frac{-1}{2} \right)^2 + 8\left(\frac{-1}{2} \right) + 3 \right] x^1 + \sum_{n=2}^{\infty} \left[a_n \left[4\left(n + \left(\frac{-1}{2} \right) \right)^2 - 1 \right] + 4a_{n-2} \right] x^n$$

$$= a_0 0 x^0 + a_1 0 x^1 + \sum_{n=2}^{\infty} \left[a_n \left[4n^2 - 4n + -1 \right] + 4a_{n-2} \right] x^n$$

Then...   (951)

$\vdots$

yielding

$$y = a_0 x^{-\frac{1}{2}} \sum_{m=0}^{\infty} \frac{(-1)^m}{(2m)!} x^{2m} + a_1 x^{-\frac{1}{2}} \sum_{m=0}^{\infty} \frac{(-1)^m}{(2m+1)!} x^{2m+1}$$

"If this last step yielded y as an arbitrary linear combination of two different series then that is the general solution to the differential equation. If the last step yielded y as just one arbitrary constant times a series, then the general solution to the original differential equation is the linear combination of the two series obtained." [222]

In our case we are in luck as we have derived the linear combination of the two different series, which is the general solution to Bessel's equation of order $1/2$

$$y = a_0 x^{-\frac{1}{2}} \sum_{m=0}^{\infty} \frac{(-1)^m}{(2m)!} x^{2m} + a_1 x^{-\frac{1}{2}} \sum_{m=0}^{\infty} \frac{(-1)^m}{(2m+1)!} x^{2m+1} \qquad (952)$$

Moreover, the series can be rewritten in terms of more well-known functions (sine and cosine).

$$y = a_0 x^{-\frac{1}{2}} \sum_{m=0}^{\infty} \frac{(-1)^m}{(2m)!} x^{2m} + a_1 x^{-\frac{1}{2}} \sum_{m=0}^{\infty} \frac{(-1)^m}{(2m+1)!} x^{2m+1}$$

$$= a_0 x^{-\frac{1}{2}} \cos x + a_1 x^{-\frac{1}{2}} \sin x \qquad (953)$$

$$= a_0 \frac{\cos x}{\sqrt{x}} + a_1 \frac{\sin x}{\sqrt{x}}$$

This series solution for l_1 is also related to the Bessel function of half integer order, also known as the spherical Bessel function.

$$j_n(z) = z^n \sum_{k=0}^{\infty} \frac{(-1)^k}{k!(2k+2n+1)!!} \left(\frac{z^2}{2} \right)^k \qquad (954)$$

$$= (-1)^k z^n \left(\frac{d}{zdz} \right)^n \frac{\sin z}{z}$$

The other solution being l_2 is related to the

Other solutions of the spherical Bessel equation are

379

$$j_n(kr) \quad \text{Bessel functions}$$
$$y_n(kr) \quad \text{Neumann functions} \qquad\qquad (955)$$
$$\left.\begin{array}{l} h_n^{(1)}(kr) \\ h_n^{(2)}(kr) \end{array}\right\} \text{Hankel Functions}$$

Such that the solutions satisfy the following properties:

j_n is the only function regular at the origin

j_n and y_n represent standing waves

$h_n^{(2)}$ is an outgoing wave, $h_n^{(1)}$ is an incoming wave.

These functions are also expressible in terms of familiar functions:

$$j_0(kr) = \frac{\sin(kr)}{kr} \qquad\qquad j_0(kr) = -\frac{\cos(kr)}{kr}$$

$$h_0^{(1)} = \frac{e^{jkr}}{jkr} \qquad\qquad h_0^{(2)} = \frac{e^{-jkr}}{jkr}$$

Higher orders of the functions are found from well-known recurrence formulas. A demonstation of the inward and outward behavior of these waves is shown below in Figure 290.

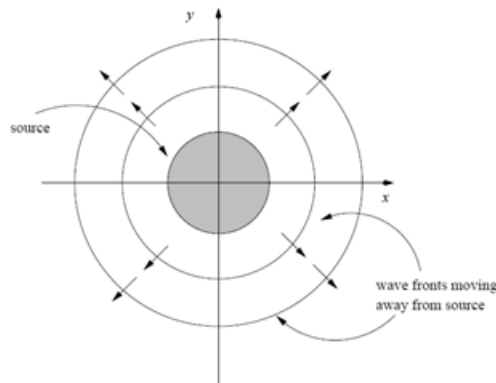Figure 290. Radiation condition; waves move away from the source. [223]

VII.3 Hankel Function Derivation

Alternatively, we can solve for the characteristic green's Function such that the solution is not composed as a series of independent (orthogonal) harmonics.

If the source is considered to reside at the origin of the coordinates, then the Green function $G(\vec{r})$ is expressed from (865) as

$$\nabla^2 G(\vec{r}) + \beta^2 G(\vec{r}) = \delta(\vec{r}) \tag{956}$$

Since the free space is assumed $G(\vec{r},\vec{r}')$ is only a function of $r = |\vec{r}|$ due to the symmetry. Now by applying the Laplacian in the spherical coordinates

$$\nabla^2 A = \frac{1}{r^2}\frac{\partial}{\partial r}\left(r^2 \frac{\partial A}{\partial r}\right) + \frac{1}{r\sin\theta}\frac{\partial}{\partial\theta}\left(\sin\theta\frac{\partial A}{\partial\theta}\right) + \frac{1}{r^2\sin^2\theta}\frac{\partial^2 A}{\partial^2\phi} \tag{957}$$

Thus we rewrite (956) as

$$\frac{d^2 G}{dr^2} + \frac{2}{r}\frac{dG}{dr} + \beta^2 G = \delta(r) \tag{958}$$

Since the right-hand side of (958) is zero except for the origin, we can rewrite this outside of the origin as

$$\frac{d^2}{dr^2}\left(rG(r)\right) + k^2\left(rG(r)\right) = 0 \tag{959}$$

Since

$$\begin{aligned}
\frac{d^2}{dr^2}\left(RG(R)\right) + k^2\left(RG(R)\right) &= \frac{1}{R}\left[\frac{d}{dr}\right]\left[\frac{d}{dr}(G)R\right] + \frac{1}{R}\frac{d}{dr}\left[G\frac{d}{dr}(R)\right] \\
&= \frac{1}{R}\left[\frac{d^2}{d^2 r}(G)R\right] + \frac{1}{R}\left[\frac{d}{dr}(G)\frac{d}{dr}(R)\right] + \frac{1}{R}\left[\frac{d}{dr}(G)\frac{d}{dr}(R)\right] + \frac{1}{R}\left[G\frac{d^2}{dr^2}(R)\right] \\
&= \frac{d^2}{d^2 r}(G) + \frac{2}{R}\frac{d}{dr}(G)
\end{aligned} \tag{960}$$

Now solving the differential equation

$$\lambda^2 + k^2\lambda = 0 \tag{961}$$

$$\lambda_{1,2} = \frac{0 \pm \sqrt{0 - 4(1)(k)}}{2} = \pm jk \tag{962}$$

Then

$$rG(r) = Ae^{-jkr} + Be^{jkr} \tag{963}$$

Such that

$$G(r) = \frac{Ae^{-jkr} + Be^{jkr}}{r} \tag{964}$$

Where A and B are arbitrary constants. Where for outgoing waves the solution is given as $\frac{Ae^{-jkr}}{r}$ and the constant is found in the text.

(a) Series solution (bilinear) derivation in unbounded space

One may construct the greens function $G(r,r')$ as an eigenfunction expansion or otherwise known as the bilinear formula (Appendix 6). Thus

$$\left.\begin{array}{l}\left(\nabla^2+k^2\right)\psi_{\vec{k}}(\vec{r})=0 \\ \nabla^2\psi_{\vec{k}}(\vec{r})=-k^2\psi_{\vec{k}}(\vec{r}) \\ \nabla^2\psi_{\vec{k}}(\vec{r})=-k^2\psi_{\vec{k}}(\vec{r}) \\ \text{where} \\ -k^2=\lambda\end{array}\right| \quad \left.\begin{array}{l}\left(\nabla^2+k'^2\right)\psi_{\vec{k}'}(\vec{r})=0 \\ \nabla^2\psi_{\vec{k}'}(\vec{r})=-k^2\psi_{\vec{k}'}(\vec{r}) \\ \nabla^2\psi_{\vec{k}'}(\vec{r})=-k^2\psi_{\vec{k}'}(\vec{r}) \\ \text{where} \\ -k'^2=\lambda_n\end{array}\right| \tag{965}$$

Where the solution of this type of equation is

$$r_{1,2}=\frac{0\pm\sqrt{0-4(1)(k)^2}}{2}=\pm jk$$
$$\psi_k=e^{r_1 r}+e^{r_2 r}=A'e^{jkr}+B'e^{-jkr}$$
vanish at the boundary ∞
$$\psi_{\vec{k}}=e^{r_1 r}+e^{r_2 r}=B'e^{-j\vec{k}\cdot\vec{r}}$$
$$\psi_{\vec{k}'}=e^{r_1 r}+e^{r_2 r}=B'e^{-j\vec{k}'\cdot\vec{r}}$$
\tag{966}

$$G(\vec{r},\vec{r}')=\sum_n\frac{\psi_n^*(\vec{r}')\psi_n(\vec{r})}{\lambda_n-\lambda} \tag{967}$$

Where $\lambda=-k^2$, $\lambda_n=-k'^2$, where the eigenfunctions are solution of

$$\left(\nabla^2+k'^2\right)\psi_{\vec{k}'}(\vec{r})=0 \tag{968}$$

That is, they are plane waves,

$$\psi_{\vec{k}'}(\vec{r})=\frac{1}{(2\pi)^{3/2}}e^{j\vec{k}'\cdot\vec{r}} \tag{969}$$

Here the factor $(2\pi)^{3/2}$ is for normalization:

$$\int\left(d\vec{k}'\right)\psi_{\vec{k}'}(\vec{r})^*\psi_{\vec{k}'}(\vec{r}')=\delta(\vec{r}-\vec{r}') \tag{970}$$

$$\int\left(d\vec{r}'\right)\psi_{\vec{k}'}(\vec{r})^*\psi_{\vec{k}'}(\vec{r}')=\delta(\vec{k}-\vec{k}') \tag{971}$$

Where we have noted that the spectrum of eigenvalues is continuous,

$$\sum_n\to\int\left(d\vec{k}\right) \tag{972}$$

Thus the eigenfunction expansion for the Green's function has the form

$$G(\vec{r},\vec{r}')=\frac{1}{(2\pi)^3}\iiint\frac{e^{-\vec{k}'\cdot\vec{r}'}e^{\vec{k}\cdot\vec{r}}}{k^2-k'^2} \tag{973}$$

Now evaluating this integral in spherical coordinates, where we write

$$\left(d\vec{k}'\right)=k'^2\,dk'd\phi'du', \quad u'=\cos\theta', \tag{974}$$

Where we have chosen the z axis to lie along the direction of $\vec{r} - \vec{r}'$. The integration over the angles is easy and is illustrated in Figure 291.

$$
\begin{aligned}
G(\vec{r},\vec{r}') &= \frac{1}{(2\pi)^3} \int_0^\infty dk' k'^2 \int_0^{2\pi} d\phi' \int_{-1}^{1} \frac{e^{jk|\vec{r}-\vec{r}'|u'}}{k^2 - k'^2} du' \\
&= \frac{1}{(2\pi)^2} \frac{1}{2} \int_{-\infty}^{\infty} \frac{dk' k'^2}{k^2 - k'^2} \frac{1}{jk'\rho} \left(e^{jk'\rho} - e^{-jk'\rho} \right),
\end{aligned}
$$

(975)
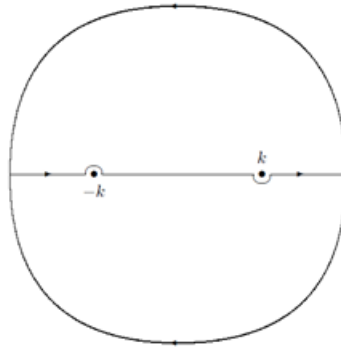
Figure 291. "Contour in the k' plane used to evaluate the integral and is closed in the upper (lower) half-plane if the exponent is positive (negative). The poles in the integrand are avoided by passing above the one on the left and below the one on the right." [220]

Defining $\rho = |\vec{r} - \vec{r}'|$, where we have replaced $\int_0^\infty$ by $\frac{1}{2}\int_{-\infty}^{\infty}$ because the integrand is even in k'^2 . We evaluate the integral by contour methods. Because now k can coincide with an eigenvalue k'^2 , we must choose the contour appropriately to define the Green's function. Suppose we choose the contour as shown in Figure 291, passing below the pole at k and above the pole at $-k$. We close the contour in the upper half plane for the $e^{jk\rho}$ and in the lower half plane for the $e^{-jk\rho}$ term. Then by Jordan's lemma, we immediately evaluate the integral:

$$
\begin{aligned}
G(\vec{r},\vec{r}') &= \frac{1}{(2\pi)^2} \frac{1}{2} \left[-\frac{2\pi j}{2k} k \frac{e^{jk\rho}}{j\rho} + \frac{2\pi j}{-2k} k \frac{e^{jk\rho}}{j\rho} \right] \\
&= -\frac{1}{4\pi} \frac{e^{jk\rho}}{\rho}
\end{aligned}
$$

(976)

(b) Series solution (bilinear) derivation in bounded space

For the Helmholtz equation in spherical coordinates we have shown that the eigenfunctions of the Laplacian are

$$j_l(kr)Y_l^m(\theta,\phi) \tag{977}$$

$$\left(\nabla^2 + k^2\right)j_l(kr)Y_l^m(\theta,\phi) = 0 \tag{978}$$

Now since by the direcht boundary conditions we know that the eigenfunctions must vanish at $r=a$.

This can be done by assuming β_{ln} is the nth zero of j_l,

$$j_l(\beta_{ln}) = 0 \qquad n = 1, 2, 3\ldots \tag{979}$$

This gives the desired eigenfunctions such that

$$\psi_{nlm}(r,\theta,\phi) = A_{nl}j_l\left(\beta_{ln}\frac{r}{a}\right)Y_l^m(\theta,\phi)$$

where

$$\psi_{nlm}(r,\theta,\phi)\Big|_{r=a} = A_{nl}j_l(\beta_{ln})Y_l^m(\theta,\phi)$$
$$\tag{980}$$

Now the eigenvalues are expressed as

$$\lambda_{ln} = -k_{ln}^2 = -\left(\frac{\beta_{ln}}{a}\right)^2 \tag{981}$$

We find the normalization parameter such that

$$\left|A_{nl}\right|^2 \int_0^a r^2 dr \left[j_l\left(\beta_{ln}\frac{r}{a}\right)\right]^2 = 1$$

where

$$\int_0^a r^2 dr j_l\left(\beta_{ln}\frac{r}{a}\right)j_l\left(\beta_{lm}\frac{r}{a}\right) = \delta_{nm}\frac{1}{2}a^3 j_{l+1}^2(\beta_{ln})$$
$$\tag{982}$$

thus

$$\left|A_{nl}\right|^2 \delta_{nm}\frac{1}{2}a^3 j_{l+1}^2(\beta_{ln}) = 1$$

$$\left|A_{nl}\right| = \frac{1}{j_{l+1}(\beta_{ln})}\sqrt{\frac{2}{a^3}}$$

And the Green's function by use of the bilinear expansion has the eigenfunction expansion

$$G_k(\vec{r},\vec{r}') = \sum_{nlm}\frac{2}{a^3}\frac{1}{j_{l+1}^2(\beta_{ln})}\frac{Y_l^m(\theta,\phi)Y_l^{m*}(\theta',\phi')j_l\left(\beta_{ln}\frac{r}{a}\right)j_l\left(\beta_{ln}\frac{r'}{a}\right)}{k^2 - \left(\frac{\beta_{ln}}{a}\right)^2}$$

or for an axially symmetric geometry
$$\tag{983}$$

$$G_k(\vec{r},\vec{r}') = \frac{2}{a^3}\sum_{nl}\frac{2l+1}{4\pi}P_l(\cos\psi)\frac{1}{j_{l+1}^2(\beta_{ln})}\frac{Y_l^m(\theta,\phi)Y_l^{m*}(\theta',\phi')j_l\left(\beta_{ln}\frac{r}{a}\right)j_l\left(\beta_{ln}\frac{r'}{a}\right)}{k^2 - \left(\frac{\beta_{ln}}{a}\right)^2}$$

VII.4 The Harmonic Equation (ϕ) Dependence

The differential equation

$$\frac{d^2\Phi}{d\phi^2} + m^2\Phi = 0 \tag{984}$$

Is better known as the harmonic equation. The solution is typically written as follows:

$$\begin{aligned}
\lambda^2 + m^2 &= 0 \\
(\lambda + jm)(\lambda - jm) &= 0 \\
\lambda &= \pm jm
\end{aligned} \tag{985}$$

Where the solution is expressed as

$$Ae^{\lambda_1\phi} + Be^{\lambda_2\phi} \tag{986}$$

Or

$$\cos(m\phi) \quad\text{or}\quad \sin(m\phi) \tag{987}$$

Such that m is an integer since $\Phi(\phi)$ must be periodic.

VII.5 The Associated Legendre Equation (θ) Dependence

The last of these equations is of the form

$$\frac{1}{\sin\theta}\frac{d}{d\theta}\left(\sin\theta\frac{d\Theta}{d\theta}\right) + \left[n(n+1) - \frac{m^2}{\sin^2\theta}\right]\Theta = 0 \tag{988}$$

By defining $x = \cos\theta$ and $y = \Theta$ we obtain,

$$(1-x^2)\frac{d^2y}{dx^2} - 2x\frac{dy}{dx} + \left[n(n+1) - \frac{m^2}{(1-x^2)}\right]y = 0 \tag{989}$$

Now since,

$$0 \le \theta \le \pi, \; -1 \le x \le 1$$

We can obtain one set of solutions, which are regular for $n \in \mathbb{Z}$, which we call the associated Legendre functions of the first kind $P_n^m(x)$. The other set of solution is the associated Legendre functions of the second kind are written as, $Q_n^m(x)$, which are singular at $|x| = 1$. Also if $m = 0$ and $n \in \mathbb{Z}$ then the solutions become orthogonal polynomials of degree n. Solutions of this nature are given by the well-known Rodrigues Formula

$$P_n(x) = \frac{1}{2^n n!}\frac{d^n}{dx^n}(x^2-1)^n \tag{990}$$

Noting that these polynomials are not orthonormal, yet are normalized such that $P_n(1)=1$. Other useful facts are such that, if $n \notin \mathbb{Z}$ then the functions $P_n(x)$ and $P_n(-x)$ are independent. Thus, if $n \in \mathbb{Z}$ than Q must be used. Also if $n \notin \mathbb{Z}$ then the functions $P_n(x)$ or $P_n^m(x)$ are not regular at $|x|=1$. For $m \neq 0$ we call these the Associated Legendre Functions otherwise just the Legendre functions. Lastly, if $m > n$ then $P_n^m(x) = Q_n^m(x) = 0$

The first few are:

$$P_0(x) = 1 \tag{991}$$

$$P_1(x) = x \tag{992}$$

$$P_2(x) = \frac{1}{2}(3x^2 - 1) \tag{993}$$

ADDITION THEOREM (PLANE WAVE AS A SUM OF SPHERICAL WAVES)

To verify this we start by using the Green's function,

$$\frac{e^{jk|\vec{r}_1-\vec{r}_2|}}{4\pi|\vec{r}_1-\vec{r}_2|} = jk\sum_{l=0}^{\infty}\begin{cases} j_l(kr_1)h_l^{(1)}(kr_2) & [r_1<r_2] \\ j_l(kr_2)h_l^{(1)}(kr_1) & [r_1>r_2] \end{cases}\sum_{m=-l}^{l}Y_l^m(\theta_1,\phi_1)Y_l^{m*}(\theta_2,\phi_2) \tag{994}$$

In the far-field for $r_2 > r_1$

$$\frac{e^{jk|\vec{r}_1-\vec{r}_2|}}{4\pi|\vec{r}_1-\vec{r}_2|} \simeq \frac{e^{jk\left[r_2-\frac{\vec{k}\cdot\vec{r}_1}{k}\right]}}{4\pi\left[r_2-\frac{\vec{k}\cdot\vec{r}_1}{k}\right]} = \frac{e^{jkr_2}e^{-j\vec{k}\cdot\vec{r}_1}}{4\pi r_2-\frac{4\pi\vec{k}\cdot\vec{r}_1}{k}} = \frac{e^{jkr_2}e^{-j\vec{k}\cdot\vec{r}_1}}{r_2\left(4\pi-4\pi\frac{\vec{k}\cdot\vec{r}_1}{kr_2}\right)} \approx \frac{e^{jkr_2}e^{-j\vec{k}\cdot\vec{r}_1}}{4\pi r_2} \tag{995}$$

$$\frac{e^{-j\vec{k}\cdot\vec{r}_1}}{4\pi}\frac{e^{jkr_2}}{r_2} = jk\sum_{l=0}^{\infty}j_l(-kr_1)h_l^{(1)}(kr_2)\sum_{m=-l}^{l}Y_l^m(\theta_1,\phi_1)Y_l^{m*}(\theta_2,\phi_2) \tag{996}$$

Applying the spherical function asymptote

$$h_l^{(1)}(kr_2) \sim (-j)^{l+1}\frac{e^{jkr_2}}{r_2} \tag{997}$$

Now applying the addition theorem for spherical harmonics

$$P_n(\cos\psi) = \frac{4\pi}{2n+1}\sum_{m=-n}^{n}Y_n^m(\theta_1,\phi_1)Y_n^{m*}(\theta_2,\phi_2) \tag{998}$$

Thus

$$\frac{e^{jkr_2}}{r_2}\frac{e^{-j\vec{k}\cdot\vec{r}_1}}{4\pi} = jk\sum_{l=0}^{\infty}j_l(-kr_1)(-j)^{l+1}\frac{e^{jkr_2}}{r_2}\frac{2l+1}{4\pi}P_n(\cos\psi)$$

$$e^{-j\vec{k}\cdot\vec{r}_1} = j\sum_{l=0}^{\infty}j_l(-kr_1)(-j)^{l+1}\frac{2l+1}{4\pi}P_n(\cos\psi)$$

$$e^{-j\vec{k}\cdot\vec{r}_1} = \sum_{l=0}^{\infty}j_l(-kr_1)(-j)^{l}\frac{2l+1}{4\pi}P_n(\cos\psi) \tag{999}$$

since

$$j(-j)^{l+1} = -(-j)^{l+2} = -(-j)^{l}(-j)^{2} = (-j)^{l}$$

Now since,

$$j_l(kr) = 2^l(kr)^l\sum_{s=0}^{\infty}\frac{(-1)^s(s+l)!}{s!(2s+2l+1)!}(kr)^{2s} = (kr)^l\sum_{s=0}^{\infty}\frac{(-1)^s}{s!(2s+2l+1)!!}\left(\frac{(kr)^2}{2}\right)^s \tag{1000}$$

Then

$$j_l(-kr) = 2^l(-kr)^l \sum_{s=0}^{\infty} \frac{(-1)^s(s+l)!}{s!(2s+2l+1)!}(-kr)^{2s} = (-kr)^l \sum_{s=0}^{\infty} \frac{(-1)^s}{s!(2s+2l+1)!!}\left(\frac{(-kr)^2}{2}\right)^s$$

$$= 2^l(kr)^l(-1)^l \sum_{s=0}^{\infty} C_s(kr)^{2s} = (-kr)^l\left(-j^2\right)^l \sum_{s=0}^{\infty} C_s(kr)^{2s} = \left(-j^2\right)^l j_l(kr) \tag{1001}$$

And upon substituting we obtain

$$e^{-j\vec{k}\cdot\vec{r}_1} = \sum_{l=0}^{\infty} j_l(kr_1)\left(-j^3\right)^l \frac{2l+1}{4\pi}P_n(\cos\psi) = e^{-j\vec{k}\cdot\vec{r}_1} = \sum_{l=0}^{\infty} j_l(kr_1)(j)^l \frac{2l+1}{4\pi}P_n(\cos\psi) \tag{1002}$$

Another way to show that a plane wave can be expressed as a sum of spherical waves is given as follows:

$$\frac{e^{j\vec{k}\cdot\vec{r}}}{4\pi r} \approx \frac{e^{jkr}}{4\pi r}e^{-jk\hat{r}\cdot\vec{r}'} = jk\frac{e^{jkr}}{4\pi r}\sum_{l,m}^{\infty}(-j)^{l+1}j_l(kr)Y_{lm}^*(\theta,\phi)Y_{lm}(\theta',\phi') \tag{1003}$$

Canceling the factor $\dfrac{e^{jkr}}{4\pi r}$ on either side, or taking the complex conjugate, we obtain the following

expansion for a scalar plane wave

$$e^{j\vec{k}\cdot\vec{r}} = \sum_{l=0}^{\infty}(j)^l j_l(kr)\sum_{m=-l}^{+l}Y_{lm}^*(\theta,\phi)Y_{lm}(\theta',\phi') \tag{1004}$$

The well-known addition theorem for the spherical harmonics states that

$$P_l(\cos\psi) = \frac{4\pi}{2l+1}\sum_{m=-l}^{l}Y_{lm}^*(\theta,\phi)Y_{lm}(\theta',\phi') \tag{1005}$$

Thus it follows that

$$e^{j\vec{k}\cdot\vec{r}} = \sum_{l=0}^{\infty}(j)^l(2l+1)j_l(kr)P_l(\cos\psi) \tag{1006}$$

Lastly, in the Fraunhofer region (far- field)

$$e^{jkr\cos(\theta-\alpha)} = \sum j^m J_m(kr)e^{jm(\theta-\alpha)} \tag{1007}$$

APPENDIX IX

SPHERICAL HARMONIC SOLUTIONS FOR THE HOMOGENOUS HELMHOLTZ EQUATION (REGULAR SPHERICAL EIGENFUNCTIONS OF THE HELMHOLTZ EQUATIONS)

It is possible to use any linear combination of the four radial functions that satisfy the Helmholtz equation. By this means the Green's function will be bounded everywhere, and on may assume

$$G(\vec{r},\vec{r}') = \sum_{l=0}^{\infty}\sum_{m=-l}^{l} A_{lm} j_l(kr') h_l^{(1)}(kr) Y_{lm}(\theta,\phi) Y_{lm}^*(\theta,\phi) \quad for \ r > r'$$

$$G(\vec{r},\vec{r}') = \sum_{l=0}^{\infty}\sum_{m=-l}^{l} A_{lm} j_l(kr) h_l^{(1)}(kr') Y_{lm}(\theta,\phi) Y_{lm}^*(\theta,\phi) \quad for \ r < r'$$

(1008)

Where A_{lm} is the expansion coefficient of the (l,m) harmonic and continuity on the surface $r = r'$ is imposed. In addition, the coefficient A_{lm} can be determined through another means of exploiting the discontinuity in the radial derivative. Thus substituting (1008) into the greens function provides

$$\left(\nabla^2 + k^2\right)G = -\delta(\vec{r}-\vec{r}') = -\frac{\delta(r-r')}{rr'\sin\theta}\delta(\theta-\theta')\delta(\phi-\phi')$$

(1009)

Next by multiplying both side by $Y_{l'm'}^*(\theta',\phi')$, and integrating the result over the entire solid angle one obtains (1010). Moreover, the orthogonality of the harmonic functions is illustrated below in Figure 292.

$$\int_{\Omega} Y_n^m(r,\theta,\phi) Y_p^q(r,\theta,\phi)^* d\Omega = \int_0^{2\pi} d\phi \int_0^{\pi} Y_n^m(r,\theta,\phi) Y_p^q(r,\theta,\phi)^* \sin\theta d\theta$$
$$= \delta_{np}\delta_{mq}$$

where δ_{np} is the Kronecker delta function $\delta_{np} = \begin{cases} 1 & n = p \\ 0 & n \neq p \end{cases}$

$$\int_{\Omega} \bullet \bullet^* d\Omega = \delta_{np}\delta_{mq}$$

Figure 292. Orthogonality of spherical harmonics. [143]

$$\int Y_{lm}(\theta,\phi) Y_{l'm'}^*(\theta',\phi') d\Omega = \delta_{ll'}\delta_{mm'}$$

(1011)

Thus we obtain

$$A_{lm}\left(\frac{d^2}{dr^2}+\frac{2}{r}\frac{d}{dr}+k^2-\frac{l(l+1)}{r^2}\right)g_l(r,r')=-\frac{\delta(r-r')}{rr'}$$

(1012)

Where

$$g_l(r,r')=\begin{cases}j_l(kr')h_l^{(1)}(kr) & r>r'\\ j_l(kr)h_l^{(1)}(kr') & r<r'\end{cases}$$

(1013)

In other words the derivative of the radial function $g_l(r,r')$ is discontinuous at $r=r'$ and thus second order derivative yields the singularity compatible with the right hand side.

$$\frac{d^2}{dr^2}g_l(r,r')=jk\frac{1}{(kr)^2}\delta(r-r')$$

(1014)

This solution has also made use of the Wronskian of the spherical Bessel functions,

$$j_l(x)\left[h_l^{(1)}(x)\right]'-j_l'(x)h_l^{(1)}(x)=j\left[j_l(x)n_l'(x)-j_l'(x)n_l(x)\right]=\frac{j}{x^2}$$

(1015)

Now one determines a rather simple result,

$$A_{lm}=jk$$

(1016)

Where the desired spherical harmonic expansion of the Green's function is given by

using the Green's function

$$\frac{e^{jk|\vec{r}-\vec{r}'|}}{4\pi|\vec{r}-\vec{r}'|}=jk\sum_{l=0}^{\infty}\begin{cases}j_l(kr)h_l^{(1)}(kr') & [r<r']\\ j_l(kr')h_l^{(1)}(kr) & [r>r']\end{cases}\sum_{m=-l}^{l}Y_{lm}(\theta,\phi)Y_{lm}^*(\theta',\phi')$$

(1017)

For a static field $k=0$ (that is $\omega=0$), and one indeed recovers the solution of the electrostatic multipole expansion.

$$\frac{1}{4\pi|\vec{r}-\vec{r}'|}=\begin{cases}\displaystyle\sum_{l=0}^{\infty}\sum_{m=-l}^{l}\frac{1}{2l+1}\frac{(r')^l}{r^{l+1}}Y_{lm}(\theta,\phi)Y_{lm}^*(\theta',\phi'), & r>r'\\[4mm] \displaystyle\sum_{l=0}^{\infty}\sum_{m=-l}^{l}\frac{1}{2l+1}\frac{r^l}{(r')^{l+1}}Y_{lm}(\theta,\phi)Y_{lm}^*(\theta',\phi'), & r<r'\end{cases}$$

(1018)

APPENDIX X

THE GREENS FUNCTION EXPANDED AS A SERIES OF ORTHONORMAL

FUNCTIONS OR MORE COMMONLY KNOWN AS THE BILINEAR FORMULA

The complete set of orthonormal eigenfunction for the Sturm-Liouville operator L satisfies the following differential equation subject to the boundary conditions.

$$\lfloor L + \lambda_n r(x) \rfloor \psi_n(x) = 0 \tag{1019}$$

"In the finite interval $a \leq x \leq b$ the complete set of orthonormal eigenfunctions $\lfloor \psi_n(x) \rfloor$, and their amplitude coefficients must satisfy the orthogonality condition of

$$\int_a^b \psi_m(x)\psi_n(x)r(x)dx = \delta_{nm} = \begin{cases} 1 & m = n \\ 0 & m \neq n \end{cases} \tag{1020}$$

If the Green's function exists, it can be represented in series form in terms of the orthonormal eigenfunctions $\{\psi_n(x)\}$ as

$$G(x,x') = \sum_n a_n(x')\psi_n(x) \tag{1021}$$

Where $a_n(x')$ are the amplitude coefficients. These can be obtained by multiplying both sides of (1021) $\psi_n(x)r(x)$, integrating from a to b, and the using (1020). It can be shown that

$$a_n(x') = \int_a^b G(x,x')\psi_n(x)r(x)dx \tag{1022}$$

Since $G(x,x')$ satisfies (956) and $\psi_n(x)$ satisfies (1019) then by multiplying (956) by $\psi_n(x)$, (1019) by $G(x,x')$, and then subtracting the two one can obtain

$$\psi_n(x)LG(x,x') - G(x,x')L\psi_n(x) = -(\lambda - \lambda_n)G(x,x')\psi_n(x)r(x) + \delta(x-x')\psi_n(x) \tag{1023}$$

Integrating (1023) between a and b, we can write that

$$\int_a^b \left[\psi_n(x)LG(x,x') - G(x,x')L\psi_n(x) \right]dx = $$
$$-(\lambda - \lambda_n)\int_a^b G(x,x')\psi_n(x)r(x)dx + \int_a^b \delta(x-x')\psi_n(x)dx \tag{1024}$$

Which by using (1022) reduces to

$$\int_a^b \left[\psi_n(x)LG(x,x') - G(x,x')L\psi_n(x) \right]dx = -(\lambda - \lambda_n)a_n(x') + \psi_n(x') \tag{1025}$$

By the symmetrical (Hermitian) property of the operator L [65]. Therefore (1025) reduces to

$$-\left(\lambda - \lambda_n\right)a_n\left(x'\right)+\psi_n\left(x'\right)=0 \tag{1026}$$

And therefore,

$$a_n\left(x'\right)=\frac{\psi_n\left(x'\right)}{\left(\lambda - \lambda_n\right)} \tag{1027}$$

Thus, the series form of the Green's function (1021) can ultimately be expressed as" [152]

$$G\left(x,x'\right)=\sum_n \frac{\psi_n\left(x'\right)\psi_n\left(x\right)}{\left(\lambda - \lambda_n\right)} \tag{1028}$$

Where $\lfloor\psi_n\left(x\right)\rfloor$ represents a complete set of orthonormal eigenfunctions for the Sturm-Liouville operator L, which satisfies the differential equation subject to the boundary conditions. This is commonly referred to the bilinear formula.

APPENDIX XI

RELATION OF SPHERICAL RANDOM ARRAY MOMENTS AND SPHERICAL ANNULAR ARRAYS TO THE PERIODIC TABLE AND HYDROGEN LIKE ATOMS

XI.I Atomic Orbitals of the Hydrogen like Atoms

The hydrogen like atoms are similar in respect to the spherical random array moments discussed thus far. I.e. the hydrogen like atom consists of a single nucleus of charge Ze and a single electron with negative charge, $-e$. The exception to this rule is the actual hydrogen atom, which is neutral. Moreoever, some of the common examples are $He^+, Li^{2+}, Be^{3+}, B^{4+}, \dots$. Solutions of these hydrogen like atomic orbitals are found using Schrodinger's equation under the specification that hydrogen-like atoms are two particle systems causing with induced interactions depending on the non-relatisitic distance. An example of the hydrogen like orbitals is found in Figure 293 and demonstrate the increasing energy levels found in the periodic table. Furthermore these orbital solutions are eigenfunctions of the one electron angular operator L in its z component L_z. Though this eigenvalue does not quantify the energy level of the atom; the principal quantum number n, however does. Nonetheless, the Hydrogen like atomic orbital is uniquely defined by the angular quantum number l, mangetic quantum number m and the principal quantum number n defining its energy level. "The Schrodinger equation of atoms or atomic ions with more than one electron has not been solved analytically, because of the computational difficulty imposed by the Coulomb interaction between electrons." [224]
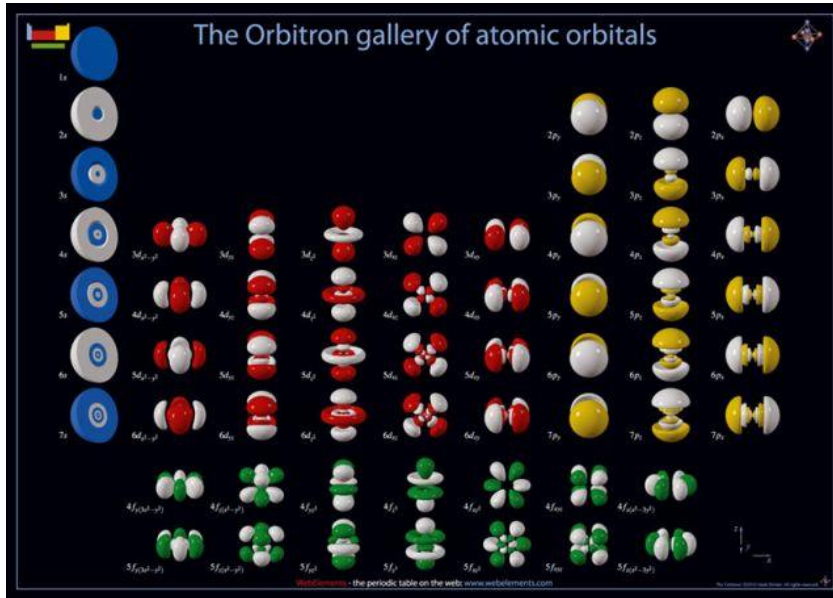
Figure 293. Example of the atomic orbitals found in the periodic table. [225]

To solve for the solutions of the hydrogen like atoms one firsts begins with Schrodinger's equation for specific Hamiltonians $\hat{H}$.

$$j\hbar\frac{\partial}{\partial t}\psi(\vec{r},t)=\hat{H}\psi(\vec{r},t)$$ (1029)

This solution is simplified by assuming a time independent solution in the absence of an external field as (1030) and is obtained by letting $\psi(\vec{r},t)\rightarrow e^{-jEt/\hbar}\psi(\vec{r})$

$$\hat{H}\psi(\vec{r})=E\psi(\vec{r})$$ (1030)

The Hamiltonian of a single-particle non-relativistic case now takes the form

$$\hat{H}=-\frac{\hbar^2}{2m_e}\nabla^2-\frac{Ze^2}{4\pi\varepsilon_0 r'}$$ (1031)

Now similar to the monopole multipole moment we derive the solutions to the Schrodinger equation of hydrogen-like atomic orbitals in a spherically symmetric potential. For instance, the potential term is (1032) similar to the first term in the spherical multipole expansion (1033).

$$V(r)=-\frac{1}{4\pi\varepsilon_0}\frac{Ze^2}{r}$$ (1032)

$$V(\vec{r})=\frac{1}{4\pi\varepsilon_0}$$ (1033)

394

Now similar to antenna theory we find the solution to these wave function by means of separation of variables

$$\psi(r,\theta,\phi)=R(r)Y_{lm}(\theta,\phi) \tag{1034}$$

And to solve this in spherical coordinates one first needs to define the kinetic energy operator as (1035) and next utilizing the solution of the spherical harmonics in (1036)

$$\frac{\hat{p}^2}{2m_0}=-\frac{\hbar^2}{2m_0}\nabla^2=-\frac{\hbar^2}{2m_0}\left[\frac{\partial}{\partial r}\left(r^2\frac{\partial}{\partial r}\right)-\hat{l}^2\right] \tag{1035}$$

$$\hat{l}^2Y_{lm}(\theta,\phi)\equiv\left\{-\frac{1}{\sin^2\theta}\left[\sin\theta\frac{\partial}{\partial\theta}\left(\sin\theta\frac{\partial}{\partial\theta}\right)+\frac{\partial^2}{\partial\phi^2}\right]\right\}Y_{lm}(\theta,\phi)=l(l+1)Y_{lm}(\theta,\phi) \tag{1036}$$

Substituting these into Schrodinger equation one obtains the one-dimensional eigenvalue equation (1037)

$$\left[-\frac{\hbar^2}{2\mu}\left(\frac{1}{r^2}\frac{\partial}{\partial r}\left(r^2\frac{\partial}{\partial r}(R(r))\right)-\frac{l(l+1)R(r)}{r^2}\right)+V(r)R(r)\right]=ER(r)$$

$$E_n=-\left(\frac{Z^2\mu e^4}{32\pi^2\varepsilon_0^2\hbar^2}\right)\frac{1}{n^2}=-\left(\frac{Z^2\hbar^2}{2\mu\varepsilon_0^2}\right)\frac{1}{n^2} \tag{1037}$$

$$\mu=\frac{m_N m_e}{m_N+m_e}$$

More importantly the solution to the wave equation of (1034) differs from the solution to the plane wave equation presented in this work since a third eigenvalue n ($n>0$) emerges from the boundary conditions imposed on R. Thus, the final expressions for the position of a hydrogen atom of the radial solution R and angular solution Y that solve the equations above in spherical coordinates, which depend on integer values of quantum numbers are provided in normalized final form given as

$$\psi_{nlm}(r,\theta,\phi)=R_{nl}(r)Y_{lm}(\theta,\phi)$$

$$\psi_{nlm}(r,\theta,\phi)=\sqrt{\left(\frac{2}{na_0}\right)^3\frac{(n-l-1)!}{2n(n+l)!}}e^{-\frac{2r}{na_0}\frac{1}{2}}\left(\frac{2r}{na_0}\right)^l L_{n-l-1}^{2l+1}\left(\frac{2r}{na_0}\right)Y_{lm}(\theta,\phi)$$

$$=\sqrt{\left(\frac{2}{na_0}\right)^3\frac{(n-l-1)!}{2n(n+l)!}}e^{-\frac{\rho}{2}}\rho^l L_{n-l-1}^{2l+1}(\rho)Y_{lm}(\theta,\phi)$$

$$\rho=\frac{2r}{na_0}, \tag{1038}$$

$$a_0=\frac{4\pi\varepsilon_0\hbar^2}{me^2}=\frac{\hbar}{m_e c\alpha}\text{Bohr radius}$$

$L_{n-l-1}^{2l+1}(\rho)=$ generalized Laguerre polynomials of degree n-l-1

$\hbar=$ reduced Plank's onstant

$m_e=$ electron mass at rest

c=speed of light

$\alpha=$ fine structure constant

Where the mass of an electron at rest is actually a reduced mass of the system, which consists of both the electron and the nucleus. Lastly it was previously states that the angular momentum operator operates on the z component. In other words the angular momentum $\boldsymbol{L}$ is a vector operator with eigenvalues of its square $L^2 = L_x^2 + L_y^2 + L_z^2$ provided by (1039). Also if this vector is projected onto an arbitrary direction it is quantized and nominally the z is given by (1040)

$$L^2 Y_{lm}(\theta, \phi) = \hbar^2 l(l+1) Y_{lm} \tag{1039}$$

$$L_z Y_{lm}(\theta, \phi) = \hbar m Y_{lm} \tag{1040}$$

Last of all L^2 and L_z commute and as a consequence share a common eigenstate, which is in accordance with Heisenberg's uncertainty principle. Otherwise unlike L^2 and L_z, the terms L_x and L_y do not commute with L_z, and because of this it is not possible to find a state that is an eigenstate of all three components simultaneously. More or less in summary the angular momentum of x and y is hard to predict, but z is. Thus, in order to find the total angular momentum of the electron one must also include the electrons spin.

In conclusion, the significance of this chapter has related the solutions of the spherical Helmholtz equation or the unbounded wave function, (plane wave eigenfunctions expressed by the plane wave expansion), similar to the wave functions of the hydrogen like atoms. The only difference in the relations is that a third quantum number n (principle quantum number) defining the energy levels of the atom are included. However, when $n=1$, the solutions are equivalent, which mean there is a wealth of connections towards array theory and quantum mechanics from this point forward. This includes pi and sigma bonds found in organic chemistry as well as shown in Figure 294, which are even quite similar to the dipole patterns of integer wavelength Figure 295.
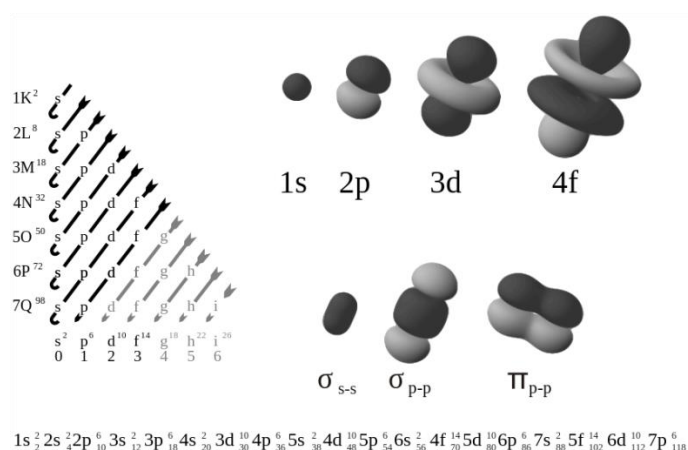

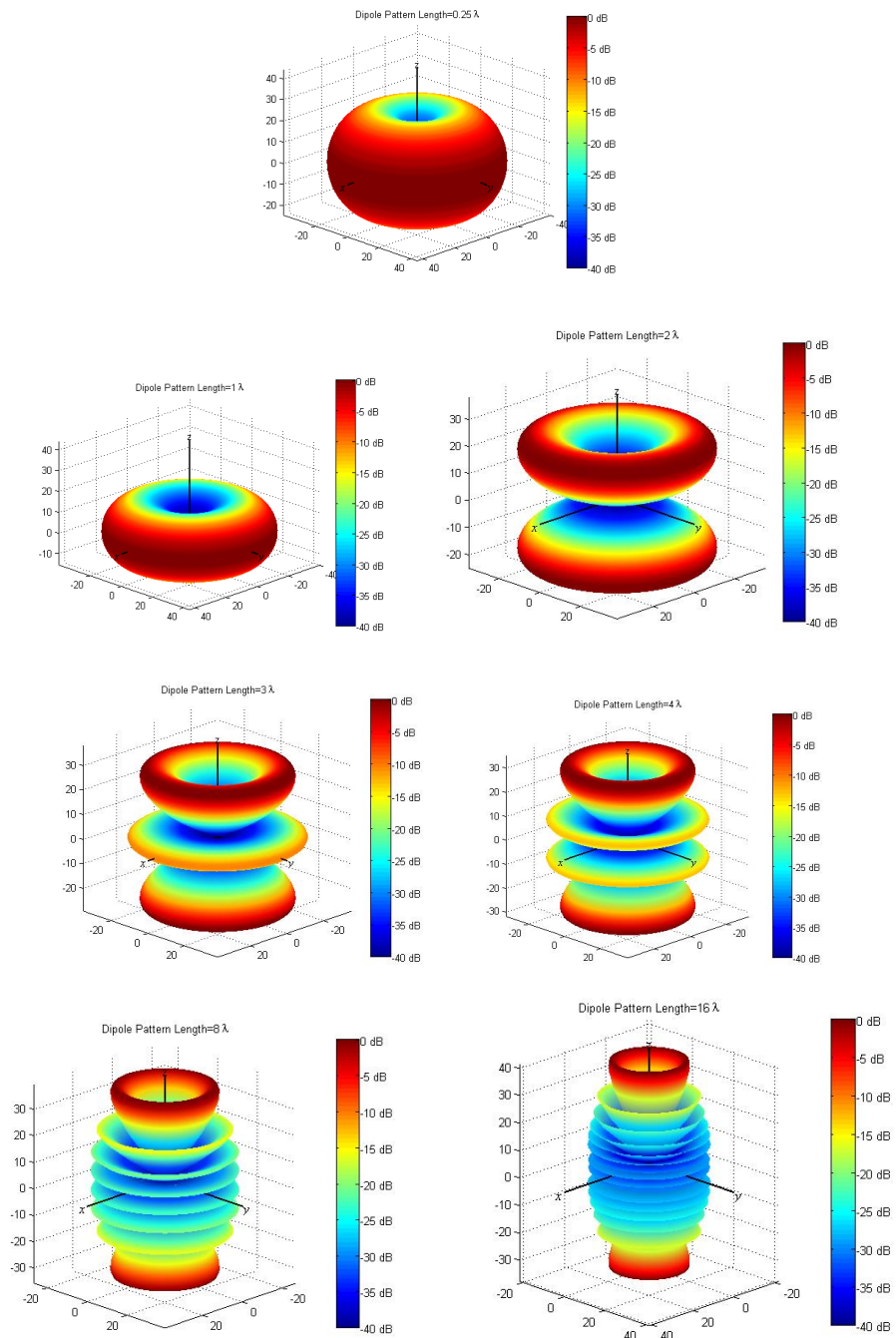Figure 294. Sigma and Pi bonds of the atomic orbitals. [224]

Figure 295. Dipole patterns of integer wavelength.

APPENDIX XII

FINDING CHARACTERISTIC FUNCTIONS WITH MATHEMATICA

To find the characteristic function of a circular random array one may use the following Mathematica command shown in (1041). This command finds the characteristic function of a Wigner semicircle distribution centered at the origin with uniform radius; also in this context known as the characteristic function of a uniformly distributed circular random array.

$$In: \; cf = CharacteristicFunction[WignerSemicircleDistribution[1],t]$$

$$Out: \quad \frac{2BesselJ[1,t]}{t} \tag{1041}$$

Another way of finding the characteristic function may be found in the following fashion. If one knows the mathematical expression of per say a semicircle in the upper half plane then one can define a probability distribution about this region given within (1042). Now once the probability distribution is known the characteristic function is easily found as shown in (1042). The normalization factor is found originally in the marginal distribution function, but in terms of this recipe it is needed for normalizing the distribution such that the joint pdf is uniformly distributed correctly.

$$In: \begin{cases} dist = ProbabilityDistribution[Sqrt[1-x \wedge 2],\{x,-1,1\}] \\ cf = CharacteristicFunction[dist,t] \\ normalizationFactor = 1/Limit[cf,t \to 0] \end{cases}$$

$$Out: \begin{cases} \left\{ \begin{array}{ll} \sqrt{1-x^2} & -1 < x < 1 \\ 0 & True \end{array} \right\} \\ \dfrac{\pi BesselJ[1,t]}{t} \\ \dfrac{2}{\pi} \end{cases} \tag{1042}$$

A marginal Distribution of a uniformly distributed circle can also be found using the following command.

$$In: \begin{cases} PDF[MarginalDistribution[\\ ProbabilityDistribution[\\ \quad 1/Pi,\{x[1],-1,1\},\{x[2], \\ -Sqrt[1-x[1] \wedge 2],Sqrt[1-x[1] \wedge 2]\}],\{2\}],\{y\}] \end{cases}$$

$$Out: \left\{ \begin{array}{ll} \dfrac{2\sqrt{1-y^2}}{\pi} & -1 < y < 1 \\ 0 & True \end{array} \right. \tag{1043}$$

APPENDIX XIII

FINDING THE INVERSE FOURIER TRANSFORM OF RANDOM ARRAYS USING

THE RADON TRANSFORM

For the case a receiver receives a beampattern at some base station it may have interest to convert this pattern to its probability density function. The Radon transform is the appropriate transform for this application. The Radon transform is an integral transform whose inverse is used to reconstruct images [149]-[151]. The Radon transform is defined as (1044) where ρ is the slope of a line and τ is its intercept.

$$R(\rho,\tau)\big[f(x,y)\big] = \int_{-\infty}^{\infty} f(x,\tau+px)dx = \int_{-\infty}^{\infty}\int_{-\infty}^{\infty} f(x,y)\delta\big[y-(\tau+px)\big]dydx \tag{1044}$$

The Radon transform is widely applicable to tomography, the creation of an image from the scattering data associated to cross-sectional scans of an object. This is also known as imaging by sections or sectioning, through the use of any kind of penetrating wave. An example of this is shown in Figure 296.
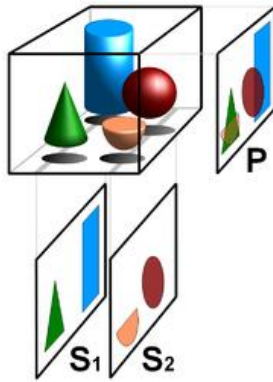

Figure 296. Radon transform. [149]

The probability density function of a uniformly distributed circle can be found using the radon transform given that a beampattern be uniformly distributed upon the receiver shown in Figure 8. This mathematics to this description is done in the following method.

Let a two dimensional cylinder function be defined by

$$f(x,y) = \begin{cases} 1 \ for \ r < R \\ 0 \ for \ r > R \end{cases} \tag{1045}$$

399

Then the Radon transform is given by (1046) and in the same process shown in [149] this becomes(1047). Upon converting $\rho = \cot \alpha$ one obtains(1048) and multiplying by the Joint PDF one obtains the Wigner Semicircle distribution of uniform radius (1049) shown in Figure 297.
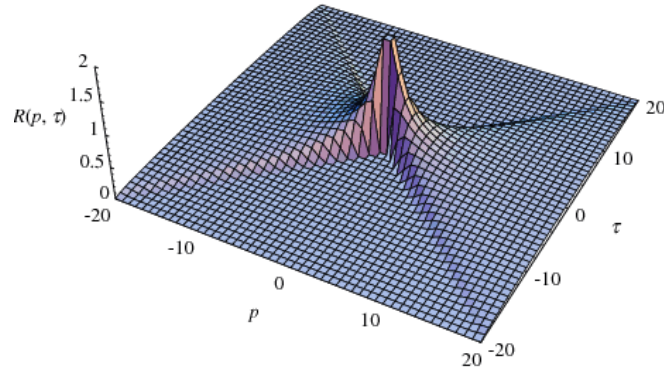

Figure 297. Uniformly distributed circular beam. [149]

$$R(\rho,\tau) = \int_{-\infty}^{\infty}\int_{-\infty}^{\infty} f(x,y)\delta(y-(\tau+px))dydx \qquad (1046)$$

$$R(\rho,\tau) = \begin{cases} \dfrac{2}{1+\rho^2}\sqrt{R^2(1+\rho^2)-\tau^2} & for\ \tau^2 < R^2(1+\rho^2) \\ 0\ otherwise \end{cases} \qquad (1047)$$

$$R'(r,\alpha) = 2\sqrt{R^2-r^2} \qquad (1048)$$

$$f(x,y)R'(r,\alpha) = \frac{1}{\pi}2\sqrt{R^2-r^2} \qquad (1049)$$

Similarly, a square radiation pattern (1051) is shown in Figure 298. Applying the Radon transform(1046) to this pattern gives (1050). Then like the previous case, a uniform distribution is found by multiplying by the Joint PDF (1053) giving (1054) (the probability density function of a box of unit length).
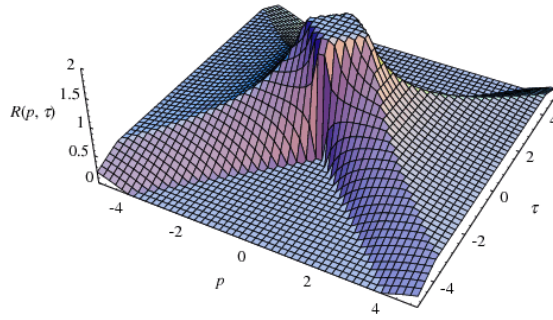
Figure 298. Uniformly distributed square beam. [149]

$$f(x,y) = \begin{cases} 1 \ for \ x,y \in [-a,a] \\ 0 \ otherwise \end{cases} \tag{1051}$$

$$R(1,1) = 2a \tag{1052}$$

$$f(x,y) = \frac{1}{4} \tag{1053}$$

$$f(x) = \frac{1}{4}r(1,1) = \frac{a}{2} = \frac{1}{2}\bigg|_{a=1} \tag{1054}$$

APPENDIX XIV

ZERNIKE POLYNOMIALS

The solutions of the Zernike poynomials are showin in Figure 299-Figure 306.

XIV.1 Order 0 {Piston}

$$\int_0^r \int_0^{2\pi} e^{jr\cos(\theta)u} r\, dr\, d\theta = \frac{2\pi J_1(u)}{u} \tag{1055}$$
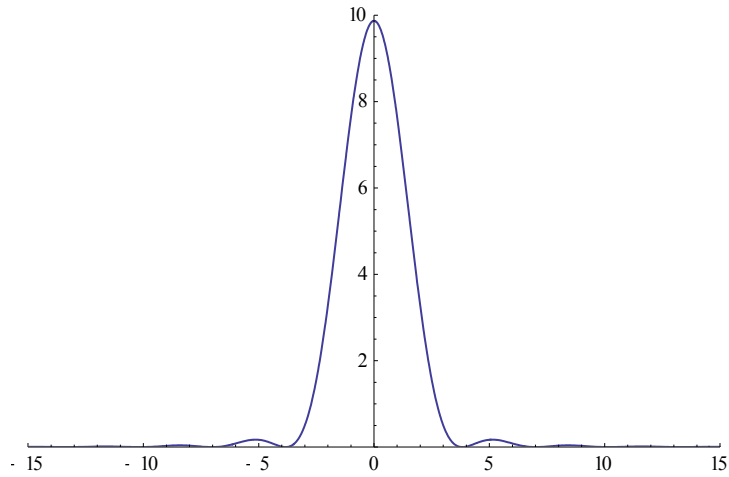

Figure 299. Order 0 {Piston}.

XIV.2 Order 1 {Tilt}

$$\int_0^r \int_0^{2\pi} 2r\sin(\theta) e^{jr\cos(\theta)u} r\, dr\, d\theta = 0 \tag{1056}$$

$$\int_0^r \int_0^{2\pi} 2r\cos(\theta) e^{jr\cos(\theta)u} r\, dr\, d\theta = \frac{4\pi j J_2(u)}{u} \tag{1057}$$
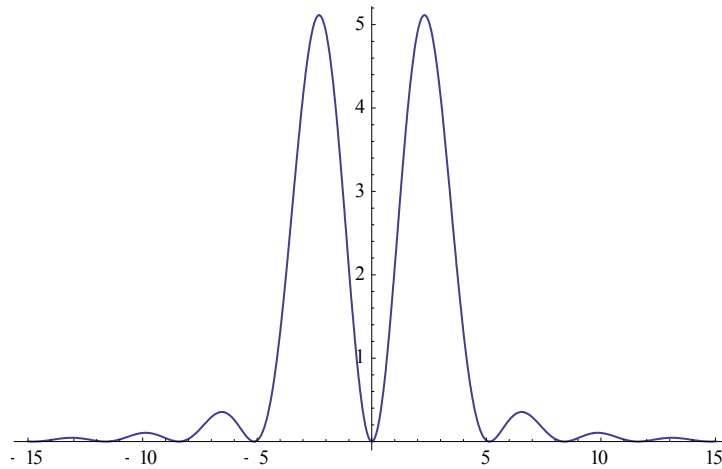
Figure 300. Order 1 {Tilt}.

XIV.3 Order 2 {Defocus, Astigmatism}

$$\int_0^r \int_0^{2\pi} \sqrt{6}\, r^2 \sin(2\theta) e^{jr\cos(\theta)u}\, r\, dr\, d\theta = 0 \tag{1058}$$

$$\int_0^r \int_0^{2\pi} \sqrt{3}\left(2r^2-1\right) e^{jr\cos(\theta)u}\, r\, dr\, d\theta = -2\sqrt{3}\pi \frac{J_3(u)}{u} \tag{1059}$$

$$\int_0^r \int_0^{2\pi} \sqrt{6}\, r^2 \cos(2\theta) e^{jr\cos(\theta)u}\, r\, dr\, d\theta = -2\sqrt{6}\pi \frac{J_3(u)}{u} \tag{1060}$$
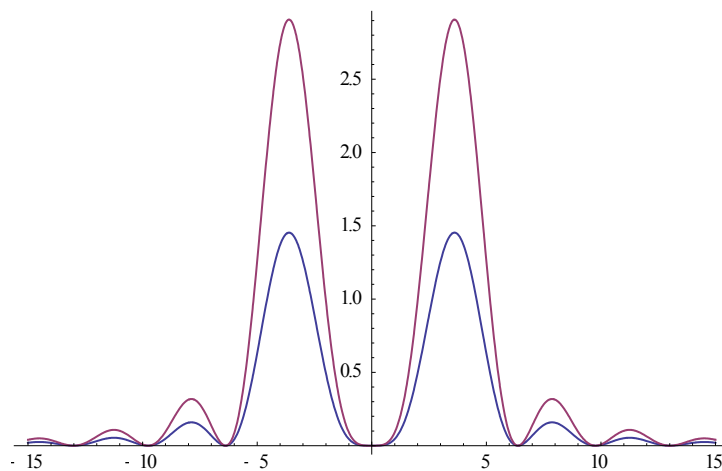

Figure 301. Order 2 {Defocus, astigmatism}.

XIV.4 Order 3{Coma, Trefoil}

$$\int_0^r \int_0^{2\pi} \sqrt{8}\, r^3 \sin(3\theta) e^{jr\cos(\theta)u}\, rdrd\theta = 0 \tag{1061}$$

$$\int_0^r \int_0^{2\pi} 8\left(3r^3 - 2r\right)\sin(\theta) e^{jr\cos(\theta)u}\, rdrd\theta = 0 \tag{1062}$$

$$\int_0^r \int_0^{2\pi} \sqrt{8}\left(3r^3 - 2r\right) e^{jr\cos(\theta)u}\, rdrd\theta = -4j\sqrt{2}\pi \frac{J_4(u)}{u} \tag{1063}$$

$$\int_0^r \int_0^{2\pi} \sqrt{8}\, r^3 \cos(3\theta) e^{jr\cos(\theta)u}\, rdrd\theta = -4j\sqrt{2}\pi \frac{J_4(u)}{u} \tag{1064}$$
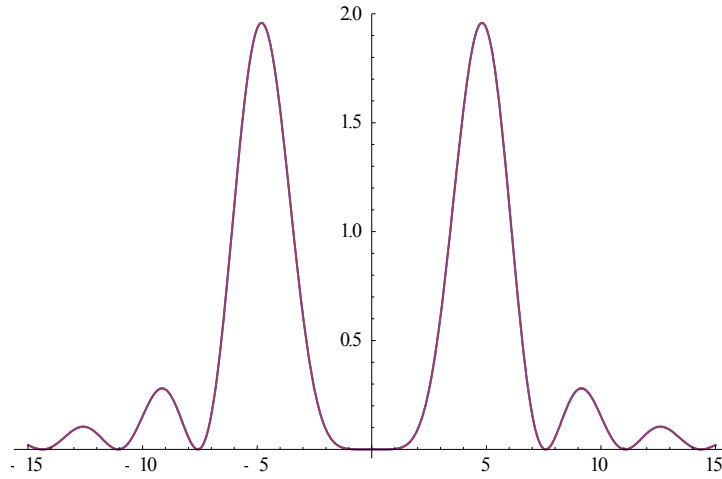

Figure 302. Order 3{Coma, trefoil}.

XIV.5 Order 4{Spherical, Secondary, Astigmatism, Tetrafoil}

$$\int_0^r \int_0^{2\pi} \sqrt{10}\, r^4 \sin(4\theta) e^{jr\cos(\theta)u}\, rdrd\theta = 0 \tag{1065}$$

$$\int_0^r \int_0^{2\pi} \sqrt{10}\left(4r^4 - 3r^2\right)\sin(2\theta) e^{jr\cos(\theta)u}\, rdrd\theta = 0 \tag{1066}$$

$$\int_0^r \int_0^{2\pi} \sqrt{5}\left(6r^4 - 6r^2 + 1\right) e^{jr\cos(\theta)u}\, rdrd\theta = \frac{2\sqrt{5}\pi\left(u\left(-48 + u^2\right)\right)J_1(u) - 12\left(-16 + u^2\right)J_2(u)}{u^4} \tag{1067}$$

$$\int_0^r \int_0^{2\pi} \sqrt{10}\left(4r^4 - 3r^2\right)\cos(2\theta) e^{jr\cos(\theta)u}\, rdrd\theta = \frac{2\sqrt{10}\pi J_5(u)}{u} \tag{1068}$$

$$\int\limits_0^r\int\limits_0^{2\pi}\sqrt{10}\,r^4\cos(4\theta)e^{jr\cos(\theta)u}\,rdrd\theta=\frac{2\sqrt{10}\pi J_5(u)}{u}\qquad(1069)$$
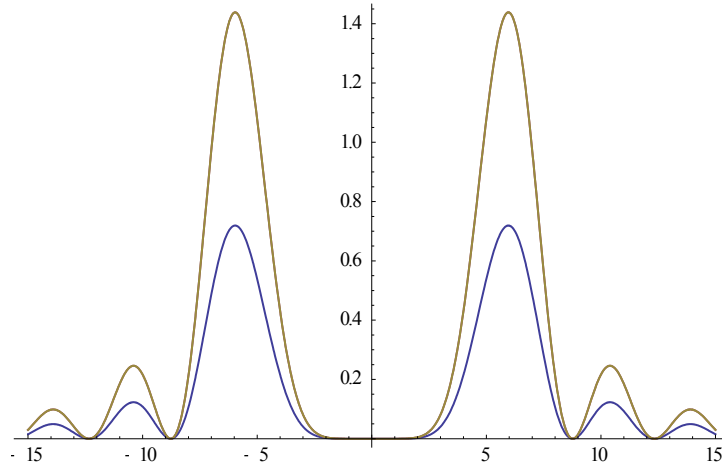

Figure 303. Order 4{Spherical, secondary, astigmatism, tetrafoil}.

XIV.6 Order 5 {Secondary Coma, Secondary Trefoil, Pentafoil}

$$\int\limits_0^r\int\limits_0^{2\pi}\sqrt{12}\,r^5\sin(5\theta)e^{jr\cos(\theta)u}\,rdrd\theta=0\qquad(1070)$$

$$\int\limits_0^r\int\limits_0^{2\pi}\sqrt{12}\left(5r^5-4r^3\right)\sin(3\theta)e^{jr\cos(\theta)u}\,rdrd\theta=0\qquad(1071)$$

$$\int\limits_0^r\int\limits_0^{2\pi}\sqrt{12}\left(10r^5-12r^3+3r\right)\sin(\theta)e^{jr\cos(\theta)u}\,rdrd\theta=0\qquad(1072)$$

$$\int\limits_0^r\int\limits_0^{2\pi}\sqrt{12}\left(10r^5-12r^3+3r\right)\cos(\theta)e^{jr\cos(\theta)u}\,rdrd\theta=\frac{4j\sqrt{3}\pi\left(u\left(\frac{-80+}{u^2}\right)J_2(u)-16\left(\frac{-30+}{u^2}\right)J_3(u)\right)}{u^4}\qquad(1073)$$

$$\int\limits_0^r\int\limits_0^{2\pi}\sqrt{12}\left(5r^5-4r^3\right)\cos(3\theta)e^{jr\cos(\theta)u}\,rdrd\theta=\frac{4j\sqrt{3}\pi J_6(u)}{u^4}\qquad(1074)$$

$$\int\limits_0^r\int\limits_0^{2\pi}\sqrt{12}\,r^5\cos(5\theta)e^{jr\cos(\theta)u}\,rdrd\theta=\frac{4j\sqrt{3}\pi J_6(u)}{u^4}\qquad(1075)$$
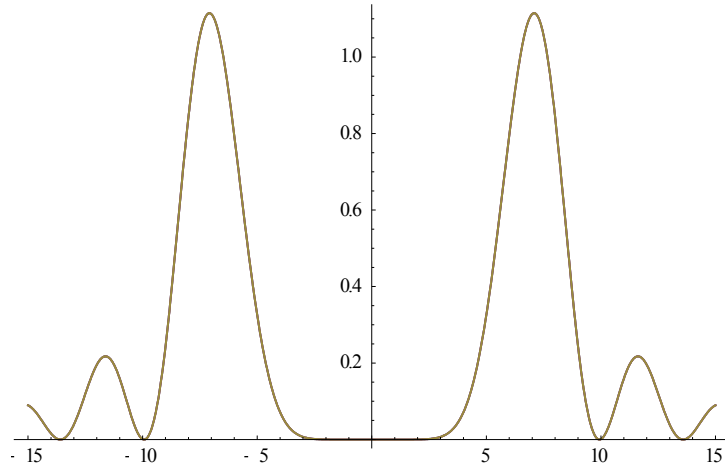
Figure 304. Order 5 {Secondary coma, secondary trefoil, pentafoil}.

XIV.7 Order 6 {Secondary Spherical, Trimary Astigmatism, Secondary Tetrafoil, Hexafoil}

$$\int_0^r \int_0^{2\pi} \sqrt{14}\, r^6 \sin(6\theta) e^{jr\cos(\theta)u}\, r dr d\theta = 0 \tag{1076}$$

$$\int_0^r \int_0^{2\pi} \sqrt{14}\left(6r^6 - 5r^4\right)\sin(4\theta) e^{jr\cos(\theta)u}\, r dr d\theta = 0 \tag{1077}$$

$$\int_0^r \int_0^{2\pi} \sqrt{14}\left(15r^6 - 20r^4 + 6r^2\right)\sin(2\theta) e^{jr\cos(\theta)u}\, r dr d\theta = 0 \tag{1078}$$

$$\int_0^r \int_0^{2\pi} \sqrt{7}\left(20r^6 - 30r^4 + 12r^2 - 1\right) e^{jr\cos(\theta)u}\, r dr d\theta =$$

$$\frac{2\sqrt{7}\pi\left(u\left(5760 - 240u^2 + u^4\right)J_1(u) - 24\left(960 - 80u^2 + u^4\right)J_2(u)\right)}{u^6} \tag{1079}$$

$$\int_0^r \int_0^{2\pi} \sqrt{14}\left(15r^6 - 20r^4 + 6r^2\right)\cos(2\theta) e^{jr\cos(\theta)u}\, r dr d\theta =$$

$$\frac{-2\sqrt{14}\pi\left(u\left(-120 + u^2\right)J_3(u) - 20\left(-48 + u^2\right)J_4(u)\right)}{u^4} \tag{1080}$$

$$\int_0^r \int_0^{2\pi} \sqrt{14}\left(6r^6 - 5r^4\right)\cos(4\theta) e^{jr\cos(\theta)u}\, r dr d\theta =$$

$$\frac{-2\sqrt{14}\pi\left(u\left(-48 + u^2\right)J_2(u) - 20\left(5760 - 240u^2 + u^4\right)J_3(u)\right)}{u^5} \tag{1081}$$

406

$$\int_0^r \int_0^{2\pi} \sqrt{14}\, r^6 \cos(6\theta) e^{jr\cos(\theta)u}\, r\, dr\, d\theta =$$

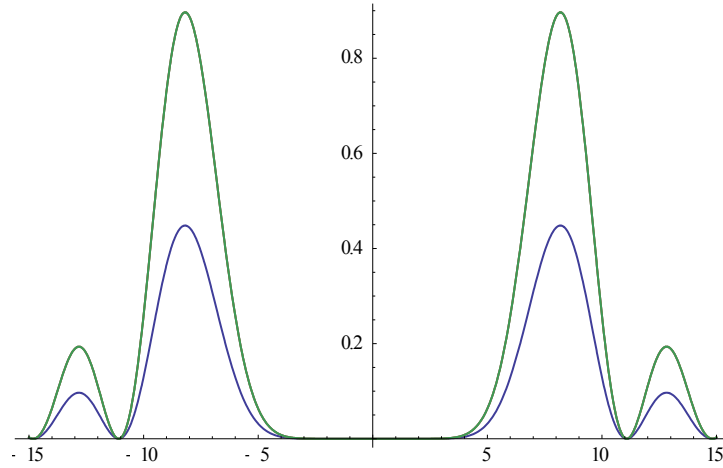$$\frac{-2\sqrt{14}\pi\left(u\left(-120+u^2\right)J_3(u)-20\left(-48+u^2\right)J_4(u)\right)}{u^4} \tag{1082}$$

Figure 305. Order 6 {Secondary spherical, trimary astigmatism, secondary tetrafoil, hexafoil}.

XIV.8 Order 7 {Trimary Coma, Trimary Astigmatism, Secondary Tetrafoil, Heptafoil}

$$\int_0^r \int_0^{2\pi} 4r^7 \sin(7\theta) e^{jr\cos(\theta)u}\, r\, dr\, d\theta = 0 \tag{1083}$$

$$\int_0^r \int_0^{2\pi} 4\left(7r^7-6r^5\right)\sin(5\theta) e^{jr\cos(\theta)u}\, r\, dr\, d\theta = 0 \tag{1084}$$

$$\int_0^r \int_0^{2\pi} 4\left(21r^7-30r^5+10r^3\right)\sin(3\theta) e^{jr\cos(\theta)u}\, r\, dr\, d\theta = 0 \tag{1085}$$

$$\int_0^r \int_0^{2\pi} 4\left(35r^7-60r^5+30r^3-4r\right)\sin(\theta) e^{jr\cos(\theta)u}\, r\, dr\, d\theta = 0 \tag{1086}$$

$$\int_0^r \int_0^{2\pi} 4\left(35r^7-60r^5+30r^3-4r\right)\cos(\theta) e^{jr\cos(\theta)u}\, r\, dr\, d\theta =$$

$$\frac{8j\pi\left(u\left(13440-360u^2+u^4\right)J_2(u)-30\left(2688-128u^2+u^4\right)J_3(u)\right)}{u^6} \tag{1087}$$

$$\int_0^r \int_0^{2\pi} 4\left(21r^7 - 30r^5 + 10r^3\right)\cos\left(3\theta\right)e^{jr\cos(\theta)u}\,r\,dr\,d\theta =$$

$$-\frac{8j\pi\left(u\left(-168+u^2\right)J_4\left(u\right)-24\left(-70+u^2\right)J_5\left(u\right)\right)}{u^4} \tag{1088}$$

$$\int_0^r \int_0^{2\pi} 4\left(7r^7 - 6r^5\right)\cos\left(5\theta\right)e^{jr\cos(\theta)u}\,r\,dr\,d\theta =$$

$$-\frac{8j\pi\left(24u\left(-70+u^2\right)J_3\left(u\right)+\left(13440-360u^2+u^4\right)J_4\left(u\right)\right)}{u^5} \tag{1089}$$

$$\int_0^r \int_0^{2\pi} 4r^7 \cos\left(7\theta\right)e^{jr\cos(\theta)u}\,r\,dr\,d\theta =$$

$$-\frac{8j\pi\left(u\left(-168+u^2\right)J_4\left(u\right)-24\left(-70+u^2\right)J_5\left(u\right)\right)}{u^4} \tag{1090}$$
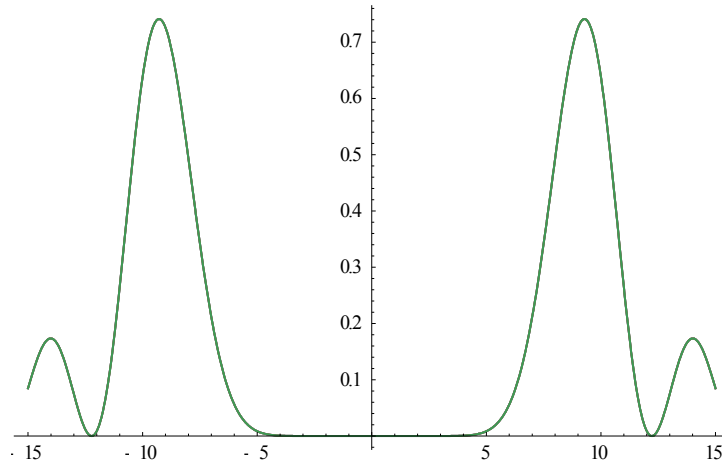

Figure 306. Order 7 {Trimary coma, trimary astigmatism, secondary tetrafoil, heptafoil}.

APPENDIX XV

PROBABLITY DISTRIBUTION CHARTS

A chart of the univariate distribution and how they are connected is illustrated in Figure 307.
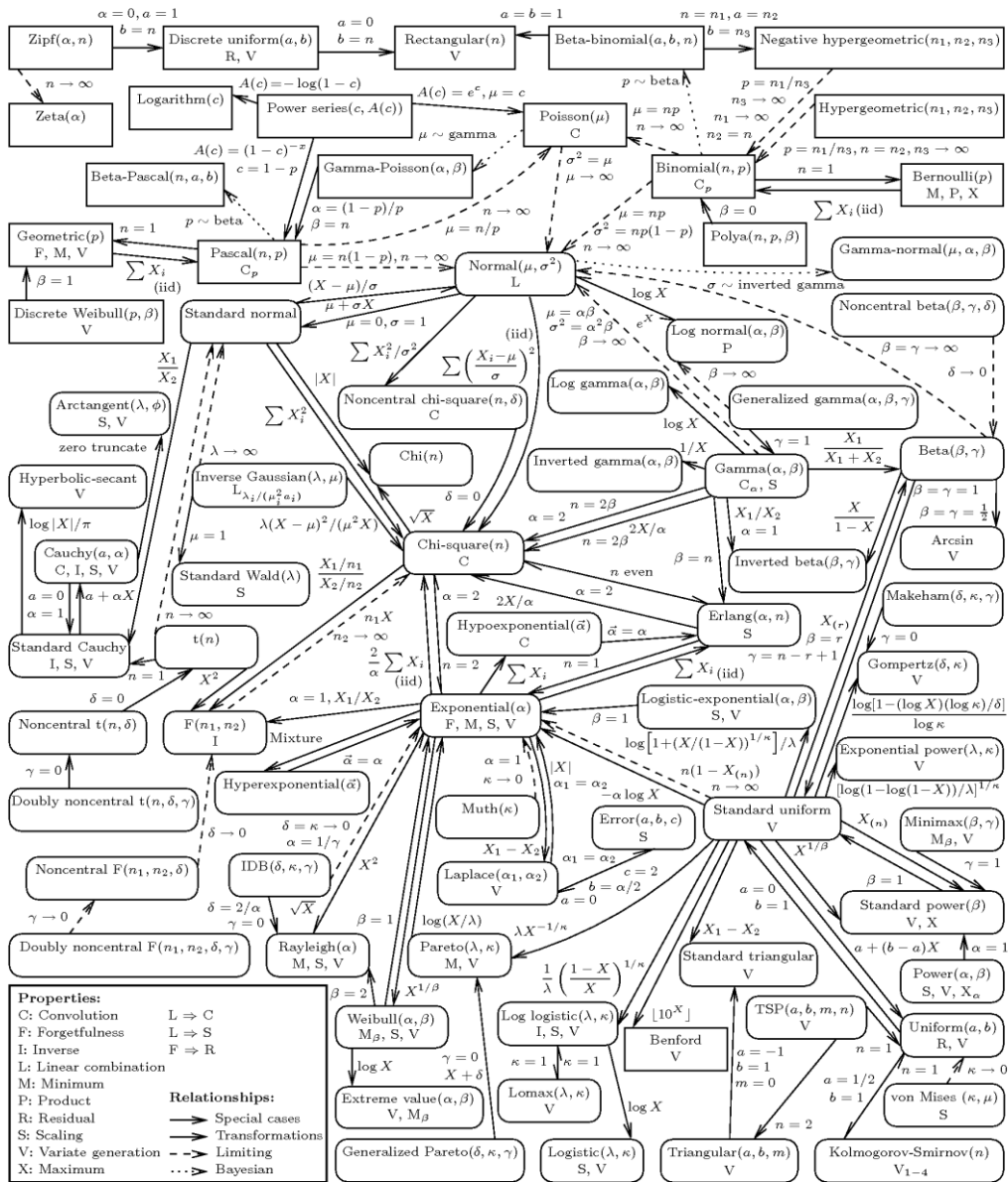
Figure 307. Univariate distribution relationships. [192]

APPENDIX XVI

MATHEMATICAL RELATIONS

XVI.1 Integral Identities

$$\int_{x_1}^{x_2} dx = x_2 - x_1 \tag{1091}$$

$$\int_{-1}^{1}\int_{-1}^{1}\cos\left(\alpha\left(x_n - x_m\right)\right)dx_n dx_m = \left|\frac{2\sin\alpha}{\alpha}\right|^2 = \left|2\mathrm{sinc}(\alpha)\right|^2 \tag{1092}$$

$$\int_{-1}^{1}\int_{-1}^{1}\sin\alpha x_n \sin\alpha x_m dx_n dx_m = 0 \tag{1093}$$

$$\int_{-1}^{1}\int_{-1}^{1}\int_{-1}^{1}\int_{-1}^{1}\left(\cos\left(\alpha\left(x_n - x_m\right) + \beta(\theta,\phi)\left(x_n - x_m\right)\right)\right)dx_n dx_m dx_n dx_m =$$
$$\left|2\frac{\sin\alpha}{\alpha}\right|^2 \left|2\frac{\sin\beta}{\beta}\right|^2 = \left|2\mathrm{sinc}\,\alpha\right|^2 \left|2\mathrm{sinc}\,\beta\right|^2 \tag{1094}$$

$$\frac{2}{\pi}\int_{-1}^{1}\sqrt{1 - x_n^2}\,dx_n = 1 \tag{1095}$$

$$J_{\upsilon}(z) = \frac{\left(\dfrac{z}{2}\right)^{\upsilon}}{\Gamma\left(\upsilon + \dfrac{1}{2}\right)\Gamma\left(\dfrac{1}{2}\right)}\int_{-1}^{1}\left(1 - t^2\right)^{\upsilon - \frac{1}{2}}\cos(zt)\,dt \quad \mathrm{Re}\,\upsilon > -\frac{1}{2} \tag{1096}$$

$$\frac{2}{\pi}\int_{-1}^{1}\left(1 - x^2\right)^{\frac{1}{2}}\cos(xt)\,dx = \frac{2J_1(x)}{x} = 2\mathrm{jinc}(x) \tag{1097}$$

$$\int_{-\pi}^{\pi}e^{-j(nx - \tau\sin x)}d\tau = 2\pi J_n \tag{1098}$$

$$J_{2n}(x) = \frac{2}{\pi}\int_{0}^{\frac{\pi}{2}}\cos(x\sin\phi)\cos(2n\phi)\,d\phi \tag{1099}$$

$$\int_{-\pi}^{\pi}e^{-j4\pi A\sin\left(\frac{\phi}{2}\right)\left(x_n - x_m\right)}d\phi = 2\pi J_o\left(4\pi A\left(x_n - x_m\right)\right) \tag{1100}$$

$$\Gamma(x) = \int_{0}^{\infty}x^{x-1}e^{-z}dz \tag{1101}$$

$$\frac{1}{2}\beta(x,y) = \frac{\Gamma(x)\Gamma(y)}{2\Gamma(x+y)} = \int_{0}^{\pi/2}\cos^{2x-1}(\theta)\sin^{2y-1}(\theta)\,d\theta \tag{1102}$$

$$\int_0^\pi \left(\sin\frac{\phi}{2}\right)^{2m} d\phi = \int_{-\pi}^0 \left(\sin\frac{\phi}{2}\right)^{2m} d\phi = \frac{\sqrt{\pi}\,\Gamma\left(m+\frac{1}{2}\right)}{\Gamma(m+1)} \tag{1103}$$

$$\int_{-\pi}^{\pi} \sin^{2m}(\theta)d\theta = \frac{4\sqrt{\pi}\,\Gamma\left(m+\frac{1}{2}\right)}{2\Gamma(m+1)} = \frac{2\sqrt{\pi}\,\Gamma\left(m+\frac{1}{2}\right)}{\Gamma(m+1)} \tag{1104}$$

$$\int_{-\pi}^{\pi} \left(2\mathrm{jinc}\left(x\sin\frac{\phi}{2}\right)\right)^2 d\phi = \sum_{m=0}^{\infty} 2^3 \frac{\Gamma\left(m+\frac{1}{2}\right)\Gamma\left(m+\frac{3}{2}\right)}{\Gamma(m+3)\Gamma(m+2)\Gamma(m+1)} \frac{\left(-1x^2\right)^m}{m!}$$

$$= \sum_{m=0}^{\infty} 8\frac{\pi}{4} \frac{\left(\frac{1}{2}\right)^{(m)}\left(\frac{3}{2}\right)^{(m)}}{(1)^{(m)}(2)^{(m)}(3)^{(m)}} \frac{\left(-1x^2\right)^m}{m!} = 2\pi\,{}_2F_3\left(\frac{1}{2},\frac{3}{2};1,2,3;-\left(x^2\right)\right) \tag{1105}$$

$$\int_x^{\infty} \frac{1}{\sqrt{2\pi}} e^{\frac{-x^2}{2}} = Q(x) \tag{1106}$$

$$\int_{-\infty}^{\infty} e^{j\alpha z} \frac{1}{\sqrt{2\pi}\sigma} e^{\frac{-z^2}{2\sigma^2}} dz = e^{\frac{-\alpha^2\sigma^2}{2}} \tag{1107}$$

$$\int_{-\pi}^{\pi} \left| e^{-\left(8\pi^2\sin^2\left(\frac{\phi}{2}\right)\right)\sigma^2} \right|^2 d\phi = 2\pi\,{}_1F_1\left(\frac{1}{2};1;-\left(2\pi\sigma\right)^2\right) \tag{1108}$$

$$\int_{-L}^{L} e^{-j\alpha x} \frac{1}{\sqrt{2\pi}\sigma} e^{\frac{-x^2}{2\sigma^2}} dx = e^{\frac{-\alpha^2\sigma^2}{2}}\left[erf\left(\frac{L-j\alpha\sigma^2}{\sqrt{2}\sigma}\right) + erf\left(\frac{L+j\alpha\sigma^2}{\sqrt{2}\sigma}\right)\right] \tag{1109}$$

$$\frac{2}{\pi}\int_{-1}^{1} \sqrt{1-x^2}\,\sin(x\alpha)dx = 0 \tag{1110}$$

$$\frac{2}{\pi}\int_{-1}^{1} \left(\sqrt{1-x^2}\right)\cos^2(x\alpha)dx = \frac{1}{2}\left(1+\frac{J_1(2\alpha(\phi))}{\alpha(\phi)}\right) \tag{1111}$$

$$\frac{2}{\pi}\int_{-1}^{1} \sqrt{1-x^2}\,\sin^2(x\alpha)dx = \frac{1}{2}\left(1-\frac{J_1(2\alpha)}{\alpha}\right) \tag{1112}$$

$$-\frac{2}{\pi}\int_{-1}^{1} \sqrt{1-z^2}\,z^2 dz = -\frac{1}{4} \tag{1113}$$

$$\int_{\left(\frac{-\phi_k}{2}\right)}^{\left(\frac{\phi_k}{2}\right)} 2\mathrm{jinc}\left(4\pi A\sin\left(\frac{\phi-\delta\phi_k}{2}\right)\right)\frac{1}{2\phi_k} d\delta\phi_k =$$

$$\frac{1}{2}\left(1-\frac{\phi}{\phi_k}\right){}_1F_2\left(\frac{1}{2};\frac{3}{2},2;-\left(\pi A(\phi-\phi_k)\right)^2\right) + \frac{1}{2}\left(1+\frac{\phi}{\phi_k}\right){}_1F_2\left(\frac{1}{2};\frac{3}{2},2;-\left(\pi A(\phi+\phi_k)\right)^2\right) \tag{1114}$$

411

$$\int_{-1}^{1}\left(1-t^2\right)\cos\left(xt\right)dt = \frac{2^{3/2}\sqrt{\pi}J_{3/2}\left(x\right)}{z^{3/2}} = 3\frac{j_1\left(x\right)}{x} = 3\mathrm{tinc}\left(x\right) \tag{1115}$$

$$\int_{-\pi}^{\pi}\left(\frac{j_1\left(z\right)}{z}\right)^2 d\phi = \frac{2\pi}{45}\left[-6\,_1F_2\left(\frac{1}{2};3,\frac{7}{2};-\left(4\pi\tilde{R}\right)^2\right) + \,_1F_2\left(\frac{1}{2};4,\frac{7}{2};-\left(4\pi\tilde{R}\right)^2\right)\right] \tag{1116}$$

$$\int_{-\pi}^{\pi}\left(\frac{j_1\left(z\right)}{z}\right)^2 d\phi = \frac{2\pi}{45}\left[-6\,_1F_2\left(\frac{1}{2};3,\frac{7}{2};-\left(4\pi\tilde{R}\right)^2\right) + \,_1F_2\left(\frac{1}{2};4,\frac{7}{2};-\left(4\pi\tilde{R}\right)^2\right)\right] \tag{1117}$$

$$\frac{3}{4}\int_{-1}^{1}\left(1-x^2\right)\cos^2\left(x\alpha\right)dx = \frac{1}{2}\left(1+\frac{3}{2}\frac{j_1\left(2\alpha\right)}{\alpha}\right) \tag{1118}$$

$$\frac{J_{3/2}\left(2x\right)}{\left(x\right)^{3/2}} = \frac{1}{\sqrt{\pi}}\int_{-1}^{1}\left(1-t^2\right)\cos\left(2xt\right)dt \tag{1119}$$

$$\int_{-1}^{1}\left(1-x^2\right)\sin^2\left(x\alpha\right)dx = \frac{1}{2}\left(1-\frac{3}{2}\frac{j_1\left(2\alpha\right)}{\alpha}\right) \tag{1120}$$

$$-\frac{3}{4}\int_{-1}^{1}\left(1-v^2\right)v^2 dv = -\frac{3}{4}\int_{-\pi/2}^{\pi/2}\cos^3\left(u\right)\sin^2\left(u\right)du = -\frac{1}{5} \tag{1121}$$

$$\frac{1}{64}\int_{-1}^{1}\int_{-1}^{1}\int_{-1}^{1}\int_{-1}^{1}\int_{-1}^{1}\int_{-1}^{1}\cos\left(\alpha\left(x_n-x_m\right)+\beta\left(y_n-y_m\right)+\chi\left(z_n-z_m\right)\right)dx_n dx_m dy_n dy_m dz_n dz_m$$
$$= \left|\mathrm{sinc}\left(x\right)\right|^2\left|\mathrm{sinc}\left(y\right)\right|^2\left|\mathrm{sinc}\left(z\right)\right|^2 \tag{1122}$$

XVI.2 Summation Identities

$$\sum_{m=1}^{N}\sum_{\substack{n=1\\n\neq m}}^{N}e^{j\alpha\left(x_n-x_m\right)} = N\left(N-1\right)\cos\left(\alpha\left(x_n-x_m\right)\right) \tag{1123}$$

$$\sum_{m=1}^{N}\sum_{\substack{n=1\\n\neq m}}^{N}e^{j\alpha\left(x_n-x_m\right)}e^{j\beta\left(y_n-y_m\right)} = N\left(N-1\right)\cos\left(\alpha\left(x_n-x_m\right)+\beta\left(y_n-y_m\right)\right) \tag{1124}$$

$$\sum_{m=1}^{N}\sum_{\substack{n=1\\n\neq m}}^{N}e^{j\alpha\left(x_n-x_m\right)}e^{j\beta\left(y_n-y_m\right)}e^{j\chi\left(z_n-z_m\right)} = N\left(N-1\right)\cos\left(\alpha\left(x_n-x_m\right)+\beta\left(y_n-y_m\right)+\chi\left(z_n-z_m\right)\right) \tag{1125}$$

XVI.3 Trigonometric Identites

1. Sum or difference

$$\sin\left(x+y\right) = \sin x\cos y + \cos x\sin y \tag{1126}$$

$$\sin\left(x-y\right) = \sin x\cos y - \cos x\sin y \tag{1127}$$

$$\cos\left(x+y\right) = \cos x\cos y - \sin x\sin y \tag{1128}$$

$$\cos(x-y)=\cos x\cos y+\sin x\sin y \tag{1129}$$

$$\tan(x+y)=\frac{\tan x+\tan y}{1-\tan x\tan y} \tag{1130}$$

$$\tan(x-y)=\frac{\tan x-\tan y}{1+\tan x\tan y} \tag{1131}$$

$$\sin^2 x+\cos^2 x=1 \tag{1132}$$

$$\tan^2 x-\sec^2 x=-1 \tag{1133}$$

$$\cot^2 x-\csc^2 x=1 \tag{1134}$$

2. Sum or difference into products

$$\sin x+\sin y=2\sin\tfrac{1}{2}(x+y)\cos\tfrac{1}{2}(x-y) \tag{1135}$$

$$\sin x-\sin y=2\cos\tfrac{1}{2}(x+y)\sin\tfrac{1}{2}(x-y) \tag{1136}$$

$$\cos x+\cos y=2\cos\tfrac{1}{2}(x+y)\cos\tfrac{1}{2}(x-y) \tag{1137}$$

$$\cos x-\cos y=-2\cos\tfrac{1}{2}(x+y)\sin\tfrac{1}{2}(x-y) \tag{1138}$$

3. Products into sum or difference

$$2\sin x\cos y=\sin(x+y)+\sin(x-y) \tag{1139}$$

$$2\cos x\sin y=\sin(x+y)-\sin(x-y) \tag{1140}$$

$$2\cos x\cos y=\cos(x+y)+\cos(x-y) \tag{1141}$$

$$2\sin x\sin y=-\cos(x+y)+\cos(x-y) \tag{1142}$$

4. Double and half angles

$$\sin 2x=2\sin x\cos x \tag{1143}$$

$$\cos 2x=\cos^2 x-\sin^2 x=2\cos^2 x-1=1-2\sin^2 x \tag{1144}$$

$$\tan 2x=\frac{2\tan x}{1-\tan^2 x} \tag{1145}$$

$$\sin\tfrac{1}{2}x=\pm\sqrt{\frac{1-\cos x}{2}}\quad\text{or }2\sin^2 x\ \text{ or 1-cos2}x \tag{1146}$$

$$\cos\tfrac{1}{2}x=\pm\sqrt{\frac{1+\cos x}{2}}\quad\text{or }2\cos^2 x\ \text{ or 1+cos2}x \tag{1147}$$

$$\tan\frac{1}{2}x = \pm\sqrt{\frac{1-\cos x}{1+\cos x}} = \frac{\sin x}{1+\cos x} = \frac{1-\cos x}{\sin x} \qquad (1148)$$

5. Series

$$\sin x = \frac{e^{jx} - e^{-jx}}{2j} = x - \frac{x^3}{3!} + \frac{x^5}{5!} - \frac{x^7}{7!} + ... \qquad (1149)$$

$$\cos x = \frac{e^{jx} + e^{-jx}}{2} = 1 - \frac{x^2}{2!} + \frac{x^4}{4!} - \frac{x^6}{6!} + ... \qquad (1150)$$

$$\tan x = \frac{e^{jx} - e^{-jx}}{j\left(e^{jx} + e^{-jx}\right)} = x + \frac{x^3}{3!} + \frac{2x^5}{15} + \frac{17x^7}{315} + .. \qquad (1151)$$

XVI.4 Special Functions

$$(2m)! = (2m-1)!!\, m!\, 2^m = \frac{\Gamma\left(m+\frac{1}{2}\right)m!\, 2^{2m}}{\sqrt{\pi}} \qquad (1152)$$

$$(2m-1)!! = \frac{\Gamma\left(m+\frac{1}{2}\right)2^m}{\sqrt{\pi}} \qquad (1153)$$

$$(2m+2) = \frac{(2m+2)!\sqrt{\pi}}{2^{2m+1} m!\, \Gamma\left(m+\frac{3}{2}\right)} \qquad (1154)$$

$$\Gamma(m+2) = (m+1)m! \qquad (1155)$$

$$x^{(n)} = \frac{\Gamma(x+n)}{\Gamma(x)} \qquad (1156)$$

$$\beta(x,y) = \frac{\Gamma(x)\Gamma(y)}{\Gamma(x+y)} \qquad (1157)$$

$$e^{jx\cos\theta} = \sum_{n=-\infty}^{\infty} j^n J_n(x) e^{jn\theta} \qquad (1158)$$

$$J_p(\alpha(\phi)) \simeq \sqrt{\frac{2}{\pi\alpha(\phi)}} \cos\left(\alpha(\phi) - \frac{\pi}{4} - \frac{p\pi}{2}\right) \qquad (1159)$$

$$J_{-n}(x) = (-1)^n J_n(x) \qquad (1160)$$

$$\left\{ e^{j\left(\frac{\pi}{2}-\xi\right)lN} + e^{j\left(\frac{\pi}{2}+\xi\right)lN} \right\} = j^{lN}\left\{ e^{jlN\xi} + e^{-jlN\xi} \right\} = 2j^{lN}\cos(lN\xi) \qquad (1161)$$

$$J_1^2(z) = \sum_{m=0}^{\infty} \frac{(-1)^m (2m+2)! \left(\dfrac{z}{2}\right)^{2m+2}}{m!(m+2)!((m+1)!)^2} \tag{1162}$$

$$\frac{J_1(2x)}{x} = \frac{2}{\pi} \int_{-1}^{1} \left(1-t^2\right)^{1/2} \cos(2xt)\,dt \tag{1163}$$

$$\frac{J_1(2\alpha)}{\alpha} = {}_0\bar{F}_1\left(;2;-\alpha^2\right) \tag{1164}$$

$$J_n(z) = \sum_{k=0}^{\infty} \left(\frac{\left(\dfrac{z}{2}\right)^{2k+1}}{\Gamma(n+1)(n+k)!} \right) = \sum_{k=0}^{\infty} \left(\frac{\dfrac{z}{2}}{\Gamma(n+1)} {}_0F_1\left(n+1;\frac{-z^2}{4}\right) \right) \tag{1165}$$

$$\frac{J_1(2x)}{x} = \frac{1}{\Gamma(2)} {}_0F_1\left(2;-x^2\right) \tag{1166}$$

$$Q(-x) = 1 - Q(x) \tag{1167}$$

$$Q(x) = \frac{1}{2} - \frac{1}{2} erf\left(\frac{x}{\sqrt{2}}\right) \tag{1168}$$

$$j_v(z)^2 = \frac{\sqrt{\pi}}{2} G_{1,\ 3}^{1,\ 1}\left(z,\frac{1}{2}\middle|\begin{matrix} & 0 & \\ v & -1/2 & -v-1\end{matrix}\right) \tag{1169}$$

$$G_{p,\ q}^{m,\ n}\left(x,r\middle|\begin{matrix} & 0 & \\ v & -1/2 & -v-1\end{matrix}\right) = \frac{1}{2\pi j} \int_l \frac{\prod_{j=1}^{m}\left[\Gamma(b_j+s)\right]\prod_{j=1}^{n}\left[\Gamma(1-a_j-s)\right]}{\prod_{j=n+1}^{p}\left[\Gamma(a_j+s)\right]\prod_{j=m+1}^{q}\left[\Gamma(1-b_j-s)\right]} z^{-s/r}\,ds \tag{1170}$$

$$\frac{j_1(z)^2}{z^2} = \frac{\left(1+z^2-\cos(2z)+z^2\cos(2z)-2z\sin(2z)\right)}{2z^6} \tag{1171}$$

$$J_{3/2}(\alpha) = \sqrt{\frac{2\alpha}{\pi}} j_1(\alpha) \tag{1172}$$

$$j_0(x) = \frac{\sin x}{x} \tag{1173}$$

$$j_1(x) = \frac{\sin x}{x^2} - \frac{\cos x}{x} \tag{1174}$$

$$j_2(x) = \left(\frac{3}{x^3} - \frac{1}{x}\right)\sin x - \frac{3}{x^2}\cos x \tag{1175}$$

$${}_0\bar{F}_1(b;z) = \sum_{k=0}^{\infty} \frac{(z)^k}{\Gamma(k+b)(b)^k k!} \tag{1176}$$

415

$$n! = \Gamma(n+1) \tag{1177}$$

XVI.5 Vector Identities

1. Rectangular coordinates

$$\vec{\nabla}\psi = \hat{a}_x \frac{\partial \psi}{\partial x} + \hat{a}_y \frac{\partial \psi}{\partial y} + \hat{a}_z \frac{\partial \psi}{\partial z} \tag{1178}$$

$$\vec{\nabla} \cdot \vec{A} = \frac{\partial A_x}{\partial x} + \frac{\partial A_y}{\partial y} + \frac{\partial A_z}{\partial z} \tag{1179}$$

$$\vec{\nabla} \times \vec{A} = \hat{a}_x \left(\frac{\partial A_z}{\partial y} - \frac{\partial A_y}{\partial z} \right) + \hat{a}_y \left(\frac{\partial A_x}{\partial z} - \frac{\partial A_z}{\partial x} \right) + \hat{a}_z \left(\frac{\partial A_y}{\partial \rho} - \frac{\partial A_x}{\partial y} \right) \tag{1180}$$

2. Cylindrical coordinates

$$\vec{\nabla}\psi = \hat{a}_\rho \frac{\partial \psi}{\partial \rho} + \hat{a}_\phi \frac{1}{\rho} \frac{\partial \psi}{\partial y} + \hat{a}_z \frac{\partial \psi}{\partial z} \tag{1181}$$

$$\vec{\nabla} \cdot \vec{A} = \frac{1}{\rho} \frac{\partial}{\partial x}(\rho A_\rho) + \frac{1}{\rho} \frac{\partial A_\phi}{\partial \phi} + \frac{\partial A_z}{\partial z} \tag{1182}$$

$$\vec{\nabla} \times \vec{A} = \hat{a}_\rho \left(\frac{1}{\rho} \frac{\partial A_z}{\partial \phi} - \frac{\partial A_\phi}{\partial z} \right) + \hat{a}_\phi \left(\frac{\partial A_\rho}{\partial z} - \frac{\partial A_z}{\partial \rho} \right) + \hat{a}_z \left(\frac{1}{\rho} \frac{\partial (\rho A_\phi)}{\partial \rho} - \frac{1}{\rho} \frac{\partial A_\rho}{\partial \phi} \right) \tag{1183}$$

3. Spherical coordinates

$$\vec{\nabla}\psi = \hat{a}_r \frac{\partial \psi}{\partial r} + \hat{a}_\theta \frac{1}{r} \frac{\partial \psi}{\partial \theta} + \hat{a}_\phi \frac{1}{r\sin\theta} \frac{\partial \psi}{\partial \phi} \tag{1184}$$

$$\vec{\nabla} \cdot \vec{A} = \frac{1}{r^2} \frac{\partial}{\partial r}(r^2 A_r) + \frac{1}{r\sin\theta} \frac{\partial}{\partial \theta}(A_\theta \sin\theta) + \frac{1}{r\sin\theta} \frac{\partial A_\phi}{\partial \phi} \tag{1185}$$

$$\vec{\nabla} \times \vec{A} = \frac{\hat{a}_r}{r\sin\theta} \left(\frac{\partial}{\partial \theta}(A_\phi \sin\theta) - \frac{\partial A_\theta}{\partial \phi} \right) + \frac{\hat{a}_\theta}{r} \left(\frac{1}{\sin\theta} \frac{\partial A_r}{\partial \phi} - \frac{\partial}{\partial r}(rA_\phi) \right) + \frac{\hat{a}_\phi}{r} \left(\frac{\partial (rA_\theta)}{\partial r} - \frac{\partial A_r}{\partial \theta} \right) \tag{1186}$$

APPENDIX XVII

INTEGRAL OF THE JINC AND TINC SQUARED FUNCTIONS

XVII.1 Jinc Squared Integral

$$\int_{-\pi}^{\pi}\left(2\,jinc\left(x\sin\frac{\phi}{2}\right)\right)^2 d\phi = \int_{-\pi}^{\pi}\left(\frac{2J_1\left(x\sin\frac{\phi}{2}\right)}{x\sin\frac{\phi}{2}}\right)^2 d\phi = 2\pi\,_2F_3\left(\frac{1}{2},\frac{3}{2};1,2,3;-(x)^2\right)$$

this is an even function so integrate only half

$$= 8\int_0^{\pi}\left(\frac{J_1\left(x\sin\frac{\phi}{2}\right)}{x\sin\frac{\phi}{2}}\right)^2 d\phi$$

From Newman and Frank the bessel function squared can be expressed as

$$J_1^2(z) = \sum_{m=0}^{\infty}\frac{(-1)^m(2m+2)!\left(\frac{z}{2}\right)^{2m+2}}{m!(m+2)!((m+1)!)^2}$$

Now letting

let $z = x\sin\left(\frac{\phi}{2}\right)$

$$8\int_0^{\pi}\left(\frac{J_1(z)}{z}\right)^2 d\phi = 8\frac{\sum_{m=0}^{\infty}\frac{(-1)^m(2m+2)!\left(\frac{z}{2}\right)^{2m+2}}{m!(m+2)!((m+1)!)^2}d\phi}{z^2}$$

$$= 8\int_0^{\pi}\sum_{m=0}^{\infty}\frac{(-1)^m(2m+2)!(z)^{2m}}{m!(m+2)!((m+1)!)^2(2)^{2m+2}}d\phi$$

plugging back z and swap the summation and integral terms

$$= 8\sum_{m=0}^{\infty}\int_0^{\pi}\frac{(-1)^m(2m+2)!(z)^{2m}}{m!(m+2)!((m+1)!)^2(2)^{2m+2}}d\phi$$

$$= 8\sum_{m=0}^{\infty}\frac{(-1)^m(2m+2)!}{m!(m+2)!((m+1)!)^2(2)^{2m+2}}\int_0^{\pi}\left(x\sin\left(\frac{\phi}{2}\right)\right)^{2m}d\phi$$

$$= 8\sum_{m=0}^{\infty}\frac{(-1)^m x^{2m}(2m+2)(2m+1)(2m)!}{m!(m+2)!(m+1)^2 m!^2(2)^{2m+2}}\int_0^{\pi}\left(\sin\left(\frac{\phi}{2}\right)\right)^{2m}d\phi$$

$$= 8\sum_{m=0}^{\infty} \frac{(-1x^2)^m 2(m+1)(2m+1)(2m)!}{m!(m+2)!(m+1)^2 m!^2 (2)^{2m+2}} \int_0^\pi \left(\sin\left(\frac{\phi}{2}\right)\right)^{2m} d\phi$$

$$= 8\sum_{m=0}^{\infty} \frac{(-1x^2)^m (2m+1)(2m)!}{m!(m+2)!(m+1)m!^2 (2)^{2m+1}} \int_0^\pi \left(\sin\left(\frac{\phi}{2}\right)\right)^{2m} d\phi$$

Using the identity $(2m)! = (2m-1)!!\, m!\, 2^m = \dfrac{\Gamma\left(m+\dfrac{1}{2}\right) m!\, 2^{2m}}{\sqrt{\pi}}$

Then

$$= 8\sum_{m=0}^{\infty} \frac{(-1x^2)^m (2m+1)(2m-1)!!\, m!\, 2^m}{m!(m+2)!(m+1)m!^2 (2)^{2m+1}} \int_0^\pi \left(\sin\left(\frac{\phi}{2}\right)\right)^{2m} d\phi$$

$$= 8\sum_{m=0}^{\infty} \frac{(2m+1)(2m-1)!!}{(m+2)!(m+1)(2)^{m+1} m!} \frac{(-1x^2)^m}{m!} \int_0^\pi \left(\sin\left(\frac{\phi}{2}\right)\right)^{2m} d\phi$$

Now using the identity $(2m)! = (2m-1)!!\, m!\, 2^m = \dfrac{\Gamma\left(m+\dfrac{1}{2}\right) m!\, 2^{2m}}{\sqrt{\pi}}$ again and substituting

$$= 8\sum_{m=0}^{\infty} \frac{(2m+1)\Gamma\left(m+\dfrac{1}{2}\right) 2^m}{(m+2)!m!(m+1)(2)^{m+1}\sqrt{\pi}} \frac{(-1x^2)^m}{m!} \int_0^\pi \left(\sin\left(\frac{\phi}{2}\right)\right)^{2m} d\phi$$

$$= 8\sum_{m=0}^{\infty} \frac{\Gamma\left(m+\dfrac{1}{2}\right)}{\Gamma(m+3)\Gamma(m+1)} \frac{(-1x^2)^m}{m!} \frac{(2m+1)}{(2m+2)\sqrt{\pi}} \int_0^\pi \left(\sin\left(\frac{\phi}{2}\right)\right)^{2m} d\phi$$

Where

$$(2m+2) = \frac{(2m+2)!\sqrt{\pi}}{2^{2m+1} m!\Gamma\left(m+\dfrac{3}{2}\right)}$$

Then

$$= 8\sum_{m=0}^{\infty} \frac{\Gamma\left(m+\dfrac{1}{2}\right)}{\Gamma(m+3)\Gamma(m+1)} \frac{(-1x^2)^m}{m!} \frac{(2m+1)2^{2m+1} m!\Gamma\left(m+\dfrac{3}{2}\right)}{(2m+2)!\sqrt{\pi}\sqrt{\pi}} \int_0^\pi \left(\sin\left(\frac{\phi}{2}\right)\right)^{2m} d\phi$$

$$= 8\sum_{m=0}^{\infty} \frac{\Gamma\left(m+\dfrac{1}{2}\right)\Gamma\left(m+\dfrac{3}{2}\right)}{\Gamma(m+3)\Gamma(m+1)} \frac{(-1x^2)^m}{m!} \frac{(2m+1)2^{2m+1} m!}{(2m+2)!\pi} \int_0^\pi \left(\sin\left(\frac{\phi}{2}\right)\right)^{2m} d\phi$$

Where

$$\Gamma(m+2) = (m+1)m!$$

$$= 8\sum_{m=0}^{\infty} \frac{\Gamma\left(m+\frac{1}{2}\right)\Gamma\left(m+\frac{3}{2}\right)}{\Gamma(m+3)\Gamma(m+1)} \frac{(-1x^2)^m}{m!} \frac{(2m+1)2^{2m+1}m!}{2(2m+1)(2m)!(m+1)\pi} \int_0^{\pi}\left(\sin\left(\frac{\phi}{2}\right)\right)^{2m} d\phi$$

substituting

$$(2m)! = \frac{\Gamma\left(m+\frac{1}{2}\right)m!2^{2m}}{\sqrt{\pi}}$$

and canceling

$$= 8\sum_{m=0}^{\infty} \frac{\Gamma\left(m+\frac{1}{2}\right)\Gamma\left(m+\frac{3}{2}\right)}{\Gamma(m+3)\Gamma(m+1)} \frac{(-1x^2)^m}{m!} \frac{1}{(m+1)m!} \frac{m!\sqrt{\pi}}{\Gamma\left(m+\frac{1}{2}\right)\pi} \int_0^{\pi}\left(\sin\left(\frac{\phi}{2}\right)\right)^{2m} d\phi$$

$$= 8\sum_{m=0}^{\infty} \frac{\Gamma\left(m+\frac{1}{2}\right)\Gamma\left(m+\frac{3}{2}\right)}{\Gamma(m+3)\Gamma(m+1)\Gamma(m+2)} \frac{(-1x^2)^m}{m!} \frac{m!}{\Gamma\left(m+\frac{1}{2}\right)\sqrt{\pi}} \int_0^{\pi}\left(\sin\left(\frac{\phi}{2}\right)\right)^{2m} d\phi$$

$$= 8\sum_{m=0}^{\infty} \frac{\Gamma\left(m+\frac{1}{2}\right)\Gamma\left(m+\frac{3}{2}\right)}{\Gamma(m+3)\Gamma(m+1)\Gamma(m+2)} \frac{(-1x^2)^m}{m!} \frac{\Gamma(m+1)}{\Gamma\left(m+\frac{1}{2}\right)\sqrt{\pi}} \int_0^{\pi}\left(\sin\left(\frac{\phi}{2}\right)\right)^{2m} d\phi$$

The integral $\displaystyle\int_0^{\pi}\left(\sin\left(\frac{\phi}{2}\right)\right)^{2m} d\phi = \frac{\sqrt{\pi}\,\Gamma\left(m+\frac{1}{2}\right)}{\Gamma(m+1)}$

To show this the definition of the gamma function is applied

$$\Gamma(z) = \int_0^{\infty} x^{z-1}e^{-x}dx$$

Using u-substitution

Let $u^2 = x$

$$dx = 2u\,du$$

$$\Gamma(z) = \int_0^\infty u^{2z-2} e^{-u^2} 2u\,du$$

$$\Gamma(z) = 2\int_0^\infty u^{2z-1} e^{-u^2}\,du \qquad [1]$$

Taking the product of two gamma functions

$$\Gamma(x)\Gamma(y) = 2\int_0^\infty u^{2x-1} e^{-u^2}\,du \cdot 2\int_0^\infty v^{2y-1} e^{-v^2}\,dv$$

$$= 4\int_0^\infty \int_0^\infty e^{-(u^2+v^2)} u^{2x-1} v^{2y-1}\,du\,dv \qquad [2]$$

Using a change of variables

$$u = r\cos(\theta)$$

$$v = r\sin(\theta)$$

$$u^2 + v^2 = r^2$$

$$du\,dv = r\,dr\,d\theta$$

$$\Gamma(x)\Gamma(y) = 4\int_0^{\pi/2} \int_0^\infty e^{-r^{22}} r^{2x-1} \cos^{2x-1}(\theta) r^{2y-1} \sin^{2x-1}(\theta) r\,dr\,d\theta$$

$$= 4\int_0^\infty e^{-r^2} r^{2(x+y)-1}\,dr \int_0^{\pi/2} \cos^{2x-1}(\theta) \sin^{2y-1}(\theta)\,d\theta$$

Using [1] from above this can be written as

$$= 2\Gamma(x+y)\int_0^{\pi/2} \cos^{2x-1}(\theta)\sin^{2y-1}(\theta)\,d\theta$$

This can be written as

$$\frac{\Gamma(x)\Gamma(y)}{2\Gamma(x+y)} = \int_0^{\pi/2} \cos^{2x-1}(\theta)\sin^{2y-1}(\theta)\,d\theta$$

Let $x = \frac{1}{2}$ and $y = m + \frac{1}{2}$

$$\frac{\Gamma\left(\frac{1}{2}\right)\Gamma\left(m+\frac{1}{2}\right)}{2\Gamma\left(\frac{1}{2}+m+\frac{1}{2}\right)} = \int_0^{\pi/2} \cos^0(\theta)\sin^{2m}(\theta)d\theta$$

$$\frac{\sqrt{\pi}\Gamma\left(m+\frac{1}{2}\right)}{2\Gamma(m+1)} = \int_0^{\pi/2} \sin^{2m}(\theta)d\theta$$

$\sin^{2m}(\theta)$ is symmetric about the line $\theta = \frac{\pi}{2}$ therefore:

$$\int_{\pi/2}^{\pi} \sin^{2m}(\theta)d\theta = \int_0^{\pi/2} \sin^{2m}(\theta)d\theta = \frac{\sqrt{\pi}\Gamma\left(m+\frac{1}{2}\right)}{2\Gamma(m+1)}$$

Therefore

$$\int_0^{\pi} \sin^{2m}(\theta)d\theta = \frac{2\sqrt{\pi}\Gamma\left(m+\frac{1}{2}\right)}{2\Gamma(m+1)} = \frac{\sqrt{\pi}\Gamma\left(m+\frac{1}{2}\right)}{\Gamma(m+1)}$$

Since $\sin^{2m}(\theta)$ is also symmetric with respect to the y-axis

$$\int_{-\pi}^{0} \sin^{2m}(\theta)d\theta = \int_0^{\pi} \sin^{2m}(\theta)d\theta = \frac{\sqrt{\pi}\Gamma\left(m+\frac{1}{2}\right)}{\Gamma(m+1)}$$

Therefore

$$\int_0^{\pi} \sin^{2m}(\theta)d\theta = \frac{2\sqrt{\pi}\Gamma\left(m+\frac{1}{2}\right)}{2\Gamma(m+1)} = \frac{\sqrt{\pi}\Gamma\left(m+\frac{1}{2}\right)}{\Gamma(m+1)}$$

$$\int_0^{\pi} \sin^{2m}(\theta)d\theta = \frac{\sqrt{\pi}\Gamma\left(m+\frac{1}{2}\right)}{\Gamma(m+1)}$$

Since $\sin^{2m}(\theta)$ is also symmetric with respect to the y-axis

$$\int_{-\pi}^{0} \sin^{2m}(\theta)d\theta = \int_0^{\pi} \sin^{2m}(\theta)d\theta = \frac{\sqrt{\pi}\Gamma\left(m+\frac{1}{2}\right)}{\Gamma(m+1)}$$

Therefore

$$\int_{-\pi}^{\pi} \sin^{2m}(\theta)d\theta = \frac{4\sqrt{\pi}\Gamma\left(m+\frac{1}{2}\right)}{2\Gamma(m+1)} = \frac{2\sqrt{\pi}\Gamma\left(m+\frac{1}{2}\right)}{\Gamma(m+1)}$$

And substituting into our earlier expression we arrive at the following

421

$$\int_{-\pi}^{\pi}\left(\frac{2J_1\left(x\sin\frac{\phi}{2}\right)}{x\sin\frac{\phi}{2}}\right)^2 d\phi = \sum_{m=0}^{\infty}8\frac{\Gamma\left(m+\frac{1}{2}\right)\Gamma\left(m+\frac{3}{2}\right)}{\Gamma(m+3)\Gamma(m+2)\Gamma(m+1)}\frac{(-1x^2)^m}{m!}\frac{\Gamma(m+1)}{\Gamma\left(m+\frac{1}{2}\right)\sqrt{\pi}}\frac{\sqrt{\pi}\Gamma\left(m+\frac{1}{2}\right)}{\Gamma(m+1)}$$

$$=\sum_{m=0}^{\infty}2^3\frac{\Gamma\left(m+\frac{1}{2}\right)\Gamma\left(m+\frac{3}{2}\right)}{\Gamma(m+3)\Gamma(m+2)\Gamma(m+1)}\frac{(-1x^2)^m}{m!}$$

The above can be rewritten as a $_2F_3$ hypergeometric formula.
To do this the pochammer symbol will be used or more formally
rising factorial $x^{(n)}$

where $x^{(n)}$ is related to the gamma function as

$$x^{(n)} = \frac{\Gamma(x+n)}{\Gamma(x)}$$

Thus

$$\left(\frac{1}{2}\right)^{(m)} = \frac{\Gamma\left(m+\frac{1}{2}\right)}{\Gamma\left(\frac{1}{2}\right)} = \frac{\Gamma\left(m+\frac{1}{2}\right)}{\sqrt{\pi}}$$

$$\left(\frac{3}{2}\right)^{(m)} = \frac{\Gamma\left(m+\frac{3}{2}\right)}{\Gamma\left(\frac{3}{2}\right)} = \frac{2\Gamma\left(m+\frac{3}{2}\right)}{\sqrt{\pi}}$$

$$\left(1\right)^{(m)} = \frac{\Gamma(m+1)}{\Gamma(1)} = \frac{\Gamma(m+1)}{1}$$

$$\left(2\right)^{(m)} = \frac{\Gamma(m+2)}{\Gamma(2)} = \frac{\Gamma(m+2)}{1}$$

$$\left(3\right)^{(m)} = \frac{\Gamma(m+3)}{\Gamma(3)} = \frac{\Gamma(m+3)}{2}$$

And

$$\frac{\left(\frac{1}{2}\right)^{(m)}\left(\frac{3}{2}\right)^{(m)}}{(1)^{(m)}(2)^{(m)}(3)^{(m)}} = \frac{4}{\pi}\frac{\Gamma\left(m+\frac{1}{2}\right)\Gamma\left(m+\frac{3}{2}\right)}{\Gamma(m+1)\Gamma(m+2)\Gamma(m+3)}$$

Making use of the above we can rewrite our expression as

$$\sum_{m=0}^{\infty}2^3\frac{\Gamma\left(m+\frac{1}{2}\right)\Gamma\left(m+\frac{3}{2}\right)}{\Gamma(m+3)\Gamma(m+2)\Gamma(m+1)}\frac{\left(-1x^2\right)^m}{m!} = \sum_{m=0}^{\infty}8\frac{\pi}{4}\frac{\left(\frac{1}{2}\right)^{(m)}\left(\frac{3}{2}\right)^{(m)}}{(1)^{(m)}(2)^{(m)}(3)^{(m)}}\frac{\left(-1x^2\right)^m}{m!}$$

$$= 2\pi\,_2F_3\left(\frac{1}{2},\frac{3}{2};1,2,3;-(x)^2\right)$$

422

$$2\pi \, _2F_3\left(\frac{1}{2},\frac{3}{2};1,2,3;-(x)^2\right)$$

XVII.2 Tinc Squared Integral

$$\int_{-\pi}^{\pi}\left(3tinc(x)\right)^2 d\phi = 9\int_{-\pi}^{\pi}\left(\frac{j_1(x)}{x}\right)^2 d\phi = 2\pi\left\{\frac{4}{5}\left[\,_1F_2\left(\frac{1}{2};4,\frac{7}{2};-\left(4\pi\tilde{R}\right)^2\right)-6\,_1F_2\left(\frac{1}{2};3,\frac{7}{2};-\left(4\pi\tilde{R}\right)^2\right)\right]\right\}$$

This is an even function and the integral reduces to,

$$18\int_{0}^{\pi}\left(\frac{j_1(x)}{x}\right)^2 d\phi$$

Subsequently applying the identity

$$j_v(z)^2 = \frac{\sqrt{\pi}}{2}G^{1,\ 1}_{1,\ 3}\left(z,\frac{1}{2}\middle|\begin{matrix}\frac{1}{2}\\v & -\frac{1}{2} & -v-1\end{matrix}\,\,\,\begin{matrix}0\\\end{matrix}\right)$$

To the spherical Bessel function squared

$$j_1(x)^2 = \frac{\sqrt{\pi}}{2}G^{1,\ 1}_{1,\ 3}\left(z,\frac{1}{2}\middle|\begin{matrix}\frac{1}{2}\\1 & -\frac{1}{2} & -2\end{matrix}\,\,\,\begin{matrix}0\\\end{matrix}\right)$$

$$\text{where } G^{1,\ 1}_{1,\ 3}\left(z,\frac{1}{2}\middle|\begin{matrix}\frac{1}{2}\\1 & -\frac{1}{2} & -2\end{matrix}\,\,\,\begin{matrix}0\\\end{matrix}\right) = \frac{\sqrt{\pi}}{2}\frac{1}{2\pi j}\int_{J_l}\left\{\frac{\prod_{j=1}^{1}\left[\Gamma(b_j+s)\right]\prod_{j=1}^{1}\left[\Gamma(1-a_j-s)\right]}{\prod_{j=2}^{1}\left[\Gamma(a_j+s)\right]\prod_{j=2}^{3}\left[\Gamma(1-b_j-s)\right]}\right\}z^{-2s}ds$$

To evaluate the above one begins by evaluating the sum of products confined within the curly braces starting with $j=1$ to obtain

$$\frac{\Gamma(1+s)\Gamma(1-s)}{1}$$

$j=2$

$$\frac{1}{\Gamma\left(\frac{3}{2}-s\right)}$$

Lastly for $j=3$

$$\frac{1}{\Gamma(3-s)}$$

Substituting the result into the expression gives

$$\frac{j_1(x)^2}{x^2} = \frac{1}{4\sqrt{\pi}j}\int_{J_l}\left\{\frac{\prod_{j=1}^{1}\left[\Gamma(b_j+s)\right]\prod_{j=1}^{1}\left[\Gamma(1-a_j-s)\right]}{\prod_{j=2}^{1}\left[\Gamma(a_j+s)\right]\prod_{j=2}^{3}\left[\Gamma(1-b_j-s)\right]}\right\}z^{-2s-2}ds$$

$$= \frac{1}{4\sqrt{\pi}j}\int_{J_l}\left\{\frac{\Gamma(1+s)\Gamma(1-s)}{\Gamma\left(\frac{3}{2}-s\right)\Gamma(3-s)}\right\}z^{-2s-2}ds$$

Now integrating along the contour of this integral gives

$$\frac{j_1(x)^2}{x^2} = \frac{\left(1 + x^2 - \cos(2x) + z^2 \cos(2x) - 2z\sin(2x)\right)}{2x^6}$$

Now letting $x = 4\pi A \sin\left(\phi / 2\right)$ gives (Yet this needs to be corrected in the future!)

$$\frac{j_1\left(4\pi \tilde{R}\sin\left(\frac{\phi}{2}\right)\right)^2}{\left(4\pi \tilde{R}\sin\left(\frac{\phi}{2}\right)\right)^2} = \frac{\begin{pmatrix} 1 + \left(4\pi \tilde{R}\sin\left(\frac{\phi}{2}\right)\right)^2 - \cos\left(8\pi \tilde{R}\sin\left(\frac{\phi}{2}\right)\right) + \left(4\pi \tilde{R}\sin\left(\frac{\phi}{2}\right)\right)^2 \cos\left(8\pi \tilde{R}\sin\left(\frac{\phi}{2}\right)\right) \\ -8\pi \tilde{R}\sin\left(\frac{\phi}{2}\right)\sin\left(8\pi \tilde{R}\sin\left(\frac{\phi}{2}\right)\right) \end{pmatrix}}{2^{13}\pi^6 \tilde{R}^6 \sin^6\left(\frac{\phi}{2}\right)}$$

And the above expression is simplified as

$$\frac{j_1\left(4\pi \tilde{R}\sin\left(\frac{\phi}{2}\right)\right)^2}{\left(4\pi \tilde{R}\sin\left(\frac{\phi}{2}\right)\right)^2} = \frac{\left(-4\pi \tilde{R}\sin\left(\frac{\phi}{2}\right)\cos\left[4\pi \tilde{R}\sin\left(\frac{\phi}{2}\right)\right] + \sin\left[4\pi \tilde{R}\sin\left(\frac{\phi}{2}\right)\right]\right)^2}{2^{12}\pi^6 \tilde{R}^6 \sin^6\left(\frac{\phi}{2}\right)}$$

Now applying the integral gives

$$18\int_0^\pi \left(\frac{j_1(x)}{x}\right)^2 d\phi = \int_0^\pi \frac{\left(-4\pi \tilde{R}\sin\left(\frac{\phi}{2}\right)\cos\left[4\pi \tilde{R}\sin\left(\frac{\phi}{2}\right)\right] + \sin\left[4\pi \tilde{R}\sin\left(\frac{\phi}{2}\right)\right]\right)^2}{2^{12}\pi^6 \tilde{R}^6 \sin^6\left(\frac{\phi}{2}\right)} d\phi$$

$$= 2\pi \left\{\frac{2}{5}\left[{}_1F_2\left(\frac{1}{2};4,\frac{7}{2};-\left(4\pi \tilde{R}\right)^2\right) - 6\,{}_1F_2\left(\frac{1}{2};3,\frac{7}{2};-\left(4\pi \tilde{R}\right)^2\right)\right]\right\}$$

APPENDIX XVIII

CANONICAL PATTERNS PLOTTED THREE DIMENSIONALLY IN DB SCALE

Examples of the radiation patterns of select distributions presented in this dissertation are shown in Figure 308-Figure 327. Negative N-sphere random array patterns $\tilde{A} = 3.35$.
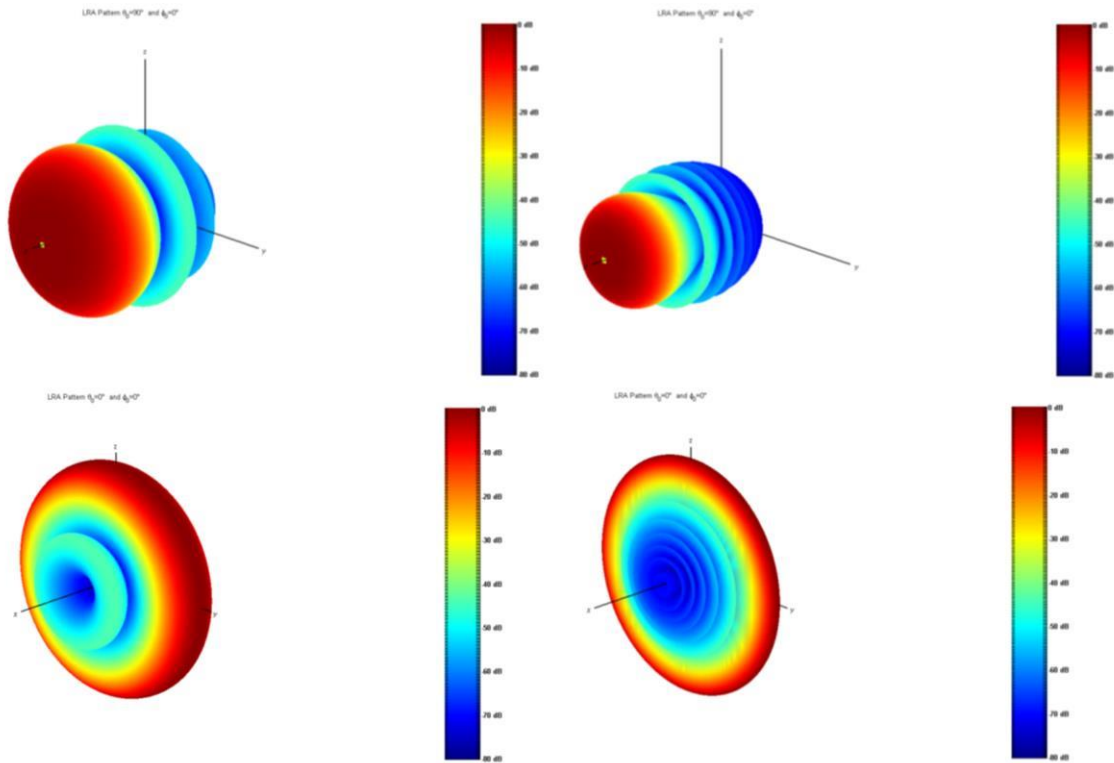
Figure 308. Linear random array $\{(\theta_0 = 90°, \ \phi_0 = 0°, \ \tilde{A} = 1)$ top left, $(\theta_0 = 90°, \ \phi_0 = 0°, \ \tilde{A} = 3.35)$ top right, $(\theta_0 = 0°, \ \phi_0 = 0°, \ \tilde{A} = 1)$ bottom left, $(\theta_0 = 0°, \ \phi_0 = 0°, \ \tilde{A} = 3.35)$, bottom right$\}$.
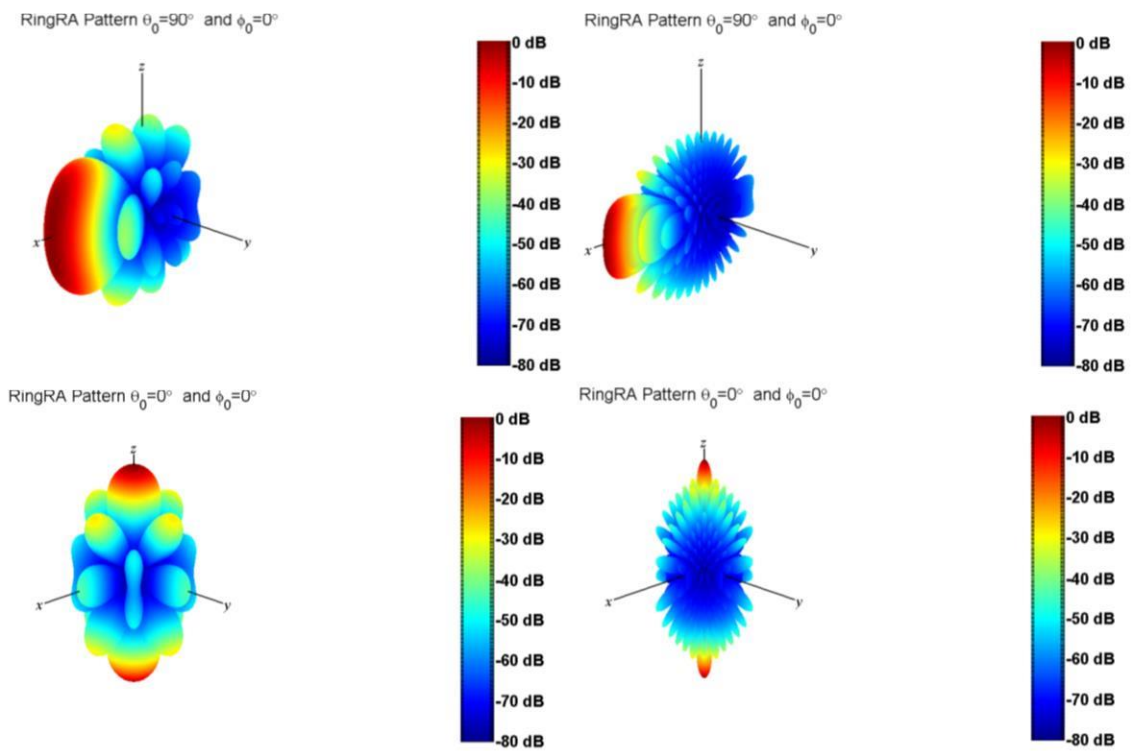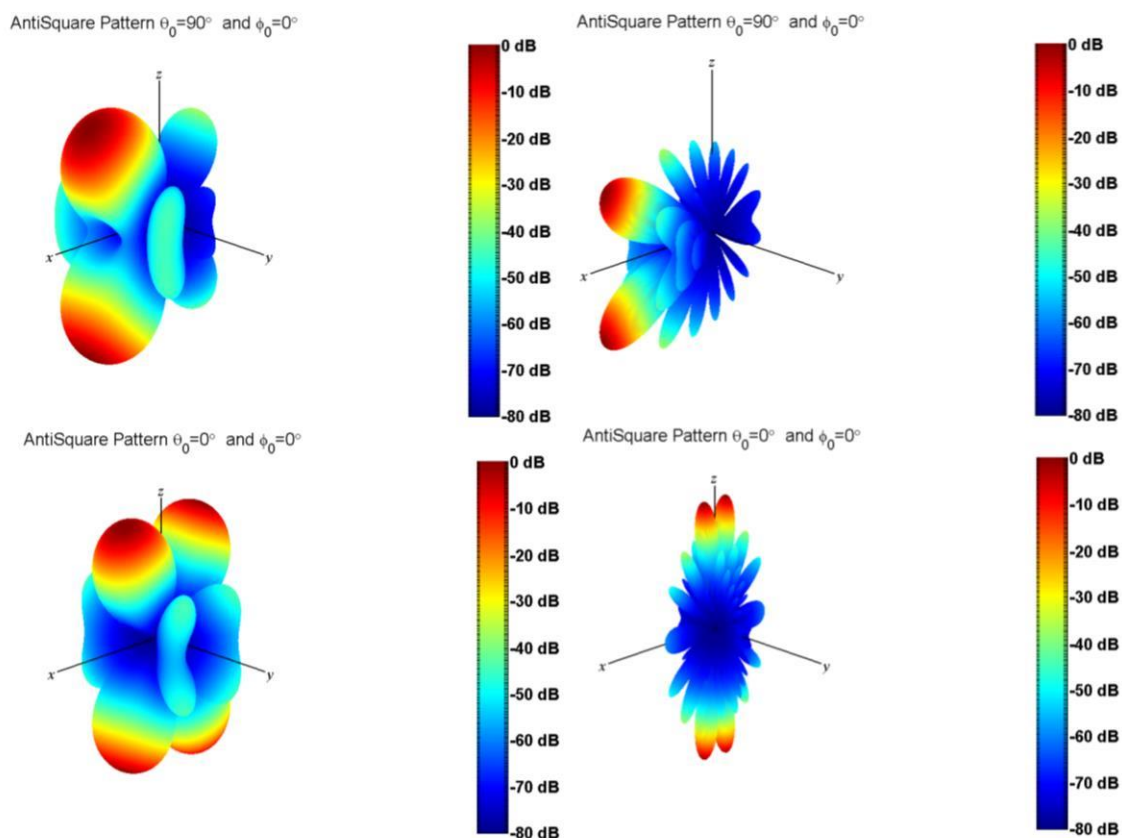
Figure 309. Ring random array $\{(\theta_0 = 90°, \ \phi_0 = 0°, \ \tilde{A} = 1)$ top left, $(\theta_0 = 90°, \ \phi_0 = 0°, \ \tilde{A} = 3.35)$ top right, $(\theta_0 = 0°, \ \phi_0 = 0°, \ \tilde{A} = 1)$ bottom left, $(\theta_0 = 0°, \ \phi_0 = 0°, \ \tilde{A} = 3.35)$, bottom right$\}$.
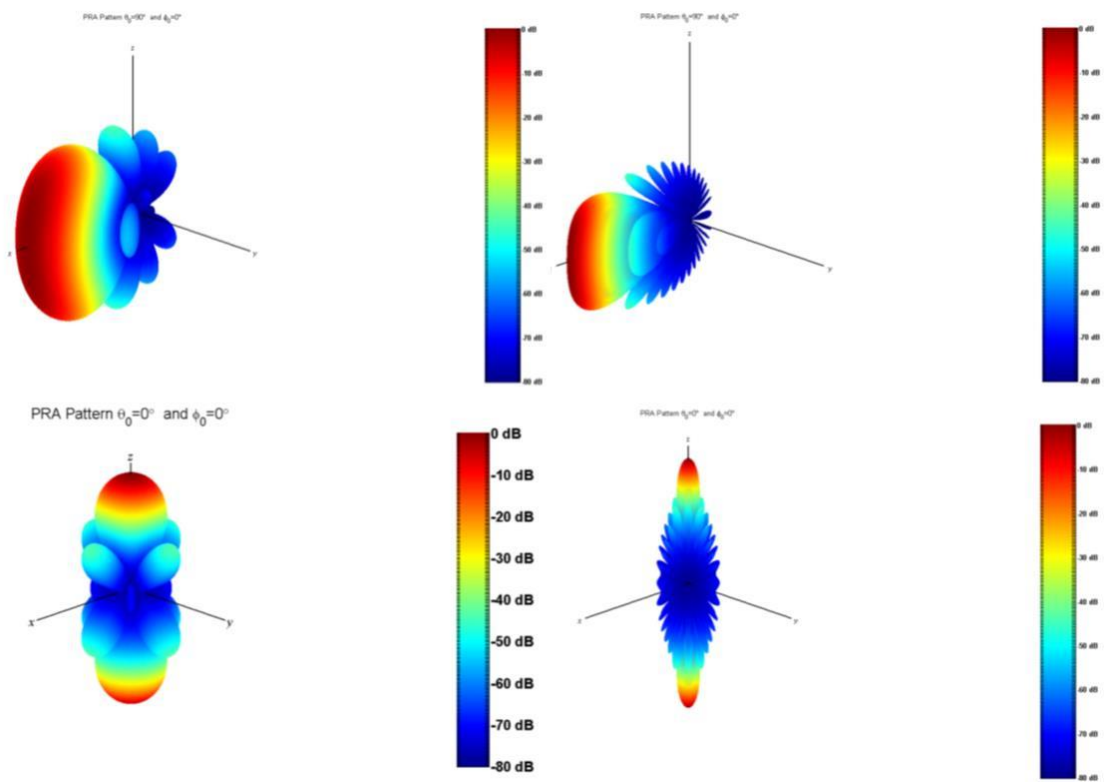
Figure 310. Planar random array $\{(\theta_0 = 90°, \ \phi_0 = 0°, \ \tilde{A} = 1)$ top left, $(\theta_0 = 90°, \ \phi_0 = 0°, \ \tilde{A} = 3.35)$ top right, $(\theta_0 = 0°, \ \phi_0 = 0°, \ \tilde{A} = 1)$ bottom left, $(\theta_0 = 0°, \ \phi_0 = 0°, \ \tilde{A} = 3.35)$, bottom right$\}$.
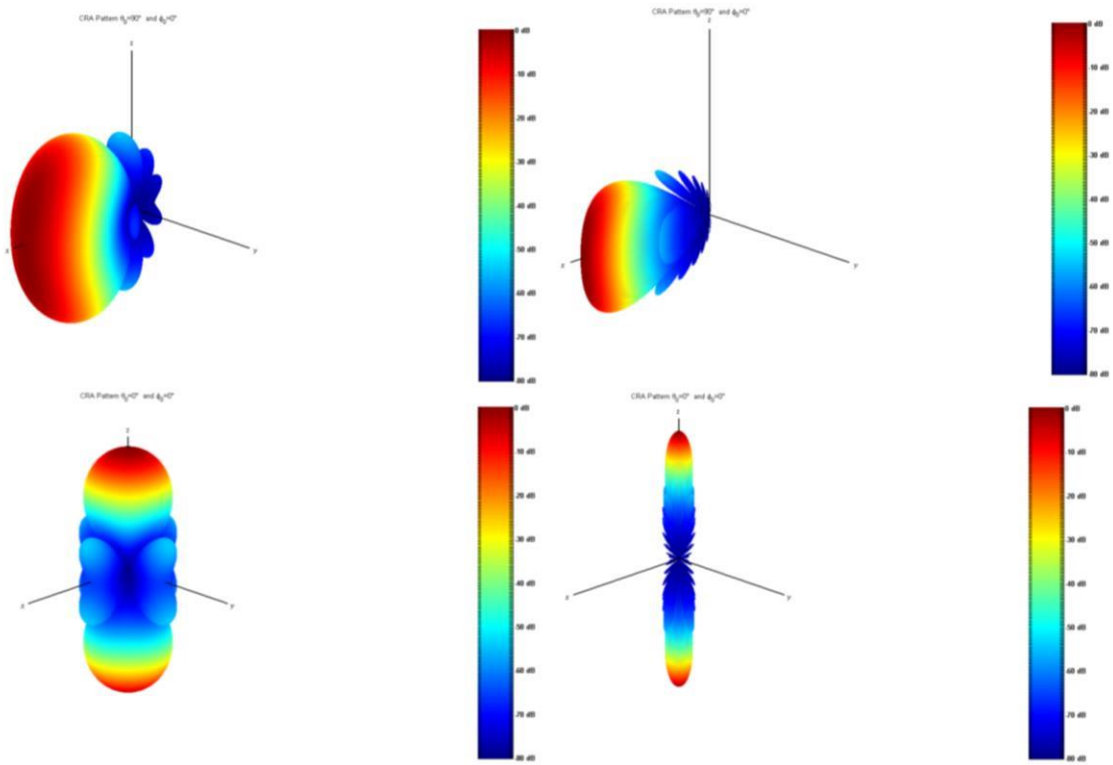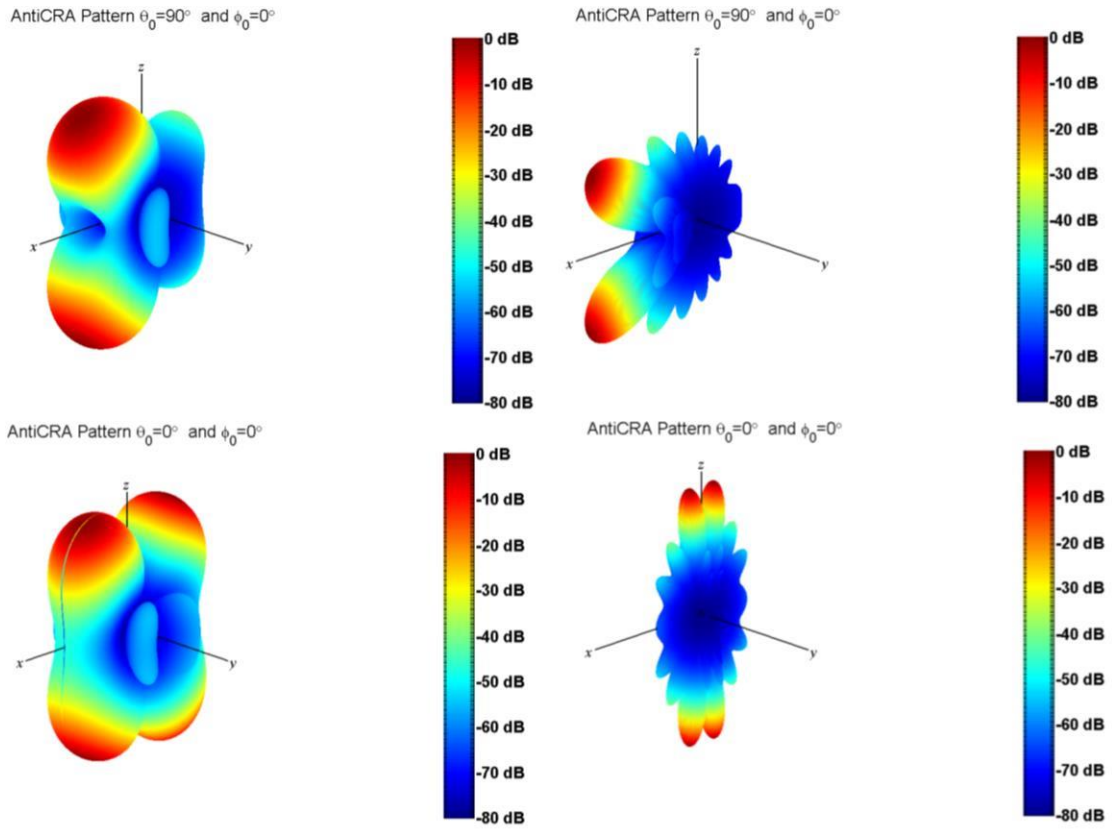
Figure 311. Circular random array $\{(\theta_0 = 90°, \phi_0 = 0°, \tilde{A} = 1)$ top left, $(\theta_0 = 90°, \phi_0 = 0°, \tilde{A} = 3.35)$ top right, $(\theta_0 = 0°, \phi_0 = 0°, \tilde{A} = 1)$ bottom left, $(\theta_0 = 0°, \phi_0 = 0°, \tilde{A} = 3.35)$, bottom right$\}$.
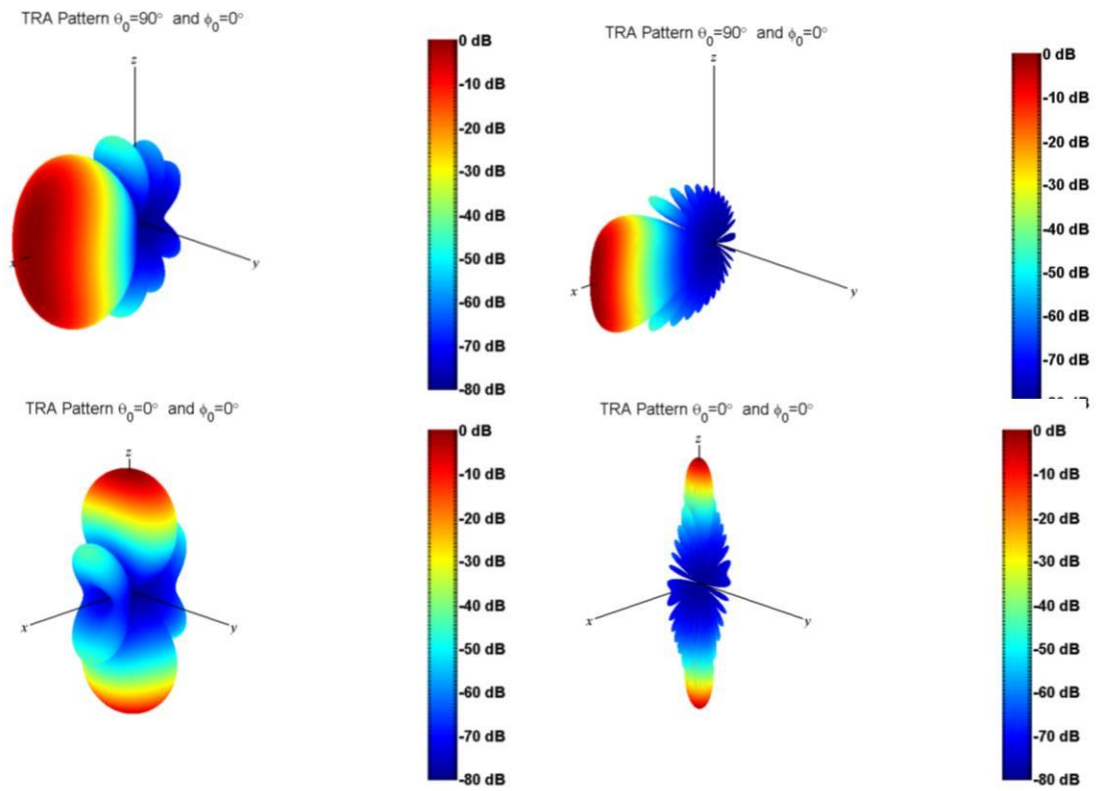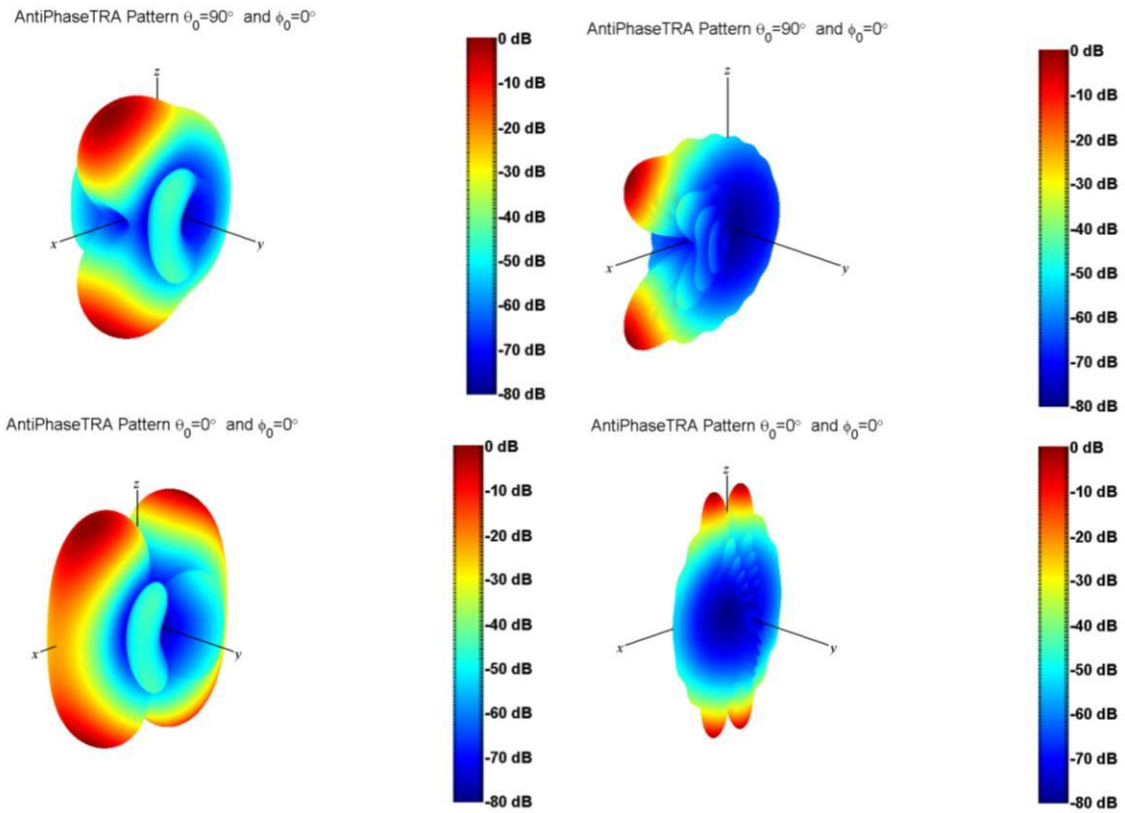
Figure 312. Triangular random array $\{(\theta_0 = 90°, \ \phi_0 = 0°, \ \tilde{A} = 1)$ top left, $(\theta_0 = 90°, \ \phi_0 = 0°, \ \tilde{A} = 3.35)$ top right, $(\theta_0 = 0°, \ \phi_0 = 0°, \ \tilde{A} = 1)$ bottom left, $(\theta_0 = 0°, \ \phi_0 = 0°, \ \tilde{A} = 3.35)$, bottom right$\}$.
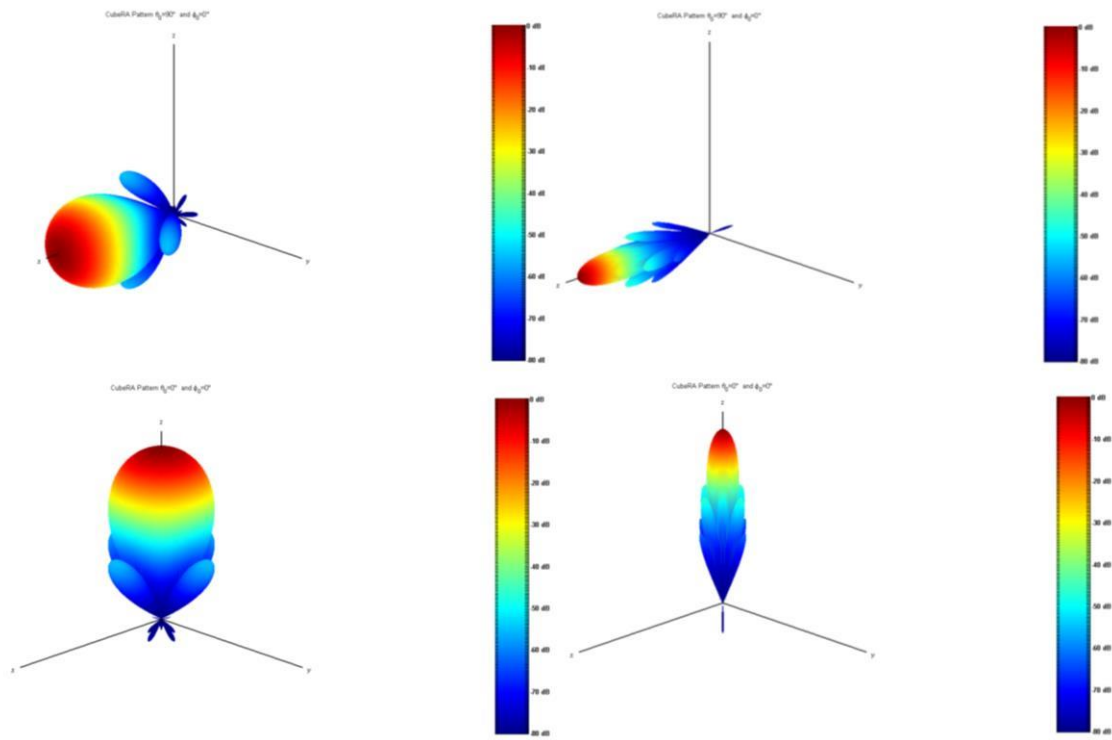
Figure 313. Cubical random array $\{(\theta_0 = 90°, \ \phi_0 = 0°, \ \tilde{A} = 1)$ top left, $(\theta_0 = 90°, \ \phi_0 = 0°, \ \tilde{A} = 3.35)$ top right, $(\theta_0 = 0°, \ \phi_0 = 0°, \ \tilde{A} = 1)$ bottom left, $(\theta_0 = 0°, \ \phi_0 = 0°, \ \tilde{A} = 3.35)$, bottom right$\}$.
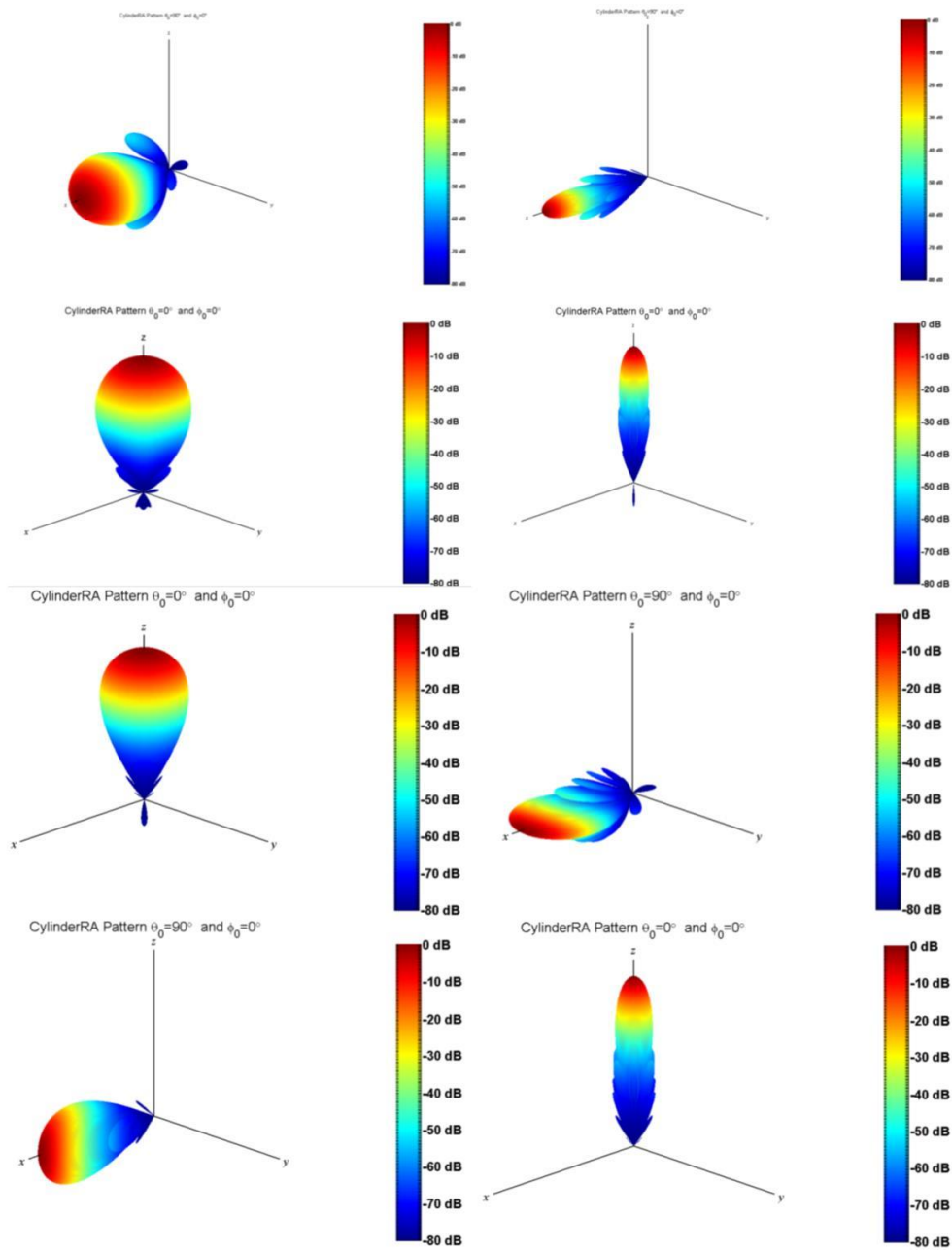
Figure 314. Cubical random array $\{(\theta_0 = 90°, \; \phi_0 = 0°, \; \tilde{A} = \tilde{B} = 1)$ top left, $(\theta_0 = 90°, \; \phi_0 = 0°, \; \tilde{A} = \tilde{B} = 3.35)$top right, $(\theta_0 = 0°, \; \phi_0 = 0°, \; \tilde{A} = \tilde{B} = 1)$ row two bottom left, $(\theta_0 = 0°, \; \phi_0 = 0°, \; \tilde{A} = \tilde{B} = 3.35)$, row two bottom right, row three bottom left $(\theta_0 = 0°, \; \phi_0 = 0°, \; \tilde{A} = 3.35, \; \tilde{B} = 1)$, row three bottom right$(\theta_0 = 90°, \; \phi_0 = 0°, \; \tilde{A} = 3.35, \; \tilde{B} = 1)$, row four bottom right$(\theta_0 = 90°, \; \phi_0 = 0°, \; \tilde{A} = 1, \; \tilde{B} = 3.35)$, row four bottom right $(\theta_0 = 0°, \; \phi_0 = 0°, \; \tilde{A} = 1, \; \tilde{B} = 3.35)\}$.

The aperture size $\tilde{B}$ is taken from the middle of the cylinder up to the top of the cylinder (half the length of the cylinder length).
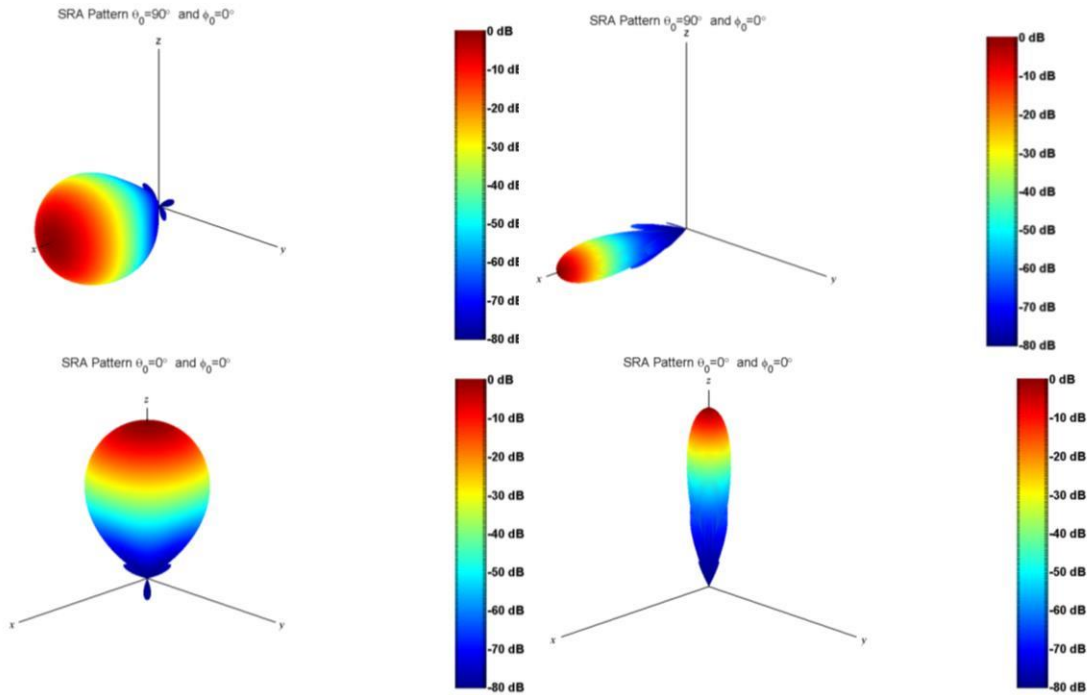
Figure 315. Spherical random array $\{(\theta_0 = 90°, \ \phi_0 = 0°, \ \tilde{A} = 1)$ top left, $(\theta_0 = 90°, \ \phi_0 = 0°, \ \tilde{A} = 3.35)$ top right, $(\theta_0 = 0°, \ \phi_0 = 0°, \ \tilde{A} = 1)$ bottom left, $(\theta_0 = 0°, \ \phi_0 = 0°, \ \tilde{A} = 3.35)$, bottom right$\}$.
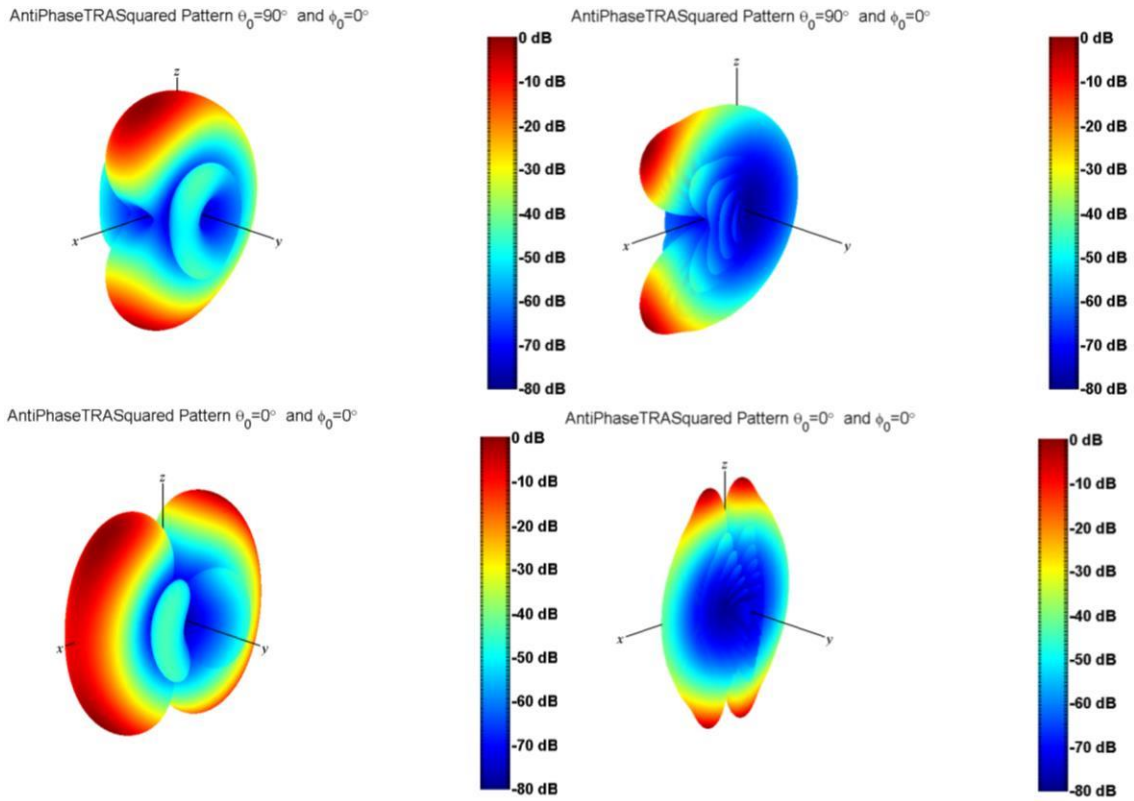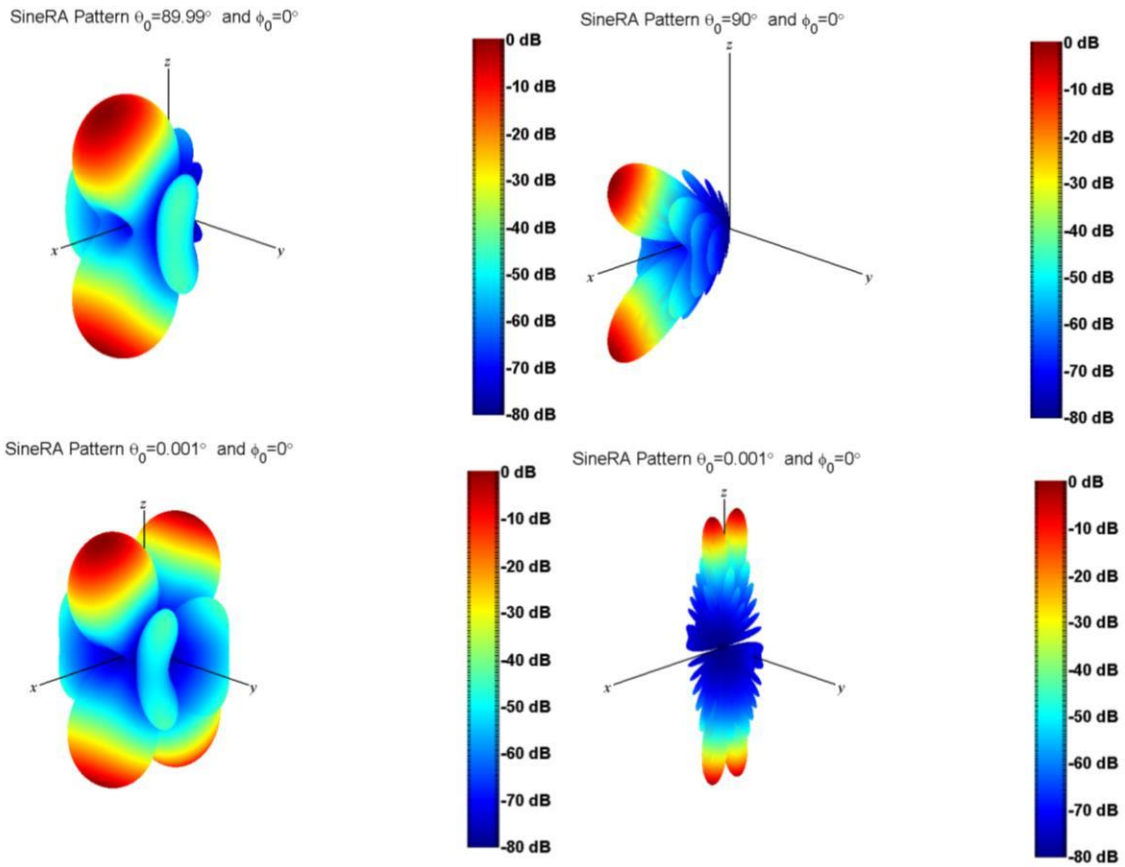
Figure 316. Anti square random array $\{(\theta_0 = 90°, \; \phi_0 = 0°, \; \tilde{A} = 1)$ top left, $(\theta_0 = 90°, \; \phi_0 = 0°, \; \tilde{A} = 3.35)$ top right, $(\theta_0 = 0°, \; \phi_0 = 0°, \; \tilde{A} = 1)$ bottom left, $(\theta_0 = 0°, \; \phi_0 = 0°, \; \tilde{A} = 3.35)$, bottom right$\}$.

Figure 317. Anti circular random array $\{(\theta_0 = 90°, \ \phi_0 = 0°, \ \tilde{A} = 1)$ top left, $(\theta_0 = 90°, \ \phi_0 = 0°, \ \tilde{A} = 3.35)$ top right, $(\theta_0 = 0°, \ \phi_0 = 0°, \ \tilde{A} = 1)$ bottom left, $(\theta_0 = 0°, \ \phi_0 = 0°, \ \tilde{A} = 3.35)$, bottom right$\}$.

Figure 318. Anti triangular random array {$(\theta_0 = 90°, \phi_0 = 0°, \tilde{A} = 1)$ top left, $(\theta_0 = 90°, \phi_0 = 0°, \tilde{A} = 3.35)$ top right, $(\theta_0 = 0°, \phi_0 = 0°, \tilde{A} = 1)$ bottom left, $(\theta_0 = 0°, \phi_0 = 0°, \tilde{A} = 3.35)$, bottom right}.
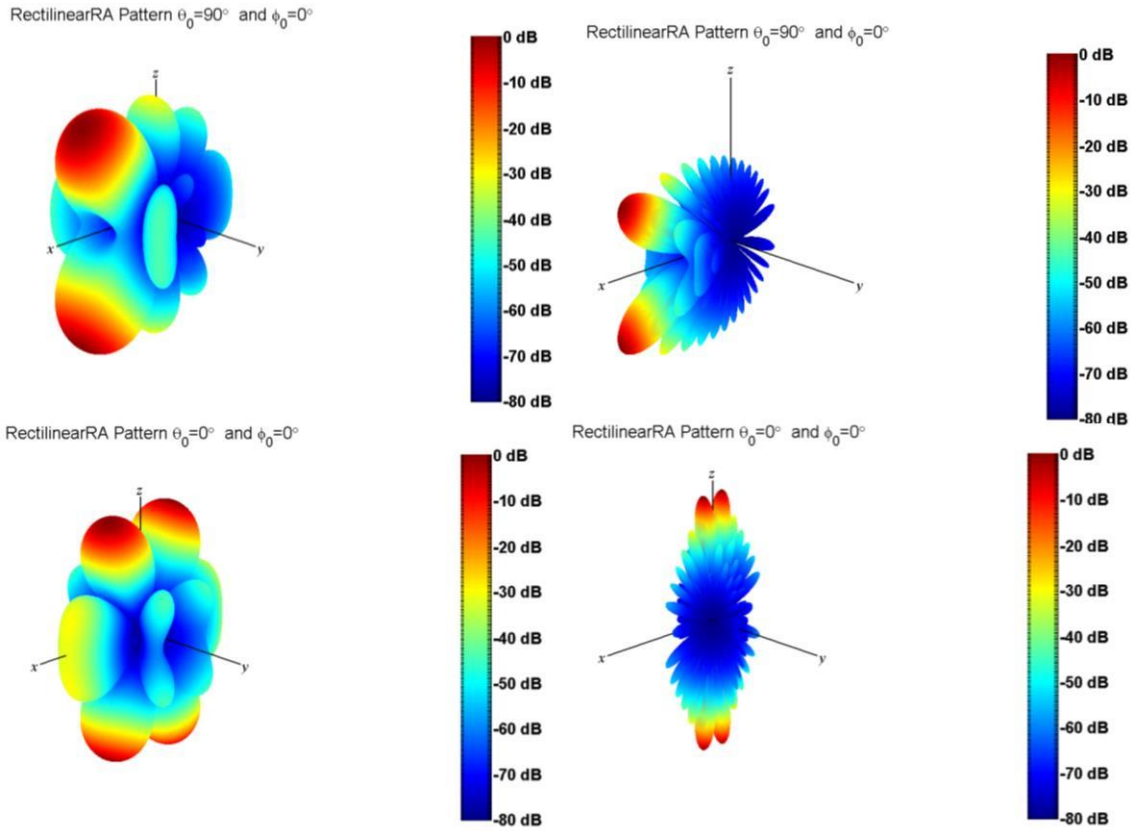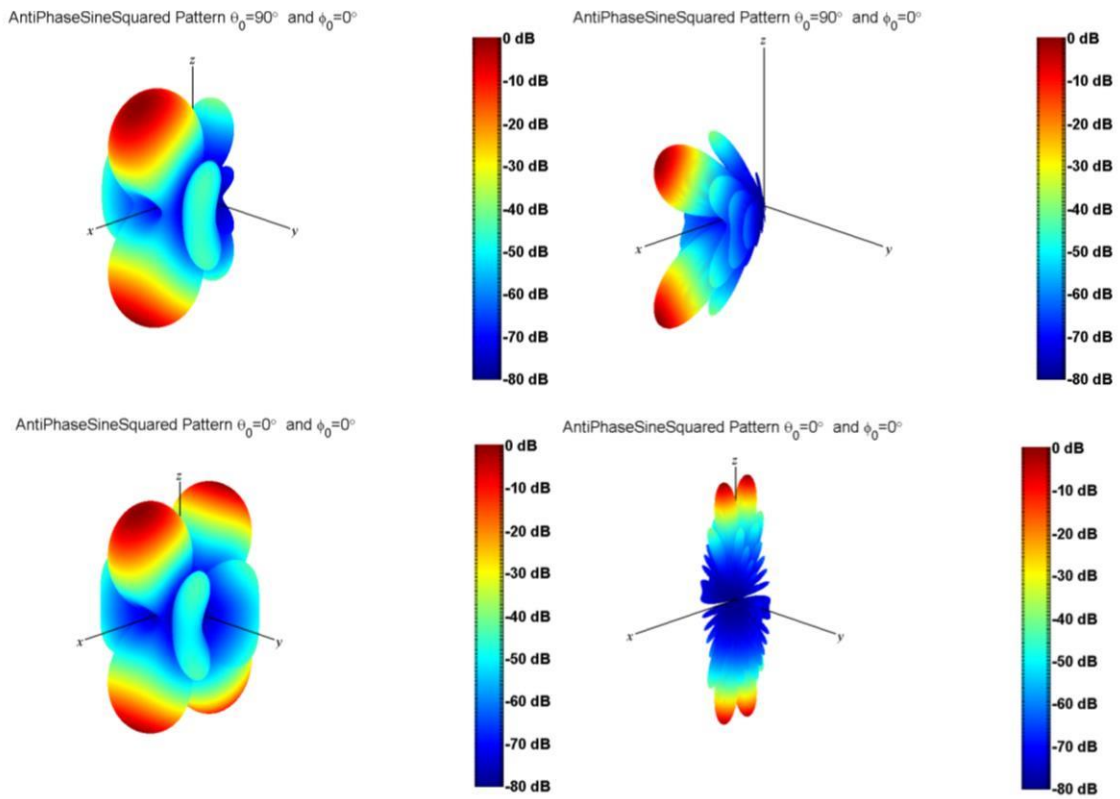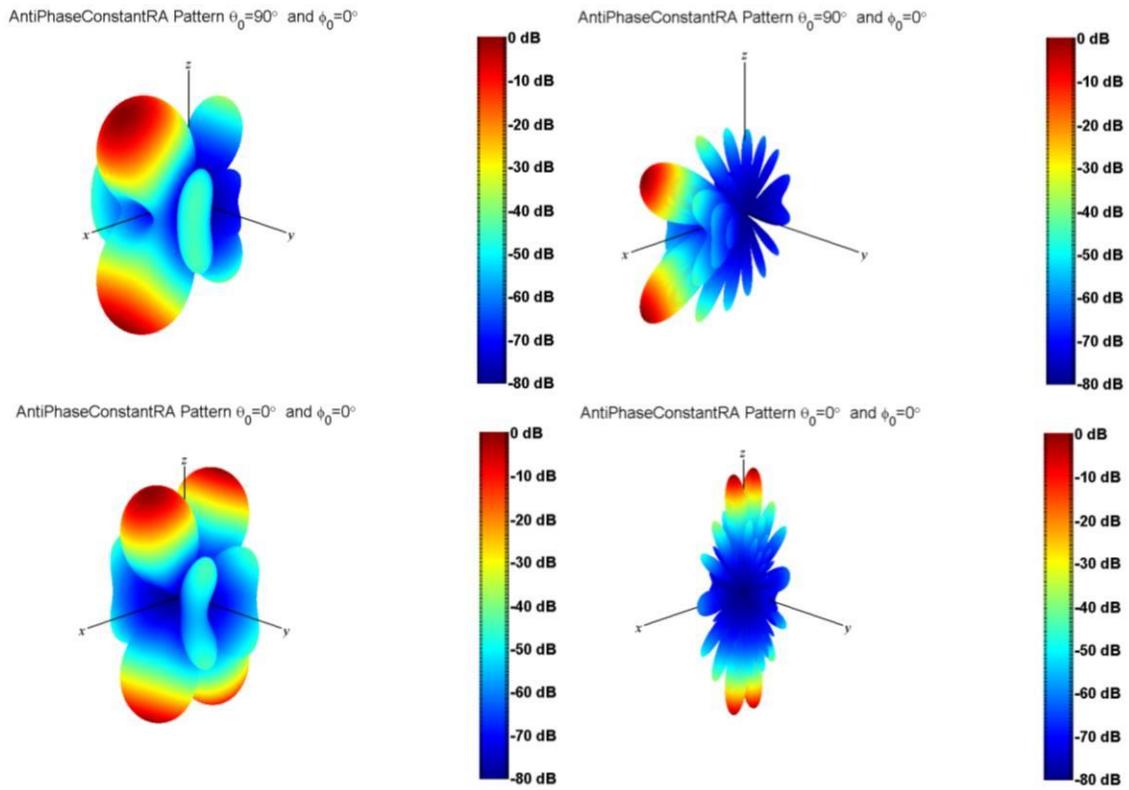
Figure 319. Reciliinear random array $\{(\theta_0 = 90°, \phi_0 = 0°, \tilde{A} = 1)$ top left, $(\theta_0 = 90°, \phi_0 = 0°, \tilde{A} = 3.35)$ top right, $(\theta_0 = 0°, \phi_0 = 0°, \tilde{A} = 1)$ bottom left, $(\theta_0 = 0°, \phi_0 = 0°, \tilde{A} = 3.35)$, bottom right$\}$.
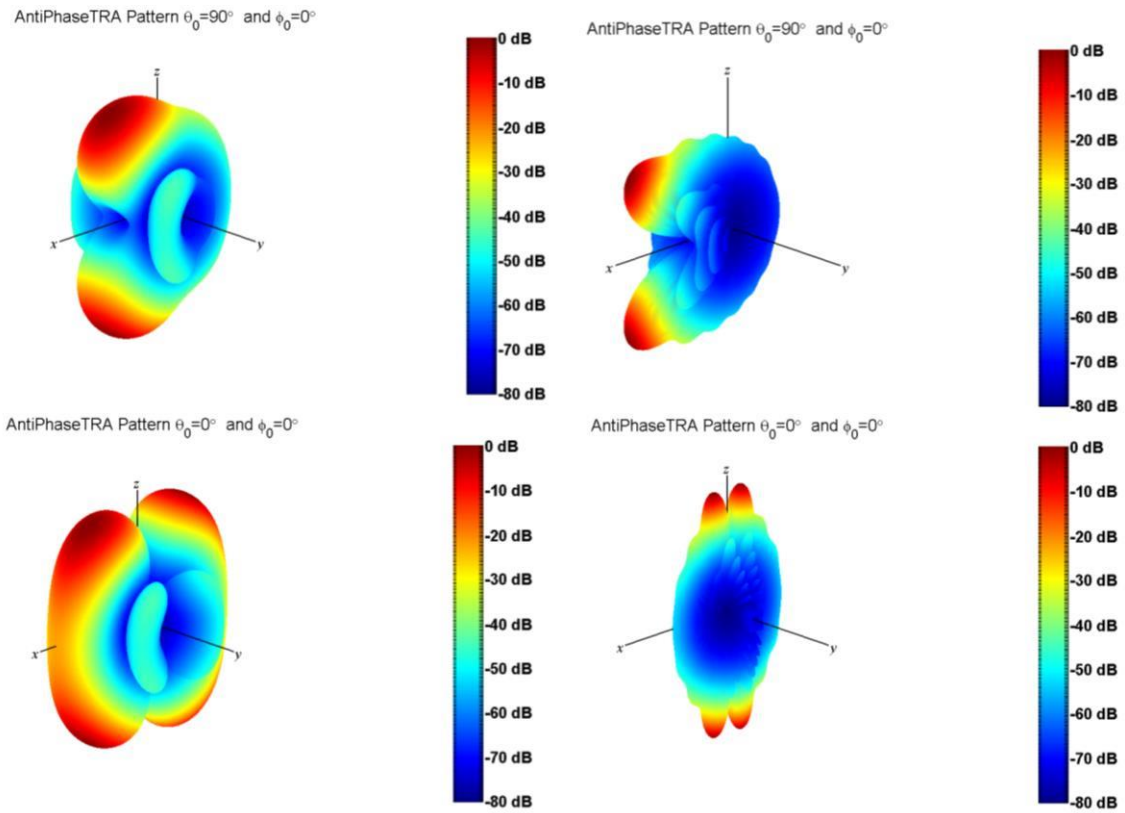
Figure 320. Antiphase triangular random array $\{(\theta_0 = 90°, \ \phi_0 = 0°, \ \tilde{A} = 1)$ top left, $(\theta_0 = 90°, \ \phi_0 = 0°, \ \tilde{A} = 3.35)$ top right, $(\theta_0 = 0°, \ \phi_0 = 0°, \ \tilde{A} = 1)$ bottom left, $(\theta_0 = 0°, \ \phi_0 = 0°, \ \tilde{A} = 3.35)$, bottom right$\}$.

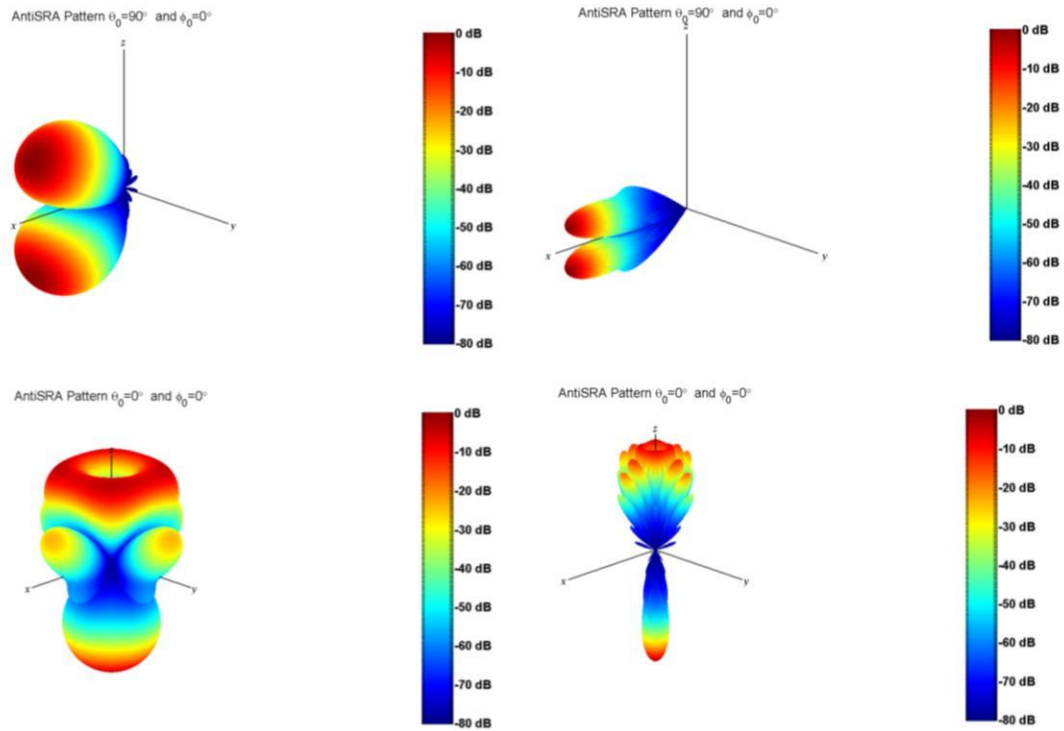Figure 321. Antiphase triangular squared random array $\{(\theta_0 = 90°, \ \phi_0 = 0°, \ \tilde{A} = 1)$ top left, $(\theta_0 = 90°, \ \phi_0 = 0°, \ \tilde{A} = 3.35)$ top right, $(\theta_0 = 0°, \ \phi_0 = 0°, \ \tilde{A} = 1)$ bottom left, $(\theta_0 = 0°, \ \phi_0 = 0°, \ \tilde{A} = 3.35)$, bottom right$\}$.

Figure 322. Sine random array $\{(\theta_0 = 90°, \ \phi_0 = 0°, \ \tilde{A} = 1)$ top left, $(\theta_0 = 90°, \ \phi_0 = 0°, \ \tilde{A} = 3.35)$ top right, $(\theta_0 = 0°, \ \phi_0 = 0°, \ \tilde{A} = 1)$ bottom left, $(\theta_0 = 0°, \ \phi_0 = 0°, \ \tilde{A} = 3.35)$, bottom right$\}$.

Figure 323. Sine-squared random array $\{(\theta_0 = 90°, \ \phi_0 = 0°, \ \tilde{A} = 1)$ top left, $(\theta_0 = 90°, \ \phi_0 = 0°, \ \tilde{A} = 3.35)$ top right, $(\theta_0 = 0°, \ \phi_0 = 0°, \ \tilde{A} = 1)$ bottom left, $(\theta_0 = 0°, \ \phi_0 = 0°, \ \tilde{A} = 3.35)$, bottom right$\}$.

Figure 324. Antiphase constant random array $\{(\theta_0 = 90°, \ \phi_0 = 0°, \ \tilde{A} = 1)$ top left, $(\theta_0 = 90°, \ \phi_0 = 0°, \ \tilde{A} = 3.35)$ top right, $(\theta_0 = 0°, \ \phi_0 = 0°, \ \tilde{A} = 1)$ bottom left, $(\theta_0 = 0°, \ \phi_0 = 0°, \ \tilde{A} = 3.35)$, bottom right$\}$.

Figure 325. Antiphase (z-plane) spherical random array $\{(\theta_0 = 90°, \ \phi_0 = 0°, \ \tilde{A} = 1)$ top left, $(\theta_0 = 90°, \ \phi_0 = 0°, \ \tilde{A} = 3.35)$ top right, $(\theta_0 = 0°, \ \phi_0 = 0°, \ \tilde{A} = 1)$ bottom left, $(\theta_0 = 0°, \ \phi_0 = 0°, \ \tilde{A} = 3.35)$, bottom right$\}$.

As can be seen from Figure 325 the antimodal distribution needs to be placed orthogonal to the beamsteering angle.
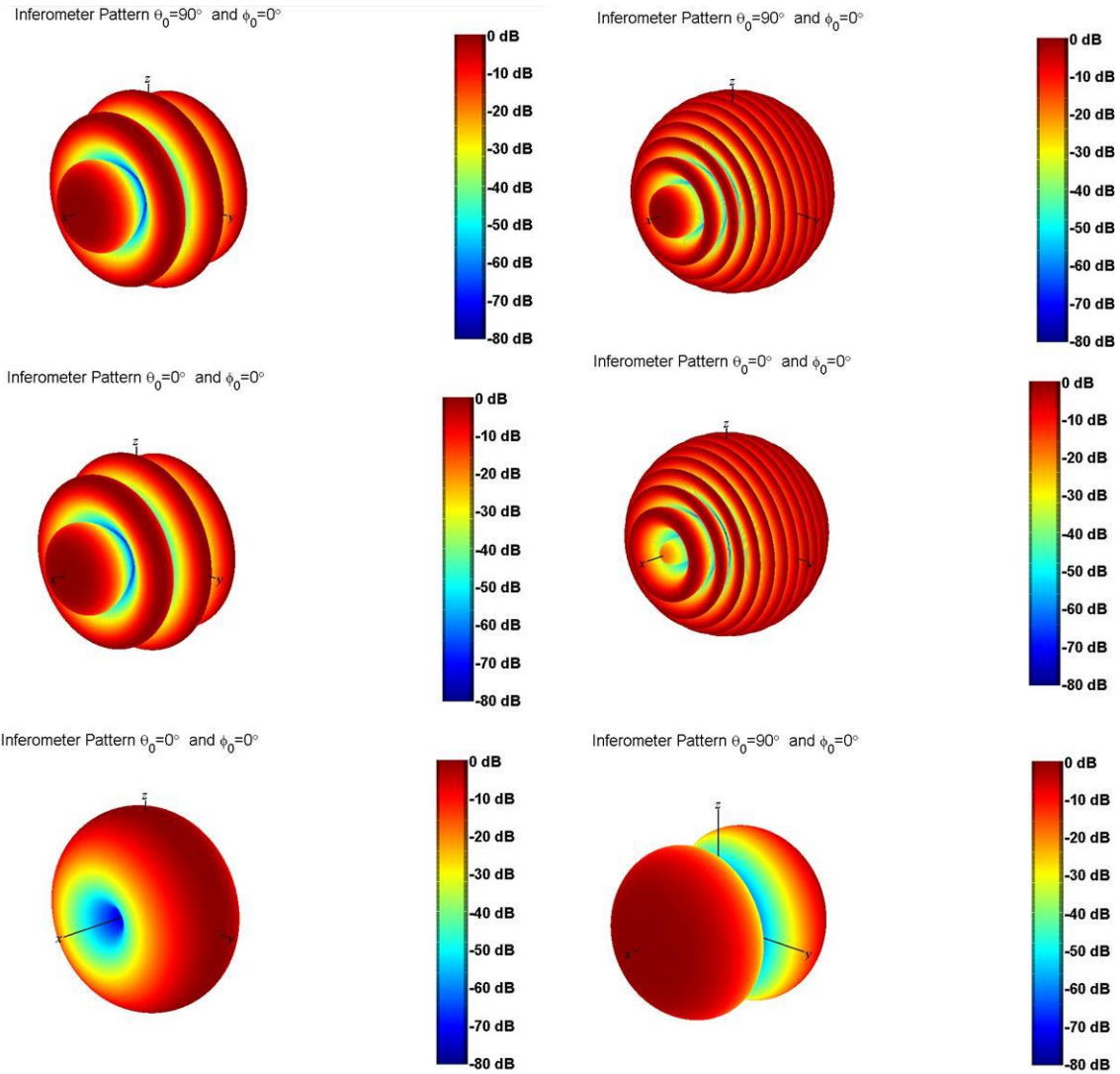
Figure 326. Inferometer random array (periodic linear array of two elements x-axis){ $\left(\theta_0 = 90°, \ \phi_0 = 0°, \ \tilde{A} = 1\right)$ top left, $\left(\theta_0 = 90°, \ \phi_0 = 0°, \ \tilde{A} = 3.35\right)$ top right, $\left(\theta_0 = 0°, \ \phi_0 = 0°, \ \tilde{A} = 1\right)$ middle left, $\left(\theta_0 = 0°, \ \phi_0 = 0°, \ \tilde{A} = 3.35\right)$, mddle right} , $\left(\theta_0 = 0°, \ \phi_0 = 0°, \ \tilde{A} = .25\right)$ (D=.5) bottom left, $\left(\theta_0 = 90°, \ \phi_0 = 0°, \ \tilde{A} = 3.35\right)$, bottom right}.
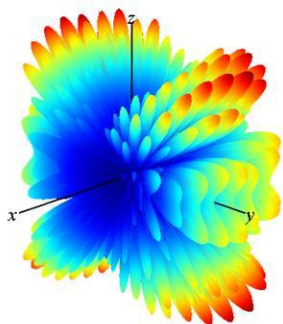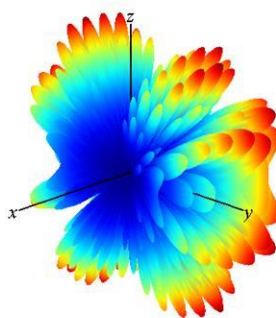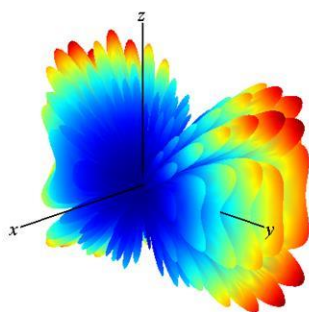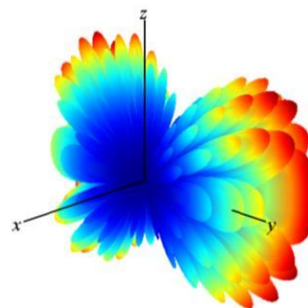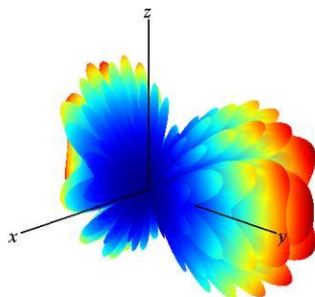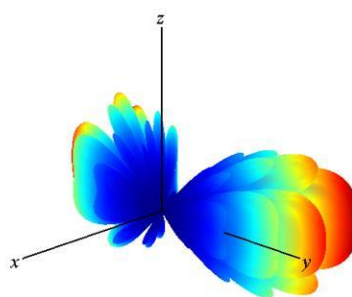
Figure 327. Negative *N*-sphere random array patterns $\tilde{A} = 3.35$.

The patterns in Figure 327 appear to be from scattering. These ricatti Bessel functions are also found in [152] in Chapter 10 with the section regarding the biconical antenna. It is likely the modes of this antenna relate to the modes of the negative *N*-sphere.